Effects of radiation shading by macrophytes on wetland hydrodynamics

Author:
Kay, Karen Louise

Publication Date:
2004

DOI:
https://doi.org/10.26190/unsworks/8847

THE UNIVERSITY OF NEW SOUTH WALES

SCHOOL OF CIVIL AND ENVIRONMENTAL ENGINEERING

Effects of Radiation Shading by Macrophytes on Wetland Hydrodynamics

by

Karen Louise Kay

Supervisor: Dr. Bruce Cathers

A thesis submitted in fulfillment
of the requirements for the degree of
Doctor of Philosophy
University of New South Wales

March 2004

Abstract

Wetlands are open, dynamic systems which are strongly influenced by meteorological forcing. In topographically shaded wetlands with no significant inflow, hydrodynamics may be driven exclusively by convective (buoyancy-induced) flows which are established by differential heating and cooling in the water body. This study considered the effects of differential heating due to radiation shading by emergent and submerged macrophytes on the hydrodynamics of a natural, low flow, freshwater wetland (Hopwoods Lagoon).

The study included characterisation of emergent macrophyte properties and measurement of shortwave radiation attenuation in the canopies of three different macrophyte species at four wetlands in the greater Sydney region. Using this data, it was determined that existing simple models from the agricultural literature could be used to predict attenuation of radiation by emergent macrophyte species.

Time-series meteorological and water temperature data from Hopwoods Lagoon were used to assess diurnal and seasonal trends in the hydrodynamic response to changes in the meteorological forcing. Differential heating between the vegetated littoral zones and open water areas created large horizontal temperature gradients, which suggested convective flows between the two zones. Observations were compared with those reported by other researchers and, while it was found that there were some similarities between different wetlands, it was also concluded that hydrodynamic flow regimes in low flow wetlands are strongly influenced by the characteristics of the endemic macrophyte communities.

An existing three-dimensional, finite element hydrodynamic model was modified as part of this study to accommodate radiation shading by emergent and submerged macrophytes, and calibrated using field data from Hopwoods Lagoon. The field observations were supplemented by hydrodynamic modelling of radiation shading, using various simulated densities of emergent and submerged macrophytes. Model results were generally supportive of the field observations, and indicated that radiation shading by submerged and emergent macrophytes could induce distinctly different convective exchanges with open water zones in the wetland.

The field and model results demonstrated that radiation shading by submerged macrophytes in littoral zones could *enhance* differential heating between vegetated littoral zones and deeper open water areas, while radiation shading by emergent macrophytes in littoral zones *opposed* differential heating due to differences in depth. This distinction has important implications for selection of macrophyte species in low flow wetlands where it is desired to promote convective mixing between vegetated and open water zones.

Acknowledgements

My (adopted!) supervisors, Dr Bruce Cathers and Associate Professor Ron Cox, have provided much encouragement and support, particularly throughout the latter part of this project. Associate Professor David Luketina, formerly of UNSW, helped to get the ball rolling in the first place. Members of the School review committees and others at the Water Research Laboratory also provided valuable input and advice along the way. John Hart and John Baird from WRL assisted in design and preparation of field equipment. Jim Tilley and Alf Wojcik from the School of Civil and Environmental Engineering helped to install and later decommission the automatic weather station.

The field work formed a very significant component of this research, and I was fortunate to have many cheerful helpers on my various wetland adventures. In particular, Natalie Marshall, who introduced me to Hopwoods Lagoon and taught me much about the Macdonald Valley, and Daryl Kay, who spent many weekends *in*, on and around the lagoon. Bronwyn, Lyn and John Maher, Alison and William Di Santo, Matthew Reilly and Nana Kay all accompanied me on field trips and even claimed to enjoy themselves! The use of the Batt's dingy and trailer and Natalie's inflatable kayak were greatly appreciated.

The ace survey team of Tim, Kirsty and Sam Egger, Daryl, Don and Irene Kay and Bronwyn Maher ensured that we completed the survey of Hopwoods Lagoon over a weekend in October 2001. The surveying equipment was generously loaned by the School of Geomatic Engineering at UNSW. Associate Professor Jean Rüeger and Mr Alan Edmunds provided advice and assistance when planning the survey.

Daniel Hickey was involved in the collection of vegetation and radiation data during the early canopy radiation experiments and Mr Van Klaphake assisted with identification of macrophyte species at the Sydney wetlands. The Hopwood family very kindly allowed research to be conducted on their beautiful property at Higher Macdonald, while the Sternbeck family provided a local point of contact. Mr Craig Tucker of Warringah Council and Mr Mark Beharrell of Pittwater Council granted permission to conduct radiation experiments at the Deep Creek wetlands and at Warriewood Wetlands, respectively.

The very patient and generous assistance of Visiting Professor Ian King at the Water Research Laboratory, author of the original RMA models, was invaluable during the hydrodynamic modelling component of the research, and is gratefully acknowledged.

Production of the thesis was a major task in itself, and again I was fortunate to have an army of assistants! My very sincere thanks must go to Daryl Kay, for all his contributions to editing, graphics and typesetting, and to Bronwyn, Lyn and John Maher, Alison Di Santo, Denise and Irene Kay and Matthew Reilly for proof reading parts of the manuscript. My good friend and TeXspert, Dr Moninya Roughan, helped to unravel some of the mysteries of LaTeX. None of this could have been achieved without the incredibly generous loan of computers from Don Kay, who also provided helpful advice regarding the graphics packages. Don Kay and Arthur Waddington also kindly allowed me time away from work to finalise the thesis, however reluctantly!

Finally, but not least, my friends and my families, the Mahers and the Kays, and particularly my husband Daryl, have been a constant source of good humour, encouragement and support throughout the duration of this project. Their patience and understanding, despite periods of neglect, has been truly amazing. I cannot thank you enough.

This research was partly funded by an Australian Postgraduate Award and scholarships from the School of Civil and Environmental Engineering and the Faculty of Engineering at UNSW.

Dedication

For my husband, Daryl,

with profound and humble thanks

– for everything.

Table of Contents

List of Figures

List of Tables

List of Symbols

Symbol	Definition - Roman Alphabet	Units
a	bed elevation	m
a	empirical coefficient used to estimate C_f	–
a_w	empirical coefficient used to estimate $f(u)$	$\mathrm{m\,s^{-1}\,hPa^{-1}}$
$a(z)$	foliage area density function	$\mathrm{m^2\,m^{-3}}$
A	empirical coefficient used to estimate R_S	–
A	aspect ratio, h/L	–
A_p	projected plant area in the direction of flow	$\mathrm{m^2}$
b	water surface elevation	m
b	empirical coefficient used to estimate C_f	–
b_w	empirical coefficient used to estimate $f(u)$	$\mathrm{hPa^{-1}}$
B	bias	–
B	empirical coefficient used to estimate R_S	–
$\mathcal{B}$	Bowen Ratio	–
B_0	surface buoyancy flux	$\mathrm{m^2\,s^{-3}}$
c_1, c_2, c_3	Nilson's coefficients for the simplified G-function	–
$C_0, \ldots, C_6$	thermistor coefficients used to calculate temperature	–
C_f	cloudiness factor	–
c_{pw}	specific heat capacity of water	$\mathrm{J\,kg^{-1}\,{}^{\circ}C^{-1}}$
c_s	volumetric heat capacity of sediments	$\mathrm{J\,m^{-3}\,{}^{\circ}C^{-1}}$
C	Chezy coefficient	$\mathrm{m^{1/2}\,s^{-1}}$
$\overline{C_D}$	bulk drag coefficient for vegetation array	–
C_{Dz}	drag coefficient for momentum, referenced to u_z	–
C_L	transfer coefficient for latent heat (Dalton number)	–
C_P	Class A evaporation pan coefficient	–
CV	coefficient of variation	–
d	characteristic stem dimension	mm
d_0	zero plane displacement height	m

d_h	hydraulic diameter	mm
D	mean spacing between canopy elements	m
D_H	diffusivity of heat	$m^2\,s^{-1}$
DL	daylength	hr
D_x, D_y, D_z	eddy diffusivities in the x, y, z directions	$m^2\,s^{-1}$
D_Y	Julian date = day of year	–
e_a	ambient vapour pressure at T_a	hPa
e_c	ambient vapour pressure in the canopy air space	hPa
e_{sat}	saturation vapour pressure at T_w	hPa
E_{aero}	evaporation rate, aerodynamic method	$m\,s^{-1}$
E_{energy}	evaporation rate, energy balance method	$m\,s^{-1}$
E_{lake}	evaporation rate from an open water body	$m\,s^{-1}$
E_{pan}	evaporation rate from evaporation pan	$m\,s^{-1}$
E_r	evaporation rate	$m\,s^{-1}$
E_{xz}	neutral flow eddy viscosity	$Pa\,s^{-1}$
EOT	equation of time	min
$f(u)$	wind-dependent vapour transport coefficient	$m\,s^{-1}\,hPa^{-1}$
F_{Dx}, F_{Dy}	drag force due to vegetation in the x, y directions	$kg\,m\,s^{-2}$
g	acceleration due to gravity (9.81)	$m\,s^{-2}$
$g_L(z, \theta_L, \varphi_L)$	inclination distribution of foliage area	–
G	heat storage flux term ($\equiv H_{NET}$)	Wm^{-2}
$G(z, \theta_L, \varphi_L)$	G-function, projection of foliage area	–
G_{BED}	bed heat flux	$J\,m^{-2}\,s^{-1}$
G_T	temperature source rate at the water surface	$m^{\circ}C\,s^{-1}$
Gr	Grashof Number	–
Gr'	effective Grashof Number	–
h	water depth	m
$\overline{h}$	mean water depth	m
h_L	canopy height	m
Δh	difference in water depths	m
h_s	depth of thermal influence in the sediments	m
H	thickness of convective flow	m
H_L	latent heat flux	Wm^{-2}
H_{NET}	net surface heat flux	Wm^{-2}
H_S	sensible heat flux	Wm^{-2}
i_{max}	maximum number of sediment layers	–
k	von Kármán constant (0.41)	–
k_s	Smagorinsky coefficient	–

K_1, K_2	conversion factors for units	–
K_h	heat transfer coefficent	$\mathrm{m\,s^{-1}}$
K_H	eddy diffusivity for heat	$\mathrm{m^2\,s^{-1}}$
K_m	mass transfer coefficent	$\mathrm{m\,s^{-1}}$
K_M	eddy diffusivity for momentum	$\mathrm{m^2\,s^{-1}}$
K_s	thermal diffusivity of sediments	$\mathrm{m^2\,s^{-1}}$
K_T	thermal diffusivity	$\mathrm{m^2\,s^{-1}}$
K_V	eddy diffusivity for water vapour	$\mathrm{m^2\,s^{-1}}$
$\mathcal{K}_{LAI}$	shortwave attenuation coefficient relative to *LAI(z)*	–
$\mathcal{K}_z$	shortwave attenuation coefficient relative to z	$\mathrm{m^{-1}}$
L	length of water body, horizontal distance	m
LN	Lake Number	–
$\mathcal{L}$	Monin-Obukhov length	m
L_e	longitude of site	°
L_s	longitude of local standard meridian	°
L_w	latent heat of vaporisation of water	$\mathrm{MJ\,kg^{-1}}$
LAI	leaf (stem) area index	$\mathrm{m^2 m^{-2}}$
$LAI(z)$	downward cumulative leaf area index at height z	$\mathrm{m^2 m^{-2}}$
m	cloud fraction	–
$\dot{m}_v$	mass flux of water vapour	$\mathrm{kg\,m^{-2}s^{-1}}$
M_V	molecular weight of vapour	$\mathrm{kg\,mol^{-1}}$
n	Manning's roughness parameter	$\mathrm{s\,m^{-1/3}}$
n_s	number of stems	–
N	buoyancy frequency	$\mathrm{s^{-1}}$
P	atmospheric pressure, water pressure	hPa, Pa
Pr	Prandtl number	–
q	specific humidity	–
q'	fluctuation in specific humidity	–
r^2	least-squares regression coefficient	–
R	rainfall	mm
R	hydraulic radius	m
R	universal gas constant (8.314×10^{-2})	$\mathrm{hPa\,m^3\,K^{-1}\,mol^{-1}}$
R_C	shortwave reflection coefficient from canopy surface	–
R_L	longwave reflection coefficient from the water surface	–
R_S	shortwave reflection coefficient from the water surface	–
R_T	mean thermistor resistance	Ω
Re	Reynolds number	–
Re_c	critical Reynolds number	–

Re_d	stem Reynolds number	–
RH	relative humidity	%
Ri	Richardson number	–
Ri_b	bulk Richardson number	–
S	slope of energy grade line	$\mathrm{m\,m^{-1}}$
S	variance	–
ΔS	change in storage depth of evaporation pan	mm
S_F	shading factor in an array of cylinders	–
ΔS_{Li}	incremental foliage area within incremental angle $\Delta\Omega_{Li}$	$\mathrm{m^2}$
$\sum_i S_{Li}$	total foliage area within the canopy volume	$\mathrm{m^2}$
S_t	Hutchinson's (1957) stability parameter	–
t	time	s
Δt	timestep	s, hr
Δt_{GMT}	time difference from Greenwich Meridian Time	hr
t_{corr}	correction to equation of time	min
t_{noon}	time of solar noon	hr
t_{solar}	solar time	hr
$t_{sunrise}$	time of sunrise	hr
t_{sunset}	time of sunrise	hr
T	temperature	K, °C
T_0	reference temperature (298 K $\approx$ 25°C)	K, °C
T_a	air temperature	K, °C
T_c	temperature of canopy elements	K, °C
T_{est}	estimated temperature	°C
T_{meas}	measured temperature	°C
T_K	temperature	K
T_s	sediment temperature	°C
T_V	virtual temperature	K
T_w	water temperature	K, °C
u	water velocity in the x direction	$\mathrm{m\,s^{-1}}$
u_*	friction velocity in air at the water surface	$\mathrm{m\,s^{-1}}$
u_{*w}	friction velocity in water column	$\mathrm{m\,s^{-1}}$
u_s	water surface drift velocity	$\mathrm{m\,s^{-1}}$
u_z	wind speed at height z	$\mathrm{m\,s^{-1}}$
U	mean velocity	$\mathrm{m\,s^{-1}}$
v	water velocity in the y direction	$\mathrm{m\,s^{-1}}$
V	resultant velocity	$\mathrm{m\,s^{-1}}$
V_C	volume fraction of mineral components in sediments	%

V_M	volume fraction of water in sediments	%
V_O	volume fraction of organic components in sediments	%
w	water velocity in the z direction	$\mathrm{m\,s^{-1}}$
W	Wedderburn number	–
z	elevation	m
z_0	aerodynamic roughness length for momentum	m
z_{0V}	aerodynamic roughness length for water vapour	m
z_M	measurement height for wind speed	m
z_V	measurement height for relative or specific humidity	m
Δz_i	thickness of sediment layer i	m

Symbol	Definition - Greek Alphabet	Units
α	orientation of boundary / shoreline	$^\circ$
α_T	thermal expansion coefficient for water	$^\circ C^{-1}$
β	solar elevation above horizon ($\beta + \theta = 90^\circ$)	$^\circ$
γ	pyschrometric coefficient	$hPa\,^\circ C^{-1}$
$\Gamma_x, \Gamma_y, \Gamma_z$	external tractions in the x, y, z directions	$Pa\,m^{-1}$
δ	solar declination	$^\circ$
δ	Dirac delta function	–
δ_H	lengthscale for rconductive heating	m
δ_R	vertical lengthscale for radiatiove heating	m
δ_{BL}	depth of the atmospheric boundary layer	m
ϵ	ratio of molecular weights of water vapour to dry air	–
ε	non-neutral eddy viscosity	$Pa\,s^{-1}$
ε'	minimum ε specified in model input	$Pa\,s^{-1}$
ε_{ac}	effective atmospheric emissivity	–
ε_c	emissivity of canopy elements	–
ε_w	emissivity of water body	–
η	underwater attenuation coefficient for shortwave radiation	m^{-1}
η^*	normalised underwater attenuation coefficient, $\eta^* = \eta\,h$	–
θ	solar zenith, from vertical ($\theta + \beta = 90^\circ$)	$^\circ$
θ_L	elevation of canopy foliage, above horizon	$^\circ$
$\overline{\theta_L}$	mean elevation of canopy foliage, above horizon	$^\circ$
θ_{SOURCE}	source / sink term for heat	$^\circ C\,s^{-1}$
θ_w	wind direction	$^\circ$
Θ_{Vz}	potential virtual temperature at elevation z	K
Θ_{Vs}	potential virtual temperature at the water surface	K
μ	viscosity	$Pa\,s^{-1}$
ν	kinematic viscosity	$m^2\,s^{-1}$
ν_s	Smagorinsky kinematic viscosity	$m^2\,s^{-1}$
ρ	water density	$kg\,m^{-3}$
ρ_0	mean water density	$kg\,m^{-3}$
ρ_a	density of dry air	$kg\,m^{-3}$
ρ_m	density of moist air	$kg\,m^{-3}$
σ	Stefan-Boltzmann constant (5.67×10^{-8})	$W\,m^{-2}\,K^{-4}$
τ	surface shear stress	Pa
τ_C	timescale for development of steady convective flows	s

τ_D	timescale for development of steady conductive flows	s
τ_W	timescale for adjustment to surface wind stress	s
$\tau_d(LAI)$	transmission coefficient for diffuse shortwave	–
τ_{PAR}	net transmission coefficient for PAR	–
τ_S	net transmission coefficient for shortwave radiation	–
ϕ	incident shortwave radiation flux	Wm^{-2}
ϕ_0	net shortwave radiation flux at the water surface	Wm^{-2}
ϕ_h	PAR flux at the bed	Wm^{-2}
$\phi_{LAI(z)}$	shortwave radiation flux at elevation z, beneath $LAI(z)$	Wm^{-2}
$\phi_{LW\downarrow}$	atmospheric (downward) longwave radiation flux	Wm^{-2}
$\phi_{LW\downarrow NET}$	net downward longwave radiation flux	Wm^{-2}
$\phi_{LW\uparrow}$	blackbody (upward) longwave radiation flux	Wm^{-2}
ϕ_{LW_C}	longwave radiation flux from canopy elements	Wm^{-2}
$\phi_{PAR(z)}$	PAR flux at elevation z	Wm^{-2}
$\phi_{PAR(h_L)}$	PAR flux above the canopy	Wm^{-2}
ϕ_z	shortwave radiation flux at elevation z	Wm^{-2}
φ	latitude of site	$^\circ$
φ_L	azimuth orientation of canopy elements, from north	$^\circ$
ψ	wind stress coefficient	–
ψ_{veg}	wind stress coefficient in emergent macrophyte zone	–
ω_h	hour angle	$^\circ$
$\Delta\Omega_{Li}$	incremental solid angle, used to calculate $g_L(\theta_L, \varphi_L)$	rad.

List of Abbreviations

AEST	Australian Eastern Standard Time
AHD	Australian Height Datum
AWS	automatic weather station
CMA	Central Mapping Authority of New South Wales
GMT	Greenwich Meridian Time
LAI	leaf area index
NIR	near infra-red (radiation)
PAR	photosynthetically-active radiation
PRT	platinum resistance thermometer
RL	reduced level
RMA-10	finite element model for three-dimensional, density-stratified flow
RMAGEN	finite element generation program used with RMA-10
RMSE	root mean squar error
UNSW	University of New South Wales
WRL	Water Research Laboratory

Chapter 1

INTRODUCTION

1.1 Background and Motivation for the Research

Wetlands are defined most simply as "wet lands", or ecosystems which are transitional between terrestrial and aquatic systems (Cowardin et al., 1979). There are many types of wetlands, both natural and constructed, and they are usually classified according to:

- the environment in which they occur, for example floodplain or estuarine, and
- the purpose for which they were created, for example stormwater treatment, flood mitigation or provision of habitat.

Wetlands may be permanent, temporary or intermittent, and the flow regime of a given wetland is often episodic and therefore highly variable with time (Brady and Riding, 1996).

The term wetland is generally restricted to marsh and swamp environments which support aquatic vegetation such as rushes, reeds and sedges (Wong et al., 1998). This definition implies that aquatic vegetation species (macrophytes) are an intrinsic component of wetlands. Macrophytes may be either emergent, submerged or floating, as shown in Figure 1.1.

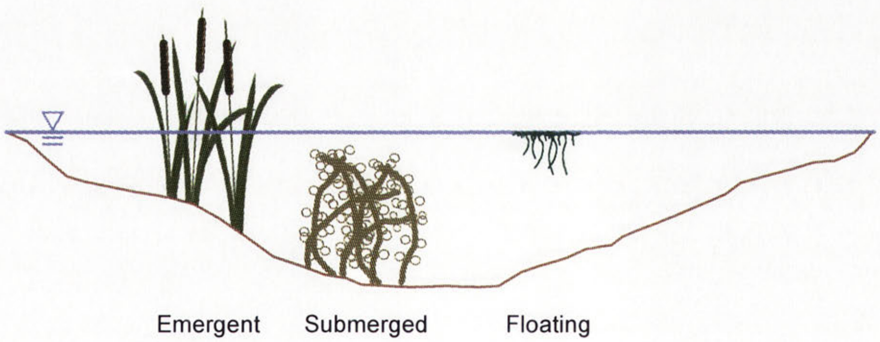

Figure 1.1: Broad classification of macrophytes according to growth form.

Wetlands are the environment's natural water purifiers and nutrient recyclers, which can enhance water quality by a number of physical and bio-chemical processes. Macrophytes are essential to these processes and serve various functions in natural and constructed wetlands. These include (Brix, 1994):

- physical filtration, distribution of flow and reduction of water velocities, which promote sedimentation

- provision of surface area for attachment of biofilms, algae and other microphytes, which absorb or assimilate bioavailable nutrients from the water column
- stabilisation of the wetland substrate and littoral zones, and oxygenation of root zones in the substrate
- insulation against extremes of temperature
- provision of habitat for water fowl and invertebrates.

Constructed wetlands can be used to improve water quality in a catchment through design to specifically emulate and optimise the natural wetland treatment mechanisms, particularly filtration, sedimentation and assimilation of bioavailable nutrients. Exchanges between macrophyte zones and open water areas are central to the effectiveness of wetland treatment processes.

Wetlands are open, dynamic systems and strongly influenced by external, meteorological forcing (Brady and Riding, 1996). In wetlands with no significant inflow, the energy driving hydrodynamic processes is derived primarily from the sun, whether directly by radiative heating, or indirectly, for example via wind-induced mixing. Convective circulations driven by differential heating of the water column are therefore particularly important in low flow wetlands, and between the major flow events in intermittent wetlands. Differential heating occurs in wetlands predominantly due to differences in depth between vegetated and open water zones, and due to attenuation of radiation fluxes by the macrophytes.

However, as will be outlined in Chapter 2, hydrodynamic processes within wetlands are not particularly well understood, despite the growing popularity of constructed wetlands. Wetlands can even become net exporters of pollutants (Mitsch and Gosselink, 1993), and inadequate performance is often attributable to poor hydrodynamic design (Somes et al., 1999). Greater understanding of hydrodynamic processes which promote wetland treatment functions during low flow periods would improve the overall effectiveness of wetlands constructed for water quality treatment (Linforth et al., 1995).

This study investigates the importance and effects of differential heating due to radiation shading by macrophytes, with a view to expanding the current knowledge of convective hydrodynamics in low flow wetlands.

1.2 Scope of the Research

The scope of the study is defined by certain physical constraints, which are outlined below.

- The study is restricted to freshwater wetlands. Buoyancy effects within the wetland can therefore be attributed to temperature differences rather than varying salinity or suspended sediment concentrations.
- The wetland comprises both open water and vegetated zones, which contain emergent and/or submerged macrophytes. Convective (buoyancy-induced) exchanges between the two zones are of primary interest.
- There is no significant, sustained net flow through the wetland. Longitudinal dispersion and hydrodynamic effects associated with concentrated inflow and outflow are therefore negligible.
- The wetland receives only diffuse, discontinuous inflow, such as runoff, and does not receive a concentrated stream of wastewater.
- The wetland is isolated from the local groundwater system and groundwater interaction can be neglected.

This description represents many natural and constructed wetlands under low flow or inter-event conditions. Hence, the physical constraints listed above do not restrict the relevance of the present study, and the findings will be applicable to a wide range of natural and constructed wetlands under low flow or inter-event conditions.

Estuarine wetlands are not considered in this study. However, they have been the subject of numerous investigations, including Roig (1994), Nepf et al. (1997a) and Nepf (1999). Wetlands receiving concentrated wastewater streams, such as sewage or industrial waste are also excluded. Extensive research efforts have also been directed at these applications of constructed wetlands, of which Hammer (1989) provides some examples.

Storm events significantly alter wetland hydrodynamics, often mixing the water column completely and creating a net flow through the system. In such cases, dispersive mixing processes associated with the flow would be expected to prevail over the convective (buoyancy-induced) exchanges which are the focus of this study. The findings of this study would then not apply. However, in most of south-eastern Australia, the duration of storms is generally much shorter than the average inter-event period (Wong and Somes, 1995), so low flow conditions are experienced much of the time. Natural wetlands may not always be isolated from a local aquifer, although constructed wetlands will often be lined with impermeable materials specifically to prevent groundwater contamination (Lawrence and Breen, 1998).

1.3 Research Objectives and Approach

This study investigates the effects of differential heating due to radiation shading by macrophytes on the hydrodynamics of a natural wetland, with a view to expanding the existing knowledge of convective hydrodynamics in constructed wetlands. Differential heating between macrophyte and open water zones in a wetland produces horizontal temperature gradients which drive convective flows between the zones. This occurs because:

- macrophytes are generally restricted to shallow, littoral zones which heat and cool more rapidly than deeper, open water zones
- emergent macrophytes shade the water surface and reduce the net shortwave radiation flux into the vegetated zone, compared with an open water zone
- submerged macrophytes attenuate shortwave radiation more rapidly with depth below the water surface compared with an unvegetated water column.

The specific objectives of this study can be summarised into three questions:

(1.) Can the attenuation of shortwave radiation by an emergent macrophyte canopy be described by simple models available in the agricultural literature, which are not known to have been previously applied to wetland macrophytes?

(2.) How does a natural wetland respond to diurnal and seasonal changes in the local meteorological forcing, and are responses consistent between different wetlands?

(3.) What are the effects of radiation shading by emergent and submerged macrophytes on convective hydrodynamics in wetlands? Are they different for the different types of macrophytes? How effective are macrophytes in promoting flows between wetland zones?

Several different techniques have been employed to address these questions, as outlined below.

(1.) **Canopy Attenuation of Shortwave Radiation**

Shortwave radiation fluxes and emergent macrophyte parameters were measured in the canopies of three common species at four different wetlands in and around Sydney, Australia. These spanned a broad range of canopy densities, from approximately $35 - 6120\,\text{stems}\,\text{m}^{-2}$ or leaf area index (LAI) of approximately $0.5 - 8.9\,\text{m}^2\text{m}^{-2}$. The field data were used to test the applicability of simple canopy attenuation models available in the literature to attenuation of shortwave radiation by emergent macrophyte species.

(2.) **Hydrodynamic Response to Meteorological Forcing**

Meteorological conditions and water temperatures were measured over an annual cycle in a natural wetland, Hopwoods Lagoon. The field data were used to estimate the magnitude and direction of horizontal convective flows between open water and macrophyte zones, and to assess zonal, diurnal and seasonal trends in the response of the wetland to the meteorological forcing. Observations at Hopwoods Lagoon were compared with those reported by researchers working in other wetlands.

(3.) **Effects of Radiation Shading by Macrophytes**

Field observations of radiation shading by emergent and submerged macrophytes were supplemented by hydrodynamic modelling. The existing three-dimensional, finite-element hydrodynamic model, RMA-10 (King, 1993) was modified to account for the influences of macrophytes on the input and distribution of heat in a shallow wetland. A model with these capabilities is not known to be readily available elsewhere. The model was calibrated using field data from Hopwoods Lagoon and simulations were undertaken to investigate the effects of varying densities of emergent and submerged macrophytes on the induced convective flows.

This study was designed to expand the existing knowledge of convective flows due to radiation shading by macrophytes in wetlands. It is anticipated that the findings could be applied specifically to improving the design of constructed wetlands with similar dimensions during low flow or inter-event periods, to promote passive mixing between macrophyte and open water zones and therefore to optimise water quality improvement. However, the results could potentially assist in the management of any partly-vegetated freshwater body with only low through-flow.

1.4 Organisation of the Thesis

Following this Introduction chapter, the thesis comprises seven further chapters which are organised as shown below.

Chapter 2 Background and Literature Review

This chapter introduces the relevant literature concerning hydrodynamic behaviour in large lakes and reservoirs, and the influences of macrophytes on similar hydrodynamic processes in wetlands.

Chapter 3 Theoretical Considerations

This chapter provides the theoretical background required to investigate the hydrodynamic response of a wetland to changes in the meteorological forcing. The relevant flow equations and important dimensionless numbers are introduced and parameterisation of the important surface energy fluxes is described for open water and emergent macrophyte zones. Scaling analyses are presented which can be used to estimate convective and advective velocities in open water and emergent macrophyte zones.

Chapter 4 Field Site Descriptions

The four field sites used in this study are introduced, and the macrophyte communities are described. The field sites were located within the Sydney metropolitan area and at Hopwoods Lagoon in the Macdonald Valley, 75 km north of Sydney.

Chapter 5 Experimental Methodology

The equipment and methodology for the experimental programmes are described in this chapter. These comprise emergent macrophyte surveys, canopy radiation experiments, underwater attenuation experiments, field hydrodynamic investigations and numerical modelling of wetland hydrodynamics.

Chapter 6 Experimental Results

The experimental results are presented and analysed in this chapter. The results of the emergent macrophyte surveys and the canopy attenuation experiments are used to test the applicability of simple models available in the agricultural literature. The results of the underwater attenuation experiments are used to estimate underwater attenuation coefficients for open water and macrophyte zones. The seasonal variation in meteorological conditions and water temperatures at Hopwoods Lagoon, and diurnal and seasonal trends in observed hydrodynamic behaviour are discussed. Field observations of radiation shading by submerged and emergent macrophytes are presented, and these are supplemented by the results of numerical modelling experiments using simulated densities of submerged and emergent macrophytes.

Chapter 7 Effects of Radiation Shading by Macrophytes

This chapter provides a summary and synthesis of the field and model observations of radiation shading by macrophytes and the effects on wetland hydrodynamics. Reference is made to findings presented in previous studies. In particular, the generality of a wetland flow classification scheme proposed by Waters (1998) is assessed, and implications for wetland design and management are considered.

Chapter 8 Conclusions

This chapter presents the conclusions of this investigation and highlights the significance of the major findings. Recommendations are also made for future research.

Appendices

The Appendices contain supplementary material, including details of supporting calculations, instrument specifications, summaries of the time-series field data, a description of the hydrodynamic model and additional field and model simulation results.

Chapter 2

BACKGROUND AND LITERATURE REVIEW

2.1 Introduction

The effects of radiation shading by macrophytes on hydrodynamic processes in wetlands is a relatively recent area of research which spans such diverse fields as crop micrometeorology and fluid dynamics. The presence of emergent macrophytes above the water surface in a wetland restricts the amount of shortwave radiation which is able to penetrate the surface, thereby reducing the net surface energy flux available to drive wetland flows. Additionally, the presence of macrophyte components beneath the water surface influences the vertical distribution of radiant energy which enters the water body and provides resistance against wetland flows. This has implications for biological and chemical processes occurring in the wetland, including the distribution of biota and the fate of pollutants.

There is an extensive body of literature concerned with the hydrodynamics of lakes and reservoirs, which are typically large, deep bodies of water. Important processes influencing the distribution of heat and constituents include thermal stratification, buoyancy-induced (convective) mixing processes and wind-induced (advective) mixing processes.

A more limited number of studies have addressed hydrodynamic processes in wetlands, which are typically smaller and shallower, and where flow regimes are often heavily influenced by macrophytes. These have generally focused on the altered surface energy fluxes due to macrophytes rather than the hydrodynamic implications, and include studies of radiation shading and wind sheltering by macrophytes. Flow resistance due to vegetation has more commonly been studied in terrestrial canopies, such as crops or forests, vegetated channels or tidal and marine canopies, and there are few studies relating directly to low flow freshwater wetlands.

This study investigates the effects of radiation shading on the hydrodynamic processes in wetlands. The following chapter provides a review of the current understanding of hydrodynamic processes in lakes and reservoirs and the influences of macrophytes on similar processes in wetlands. Mathematical description of the flow field, parameterisation of the surface energy fluxes and scaling of the resulting convective and advective flows is addressed in Chapter 3.

2.2 Hydrodynamic Processes in Lakes and Reservoirs

Hydrodynamic processes control the distribution of heat and other constituents within a water body, and can therefore strongly influence the distribution of nutrients, biota and oxygen, and the fate of pollutants within a system. A substantial effort has been expended researching the response of lakes and reservoirs to changes in meteorological forcing, and the resulting temperature gradients and circulation regimes. This knowledge has been exploited as a useful starting point by researchers interested in wetland hydrodynamics.

Most lakes become vertically stratified for at least part of the annual cycle, due to heating by shortwave radiation which penetrates into the water column. Because the shortwave radiation flux is attenuated with depth, the resulting vertical temperature and density gradient stabilises the water body and restricts vertical mixing. Various buoyancy-induced and mechanical mixing processes work to erode the stability of the stratification and redistribute heat within the water body. However, a spatially-variable, vertical stratification profile can also create lateral stratification and induce horizontal, buoyancy-induced exchanges (Imberger and Patterson, 1990). Inertia in the flow response to changes in the meteorological forcing means that the flow is generally not in phase with the diurnal heating cycle (Monismith et al., 1990), and this unsteadiness has important implications for the resulting flow regimes.

The following sections provide an overview of the development of thermal stratification in lakes and reservoirs, and measures of the stability of the stratification. Convective (buoyancy-induced) and advective (wind-induced) mixing processes which act to destabilise vertical stratification are also discussed, including differential heating and cooling, penetrative convection, upwelling and differential deepening. This brief review serves as a necessary preview to a discussion of the effects of macrophytes on the hydrodynamics of wetland systems, which is included in Section 2.3.

2.2.1 Thermal Stratification

Stratification occurs in a water body due to density gradients, and may be either vertical or horizontal, although the term usually applies to vertical layering. Stratification may be caused by differences in temperature, salinity or the concentration of suspended sediments.

Density stratification due to temperature variation is the most common in freshwater ecosystems, and the only type of stratification considered in the present study (Section 1.2).

A vertically-stratified water column in which the density increases with depth is inherently stable because the centre of mass is situated beneath the centre of buoyancy (Sturman and Ivey, 1998). Stratification develops in response to heating by shortwave radiation and can be eroded by wind- and buoyancy-induced mixing processes.

A vertically-stratified water column is conventionally described in terms of three layers (Wetzel, 1983).

- The **epilimnion** is an upper layer of warm, buoyant, well-mixed and comparatively turbulent water.
- The **metalimnion** is a transitional layer between the epilimnion and hypolimnion, within which the **thermocline** coincides with the maximum rate of change of temperature with depth.
- The **hypolimnion** is a lower layer of cool, dense, essentially quiescent water underlying the metalimnion.

Imberger (1985) demonstrated that the epilimnion is not always well mixed and neither is it in a state of constant or uniform turbulence. Instead, he defined a **diurnal surface layer** as the depth of water which responds directly to the momentum and turbulence introduced by the surface wind stress and to the surface thermal fluxes. This surface layer is delimited at the lower boundary by the **parent thermocline**, which is defined as the thermocline produced by the most significant mixing event in the recent past.

A typical temperature profile from a thermally stratified lake is shown in Figure 2.1, although the layering may be less distinct in a shallow water body. The depth required for a water body to stratify is dependent on a number of factors, including the surface area, depth-volume relationships, exposure to prevailing meteorological conditions and the geographic and topographic location (Wetzel, 1983). Recently, Wells and Sherman (2001) argued that significant stratification could only occur when a lake or reservoir included shallow areas which accounted for more than 50% of the total surface area, where the ratio of the mean depth of shallow areas to the mean depth of deeper areas <0.5.

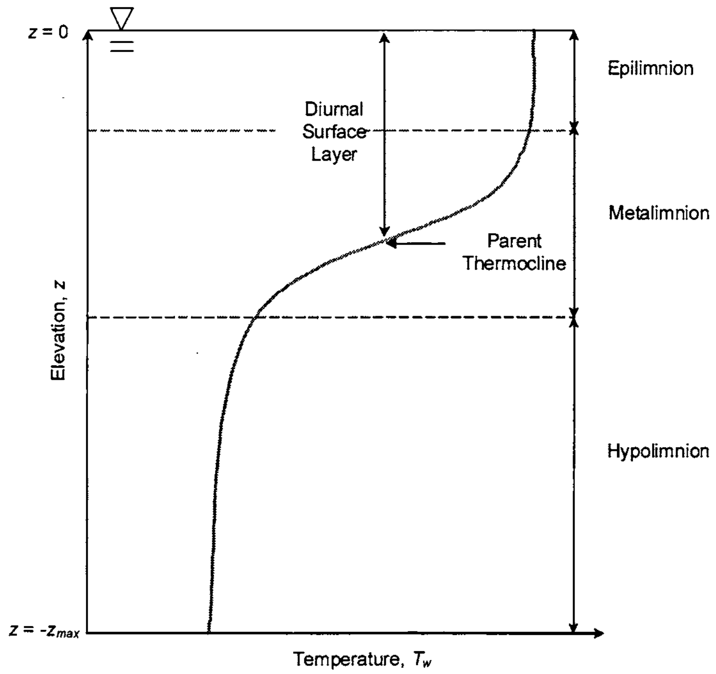

Figure 2.1: Typical thermal profile in a stratified lake or reservoir in summer.

2.2.1.1 Stability of Vertical Stratification

The stability of vertical stratification is defined as the resistance of the water column to turbulent mixing and destratification (Wetzel, 1983). The stability or intensity of the stratification can be quantified by the **buoyancy frequency** N (s^{-1}), which is calculated as follows (Turner, 1973):

$$N^2 = -\frac{g}{\rho}\frac{\partial \rho}{\partial z} \tag{2.1}$$

where z = depth over which the shortwave radiation is absorbed (m)
= positive when measured up from the water surface
$-\partial\rho/\partial z$ = density gradient ($\mathrm{kg\,m^{-4}}$).

The gradient **Richardson number** is more commonly used to quantify the stability of the thermal stratification (Turner, 1973):

$$Ri = N^2 \Big/ \left(\frac{\partial u}{\partial z}\right)^2 = -\frac{g}{\rho}\frac{\partial \rho}{\partial z} \Big/ \left(\frac{\partial u}{\partial z}\right)^2 \tag{2.2}$$

where the first term represents the stability of the stratification and the second term represents the velocity shear. The water column is sufficiently stable to suppress turbulent shear mixing when $Ri > 0.4$, and unstable when $Ri < 0.25$ (Turner, 1973).

Other stability criteria have also been proposed for use in lakes and reservoirs, but these are not directly applicable to the present study.

- Hutchinson (1957) defined a stability parameter S_t which was a function of the local elevation, the elevation of the lake's centre of volume, the area and water density. However, this parameter accounts only for the stabilising influence of stratification and does not consider destabilising influences such as wind-induced mixing and through-flow.
- The dimensionless Wedderburn number W is often employed as a bulk indicator of the stability of a stratified lake or reservoir and the deepening regime of the diurnal mixed layer. This number represents the ratio of baroclinic pressure forces to surface wind-induced forces, per unit width of lake (Imberger, 1985). It is based on a simple, two-layer representation of a stratified lake and is a steady-state parameter.
- The Lake Number L_N (Imberger and Patterson, 1990) is calculated at the point where upwelling commences (that is, where the metalimnion intersects the water surface) and relates the strength of vertical stratification to the forces induced by surface wind stresses. It is also a steady state parameter.

Unfortunately, the meteorological forcing rarely lasts sufficiently long to produce a steady flow, so the application of W and L_N is somewhat limited (Stevens and Imberger, 1996), especially in smaller water bodies.

2.2.1.2 Classification Schemes Based on Thermal Structure

There are several classification schemes for lakes and reservoirs based on thermal structure and seasonal patterns in the stratification and mixing cycles. The most widely used is that of Hutchinson (1957), which was developed from earlier schemes proposed by Forel and Whipple (Wetzel, 1983). Hutchinson's classification scheme is based on the frequency of circulation in a water body, assuming that the water is deep enough to form a hypolimnion. In order of increased frequency of mixing, stratified lakes may be classified as indicated below (Wetzel, 1983).

- **Amictic** lakes occur in high altitude, high latitude locations and never mix, because they are perennially covered with ice and thus essentially isolated from the environment.

- **Oligomictic** lakes occur in tropical climates and mix rarely, at irregular intervals.
- **Monomictic** lakes occur as either:
  - ***cold monomictic*** lakes in high altitude climates, which mix only once a year during summer, or
  - ***warm monomictic*** lakes in warm temperate climates, which stratify during summer and mix only once a year during winter.
- **Dimictic** lakes occur in cool temperate climates and mix freely twice a year, during spring and autumn. They display stable stratification during summer and inverse stratification beneath an ice cover during winter.
- **Polymictic** lakes mix frequently and occur as either:
  - ***cold polymictic*** lakes in equatorial regions where there is little seasonal variation in air temperatures, or
  - ***warm monomictic*** lakes in warm temperate or tropical climates.

This classification scheme applies to ***holomictic*** lakes which mix over the full depth, while lakes which mix over only the upper part of the water column are defined as ***meromictic*** (Hutchinson, 1957). Additional classification schemes are available for meromictic conditions, although shallow lakes or wetlands are unlikely to be classified as meromictic, and these are not considered further. A modified thermal classification scheme proposed by Waters (1998) for wetlands is reviewed in Section 2.3.4.

2.2.2 Buoyancy-Induced (Convective) Mixing Processes in Open Water

Buoyancy-induced mixing processes arise from density or temperature gradients in a water body, which may be either horizontal or vertical.

- Horizontal temperature and density gradients develop in response to differential heating or cooling between adjacent areas, which can produce unsteady, three-dimensional convective flows. Horizontal convective flows have been observed with velocities up to $5\,\mathrm{cm\,s^{-1}}$ (Monismith et al., 1990), which can transport water from littoral zones to the pelagic zones of small lakes within hours and greatly enhance overall horizontal transport (Imberger and Patterson, 1990).

- Vertical density gradients develop in response to heat fluxes at the surface and/or bed. If stable (with the density increasing with increasing depth), such gradients can suppress or completely prevent vertical mixing, while unstable density gradients cause substantial vertical mixing.

2.2.2.1 Differential Heating and Cooling in Lakes and Reservoirs

Differential heating and cooling may occur in lakes or reservoirs via a number of processes. This may result, for example, from (Monismith et al., 1990; Imberger and Patterson, 1990):

(1.) a uniformly distributed surface heat flux incident on a body of water of variable depth, which allows more rapid heating and cooling in shallow areas than in the deeper regions, or

(2.) differences in the depth of penetration of shortwave radiation into the water column or differences in the absorption of shortwave radiation within the water column due to variation in turbidity, or

(3.) variable exposure to a surface wind stress, which reduces latent and sensible heat fluxes in sheltered areas compared with exposed regions.

The **heating phase** is defined as that part of the diurnal meteorological cycle when the net surface heat flux is positive, which leads to warming of the diurnal surface layer. The **cooling phase** occurs when the net surface heat flux is negative, which causes cooling of the surface layer.

Differential heating and cooling are shown schematically in Figure 2.2. Surface flows induced by **differential heating** during the diurnal **heating phase** are typically (Monismith et al., 1990; Sturman et al., 1996):

- directed from the warmer littoral zones towards the cooler pelagic regions
- shallow, stable and across the top of a strongly stratified water column.

In contrast, surface flows induced by **differential cooling** during the **cooling phase** are typically (Monismith et al., 1990; Farrow and Patterson, 1993):

- opposite in direction to the heating phase flows, and directed from the pelagic regions towards the littoral zones

- driven by a cool bed current from the littoral zones into the deeper, pelagic water
- unstable and turbulent, and often also mixed vertically by penetrative convection (Section 2.2.2.2, page 20)
- relatively deep compared with the stable, laminar flows induced by differential heating.

Because the surface currents are deeper, discharges due to a destabilising, cooling forcing generally exceed those due to a stabilising, heating forcing (Sturman and Ivey, 1998). Calm conditions are required for the development of appreciable horizontal temperature gradients and induced convective currents, and strong advective mixing may impede or prevent development of the convective circulation (Horsch and Stefan, 1988). The shallower heating phase flows are also more susceptible to wind effects than the deeper horizontal flows associated with differential cooling (Monismith et al., 1990). Convective currents are therefore more likely to form near sheltered shores in smaller lakes.

Despite these differences, there are also some similarities between the flows induced by differential heating and cooling. They are both characterised by low aspect ratio, defined as the depth to length of the surface flow (Sturman et al., 1996) and are likely to be

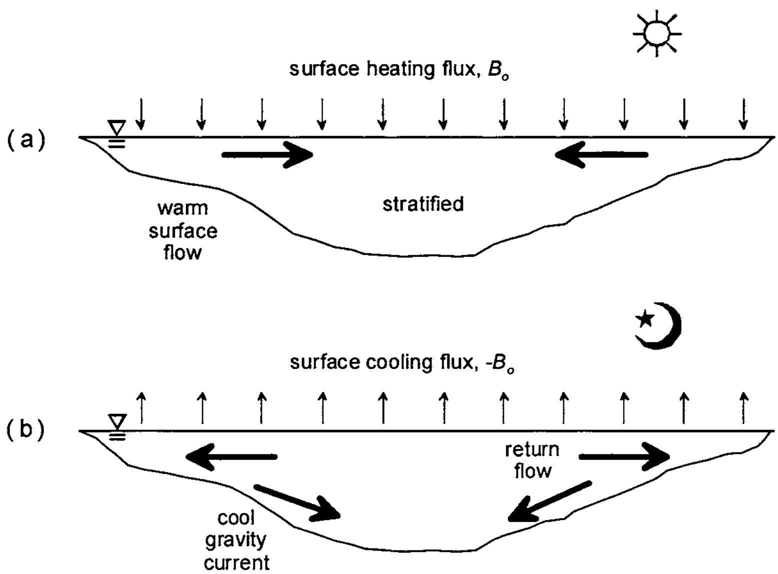

Figure 2.2: Typical convective flows in a lake or reservoir induced by (a) differential heating and (b) differential cooling.

unsteady. This is because the direction and magnitude of the meteorological forcing is variable over the diurnal, seasonal and annual cycles, while the times required to establish steady state flows under either stabilising or destabilising buoyancy regimes are of the same order of magnitude as the diurnal forcing (discussed further in Section 3.8.1.1). In the field, convective flows have been observed to lag the meteorological forcing by several hours (Monismith et al., 1990; Imberger and Patterson, 1990) and it was concluded by the former that the flow in reservoir sidearms is strongly dominated by inertia. The induced convective flows generally persist until a sufficiently strong baroclinic gradient is established to arrest the flow (Monismith et al., 1990), either when the flux weakens or changes direction.

Differential Heating and Cooling due to Depth Variation

This process is important in lakes and reservoirs and has received considerable attention in a range of field, laboratory and numerical experiments.

In numerical and laboratory experiments in a triangular cavity subjected to a uniform surface cooling flux over a region of increasing depth, Horsch and Stefan (1988) observed greater net cooling at the shallow end. The resulting convectively unstable surface layer interacted substantially with the stable underlying water and formed a cold undercurrent flowing down the slope and a return flow along the surface. The horizontal extent of the convective current was found to be limited by the duration of the cooling period. James and Barko (1991) observed similar convective exchanges between vegetated littoral zones and pelagic zones in a reservoir in Wisconsin, USA during overnight cooling on warm, calm evenings when wind-induced circulation could be discounted.

In later numerical experiments conducted in a triangular cavity representing a reservoir sidearm, Farrow and Patterson (1993) observed the temperature response in the water to lag the reversal in surface forcing between uniform heating and cooling by approximately one quarter of a period. Consistent with the expectations of Monismith et al. (1990), they suggested that the temperature gradient in a typical sidearm would not reverse direction until $\sim 6\,\mathrm{hr}$ after a change in the sign of the net heat flux. In field and laboratory experiments, Wells and Sherman (2001) observed gravity currents generated in shallow regions of a reservoir by prolonged surface cooling, and suggested that these currents could begin to stratify the deep region. However, this occured only when the ratio of the surface areas of deep and shallow zones was less than one, and the mean depth of the shallow areas was less than half the mean depth of the deep regions.

Sturman and Ivey (1998) also investigated the effects of unsteadiness in the buoyancy forcing on the resulting circulation processes in a rectangular cavity. Inertia was found to be important when the surface buoyancy flux was switched from destabilising to stabilising. A weak residual flow from the destabilising forcing persisted after the change in forcing, and this influenced the approach to steady state flow under the stabilising buoyancy flux. When the cavity was modified to incorporate a shallow shelf connected to the main cavity by a slope, a laminar surface flow was initiated in the shallow area in response to a uniform surface heating flux. A return flow developed underneath, but unlike the surface cooling experiments of Horsch and Stefan (1988), there was no net flow down the slope.

Collectively, the laboratory and numerical experiments demonstrated the importance of horizontal convective flows induced by a uniform surface heating or cooling flux applied across an area of variable depth. Despite the limitations imposed by the physical constraints of the cavities and the associated boundary conditions, convective flows with similar features have also been observed in lakes and reservoirs. It is expected that similar processes might apply in wetlands.

Differential Heating and Cooling due to Variable Absorption of Shortwave Radiation

This process can cause large temperature differences between areas with differential absorption of shortwave radiation.

Patterson (1984) investigated transient natural convection in a rectangular cavity with a low aspect ratio. The flow was driven by internal buoyancy sources and sinks, which could represent horizontal variation in attenuation of shortwave radiation. Using scaling analysis, he demonstrated that several transitional flow regimes could be generated by the horizontal temperature gradients, leading ultimately to a purely conductive, transitional or convective steady state flow. The model of Patterson (1984) applied to a rectangular cavity subject to temporally-invariant internal heat sources (or sinks) which permitted evolution of steady state flow. As discussed previously, this is unlikely to occur in a field situation where the meteorological forcing varies over a diurnal cycle. However, features of the flow response described by Patterson (1984) have been observed in the field due to differential absorption of radiation.

Imberger and Patterson (1990) reported on the formation of a lens of warm water in a turbid region of the Canning Reservoir in Western Australia. This warm lens was underlain by water considerably cooler than at a similar depth at nearby, less turbid sites. The temperature gradients were observed to drive a buoyant surface flow as the warm lens spread out, and an intrusive flow at mid-depth, which the authors termed a "thermal siphon". Similar processes are expected to be important due to increased radiation absorption by macrophytes in wetlands, as discussed in Section 2.3.1, and of primary interest to the present study.

Differential Heating and Cooling due to Variation in Surface Wind Stresses

Differential wind exposure leads to differences in the latent and sensible heat fluxes, which influence the net surface heat flux. However, unless the reservoir is very large and/or the sheltered areas significantly more protected than the main impoundment, differences in the latent and sensible heat fluxes due to differential wind exposure are unlikely to be as important as differential heating due to variation in depth or absorption of shortwave radiation.

2.2.2.2 Penetrative Convection

Penetrative convection is a vertical mixing process which occurs in response to a negative or cooling buoyancy flux at the water surface. Surface cooling has two main effects (Imberger, 1985; Imberger and Patterson, 1990):

(1) thermals induced by penetrative convection descend from the surface and erode an existing stable thermal structure beneath the surface layer

(2) this cooling reduces the density difference between the surface layer and the underlying water, which decreases the stability of the water column and increases its susceptibility to future wind-induced mixing.

The thermals induced by penetrative convection are discrete parcels of fluid with characteristic dimension much smaller than the water depth. Descending thermals entrain fluid immediately surrounding them, to satisfy continuity, and leave behind a wake of entrained fluid, while remaining otherwise distinct from the surrounding flow (Turner, 1973). In contrast, wind-induced turbulent eddies possess characteristic dimensions ranging from the depth of the water column down to the Kolmogorov scale, at which the turbulent kinetic energy is dissipated as heat (Tennekes and Lumley, 1972). The rate of entrainment due to penetrative convection is therefore considerably less than mixing due to wind-induced shear production (discussed in Section 2.2.3).

Horsch and Stefan (1988) suggested that the thermals could be thought of as a mechanism to uniformly distribute a surface heat loss over the depth of the water column. Where the water depth varies because of a sloping bed, a similar amount of heat is extracted from areas of different depth, which creates horizontal temperature differences. These can generate horizontal convective flows, as described on page 18.

Pure penetrative convection was documented by Imberger (1985) in Wellington Reservoir on a summer evening when the air was completely still and the air temperature was 12°C cooler than the water surface. A distinctly unstable layer formed beneath the water surface, generated by falling thermals. The net vertical heat flux in the water column was calculated from the time rate of change of temperatures in the surface mixed layer, and it was found that most of the heat gained by the water body during the day was lost by penetrative convection overnight.

2.2.3 Wind-Induced (Advective) Mixing Processes in Open Water

Wind-induced mixing processes occur in several ways, and may be due to (Waters, 1998):

- transfer of momentum across the water surface, which causes horizontal advection or turbulence and vertical mixing in the surface layer, or
- breaking of wind-induced waves, either at the shore or upon encountering an obstacle in the flow.

Although most wind-induced horizontal transport in water bodies is via advection, differential exposure to surface wind stresses can lead to differential deepening of the surface mixed layer, and cause horizontal convective exchanges.

Wetzel (1983) defined currents as non-periodic movements of water, and noted that wind-induced currents generally dominate near the surface. The action of a wind stress across the water surface induces a downwind current in the surface layer and a weak upwind flow below the surface layer (Imberger, 1985), to satisfy continuity. Cheung and Street (1988) found that the speed of currents immediately below the water surface varied linearly with depth for wind speeds up to a threshold of around $6\,\mathrm{m\,s^{-1}}$, and logarithmically at greater depth.

2.2.3.1 Seiches and Upwelling

Seiches are lake-scale oscillations (standing waves) which occur in response to wind-induced tilting or set-up of the water surface and the metalimnion (Wetzel, 1983). Surface seiches affect the motion of the entire water mass regardless of the state of stratification, and have maximum amplitude at the surface (Wetzel, 1983). They are due to external influences and are not related to density gradients. Internal seiches occur in the metalimnion of stratified water bodies and are baroclinic (Hutter, 1984). These internal standing waves have much greater amplitude and up to an order of magnitude longer period than surface seiches (Wetzel, 1983). Internal waves can produce considerable mixing between the epilimnion and the metalimnion.

Under weak winds, mixing processes are essentially one-dimensional, so seiching and entrainment at the base of the surface mixed layer can be decoupled (Imberger, 1985). The assumption of one-dimensionality breaks down under severe wind conditions, when horizontal advection becomes important (Imberger, 1985) and the response of the surface mixed layer to strong winds is more complicated. As a result of the set-up, stronger winds induce downwelling and upwelling at opposite ends of the lake while horizontal advection redistributes the upwelling water within the surface layer. The reader is referred to Imberger (1985) and Imberger and Patterson (1990) for a more comprehensive discussion of upwelling, which is not considered in detail in the present study.

2.2.3.2 Differential Deepening

Differential deepening is defined as a variation in the surface layer deepening due to spatial variation in wind exposure. Greater wind stresses in exposed areas cause a more rapid local deepening of the surface layer and a greater introduction of momentum (Imberger and Patterson, 1990). This can lead to substantial horizontal variation in the depth and temperature of the mixed layer (Imberger and Parker, 1985). In a reservoir, differential deepening typically occurs due to topographic shading in a sidearm relative to the main impoundment.

Differential deepening in a stratified fluid leads to horizontal pressure gradients, which are ultimately averaged across the surface layer by convective circulations. Horizontal flows have been observed with velocities up to $5\,\mathrm{cm\,s^{-1}}$ (Imberger and Parker, 1985). These intrusion velocities were greater than could be accounted for directly by the wind stress, and during windy periods, momentum was transmitted to the metalimnion before the wind-induced mixing could penetrate to that depth (Imberger, 1985). The differential deepening response of the mixed-layer may change with time, even under a constant wind stress (Maxworthy and Monismith, 1988). However, mixed layer deepening can persist after the wind ceases (Imberger, 1985) if a horizontal pressure gradient exists, and thus continue to influence the horizontal redistribution of pollutants and biota in lakes.

Wind sheltering by emergent macrophytes in the vegetated zone of a wetland displays some similarities to the differential deepening described above, and will be considered in Section 2.3.2.

2.3 Effects of Macrophytes on Hydrodynamic Processes

As shown in the preceding sections, the hydrodynamic processes in lakes and reservoirs are driven by the meteorological forcing. Hydrodynamic processes control the distribution of heat and other constituents within a water body, and therefore strongly influence the fate of pollutants. In a wetland, most of the microbial activity important to nutrient assimilation and filtration occurs in the macrophyte zones, so the delivery of water and pollutants to these sites is crucial for water quality improvement. Both buoyancy- and wind-induced mixing processes are important for flushing between the macrophyte and open water zones. Wetland circulation is strongly influenced by the presence of macrophytes, which can introduce complex three-dimensional flow behaviour.

Although the physical scale of wetlands is generally much smaller than the lakes and reservoirs discussed previously, many of the flow regimes described in Section 2.2 have also been documented in wetlands. In general, wetlands distribute heat over smaller depths than lakes or reservoirs and are subject to greater differential heating (via radiation shading) and differential exposure to wind stresses (via wind sheltering) than larger water bodies (Andradóttir and Nepf, 2000a). Wetlands are also more responsive to changes in meteorological forcing and display hydrodynamic changes on much shorter time scales than lakes (Waters, 1998). Important factors in wetlands are the modified surface energy fluxes due to the presence of macrophytes, the increased attenuation of shortwave radiation within the water column by submerged macrophytes, and the flow resistance introduced by the vegetation.

The following sections provide an overview of the current literature addressing radiation shading, wind sheltering, and flow resistance due to vegetation in wetlands. Several researchers have documented the effects of macrophytes on surface energy fluxes (parameterisation schemes are given in Chapter 3), although few have extended this to a consideration of the implications for wetland hydrodynamics. This is an objective of the present study.

2.3.1 Radiation Shading by Wetland Macrophytes

Radiation shading by wetland macrophytes is a special case of the differential heating described in Section 2.2.2. Rather than a uniform surface heat flux being absorbed by a water column of variable depth, radiation shading in a wetland may comprise either:

(1.) a surface heat flux which is lower in vegetated zones than in open water, due to attenuation by an emergent canopy, and/or

(2.) more rapid attenuation of shortwave radiation with depth in macrophyte zones than in open water, due to the presence of submerged macrophyte components.

Differential heating may be enhanced or mitigated if the water depth also varies significantly between the macrophyte and open water zones.

Emergent macrophytes contribute to the first two of these radiation shading mechanisms, and are the primary focus of the present investigation, although floating macrophytes can also reduce the surface heat flux. However, shortwave radiation which penetrates the surface is likely to be minimal beneath a floating mat, so the further attenuation of shortwave radiation with depth would be negligible. Submerged macrophytes would not affect the surface heat fluxes directly, but could affect the upward longwave radiation, latent and sensible heat fluxes if rapid underwater attenuation of shortwave radiation substantially increased water temperatures near the surface.

There are numerous studies concerning the attenuation of shortwave radiation by the canopies of commercial crop species, many of which have a similar canopy structure to the common emergent macrophyte species, and some simple parameterisation schemes are outlined in Chapter 3. There is also some evidence in the literature of radiation shading by macrophytes, although few studies have examined the influences of the radiation shading on wetland hydrodynamics.

2.3.1.1 Radiation Shading by Floating Macrophytes

In field experiments, Dale and Gillespie (1976) found that the surface temperatures of floating macrophytes exceeded water temperatures measured 2 cm below the floating mat, and surface water temperatures measured in an adjacent open water zone. At greater depth, the diurnal temperature range was smaller in the vegetated zone than in the open water. Although the horizontal temperature difference would have created a horizontal pressure gradient, the potential for convective exchange between macrophyte and open water zones was not discussed.

Coates and Patterson (1993) used numerical and laboratory experiments to investigate the development of unsteady natural convective flows due to unequal absorption of radiation at the surface in an insulated cavity. They used an opaque layer to simulate floating vegetation, which was assumed to absorb all radiation. From scaling arguments, they predicted an intrusion velocity of $\sim 9\,\mathrm{mm\,s^{-1}}$ for a typical lake of depth 1 m and an illuminated length of 100 m (half the total length). However, this experiment did not explicitly account for the effects of diurnal variation in light intensity or the presence of macrophytes extending into the flow.

Coates and Ferris (1994) extended the work of Coates and Patterson (1993) to include small floating macrophytes and an adjacent open water area. They used the same laboratory chamber and opaque surface layer as Coates and Patterson (1993), so the presence of the root mass was the only difference. The root masses of floating *Lemna* and *Azolla* species were found to displace the buoyant intrusion current downwards, but did not prevent its formation. This occurred even at relatively low plant densities. Neither the experiments of Coates and Patterson (1993) nor Coates and Ferris (1994) allowed for the transmission of light through the floating macrophytes and the associated heating or cooling of the macrophyte surface by evapotranspiration or surface wind effects. However, both papers acknowledged that these additional factors would probably be important in a field situation.

2.3.1.2 Radiation Shading by Emergent Macrophytes

Waters and Luketina (1998) observed vertical and horizontal temperature differences in a shallow wetland containing emergent *Typha orientalis* and *Schoenoplectus validus.* Under high radiation loading in summer, vertical temperature differences of up to 10°C were observed over a depth of 1.0 m in a densely vegetated *Typha* zone. Vertical temperature differences in the adjacent open water were generally less than half this value. Winter temperature differences were lower than those observed in summer. Lateral temperature differences between the two zones generally reversed direction on a diurnal time scale during winter, but maintained a consistent direction for several days to weeks at a time during summer. They concluded that these temperature differences led to horizontal convective exchanges between the two zones.

Waters (1998) observed that radiation shading in a densely vegetated zone in Manly Dam, Sydney, reduced the radiation input so it warmed less than the main reservoir. Scaling analyses suggested buoyancy-driven convections would achieve steady state quickly to establish a balance between buoyancy-induced lateral forcing and vegetation resistance. Estimated velocities were $\sim 1\,\mathrm{mm\,s^{-1}}$, which is consistent with Coates and Patterson (1993). However, differential absorption of shortwave radiation beneath the water surface between vegetated and open water zones was not explicitly considered.

Insulation by emergent macrophytes can also give rise to differential cooling and convective circulation, as the macrophyte zones tend to retain heat and generally cool more slowly than adjacent open water areas. Such convective currents were observed by Oldham and

Sturman (2001), who used scaling arguments and field experiments to investigate the time scales of convective flushing of shallow vegetated regions subjected to a destabilising buoyancy flux. They found the time scales of convective flushing were short, even in the presence of dense vegetation, and declared that convective circulation due to differential heating and cooling was important for mixing between vegetated and open water areas.

2.3.1.3 Radiation Shading by Submerged Macrophytes

Investigating the influences of macrophytes on vertical temperature gradients in shallow water bodies, Dale and Gillespie (1977) found that diurnal cycles of stratification could develop in a shallow lake containing zones of submerged macrophytes. Vertical temperature gradients were found to be positively correlated with biomass and radiation load. Much larger vertical temperature gradients developed in the macrophytes than in adjacent unvegetated areas. While near bed temperatures remained relatively constant, diurnal fluctuations in the water surface temperature led to diurnal cycles in vertical temperature gradients. These were similar to the observations reported by Waters and Luketina (1998) between open water zones and areas supporting emergent macrophytes.

Waters (1998) suggested that buoyancy-driven convection would be insignificant in a wetland containing submerged macrophytes but no emergent macrophytes, because there would be no radiation shading above the water surface. The present study questions this, and presents evidence that convective currents are indeed induced between open water and submerged macrophyte zones due to differential heating via differential absorption of radiation. As discussed with reference to the field data in Chapter 6, the relative importance of shortwave radiation attenuation both *above* and *below* the water surface largely determines the direction of horizontal temperature differences between open water and vegetated zones.

The likely magnitude of buoyancy-induced convective currents in wetlands is considered in Section 3.8.3. The influences of radiation shading by wetland macrophytes on convective circulations are discussed with reference to the field data in Chapter 6.

2.3.2 Wind Sheltering by Wetland Macrophytes

No studies were located in the literature which explicitly considered convective processes induced by differential wind exposure in a wetland. However, it is expected that a situation similar to differential deepening due to topographic shading in a reservoir (Section 2.2.3.2) could arise due to wind sheltering by macrophytes. Wind sheltering by macrophytes has been documented previously, as described below, but the influence of wind sheltering on wetland hydrodynamics in general, and convective exchanges in particular, has not.

Danard and Murty (1994) presented calculations showing that an emergent macrophyte canopy would significantly reduce the wind stress at the water surface, compared with an open water surface. They used separate drag coefficients for the submerged vertical surfaces of the canopy elements, the top of the macrophyte canopy and the water surface. Their calculations demonstrated that, under a wind blowing from the open water towards an emergent canopy, the effective wind stress at the water surface was an order of magnitude lower at the water surface beneath the macrophytes.

Waters (1998) extended the calculations of Danard and Murty (1994) to obtain an estimate of the turbulent velocities in the water column beneath a 1.7 m tall *Typha orientalis* canopy. His analysis suggested that velocities within the macrophyte zone would be less than 40% of those outside the vegetation, and he presented supporting field data. Acoustic Doppler velocimetry (ADV) data showed reduced levels of turbulence and a smaller influence of surface waves in the macrophyte zones. In open water areas, turbulence was highest at the water surface where generated by wind shear, and progressively weaker with depth as it was dissipated. In macrophyte zones, the turbulence intensity was similar over the upper parts of the water column but lower near the base. This was considered inconsistent with wind-generated turbulence. The additional turbulence at mid-depths in the vegetated zones was interpreted as being due to vortex shedding by surface waves on impact with the vegetation.

Luketina and Kay (2000) used a simple numerical model to examine convective circulation between a well mixed open water zone and an emergent macrophyte zone where wind-induced vertical mixing was precluded. Commencing from an isothermal state and neglecting advective effects and vegetation drag, they suggested that a double-cell circulation regime could develop due to wind sheltering, where radiation shading was insignificant. The convective exchanges comprised a warm surface current from the vegetation towards the cooler open water and a cold gravity current from the cool bed in the vegetation towards the open water, with a return flow around mid-depth.

Other types of wetland vegetation can also reduce the effects of wind at the water surface. For example, Dale and Gillespie (1976) demonstrated that floating leaves of *Lemna* and other species reduced the degree of wind-induced mixing in the underlying water column. Numerous laboratory and field studies focusing on coastal and estuarine environments have confirmed that seagrasses, kelp and other marine species significantly reduce mean streamwise velocities, turbulence intensities and mixing compared with unvegetated areas. Wallace (2003) provided a comprehensive recent review of such studies. Although the marine and wetland flow regimes are vastly different, submerged wetland macrophytes would be expected to reduce wind-induced turbulence in the water column compared with an unvegetated wetland zone, even if the wind shear at the surface was identical. This could potentially lead to horizontal temperature gradients and hence convective flows between the two zones.

Other studies have also presented evidence that an emergent canopy reduces the extent of wind-induced turbulence and dampens wave energy at the water surface, compared with an unvegetated zone. Further details are given by Nepf et al. (1997b), Nepf (1999) and Andradóttir and Nepf (2000a), for example, although the implications of this for buoyancy-induced, convective exchanges were not considered.

The expected magnitude of wind-induced currents in wetlands is considered in Section 3.8.4, while the influences of wind sheltering by wetland macrophytes on convective circulations are discussed with reference to the field data in Chapter 6.

2.3.3 Flow Resistance due to Wetland Macrophytes

Although there is a substantial body of literature concerned with flow resistance in vegetated channels (see for example, Petryk and Bosmajian, 1975; Chen, 1976 and Naot et al., 1996) and tidal wetlands or marine environments (see for example, Roig, 1994 and Wallace, 2003), flow in wetlands is generally quite distinct from these, and has only recently received attention by researchers. Important among the characteristics of wetland flows which distinguish them from marine or open channel flows are that (Tsihrintzis and Madiedo, 2000):

- slopes are small, water depths are shallow and the bed levels may be highly variable within the shallow flow
- flows are generally laminar or transitional, rather than turbulent
- the type and density of wetland macrophytes are different from marine species and vegetation in channels
- areas may be only intermittently flooded, and there may be channeling within the wetland
- the ratio of flow depth to emergent macrophyte height is generally low compared with marine flows and grassed channels
- the magnitude and direction of wetland velocities are highly variable with location, due to the spatial heterogeneity of the macrophytes.

Tsihrintzis and Madiedo (2000) undertook a comprehensive review of available theoretical, laboratory and field investigations concerning the resistance due to vegetation in marsh wetlands, which they defined as wetlands supporting emergent herbaceous vegetation. They noted that the influence of vegetation on flow resistance is difficult and complex to model, because transport processes, roughness, drag and turbulence due to emergent macrophytes are still not well understood.

Unfortunately, most of the contributing studies were conducted with flow regimes significantly outside those expected in the present investigation, and are therefore not directly applicable. However, Tsihrintzis and Madiedo (2000) did present some general observations.

- Flow in wetlands is often controlled by the vegetation resistance, which is much higher than in comparable open channel flow.
- Vegetation density varies with depth, and hence the roughness and velocities are also highly variable with depth
- For submerged macrophytes, overall flow resistance generally peaks at low velocities and shallow flow depths, then decreases as either velocity or depth increases.

- For emergent macrophytes, the change in flow resistance with depth appears to be dependent on the depth-variation in vegetation morphology and density.

- The flexibility of the vegetation significantly influences the flow resistance, and resistance generally increases with increasing vegetation stiffness. Flexible vegetation bends with the flow and thus offers less resistance.

The obstructions introduced by macrophytes in a flow field increase resistance to the flow over that experienced in their absence. Roig (1994) identified four important physical mechanisms which dissipate energy in flow through wetland vegetation:

- **form drag** or pressure drag due to the hydrodynamic pressure difference which arises from flow separation around the vegetation elements
- **skin friction** or viscous drag due to friction along the perimeter of the vegetation
- **wave drag** due to deformation of the water surface by emergent vegetation
- energy losses due to **fluid viscosity** and **vegetation-induced turbulence**.

The form drag and skin friction are conventionally summed to give a total drag force, and it is this total drag force that is important in a wetland. Wave drag is not likely to be significant in a freshwater wetland with low flow velocities, and is not considered further in the present study. Energy losses due to fluid viscosity and vegetation-induced turbulence are generally modelled using a turbulence sub-model (Roig, 1994). This is described in the context of the present study in relation to the hydrodynamic modelling in Section 6.6.1.5.

2.3.3.1 Studies of Flow Resistance due to Macrophytes

The resistance to flow due to aquatic vegetation has traditionally been modelled using a derivation from Manning's equation or the Chezy equation (see for example, Feng and Molz, 1997; Somes et al., 1999; Hsu et al., 1999). Manning's equation is generally expressed as follows:

$$U = \frac{1}{n} R^{2/3} S^{1/2} \tag{2.3}$$

while the Chezy equation is given by:

$$U = C\sqrt{RS} \quad \Rightarrow \quad C = \frac{R^{1/6}}{n} \tag{2.4}$$

where U = mean flow velocity ($\mathrm{m\,s^{-1}}$)

n = Manning's roughness parameter ($\mathrm{s\,m^{-1/3}}$)

R = hydraulic radius (m)

S = slope of the energy grade line ($\mathrm{m\,m^{-1}}$)

C = Chezy coefficient ($\mathrm{m^{1/2}\,s^{-1}}$).

The simplicity of such an approach is attractive, although the formulation is strictly only applicable to fully-developed turbulent flow. Through the use of the hydraulic radius, the Manning and Chezy equations also imply that bottom drag dominates (Kadlec, 1990), whereas drag due to vegetation components is expected to be more important in most wetlands, except very close to the bed (Nepf et al., 1997b).

In the laminar and transitional flow regions, Tsihrintzis and Madiedo (2000) suggested that the Manning and Chezy equations would be valid only if the roughness parameter was determined as a function of the flow conditions, via the flow Reynolds number $Re = U\,h/\nu$, where h is the flow depth (the significance of the Reynolds number is discussed further in Section 3.2.1). The exact relationship between n and Re is unclear for low Re (laminar) flow, although it is known that the value of n generally increases as Re decreases in the laminar flow region, for a given vegetation condition and flow depth (Hosokawa and Furukawa, 1992). Reviewing studies where the Manning equation has been applied to flows containing wetland macrophytes, Tsihrintzis and Madiedo (2000) commented that values of the roughness parameter n ranged over nearly three orders of magnitude. They attributed this to the variety of conditions under which data had been collected.

Hammer and Kadlec (1986) suggested that flow through wetland vegetation could be conceptualised as flow through a porous medium. Two porosity scales were identified, a fine scale porosity through the plant stems and vegetation debris in the water column, and a coarse scale porosity due to variation in wetland bathymetry, channels and mounds in the wetland. They also noted that the porosity scales could be expected to vary with depth. They presented a one-dimensional model developed from a balance between the gravitational and pressure forces, and the frictional drag forces. Unfortunately, the one-dimensional flow assumption is unlikely to be satisfied in most low flow wetlands, and is not considered further.

Oldham and Sturman (2001) also used theory for flow through a porous medium in experiments to determine the time scales for convective flushing in littoral zones of wetlands. They assumed that resistance to flow was substantially lower in the vertical than the horizontal direction, and derived an inertial drag coefficient for horizontal flow across the array which depended on the ratio of vertical to horizontal permeability. Their model applies to circular stems and is valid in the range $1.25 \leq D/d \leq 2.5$, where d is the mean stem diameter (m) and D is the mean spacing between stems (m). This equates to a high stem density range of 1600 to $6400\,\mathrm{m}^{-2}$ for stems with $d \sim 0.01\,\mathrm{m}$. Given this high stem density range and the difficulty in determining the vertical and horizontal permeabilities, this method is not considered further.

In flow containing closely spaced elements, Roig (1994) argued that interference between neighbouring elements meant the loss of energy due to viscous and turbulent effects could not be easily separated from energy losses due to form drag and skin friction associated with the vegetation. Using dimensional reasoning and laboratory experiments, she developed a bulk resistance parameterisation in two-dimensional, depth-averaged flow. This related the resistance force to simple physical characteristics of the vegetation, including the stem density, diameter and length. The model was developed for arrays of rigid cylinders with depth-variable diameter and length, and non-uniform stem spacing, and was successfully validated using field data. Unfortunately, because the model was calibrated for high Re, turbulent tidal flows, it is not directly applicable to the present investigation, and is not considered further.

Effects of Flexibility on Flow Resistance due to Macrophytes

Fathi-Maghadam and Kouwen (1997) investigated the effects of non-rigid roughness due to emergent vegetation using dimensional analysis extending from a form of the Darcy-Weisbach friction factor. Unfortunately, their study was restricted to fully turbulent flow conditions, which means that the results may not be directly applicable to laminar or transitional flows. However, they did observe that flow resistance due to flexible vegetation is dependent on the momentum-absorbing area of the canopy. This is a function of the cumulative plant surface area per unit volume rather than the projected or frontal area which becomes invalid if canopy elements are deflected by the flow. They also observed reduced drag due the deflection of flexible vegetation components in laboratory experiments using pine and cedar saplings.

If flow velocities are sufficiently small that there is only minimal bending of macrophyte elements, the macrophytes behave essentially as if they are rigid and the projected area is independent of the flow velocity (Petryk and Bosmajian, 1975). This is likely to be the case in most wetlands with only low flow velocities.

The effects of stem flexibility were examined by Nepf et al. (1997b) using emergent flexible plastic strips attached to the top of rigid cylinders. The flexible part of the canopy was observed to produce greater drag and measured velocities were smaller than in the underlying, rigid region.

Effects of Depth on Flow Resistance due to Macrophytes

Kadlec (1990) examined data available from several previous studies and observed that the average resistance due to vegetation decreased as the flow depth increased. Unfortunately, only limited details were provided describing the vegetation and it is not clear from his work whether or not the vegetation remained emergent with the increasing flow depth.

Wu et al. (1999) investigated the variation in vegetation roughness with flow depth, using laboratory studies which simulated the vegetation by a stiff horsehair mattress. They observed that the resistance due to the vegetation decreased with increased flow depth while the vegetation was emergent. When the vegetation became submerged, the resistance initially increased slightly then decreased to an approximately constant value as the flow depth (and Re) increased.

In contrast, in laboratory experiments over a range of flow depths containing pine and cedar saplings, Fathi-Maghadam and Kouwen (1997) found that resistance values increased as the flow depth increased. The foliage area increased with height above the bed, so a larger vegetation area obstructed the flow as the depth increased.

Effects of Macrophytes on Turbulence and Diffusivity

Much of the research concerning the effects of vegetation on turbulence and diffusivity in flows has been conducted in terrestrial environments such as commercial crops or forests (see for example, Raupach and Thom, 1981 and Finnigan, 2000). Fewer researchers have addressed these issues in aquatic environments. Among these, Waters (1998) measured lower flow velocities and reduced turbulence within zones of emergent *Typha orientalis* than in adjacent unvegetated zones in a natural wetland. In laboratory flume experiments, Wilson et al. (2003) also observed reduced shear-generated turbulence in arrays of flexible rods (stipes), than in "unvegetated" experiments, which they attributed to inhibited momentum exchange with the surrounding flow.

Nepf et al. (1997a) conducted laboratory experiments in a flume containing 0.6 and 1.2 cm diameter hardwood dowels to simulate emergent macrophytes at stem densities in the range from 200 to 2000 m^{-2}. Experiments were also conducted with plastic strips attached to the dowels to simulate flexible vegetation. They found that the larger surface area and greater flexibility of the "leaves" produced greater drag and reduced velocities in the upper canopy region than in the underlying stiff, cylinder area, and the velocity difference increased as the stem area increased. Wilson et al. (2003) also reported greater drag and reduced velocities in the upper canopy region when flexible foliage fronds were attached to rods or stipes.

Nepf et al. (1997a) observed that the horizontal diffusivity within the stiffer cylinder region remained largely unaffected by the flexible canopy component, while the diffusivity was considerably lower in the flexible region than in the cylinder region. The wakes produced by the flexible strips were not as strong as those produced by individual cylinders, which led them to conclude that stiff canopies generate higher turbulent diffusion than flexible canopies, under comparable flow conditions. Wilson et al. (2003) also concluded that more flexible canopies experience greater drag forces but reduced shear-generated turbulence, and therefore diffusion, than more rigid canopies.

The turbulence intensity was observed to peak near the top of the canopies in fully submerged flow (Wilson et al., 2003), similar to observations made in terrestrial canopies (Finnigan, 2000) and marine canopies (Wallace, 2003). In canopies comprising flexible foliage attached to more rigid stems, the turbulence intensity peaked near the interface between the rigid and flexible components (Nepf et al., 1997a).

2.3.3.2 Parameterisation of Flow Resistance due to Macrophytes

Parameterisation of the flow resistance due to vegetation in the context of the present study is considered in Section 3.2.2.

2.3.4 Wetland Convective Flow Classification Scheme

While the thermal classification scheme of Hutchinson (1957) has some applications to wetland thermal classification, wetlands are generally much smaller and certainly shallower than lakes and reservoirs. Wetlands also display changes in hydrodynamic behaviour on comparatively short time scales. Whereas vertical stratification is often the dominant feature of the thermal structure of a lake or reservoir, in a wetland it is more likely to be strong horizontal temperature gradients and buoyancy-induced horizontal currents between open water and macrophyte zones.

Waters (1998) proposed a classification scheme for the convective regime in wetlands which considers both diurnal and seasonal cycles in the thermal structure. He defined:

- **ordinary convection** as the case where a buoyant surface convective current moves from the open water zone into the macrophyte zone
- **reversed convection** as the opposing case, where buoyancy-driven surface flows are induced from the macrophyte zone into the open water.

In a **monoconvective** wetland, the direction of the convective circulation is maintained throughout the diurnal cycle, whereas in a **diconvective** wetland, the convective currents reverse direction during the diurnal cycle. These concepts are illustrated in Figure 2.3. Note that his scheme implies a two level flow comprising a single convective circulation cell.

The classification scheme also allows for **aconvective** conditions, when convective currents are not induced. This may be either because the area of the macrophyte zones is very much larger than the open water and/or the flow resistance due to the vegetation is very high, or because the water temperatures are close to 4°C, so changes in density with temperature are marginal. A **wind-dominated** or advective state was also defined, where wind-induced mixing processes dominate over convective exchanges.

With the exception of the aconvective states, Waters (1998) observed each of these con-

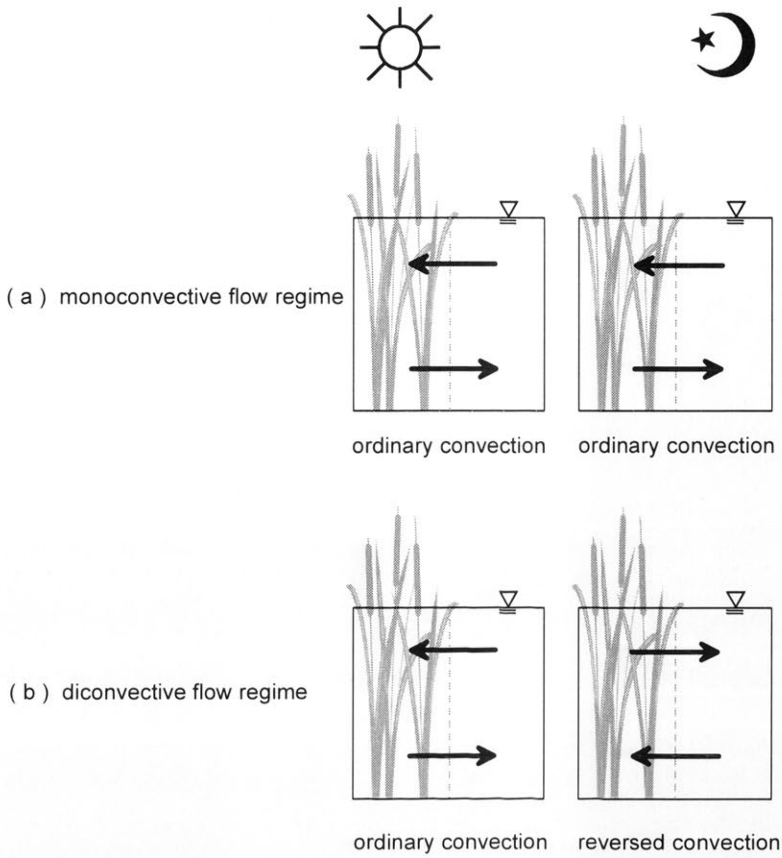

Figure 2.3: Illustration of the convective flow classification scheme proposed by Waters (1998), based on his Figure 7.1: (a) monoconvective and (b) diconvective flow regime.

vective regimes in a wetland zone at Manly Dam in Sydney, and noted significant seasonal variation. He found that strong lateral stratification between macrophyte and open water zones and resulting buoyancy-induced flows were the dominant feature of the thermal structure in Manly Dam. The wetland was typically monoconvective during summer and diconvective in winter. In summer, large temperature differences persisted between the macrophyte and open water zones for periods of several days to weeks at a time. Although Waters (1998) commented that the conditions under which the hydrodynamic regime would change from convective to advective were uncertain, this author expects it to depend on the relationship between wind speed and horizontal temperature differences, influenced by the density of macrophytes.

Waters (1998) cautioned that his classification scheme could only be considered tentative until further research investigated the degree to which lateral stratification and horizontal convection occurred in other wetlands. As part of the present study, the generality of his wetland classification scheme is assessed when applied to a wetland in another location with a different geometry, hydrological regime, and macrophyte community. Field observations of wetland hydrodynamics, including convective (buoyancy-induced) and advective (wind-induced) processes, are discussed in Chapter 6.

2.4 Summary

Much of the work that has previously been conducted into hydrodynamic processes in water bodies has been concerned with the hydrodynamics of lakes and reservoirs, while wetlands have only received attention relatively recently. These hydrodynamic processes are ultimately driven by the meteorological forcing to which the water body is exposed, and while the effects of macrophytes on the surface energy fluxes can to some extent be extrapolated from research undertaken in commercial crops, the implications for wetland hydrodynamic processes have not been extensively studied. At a smaller scale than the lakes and reservoirs, important factors in wetlands are understood to be radiation shading and wind sheltering by macrophytes, shorter response times to changes in the meteorological forcing and increased flow resistance due to the vegetation.

From this review, it is clear that there are opportunities to:

- confirm the applicability of existing shortwave radiation attenuation models in the agricultural literature to attenuation of shortwave radiation by emergent macrophyte species, and hence to quantify the degree of radiation shading by the macrophytes
- investigate the development of vertical and horizontal temperature stratification in a natural wetland as a result of radiation shading by macrophytes, and temporal variation in the resulting convective circulation regimes
- examine the influences of macrophyte type (emergent or submerged), density and distribution on radiation shading and the resulting convective circulation regimes in a natural wetland
- consider the relative importance of the convective (buoyancy-induced) and advective (wind-induced) hydrodynamic processes in a natural wetland.

This thesis aims to address such issues.

Chapter 3

THEORETICAL CONSIDERATIONS

3.1 Introduction

The previous chapter has indicated that macrophytes can significantly influence the hydrodynamic processes in a wetland, compared with an unvegetated water body. Important factors in wetlands are the smaller scale of the water body, radiation shading and wind sheltering by macrophytes, the shorter response time of the body to changes in the meteorological forcing and increased flow resistance due to the macrophytes.

This chapter provides the theoretical background required to investigate the hydrodynamic response of a natural wetland to changes in the meteorological forcing, and in particular, the effects of radiation shading by macrophytes on wetland hydrodynamics. The hydrodynamic and thermodynamic flow equations are introduced in Section 3.2, along with important dimensionless numbers which assist in understanding the flow behaviour. Incorporation of the flow resistance due to the macrophytes is then considered in Section 3.2.2.

An overview is given in Section 3.3 of the parameterisation of the important surface energy exchanges which ultimately drive the wetland hydrodynamics, including radiation fluxes, latent and sensible heat fluxes and the effects of atmospheric stability on these surface heat fluxes. This is extended in Section 3.4 to include the effects of macrophytes on the surface energy fluxes. In both cases, particular attention is paid to the shortwave radiation flux which is the most important component of the heat flux between the atmosphere and the water body. Simple models available in the agricultural literature to describe attenuation of shortwave radiation by a vegetation canopy are also reviewed briefly. Consideration is given in Sections 3.5 to 3.7 to heating due to shortwave radiation and other (non-surface) wetland energy fluxes.

Scaling analyses are presented in Section 3.8, which were conducted to obtain order of magnitude estimates for the convective and advective velocities expected in the open water and macrophyte zones of a natural wetland. These estimates are compared with the observed wetland hydrodynamic behaviour in Chapter 6.

3.2 Hydrodynamic and Thermodynamic Equations

The behaviour of a fluid in a wetland can be described using:

- the Navier-Stokes equations, which are based on momentum
- the continuity equation for conservation of mass
- an energy equation for conservation of thermal energy.

The Boussinesq assumption applies to a fluid subject to small variations in density, whereby density changes due to pressure changes are assumed negligible and density changes due to temperature changes are important only as they directly affect buoyancy (Garratt, 1992).

Momentum Equations

The Navier-Stokes or momentum equations can be expressed as follows:

$$\frac{\partial u}{\partial t} + u\frac{\partial u}{\partial x} + v\frac{\partial u}{\partial y} + w\frac{\partial u}{\partial z} = -\frac{1}{\rho_0}\frac{\partial P}{\partial x} + \nu\left(\frac{\partial^2 u}{\partial x^2} + \frac{\partial^2 u}{\partial y^2} + \frac{\partial^2 u}{\partial z^2}\right) + \Gamma_x \quad (3.1)$$

$$\frac{\partial v}{\partial t} + u\frac{\partial v}{\partial x} + v\frac{\partial v}{\partial y} + w\frac{\partial v}{\partial z} = -\frac{1}{\rho_0}\frac{\partial P}{\partial y} + \nu\left(\frac{\partial^2 v}{\partial x^2} + \frac{\partial^2 v}{\partial y^2} + \frac{\partial^2 v}{\partial z^2}\right) + \Gamma_y \quad (3.2)$$

$$\frac{\partial w}{\partial t} + u\frac{\partial w}{\partial x} + v\frac{\partial w}{\partial y} + w\frac{\partial w}{\partial z} =$$
$$-\frac{1}{\rho_0}\frac{\partial P}{\partial z} + \nu\left(\frac{\partial^2 w}{\partial x^2} + \frac{\partial^2 w}{\partial y^2} + \frac{\partial^2 w}{\partial z^2}\right) + g\,\alpha_T\,(T - T_0) + \Gamma_z \quad (3.3)$$

where
x, y, z = the Cartesian coordinate system
u, v, w = instantaneous velocities in the x, y, z directions ($\mathrm{m\,s^{-1}}$)
t = time (s)
ρ_0 = reference water density ($\mathrm{kg\,m^{-3}}$)
P = pressure (Pa)
ν = kinematic viscosity ($\mathrm{m^2\,s^{-1}}$)
$\Gamma_x, \Gamma_y, \Gamma_z$ = external tractions operating on the system ($\mathrm{Pa\,m^{-1}}$)
g = acceleration due to gravity ($\mathrm{m\,s^{-2}}$)
α_T = thermal expansion coefficient ($^\circ\mathrm{C}^{-1}$)
T, T_0 = temperature, reference temperature ($^\circ$C).

Use of the reference or average density and temperature in the fluid (ρ_0 and T_0) is a consequence of the Boussinesq assumption. This also allows an assumption that the thermal expansion coefficient (α_T) is essentially constant for relatively small changes in the temperature of the fluid. External tractions or body forces ($\Gamma_x, \Gamma_y, \Gamma_z$) acting on the fluid might include geostrophic forces (such as the Coriolis force), wind stresses or resistance forces due to obstructions in the flow. Resistance due to emergent macrophytes in a wetland is conventionally incorporated as a body force term, and is considered in Section 3.2.2.

Briefly considering the significance of each of the terms in the momentum equations, on the left hand side of Equations (3.1) to (3.3):

- the first term represents unsteady effects
- the remaining terms represent convective and/or advective effects, in this project depending on the mechanism responsible for the fluid motion.

On the right hand side of these equations:

- the first term represents the influence of a pressure gradient on the flow
- the (bracketed) second to fourth terms represent the influence of fluid viscosity
- the final term represents the external tractions operating on the systems
- in Equation (3.3), the second last term represents the influence of buoyancy on the flow.

The terms in the momentum equations are discussed in more detail in many fundamental fluid mechanics texts, including Tennekes and Lumley (1972) and Townsend (1976).

Continuity Equation

In an incompressible fluid, the mass conservation or continuity equation is expressed as follows:

$$\frac{\partial u}{\partial x} + \frac{\partial v}{\partial y} + \frac{\partial w}{\partial z} = 0 \tag{3.4}$$

Thermal Energy Equation

The conservation of thermal energy is expressed by an advection-diffusion equation, as follows:

$$\frac{\partial T}{\partial t} + u\frac{\partial T}{\partial x} + v\frac{\partial T}{\partial y} + w\frac{\partial T}{\partial z} = D_H\left(\frac{\partial^2 T}{\partial x^2} + \frac{\partial^2 T}{\partial y^2} + \frac{\partial^2 T}{\partial z^2}\right) + \vartheta_S = 0 \tag{3.5}$$

where D_H = coefficient of thermal diffusivity ($m^2\,s^{-1}$)

ϑ_S = source / sink term for heat ($^\circ C\,s^{-1}$)

and other variables are as previously defined.

3.2.1 Important Dimensionless Numbers

Several dimensionless numbers have been used during previous investigations concerning buoyancy-driven flows in stratified fluids, and these are useful in estimating the flow regimes likely to be encountered in wetlands. The most important dimensionless numbers relevant to the present study are the Reynolds number and the Grashof number.

3.2.1.1 Reynolds Number, Re

The Reynolds number relates the inertial and viscous effects in a flow, as follows:

$$Re = \frac{U\,h}{\nu} \tag{3.6}$$

where U = mean flow velocity ($m\,s^{-1}$)

h = a characteristic length scale for the flow, often the flow depth (m)

ν = kinematic viscosity ($m^2\,s^{-1}$).

At small Re, viscous forces dominate over inertial effects associated with the horizontal movement of the fluid, and the flow is laminar. At large Re, the inertial forces predominate and the flow is turbulent. There is a critical value Re_c, below which laminar flow will always occur, although Re_c is a function of the boundary geometry, and hence varies with situation. There is also a transitional phase when $Re > Re_c$ before the flow can be considered fully turbulent.

If flow in the open water section of a wetland could be approximated by flow in a wide open channel, Tsihrintzis and Madiedo (2000) suggest that the transitional range could span $100 < Re_c \leq 1 \times 10^4$. The expected value of the Reynolds number in a "typical" wetland (see Section 3.8) with $U \sim O(10^{-2})\,m\,s^{-1}$, $h \sim O(10^{-1})\,m$ and $\nu \sim O(10^{-6})\,m^2\,s^{-1}$ is:

$$Re = \frac{U\,h}{\nu} \sim \frac{(10^{-2})\,(10^{-1})}{(10^{-6})} \sim (10^3) \tag{3.7}$$

which suggests transitional flow.

The Stem Reynolds Number for Flows Containing Macrophytes, Re_d

In a flow containing obstructions, such as macrophytes in a wetland, the stem Reynolds number is more appropriate. Assuming that the macrophytes can be represented by circular cylinders, the characteristic flow dimension is the mean stem diameter d (m) and:

$$Re_d = \frac{U\,d}{\nu} \tag{3.8}$$

Using the stem Reynolds number, flows are conventionally classified as laminar when $Re_d < 3$ and turbulent when $Re_d > 4 \times 10^4$ (Schlichting, 1962), with a transitional flow regime between these critical values. Assuming a mean stem diameter d ~O(10^{-2}) m in the "typical" wetland considered above:

$$Re_d = \frac{U\,d}{\nu} \sim \frac{(10^{-2})\,(10^{-2})}{(10^{-6})} \sim (10^2) \tag{3.9}$$

which also falls within the transitional flow regime. This flow classification is consistent with the findings of Tsihrintzis and Madiedo (2000), for example, that flow in wetlands is rarely turbulent.

3.2.1.2 Grashof Number, Gr

The Grashof number relates the strength of the buoyancy forcing to viscous forces which tend to dampen convective flows:

$$Gr = \frac{g\,\alpha_T\,\Delta T\,h^3}{\nu^2} \tag{3.10}$$

where ΔT is the temperature difference between fluid layers (°C) and other variables are as previously defined.

At small Gr, viscous dampening tends to suppress buoyancy-induced movements, and heat transport occurs primarily at the molecular scale. At large Gr, the buoyancy forces dominate the viscous effects and heat transport occurs largely by convection. Flow classification using the Grashof number is discussed in more detail in Section 3.8.1 in relation to the scaling of convective and advective flows in a wetland.

In the "typical" wetland with α_T ~O(10^{-4})°C^{-1} and ΔT ~O(10^0)°C, the expected magnitude of the Grashof number is:

$$Gr = \frac{g\,\alpha_T\,\Delta T\,h^3}{\nu^2} \sim \frac{(10^1)\,(10^{-4})\,(10^0)\,(10^{-1})^3}{(10^{-6})^2} \sim (10^6) \tag{3.11}$$

This suggests that buoyancy forces will dominate, and convective flows will be important.

3.2.2 Parameterisation of Flow Resistance due to Macrophytes

The resistance force due to macrophytes in the flow is accommodated in the horizontal momentum equations as a body force term. As discussed in Section 2.3.3, this resistance force is usually parameterised as a total drag force ($\mathrm{kg\,m\,s^{-2}}$):

$$F_D = \frac{1}{2}\rho C_D A_p U^2 \tag{3.12}$$

where
ρ = water density ($\mathrm{kg\,m^{-3}}$)
A_p = projected plant area in the direction of flow ($\mathrm{m^2}$)
U = mean velocity ($\mathrm{m\,s^{-1}}$)
C_D = dimensionless bulk drag coefficient.

The drag coefficient is difficult to measure for natural vegetation (Petryk and Bosmajian, 1975) and wetland macrophytes are often simulated by circular cylindrical rods. These are indeed representative of many common emergent species, including *Juncus* and *Eleocharis* species (Sainty and Jacobs, 1981). The drag force on an isolated circular cylinder or an array of cylinders has been studied previously, as outlined below.

3.2.2.1 Drag on an Isolated Cylinder

The drag coefficient for an isolated circular cylinder of infinite length is influenced by the surface roughness of the cylinder and the structure of the downstream wake. Assuming uniform surface roughness characteristics, it is dependent on the stem Reynolds number Re_d, which is a function of the mean flow velocity and the characteristic stem dimension. The drag coefficient can be approximated over the range from laminar to turbulent flow as summarised in Table 3.1. Using this relationship, the drag coefficient varies from $C_D = 10$ at $Re_d = 1$, to $C_D = 1.15$ at $Re_d = 4 \times 10^4$, reflecting the general decrease in C_D with increasing Re_d.

3.2.2.2 Drag on an Array of Cylinders

In an array of cylinders, the drag coefficient is additionally influenced by the interaction between neighbouring elements, and sheltering by upstream elements reduces the drag on downstream elements (Raupach, 1992). In a study involving emergent macrophytes, Naot

Flow Regime	Stem Reynolds number	Drag Coefficient	Reference
Laminar	$Re_d < 3$	$C_D = 10 / Re_d$	Kadlec (1990)
Transitional	$3 \leq Re_d < 10^3$	$C_D = \left(10^3 / Re_d\right)^{0.25}$	Schlichting (1962)
Turbulent	$10^3 \leq Re_d \leq 4 \times 10^4$	minimum of: 1.15 and $0.976 + \left[(10^{-3} Re_d - 2)/20.5\right]^2$	Schlichting (1962)

Table 3.1: Variation in the drag coefficient for an emergent circular cylinder of infinite length, as a function of the stem Reynolds number.

et al. (1996) used a shading factor, S_F to estimate the average drag force in an array of randomly distributed circular rods. This led to:

$$F_D = \frac{1}{2} \rho C_D S_F n_s d h A_p U^2 \tag{3.13}$$

where n_s = average stem density per unit horizontal area (m^{-2})
d = stem diameter (m)
h = water depth (m)

and other variables are as previously defined. The quantity ($n_s d h$) is a non-dimensional vegetation density, and the shading factor is given by:

$$S_F = 1 - d/D \left(1 - 0.5 \sqrt{d/D}\right) \tag{3.14}$$

where $D = 1/\sqrt{n_s}$ is the mean spacing between stems (m). The drag coefficient in Equation (3.13) is approximated as shown in Table 3.1.

In general, the flow resistance increases with increasing vegetation density (Tsihrintzis and Madiedo, 2000), although the drag on individual elements decreases due to sheltering by upstream elements. The flow resistance is influenced by both the stem spacing D/d and by the relative flow depth h/d, and generally increases as D/d decreases (Roig, 1994). In wind tunnel studies, in situ drag coefficients have been found to be smaller than measured drag coefficients for individual elements by factors of up to 3 or 4 (Finnigan, 2000). There are not known to be any analogous studies simulating flow through wetland macrophytes.

The flow resistance also depends on the arrangement of the elements in an array. Tsihrintzis and Madiedo (2000) reported that the flow resistance is comparatively lower when a smaller cumulative frontal area is directly exposed to the flow, for example a square array would be expected to offer less resistance than a staggered array of cylinders.

3.2.2.3 Drag on Non-Cylindrical Elements

Not all macrophyte communities can be represented by arrays of regularly-spaced cylindrical rods. The field situation is typically more complex, with additional factors to consider including (Roig, 1994):

- plant morphology, including stem shape, branching, and variation in stem height and diameter
- spatial heterogeneity, including clumping and variation in horizontal plant distribution with depth
- variation in surface characteristics and therefore roughness.

A net resistance force such as that proposed by Roig (1994) is clearly more applicable than a simple drag force parameterisation based on arrays of cylinders. However, laboratory experiments would be required to calibrate her equation for lower Re_d flow through non-cylindrical vegetation. Such work could constitute a research project in its own right and is beyond the scope of the present study. Instead, a drag force parameterisation is implemented in this study, while acknowledging its limitations.

3.3 Parameterisation of Surface Energy Fluxes

It is well established that the major external inputs of energy into a standing water body occur across the surface (Henderson-Sellers, 1984), and that these drive the hydrodynamics of the water body. Major energy inputs include thermal energy from shortwave and longwave radiation, transfer of latent and sensible heat and mechanical energy due to the action of winds. The major components of the heat budget at a water surface are shown schematically in Figure 3.1, and include:

- Radiative heat fluxes include:
  - shortwave radiation, ϕ
  - atmospheric or downward longwave radiation, $\phi_{LW\downarrow}$
  - blackbody or upward longwave radiation, $\phi_{LW\uparrow}$

- Latent heat H_L, which is either lost from the water body during evaporation, or added during the reverse process of condensation
- Sensible heat H_S, which may be either gained by or lost from the water surface by conduction, as a result of a temperature difference between the water surface and the overlying air mass.

The latent and sensible heat fluxes are dependent on wind speed and convective processes above the water surface, while the radiation fluxes are independent of momentum exchange. The magnitude of the net surface energy input is therefore determined by meteorological conditions (Fischer et al., 1979), and the properties of the water surface.

The net surface heat flux can be calculated as follows:

$$H_{NET} = (1 - R_S)\,\phi + (1 - R_L)\,\phi_{LW\downarrow} - \phi_{LW\uparrow} + H_L + H_S \tag{3.15}$$

where
H_{NET} = net surface heat flux (Wm^{-2})
ϕ = incident shortwave radiation flux (Wm^{-2})
R_S = dimensionless reflection coefficient for shortwave radiation
$\phi_{LW\downarrow}$ = incident atmospheric longwave radiation flux (Wm^{-2})
R_L = dimensionless reflection coefficient for atmospheric longwave
$\phi_{LW\uparrow}$ = upward longwave radiation flux (Wm^{-2})
H_L = latent heat flux (Wm^{-2})
H_S = sensible heat flux (Wm^{-2}).

3.3.1 Sign Convention for Surface Heat Fluxes

The surface heat fluxes are defined as positive when they are directed into the water body (heat gain) and negative when directed away from the water (heat loss). Following this convention:

- shortwave radiation is positive during the day and zero overnight
- atmospheric longwave radiation is always positive
- upward longwave radiation is always negative
- latent and sensible heat fluxes may be either positive or negative, depending on the temperature of the water surface and conditions in the atmospheric boundary layer.

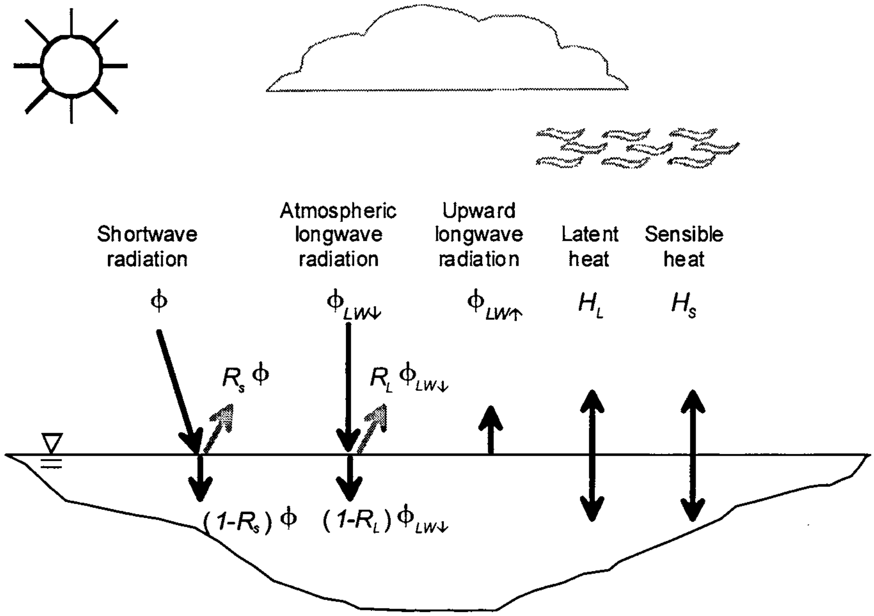

Figure 3.1: Radiation and major thermal fluxes at the water surface in an unvegetated water body.

The net heat budget is dominated by shortwave radiation during the day, when the atmospheric and upward longwave radiation are approximately equal in magnitude but opposite in sign. The latent and sensible heat fluxes are generally considerably smaller than the radiation fluxes. The net longwave radiation flux is important overnight when shortwave radiation is zero and wind speeds are generally low. Latent and sensible heat fluxes are often important during the afternoon and early evening when an unstable atmosphere will enhance vertical transport processes across the water surface (Souch et al., 1996).

3.3.2 Radiation Fluxes at the Water Surface

3.3.2.1 Shortwave Radiation Flux, ϕ

Shortwave radiation is defined as the component of the solar spectrum with wavelengths between 100 nm and 4000 nm, although there is some inconsistency between different researchers. For example, Ross (1975) uses 350 to 3500 nm, Imberger and Patterson (1990) us 300 to 1000 nm and Wetzel and Likens (1991) use 300 to 3000 nm. However, global shortwave radiation is typically measured between 300 and 2800 nm.

Photosynthesis is stimulated by radiation within the waveband from 400 to 700 nm, which is defined as photosynthetically active radiation (PAR). On a cloudless day, the ratio of PAR to total energy in the extraterrestrial solar spectrum is approximately 45 to 48 % (Monteith and Unsworth, 1990; Wetzel and Likens, 1991). This corresponds to approximately 47 to 50 % of the total energy in the global shortwave radiation band, if it is assumed that global shortwave radiation accounts for approximately 96 % of the total solar spectrum (Ross, 1975). The exact ratio depends on the definition of the PAR and global wavebands. The relationship adopted in the present study is discussed in Section C.2 in Appendix C.

Global shortwave radiation comprises both direct and diffuse shortwave radiation.

- **Direct shortwave radiation** is unidirectional and unpolarised. Although the solar radiation emitted by the sun is nearly constant at 1350 to 1400 Wm^{-2} (Ayra, 1988), the incident shortwave radiation flux varies both spatially and temporally because the radiation is attenuated by atmospheric absorption, reflection and scattering before reaching the earth's surface. Hence direct shortwave radiation contributes around 90% of the total incident shortwave radiation flux around solar noon on cloudless days (Norman, 1975) but the fractional component decreases under cloud. The effects of clouds on the direct shortwave radiation flux are extremely difficult to quantify and most shortwave radiation prediction models either apply to cloudless conditions or incorporate simple empirical relationships.
- **Diffuse shortwave radiation** is dominated by shorter wavelengths and occurs after scattering by aerosols and other molecules in the atmosphere. It is the only component of shortwave radiation before sunrise and after sunset (Rosenberg, 1974). The relative importance of the diffuse shortwave radiation component is determined by the cloud cover. On cloudless days, diffuse radiation is approximately 10 % of global shortwave radiation (Bukata et al., 1995), but around 50 % of global shortwave radiation when the sun is obscured by heavy cloud (Monteith and Unsworth, 1990).

The incident shortwave radiation flux can be calculated from standard astronomical formulae which are avaliable in many standard references, including Burman and Pochop (1994). However, the incident shortwave radiation flux is more commonly measured directly, which is the approach adopted in the present investigation.

Net Shortwave Radiation Flux, ϕ_0

Of the shortwave radiation flux which passes through the atmosphere, a fraction is reflected from the water surface (see Figure 3.1) while the net shortwave radiation flux is transmitted across the surface and into the water column:

$$\phi_0 = \tau_S \, \phi = (1 - R_S) \, \phi \tag{3.16}$$

where ϕ_0 = net shortwave radiation flux across the water surface ($\mathrm{Wm^{-2}}$)

ϕ = incident shortwave radiation flux ($\mathrm{Wm^{-2}}$)

τ_S = dimensionless surface transmission coefficient

R_S = dimensionless reflection coefficient for shortwave radiation.

The reflection coefficient is dependent on a combination of three factors, as outlined below.

Shortwave Reflection Coefficient from a Water Surface, R_S

The shortwave reflection coefficient at the water surface is most significantly influenced by three factors (Bukata et al., 1995; Chapra, 1997) as shown in Figure 3.2.

(a) The **angle of incidence of the direct shortwave radiation beam** is a function of the solar zenith angle θ which varies according to season, time of day and geographic location. Under cloudless conditions, $R_S \sim 5\,\%$ while $\theta \leq 50\,^\circ$ but increases rapidly towards $100\,\%$ near sunrise and sunset.

(b) The **degree of cloud cover** determines the relative proportions of direct and diffuse radiation. The value of R_S is relatively insensitive to the degree of cloud cover while $\theta \leq 60\,^\circ$, but decreases as cloud cover increases at higher θ.

(c) The **roughness of the water surface** is a function of the local wind climate. The value of R_S is essentially independent of wind speed for speeds of up to $50\,\mathrm{km\,h^{-1}}$ ($13.9\,\mathrm{m\,s^{-1}}$) while $\theta \leq 60\,^\circ$. When θ is higher, R_S is greater for lower wind speeds which maintain a smoother water surface.

The shortwave reflection coefficient may be estimated from Figure 3.2, or calculated using an empirical relationship, such as that proposed by Anderson (cited by Gangopadhyaya et al., 1966). This relationship calculates R_S as a function of the solar elevation and empirical coefficients related to the degree of cloud cover, but does not consider the effect of wind speed:

$$R_S = A \, \beta^B \tag{3.17}$$

where β = solar elevation ($^\circ$ above the horizon)

A, B = empirical coefficients which incorporate the effects of cloud cover and which are given in Table 3.2.

The solar elevation can be calculated using standard formulae, as shown in Section A.1 of Appendix A. Strictly, a reflection coefficient should be defined for both the direct and diffuse components of the global shortwave radiation flux, although a combined shortwave reflection coefficient is usually adequate (Bukata et al., 1995), especially when the flux components are not measured separately.

	Cloudless	Scattered Cloud	Broken Cloud	Overcast
Cloud Fraction	0	0.1 to 0.5	0.6 to 0.9	1.0
Coefficient A	1.18	2.20	0.95	0.35
Coefficient B	-0.77	-0.97	-0.75	-0.45

Table 3.2: Empirical coefficients used to calculate the shortwave reflection coefficient as a function of solar elevation and degree of cloud cover (after Anderson, cited by Gangopadhyaya et al., 1966).

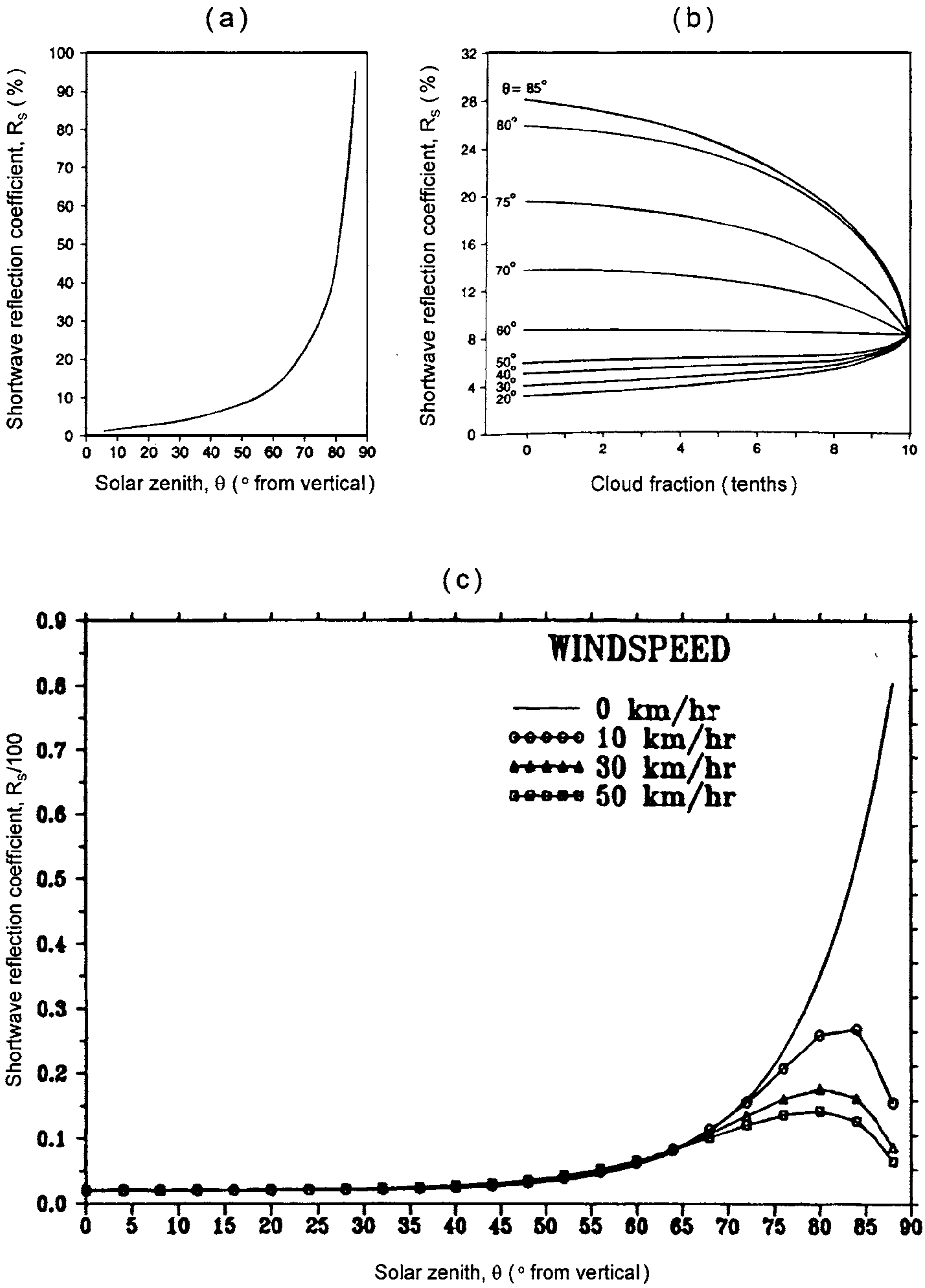

Figure 3.2: Variation in shortwave reflection coefficient with (a) the solar zenith, (b) the degree of cloud cover and the solar zenith and (c) the roughness of the water surface and the solar zenith (adapted from Bukata et al., 1995).

3.3.2.2 Longwave Radiation Fluxes, ϕ_{LW}

Longwave radiation is defined as the component of the solar spectrum with wavelengths in the range from 4 to 100 μm (Henderson-Sellers, 1984). Any substance with a temperature greater than absolute zero (0° K ~ -273°C) will emit longwave radiation. At the water surface, longwave radiation comprises both downward radiation from the atmosphere and upward radiation from the water surface, and it is the balance of these two fluxes which contributes to heating of the water column. While absolute values of the downward and upward longwave radiation fluxes may be large, their net effect is generally small during the day compared with the shortwave radiation flux. Overnight, however, there can be a significant imbalance between downward and upward longwave radiation.

Atmospheric Longwave Radiation, $\phi_{LW\downarrow}$

A blackbody is an ideal radiator which absorbs thermal energy and transforms it into longwave radiation at the maximum rate allowed by the laws of thermodynamics (Guyot, 1998). Blackbodies emit longwave radiation according to the Stefan-Boltzmann law:

$$\phi_{LW} = \sigma T^4 \tag{3.18}$$

where ϕ_{LW} = longwave radiation flux emitted by a unit area of a planar surface into an imaginary hemisphere surrounding it (Wm^{-2})

σ = Stefan-Boltzmann constant

= 5.67×10^{-8} Wm^{-2} K^{-4}

T = temperature of the blackbody (K).

It is preferable to measure longwave radiation fluxes directly, although the atmospheric longwave radiation flux is often estimated from blackbody radiation theory using an equation of the form:

$$\phi_{LW\downarrow} = (1 - R_L)\, \varepsilon_{ac}\, \sigma\, T_a^4\, C_f \tag{3.19}$$

where R_L = dimensionless longwave reflection coefficient

ε_{ac} = dimensionless effective atmospheric emissivity

σ = Stefan-Boltzmann constant (Wm^{-2} K^{-4})

T_a = air temperature (K)

C_f = dimensionless cloudiness factor.

These variables are determined as outlined in the following sections.

Longwave Reflection Coefficient from a Water Surface, R_L

The longwave reflection coefficient from a water surface is small, and generally assumed to be constant at $R_L = 0.03$ (Henderson-Sellers, 1984). The reflection of longwave radiation increases slightly with decreasing solar elevation, to a maximum at grazing angles of incidence (Monteith and Unsworth, 1990). This small variation is usually neglected, and is similarly neglected in the present study.

Atmospheric Emissivity, ε_{ac}

The atmospheric emissivity accounts for the deviation of the atmosphere from ideal black-body behaviour. It is defined as the ratio of actual to theoretical longwave radiation over a given waveband (Monteith and Unsworth, 1990). Numerous semi-empirical relationships have been proposed to determine the *effective* atmospheric emissivity using measurements made near the ground surface. These are generally calculated from the air temperature, the ambient vapour pressure, or a combination of the two. The most common relationships are dependent only on the air temperature, and assume that vapour pressure is essentially a function of air temperature (Swinbank, 1963). These include the equations of Swinbank (1963) and Idso and Jackson (1969). These give very similar values for the effective atmospheric emissivity, although Henderson-Sellers (1984) suggests that the latter agrees better with observations when $T_a < 10°\text{C}$ (283K).

The equation of Idso and Jackson (1969) is:

$$\varepsilon_{ac} = 1.0 - 0.261 \exp\{-7.77 \times 10^{-4} (T_a - 273)^2\} \tag{3.20}$$

where T_a (K) is the air temperature, which is generally measured at around 2 m elevation.

Cloudiness Factor, C_f

The cloudiness factor accounts for the effect of clouds on the atmospheric longwave radiation flux. Empirical formulae exist to compute the cloudiness factor from observed cloud cover or the ratio of measured to total available sunshine hours. The latter approach is only really applicable to timesteps of one day or longer, and is not considered further.

The general form of the cloudiness factor is (Brutsaert, 1982):

$$C_f = \left(1 + a m^b\right) \tag{3.21}$$

where a, b = empirical coefficients (dimensionless)

m = dimensionless cloud fraction

= proportion of the sky covered by cloud.

The value of a is dependent on the type of cloud, and ranges from 0.04 for fine, high Cirrus clouds, to 0.25 for dense Nimbostratus clouds or fog (Brutsaert, 1982). The coefficient values of $a = 0.17$ and $b = 2$ used by Fischer et al. (1979) are adopted in this study.

Upward Longwave Radiation, $\phi_{LW\uparrow}$

The longwave radiation flux emitted from the ground surface is usually assumed to be isotropic (Ross, 1981), and the longwave radiation flux emitted from the water surface is similarly assumed isotropic. This can be calculated from the Stefan-Boltzmann law using an equation similar to Equation (3.19):

$$\phi_{LW\uparrow} = -\,\varepsilon_{\mathrm{w}}\,\sigma\,T_w^4 \tag{3.22}$$

where ε_{w} = dimensionless emissivity of the water

σ = Stefan-Boltzmann constant ($\mathrm{Wm^{-2}\,K^{-4}}$)

T_w = water surface temperature (K).

The negative sign indicates that the flux is directed out of the water column.

Water Surface Emissivity, ε_{w}

Within the range of temperatures encountered at the earth's surface, most natural materials behave approximately as ideal radiators (Bukata et al., 1995). This includes water, vegetation and soil, which all exhibit an emissivity of $\varepsilon_{\mathrm{w}} > 0.9$ (Ayra, 1988). The emissivity of water is generally given as $\varepsilon_{\mathrm{w}} \sim 0.97$ (Hutchinson, 1957).

3.3.3 Other Energy Fluxes at the Water Surface

Aside from the radiation fluxes, the major heat fluxes at the water surface are the latent and sensible heat fluxes. These are strongly dependent on the exchange of momentum across the air-water interface, which is in turn influenced by the stability of the atmospheric boundary layer.

3.3.3.1 Effects of Atmospheric Stability on Surface Energy Fluxes

The conditions in the atmospheric boundary layer above a water surface determine the shape of the wind profile above that surface. The wind profile influences the magnitude of the surface fluxes of water vapour, heat and other constituents, while radiation fluxes are not directly affected. Above a relatively uniform surface, the atmospheric boundary layer can be roughly divided into three main regions (Brutsaert, 1982), as shown in Figure 3.3.

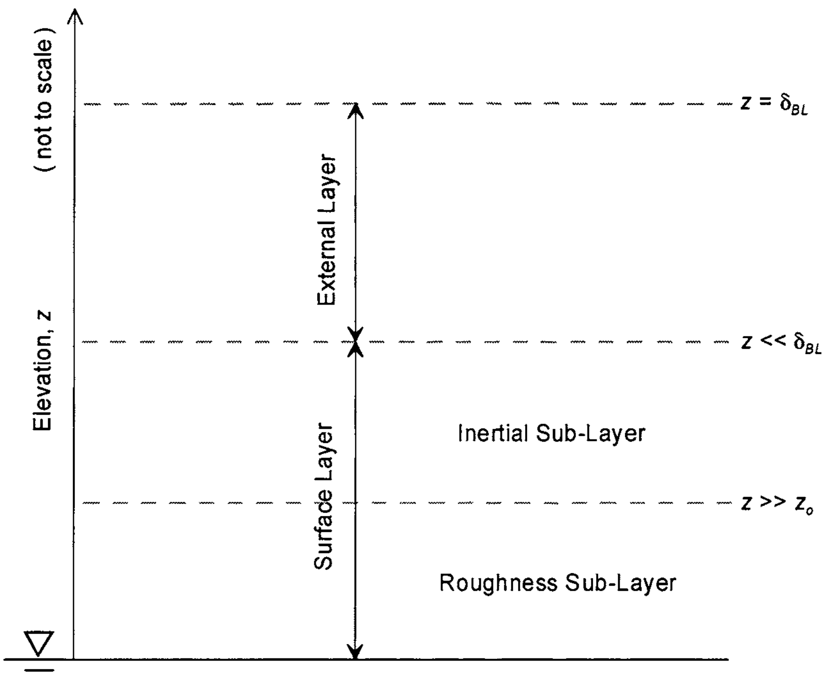

Figure 3.3: Main regions of the atmospheric boundary layer, where δ_{BL} is the depth of the boundary layer and z_0 is the aerodynamic roughness length, defined in Section 3.3.3.2 (adapted from Styles, 1997).

Above a water surface, the atmospheric surface layer is most important in the vertical transport of momentum, water vapour and heat, and comprises two regions.

(1.) A **dynamic or roughness sub-layer** exists adjacent to the water surface, where air flow is directly dependent on the water surface characteristics. In smooth flow conditions, the dynamic sub-layer extends up from the surface to $z \sim (30\,\nu\,/\,u_*)$. In rough flow conditions the layer depth is of the order of the mean height of the surface roughness elements, for example the height above the mean surface elevation of surface waves or emergent vegetation.

(2.) An **inertial sub-layer** exists above the dynamic layer, where air flow is no longer strongly influenced by local water surface characteristics. The effects of the earth's rotation are negligible and the vertical fluxes of momentum and scalar constituents are essentially constant with elevation. The height of the inertial sub-layer can extend up to several tens of metres above the surface.

An **external layer** exists above the atmospheric surface layer, where air flow is influenced by both the properties of the surface and by larger-scale processes associated with the Earth's rotation. The height of the external layer ranges from tens of metres to several thousand metres, beyond which the free atmosphere is no longer influenced by surface characteristics.

Vertical transport in the atmosphere is governed by convective processes (Thom, 1975; Monteith and Unsworth, 1990), of which there are three modes.

- **Free convection** occurs where vertical transport processes are governed by buoyancy forces associated with vertical density gradients. This is common during light winds or calm periods.
- **Forced convection** prevails where vertical motion is generated and maintained purely by frictional forces arising from the interaction of the atmosphere with the water surface, for example during windy periods.
- **Mixed convection** results where the vertical transport regime is determined by both forced and free convection. This is common during the daytime, although the relative importance of the two processes varies with time.

The stability of the atmospheric boundary layer can significantly influence the transport of momentum and scalar constituents at the air-water interface. Depending on atmospheric stability, convective processes may be either enhanced or suppressed, compared with the neutrally stable case. The atmosphere is considered **neutrally stable** when the vertical temperature gradient is equal to the adiabatic lapse rate, $-dT/dz \approx 1°\text{C}/100\,\text{m}$. The vertical wind profile can only be considered logarithmic over an ideal site when the atmosphere is neutrally stable. In non-neutral conditions, the vertical profiles of wind, water vapour and heat deviate from the logarithmic forms observed under neutral conditions (Smith, 1989).

The atmosphere is **unstable** when the rate of decrease of the air temperature gradient with elevation exceeds the adiabatic lapse rate. Under these conditions, buoyancy forces enhance vertical transport. Light warm air near the ground tends to rise, and a parcel of air moved to a higher elevation will continue to rise due to buoyancy forces. Vertical motion will tend to be enhanced with increasing elevation.

In contrast, when the rate of air temperature decrease with elevation is less than the adiabatic lapse rate, the atmosphere is **stable** or super-adiabatic. This is also known as a temperature inversion, and vertical transport is suppressed. If a parcel of air is moved to a higher elevation without exchanging heat across its boundaries, it will become negatively-buoyant and sink again, with a corresponding reduction in overall vertical motions.

The effects of atmospheric stability on the vertical eddy structure are shown schematically in Figure 3.4.

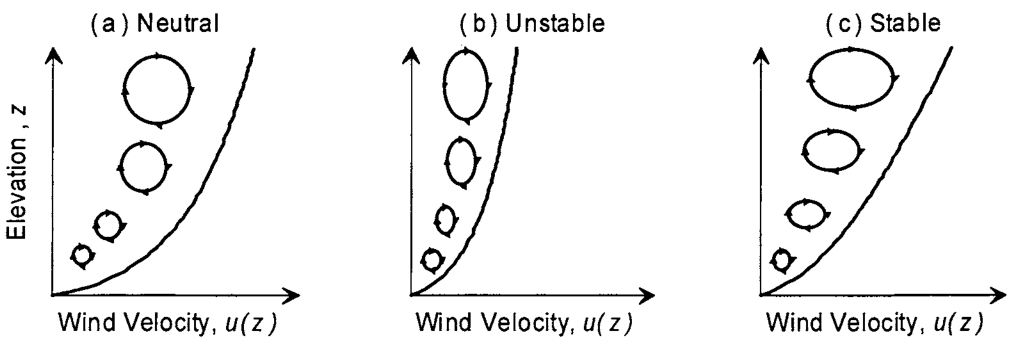

Figure 3.4: Vertical wind profiles and eddy structures for (a) neutrally-stable, (b) unstable and (c) stable atmospheric conditions (adapted from Thom, 1975).

Many seasonal hydrodynamic models fail to consider the effects of atmospheric stability on vertical transport processes at the water surface. However, over shorter time scales of hours to days, the influence of atmospheric stability on the transfer of momentum, latent and sensible heat is significant and should be accounted for (Imberger and Patterson, 1990). Fischer et al. (1979) suggest that latent and sensible heat fluxes can increase by as much as 40% in unstable conditions, and decrease by a similar amount when the atmosphere is stable.

Where detailed measurements are available to give non-dimensional profiles of wind, sensible heat and specific humidity, corrections can be made to the bulk transfer equations to account for atmospheric stability. These are based on a dimensionless stability function (Dyer and Hicks, 1970) which depends on the Monin-Obukhov stability parameter ($z\,/\,\mathcal{L}$). Alternatively, proxy variables such as the bulk Richardson number can be used to indicate the stability of the boundary layer near the water surface.

The bulk Richardson number, Ri_b, represents the ratio of buoyancy forces to wind shear forces, as follows (Donelan, 1990):

$$Ri_b = \frac{g\,z\,(\Theta_{V_z} - \Theta_{V_s})}{\Theta_{V_z}\,u_z^2} \tag{3.23}$$

where	g	=	acceleration due to gravity ($\mathrm{m\,s^{-2}}$)
	u_z	=	wind speed ($\mathrm{m\,s^{-1}}$) at elevation z (m), generally 10 m
	Θ_{V_z} and Θ_{V_s}	=	potential virtual temperatures (K) at height z and at the water surface, respectively.

The potential virtual temperature is the temperature of a parcel of dry air at the same density as moist air with given specific humidity, temperature and pressure, when the air is brought adiabatically from ambient conditions to a standard pressure of $P_0 = 1000\,\mathrm{hPa}$ (Brutsaert, 1982). It is calculated as shown in Appendix A.

Using the bulk Richardson number, the stability of the atmospheric boundary layer at the water surface is classified as follows:

$$\begin{array}{lrcccl} \text{unstable} & & & Ri_b & < & 0.0 \\ \text{neutral} & 0.0 & < & Ri_b & < & 0.01 \\ \text{stable} & 0.01 & < & Ri_b & & \end{array} \tag{3.24}$$

3.3.3.2 Surface Momentum Exchange

Momentum exchange across the water surface is important not only for mechanical mixing processes, but because the latent and sensible heat fluxes are related to momentum exchange. Fluxes of momentum, moisture and heat across the air-water interface are driven primarily by frictional resistance to winds blowing across the surface (Thom, 1975). The wind-induced surface shear stresses are influenced by (Fischer et al., 1979):

- wind speed
- water surface conditions and fetch length
- variability in the local wind climate
- stability of the adjacent atmospheric boundary layer.

The wind speed is generally the dominant factor determining the magnitude of the shear stress at the water surface.

In neutral conditions and over a fetch of uniform roughness, the variation in wind speed with height above a surface is described by the logarithmic wind profile:

$$u_z = \left(\frac{u_*}{k} \right) ln \left(\frac{z}{z_0} \right) \tag{3.25}$$

where	u_z	=	mean wind speed ($\mathrm{m\,s^{-1}}$) at height z (m) above the surface
	u_*	=	friction velocity in the air adjacent to the water surface ($\mathrm{m\,s^{-1}}$)
	k	=	von Kármán constant (approximately 0.41)
	z_0	=	aerodynamic roughness length for momentum (m).

This is strictly only valid when the measurement height, z is considerably larger than the aerodynamic roughness length, z_0 (Brutsaert, 1982). The effects of non-neutral atmospheric stability on the vertical wind profile were addressed in Section 3.3.3.1.

The friction velocity quantifies the turbulent velocity fluctuations in the air (Monteith and Unsworth, 1990). The friction velocity in the air u_* is defined by:

$$u_* = \sqrt{\frac{\tau}{\rho_a}} \tag{3.26}$$

where τ is the shear stress at the water surface and ρ_a is the air density.

Assuming the shear stress is constant at the water surface, the wind-induced friction velocity in the water column is given by:

$$\tau = \rho_a u_*^2 = \rho u_{*w}^2 \qquad \Rightarrow \qquad u_{*w} = \sqrt{\frac{\rho_a}{\rho}}\, u_* = \sqrt{\frac{\rho_a}{\rho}} \left(\frac{k}{ln(z/z_0)} \right) u_z \tag{3.27}$$

where u_{*w} = friction velocity in the water column ($\mathrm{m\,s^{-1}}$)

ρ = water density ($\mathrm{kg\,m^{-3}}$)

and other variables are as previously defined.

Equations (3.25) and (3.27) assume the zero-slip boundary condition, which causes the wind speed to decrease dramatically close to the water surface to virtually zero at the surface. When the water surface is non-stationary, the water surface velocity should be taken into account by replacing the wind speed u_z with the relative wind speed $(u_z - u_s)$, where u_s is the surface mean water velocity (Imberger and Patterson, 1990). When the surface water velocity is not available, the drift velocity is often neglected. However, u_s can be approximated by the friction velocity in the water column, which can be estimated via Equation (3.27) from the wind speed at 10 m elevation (Hicks, 1972):

$$u_s \sim u_{*w} \sim 0.035 \times u_{10} \tag{3.28}$$

Aerodynamic Roughness Length over a Water Surface, z_0

The aerodynamic roughness length is defined by Equation (3.25), and related to the height, density and distribution of surface roughness elements. It is a length scale that characterises the effectiveness of the surface as a momentum absorber, and is typically one order of magnitude smaller than the physical height of the surface roughness elements (Thom, 1975).

Depending on the condition of the water surface, the aerodynamic roughness length can be parameterised as follows (Donelan, 1990):

Smooth flow $$z_0 = \frac{0.11\,\nu}{u_*} \qquad u_* < 2(\nu g)^{1/3} \tag{3.29}$$

Rough flow $$z_0 = \frac{0.014\,u_*^2}{g} \qquad u_* \geq 2(\nu g)^{1/3} \tag{3.30}$$

where ν = kinematic viscosity of the water ($\mathrm{m^2\,s^{-1}}$)

g = acceleration due to gravity ($\mathrm{m\,s^{-2}}$).

It is generally accepted that the water surface is smooth under light winds, and z_0 may even have a lower value than given by Equation (3.29) for extremely smooth conditions (Brutsaert, 1982). Many studies in the literature report values for z_0 over a smooth water surface, ranging from 3×10^{-3} mm (Craig and Banner, 1994) to 6.0 mm (Guyot, 1998). The value of z_0 is generally lower over shallow water (Brutsaert, 1982), and an average of $z_0 = 0.23$ mm is often adopted. This value was used as a starting point in the present study.

The water surface is no longer smooth under moderately strong winds with well-developed waves and the roughness length increases with wind speed according to the equation of Charnock, Equation (3.30). Rough surface conditions are unlikely to develop in a wetland with a limited fetch and relatively shallow depth, and are therefore not considered further in this study.

Drag Coefficient for Surface Momentum Exchange, C_{Dz}

Fluxes of momentum and the related fluxes of water vapour and heat across a water surface may also be described in terms of a drag coefficient and bulk transfer equations rather than the aerodynamic roughness length. In a neutral boundary layer, the dimensionless drag coefficient for momentum can be related to z_0, as follows (Garratt and Hicks, 1973):

$$C_{Dz} = k^2 \left[ln \left(\frac{z_M}{z_0} \right) \right]^{-2} \tag{3.31}$$

where C_{Dz} is referenced to wind speed measurements made at height z_M. For wind speeds of $u_{10} \leq 4\,\mathrm{m\,s^{-1}}$, Hicks (1972) found the value of the drag coefficient to be relatively constant at $C_{D_{10}} \sim 1.0 \times 10^{-3}$ at sites in Bass Strait and Lake Michigan. For $u_{10} \geq 4\,\mathrm{m\,s^{-1}}$ the drag coefficient increased slightly and approximately linearly with u_{10}.

Over shallow water ($h < 2.5$ m) Hicks et al. (1974) found that the surface remained aerodynamically smooth for $u_{10} \geq 10\,\mathrm{m\,s^{-1}}$. They suggested a constant value of $C_{D_{10}} = 1.0 \times 10^{-3}$ in shallow water, and cited other studies in support of their findings. From Equation (3.31), this corresponds to $z_0 \sim 0.23$ mm, as reported earlier. The effects of atmospheric stability on the drag coefficient must be accounted for, as discussed in Section 3.3.3.1, while the value of z_0 is unaffected by atmospheric stability.

3.3.3.3 Latent Heat Flux, H_L

The latent heat flux is associated with evaporation or condensation, and represents a significant component of the heat flux across a water surface. Latent heat transfer generally occurs due to evaporation rather than condensation, which results in a heat loss from the water column.

Two requirements must be satisfied to permit evaporation from a water surface (Penman, 1948):

(1.) a supply of energy to provide the latent heat of vaporisation, acquired mainly from shortwave radiation

(2.) a mechanism to transport water vapour away from the surface, which depends on the wind velocity and the vapour pressure deficit above the surface.

The latent heat flux can be separated into two components, H_L and H_{L2} (Henderson-Sellers, 1984). The major component is the energy used for evaporation, which is directly involved in the change of state (H_L):

$$H_L = -\rho\, L_w\, E_r \tag{3.32}$$

while the second, comparatively minor component, is the energy carried away by the evaporating water (H_{L2}):

$$H_{L2} = -\rho\, c_{pw}\, (T_w - T_0) \tag{3.33}$$

where
ρ = water density ($\mathrm{kg\,m^{-3}}$)
L_w = latent heat of vaporisation of water ($\mathrm{J\,kg^{-1}}$)
E_r = evaporation rate ($\mathrm{m\,s^{-1}}$)
c_{pw} = specific heat capacity of water at temperature T_w ($\mathrm{J\,kg^{-1}\,{}^\circ C^{-1}}$)
T_w = water temperature (°C)
T_0 = reference temperature (usually 298 K $\sim$ 25°C).

The negative sign indicates that the latent heat flux due to evaporation represents a loss from the water body. The density, latent heat of vaporisation and specific heat capacity are all dependent on the water temperature, T_w and can be calculated as shown in Appendix A. Because $L_w >> c_{pw}\,(T_w - T_0)$, then $H_L >> H_{L2}$, and the second component is usually neglected (Henderson-Sellers, 1984), as is the case in the present study.

There is no universally-accepted method for calculating evaporation from an open water body, and several methods are available, including:

- water balance methods
- evaporation pan methods
- energy balance methods
- aerodynamic methods
- combination methods
- eddy measurement methods.

Not all of these are suitable for use over short time steps of $\Delta t \leq 1$ hr, and the instrumentation requirements for others are not always easy to satisfy. The features, advantages and disadvantages of these methods are summarised in Section A.2 in Appendix A. Of these, the aerodynamic and eddy measurement methods are most suitable for the present study. Ideally, eddy measurement techniques would be used, although the expense and fragility of the instruments required for eddy measurements precluded their use in the long term field deployment of the present investigation. Instead, the latent heat flux was estimated using an aerodynamic method, as outlined below.

Estimation of Latent Heat Flux using Aerodynamic Methods

Under conditions of forced convection the evaporation rate is controlled by the humidity gradient in the air adjacent to the water surface and the wind speed across the surface (Chow et al., 1988). The latent heat flux is estimated from the evaporation rate using some form of the equation first proposed by Dalton in 1802:

$$H_L = -\rho \, L_w \, E_{aero} \qquad \text{where} \qquad E_{aero} = f(u)\,(e_{sat} - e_a) \tag{3.34}$$

and $f(u)$ = dimensionless wind-dependent vapour transport coefficient

$(e_{sat} - e_a)$ = vapour pressure deficit (hPa).

The vapour transport coefficient commonly takes the form:

$$f(u) = a_w + b_w \, u_z \tag{3.35}$$

where a_w ($\mathrm{m\,s^{-1}\,hPa^{-1}}$) and b_w ($\mathrm{m\,s^{-1}\,hPa^{-1}}$ per $\mathrm{m\,s^{-1}}$) are empirical coefficients and u_z ($\mathrm{m\,s^{-1}}$) is the wind speed at height z.

However, the values of these coefficients are site specific and therefore extremely variable. They are also only strictly applicable to seasonal time scales or longer. This approach is not considered further in this study.

Thornwaite-Holzman Equation

The Thornwaite-Holzman equation provides an alternative aerodynamic expression for the mass flux of water vapour which can be used to calculate the evaporation rate (Chow et al., 1988):

$$\dot{m}_v = \frac{K_V\, k^2\, \rho_m\, (q_1 - q_2)\, (u_2 - u_1)}{K_M\, [\ln(z_2 / z_1)]^2} \tag{3.36}$$

where $\dot{m}_v$ = mass flux of water vapour ($\mathrm{kg\,m^{-2}s^{-1}}$)

K_V, K_M = eddy diffusivities for water vapour and momentum, respectively ($\mathrm{m^2\,s^{-1}}$)

k = dimensionless von Kármán constant (0.41)

ρ_m = density of moist air ($\mathrm{kg\,m^{-3}}$)

q_1, q_2 = dimensionless specific humidities at heights z_1 and z_2

u_1, u_2 = wind speeds at these heights ($\mathrm{m\,s^{-1}}$).

The similarity hypothesis states that $K_V = K_M$ (Thom, 1975), when the atmosphere is neutrally stable. However, Webb (1970) reported no significant variation in the ratio of K_V to K_M in unstable or stable atmospheric conditions within the range $-0.1 < Ri < 0.2$ and perhaps extending to $Ri < 1$. The effects of atmospheric stability can be taken into account as discussed in Section 3.3.3.1.

Equation (3.36) requires the measurement of specific humidity and wind speed at two heights. This can be simplified by assuming that the wind speed reduces to zero at the aerodynamic roughness height, $z_1 = z_0$ and that the air is saturated with moisture there (Chow et al., 1988). The specific humidity q can be expressed in terms of the vapour pressure and the ambient air pressure at a given height, as:

$$q = 0.622\, e / P \tag{3.37}$$

where e = vapour pressure (hPa)

P = ambient air pressure (hPa).

The vapour pressure at height z_M is the ambient vapour pressure in the air e_a, while the vapour pressure at height $z_1 = z_0$ is the saturation vapour pressure at the water surface temperature e_{sat}.

Using Equation (3.37), the latent heat flux under conditions of forced convection can be calculated from a form of Equation (3.36):

$$H_L = \dot{m}_v K_2 L_w = \frac{0.622 K_2 L_w k^2 \rho_m (e_{sat} - e_a) u_z}{P[\ln(z_M / z_0)][\ln(z_V / z_{0V})]} \tag{3.38}$$

where z_M = measurement height for wind speed (m)

z_V = measurement height for specific or relative humidity (m)

z_0 = aerodynamic roughness height for transfer of momentum (m)

z_{0V} = roughness height for transfer of water vapour (m)

k = dimensionless von Kármán constant (0.41)

K_2 = conversion factor for units.

In general, $z_{0V} \neq z_0$, but the value of z_{0V} is extremely difficult to determine experimentally and only limited field data are available. Over a smooth water surface, and making use of Equation (3.29), Brutsaert (1982) suggested:

$$z_{0V} \sim \frac{0.624\,\nu}{u_*} \sim 0.624 \left(\frac{z_0}{0.11}\right) \sim 5.7\, z_0 \tag{3.39}$$

This leads to values which are broadly consistent with field values reported by Brutsaert (1982) for lakes under low wind conditions.

The Thornwaite-Holzman equation is suitable for estimating the latent heat flux when $\Delta t \leq 1\,\mathrm{hr}$ (Gangopadhyaya et al., 1966), provided the effects of atmospheric stability can be incorporated (Brutsaert, 1982), as described in Section 3.3.3.1.

Estimation of the Free Convection Latent Heat Flux

Under conditions of free convection which occur when winds are light or absent, evaporation is driven by buoyancy-induced convective air movements adjacent to the water surface. These maintain a relatively high temperature gradient between the water surface and the overlying air, and the latent heat transfer ($\mathrm{Wm^{-2}}$) is proportional to the temperature difference across the air-water interface:

$$H_L = K_h (T_w - T_a)(\rho_m c_p) \tag{3.40}$$

where K_h = heat transfer coefficient ($\mathrm{m\,s^{-1}}$)

T_w = water surface temperature (°C)

T_a = air temperature (°C)

c_{pw} = specific heat capacity of water at T_w ($\mathrm{J\,kg^{-1}\,{}^{\circ}C^{-1}}$)

ρ_m = density of moist air ($\mathrm{kg\,m^{-3}}$).

The heat transfer coefficient can be derived from heat transfer theory using a flat-plate analogy for the water surface (Rubin and Atkinson, 2001):

$$K_h = 0.14 \left[\frac{g\,\alpha\,\kappa_T^2\,(T_w - T_a)}{\nu} \right]^{1/3} \tag{3.41}$$

where α = thermal expansion coefficient of water ($\mathrm{{}^{\circ}C^{-1}}$)

κ_T = thermal diffusivity of water ($\mathrm{m^2\,s^{-1}}$)

ν = kinematic viscosity of water ($\mathrm{m^2\,s^{-1}}$).

Applying the Reynolds' analogy and assuming that the vapour transport and heat transport rates across the surface are equal (Rubin and Atkinson, 2001), the heat transfer coefficient is equal to a mass transfer coefficient, K_m ($\mathrm{m\,s^{-1}}$). The mass flux of water vapour is then proportional to the difference between the saturated vapour density, $\rho_{m\,sat}$ and the ambient vapour density, ρ_m:

$$\dot{m}_v = K_m\,(\rho_{m\,sat} - \rho_m) \tag{3.42}$$

This can be related to the vapour pressure deficit ($e_{sat} - e_a$) via the ideal gas law (Rubin and Atkinson, 2001), which leads to the latent heat flux under conditions of free convection:

$$\begin{aligned} H_L &= \dot{m}_v\,K_2\,L_w \\ &= 0.14\,K_2\,L_w\,\frac{M_V}{R\,T_V} \left[\frac{g\,\alpha\,\kappa_T^2\,(T_w - T_a)}{\nu} \right]^{1/3} (e_{sat} - e_a) \end{aligned} \tag{3.43}$$

where M_V = molecular mass of water vapour

= $18.016 \times 10^{-3}\ \mathrm{kg\,mol^{-1}}$

R = universal gas constant

= $8.314 \times 10^{-2}\ \mathrm{hPa\,m^3\,K^{-1}\,mol^{-1}}$

T_V = virtual air temperature (K), calculated as shown in Appendix A.

The free convection latent heat flux provides a lower bound estimate on the latent heat flux when winds are light or absent. Comparisons were made between the latent heat fluxes calculated using Equation (3.38) and Equation (3.43) over a range of air and water temperatures (10°C< T_a <25°C and 15°C< T_w <30°C) where evaporation would be expected. Previewing the field monitoring results (Chapter 6), the air temperatures often exceeded the water temperatures when T_a > 25°C, so evaporation would not have been expected and the comparisons were not made over a greater temperature range. The results indicated that the wind speed threshold for equality of the forced and free convection latent heat fluxes was generally around $0.1\,\mathrm{m\,s^{-1}}$ and always between $0.05\,\mathrm{m\,s^{-1}}$ and $0.13\,\mathrm{m\,s^{-1}}$ for the specified temperatures, humidity and atmospheric pressure. Equation (3.38) can therefore be used with a lower threshold wind speed of $0.1\,\mathrm{m\,s^{-1}}$ to determine the latent heat flux under conditions of both free and forced convection. The results are summarised in Figure A.1 in Appendix A (page 380).

3.3.3.4 Sensible Heat Flux, H_S

The sensible heat flux is associated with the conduction of heat between the water surface and the overlying air mass. The direction of the sensible heat flux may be either:

- **positive** (into the water column) when the air is warmer than the water, as is commonly the case during the day, or
- **negative** (out of the water column) when the water is warmer than the air, which is more typical overnight.

The sensible heat flux is usually less important than the radiation and latent heat fluxes over a water body, in contrast to the common situation over land (Ayra, 1988). Similar to the latent heat flux, the sensible heat flux is dependent on turbulent transport processes in the water surface layer, and hence strongly influenced by local meteorological conditions. The sensible heat flux is most commonly measured directly using eddy methods, in a manner analogous to that for the latent heat flux, or estimated from the latent heat flux using the Bowen Ratio. Since eddy measurements were precluded in the present study, the Bowen Ratio method was used.

Estimation of Sensible Heat Flux using the Bowen Ratio

The Bowen Ratio ($\mathcal{B}$) is the ratio of the sensible heat flux to the latent heat flux, and can be calculated from measurements of temperature and vapour pressure at two different heights, as follows (Chow et al., 1988):

$$H_S = \mathcal{B}\, H_L \quad \text{where} \quad \mathcal{B} = \gamma \left(\frac{T_2 - T_1}{e_2 - e_1} \right) = \gamma \left(\frac{T_w - T_a}{e_{sat} - e_a} \right) \tag{3.44}$$

where γ is the psychrometric coefficient (hPa °C^{-1}). This coefficient is calculated as shown in Appendix A.

This method also makes use of the similarity hypothesis for the eddy diffusivities for momentum, water vapour and heat ($K_M = K_V = K_H$). This is valid in a neutral boundary layer, but often assumed to apply under other stability conditions (Thom, 1975). In the absence of eddy measurements, the Bowen Ratio provides a simple method for estimation of the sensible heat flux if the latent heat flux is known. However, any errors in estimation of the latent heat flux will be transferred and possibly increased through the sensible heat flux.

3.4 Effects of Macrophytes on Surface Energy Fluxes

The presence of an emergent macrophyte canopy is expected to significantly influence the radiation and other surface energy fluxes, compared with an unvegetated water body. Modifications to the surface fluxes described in Section 3.3 are primarily dependent on the structural properties of the canopy. It is not the objective of this study to describe the energy regime within the emergent macrophyte canopy in great detail, but rather to determine the energy fluxes at the water surface beneath the canopy. This is shown schematically in Figure 3.5. Hence, an understanding of the radiation regime and fluxes of latent and sensible heat within the canopy volume are important only insofar as they influence the energy fluxes at the water surface.

The shortwave radiation flux is the most important contributor to the net heat flux between the atmosphere and a stand of vegetation (Ross, 1975), and predicting the net shortwave radiation flux at the water surface beneath an emergent canopy is one of the primary objectives of this study. Hence, particular emphasis is placed on the structural properties influencing attenuation of shortwave radiation by an emergent macrophyte canopy. Fortunately, extensive work has been published addressing energy exchanges between the air and the canopies of commercial crops, many of which have a similar canopy architecture to the common emergent macrophyte species.

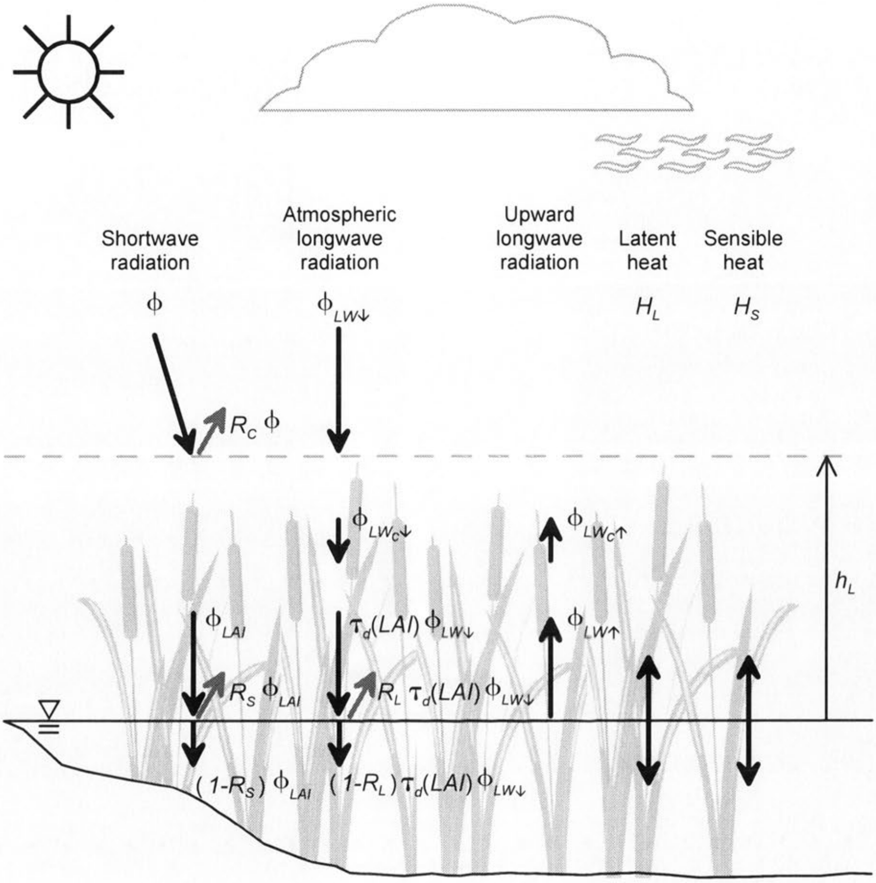

Figure 3.5: Radiation and major thermal fluxes at the water surface beneath an emergent macrophyte canopy.

3.4.1 Structural Properties of an Emergent Macrophyte Canopy

The structural properties of a canopy describe the arrangement of canopy elements in space, and the important structural attributes are (Asrar and Myneni, 1991):

(1.) vertical distribution of foliage area

(2.) orientation of canopy foliage

(3.) horizontal dispersion of canopy elements.

3.4.1.1 Vertical Distribution of Foliage

The vertical distribution of foliage area is conventionally described by the foliage area density function and the leaf area index (Ross, 1975).

- The **foliage area density function**, *a(z)*, is the one-sided foliage area per unit volume of canopy at elevation z (m), with units of $\mathrm{m^2\,m^{-3}}$.

- The **leaf area index**, *LAI*, ($\mathrm{m^2m^{-2}}$) is the total one-sided foliage surface area enclosed within a vertical cylinder of unit cross-sectional area and height h_L, where h_L is the canopy height (m). Typical values of LAI range from 3 to 5 for species with predominantly horizontal elements, and may be as high as 10 for predominantly vertical canopies (Monteith and Unsworth, 1990).

- The **downward cumulative leaf area index**, *LAI(z)*, is more commonly used in canopy radiation studies, where *LAI(z)* is the total one-sided foliage area enclosed within a vertical cylinder of unit cross-sectional area between the top of the canopy and elevation z:
$$LAI\,(z) = \int_z^{h_L} a(z)\,dz \tag{3.45}$$
By definition, $LAI{=}LAI(0)$ at the water surface. The canopies of many common emergent macrophyte species actually comprise stems rather than leaves, and a stem area index can be defined analogously to the leaf area index. However, the term LAI is retained here for consistency with the literature.

According to Norman (1975), LAI is the most important structural parameter when determining the attenuation of shortwave radiation by a canopy, so field efforts should be focused accordingly. Detailed measurements of the foliage orientation and inclination distributions are laborious and time-consuming, so assumptions are commonly made about the nature of these distributions, as described below. The predominant canopy element for many common emergent macrophyte species is a stem which can be approximated by a simple geometrical shape, so it is only necessary to consider one type of element. In canopies with more complex structures it may be necessary to consider stems, leaves and flower structures separately, and to combine the results.

3.4.1.2 Orientation of Canopy Foliage

Ross (1975) demonstrated that the transfer of shortwave radiation through a plant canopy is strongly dependent on the inclination and azimuth of canopy foliage. Geometrical characteristics of individual plants can be treated as random variables, and the inclination and the azimuth orientation of the canopy foliage can therefore be assumed independent of one another (Ross, 1981).

Inclination Distribution Function

The orientation of any canopy element can be described in terms of an elevation above the horizon (θ_L) and an azimuth orientation from north (φ_L). While the technical literature uses the inclination from the vertical of the normal to a canopy element, Figure 3.6 shows that this is numerically equal to the elevation of a canopy element above the horizon. The latter will be used hereafter for simplicity, although the term "inclination distribution" will be retained.

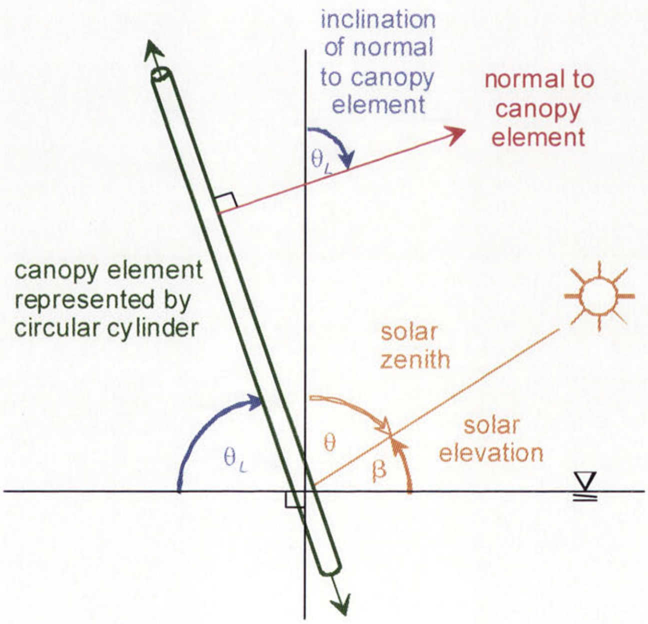

Figure 3.6: Schematic illustration of the equivalence between the inclination of the normal to a canopy element and the elevation of the canopy element above the horizon, θ_L.

The distribution function for all elements within a canopy can be described by dividing the upper hemisphere into portions of equal incremental solid angle $\Delta\,\Omega_L = \sin\theta_L\,\Delta\,\theta_L\,\Delta\,\varphi_L$

and determining the fraction of total foliage contained within each increment. The inclination distribution function for the canopy is then determined as follows (Ross, 1981):

$$\frac{1}{2\pi}\, g_L(\theta_L, \varphi_L) \;=\; \frac{1}{\Delta\Omega_{Li}}\, \frac{\Delta S_{Li}}{\sum_i S_{Li}} \tag{3.46}$$

where ΔS_{Li} = incremental foliage area (m^2) contained within the solid incremental angle $\Delta\Omega_{Li}$ (rad)

$\sum_i S_{Li}$ = total foliage area within the canopy volume (m^2).

As a probability distribution, this function must satisfy the following condition (Ross, 1981):

$$\frac{1}{2\pi}\int_0^{2\pi} d\varphi_L \int_0^{\pi/2} g_L(\theta_L, \varphi_L) \sin\theta_L \, d\theta_L \;\equiv\; 1 \tag{3.47}$$

However, it is generally assumed that there is no azimuth preference, so Equation (3.47) reduces to (Ross, 1981):

$$\int_0^{\pi/2} g_L(\theta_L) \sin\theta_L \, d\theta_L \;=\; 1 \tag{3.48}$$

where $g_L(\theta_L)$ is the probability of a stem having an elevation of θ_L above the horizon.

The G-Function

The G-function was introduced by Ross and Nilson (Ross, 1981) in preference to the inclination distribution function defined above. The G-function is a dimensionless projection of the leaf area distribution, which accounts for the vertical distributions of leaf inclination and azimuth orientation, and the influences of these on the shadow projected by the canopy onto a horizontal plane. Assuming no azimuth preference, the G-function is defined as follows:

$$G(z, \theta, \theta_L) \;=\; \int_0^{\pi/2} g_L(z, \theta_L)\, A(\theta, \theta_L) \sin\theta_L \, d\theta_L \tag{3.49}$$

where θ = solar zenith angle, from the vertical

$g_L(z, \theta_L)$ = foliage area inclination at elevation z or depth *LAI(z)*

and $A(\theta, \theta_L)$ accounts for the combined effects of solar elevation and canopy inclination on the projected area of the canopy. This mathematical expression of the G-function is quite complex and difficult to apply. Simple expressions for the G-function for some common canopy distributions are summarised in Table 3.3.

Assumed distribution of canopy elements	Inclination distribution function (1) $g_L(z, \theta_L)$	G-function $G(\theta)$ (2)
Horizontal or planophile (3)	$\delta(\theta_L - 0)$ (5)	$\cos\theta$
Vertical or erectophile (4)	$\delta(\theta_L - \pi/2)$	$2/\pi \sin\theta$
Uniform or spherical	1	1/2

Notes to Table:

1. Assumes no azimuth preference
2. θ is the solar zenith (from vertical)
3. Predominantly horizontal when all canopy elements are within 15° ($\pi/12$) of the horizon
4. Predominantly vertical when all canopy elements are within 15° ($\pi/12$) of the vertical
5. δ is the Dirac delta function

Table 3.3: Simplified expressions for the G-function for common canopy distributions (from Ross, 1981).

Nilson (1991) presented an approximation to the G-function for other canopy inclination distributions, where there is no azimuth preference. The G-function is calculated as a weighted function of the G-function for the uniform, vertical and horizontal canopy distributions given in Table 3.3:

$$
\begin{aligned}
G(z, \theta, \theta_L) &\sim c_1 \left[G(z, \theta)_{\text{uniform}}\right] + c_2 \left[G(z, \theta)_{\text{vertical}}\right] + c_3 \left[G(z, \theta)_{\text{horizontal}}\right] \\
&= c_1 \left[\frac{1}{2}\right] + c_2 \left[\frac{2}{\pi}\sin\theta\right] + c_3 \left[\cos\theta\right] \qquad (3.50)
\end{aligned}
$$

The coefficients c_1, c_2 and c_3 are derived from a discrete inclination function where:

$g_{L1}(z, \theta_L)$ is defined over the interval 0° to 15° above the horizon

$g_{L2}(z, \theta_L)$ is defined over the interval 15° to 30° above the horizon

$\vdots \quad \vdots$

$g_{L6}(z, \theta_L)$ is defined over the interval 75° to 90° above the horizon.

Nilson's coefficients are calculated as follows, where $c_1 + c_2 + c_3 = 1.0$:

$$
\begin{aligned}
c_1 &= \left[1 - g_{L1}(z, \theta_L) - g_{L6}(z, \theta_L)\right] / 0.707 \\
c_2 &= g_{L6}(z, \theta_L) - 0.259\, c_1 \\
c_3 &= 1 - c_1 - c_2 \qquad (3.51)
\end{aligned}
$$

The weighting in the calculation of the coefficients suggests that the simplified coefficients are probably best representative of the G-function when the measured inclination distribution function differs only slightly from a spherical or uniform distribution.

3.4.1.3 Horizontal Dispersion of Canopy Elements

The horizontal distribution of canopy elements within monocultural stands has been referred to in the literature as the dispersion, to distinguish it from the vertical distribution of canopy elements. Three common canopy dispersion models are illustrated in Figure 3.7, and the features of these are summarised in Table 3.4.

In modelling applications, the canopy foliage is generally assumed to be randomly dispersed, which implies horizontal homogeneity (Ross, 1981). However, experimental data of Ross (1981) indicate that this assumption is not always valid, and that the distribution of plants within a natural canopy instead tends more towards a clumped or a semi-regular dispersion. Further complications arise when the dispersion varies between horizontal layers within a canopy. Despite this, Lantinga et al. (1999) report that the effects of variations tend to compensate over the depth of the canopy, so there are no significant effects on the net attenuation of shortwave radiation.

For simplicity, and given the reasoning above, it is assumed in this study that the emergent macrophytes are randomly dispersed, and that the dispersion is equivalent at all levels in the canopy. It is also assumed that the horizontally-homogeneous canopy is infinite in extent (Myneni et al., 1991), so that boundary effects at the edges of the canopy can be neglected.

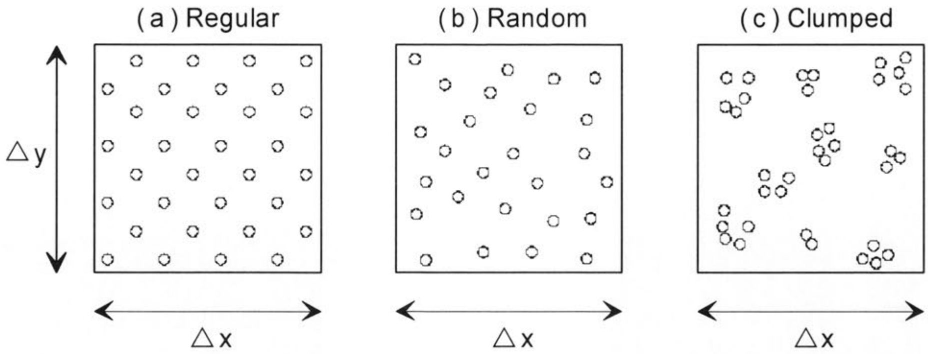

Figure 3.7: Three common canopy dispersion models: (a) regular dispersion, (b) random dispersion and (c) clumped dispersion.

Regular Canopy Dispersion
Individual plants are located at the nodes of a parallelogram grid with equal dimensions
Small gaps in the foliage, therefore maximal coverage of the substrate
No significant degree of mutual shading
Net canopy attenuation of shortwave radiation is higher than for random distribution
Does not occur in natural communities, but common in cultivated stands
Random Canopy Dispersion
Equal probability of plant occurrence at any point within the canopy area
Commonly adopted when modelling attenuation of shortwave radiation by a canopy
Common in cultivated crops
Clumped Canopy Dispersion
Individual plants grow close together in groups
Large gaps are common in the foliage, therefore lower coverage of the substrate
Considerable mutual shading
Net attenuation of shortwave radiation by the canopy is greater than for a random dispersion
Predominant canopy dispersion in natural communities

Table 3.4: Characteristics of three common dispersion models for a plant canopy (from Ross, 1981; Lantinga et al., 1999; Lemur and Blad, 1974).

3.4.1.4 Optical Properties of a Canopy

The optical properties of the canopy foliage control the shortwave radiation field within the canopy volume and are commonly defined in terms of the absorption, transmission, and reflection coefficients. These should sum to unity for any given foliage surface.

As discussed by Ross (1981) and Guyot (1998), the optical properties of a canopy foliage are dependent on a number of factors, including the structure and surface characteristics of the canopy foliage, the moisture content and the age and health of the canopy foliage. The optical properties are also influenced by the solar elevation, which varies with time of day and season.

The attenuation of shortwave radiation by a canopy is simplified for photosynthetically-active radiation (PAR) compared with global shortwave radiation, due to the high absorption of radiation in the PAR waveband. Up to 90 % of the incident PAR is absorbed by green plants, compared with only 40 to 75% for global shortwave radiation (Ross, 1981). Vegetation has very low transmittance ($< 5\%$) in the PAR waveband and this is often neglected. Reflection by a canopy is low in the PAR waveband ($< 15\%$), but up to 30% in the global shortwave radiation band (Gates, 1980). The PAR reflection coefficient is often neglected completely. Multiple scattering can also be neglected. Modelling results based on PAR are therefore less sensitive to the optical properties of the canopy than other wavebands (Torssell and McPherson, 1977), including the global shortwave radiation band.

3.4.1.5 Spatial and Temporal Variation in Canopy Properties

The structural and optical properties of a canopy are constant neither in space nor in time, and spatial and temporal variability in these properties should be considered when modelling the attenuation of shortwave radiation by a canopy. Spatial averages are often implemented, which implies that the canopy is horizontally homogeneous, and that mean canopy properties vary only with height above the water surface.

The shortwave radiation field within a canopy also varies over a number of different time scales, including (Ross, 1975):

- very rapid fluctuations with a period of the order of seconds, due to wind-induced movement of canopy elements

- fluctuations with a period of around 10 minutes, due to the movement of clouds
- fluctuations with a period of around one hour, due to the movement of the sun across the sky
- diurnal variation
- annual variation, including seasonal changes to canopy structure and density.

The higher frequency fluctuations do not appear to significantly affect the mean attenuation of shortwave radiation by a canopy (Norman, 1975), although changes in solar elevation, diurnal and seasonal variation are significant.

3.4.2 Effects of Macrophytes on Radiation Fluxes

3.4.2.1 Shortwave Radiation Flux Beneath an Emergent Canopy

The two components of the global shortwave radiation flux within and beneath a plant canopy are (Ross, 1975):

- **direct shortwave** radiation, which comprises directional shortwave radiation which penetrates through gaps in the canopy without interception by the canopy foliage
- **diffuse shortwave** radiation, which comprises shortwave radiation which has been scattered during passage through the atmosphere or scattered by the canopy foliage.

It is not easy to measure the shortwave radiation components individually, and a net downward or upward shortwave radiation flux is usually monitored instead. The direct shortwave radiation flux may exceed the diffuse flux in shaded areas by several orders of magnitude, and the latter is generally neglected under cloudless conditions (Ross, 1975). Modelling efforts concentrate on the direct shortwave radiation component, which is the approach adopted here.

Most of the relevant literature is concerned with modelling the radiation regime in agricultural crops (for example, Ross, 1975; Nilson, 1991). It appears that the study of Waters (1998) is the only work which explicitly considers shortwave radiation fluxes in an emergent macrophyte canopy and it was limited to a single series of measurements at one site on one afternoon. However, many of the common emergent macrophytes have a similar canopy structure to agricultural species. The following sections provide a review of simple models for predicting canopy attenuation of shortwave radiation.

Net Transmission of Shortwave Radiation through a Canopy

Ross (1975) calculated the theoretical net transmission coefficients for global shortwave radiation (τ_S) and PAR (τ_{PAR}) through a canopy, as shown in Figure 3.8. The net transmission coefficient is defined as the proportion of the total incident shortwave radiation which is transmitted through the canopy to the water surface.

From Figure 3.8 it can be seen that the correlation between the net transmission coefficients is highly linear for $\tau_{\mathrm{PAR}} \geq 0.23$ ($r^2 > 0.99$ for $n = 6$):

$$\tau_S = 0.78\,\tau_{\mathrm{PAR}} + 0.22 \tag{3.52}$$

where τ_S = net transmission coefficient for global shortwave radiation

τ_{PAR} = net transmission coefficient for PAR.

However, τ_S is significantly overestimated by this relationship for smaller τ_{PAR}. Linear regression through all of the data points of Ross (1975) produces a less satisfactory

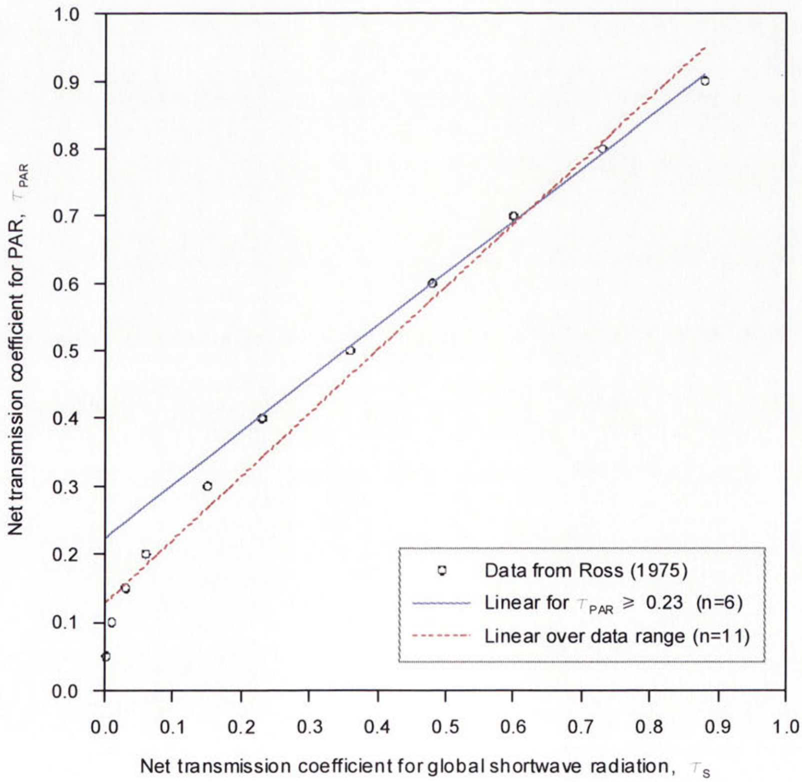

Figure 3.8: Relationship between the theoretical net transmission coefficients for global shortwave radiation and PAR, as calculated by Ross (1975). Data from his Table IX, p.39.

relationship ($r^2 = 0.98$ for $n = 11$), which overestimates τ_S when $\tau_{PAR} > 0.73$ and underestimates τ_S when $\tau_{PAR} < 0.03$.

Equation (3.52) has been adopted in this investigation, noting that it is strictly valid only within the range $0.2 < \tau_{PAR} < 0.9$, and that it overestimates τ_S for lower net transmission of PAR. However, as discussed in Section 6.3.3, most of the measured net transmission coefficients for PAR were greater than 0.2, and Equation (3.52) is therefore generally applicable.

Simple Models for Attenuation of Shortwave Radiation by a Canopy

There are numerous detailed and complex models available in the literature to predict the shortwave radiation regime within a plant canopy, although the data requirements and computational effort are unwarranted when only the net transmission of shortwave radiation is required. This can often be achieved using a relatively simple model. The simple canopy radiation models reviewed here assume that the canopy is horizontally homogeneous, so the canopy properties can be assumed to vary only with height above the water surface. As discussed by Goudriaan (1977), Ross (1981) and Guyot (1998), this is a common assumption in canopy modelling.

The simple models also assume that any radiation intercepted by canopy foliage is absorbed, with negligible reflection, scattering or re-emission. As discussed earlier, this is not a valid assumption for the global shortwave radiation spectrum, but is reasonable for photosynthetically-active radiation (Ross, 1981). The PAR waveband is modelled in this study, and in this context, simple models are defined as those which do not explicitly account for transmission or reflection of PAR within the canopy.

The simple canopy radiation models can be broadly classified as either empirical or theoretical. Both represent the canopy by an array of simple geometrical structures with characteristic dimensions and consider the shadows they cast on the substrate. They are generally restricted to canopies of a single species with a relatively simple structure. For example, many common emergent macrophytes can be represented by vertical cylinders or long, narrow rectangles with characteristic dimensions at various heights above the water surface.

The most common of the simple canopy attenuation models is Beers Law, which describes the exponential attenuation of radiation within a medium. There are several forms of Beers law, which share a common set of assumptions. These assumptions are discussed in detail by Rosenberg (1974) and Larsen and Kershaw (1996), and include the following:

- the canopy is a three-dimensionally homogeneous medium
- canopy foliage is randomly dispersed
- the optical properties of the canopy are isotropic and constant in time
- the canopy foliage is inclined horizontally
- the shortwave radiation flux is isotropic
- all incident shortwave radiation is absorbed by canopy foliage, with no reflection or transmittance
- the shortwave attenuation coefficient is constant with depth and time.

Most of these assumptions represent gross simplifications of conditions in natural plant canopies, but despite the shortcomings, Beers Law is very widely employed. Ross (1981) suggested that Beers Law should be used only as a first approximation to a much more complex process, although it has successfully approximated field measurements of the net shortwave radiation and PAR profiles within and beneath a canopy (see for example Miller, 1981; Goudriaan, 1977; Larsen and Kershaw, 1996; Monteith and Unsworth, 1990). The simple canopy attenuation models are reviewed briefly in the following sections and evaluated with reference to field PAR data in Chapter 6.

Beers Law using Depth of Penetration into the Canopy

The simplest empirical form of Beers Law models the attenuation of PAR as a function of the depth of penetration into the canopy:

$$\phi_z = \phi \exp\left[-\mathcal{K}_z \left(h_L - z \right)\right] \tag{3.53}$$

where

ϕ_z	=	PAR flux within the canopy (Wm^{-2}) at height z (m)
ϕ	=	PAR flux above the canopy (Wm^{-2})
$\mathcal{K}_z$	=	attenuation coefficient (m^{-1})
h_L	=	canopy height above the water surface (m)
$(h_L - z)$	=	depth of penetration into the canopy (m).

The attenuation coefficient is derived from field PAR measurements at various levels in the canopy.

Because this form of Beers Law doesn't explicitly account for the structural properties of the canopy, it is difficult to compare between different canopy types and densities (Norman, 1975). Shortwave radiation data from field measurements is required to determine site-specific attenuation coefficients.

Beers Law using Leaf Area Index

An alternative empirical form of Beers Law replaces the depth of penetration with the downward cumulative leaf area index:

$$\phi_{LAI(z)} = \phi \exp\left[-\mathcal{K}_{LAI}\, LAI(z)\right] \tag{3.54}$$

where $LAI(z)$ = downward cumulative leaf area index ($m^2 m^{-2}$) at height z (m)

ϕ_{LAI} = PAR flux in the canopy below $LAI(z)$ (Wm^{-2})

$\mathcal{K}_{LAI}$ = dimensionless attenuation coefficient.

The attenuation coefficient can be derived from field radiation measurements. This empirical form of Beers Law is preferred over Equation (3.53) because it incorporates vertical variability in the canopy structure through the $LAI(z)$ term (Miller, 1981).

Beers Law using Geometrical Shape Factors

The $\mathcal{K}_{LAI}$ coefficient can also be derived using a purely theoretical or geometrical approach, obviating the need for field PAR measurements. Ross (1981) outlined a geometrical shape factor method, where the shape factor is defined as the area of horizontal shadow cast by a canopy, per unit horizontal canopy area. Monteith and Unsworth (1990) demonstrated that the shape factor is numerically equal to the $\mathcal{K}_{LAI}$ coefficient. Shape factors are available for some common canopy inclination models, as shown in Table 3.5.

For a simple canopy structure, use of the geometrical shape factors should improve predictions compared with the empirical forms of Beers Law. The shape factor accounts for the vertical variability in the canopy structure through the LAI term, and also considers the solar elevation β, and mean inclination of canopy foliage $\overline{\theta}_L$. If LAI and the canopy inclination can be estimated, and β is calculated from standard astronomical formulae (see Appendix A), there is no requirement for field measurements.

Canopy Inclination Model	Geometrical Shape Factor $\equiv \mathcal{K}_{LAI}$
Horizontal distribution	1
Vertical distribution	$\frac{2}{\pi}\cot\beta$
Uniform or Spherical distribution	$1/(2\sin\beta)$
Inclined Canopy (i) $\beta \geq \overline{\theta}_L$	$\cos\overline{\theta}_L$
(ii) $\beta < \overline{\theta}_L$	$\frac{1}{\pi}[(\pi - 2\theta_0)\cos\overline{\theta}_L + 2\sin\overline{\theta}_L\cot\beta\sin\theta_0]$

Notes to Table:

- β is the solar elevation above the horizon
- $\overline{\theta}_L$ is the mean elevation of the canopy elements above the horizon
- $\theta_0 = \cos^{-1}(\tan\beta\cot\theta_L)$

Table 3.5: Geometrical shape factors for common canopy inclination models, assuming no azimuth preference and a random canopy dispersion (Monteith and Unsworth, 1990).

Beers Law using the G-function

As outlined on page 74, the G-function takes into account the variation of foliage area, leaf inclination and azimuth orientation with height, and the influences of these factors and solar elevation on the shadow projected by a canopy. An attenuation coefficient can be calculated from the G-function as follows (Ross, 1975):

$$\mathcal{K}_{LAI} = \frac{G(z, \theta, \theta_L)}{\cos\theta} = \frac{G(z, \theta, \theta_L)}{\sin\beta} \tag{3.55}$$

This attenuation coefficient has advantages over the previous methods, because it allows for a distribution of canopy inclination angles and for changes in the solar elevation. It also allows for variation in the foliage density with elevation.

3.4.2.2 Longwave Radiation Beneath an Emergent Canopy

The longwave radiation regime within a plant canopy comprises four main components (Ross, 1975):

- downward radiation from the atmosphere which has not been intercepted by foliage higher in the canopy ($\phi_{LW\downarrow}$)
- downward radiation emitted from foliage higher in the canopy ($\phi_{LW_{C\downarrow}}$)
- upward radiation emitted from foliage lower in the canopy ($\phi_{LW_{C\uparrow}}$)
- upward longwave radiation from the underlying water surface which has not been intercepted by foliage lower in the canopy ($\phi_{LW\uparrow}$).

Net Downward Longwave Radiation Flux, $\phi_{LW_{C\downarrow}}$

Assuming that fluxes of longwave radiation from the atmosphere, the water surface and the canopy foliage are all isotropic, the net downward longwave radiation flux at the water surface beneath an emergent canopy is calculated from (Ross, 1975):

$$\begin{aligned}\phi_{LW\downarrow NET} &= \phi_{LW_C} - \tau_d(LAI)\,(\phi_{LW_C} - \phi_{LW\downarrow}) \\ &= \{1 - \tau_d(LAI)\}\,\phi_{LW_C} + \tau_d(LAI)\,\phi_{LW\downarrow} \end{aligned} \tag{3.56}$$

where ϕ_{LW_C} = longwave radiation flux from canopy foliage (Wm^{-2})

$\phi_{LW\downarrow}$ = atmospheric longwave flux above the canopy (Wm^{-2})

$\tau_d(LAI)$ = dimensionless surface transmission coefficient for $\phi_{LW\downarrow}$.

<u>*Surface Transmission Coefficient for Atmospheric Longwave Radiation,* $\tau_d(LAI)$</u>

Given the assumption of isotropic atmospheric longwave radiation, the transmission coefficient for atmospheric longwave radiation can be approximated by the canopy transmission coefficient for (isotropic) diffuse shortwave radiation (Ross, 1975):

$$\tau_d(LAI) = 2\int_0^{\pi/2} \exp\left[-\mathcal{K}_{LAI}\,LAI\right]\cos\theta\sin\theta\,\mathrm{d}\,\theta \tag{3.57}$$

where θ = solar inclination from the vertical ($^\circ$)

$\mathcal{K}_{LAI}$ = shortwave attenuation coefficient (m^2m^{-2})

LAI = downward cumulative leaf area index (m^2m^{-2}).

Longwave Radiation from Canopy Foliage, ϕ_{LW_C}

The longwave radiation flux from canopy foliage is calculated using the Stefan-Boltzmann law:

$$\phi_{LW_C} = \pm\,\varepsilon_c\,\sigma\,T_c^{\,4} \tag{3.58}$$

where ε_c = canopy emissivity (assumed constant at $\varepsilon_c = 1.0$)

σ = Stefan-Boltzmann constant ($Wm^{-2}\,K^{-4}$)

T_c = surface temperature of the canopy foliage (K).

The downward canopy longwave radiation flux is positive and the upward canopy longwave radiation flux is negative.

Longwave radiation exchanges within the canopy tend to equalise temperatures throughout the canopy volume, and between different canopy elements (Miller, 1981). The temperature of the canopy foliage is often assumed constant and equal to the air temperature within the canopy, so the canopy longwave radiation flux can be assumed isotropic. This assumption is valid provided water supply is not a limiting factor and the ambient relative humidity is not excessively high or low (Ross, 1981), whereupon the foliage temperature could vary considerably from the surrounding air temperature. If water was a limiting factor, the temperature of illuminated leaves would rise above the air temperature as they absorbed radiation, while the temperature of shaded leaves would remain close to the air temperature.

Longwave Reflection from Canopy Foliage

The reflection of longwave radiation from the surface of canopy foliage is generally $< 5\%$ and often ignored (Ross, 1975; Zhang et al., 1997). This is a reasonable assumption, given the high absorption of longwave radiation by green plants (Monteith and Unsworth, 1990).

Longwave Emissivities for Emergent Macrophytes, ε_C

No studies could be located which reported the longwave emissivities for emergent macrophytes, although many commercial crops have similar structural properties. Longwave emissivities for a selection of grass and crop species are given in Table 3.6. The slight departure from ideal blackbody behaviour is often ignored, and leaves or stems are generally assumed to have a longwave emissivity of 1.0.

Vegetation Surface	Longwave Emissivity		References
	Lower Value	Upper Value	
Long grass (1 m)	0.90	0.95	Ayra (1988), Guyot (1998)
Short grass (0.2 m)	0.90	0.95	Ayra (1988), Guyot (1998)
Agricultural crops	0.90	0.99	Guyot (1998)
Maize	0.94	0.95	Monteith and Unsworth (1990)
Sugar cane	0.99	0.99	Monteith and Unsworth (1990)

Table 3.6: Longwave emissivities for selected vegetation species with structural properties similar to common emergent macrophyte species.

Longwave Reflection from the Water Surface, R_L

The reflection of atmospheric longwave radiation from the water surface beneath an emergent canopy is small, and assumed similar to that for open water, $R_L = 0.03$.

Upward Longwave Radiation Beneath an Emergent Canopy, $\phi_{LW\uparrow}$

The upward longwave radiation flux from the water surface is calculated according to the Stefan-Boltzmann law, Equation (3.22), which is repeated below:

$$\phi_{LW\uparrow} = -\varepsilon_{\mathrm{w}}\,\sigma\,T_w^4$$

where ε_{w} = dimensionless emissivity of the water
σ = Stefan-Boltzmann constant ($\mathrm{Wm^{-2}\,K^{-4}}$)
T_w = water surface temperature (K).

The upward longwave radiation flux is a function of the water surface temperature and emissivity, and only indirectly affected by the presence of the canopy.

3.4.3 Effects of Emergent Macrophytes on Other Surface Energy Fluxes

3.4.3.1 Momentum Exchange Beneath an Emergent Canopy

The exchange of heat, moisture and other scalars between a vegetation canopy and the atmosphere is driven by the turbulent wind field (Finnigan, 2000). Within a canopy, the flux of momentum is no longer conservative with elevation, as momentum is absorbed by interaction with the canopy elements. This occurs primarily in the upper reaches of the canopy, so the momentum flux at the underlying surface is generally very low (Guyot, 1998). Linacre et al. (1970) found wind speeds measured over a swamp of *Typha orientalis* and *Typha domingensis* were less than those measured simultaneously over a nearby lake in a similar topographic setting. Waters (1998) demonstrated that the wind-induced shear velocity in the water beneath a canopy of emergent *Typha orientalis* was considerably smaller than in an open water zone exposed to the same wind forcing.

Constant stress layers develop above the canopy and in a thin layer close to the water surface (Niedoroda et al., 1991) while the velocity profile within the canopy is approximately exponential (Cionco, 1972). A displaced logarithmic wind profile is commonly applied in the constant stress layer above a plant canopy (Thom, 1975), as shown in Figure 3.9.

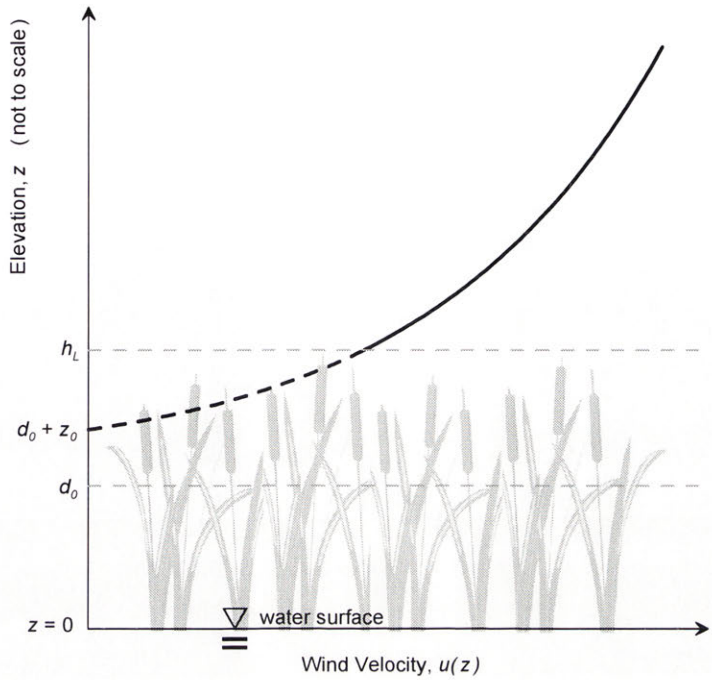

Figure 3.9: Displaced wind profile above an emergent macrophyte canopy.

Assuming fully turbulent flow in neutrally-stable conditions:

$$u_z = \left(\frac{u_*}{k} \right) ln \left(\frac{z - d_0}{z_0} \right) \tag{3.59}$$

where d_0 is the zero-plane displacement height (m) and the other variables are as defined earlier.

This is a more general form of Equation (3.25), which takes into account the height and the roughness of the surface elements. Both z_0 and d_0 can be calculated if the drag profile within the canopy is known (Raupach and Thom, 1981), but they are most commonly estimated using empirical formulae. Simple relationships and typical values of these parameters are given below.

Aerodynamic Roughness Length of an Emergent Canopy, z_0

The roughness of a vegetated surface is determined by the canopy height, structure and flexibility of the canopy elements, canopy density and distribution of the foliage area within the canopy volume. Shaw and Pereira (1982) found the aerodynamic roughness length to be a unimodal function of the canopy density:

- in **sparse canopies** (nominally $LAI \leq 1.0$):
  - z_0 increases with increasing canopy density
  - effective canopy roughness is greatest when the foliage density is concentrated in the upper layers of the canopy, which are exposed to higher wind speeds
- in **dense canopies** ($LAI \geq 5.0$):
  - z_0 decreases with increasing canopy density as the flow progressively skims across the canopy rather than penetrating through the canopy array
  - effective roughness is least when the foliage area is concentrated near the top of the canopy, providing a smoother surface to the air flow
  - effective roughness is greatest when the top of the canopy is relatively open, allowing momentum to penetrate deeper into the canopy.

The foliage density of most common emergent macrophyte species decreases with increasing height above the water surface. Note that there is no universal acceptance as to what value for LAI constitutes a sparse or a dense canopy. Ross (1981) provided examples of agricultural crops with LAI typically in the range from 2 to 3, but as high as 8, while Del Pozo and Dennett (1999) cited a "dense" crop with LAI=6. As discussed in Chapter 6, in this study a canopy with $LAI \leq 1.0$ is considered sparse while a canopy with $LAI \geq 5.0$ is considered dense.

The value of z_0 depends only on the surface roughness for low to moderate wind speeds, although Panofsky and Dutton (1984) argue that z_0 may be dependent on wind speed for flexible roughness elements. The stems of many common emergent macrophyte species are flexible, so the possible wind-speed dependence of z_0 should be acknowledged.

The aerodynamic roughness length is commonly estimated from the mean height of surface roughness elements, or the mean canopy height. For a variety of surfaces, Brutsaert (1982) reported that $0.06\,h_L < z_0 < 0.238\,h_L$. Smith (1991) suggested $z_0 = 0.123\,h_L$, while Jackson (1981) reported an average $z_0 = 0.15\,h_L$ for vegetation. Table 3.7 shows the range of z_0 values reported in the literature for crops resembling common emergent macrophyte species. These values apply to aerodynamic roughness length over a land surface, and are expected to differ over a water surface which is not necessarily stationary. However, in the absence of literature specific to emergent macrophytes, these values can be used as initial estimates.

Canopy Description	Canopy Height h_L (m)	Aerodynamic Roughness z_0 (mm)	References
Vegetation	1 – 2	200	Garratt (1992)
Grass - thin	0.5	50	Garratt (1992)
Grass - sparse	0.45	18	
Grass - sparse	0.65	39	
Grass - long	N/A	6.5 – 50	Brutsaert (1982)
	N/A	23	Guyot (1998)
	N/A	50	Panofsky and Dutton (1984)
	N/A	40 – 100	Burman and Pochop (1994)
Agricultural crops	N/A	1.2 – 220	Burman and Pochop (1994)
	N/A	50 – 200	Guyot (1998)
	N/A	400 – 700	Brutsaert (1982)
Wheat	1.0	50	Garratt (1992)
Corn	0.8	64	Garratt (1992)
Sugar cane	N/A	40 - 90	Burman and Pochop (1994)

Table 3.7: Typical values of the aerodynamic roughness length z_0 for various vegetation canopies, neglecting any wind speed dependence for flexible canopy elements.

Zero Plane Displacement Height, d_0

The zero-plane displacement height is defined as the height of the aerodynamic origin (Raupach, 1992) and also interpreted as the mean level of momentum absorption by the canopy (Thom, 1975). The canopy is assumed to be horizontally uniform, as discussed in Section 3.4.2.1. The zero-plane displacement height increases from $d_0 \sim 0$ in a very sparse canopy to $d_0 \sim h_L$ in a very dense canopy (Shaw and Pereira, 1982).

The zero-plane displacement height can be estimated from the mean height of the canopy roughness elements, h_L. Jackson (1981) suggested $d_0 \,/\, h_L = 0.7$ over a large range of z_0, while Brutsaert (1982) reported $d_0 \,/\, h_L \sim 2/3$ for natural crop surfaces. The ratio $d_0 \,/\, h_L$ is less sensitive to the nature of the surface or other environmental factors than the relationship between z_0 and h_L, and also relatively insensitive to the method used to calculate it (Brutsaert, 1982). Relationships between z_0, d_0 and h_L are better defined for denser canopies than sparse canopies (Shaw and Pereira, 1982).

Strictly, the zero-plane displacement height varies with atmospheric stability, although d_0 is often estimated during conditions of neutral stability and assumed to apply when the atmosphere is unstable (Garratt, 1992). Garratt (1992) even suggested that d_0 could be ignored if $z_M > 10\,h_L$, where z_M is the wind measurement height.

3.4.3.2 Latent Heat Flux Beneath an Emergent Canopy

In the macrophyte zones of a wetland, evapotranspiration comprises both evaporation from the water surface and transpiration from the macrophytes. The latent heat flux is a major energy sink in many wetlands and often remains negative throughout the evening, sustained by heat loss from the water column. During summer, Souch et al. (1996) found that the latent heat flux accounted for nearly 50% of the net radiation flux during the day, while the sensible heat flux was less than 20%, and the remainder of the net radiation flux was used to heat the water column.

There is apparently conflicting evidence in the literature as to whether emergent macrophytes increase or decrease the overall evaporation from a wetland, compared with an unvegetated body of water (Koch and Rawlik, 1993). Some researchers report increased evapotranspiration from emergent macrophyte zones (for example, Sanchez-Carrillo et al., 2001). Some found reduced evapotranspiration from macrophyte zones (for example, Linacre et al., 1970), while others found no significant difference between vegetated and unvegetated zones (for example, Abtew, 1996). An energy budget approach suggests that evapotranspiration should be lower from a vegetated zone than an unvegetated zone, because the net radiation flux is generally lower. However, an aerodynamic approach suggests that the rougher surface would increase turbulence in the adjacent boundary layer and hence increase transpiration, with all other factors being equal (Linacre et al., 1970). Additionally, emergent macrophytes shelter the water surface from winds, which would reduce evaporation at the water surface.

However, more consistent trends emerge from these apparently conflicting findings when the "oasis effect" is considered. This oasis effect (Linacre, 1975; Anderson and Idso, 1987; Idso and Anderson, 1988) is due to the occurrence of a water body in a relatively dry environment. Horizontal advection of sensible heat appears to stimulate enhanced transpiration from the exposed perimeter of the macrophytes, which suggests that the peripheral surface area is more important than the horizontal surface area. Consequently (Idso and Anderson, 1988):

- evapotranspiration from exposed narrow stands of emergent macrophytes exceeds evapotranspiration from a similar horizontal area of open water
- evapotranspiration from a more extensive stand of macrophytes is similar to or less than evapotranspiration from a similar open water area
- shorter denser canopies offer greater aerodynamic resistance to evapotranspiration than taller canopies.

The purpose of this study is to quantify the heat fluxes across the water surface, rather than the variation in fluxes within the canopy volume. With respect to evapotranspiration, it is assumed that the energy for transpiration from the macrophytes is provided primarily by radiation absorbed within the canopy rather than from heat stored in the water body. The latent heat flux at the underlying water surface is then approximated by the evaporative flux alone. Parameterisation schemes are therefore similar to those outlined in Section 3.3.3.3 for evaporation from an open water surface into the overlying atmosphere, and the discussion in Section 3.3.3.3 applies equally here.

The emergent macrophyte zone can be represented as a three layer system, comprising the water column (the substrate), the canopy volume (the roughness sub-layer) and the overlying atmosphere. Under this scheme, the latent heat flux at the water surface in the vegetated zone is only directly influenced by conditions in the water body and in the canopy volume, although both of these layers are influenced by atmospheric conditions. It can be noted that:

- the net radiation flux at the water surface beneath an emergent canopy is generally less than at an open water surface (Sections 3.3.2 and 3.4.2)
- the saturation vapour pressure in both zones is a function of the water surface temperature, so although the water temperatures will be different, the approach to calculating e_{sat} is identical

- the ambient vapour pressure is a function of the ambient temperature and relative humidity, so although generally $T_c > T_a$ and $RH_c > RH_a$, the approach to calculating e_a is identical in both zones.

Under conditions of forced convection and assuming that the effects of atmospheric stability are accounted for, the latent heat flux at the water surface beneath an emergent canopy can be calculated from a form of Equation (3.36):

$$H_L = -\frac{0.622\, K_2\, L_w\, k^2\, \rho_m\,(e_{sat} - e_a)\, u_z}{P\{\ln[(z_M - d_0)/z_0)]\}\{\ln[(z_V - d_0)/z_{0V}]\}} \tag{3.60}$$

where z_M = measurement height for wind speed (m)

d_0 = zero-plane displacement height (m)

z_0 = aerodynamic roughness length for momentum (m)

z_V = measurement height for relative or specific humidity (m)

z_{0V} = aerodynamic roughness length for water vapour (m)

and other variables are as previously defined. As discussed in Section 3.3.3.3, the latent heat flux under conditions of free convection in light winds was accounted for by imposing the lower wind speed threshold of $0.1\,\mathrm{m\,s^{-1}}$.

The value of z_{0V} is extremely difficult to determine experimentally, but can be estimated empirically. In a vegetation canopy and at other permeable rough surfaces, the value of $\ln(z_0/z_{0V})$ is relatively insensitive to the nature of the flow (Garratt and Hicks, 1973), and Brutsaert (1982) suggested $z_{0V}/z_0 \sim 1/7$ to $1/12$.

3.4.3.3 Sensible Heat Flux Beneath an Emergent Canopy

As for the latent heat flux beneath an emergent canopy, because it is the sensible heat flux across the water surface that is under consideration rather than the sensible heat flux between the canopy volume and the atmosphere, much of the discussion from Section 3.3.3.4 applies directly. The sensible heat flux is expected to be smaller at the water surface in an emergent macrophyte zone than an adjacent open water area, given the reduced air velocities beneath the canopy. However, the temperature gradient $T_w - T_a$ could be either larger or smaller than that in the open water area, depending on the canopy density.

In the absence of eddy measurements, the sensible heat flux beneath an emergent canopy can be estimated from the latent heat flux in the emergent zone using the Bowen Ratio, similar to Equation (3.44):

$$H_S = \mathcal{B}\, H_L \quad \text{where} \quad \mathcal{B} = \gamma \left(\frac{T_w - T_C}{e_{sat} - e_C} \right) \tag{3.61}$$

where γ = dimensionless psychrometric coefficient, which is calculated as shown in Appendix A

T_w , T_C = water surface and canopy air temperatures (°C)

e_{sat} = saturation vapour pressure (hPa)

e_C = ambient vapour pressure in the canopy air space (hPa).

This is a simple method for estimating the sensible heat flux, although any errors in estimation of the latent heat flux will be transferred and possibly increased through the sensible heat flux.

3.5 Heating due to Shortwave Radiation

Shortwave radiation which penetrates the surface of a water body is either absorbed or scattered by the water or by solutes or suspended material (Wetzel and Likens, 1991). Absorption of radiation and dissipation as heat strongly influences the thermal structure and circulation patterns in a body of water.

Attenuation of shortwave radiation with depth in a water body is commonly modelled using a form of Beers Law, which describes the exponential decrease in light intensity with passage through a medium. This form of Beers Law is expressed as follows (Kirk, 1983):

$$\phi_z = \phi_0 \exp\, [-\eta\, z] \tag{3.62}$$

where ϕ_z = shortwave radiation flux at depth z (Wm^{-2})

ϕ_0 = shortwave radiation flux at the water surface (Wm^{-2})

η = mean attenuation coefficient (m^{-1}).

Attenuation coefficients can be derived from field measurements at two or more depths. The relationship between water depth and attenuation of shortwave radiation with different values of η is shown in Figure 3.10. It is evident that in clear waters (for example $\eta = 0.5\,\text{m}^{-1}$), nearly 10% of the surface shortwave radiation flux ϕ_0 is transmitted to a

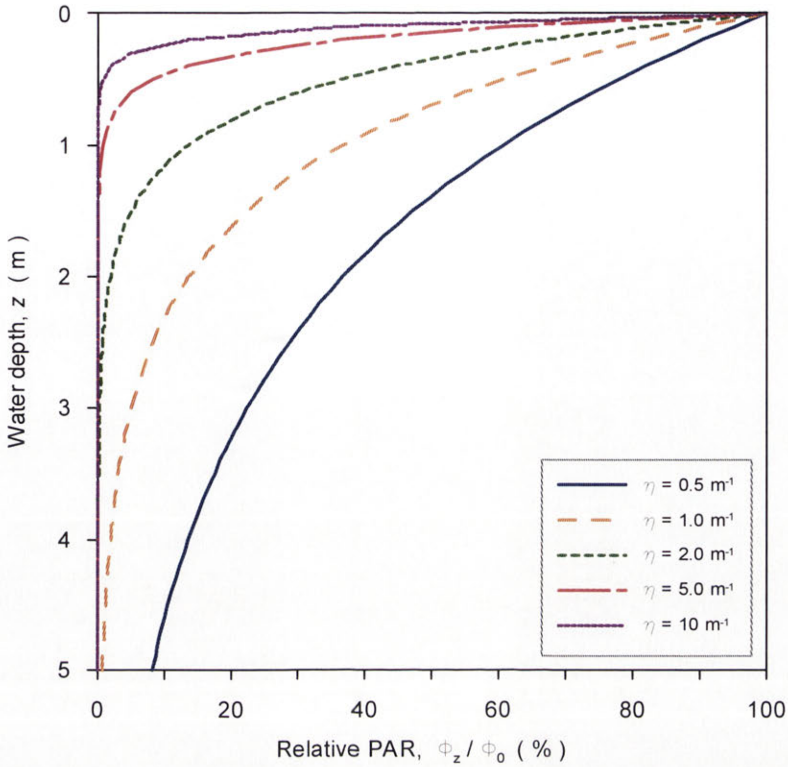

Figure 3.10: Attenuation of shortwave radiation as a function of attenuation coefficient η and depth below the water surface z.

depth of 5 m. By contrast, in highly turbid water (for example $\eta = 10.0\,\mathrm{m}^{-1}$), $< 1\%$ of ϕ_0 is transmitted to a depth of 5 m.

As discussed in Section 3.4.2.1 (page 82), Beers Law applies strictly only to monochromatic light travelling through a homogeneous medium, although a mean attenuation coefficient is generally employed. This is reasonable, after the shorter (ultra violet) and longer (infra red) wavelengths are filtered immediately beneath the surface (Benoit and Hemond, 1996).

Henderson-Sellers (1984) and Zaneveld and Spinrad (1980) each proposed alternative models to account for the rapid initial attenuation of shortwave radiation immediately beneath the water surface. However, it is unnecessary to account for this filtering of wavelengths at the extreme ends of the shortwave radiation spectrum if the attenuation coefficient is derived from measurements of PAR rather than global shortwave radiation. This argument is consistent with Stefan et al. (1983), who reported that PAR attenuation was approximated very well by Equation (3.62) without the need for modification near the surface. Their measurements were made at 0.1 m depth intervals to a depth of 2 m in the turbid waters of Lake Chicot in Arkansas, USA.

More complex forms of Beers Law are also available which account separately for the different wavelengths and the effects of chlorophyll, colour and suspended organic and inorganic substances (see for example, Blom et al., 1994; Salençon and Thébault, 1996). These models require significantly more data and additional instrumentation, and are not considered further in the present study.

The attenuation coefficient (η) for global shortwave radiation in natural water bodies ranges from $0.2\,\mathrm{m}^{-1}$ for very clear, oligotrophic lakes, to greater than $4.0\,\mathrm{m}^{-1}$ for highly stained waters (Wetzel, 1983). Cristofor et al. (1994) reported $\eta \leq 12.05\,\mathrm{m}^{-1}$ in partially-vegetated, shallow lakes of the Danube Delta. Mean attenuation coefficients for PAR in Australian inland waters range from $0.21\,\mathrm{m}^{-1}$ in clear Tasmanian lakes to greater than $10\,\mathrm{m}^{-1}$ in Lake George, New South Wales (Kirk, 1983).

Attenuation coefficients generally increase with increasing turbidity, colour, algal or macrophyte growth (Henderson-Sellers, 1984). Algae and suspended sediments are usually the primary contributors to light attenuation in shallow eutrophic lakes (Blom et al., 1994). The attenuation coefficient increases slightly near sunrise and sunset, due to increased solar zenith and therefore greater pathlength of the solar beam. However, Kirk (1983) reported the variation was minimal for $10° \leq \beta \leq 80°$.

The change in temperature ΔT of a volume of water in a time interval Δt due to absorption of shortwave radiation is calculated as follows (Henderson-Sellers, 1984):

$$\frac{\Delta T}{\Delta t} = \frac{\eta\, \phi_z}{\rho\, c_{pw}} = \frac{\eta\, \phi_0}{\rho\, c_{pw}} \exp\left(-\eta\, z\right) \tag{3.63}$$

where
ϕ_z = shortwave radiation flux at depth z (Wm^{-2})
ϕ_0 = shortwave radiation flux at the water surface (Wm^{-2})
ρ = water density ($\mathrm{kg\,m}^{-3}$)
c_{pw} = specific heat capacity of water ($\mathrm{J\,kg}^{-1}\,{}^{\circ}\mathrm{C}^{-1}$)
η = attenuation coefficient for shortwave radiation (m^{-1})
z = depth over which the shortwave radiation is absorbed (m).

Both ρ and c_{pw} are temperature dependent, and calculated as shown in Appendix A.

3.6 Parameterisation of the Bed Heat Flux

In shallow water bodies, thermal fluxes may occur between the water column and the underlying sediments due to conduction, or by direct shortwave radiative heating of these sediments (Wetzel, 1983). In this context, the "sediments" comprise the minerals, organic components and water which collectively form the wetland substrate.

In general, the relative importance of the bed heat flux in the overall heat budget of a wetland increases as the water depth decreases and the clarity of the water increases. Diurnal cycles can be expected in the magnitude and direction of the sediment heat flux, and hence steady-state assumptions are inappropriate when modelling diurnal hydrodynamic cycles. However, because it is difficult to measure directly, the bed heat flux has often been neglected in hydrodynamic modelling (Benoit and Hemond, 1996).

3.6.1 Bed Heat Flux due to Conduction at the Sediment Interface

Where it is necessary to consider the bed heat flux, it is generally assumed that conduction in the vertical direction exceeds any horizontal conduction (Fang and Stefan, 1996). If it is also assumed that the thermal diffusivity of the sediments is independent of temperature (Brutsaert, 1982), the sediment temperature distribution can be estimated using the one-dimensional unsteady heat transport equation (Fang and Stefan, 1996):

$$\frac{\partial T_s}{\partial t} = K_s \frac{\partial^2 T_s}{\partial z^2} \tag{3.64}$$

where T_s = sediment temperature (°C)

z = depth beneath the water-sediment interface (m)

K_s = thermal diffusivity of the sediments ($\mathrm{m^2\,s^{-1}}$).

Values of K_s reported in the literature range from 3.3×10^{-7} to $1.23\times10^{-6}\ \mathrm{m^2\,s^{-1}}$ for lake sediments (Benoit and Hemond, 1996; Fang and Stefan, 1998; Deas and Lowney, 2000). Equation (3.64) is solved for the temperatures throughout the sediment layer using the water temperature at the water-sediment interface as the upper boundary condition, and a zero heat flux at the lower sediment boundary, h_s.

The depth of thermal influence of the sediments (h_s) is the depth below which sediment temperatures are assumed constant and essentially independent of the overlying water body (Fang and Stefan, 1996). This depth is limited by the relatively low thermal conductivity of typical sediments compared with water (Benoit and Hemond, 1996), and is generally less than a few metres. Jin et al. (2000) assumed a depth of influence of h_s = 0.3 m in Lake Okeechobee in Florida, USA, which has an average depth of less than 3 m. Fang and Stefan (1998) reported that diurnal cycles in sediment temperatures were generally only perceptible to depths of around 0.3 m.

The bed heat flux is calculated from the rate of change of the sediment temperature distribution over the depth of thermal influence, as follows:

$$G_{BED} = -\, c_s \int_0^{h_s} \frac{\partial T_s}{\partial t}\, dz \tag{3.65}$$

where G_{BED} = bed heat flux between the water and sediments ($\mathrm{J\,m^{-2}s^{-1}}$)

c_s = volumetric heat capacity of the sediments ($\mathrm{J\,m^{-3}\,{}^{\circ}C^{-1}}$).

Values of c_s reported in the literature range from $1.4{\times}10^6$ to $3.8{\times}10^6\,\mathrm{J\,m^{-3}\,{}^{\circ}C^{-1}}$ for lake sediments (Fang and Stefan, 1998). The value of c_s can be estimated from physical parameters of the sediments, bulk density, moisture content and organic content, as shown in Appendix A. The integral term is positive when the sediments are being heated by conduction from the water column. Following the convention adopted at the beginning of this chapter, the negative sign is introduced in Equation (3.65) so that G_{BED} is positive when heat is directed into the water column from the sediments.

3.6.2 Bed Heat Flux due to Shortwave Radiation

Sediment heating due to shortwave radiation is only likely to be significant in very clear or very shallow water bodies, and is generally a minor component of the bed heat budget (Benoit and Hemond, 1996). Where important, direct heating due to shortwave radiation can be estimated using a form of Beers Law:

$$\phi_h = \phi_0 \exp\,[-\,\eta\, h] \tag{3.66}$$

where ϕ_h = shortwave radiation flux at the bed ($\mathrm{Wm^{-2} \equiv J\,m^{-2}s^{-1}}$)

ϕ_0 = shortwave radiation flux at the water surface ($\mathrm{Wm^{-2}}$)

η = underwater attenuation coefficient ($\mathrm{m^{-1}}$)

h = water depth (m).

Heating due to shortwave radiation was discussed in Section 3.5.

3.7 Other Wetland Energy Fluxes

The preceeding sections have provided an overview of the importance and estimation of the primary energy fluxes at the water surface in a wetland. Several other energy fluxes can be significant in certain situations and these are shown in Figure 3.11. However, most of these are relatively minor and mentioned only briefly.

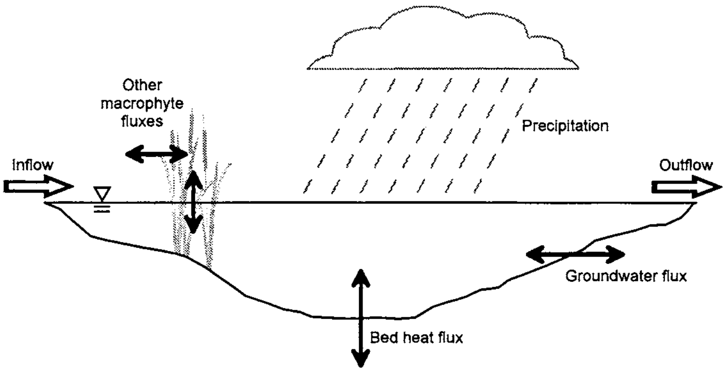

Figure 3.11: Other wetland energy fluxes.

3.7.1 Stream Inflow and Outflow

Inflow and outflow may represent significant energy fluxes in a wetland, particularly during wet weather. Energy fluxes associated with inflow may comprise (Fischer et al., 1979):

- kinetic energy, due to the velocity of the inflow
- potential energy, if there is a change in elevation between the centres of mass of the inflow and the water body
- thermal energy, if the temperature of the inflow differs significantly from that of the wetland.

Energy fluxes may arise more indirectly from outflow, which can generate internal waves (seiches) if the outflow velocity is sufficient and the wetland is thermally stratified (Fischer et al., 1979).

However, as outlined in Section 1.2, this study is concerned primarily with the hydrodynamic response of a wetland during inter-event periods, when inflow and outflow are generally small. Energy fluxes associated with inflow and outflow are therefore beyond the scope of this study. Also, as described in Section 4.4, inflow and outflow were negligible at the Hopwoods Lagoon field site during the study period.

3.7.2 Precipitation

Direct precipitation onto a wetland could potentially change the water surface temperature and cause localised vertical mixing, although the energy exchange is generally considered negligible (Henderson-Sellers, 1984; Andradóttir and Nepf, 2000). Precipitation could also contribute energy indirectly via surface inflow, as mentioned above.

Waters et al. (1994) used scaling analyses with dimensions and meteorological variables for a "typical" wetland to determine the relative importance of rainfall and other external processes on mixing in wetlands. They suggested that the energy fluxes associated with rainfall were less significant for mixing than fluxes due to wind-induced mixing or penetrative convection. The smaller radiation, latent and sensible heat fluxes typically experienced during rainfall events generally have more significant effects on wetland hydrodynamics than direct precipitation.

Given the comments above, and the focus of the present investigation on wetland hydrodynamics during dry, inter-event periods, the direct effects of rainfall on energy fluxes in a wetland are not considered further.

3.7.3 Groundwater Flux

Groundwater fluxes can be important in the water budget of a wetland which is hydrologically integrated with the local or regional groundwater system. Groundwater fluxes can also contribute to the energy budget if the groundwater temperature differs significantly from the temperature of the water column. However, groundwater fluxes are difficult to quantify and therefore generally neglected or uncertain (Hunt et al., 1996).

As outlined in Section 1.2, groundwater interactions are outside the scope of the present investigation, and not considered further. This is not an unreasonable assumption for applications involving free-surface constructed wetlands, where the water body is likely to be hydrologically isolated from the local aquifer. Constructed wetlands may be isolated to prevent contamination of the local groundwater by pollutants removed in the wetland

(Lawrence and Breen, 1998) or because of the difficulties associated with construction in saturated soils. Also, as described in Section 4.4, data from the primary field investigation site suggest that groundwater interaction was insignificant during the study period.

3.7.4 Other Energy Fluxes Associated with Macrophytes

In more detailed studies of the macrophyte canopy, other energy fluxes associated with the macrophytes might be considered, including:

- the cycling of potential chemical energy due to photosynthesis and respiration
- absorption, storage and conduction of heat by canopy foliage
- heat storage within the canopy volume.

However, the rate at which heat is stored by photosynthesis is almost always negligible (Gates, 1980), and the absorption, conduction and storage of heat within the canopy air space is generally insignificant compared with the other terms in the heat budget (Zhang et al., 1997). Inclusion of these macrophyte fluxes would constitute a detailed study in its own right, and is beyond the scope of the present investigation.

3.8 Scaling Horizontal Convective and Advective Flows in Wetlands

Scaling analysis allows estimates to be made of various flow parameters using appropriate scale variables and relationships between terms in the hydrodynamic and thermodynamic equations. The objective of the following analyses was to obtain order of magnitude estimates for the convective and advective velocities expected in the open water and macrophyte zones of a "typical" wetland. These estimates were used as a basis for interpreting the observed wetland hydrodynamics which are discussed in Chapter 6. In this context, a typical wetland is defined as one having dimensions similar to those encountered during the field studies, as described in Chapter 4.

3.8.1 Convective Flows in Open Water

Patterson (1984) investigated unsteady natural convection in a rectangular cavity of small aspect ratio. He found that flows driven by internal sources of heating or cooling could be classified as either conductive, transitional or convective, depending on the relationship between the Grashof number, the Prandtl number Pr and the aspect ratio A.

Coates and Patterson (1993) later investigated unsteady natural convection in a rectangular cavity with non-uniform absorption of radiation across the water surface. They reported that, following an initial inertial period, horizontal flows typically became either viscous or energy limited, depending on the relationship between the Grashof number, the mean underwater attenuation of radiation and the geometry of the system.

Farrow and Patterson (1993) considered the response of a triangular cavity (simulating a reservoir sidearm) to diurnal heating and cooling and found that flow was inertia-dominated in the deeper regions but viscous-dominated in the shallow littoral areas. The shallow areas absorbed more heat per unit volume during the day than the deeper regions and cooled more rapidly overnight, leading to horizontal pressure gradients between the two zones.

Aspects of the scaling analyses described by these researchers are useful in the present study, as outlined below.

3.8.1.1 *Initiation of Heating and Convective Flows in Open Water*

Heating in an essentially isothermal and quiescent fluid subject to a surface heat flux H_{NET} commences by absorption of radiation beneath the water surface. Assuming that shortwave radiation is absorbed with depth according to Beers Law, Equation (3.62) from page 94, the vertical length scale for radiative heating will be $\delta_R \sim 1/\eta$ (Coates and Patterson, 1993), where η is the mean underwater attenuation coefficient (m^{-1}). As radiative heating progresses, heat will be transported within the fluid by conduction (molecular diffusion) with horizontal and vertical length scales of $\delta_H \sim (D_H \, \tau)^{1/2}$, until such time as $\delta_H \geq \delta_R$ (D_H is the coefficient of molecular diffusion for heat). This critical time scale, corresponding to $\delta_H \approx \delta_R$ is $\tau_{RC} \sim h^2/\eta_*^2 \, D_H$, where $\eta_* = \eta \, h$ is the mean underwater attenuation coefficient normalised over the depth of the water column, h.

Comparing τ_{RC} with the time scale required to develop steady state flows under purely conductive conditions, $\tau_D \sim h^2 / D_H$ (Farrow and Patterson, 1993), it is apparent that $\tau_{RC} < \tau_D$ whenever $\eta_* > 1$. As discussed in Section 3.5 (page 94), $\eta_* > 1$ would be expected in all but the clearest of natural water bodies, and hence steady state conductive flow is unlikely to be achieved. Other studies have also shown that steady state flow is unlikely to develop in natural water bodies subjected to diurnal meteorological forcing (see, for example, Horsch and Stefan, 1988; Sturman et al., 1996 and Sturman and Ivey, 1998).

Vertical temperature gradients develop due to the attenuation of shortwave radiation with depth below the surface, as shown in Equation (3.63) on page 96. Horizontal temperature gradients develop due to differences in either the internal distribution of heat between two locations or the net heat flux at the water surface. The former was studied in detail by Patterson (1984) and the latter by Coates and Patterson (1993). The following scale variables are now introduced: L for horizontal distance, H for the thickness of the convective flow, $\Delta T/L$ for the horizontal temperature gradient, U for the horizontal convective velocity and τ for time.

For internally-driven heating, there is initially a balance in Equation (3.5) on page 42 between the unsteady term and the heat source term, ϑ_S (Patterson, 1984), which gives a scale for the growth of the horizontal temperature difference:

$$\frac{\partial T}{\partial t} \sim \vartheta_S \qquad \Rightarrow \qquad \Delta T \sim \vartheta_S \, \tau \tag{3.67}$$

This relationship prevails while the time since inception is less than the timescales required for convection or conduction to dominate the unsteady term, $\tau_C \sim L/U$ or $\tau_D \sim L^2/D_H$, respectively.

The horizontal temperature gradient establishes a pressure gradient which drives a horizontal circulation. Balancing this pressure gradient and the buoyancy term leads to (Patterson, 1984):

$$\frac{\partial P}{\partial x} \sim \rho_0 \, g \, \alpha_T \frac{\partial T}{\partial x} \partial z \qquad \Rightarrow \qquad \frac{\Delta P}{L} \sim \rho_0 \, g \, \alpha_T \frac{\vartheta_S \, \tau}{L} H \tag{3.68}$$

Applying Equation (3.68) in the horizontal momentum equation to balance the unsteady term gives a scale for the horizontal convective velocity (Patterson, 1984) as:

$$\frac{\partial u}{\partial t} \sim -\frac{1}{\rho_0} \frac{\partial P}{\partial x} \qquad \Rightarrow \qquad U \sim g \, \alpha_T \frac{\vartheta_S \, \tau^2}{L} H \tag{3.69}$$

Using Equation (3.67) it can be seen that Equation (3.69) is similar to the horizontal convective velocity scale derived by Monismith et al. (1990) for a suddenly-imposed horizontal temperature gradient of $\Delta T/L$ along the sidearm of a reservoir:

$$U \sim (g \, \alpha_T \Delta T H)^{1/2} \tag{3.70}$$

Expected Horizontal Convective Velocities in an Open Water Zone

For the moment assuming the validity of the preceding analyses in the open water zones in a wetland, an estimate can be made for the magnitude of the horizontal convective velocity using Equation (3.69). For initial flow times $\tau \leq 1\,\text{hr}$ in a "typical" wetland with $H \sim$O(10^{-1}) m, $\Delta T \sim$O(10^{0}) °C and $L \sim$O(10^{2}) m:

$$U \sim g \, \alpha_T \frac{\Delta T \, \tau}{L} H \sim (10^1)(10^{-4}) \frac{(10^0)(10^3)}{(10^2)} (10^{-1}) \sim 10^{-3} \;\; \text{m}\,\text{s}^{-1}$$

This is considerably smaller than the convective velocities estimated by Monismith et al. (1990) for exchange flows between the sidearm and main impoundment of a typical reservoir, where the physical scales are much larger: $L \sim$O(10^{3}) m and $H \sim$O(10^{0}) m. In both wetlands and reservoirs, the free convective velocities could be either enhanced or arrested by wind-induced, horizontal advective flows, as discussed in Section 3.8.2.

Patterson (1984) also expressed the initial convective velocity scale in terms of an effective Grashof number (Gr'), which he used to classify the developing flow into conductive, transitional or convective flow regimes:

$$Gr' = \frac{g\,\alpha_T\,\vartheta_S\,H^3\,L^2}{\nu^3} \equiv \frac{g\,\alpha_T\,\Delta T\,H^3\,L^2}{\tau\,\nu^3} \tag{3.71}$$

Substituting Equation (3.69) into Equation (3.71) gives the initial horizontal convective velocity scale as:

$$U \sim \frac{Gr'\,\nu^3\,\tau^2}{H^2\,L^3} \tag{3.72}$$

Flow classification following initial flow establishment is discussed in the following sections.

3.8.1.2 Expected Flow Regimes in Open Water

Patterson (1984) found that horizontal flows driven by internal horizontal temperature or pressure gradients could be broadly classified into three flow regimes. These depend on the relationship between the effective Grashof number Gr' and combinations of the Prandtl Number $Pr = \nu/D_T > 1$ and the aspect ratio $A = H/L$, as follows:

- **conductive**: $Gr' < Pr^{-2}$, where the flow is dominated by conduction
- **transitional**: $Pr^{-2} < Gr' < Pr^{-2}\,A^{-4}$
- **convective**: $Gr' > Pr^{-2}\,A^{-4}$, where the flow is dominated by convection.

A number of subregimes were also identified within the transitional flow regime but are not considered here.

Again assuming the validity of Patterson's work in the open water zones in a "typical" wetland with the scales shown in the previous section, $H \sim O(10^{-1})\,\mathrm{m}$, $\Delta T \sim O(10^{0})\,°\mathrm{C}$, $L \sim O(10^{2})\,\mathrm{m}$ and $\nu \sim O(10^{-6})\,\mathrm{m^2\,s^{-1}}$:

$$Gr' = \frac{g\,\alpha_T\,\Delta T\,H^3\,L^2}{\tau\,\nu^3} \sim \frac{(10^1)\,(10^{-4})\,(10^0)\,(10^{-1})^3\,(10^2)^2}{(10^3)\,(10^{-6})^3} \sim 10^{13} \tag{3.73}$$

If $Pr = 7.14$ (non-turbulent flow) and $A \sim O(10^{-3})$, then:

$$Pr^{-2} \sim O(10^{-1}) - O(10^{-2}) \qquad A^{-4} \sim O(10^{10}) - O(10^{11}) \quad \Rightarrow \quad Pr^{-2}\,A^{-4} \sim O(10^{10}).$$

Hence $Gr' \gg Pr^{-2} A^{-4}$, and horizontal flow in the core region of the wetland is expected to be dominated by convection.

3.8.1.3 Horizontal Heating and Cooling Phase Flows in Open Water

Meteorological forcing is partly determined by the surface buoyancy flux B_0 ($\mathrm{m^2\,s^{-3}}$), which can be determined from the net surface heat flux defined in Equation (3.15), as follows (Imberger, 1985):

$$B_0 = \frac{g\,\alpha_T\,H_{NET}}{\rho_0\,c_{pw}} \tag{3.74}$$

where α_T = thermal expansion coefficient ($^\circ\mathrm{C}^{-1}$)
H_{NET} = net surface heat flux ($\mathrm{Wm^{-2}}$)
ρ_0 = mean water density ($\mathrm{kg\,m^{-3}}$)
c_{pw} = specific heat capacity of water ($\mathrm{J\,kg^{-1}\,^\circ C^{-1}}$).

The buoyancy flux is positive when $H_{NET} > 0$, and this constitutes the **heating phase** of the diurnal cycle. Heating phase flows are typically shallow and laminar, and occur across the top of a stable vertical stratification (Sturman and Ivey, 1998) which is reinforced by the positive surface buoyancy flux. In the absence of significant wind-induced mixing, vertical heat transport during the heating phase will occur primarily by conduction along the vertical temperature gradient.

The **cooling phase** occurs when H_{NET} and B_0 are negative, and results in surface cooling. Cooling phase flows are generally deeper and unstable, and may be mixed vertically by penetrative convection (Sturman and Ivey, 1998). These researchers also presented scaling analyses which demonstrated that the volume of water convected during the cooling phase generally exceeds that during the heating phase.

In laboratory experiments, horizontal convective velocities in both heating phase (stabilising) and cooling phase (destabilising) flows were found to scale with the magnitude of the buoyancy flux and the length of the forcing region (Sturman et al., 1996; Sturman and Ivey, 1998). This is consistent with the work first proposed by Phillips (1966):

$$U \sim (B_0\,L)^{1/3} \tag{3.75}$$

In this application, L is the length of the forcing region exposed to the surface heat flux.

Expected Horizontal Convective Velocities in an Open Water Zone

For a typical $H_{NET} \sim O(10^2)\,\mathrm{Wm^{-2}}$ in temperate latitudes (see Figure 6.20 on page 245 for the observed annual variation in H_{NET} at Hopwoods Lagoon), the net surface buoyancy flux is:

$$B_0 = \frac{g\,\alpha_T\,H_{NET}}{\rho_0\,c_{pw}} \sim \frac{(10^1)\,(10^{-4})\,(10^2)}{(10^3)\,(10^3)} \sim 10^{-7} \quad \mathrm{m^2\,s^{-3}} \tag{3.76}$$

From Equation (3.75) with $L \sim O(10^2)$, the expected horizontal convective velocities in open water are $U \sim O(10^{-2})\,\mathrm{m\,s^{-1}}$. While this is larger than the initial horizontal convective flows estimated for a wetland in Section 3.8.1.1, it is not unreasonable for the continued evolution of flow from an essentially quiescent and isothermal state.

3.8.1.4 Penetrative Convection in Open Water

During the cooling phase when the water surface is subjected to a negative or destabilising buoyancy flux, vertical conductive heat transport is supplemented by penetrative convection. Thermals induced by surface cooling are negatively buoyant and descend from the surface, eroding the existing thermal structure and entraining the surrounding fluid as they fall (Turner, 1973). In the initial stages of their fall, the vertical velocity (w) of thermals generated by penetrative convection has been found both theoretically and experimentally to scale with the magnitude of the negative surface buoyancy flux and the depth below the surface (Sturman and Ivey, 1998). Wells and Sherman (2001) cited the work of Adrian et al. (1986), who determined from experimental and theoretical work that the coefficient of proportionality in Equation (3.77) was 0.6:

$$w \sim (\,B_0\,H\,)^{1/3} \approx 0.6\,(\,B_0\,H\,)^{1/3} \tag{3.77}$$

Expected Penetrative Convective Velocities in an Open Water Zone

In open water zones and for a typical $H_{NET} \sim O(10^2)\,\mathrm{Wm^{-2}}$ and $B_0 \sim O(10^{-7})\,\mathrm{m^2\,s^{-3}}$, the thermals driven by penetrative convection would be expected to have a vertical velocity of:

$$w \sim (\,B_0\,H\,)^{1/3} \sim \Big[(10^{-8})\,(10^{-1})\Big]^{1/3} \sim 10^{-3} \quad \mathrm{m\,s^{-1}} \tag{3.78}$$

which is smaller than the estimated horizontal convective velocities. This comparison between horizontal and vertical convective velocities highlights the potential importance of horizontal convective flows in distributing constituents within water bodies such as wetlands, in the absence of strong winds and advective mixing processes.

3.8.2 Advective Flows in Open Water

In addition to the buoyancy-induced, free convective motions considered above, forced convection may occur in wetlands during windy periods due to wind-induced horizontal currents (Monismith et al., 1990). As outlined in Section 3.3.3.2, the surface drift velocity u_s can be approximated from the wind speed at 10 m elevation via Equation (3.28) from page 62:

$$u_s \sim u_{*w} \sim 0.035 \times u_{10}$$

Depending on the direction of the horizontal temperature gradient and the prevailing winds, forced convection or wind-induced advective currents may either enhance or arrest buoyancy-driven free convection currents. Assuming opposing directions, the wind speed required over time τ to balance a given horizontal temperature gradient $\Delta T/L$ can be estimated from Equations (3.69) and (3.28), as follows:

$$0.035 \times u_{10} \sim g\,\alpha_T \frac{\Delta T\,\tau}{L} H \qquad \Rightarrow \qquad u_{10} \sim \frac{g\,\alpha_T}{0.035}\,\tau H\,\frac{\Delta T}{L} \tag{3.79}$$

Expected Advective Velocities in an Open Water Zone

Figure 3.12 shows the mean wind speed u_{10} required to balance the horizontal temperature gradient over a time τ (hr), for a convective surface layer of depth around $H = 0.5$ m. For relatively small temperature gradients of less than $0.05°\mathrm{C\,m^{-1}}$ established over a short timescale of less than 1 hr, relatively modest wind speeds of $<5\,\mathrm{m\,s^{-1}}$ could balance the horizontal temperature gradient and arrest the resulting convective flow. The required wind speed increases dramatically for long-established temperature gradients, as might be expected in the later parts of the diurnal heating or cooling cycles.

However, winds are inherently unsteady (Maxworthy and Monismith, 1988), and the time scale for adjustment of the mixed layer turbulence to a change in the surface wind stress is $t_W \sim (H\,/\,u_*)$, where u_* is the friction velocity at the water surface. This is of the order of minutes and relatively short compared with the convective processes considered in Section 3.8.1 (Imberger, 1985; Spigel et al., 1986; Stevens et al., 1996). Hence, the surface layer could be expected to respond more rapidly to changes in the wind climate than to changes in the net surface heat flux or surface buoyancy flux.

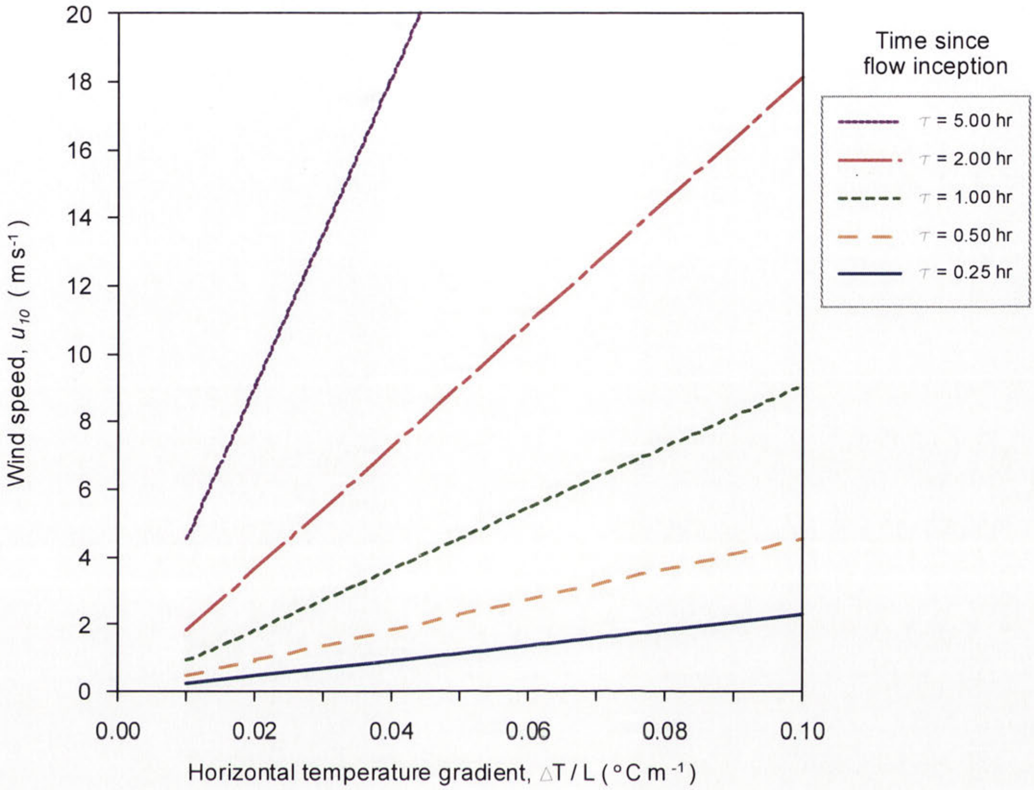

Figure 3.12: Mean wind speed required to balance a horizontal temperature gradient of $\Delta T/L$ established over a period τ since flow inception, with a convective flow depth of $H \sim 0.5\,m$.

3.8.3 Convective Flows in Macrophyte Zones

The presence of macrophytes could either enhance or reduce horizontal temperature gradients compared with those expected in open water containing no vegetation, because:

- if emergent macrophytes reduce the net surface heat flux in the macrophyte zones, the horizontal temperature difference from the open water zone at the water surface would increase due to radiation shading
- if submerged macrophyte components increased the attenuation of shortwave radiation with depth below the water surface, horizontal temperature differences from the open water zone could decrease in the shallow regions but increase at depth.

Only a limited number of studies have presented scaling analyses for flows through macrophyte zones. Waters (1998) reviewed several studies of flow through vegetation and conducted scaling analyses in a wetland with depth h=0.5 m and length L=10 m. He stated that it was the drag term which most distinguishes flows through macrophytes from those in open water, and his two-dimensional (laterally-averaged) analysis confirmed that the vegetation drag term was significant in the horizontal momentum equations. Oldham and Sturman (2001) extended the work of Sturman et al. (1999) to include the effect of vegetation on convective flushing in the shallow regions of wetlands. They concluded that convective flushing is a significant mechanism in sheltered wetlands, interpreted by this author to be wetlands where advective flows are negligible.

In the following analyses, the flow resistance due to macrophytes is incorporated in the Γ_x and Γ_y terms in the horizontal momentum equations using the drag force parameterisation in Section 3.2.2.

3.8.3.1 Steady State Analysis for Flows through Macrophytes

Waters (1998) conducted scaling analyses for buoyancy-induced two-dimensional (horizontally-averaged) flows in a wetland containing emergent macrophytes ($h = 0.5$ m and $L = 10$ m). An order of magnitude analysis suggested that the unsteady, advective and viscous terms in the horizontal momentum equation were less significant than the buoyancy and drag terms, and he assumed a balance between the buoyancy and drag terms.

From Section 3.8.1.1 (page 104), a horizontal temperature gradient will establish a horizontal pressure gradient or buoyancy forcing which drives a horizontal flow. Following the reasoning of Waters (1998) and applying this in the horizontal momentum equation to balance the drag force leads to:

$$\frac{\partial P}{\partial x} \sim \frac{1}{2}\rho_0 C_D A_p U^2 \qquad \Rightarrow \qquad \rho_0\, g\, \alpha_T \frac{\Delta T}{L} H \sim \frac{1}{2}\rho_0 C_D A_p U^2 \tag{3.80}$$

where A_p is the total projected area of vegetation per unit volume ($m^2\,m^{-3}$) and other variables are as defined earlier (page 45).

The horizontal convective velocity can then be estimated from:

$$U \sim \left(\frac{2}{C_D A_p} g\, \alpha_T \frac{\Delta T}{L} H \right)^{1/2} \tag{3.81}$$

although further manipulation is required because the drag coefficient is a function of the stem Reynolds number and hence the velocity, as shown in Table 3.1 (page 46).

In the **laminar flow regime** when $Re_d < 3$, $C_D = 10 / Re_d$ and:

$$U \sim \left[\frac{2}{A_p} \left(\frac{U\,d}{10\,\nu} \right) g\,\alpha_T \frac{\Delta T}{L} H \right]^{1/2} \sim \frac{d}{5\,\nu\,A_p} g\,\alpha_T \frac{\Delta T}{L} H \tag{3.82}$$

In the **transitional flow regime** when $3 \leq Re_d < 10^3$, $C_D = \left(10^3 / Re_d\right)^{0.25}$ and:

$$U \sim \left[\frac{2}{A_p} \left(\frac{U\,d}{1000\,\nu} \right)^{1/4} g\,\alpha_T \frac{\Delta T}{L} H \right]^{1/2} \sim \left[\frac{2}{A_p} \left(\frac{d}{1000\,\nu} \right)^{1/4} g\,\alpha_T \frac{\Delta T}{L} H \right]^{4/7} \tag{3.83}$$

In the **turbulent flow regime** when $10^3 \leq Re_d \leq 4 \times 10^4$, $C_D \approx 1$ and:

$$U \sim \left[\frac{2}{A_p} g\,\alpha_T \frac{\Delta T}{L} H \right]^{1/2} \tag{3.84}$$

As discussed in Section 2.3.3 (page 29) and estimated from the expected Re_d (page 44), the flow in wetlands is generally laminar or transitional rather than fully turbulent. Equation (3.84) is therefore not likely to apply. Note also that these estimates for the horizontal convective velocities are not strictly applicable near the water surface or the bed of the wetland, because the implications of the free surface and non-slip boundary conditions have not been considered (Waters, 1998). However, they can provide a useful indication of the likely magnitude of buoyancy-induced velocities through macrophytes.

The magnitude of the projected plant area per unit volume A_p ($\mathrm{m^2\,m^{-3}}$) in Equation (3.81) can be estimated as follows. A unit horizontal area of wetland contains n_s stems, and it can be assumed from the field survey results reported in Chapter 6 that $n_s \sim O(10^2)$. The total projected area of these stems in the direction of flow over a depth $h \sim O(10^{-1})$ m is $(n_s\,d\,h)$, where $d \sim O(10^{-2})$ m is the mean stem diameter. The volume is $1 \times 1 \times h\,\mathrm{m^3}$. Hence, the projected vegetation area per unit volume is:

$$A_p = \frac{n_s\,d\,h}{1 \times 1 \times h} = n_s\,d \sim (10^2)\,(10^{-2}) \sim (10^0)\,\mathrm{m^2\,m^{-3}} \tag{3.85}$$

Expected Horizontal Convective Velocities in a Macrophyte Zone

Assuming the length, depth and temperature difference scales adopted earlier for the open water scenario, an estimate can be made for the horizontal convective velocity in the macrophyte zone when the buoyancy forcing is balanced by the vegetation drag. For flow in the transitional regime, Equation (3.83) suggests:

$$U \sim \left[\frac{2}{(10^0)} \left(\frac{(10^{-2})}{(10^3)\,(10^{-6})} \right)^{1/4} (10^1)\,(10^{-4})\,\frac{(10^0)}{(10^2)}\,(10^{-1}) \right]^{4/7} \sim (10^{-23/7})\,\mathrm{m\,s^{-1}} \quad (3.86)$$

which is approximately $O(10^{-3})\,\mathrm{m\,s^{-1}}$. This is an order of magnitude smaller than the horizontal convective flows expected during the heating and cooling phases in open water areas devoid of vegetation (Section 3.8.1.3).

The above estimates are consistent with convective velocities of 9–12 $\mathrm{mm\,s^{-1}}$ calculated by Waters (1998) from measured horizontal temperature differences in an emergent *Typha orientalis* wetland in Sydney. He assumed a balance between the buoyancy and drag forces and calculated the drag coefficient for a transitional flow. The estimated magnitude of the horizontal convective velocity is also consistent with velocities in the range 1–10 $\mathrm{mm\,s^{-1}}$ measured by Oldham and Sturman (2001) in a wetland containing *Schoenoplectus validus* in Perth, Western Australia.

3.8.3.2 Unsteady Flow Analysis through Macrophyte Zones

The preceding analysis has assumed that the flow is essentially steady, although scaling performed for flows in open water zones in wetlands (Section 3.8.1.1) suggested that steady state flows are unlikely to become established in response to diurnal cycles in meteorological forcing. Assuming that convective velocities through macrophyte zones would not exceed those in open water zones, they would be expected to be $\sim O(10^{-2})\,\mathrm{m\,s^{-1}}$ or smaller. Over a distance of $L \sim O(10^2)$ m in a "typical" wetland, the timescale for convective flow is therefore:

$$\tau_C \sim \frac{L}{U} \sim \frac{(10^2)}{(10^{-2})} \sim (10^4)\,\mathrm{s} \quad (3.87)$$

The expected order of magnitude of the unsteady term in the momentum equations is then:

$$\frac{\partial u}{\partial t} \sim \frac{U}{\tau_C} \sim \frac{(10^{-2})}{(10^4)} \sim (10^{-6})\,\mathrm{m\,s^{-2}} \quad (3.88)$$

With the approximations used when examining the open water convective flows, the horizontal buoyancy forcing would be expected to have a magnitude of:

$$g\,\alpha_T\,\frac{\Delta T}{L}\,H \sim (10^1)\,(10^{-4})\,\frac{(10^0)}{(10^2)}\,(10^{-1}) \sim (10^{-6})\,\mathrm{m\,s^{-2}} \quad (3.89)$$

The expected magnitude of the drag force due to the macrophytes would be:

$$F_D \sim \frac{1}{2}\, C_D\, A_p\, U^2 \sim (10^0)\,(10^{-2})\,(10^{-2})^2 \sim (10^{-6})\,\mathrm{m\,s^{-2}} \tag{3.90}$$

The unsteady, buoyancy and drag terms are expected to be of a similar order of magnitude, while order of magnitude estimates indicate that the remaining (advective and viscous) terms in the horizontal momentum equations would be smaller. It therefore seems reasonable that the drag force could be balanced by either the buoyancy forcing in Equation (3.80) or the unsteady term, as follows:

$$\frac{\partial u}{\partial t} \sim F_D \qquad \Rightarrow \qquad \frac{U}{\tau} \sim \frac{1}{2}\, C_D\, A_p\, U^2 \qquad \Rightarrow \qquad U \sim \frac{2}{\tau\, C_D\, A_p} \tag{3.91}$$

Note that this latter balance assumes there is no horizontal temperature difference, and therefore no buoyancy-induced or horizontal pressure forcing in the wetland.

Expected Horizontal Velocities in the Absence of Buoyancy Forcing

Again assuming the horizontal length, depth and temperature difference scales adopted earlier, an estimate can be made for the horizontal convective velocity in the macrophyte zone when the vegetation drag is balanced by the unsteady term in the momentum equations. For flow in the transitional regime, Equation (3.91) leads to:

$$U \sim \frac{2}{\tau\, A_p}\left(\frac{U\, d}{1000\,\nu}\right)^{1/4} \sim \left[\frac{2}{\tau\, A_p}\left(\frac{d}{1000\,\nu}\right)^{1/4}\right]^{4/3} \sim \left[\frac{2}{(10^4)\,(10^0)}\left(\frac{(10^{-2})}{(10^3)\,(10^{-6})}\right)^{1/4}\right]^{4/3} \tag{3.92}$$

which is $\mathrm{O}(10^{-5})\,\mathrm{m\,s^{-1}}$. This is somewhat smaller than the magnitude of the horizontal convective velocity estimated to result from a balance between the buoyancy forcing and vegetation drag.

These analyses imply that the very small unsteady convective velocities estimated to arise from a balance between the unsteady and vegetation resistance terms in the absence of any buoyancy forcing would be overcome by buoyancy-driven, convective flows if a horizontal temperature gradient was to develop. Hence, the horizontal velocities estimated in the absence of a buoyancy forcing can be considered a lower bound on the horizontal velocity in a macrophyte zone. It seems more likely that the drag force due to the macrophytes would be balanced by a combination of the buoyancy forcing and the unsteady term in the horizontal momentum equations, and that the resulting horizontal flows would have a velocity intermediate within the range from $\mathrm{O}(10^{-5})$ to $\mathrm{O}(10^{-3})\,\mathrm{m\,s^{-1}}$.

3.8.3.3 Penetrative Convection in Macrophyte Zones

The effects of macrophytes on penetrative convection in wetlands is not known to have been studied directly. From Equation (3.77), the magnitude of the vertical convection thermals is proportional to the surface buoyancy flux, and Waters (1998) postulated that the smaller estimated surface heat transfers in macrophyte zones would reduce the velocity of the thermals from those expected in open water. He also suggested that the shear imposed by the no-slip boundary condition along the surface of the macrophytes would further reduce the fall velocity, and concluded that these effects would reduce the length scale of mixing within the macrophyte zones.

While not directly investigating penetrative convection, Oldham and Sturman (2001) found the vertical permeability to exceed the horizontal permeability in a laboratory array of dowels by a factor of around 1000. This suggests that the macrophytes would impede vertical convective flows less significantly than horizontal convective exchanges.

Without further information, it is assumed that the vertical velocity of thermals generated by penetrative convection would scale with the magnitude of the surface buoyancy flux B_0 and the fall depth H, as per Equation (3.77) on page 107, while acknowledging that B_0 would be lower in the macrophyte zones than in the open water.

Expected Penetrative Convective Velocities in a Macrophyte Zone

Assuming that $H_{NET} \sim \mathrm{O}(10^2)\,\mathrm{Wm^{-2}}$ and $B_0 \sim \mathrm{O}(10^{-7})\,\mathrm{m^2\,s^{-3}}$ in the macrophyte zones of a "typical" wetland, the thermals driven by penetrative convection would be expected to have a vertical velocity of:

$$w \sim (\,B_0 H\,)^{1/3} \sim \left[(10^{-8})\,(10^{-1})\right]^{1/3} \sim 10^{-3} \quad \mathrm{m\,s^{-1}} \tag{3.93}$$

This is of the same order of magnitude as the expected velocity of descending thermals in open water zones and the estimated horizontal convective velocities in macrophyte zones. Penetrative convection could therefore be expected to play an important role in differential cooling in macrophyte zones of wetlands.

3.8.4 Advective Flows in Macrophyte Zones

Forced convection due to wind-induced horizontal currents is expected to be less important in macrophyte zones than in open water zones, because of wind speed attenuation and flow resistance by the macrophytes. The surface drift velocity in the water column will no longer be a simple function of the wind speed in the air as it was assumed for an open water surface (page 108). Instead, the relationship between the surface drift velocity and the wind speed will depend on the height, structure, density and flexibility of the macrophyte canopy, as discussed in Section 3.4.3.1. Two scenarios are considered.

Scenario 1:

The flow in a macrophyte zone is assumed to result from a balance between the buoyancy-induced horizontal pressure gradient and the vegetation drag term. From Equation (3.83) on page 111, if the induced convective flow was just balanced by an advective flow in the opposing direction, the surface drift velocity would be:

$$u_s \sim \left[\frac{2}{A_p} \left(\frac{d}{1000\,\nu} \right)^{1/4} g\,\alpha_T \frac{\Delta T}{L} H \right]^{4/7} \tag{3.94}$$

where a transitional flow regime has been assumed when calculating the drag coefficient. This suggests that the surface drift velocity would be proportional to $(\Delta T/L)^{4/7}$, with all other variables held constant.

Scenario 2:

Here the flow in a macrophyte zone is based on a balance between the unsteady and vegetation drag terms. Equation (3.91) on page 113 indicates that the induced flow is independent of any horizontal temperature difference and instead a function of the time since flow inception, τ. The surface drift velocity required to just balance such a flow would be:

$$u_s \sim \left[\frac{2}{\tau\,A_p} \left(\frac{d}{1000\,\nu} \right)^{1/4} \right]^{4/3} \tag{3.95}$$

Expected Advective Velocities in a Macrophyte Zone

Figure 3.13 shows the surface drift velocity required to just balance the horizontal flows described by Equations (3.94) and (3.95), for a flow depth of $H = 0.5\,\text{m}$. In preparing these graphs, it has been assumed that $A_p = n_s\, d = 200\,(0.01) = 2\,\mathrm{m}^2\,\mathrm{m}^{-3}$, based on field survey results for *Typha domingensis* (described in Chapter 6). For Scenario 1, the surface drift velocity ranges from 2–7 $\mathrm{mm\,s}^{-1}$, is shown in Figure 3.13 (a) for horizontal temperature gradients in the range from 0.01–0.1°C m^{-1}. For Scenario 2, where there is a balance between the unsteady terms and vegetation drag, Figure 3.13 (b) shows that the surface drift velocity declines rapidly from <0.25 $\mathrm{mm\,s}^{-1}$ with increasing time since the flow inception. This suggests that even a very slight advective flow would readily overcome any horizontal flow induced by a balance between the unsteady and vegetation drag terms in the horizontal momentum equations.

Note that the graphs in Figure 3.13 are not directly comparable with Figure 3.12 for the open water zone, which relates to the wind speed in the air (u_{10}) rather than the drift velocity in the water (u_S). In either of the two scenarios for a macrophyte zone, the wind speed above the macrophytes could be up to an order of magnitude larger (Danard and Murty, 1994), depending on the physical properties of the canopy. Waters (1998) reported that water velocities beneath an approximately 1.0m high *Typha orientalis* canopy were < 40% of those in an adjacent open water zone.

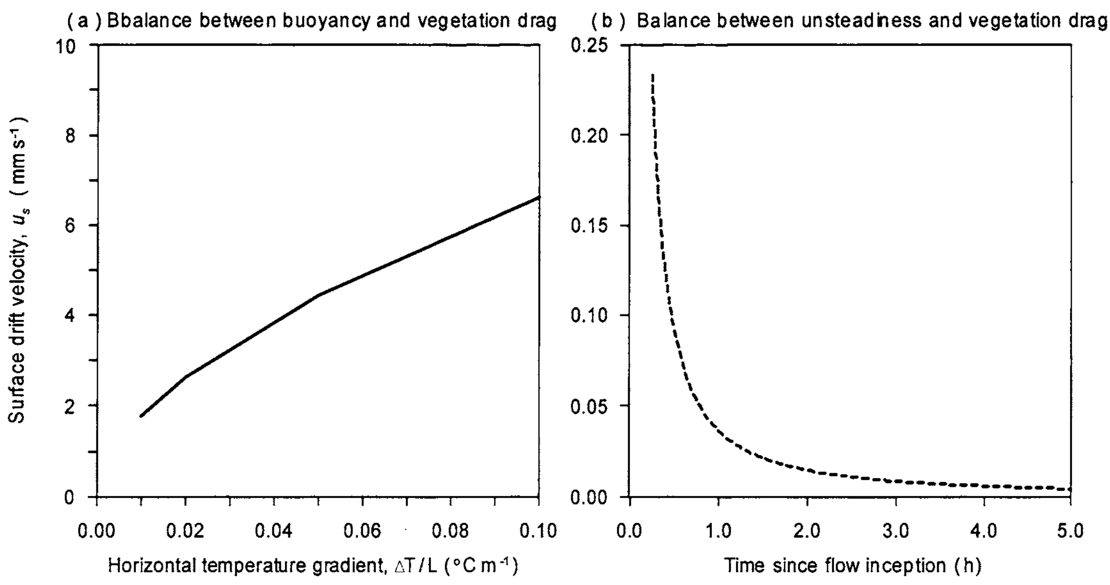

Figure 3.13: Surface drift velocities required to balance horizontal flows through macrophyte zones when resulting from a balance between (a) the buoyancy forcing and vegetation drag and (b) the unsteady term and vegetation drag. The flow depth is $H \sim 0.5\,m$.

3.9 Summary

This chapter has presented the relevant theory and scaling analyses which will be applied when interpreting the results of the field investigations and hydrodynamic simulation experiments. The flow equations and major surface energy fluxes have been considered for an unvegetated water body, and the effects of macrophytes on these have then been included. Scaling analyses have provided estimates of the horizontal convective and advective velocities likely to be induced in a natural wetland by various meteorological forcing scenarios. The next chapter introduces the field sites utilised in this study, while subsequent chapters outline the experimental methodology and results, and discuss the effects of radiation shading by macrophytes on the hydrodynamics in a natural wetland.

Chapter 4

FIELD SITE DESCRIPTIONS

4.1 Introduction

Field investigations were conducted at three sites in the northern Sydney metropolitan area, and at a fourth site in the Macdonald Valley, 75 km north-west of Sydney. The locations of the field sites are shown in Figure 4.1. The three Sydney sites were used for emergent macrophyte surveys and canopy shortwave radiation experiments. Longer term monitoring experiments were conducted at Hopwoods Lagoon in the Macdonald Valley. These included the collection of meteorological and water temperature data, additional canopy shortwave radiation experiments and experiments to measure underwater attenuation of shortwave radiation.

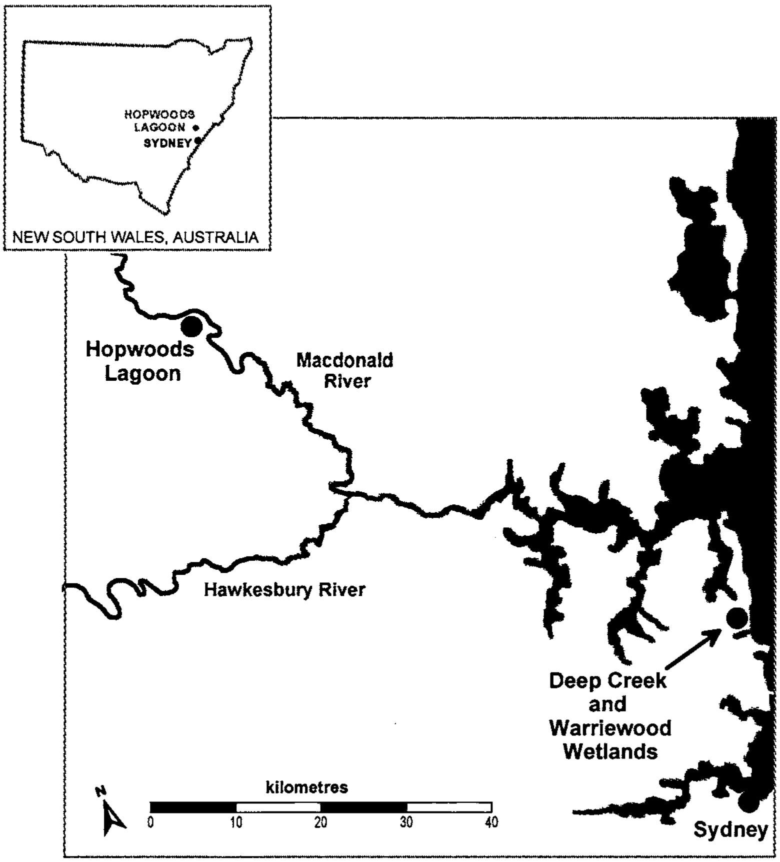

Figure 4.1: Location of field sites at Deep Creek (two sites), Warriewood Wetlands and Hopwoods Lagoon.

This chapter commences with a summary of the important characteristics at the four wetland sites. A more detailed description is then provided of the location and features of the four field sites. Particular attention is given to the macrophyte species present at each wetland, and photographs are included of the dominant species. The description for Hopwoods Lagoon is more comprehensive than those for the Sydney wetlands, and includes details of the wetland bathymetry and water level variation. This increased level of detail reflects the more extensive field investigation programme conducted at Hopwoods Lagoon. The field experimental methodology is outlined in Chapter 5 and results are presented and discussed in Chapter 6.

4.1.1 Summary of Wetland Characteristics

Important characteristics of the four wetland field sites are summarised in Table 4.1, and described in more detail in the remainder of this chapter.

Wetland Identification	Deep Creek *Typha* DCT	Deep Creek *Juncus* DCJ	Warriewood Wetlands WW	Hopwoods Lagoon HL
Location	northern Sydney	northern Sydney	northern Sydney	north-west of Sydney
Topography	coastal floodplain	coastal floodplain	coastal floodplain	narrow river valley
Area	~0.5 ha	< 0.5 ha	~8 ha	~6.5 ha
Depth	1.2 m	0.3 m	1.2 m	3.2 m
Emergent Macrophytes	*Typha domingensis* *Phragmites australis* *Triglochin procerum* *Eleocharis* species	*Juncus kraussii* *Phragmites australis*	*Typha domingensis* *Phragmites australis*	*Eleocharis sphacelata* *Triglochin procerum* *Juncus* species *Paspalum* species *Ludwidgia* species
Submerged Macrophytes	–	–	–	*Hydrilla verticillata* *Potamogeton* species
Further Details	Section 4.2.1 page 121	Section 4.2.2 page 123	Section 4.3 page 126	Section 4.4 page 128

Table 4.1: Summary of important characteristics at the four wetlands. Note that depths are relative to the water surface level at the time of measurement.

These four wetlands were selected to allow contrasts and comparisons between:

- three species of emergent macrophytes with different canopy structures and densities (*Typha domingensis*, *Juncus kraussii* and *Eleocharis sphacelata*)
- two different sites supporting near-monocultural stands of *Typha domingensis* (Deep Creek and Warriewood Wetlands).

4.2 Deep Creek Wetlands, Sydney

The Deep Creek wetlands are located on the floodplain of Deep Creek, a small coastal creek which drains to Narrabeen Lakes in northern Sydney (approximately 33°45'S, 151°18'E). The wetlands are located approximately 250 m from the main creek channel and within 100 m of the shore of Narrabeen Lakes, although the floodplain was never completely inundated during the experimental period from 1999 to 2001. The surrounding topography rises gently from the floodplain. The wetlands are located adjacent to Wakehurst Parkway, and are otherwise bounded by native coastal vegetation.

Two wetland areas were selected at Deep Creek to investigate the attenuation of shortwave radiation by emergent macrophytes. These sites were designated Deep Creek *Typha* (DCT) and Deep Creek *Juncus* (DCJ), after the principal macrophyte species observed at each site. Major features in the vicinity of the Deep Creek *Typha* and *Juncus* wetlands are shown in Figure 4.2. The Deep Creek wetlands were selected over alternative sites for canopy shortwave radiation experiments for several reasons. Favourable site attributes included:

- the near-monocultural species composition at each site, which simplified the characterisation of each canopy
- the contrast in macrophyte species and canopy density between the two adjacent wetland sites
- the proximity of the sites to the Water Research Laboratory, where the research was based
- the relatively low vandalism risk, given that the wetlands were accessible only by wading.

4.2.1 Deep Creek *Typha* Wetland

The Deep Creek *Typha* wetland covers an area of approximately 0.5 ha with a maximum depth of 1.2 m. Most of the wetland area is vegetated, predominantly by the emergent macrophyte *Typha domingensis* (Narrowleaf Cumbungi). *Typha domingensis* is a native perennial species which grows in fresh to brackish water, in depths of up to 2 m. *Typha* comprises relatively flat leaf blades which grow to heights of several metres out of cylin-

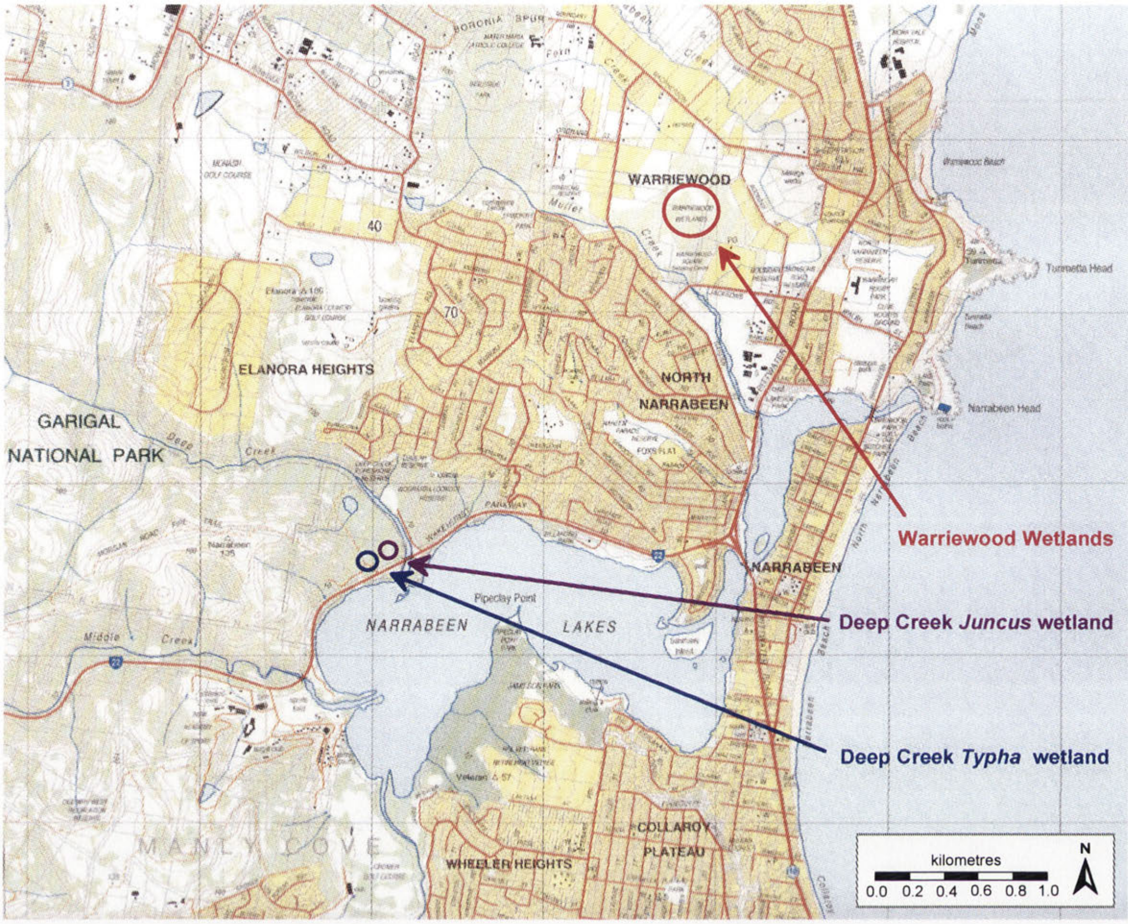

Source: base map from CMA (2000).

Figure 4.2: Major features in the vicinity of the Deep Creek Typha and Juncus wetlands, and Warriewood Wetlands.

drical, pithy stems (Sainty and Jacobs, 1981). A *Typha* canopy typically contains live green stems, dead brown stems and cylindrical flower stems, although no flower stems were observed at the Deep Creek *Typha* wetland during the period from 1999 to 2001.

The wetland also supports more limited numbers of several other emergent macrophyte species. *Phragmites australis* (Common Reed) grows primarily in shallower water around the perimeter, while *Triglochin procerum* (Water Ribbons) is scattered throughout the *Typha*. A small species of *Eleocharis* (possibly *Eleocharis acuta*) was also observed during 2001. Terrestrial vegetation fringing the wetland comprises mainly native *Acacia* and *Casuarina* shrubs.

Figure 4.3(a) shows the Deep Creek *Typha* wetland in July 1999, while the *Typha* was in senescence. Dead brown stems significantly outnumbered fresh *Typha* stems and stems of other macrophyte species. Figure 4.3(b) shows a detail of vegetation in November 1999, including brown stems and fresh regrowth of *Typha domingensis*, stems of *Phragmites australis* and *Triglochin procerum.* The quantity of vegetation debris floating on the water surface was typical of that observed throughout the field investigation period from 1999 to 2001.

4.2.2 Deep Creek *Juncus* Wetland

The Deep Creek *Juncus* wetland covers an area of less than 0.5 ha with a maximum depth of 0.30 m. The Deep Creek *Juncus* wetland is located approximately 150 m to the east of the *Typha* wetland, and supports a virtual monoculture of the emergent macrophyte *Juncus kraussii* (Sea Rush). *Juncus kraussii* is a native perennial species which grows to heights of around 1.5 m above the water surface (Sainty and Jacobs, 1981). The canopy comprises an extremely dense array of narrow, near-cylindrical stems with flowers subtended from the stems.

The wetland also supports more limited numbers of *Phragmites australis*, although the *Phragmites* is not restricted to the perimeter of the wetland, as at the nearby *Typha* site. Terrestrial vegetation fringing the *Juncus* wetland is similar to that around the *Typha* wetland.

Figure 4.4(a) shows the dense *Juncus kraussii* canopy in November 1999, with very low transmission of shortwave radiation to the underlying water surface. Figure 4.4(b) shows typical stems and flower heads of *Juncus kraussii.*

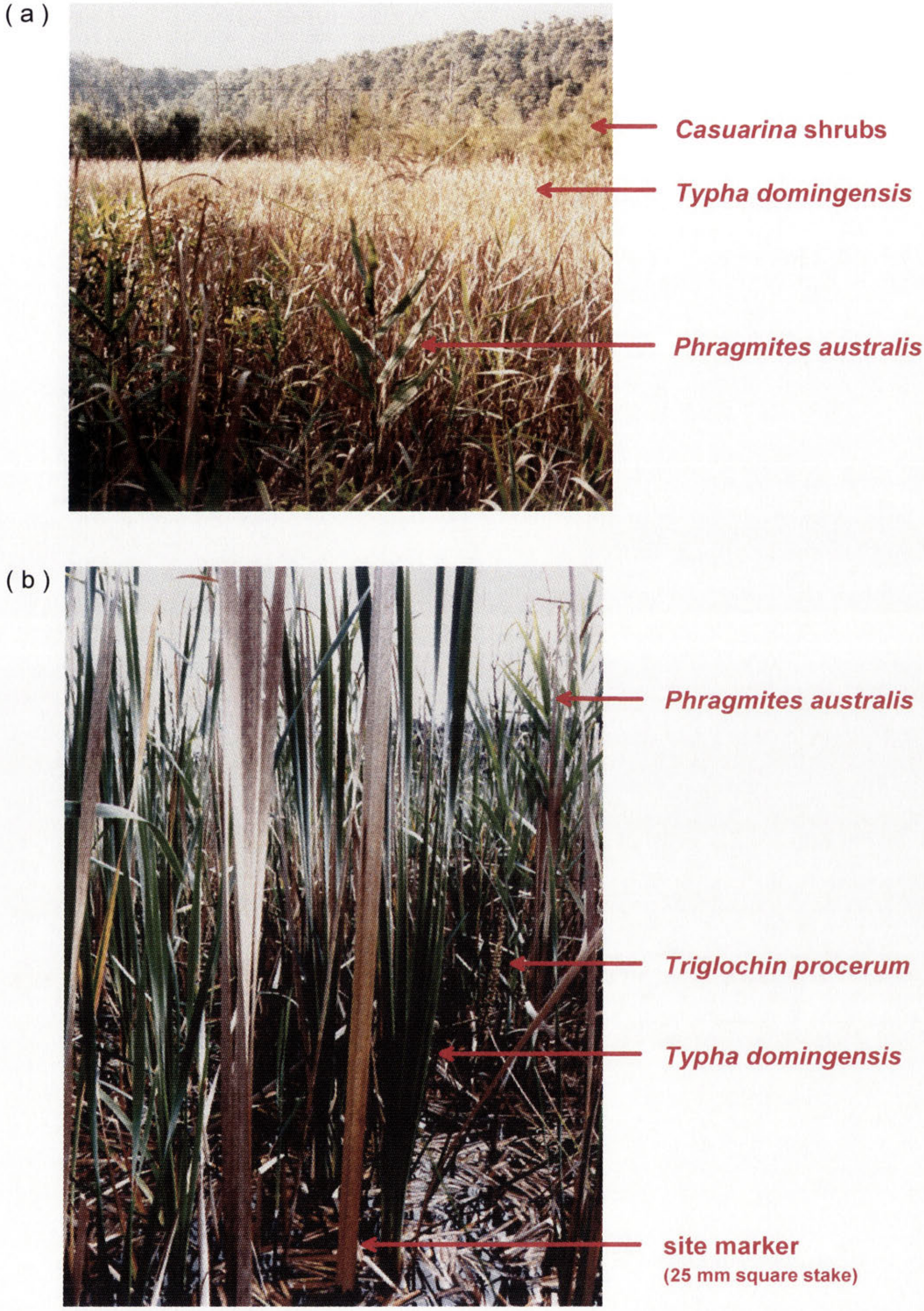

Figure 4.3: Views of the Deep Creek Typha wetland:

(a) from the south in July 1999, showing Typha domingensis in senescence, and

(b) detail of macrophytes in November 1999, showing Typha domingensis, Phragmites australis and Triglochin procerum.

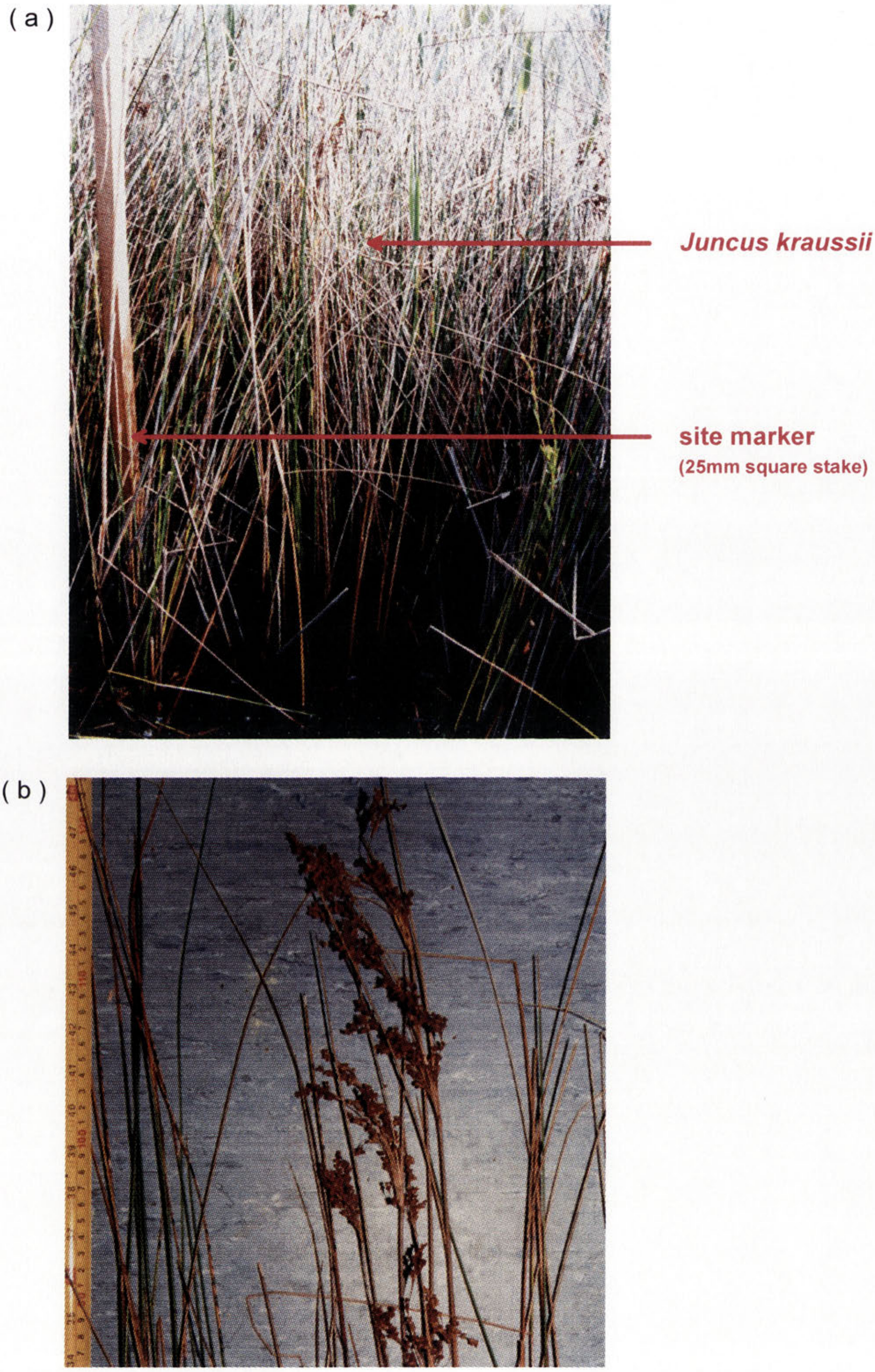

Figure 4.4: Views of the Deep Creek Juncus wetland:

(a) in November 1999, showing the dense Juncus kraussii canopy, and

(b) detail of stems and flowers of Juncus kraussii (height above the water surface).

4.3 Warriewood Wetlands, Sydney

Warriewood Wetlands are located approximately 2.5 km north east of the Deep Creek wetlands. They are situated adjacent to Mullet Creek, which also drains to Narrabeen Lakes. The wetlands cover an area of approximately 8 ha with a water depth of ~ 1 m in the vicinity of the experimental sites. The topography is relatively flat in the immediate vicinity of the wetlands, and surrounding landuses are predominantly residential or recreational. Major topographic features in the vicinity of Warriewood Wetlands are shown in Figure 4.2.

Approximately half of the wetland area is vegetated, predominantly with the emergent species, *Typha domingensis* and *Phragmites australis.* As at the Deep Creek *Typha* wetland, the *Phragmites* is generally restricted to shallower water about the wetland perimeter, while the *Typha* dominates the deeper regions. Unlike the Deep Creek wetland, however, the *Typha* canopy at Warriewood included stems which had flowered in previous seasons, as shown in Figure 4.5(a).

An extensive mat of the fine-leaved floating fern, *Azolla filiculoides* was observed within the *Typha* stand during site visits in September and October 1999. This completely obscured the water surface in some areas of the wetland, as shown in Figure 4.5(b). Terrestrial vegetation surrounding Warriewood Wetlands is similar to that observed elsewhere in the region, and comprises mainly *Acacia* and *Casuarina* species.

The sites at Warriewood Wetlands were selected for shortwave radiation profile experiments for reasons similar to those for the Deep Creek wetlands, primarily for the near-monocultural stand of *Typha domingensis* and because of the proximity to the Water Research Laboratory. However, only limited areas of the wetland were readily accessible, so experiments were restricted to sites adjacent to a shallow, submerged walkway installed by Pittwater Council. The selected sites could only be accessed from these submerged walkways.

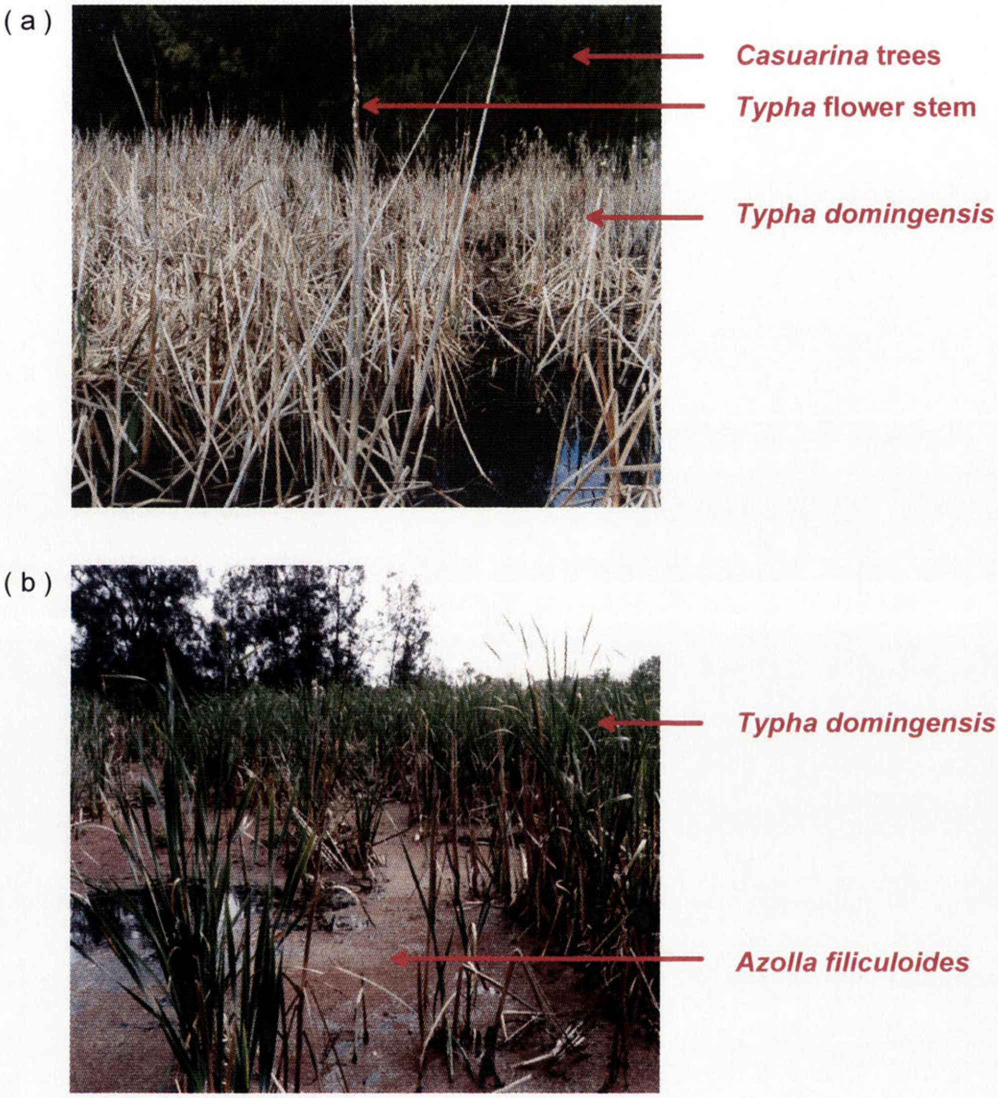

Figure 4.5: Views of the Typha domingensis *canopy at Warriewood Wetlands:*
(a) in senescence in July 1999, showing remnant flower stems in the foreground and Phragmites australis *and* Casuarina *trees in the background, and*
(b) in November 1999, showing significant fresh growth of Typha domingensis*, together with extensive growth of the floating* Azolla filiculoides*.*

4.4 Hopwoods Lagoon, Macdonald Valley

Hopwoods Lagoon is located on the floodplain of the Macdonald River, 75 km north-west of Sydney (approximately 33°13'S, 150°56'E). The lagoon is a natural wetland formed in a meander cutoff of the Macdonald River (Smeulders, 1999), which is a tributary of the Hawkesbury River. Major features in the vicinity of Hopwoods Lagoon are shown in Figure 4.6. The lagoon has a maximum depth of around 3.2 m and covers an area of approximately 6.5 ha, within a relatively small catchment area (< 100 ha). The lagoon can be classified as polymictic (Hutchinson, 1957), and generally mixes on a diurnal basis.

Figure 4.6: Aerial photograph showing major features in the vicinity of Hopwoods Lagoon (20 July 2000).

4.4.1 Hydrology and Hydrogeology

At its closest, the Macdonald River is located approximately 70 m from the lagoon. There is an intermittent link to the river along a shallow, narrow channel, although the lagoon appears to be hydrologically isolated from the river for most of the time. According to Henry (1977), the relatively high river banks in the vicinity of Hopwoods Lagoon were breached by floodwaters on only four occasions between 1867 and 1977, although Marshall (2001) reported a further inflow to the lagoon from the river in August 1998.

Apart from direct runoff, the only surface inflow to the lagoon is via two intermittent watercourses in the south-western area of the catchment, which exhibit surface flow for a short period after prolonged rainfall. Examination of the time-series records of water level variation and mean evaporation in the lagoon suggests that there is no significant groundwater interaction (Figure 6.17, page 239).

4.4.2 Geology and Sediments

Hopwoods Lagoon is situated within Quaternary alluvial sediments and is underlain by the Narrabeen Group, which comprises interbedded quartz-lithic sandstone and shales (Ryan et al., 1996). Four sediment cores were extracted from the central area of Hopwoods Lagoon in June and August 1999 by Smeulders (1999), with a maximum depth of 143 cm. The upper 12 to 15 cm of the cores comprised sand and relatively unconsolidated, gelatinous fluvial sediment (vegetation debris, sand, silt and clay). These were underlain by compacted to very densely compacted clay strata, interbedded with densely compacted layers of fibrous organic material.

Physical properties determined from core samples were used to calculate the volumetric heat capacity of the sediments, as described in Section 6.6.1.3 and Appendix A.

4.4.3 Topography

The Macdonald Valley is narrow, and bounded by sandstone ridges which rise to 250 m within 500 m of Hopwoods Lagoon. The elevated ground is vegetated predominantly with native open forest and woodland species (Ryan et al., 1996), while the river floodplain is largely cleared for agriculture. The sandstone ridges and a knoll adjacent to the lagoon create topographic shading and influence the local wind climate.

4.4.4 Macrophyte Species

The wetland supports stands of the emergent macrophyte *Eleocharis sphacelata* (Tall Spikerush) at the north-eastern and the western ends of the lagoon. *Eleocharis sphacelata* is a native perennial species which grows in stationary to slow moving water bodies up to 2.5 m deep. The canopy comprises individual cylindrical stems which grow up to two metres above the water surface and up to 15 mm in diameter from tuberous roots (Sainty and Jacobs, 1994). The emergent *Triglochin procerum* was also observed growing in water up to 1 m deep. Figure 4.7(a) shows adjacent stands of *Eleocharis sphacelata* and *Triglochin procerum* at the northern end of Hopwoods Lagoon, while Figure 4.7(b) shows the *Eleocharis* canopy in more detail.

Submerged macrophytes occur in dense mats throughout the lagoon, and principally comprise *Hydrilla verticillata* (Water Thyme) and a *Potamogeton* (Pondweed) species. Both species send flowering shoots to the water surface during spring. The extent of the submerged vegetation can be seen clearly on the aerial photograph (Figure 4.6, page 128).

The *Eleocharis* declined in area and density throughout the monitoring period, possibly due to the destructive nesting and feeding behaviour of water fowl which increased in number during the same period. The extent of the submerged vegetation increased with time, and may also have impacted adversely on the distribution of the *Eleocharis*.

Littoral vegetation at Hopwoods Lagoon includes *Juncus usitatus* and several other species of *Juncus*, *Paspalum* and *Ludwidgia* species (Sainty and Jacobs, 1981).

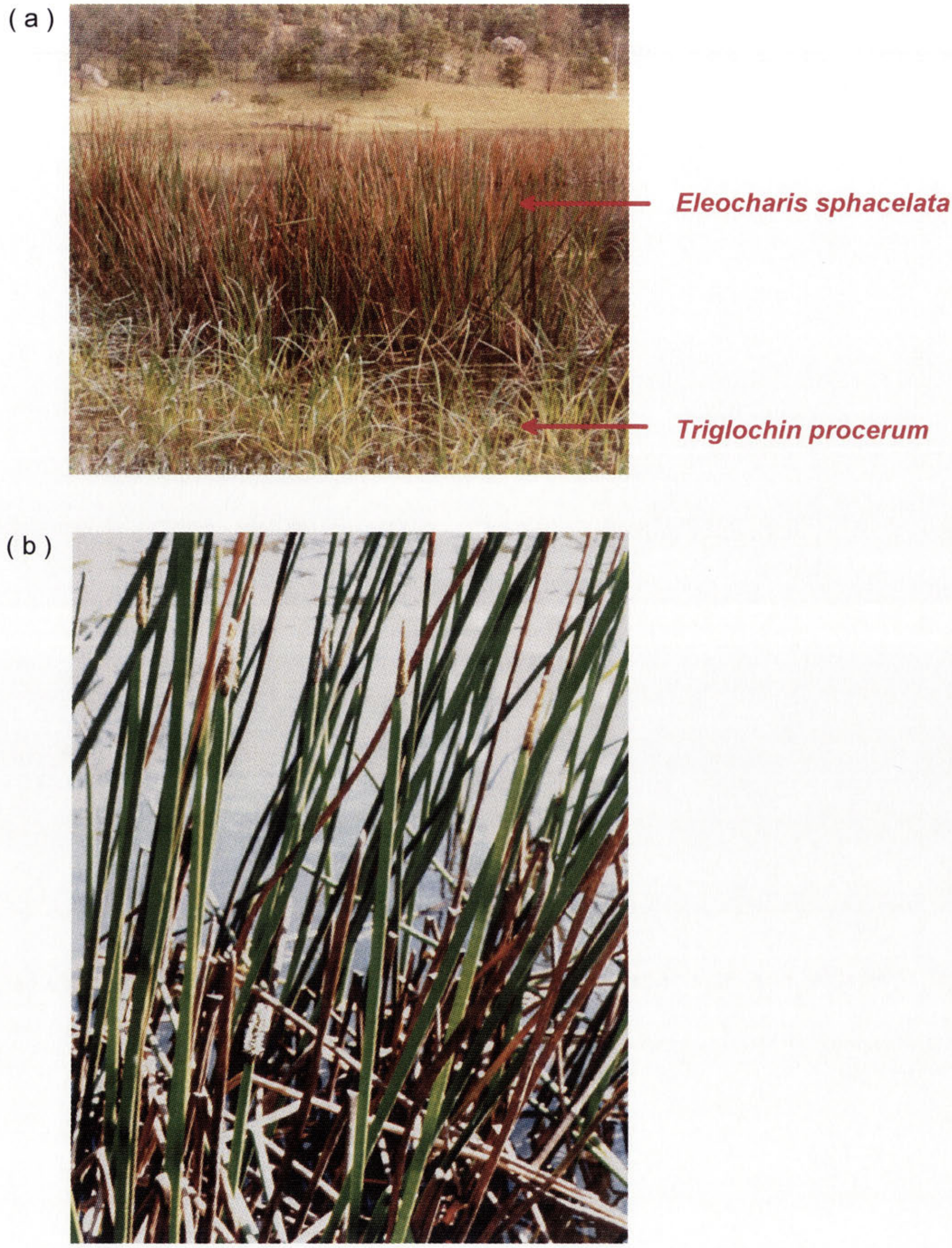

Figure 4.7: Views of the emergent macrophytes at Hopwoods Lagoon:

(a) *Eleocharis sphacelata* and *Triglochin procerum* in June 2000, with the *Eleocharis* afflicted by a rust-coloured blight, and

(b) detail of the *Eleocharis sphacelata* in September 2000, showing flowering stems.

4.4.5 Site Selection

Hopwoods Lagoon was selected for the longer term monitoring of meteorological conditions and water temperatures despite its distance from the Water Research Laboratory. Favourable site attributes which outweighed this disadvantage of distance included:

- the opportunity to complement an existing research programme being undertaken by Natalie Marshall (School of Geography, UNSW) at Hopwoods Lagoon and several other floodplain wetlands in the Macdonald Valley
- the small catchment area and limited surface inflows and outflows, which simplified the hydrology of the site
- the existence of distinct open water and vegetated areas of various depths for water temperature monitoring
- the presence of mature, near-monocultural stands of a different emergent macrophyte species from those studied in Sydney, for further shortwave radiation profile experiments
- the relatively undeveloped nature of the catchment, which is not permanently occupied and used mainly for low intensity grazing of cattle
- the low vandalism risk, with the lagoon located on private property 20 km from the nearest town and not visible from the road.

4.4.6 Bathymetric Survey of Hopwoods Lagoon

A bathymetric survey was conducted to determine the subsurface geometry of Hopwoods Lagoon. The survey provided information on the depth-dependence of the various vegetation zones and geometric input for the hydrodynamic modelling.

The bathymetric survey was conducted in October 2001 using Nikon DTM-300 surveying instruments. The bathymetric profile of the lagoon was constructed from a large number of linear transects between the northern and southern shores, with bed levels taken from a boat. A total of 594 points were surveyed, on a grid with a spacing of between 10 m and 20 m. The distribution of macrophytes within the lagoon was also recorded during the survey.

Elevations were recorded to ± 0.01 m, although the bed levels were possibly in error by as much as 0.05 to 0.10 m, given the soft and uneven nature of the sediment-water interface. On the shore, survey closure readings between the three survey station points were within ± 0.04 m in the horizontal and ± 0.02 m in the vertical. The site survey was related to AHD by overlaying the survey contours with the Auburn 9031-1-S 1:25 000 topographic map (CMA, 1976), in the absence of a nearby trig station or state survey mark.

Contours were created from the Hopwoods Lagoon survey data using the inbuilt Kriging function within the software contouring package, Surfer (Golden Software, Inc). Bathymetric contours are shown in Figure 4.8. Two distinctive features of the bathymetry of Hopwoods Lagoon are the relative shallow, semi-enclosed embayment at the north-eastern end, and the steep slope along the north-western shore of the lagoon. The deepest point is located close to this steep shore, with a bed elevation of 13.54 m. The perimeter slope was more gradual and approximately uniform around the remainder of the lagoon.

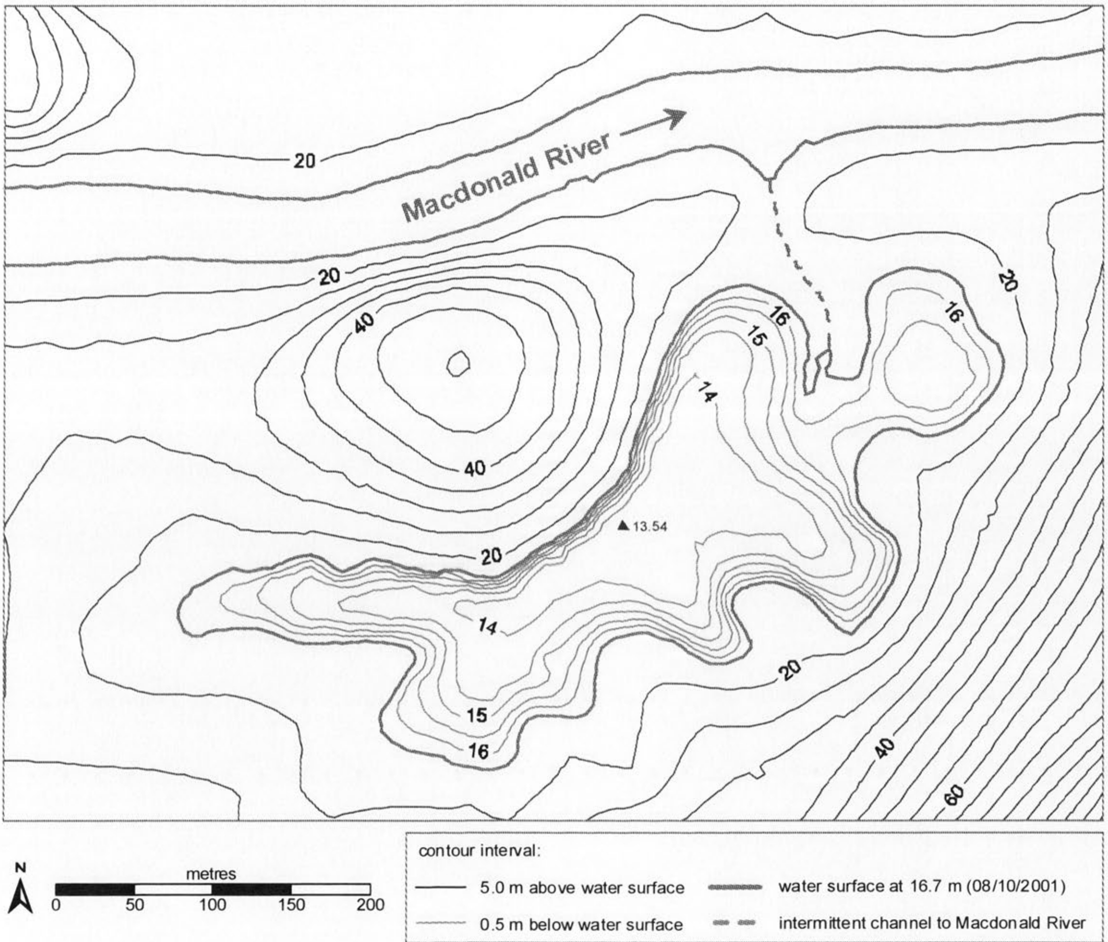

Figure 4.8: Topographic and bathymetric contours derived from the survey at Hopwoods Lagoon and the Auburn 9031-1-S 1:25 000 topographic map (CMA, 1976).

4.4.7 Water Level Variation at Hopwoods Lagoon

Variation in the water surface elevation was required to asses the hydrological regime at Hopwoods Lagoon, and to provide input for the hydrodynamic modelling. Water temperature measurement depths were also defined relative to the water surface elevation, because some measurements were made at fixed depths below the water surface.

The water surface elevation was gauged against an aluminium survey staff located at the northern end of Hopwoods Lagoon. The staff gauge was installed and maintained by Natalie Marshall of the School of Geography at UNSW, who also provided water level data for dates prior to February 2000. Water levels were measured manually and recorded to ± 0.01 m. Water surface elevation was related to staff gauge level using the site survey data:

$$\text{water level (m, AHD)} = \text{gauge level} + 7.06 \tag{4.1}$$

The water level variation at Hopwoods Lagoon is shown in Figure 4.9, which indicates a similar seasonal cycle in 2000 and 2001. The water level increased by 0.76 m during a flood in August 1998, when water entered the lagoon from the Macdonald River along the narrow tie-channel at the northern end of the lagoon (N. Marshall, pers. comm.).

The peak water surface elevation of 17.25 m in March 2001 was almost 1.2 m higher than the minimum elevation prior to the flood of August 1998, although the annual water level range was a more modest 0.42 m in 2000 and 0.65 m in 2001. Smeulders (1999) reported anecdotal evidence that suggested the lagoon had not dried out completely during living memory. However, an aerial photograph reproduced from 1941 (Henry, 1977) shows much lower water levels and a significantly reduced water surface area, with the north-eastern embayment completely dry.

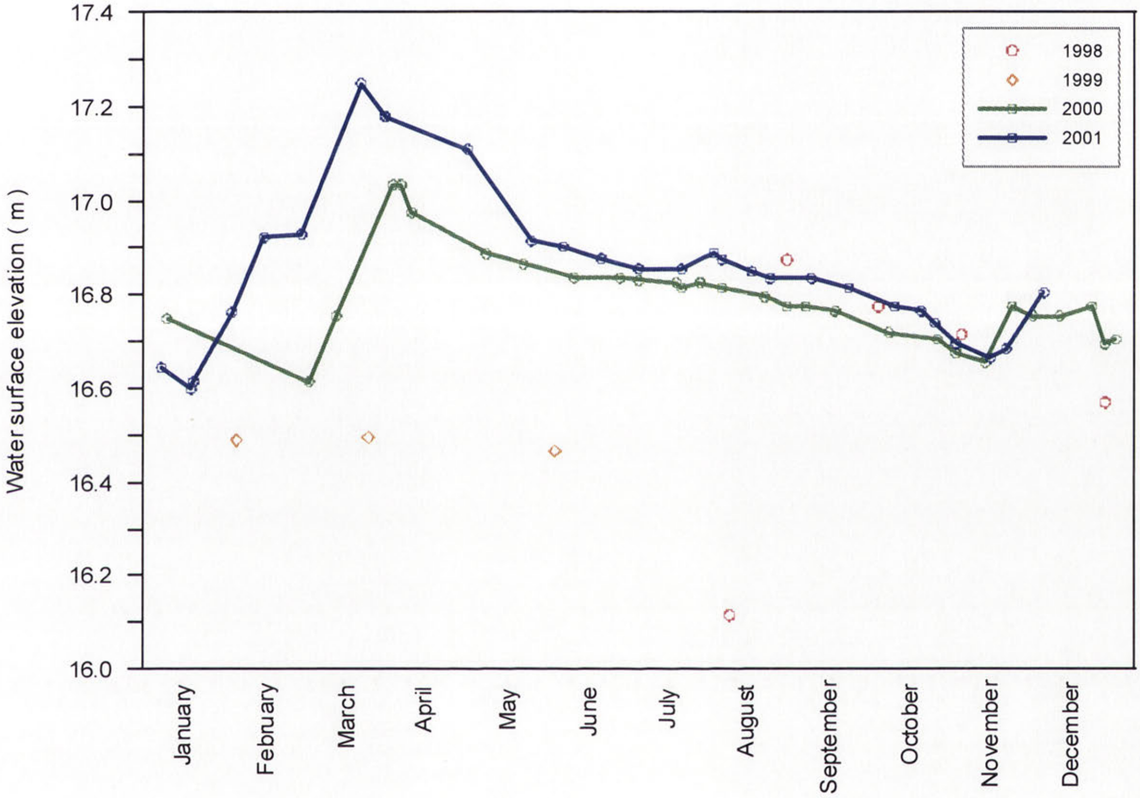

Figure 4.9: Time-series variation in water surface elevation at Hopwoods Lagoon.

Chapter 5

EXPERIMENTAL METHODOLOGY

5.1 Introduction

The field investigation programme was designed to obtain data which could be used to:

- test the applicability of simple canopy and underwater shortwave radiation attenuation models proposed in the literature
- examine diurnal and seasonal hydrodynamic behaviour in a natural wetland and
- provide input data for the hydrodynamic modelling experiments.

A series of field experiments was conducted at the Deep Creek and Warriewood Wetlands in Sydney and at Hopwoods Lagoon in the Macdonald Valley. These field sites were described in Chapter 4. The methodology for emergent macrophyte surveys undertaken to characterise macrophyte properties is described in Section 5.2, while the canopy radiation and underwater shortwave radiation attenuation experiments are described in Sections 5.3 and 5.4, respectively.

Numerical modelling of the effects of radiation shading on wetland hydrodynamics was undertaken using the existing RMA-10 code, which was modified by the present author to incorporate a generalised macrophyte shading module. The model was validated using field data from Hopwoods Lagoon and used to examine radiation shading in wetlands over a greater range of macrophyte properties than could be examined in the field. The numerical modelling methodology is described in Section 5.6.

The results of the experimental programme are analysed and discussed in Chapter 6.

5.2 Emergent Macrophyte Surveys

The presence of emergent macrophytes in a wetland significantly alters the energy fluxes across the air-water interface, compared with an unvegetated zone. Attenuation of these fluxes above the water surface is a function of the structural properties (foliage area and distribution) of an emergent macrophyte canopy. Emergent macrophyte surveys were conducted to determine the physical characteristics of the macrophyte canopies. The macrophyte data were used with the results of the canopy attenuation experiments to examine simple canopy attenuation models described in the literature. Macrophyte data were also used as input to the hydrodynamic model when calculating the modified surface energy fluxes in macrophyte zones.

The specific objectives of the emergent macrophyte surveys were to determine for each wetland, and for each series of canopy attenuation experiments:

(1.) the canopy height, h_L

(2.) the macrophyte stem density as a function of height, $n_s(z)$

(3.) the mean stem dimensions as a function of height, $d(z)$

(4.) the foliage area density, $a(z)$, and downward cumulative leaf area index, *LAI(z)*, as a function of height, and

(5.) the inclination of the foliage area, $g_L(\theta)$.

Typical stands of the emergent macrophytes at the four wetlands were depicted in Chapter 4. The macrophyte surveys were conducted during the seasons indicated in Table 5.1, in conjunction with the canopy attenuation experiments.

The macrophyte surveys were restricted to emergent species because these are the most commonly identified wetland macrophytes and the most extensively used in constructed wetlands. Moreover, the existing literature suggests that emergent macrophytes have a more significant influence on the surface energy fluxes in a wetland than non-emergent species.

The macrophyte surveys were designed to allow efficient collection of comparable vegetation data at each site and on each sampling occasion. From comprehensive reviews of vegetation sampling techniques available in the literature (Dennis and Isom, 1984; Moore

Wetland and Dominant Species		Dates of Emergent Macrophyte Surveys		
Deep Creek *Typha*	DCT	Winter	Spring	Autumn
Typha domingensis		26 Aug 1999	26 Nov 2000	17 Apr 2001
Warriewood Wetlands	WW	–	Spring	–
Typha domingensis		–	17 Oct 1999	–
Deep Creek *Juncus*	DCJ	Winter	–	–
Juncus kraussii		26 Aug 1999	–	–
Hopwoods Lagoon	HL	Winter	–	Autumn
Eleocharis sphacelata		3 Sep 2000	–	1 Apr 2001

Table 5.1: Dates of emergent macrophyte surveys.

and Chapman, 1986), a selective sampling regime was chosen for the macrophyte surveys. Quadrats were established at representative sites within each wetland, because access restrictions precluded a more statistically robust, random sampling regime. It is acknowledged that there is some inherent bias in such selective sampling (Gertz, 1984), however the results were considered sufficiently representative of overall canopy conditions for the purposes of this investigation.

It was assumed that the macrophyte canopies were horizontally homogeneous, with structural properties which varied only with height above the water surface. This assumption is commonly adopted in micrometeorological and plant actinometrical studies (Ross (1981), Ayra (1988), Miller (1981), Goudriaan (1977)) because it reduces the mathematical complexity of the system. It was also assumed that mean values could be obtained for the canopy structural parameters using results from a number of discrete sampling locations (Guyot, 1998), which were assumed to be representative of mean canopy conditions.

The canopy structural properties were determined as outlined in the following sections.

5.2.1 Canopy Height, h_L

The canopy height is fundamental in describing the structure of an emergent macrophyte canopy, and used directly in some simple canopy attenuation models. The canopy height was determined as the *in situ* height above the water surface of the tallest stem of the dominant macrophyte species.

While the mean canopy height defines the height at which the stem density is concentrated within the canopy, the maximum canopy height is the height below which shortwave radiation is attenuated, and therefore the relevant parameter in the present study.

The maximum canopy heights at each wetland are reported in Section 6.2.1.

5.2.2 Stem Density, $n_s(z)$

The stem density is defined as the number of individual emergent macrophyte stems or shoots per unit area of water surface. Stem densities were required to calculate the foliage area within the emergent macrophyte canopies. The stem density was determined at each wetland as described below.

- Square-shaped quadrats were defined at each sampling site using a compass and steel tape measure, and marked at the four corners using stakes driven into the substrate. Quadrat areas were 1 m by 1 m in the *Typha* and *Eleocharis* stands at Deep Creek, Warriewood Wetlands and Hopwoods Lagoon, and 30 cm by 30 cm and 60 cm by 60 cm in the dense Deep Creek *Juncus* wetland, where stem counting over a larger area would have been prohibitive.
- The corner stakes were marked at height intervals of 0.2 m above the water surface, and the quadrat was delineated by a cord secured around the perimeter.
- The number of stems of each species which intersected the horizontal quadrat area was recorded for each height increment. Counting was undertaken simultaneously by two people to minimise errors. Stems were counted if any part of the stem intersected the quadrat area, whether or not it was rooted within the quadrat. Goldsmith et al. (1986) advocate counting based on root position rather than the occurrence of aerial plant components in the quadrat. However, this method was impractical for wetland species with submerged roots. It was also observed that the numbers of stems entering and leaving the quadrats were approximately balanced.

The stem densities at each wetland are reported in Section 6.2.2.

5.2.3 Stem Dimensions, $d(z)$

The mean stem dimensions were required with the stem densities to calculate the distribution of foliage area within each of the emergent macrophyte canopies. The characteristic stem dimensions were defined as:

- **mean stem width** for the flat, approximately rectangular stems of *Typha domingensis* and *Triglochin procerum*
- **mean stem diameter** for the near-cylindrical stems of *Juncus kraussii, Eleocharis sphacelata* and *Phragmites australis.*

Representative samples were removed from each wetland and the stem dimensions were measured in the laboratory. Stem samples were considered representative if they included all types of stems observed within the quadrats, with approximately 50 individuals of the dominant stem type. Stems were sampled from an area not less than a single quadrat, but the total number of stems was restricted to limit ecosystem damage. Stems were transported and stored in water and measured as soon as possible after sampling to minimise dimension changes due to dehydration.

Stem dimensions were measured at 0.2 m intervals above the water surface, using a Mitutoyo dial gauge with 0.05 mm divisions, and recorded to the nearest 0.1 mm. The sample mean and standard deviation were calculated for each 0.2 m height interval above the water surface, for each macrophyte species at each wetland.

The characteristic stem dimensions are reported in Section 6.2.3.

5.2.4 Foliage Area Density, $a(z)$, and Leaf Area Index, $LAI(z)$

The foliage area density function was required to calculate the downward cumulative leaf area index, which was used with the results of the canopy attenuation experiments to examine simple canopy attenuation models. The foliage area density function and the downward cumulative leaf area index were defined on page 72, and calculated for each macrophyte canopy as discrete functions defined at intervals of 0.2 m above the water surface.

The foliage area density and the downward cumulative leaf area index for each canopy included the foliage area contributed by all species at the site, not only the dominant *Typha, Juncus* or *Eleocharis* stems. A mean *LAI(z)* for each wetland was calculated as the weighted mean of the *LAI(z)* at each site at that wetland. The weighting function at each measurement height was calculated from the stem density at each contributing site, expressed as a proportion of the total number of stems at all sites. The calculation methodology is described in more detail in Section B.3 in Appendix B.

The weighted mean downward cumulative leaf area index for each wetland is reported in Section 6.2.4.

5.2.5 Foliage Area Inclination, $g_L(\theta)$

The orientation of the foliage area was required as input in some simple canopy attenuation models. As discussed in Section 3.4, the orientation of foliage area is typically described in terms of the inclination angle (from the vertical), the azimuth (or bearing from north) and the height in the canopy. The depth below the top of the canopy, or *LAI(z)*, is sometimes used instead of depth. It is commonly assumed that there is no azimuth preference in the foliage orientation (Ross, 1981), especially in natural communities, as was adopted in this study. It was also assumed that the foliage inclination was constant with height above the water surface, which was considered reasonable for the predominantly vertical *Typha*, *Juncus* and *Eleocharis* canopies.

The foliage area inclination for each canopy was estimated by inspection, and distributed across six inclination classes of 15°. Ross (1981) described several laborious methods for determining the foliage area inclination more precisely, however these were impractical in the present study due to access restrictions in the wetlands.

The estimated distribution of the foliage area inclination at the four wetlands is reported in Section 6.2.5.

5.3 Canopy Attenuation Experiments

Shortwave radiation is attenuated with depth of penetration beneath the top of a macrophyte canopy, and either reflected from foliage surfaces, absorbed by the canopy elements, or transmitted through the canopy without interception. Shortwave radiation fluxes at the water surface beneath an emergent macrophyte canopy are therefore less than those in the absence of vegetation.

The objectives of the canopy attenuation experiments were to:

- expand the existing data set available in the literature by measuring vertical attenuation of shortwave radiation within the macrophyte canopies of three different species, with a range of stem densities, at four wetlands
- use the vertical attenuation data to examine the applicability of simple canopy attenuation models described in the literature
- select a simple canopy attenuation model for incorporation in the wetland hydrodynamic model.

Attenuation experiments were conducted at the four wetlands between August 1999 and April 2001. The experiments were repeated at different times of the year at the Deep Creek *Typha* wetland and at Hopwoods Lagoon, to examine seasonal variation in attenuation of shortwave radiation by the *Typha* and *Eleocharis* canopies. Measurements were made at different times during the day and at a number of sites at each wetland to provide temporal and spatial canopy attenuation data. The number of sites at each wetland was minimised ($\leq$ 3) so the number of radiation profiles could be maximized at each site, within the period available for experiments.

Profile measurements were conducted only when the day commenced with cloudless skies. Measurements under clear skies ensured the proportions of direct and diffuse radiation were relatively consistent between different times and on different days (Ross, 1981), since scattering by clouds increases the proportion of diffuse to direct shortwave radiation. However, this also influenced the timing of measurements and restricted the total number of clear sky radiation profiles, because profile measurements were clearly affected if clouds appeared (see Section 5.3.1).

Shortwave radiation was measured within the macrophyte canopies using a cosine-corrected, LI-COR model 192SA quantum sensor, sensitive to photosynthetically active radiation (PAR) in the waveband 400 to 700 nm. The sensor specifications and calibration factors are given in Appendix C. As discussed in Section 3.3.2.1, the PAR waveband contains approximately 50 percent of the energy in the global shortwave spectrum under clear skies (Guyot, 1998). This ratio was confirmed in the field by comparing output from the PAR sensor and the global pyranometer operated at Hopwoods Lagoon. The relationship is shown in Figure C.1 and Table C.2 in Appendix C.

Modelling the transmission of shortwave radiation through a canopy is simpler for PAR compared with global shortwave radiation (300 to 2800 nm), due to the high absorption of radiation in the PAR waveband. Multiple scattering (reflection) of PAR within the canopy can therefore be neglected, and consequently, modelling results based on PAR are less sensitive to the optical properties of the canopy than other wavebands (Torssell and McPherson, 1977), including global shortwave radiation. In these experiments, it was assumed that PAR was either attenuated (absorbed) by canopy elements or transmitted without interception.

Each canopy radiation profile comprised a vertical series of radiation measurements made at the water surface and at height intervals of 0.1 to 0.2 m from the water surface to the top of the macrophyte canopy, with an additional, reference measurement above the canopy. At each height, the PAR sensor was scanned once every 5 s for a period of one minute, and the average was calculated.

The PAR sensor was moved vertically through the canopy using a set of telescopic poles, as shown in Figure 5.1. These allowed the sensor to be raised to any height.

All measurements were made with the sensor located due north of the telescopic pole, which minimised differential shading effects throughout the day. Reflection from the matte PVC and aluminium surfaces of the pole assembly was assumed to be negligible. Reflection from the water surface did not influence attenuation of radiation by the canopy *above* the surface, and was considered separately.

5.3.1 Reliability of Sampling Regime

The reliability of the 5 s sampling regime in describing average PAR conditions over each one minute period was assessed using the coefficient of variation (CV). This coefficient describes the relative variation in a sample, and is calculated as follows:

$$CV = \frac{\text{standard deviation}}{\text{mean}} \times 100\,\% \tag{5.1}$$

The CV was calculated for the above canopy reference PAR measurements ($\phi_{PAR(z)}$ when $z \geq h_L$) for each radiation profile, and the results are reported in Table 5.2. Any variation in the above-canopy measurements should be independent of local canopy properties and affected only by factors remote from the measurement site, for example topographic shading in the early morning or late afternoon.

The data in Table 5.2 indicate that the 5 s sampling regime was generally reliable in representing the average, clear sky PAR conditions over a period of one minute, as the coefficient of variation was in most cases $< 1\%$. A reliability of $CV \leq 5\%$ was considered

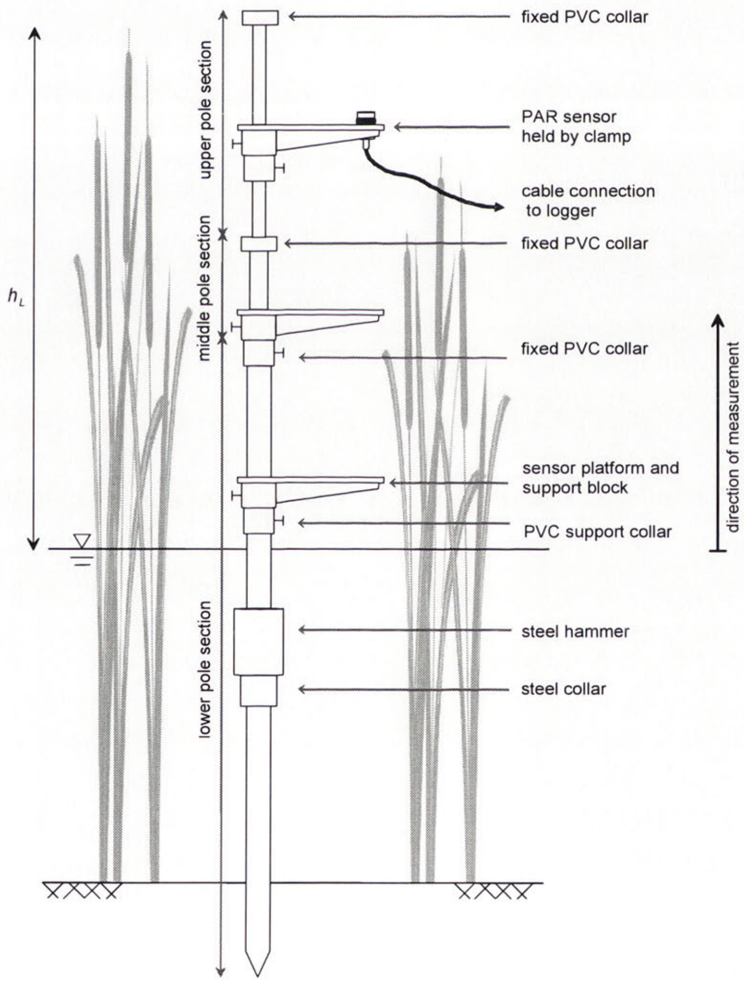

Figure 5.1: Experimental apparatus for measurement of shortwave radiation within an emergent macrophyte canopy (not to scale).

acceptable for this series of experiments. Notable exceptions where $CV > 5\%$ could generally be explained with reference to specific observations noted at the time of the experiments, as outlined below.

- At the **Deep Creek *Typha*** wetland, some measurements made after 15:00 on **19 August 1999** were affected by partial shading from shrubs surrounding the wetland. It is likely that observed variability in the measured PAR intensity resulted from differential shading as the shrubs moved in response to light winds. The variation in the 5 s measurements taken around 15:35 coincided with a band of thin high cloud noted over the southern horizon. The high variance in the measurements taken around 13:39 at site DCT3 cannot be explained by the observed meteorological conditions at the time, and it is hypothesized that two low measurements during the one minute period may have been due to birds or insects passing across the face of the sensor.
- At the **Deep Creek *Typha*** wetland, measurements made after 13:50 on **23 November 2000** appeared to have been influenced by a bank of clouds which approached from the south.
- At the **Deep Creek *Juncus*** wetland, some measurements made before about 08:30 appeared to have been influenced by partial shading from shrubs surrounding the wetland. On **14 August 1999**, cloud began to approach from the west around 08:15. The clouds were fast moving and partially obscured the sun at times after 08:30. Measurements taken on **17 August 1999** were all potentially influenced by fine cirrus clouds which developed from a small band on the horizon into a thick band of cumulus clouds around noon, and these obscured the sun.

All profiles with $CV > 10\%$ for above-canopy measurements and any profiles with $CV > 5\%$ which were known to be cloud-affected were removed from the clear sky canopy attenuation dataset. Other profiles with $CV > 5\%$ were retained but used with caution in subsequent analyses.

<u>Notes to Table 5.2</u> (following pages).

Relative PAR profile not considered in subsequent analyses because:

(1) $CV > 10\%$

(2) measurements made within 2 hr of sunrise or sunset (see Section 5.3.2).

Wetland and Dominant Species	Date of Measurement	Site ID	Profile Start (AEST)	PAR Sensor Response Mean (mV)	St. Dev. (mV)	CV (%)	Notes see p.147
Deep Creek *Typha* *Typha domingensis*	19 Aug 1999	DCT1	08:32	4.423	0.009	< 1	
			10:04	6.328	0.008	< 1	
			11:35	7.062	0.010	< 1	
			13:20	6.236	0.006	< 1	
			14:49	4.316	0.007	< 1	
			16:01	0.693	0.017	2.5	2
		DCT2	09:29	5.747	0.007	< 1	
			11:04	6.832	0.019	< 1	
			12:53	6.462	0.006	< 1	
			14:30	4.643	0.008	< 1	
			15:35	0.815	0.137	16.8	1,2
			16:45	0.242	0.001	< 1	2
			17:01	0.151	0.002	1.4	2
		DCT3	09:04	4.891	0.007	< 1	
			10:45	6.264	0.005	< 1	
			11:58	6.553	0.021	< 1	
			13:39	5.196	1.108	21.3	1
			15:15	1.630	0.134	8.2	
			16:18	0.367	0.002	< 1	2
	23 Nov 2000	DCT1	13:33	8.820	0.010	< 1	
		DCT2	09:47	9.707	0.186	1.9	
			10:23	9.914	0.015	< 1	
			11:02	10.002	0.010	< 1	
			12:20	9.951	0.014	< 1	
			14:13	8.338	0.912	10.9	1
		DCT3	12:48	9.599	0.010	< 1	
			14:40	6.077	2.902	47.8	1
	26 Nov 2000	DCT1	10:25	9.926	0.011	< 1	
			10:52	10.070	0.010	< 1	
			13:11	9.363	0.014	< 1	
			13:29	9.040	0.013	< 1	
		DCT2	12:40	9.849	0.015	< 1	
		DCT3	11:25	10.130	0.010	< 1	
			11:42	10.158	0.022	< 1	
			13:52	8.722	0.012	< 1	
			14:18	8.214	0.017	< 1	
	17 Apr 2001	DCT1	11:49	7.304	0.010	< 1	
			12:11	7.361	0.008	< 1	
			13:40	6.161	0.008	< 1	
			14:00	5.720	0.013	< 1	
			14:46	4.712	0.009	< 1	
		DCT2	10:54	6.992	0.008	< 1	
			11:18	7.233	0.010	< 1	
			12:49	6.851	0.009	< 1	
			13:09	6.402	0.008	< 1	
			14:25	4.749	0.005	< 1	

Table 5.2: Mean, standard deviation and coefficient of variation for the 5 s, reference PAR measurements made above the canopy, $\phi_{PAR(h_L)}$.

Wetland and Dominant Species	Date of Measurement	Site ID	Profile Start (AEST)	PAR Sensor Response Mean (mV)	PAR Sensor Response St. Dev. (mV)	PAR Sensor Response CV (%)	Notes see p.147
Warriewood Wetlands *Typha domingensis*	30 Sep 1999	WW1	09:12	7.539	0.010	< 1	
			11:03	9.738	0.029	< 1	
			12:18	8.613	0.008	< 1	
			13:17	7.836	0.014	< 1	
			14:28	6.185	0.009	< 1	
		WW2	10:35	8.680	0.008	< 1	
			11:51	8.799	0.015	< 1	
			12:51	8.300	0.413	5.0	
			14:01	7.105	0.013	< 1	
			15:11	5.194	0.140	2.7	
Deep Creek *Juncus* *Juncus kraussii*	12 Aug 1999	DCJ1	07:32	0.832	0.099	11.9	1,2
			08:26	2.733	0.050	1.8	2
			09:15	5.106	0.051	< 1	
			10:13	6.140	0.005	< 1	
		DCJ2	07:51	3.053	0.010	< 1	2
			08:49	4.765	0.010	< 1	
			09:39	5.963	0.009	< 1	
			10:35	6.854	0.013	< 1	
	14 Aug 1999	DCJ1	06:57	0.431	0.013	3.1	2
			07:48	1.156	0.110	9.5	2
			08:34	1.703	0.005	< 1	
			09:31	6.914	1.453	21.0	1
		DCJ2	07:17	0.484	0.015	3.1	
			08:06	4.367	0.075	1.7	
			08:51	3.808	0.460	12.1	1
			10:53	5.169	2.268	43.9	1
	17 Aug 1999	DCJ1	09:38	5.201	0.097	1.9	
			10:29	6.213	0.045	< 1	
			11:51	4.340	0.110	2.5	
			12:39	2.625	0.002	< 1	
		DCJ2	10:02	6.250	0.138	2.2	
			10:46	6.155	0.105	1.7	
			12:11	5.572	0.375	6.7	
Hopwoods Lagoon *Eleocharis sphacelata*	27 Jul 2000	HL2	10:17	6.187	0.006	< 1	
			10:41	6.774	0.034	< 1	
			11:12	6.920	0.012	< 1	
			11:36	7.141	0.013	< 1	
	27 Aug 2000	HL2	08:28	5.714	0.005	< 1	
			08:59	5.921	0.006	< 1	
	03 Sep 2000	HL2	10:47	7.170	0.005	< 1	
	01 Apr 2001	HL1	10:56	7.554	0.006	< 1	
			11:14	7.578	0.008	< 1	
			12:15	7.401	0.006	< 1	

Table 5.2 (continued): Mean, standard deviation and coefficient of variation for the 5 s, reference PAR measurements made above the canopy, $\phi_{PAR(h_L)}$.

5.3.2 Canopy Relative PAR Attenuation Profiles, $\phi_{PAR(z)}\,/\,\phi_{PAR(h_L)}$

The relative PAR at elevation z above the water surface is defined as $\phi_{PAR(z)}\,/\,\phi_{PAR(h_L)}$, where $\phi_{PAR(z)}$ is the PAR flux (Wm^{-2}) at elevation z (m) and $\phi_{PAR(h_L)}$ (Wm^{-2}) is the incident or reference PAR flux above the canopy.

Because only one PAR sensor was available for the canopy attenuation experiments, measurements could not be made simultaneously within and above the canopy. The error associated with using a single sensor to make sequential measurements was assessed by calculating the predicted variation in unattenuated PAR over the average measurement period. The movement of the sun is symmetrical about solar noon, and the variation in PAR can be approximated by a sinusoidal curve (Monteith and Unsworth, 1990) as follows:

$$\phi_{PAR(t)} = \phi_{PAR(max)} \sin\left\{\frac{\pi t}{DL}\right\} \tag{5.2}$$

where $\phi_{PAR(max)}$ = maximum PAR at solar noon (Wm^{-2})
t = time after sunrise (hr)
DL = daylength (hr).

The time of sunrise and the daylength can be calculated as shown in Appendix A.

The average measurement period for all individual canopy attenuation profiles was 0:19:21 $\pm$ 0:04:59 (from commencement at the water surface to completion above the canopy). Figure 5.2 shows the variation in PAR as a function of the maximum PAR at solar noon, according to Equation (5.2). Note that temporal variation is shown as relative time of day between sunrise ($t/DL = 0$) and sunset ($t/DL = 1.0$), with solar noon at $t/DL = 0.5$.

The relative change in predicted PAR over the preceding 20 min period approximating a single canopy attenuation profile is also shown in Figure 5.2. This latter curve indicates that the variation in predicted PAR over the preceding 20 min period is $\sim$ 100% near sunrise and sunset. Because the reference PAR measurement was the final measurement in each profile, it overestimated the 20 min average PAR conditions at $z = h_L$ during the morning and underestimated during the afternoon. Consequently, relative PAR attenuation at other $z < h_L$ could be underestimated during the morning and overestimated during the afternoon if calculated using the measured reference PAR to represent above-

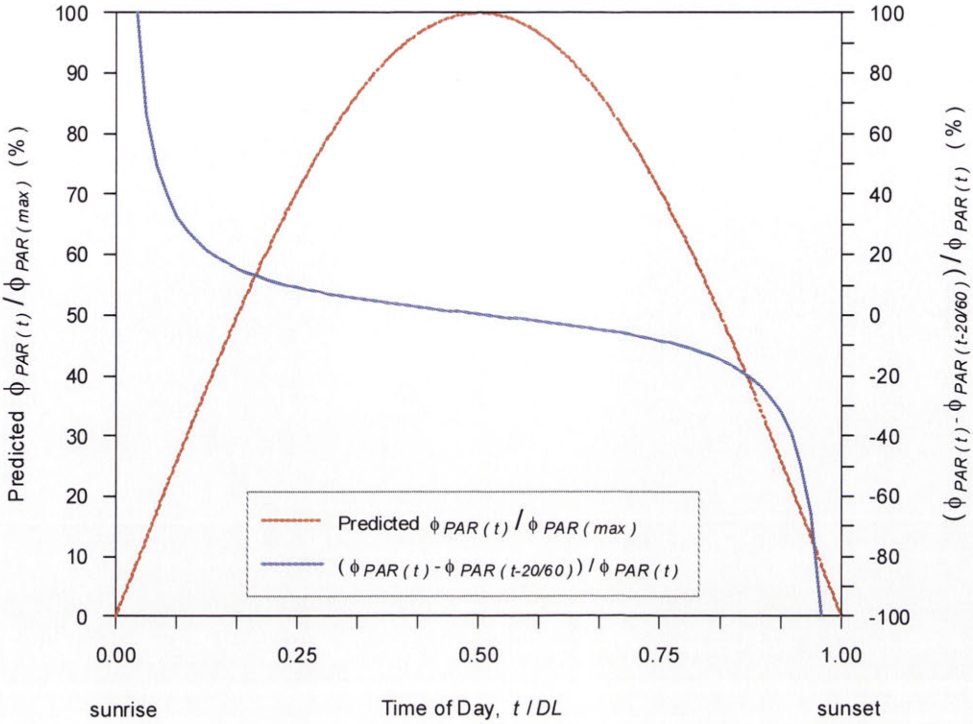

Figure 5.2: Temporal variation in predicted reference PAR, where t is the time (hr) since sunrise and DL is daylength (hr).

canopy PAR conditions over the entire profile period. The expected error is $< 5\%$ within 2 hr of solar noon, but could exceed 15% for profiles measured within two hours of sunrise or sunset. Given this uncertainty, profiles measured within 2 hr of sunrise or sunset were removed from the data set and not used in further analyses.

Relative PAR profiles were determined for the remaining canopy attenuation profiles by dividing the 1 min mean of the 5 s PAR measurements at each height by the 1 min mean of the 5 s reference PAR measurements at $z \geq h_L$. The canopy relative PAR profiles are presented and discussed in Section 6.3.

5.4 Underwater Attenuation Experiments

Of the energy fluxes described in Chapter 2, only shortwave radiation penetrates to any significant depth below the water surface. The shortwave radiation flux is attenuated with depth due to scattering by suspended matter and absorption by water molecules and suspended materials.

The objectives of the underwater shortwave radiation experiments were to:

- expand the existing data set available in the literature by measuring vertical attenuation in the coloured waters of the natural wetland at Hopwoods Lagoon
- use the vertical attenuation data to examine the applicability of Beers Law for underwater radiation attenuation
- determine representative underwater attenuation coefficients for use in the wetland hydrodynamic model.

Underwater shortwave radiation experiments were conducted at Hopwoods Lagoon in January, April and October 2001. The experiments were repeated at different times of the day and during several seasons to examine temporal variation in underwater attenuation of radiation. Experiments were conducted at both open water and vegetated sites to examine the influence of submerged macrophytes on the underwater attenuation of radiation.

As for the canopy attenuation experiments, underwater attenuation experiments were only conducted under cloudless skies. This unfortunately restricted the total number of successful underwater profiles to a small number, because many attempted experiments had to be abandoned due to development of overcast conditions.

Shortwave radiation data were measured in the PAR waveband using the LI-COR model 192SA quantum sensor with the calibration factor for water. The sensor specifications and calibration factors are given in Appendix C.

The PAR sensor was supported by a 10 cm diameter sleeve of PVC pipe which was raised and lowered along a timber dowel, as shown in Figure 5.3. The depth of the sensor was controlled by a pulley system which was operated remotely from a boat. The boat was stabilised using two moorings and the sensor was always lowered from the sunny side of the boat, to minimise shading effects (Kirk, 1983).

Underwater attenuation of radiation is greater in the infrared and ultraviolet wavelengths than in the visible and PAR wavebands (Kirk, 1983). The underwater attenuation of PAR with depth was therefore expected to be slightly less than underwater attenuation of global shortwave radiation, although no studies were located which directly compared attenuation of PAR and global shortwave radiation. The attenuation coefficients derived from PAR measurements were therefore used as initial estimates for attenuation of global shortwave radiation in the hydrodynamic modelling. It is acknowledged, however, that attenuation of global shortwave radiation would probably be slightly higher than attenuation of PAR.

Measurements were made just above and just below the water surface, and at depth intervals ranging from 0.025 m near the surface, to 0.25 m nearer the bed. The sensor was scanned once every 5 s for a period of one minute, which minimised high frequency variation due to surface ripples and allowed each radiation profile to be completed within a short enough interval that changes in solar elevation were small. The reliability of such a sampling regime was addressed in Section 5.3.1.

All underwater PAR measurements were made relative to the water surface at the time of measurement, and only downward PAR was measured. The total depth would have

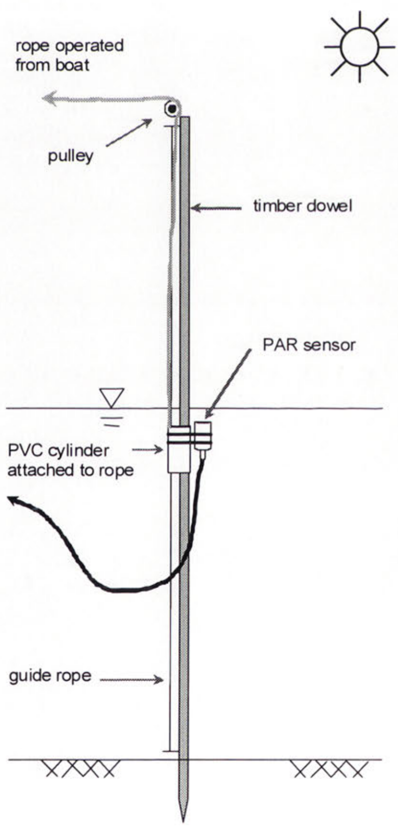

Figure 5.3: Experimental apparatus for measurement of underwater attenuation at Hopwoods Lagoon (not to scale).

affected the instrument response at any location only if there was considerable reflection from the bed and multiple scattering within the water column. However, the sediments were dark in colour and not highly reflective at Hopwoods Lagoon so such effects could be neglected.

5.4.1 Underwater Relative PAR Profiles, $\phi_{PAR(z)} \,/\, \phi_{PAR(0)}$

Analogous to the relative PAR profiles through the canopy, the underwater relative PAR at any depth z below the water surface is defined by the ratio of $\phi_{PAR(z)}$ to $\phi_{PAR(0)}$, where $\phi_{PAR(0)}$ is the net PAR flux at the water surface. In these experiments, the reference PAR flux was measured just below the water surface ($z < 0.005\,\mathrm{m}$) so that reflection at or above the water surface could be neglected in the calculation of relative PAR.

Relative PAR profiles were determined for each experiment from the 1 min mean of the 5 s PAR measurements at each depth and the 1 min mean of the 5 s reference PAR measurements made just below the water surface, as per LaPerriere and Edmundson (2000).

The average measurement period for the individual underwater attenuation profiles was 0:30:36±0:06:08 (from commencement at the water surface to completion at depth). Following the reasoning in Section 5.3.2 (page 150), relative PAR attenuation could therefore be overestimated during the morning and underestimated during the afternoon by using the mean reference PAR measured at the beginning of the profile to represent the average PAR over the 30 min profile period. Expected errors would be most significant ($> 20\%$) for profiles measured within two hours of sunrise or sunset, but within $\sim 7.5\%$ for profiles measured within 2 hours of solar noon. However, none of the underwater experiments were conducted within 2 hours of sunrise or sunset, and most were completed within 2 hours of solar noon.

Underwater shortwave radiation measurements and canopy attenuation experiments were undertaken at separate times because only a single sensor was available for both. However, subject to meteorological constraints, measurements were made as close together as possible so that solar conditions would have been similar. Both types of measurements were made under clear skies so that any potential variability due to clouds could be neglected.

The underwater relative PAR profiles are presented and discussed in Section 6.4.

5.5 Field Monitoring of Wetland Hydrodynamics

The main external sources of energy driving wetland hydrodynamics are atmospheric, and can be parameterised in terms of meteorological variables. Meteorological data were collected at Hopwoods Lagoon to provide information on diurnal and seasonal cycles in meteorological forcing, and were used as input in the hydrodynamic model. Water temperatures were measured to determine the response of the wetland to temporal variation in the meteorological forcing. The water temperature data were also used to calibrate and validate the hydrodynamic model.

The objectives of the field hydrodynamic experiments were to:

- expand the existing data set available in the literature by monitoring the hydrodynamic response to changes in meteorological forcing in the natural wetland at Hopwoods Lagoon
- compare and contrast the observed hydrodynamic responses with those reported by other researchers, particularly Waters (1998), who conducted similar experiments in Manly Dam
- provide data for input to and calibration of the wetland hydrodynamic model.

Water velocities were not measured directly at Hopwoods Lagoon because the magnitude of the expected velocities (Section 3.8) was smaller than the lower threshold of the available Acoustic Doppler Velocimeter ($3\,\mathrm{cm\,s^{-1}}$, SonTek, 1998). However, convective velocities were inferred from measured temperature differentials, as per Ostrovsky et al. (1996), James and Barko (1991) and Waters (1998).

Diurnal and seasonal variation in wetland hydrodynamics could be interpreted from the monitoring program described in the following sections. The observed diurnal and seasonal variation in hydrodynamic behaviour at Hopwoods Lagoon during the monitoring period is discussed in Section 6.5.

5.5.1 Monitoring of Meteorological Conditions

An automatic weather station (AWS) was used to monitor meteorological conditions at Hopwoods Lagoon between 4 February 2000 and 12 November 2001. The monitoring instruments and the collection and processing of meteorological data are described below.

5.5.1.1 Meteorological Monitoring Instruments

The AWS was installed within a fenced enclosure on the south-eastern shore of Hopwoods Lagoon. This site was selected as the most open (least sheltered) and most level site adjacent to the lagoon (Figure 4.6 on page 128). Meteorologic conditions at the weather station were clearly influenced by the surrounding topography (see Section 4.4 on page 128), but within the context of this local topography, were considered representative of conditions over the small lagoon catchment.

The weather station comprised a number of electronic sensors supported by a 10 m mast stabilised by steel guys. The base of the mast was restrained by a hardwood timber plinth embedded into the soil, with its upper surface at an elevation of 22.2 m relative to AHD. The AWS measured:

- **wind direction** using a wind vane
- **wind speed** using a cup anemometer
- **air temperature** using a platinum resistance thermometer
- **relative humidity** using a capacitive sensor
- **barometric pressure** using a pressure transducer
- **shortwave radiation** using a global pyranometer
- **rainfall** using a tipping bucket pluviometer.

All sensors were factory calibrated prior to field installation. Where possible, the factory calibration of the AWS sensors was checked by simple comparison using other sensors maintained by the Hydrology Department of the School of Civil and Environmental Engineering at UNSW. This comprised a series of spot checks over a period of several hours on a number of occasions rather than a formal calibration process. The comparisons were all successful, but no detailed notes were taken. The instrument specifications are given in Appendix C.

An additional, manually monitored, storage rain gauge was installed beside the tipping bucket pluviometer in June 2000 for comparison with the pluviometer throughout the remainder of the monitoring period. Net pan evaporation was measured using a Class A evaporation pan situated near the automatic weather station, on the south-western shore

Meteorological Variable	Scanning Interval	Logging Interval	Meteorological Data Calculated and Recorded by the Data Logger
Wind direction	20 s	10 min	vector mean and standard deviation wind direction
Wind speed	20 s	10 min	vector mean and standard deviation wind speed
Air temperature	1 min	10 min	mean air temperature
Relative humidity	10 min	10 min	instantaneous relative humidity only
Barometric pressure	1 min	10 min	mean barometric pressure
Shortwave radiation	1 min	10 min	mean shortwave radiation
Rainfall	at bucket tip	10 min	cumulative rainfall

Table 5.3: Scanning and logging intervals for the sensors of the automatic weather station.

of Hopwoods Lagoon. The evaporation pan was installed in October 2000 and maintained by Natalie Marshall of the School of Geography at UNSW.

5.5.1.2 Collection and Processing of Meteorological Data

The objective of the meteorological data collection programme was to quantify the meteorological forcing in the vicinity of Hopwoods Lagoon. For most of the AWS sensors, the data were stored as an average value calculated from multiple measurements during each 10 min period, as shown in Table 5.3. Relative humidity measurements were made only once every 10 min, because the power requirements of the sensor made it inefficient to scan more regularly. The 10 min vector mean wind speed and direction were calculated as shown in Section D.1 in Appendix D.

Output from the weather monitoring instruments was logged by a Data Electronics model DT50 data logger and stored on a 1 MB memory card. The logger was installed in a weatherproof enclosure attached to the mast. The data logger and weather monitoring instruments were powered by a 12 V battery which was recharged via a 5 W solar panel.

The logger was accessed using an RS232 cable from a laptop computer, via the Data Electronics *DTWin* interface software. Data were periodically downloaded from the memory of the logger to the laptop, typically every two to three weeks. Despite this frequency of site visits, some meteorological data were lost during the monitoring period. The periods of data loss and reasons for these are summarised in Table D.1 in Appendix D. Overall, the data losses accounted for 37.5 days (or $\sim$6%) over the total monitoring period of 646 days.

An overview of the meteorological conditions at Hopwoods Lagoon throughout the monitoring period is given in Section 6.5.1.

5.5.2 Monitoring of Water Temperatures

Water temperatures were monitored at various depths at Hopwoods Lagoon between May 2000 and November 2001, in both vegetated and unvegetated zones of the lagoon. The following sections describe the monitoring instruments and the collection and processing of water temperature data.

5.5.2.1 Water Temperature Monitoring Instruments

Water temperatures were monitored at Hopwoods Lagoon using two sets of Thermometrics thermistors. Both sets of thermistors were deployed in the field within sheaths of transparent PVC tubing to minimise heat conduction along the stainless steel casing (Waters, 1998). The thermistor specifications are given in Appendix C. Each set of thermistors was calibrated simultaneously in the laboratory to $\pm 0.1°C$ against a calibrated platinum resistance thermometer, over temperature ranges of:

- 3.6 to 33.2°C for the primary thermistors, designated T1 to T16
- 6.0 to 38.3°C for the additional thermistors, designated T21 to T28.

Details of the thermistor calibration experiments and results are provided in Appendix E. The performance of the thermistors was verified in the field, by comparing temperatures given by the primary and additional thermistors when deployed immediately adjacent to one another. Post-deployment verification checks were also conducted in the laboratory, as detailed in Appendix E. These experiments indicated that thermistors T1 and T21 exceeded the calibration error of $\pm 0.1°C$ at the end of the monitoring period. Temperatures given by these thermistors were therefore considered with caution in all further analyses.

Both sets of thermistors were connected via shielded two-wire cables and weatherproof connectors to Data Electronics model DT505 data loggers. The loggers were powered by 12 V batteries and housed in weatherproof enclosures, the primary logger supported on a scaffold at the shore of the lagoon, and the additional logger in a floating container moored near the monitoring site.

5.5.2.2 Collection and Processing of Water Temperature Data

Thermistors T1 to T16 were deployed in vertical arrays throughout the monitoring period at three primary monitoring locations, which are described in Section 5.5.2.3. Thermistors T21 to T28 were deployed for shorter periods at 10 additional sites distributed throughout the wetland. The thermistors were deployed using a method similar to that described by Waters (1998), at fixed depths below the water surface or at fixed heights above the bed.

The thermistors were logged every hour as resistances and later converted to temperatures using the calibration polynomials given in Table E.4 in Appendix E (for the primary thermistors) or Table E.5 (for the additional thermistors). The power requirements of the available instruments precluded a shorter monitoring interval without more frequent visits to site. However, field trials conducted in July 2000 and verified in November 2000 indicated that a sampling interval of 1 hr could represent 15 min variation in water temperatures in the open water zone of the wetland to within $\pm 0.5°C$ at the water surface and less with depth. As discussed in Section F.1 in Appendix F, this was sufficient to distinguish temporal and spatial trends in the water temperature data.

As shown in Figure 5.4, the fixed depth thermistors were deployed from a float, which comprised a 1 m length of PVC pipe inserted through a 100 mm diameter polystyrene ball. The float moved vertically along a timber dowel with changes in water surface elevation. The fixed elevation thermistors were deployed beneath a pair of submerged polystyrene floats anchored to a solid weight. The submerged floats maintained the rope in an approximately vertical position above the bed.

One thermistor was also deployed 50 mm above the water surface within the *Eleocharis* canopy to monitor the air temperature within the vegetated zone. The canopy air temperature data were input to the hydrodynamic model to calculate longwave radiation fluxes within the emergent canopy (as defined by Equation (3.58), page 85). Selected data series were used for model calibration and simulation runs, as described in Section 5.6.4.3.

The water temperature monitoring regime was selected to allow:

- monitoring of surface energy fluxes and fluxes near the water-sediment interface, where the most significant vertical temperature gradients were expected
- assessment of diurnal and seasonal cycles in the vertical temperature distribution at specific locations in open water and vegetated zones of the lagoon
- comparison of the temperature responses of different open water and vegetated zones to the same meteorological forcing
- quantification of horizontal temperature differentials between the different wetland zones
- estimation of the magnitude and direction of horizontal velocities between the different wetland zones.

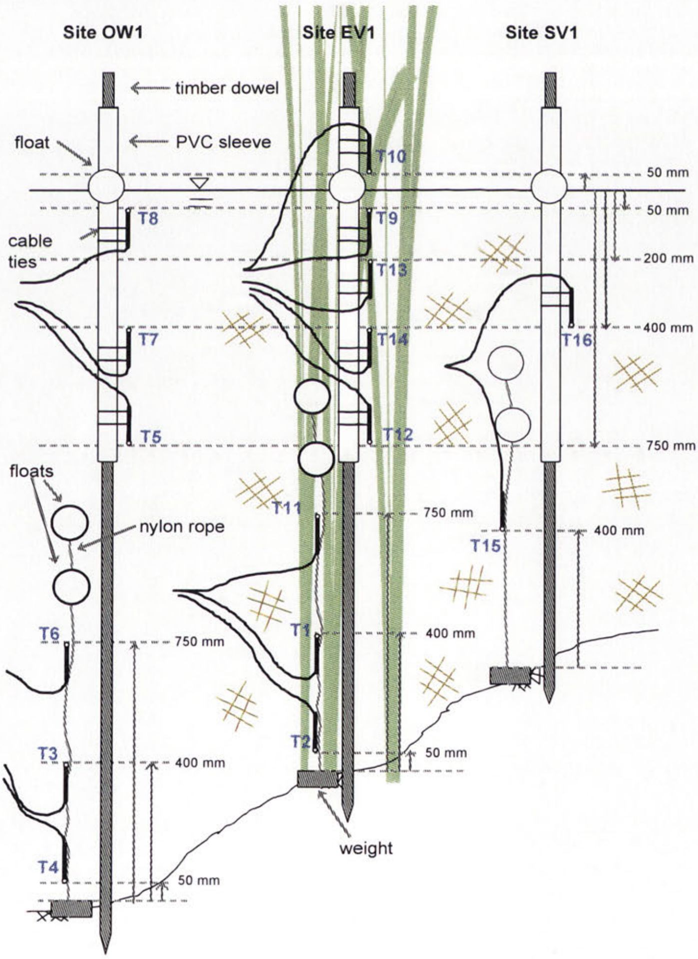

Figure 5.4: Thermistor deployment depths at Sites OW1, EV1 and SV1 (not to scale).

5.5.2.3 Water Temperature Monitoring Locations

The water temperature monitoring locations are shown in Figure 5.5. The primary monitoring locations were designated Sites OW1, EV1 and SV1, as described below. These three sites were selected for their proximity to each other and to a suitable location for the data logger enclosure.

Additional locations were used to monitor water temperatures in open water and vegetated zones in other parts of the lagoon. The additional monitoring locations were numbered sequentially and identified according to the zone in which they were situated (OW for open water, EV for emergent vegetation or SV for submerged vegetation), as shown in Figure 5.5. The monitoring periods and locations of the primary and additional thermistors are listed in Tables F.2 and F.3, respectively, in Appendix F.

An overview of water temperature variation at Hopwoods Lagoon throughout the monitoring period is given in Section 6.5.2.

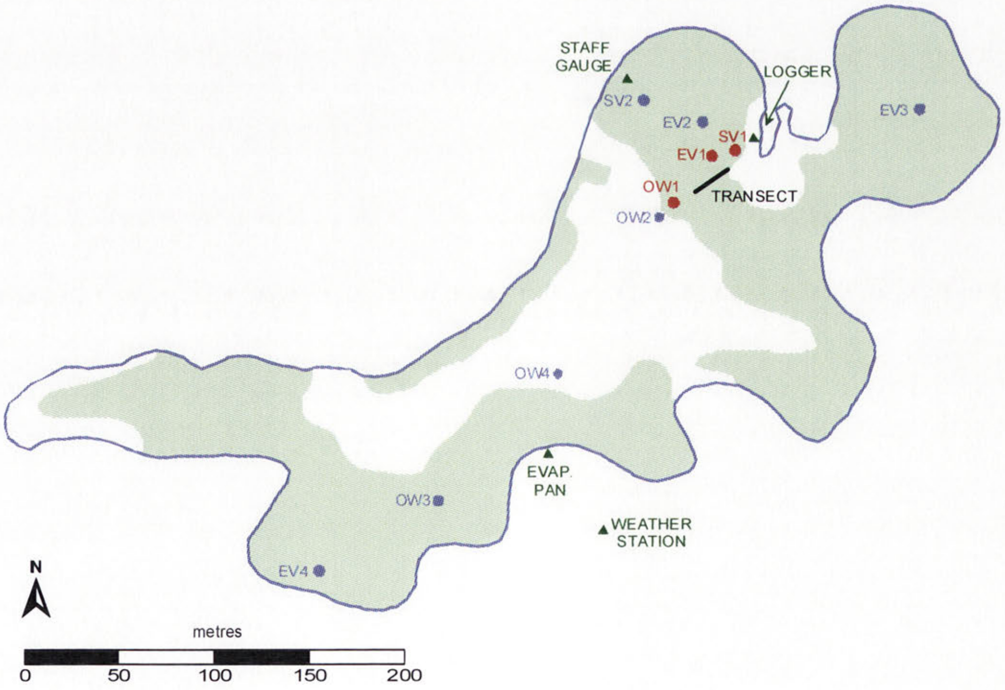

Figure 5.5: Water temperature monitoring locations at Hopwoods Lagoon. The shading indicates the extent of emergent and submerged macrophytes as surveyed in October 2001.

Site OW1, Open Water Zone (bed RL 14.15 m)

Site OW1 was located in the open water zone at the northern end of Hopwoods Lagoon, adjacent to the main zone of emergent *Eleocharis sphacelata*. The water depth ranged from 2.45 m to 3.10 m over the monitoring period. Site OW1 was free from vegetation at the time of deployment, although the submerged *Hydrilla verticillata* encroached into this area of the lagoon during 2001. As shown in Figure 5.5, Site OW1 was effectively surrounded by submerged macrophytes by October 2001.

Site EV1, Emergent Vegetation Zone (bed RL 14.80 m)

Site EV1 was located in the main stand of emergent *Eleocharis sphacelata* at the northern end of Hopwoods Lagoon. The water depth ranged from 1.80 m to 2.45 m over the monitoring period. The top of the *Eleocharis* canopy was approximately 1 m above the water surface at Site EV1 and submerged *Hydrilla verticillata* was also present.

Site SV1, Submerged Vegetation Zone (bed RL 15.35 m)

Site SV1 was located in a zone of submerged macrophyte between the emergent macrophytes and the shore at the northern end of Hopwoods Lagoon. The water depth ranged from 1.25 m to 1.90 m over the monitoring period. The site was vegetated by submerged mats of *Hydrilla verticillata*, which comprised whorls of small leaves around a narrow stem.

5.6 Numerical Modelling of Wetland Hydrodynamics

A hydrodynamic model was used to investigate the response at Hopwoods Lagoon to changes in meteorological forcing, and the effects of radiation shading by macrophytes. The existing three-dimensional finite element program RMA-10 (King, 1993) was modified by the present author to account for the influences of both emergent and submerged macrophytes on the input and distribution of heat in a wetland. Modifications to the model included the introduction of alternative surface energy fluxes in the emergent macrophyte zones, spatially-variable attenuation of shortwave radiation beneath the surface and introduction of a bed heat flux as a lower thermodynamic boundary condition.

The specific objectives of the numerical modelling experiments were to:

- simulate diurnal cycles in the temperature structure of a natural wetland during different seasons with different meteorological forcing conditions
- compare simulated water velocities with those inferred from field data and scaling analyses, giving consideration to possible convective circulation regimes identified in the literature
- examine the influences of radiation shading by both emergent and submerged macrophytes on temperature stratification and convective circulation patterns induced in a partially-vegetated natural wetland.

RMA-10 is a three dimensional, finite element model which solves the Reynolds form of the Navier-Stokes equations using Newton-Raphson iteration. The hydrostatic pressure assumption is applied and the model assumes the validity of eddy viscosity concepts. The governing equations and parameterisation of boundary conditions are presented in Appendix H, including details of amendments made to RMA-10 by the author. A more comprehensive description of the structure and capabilities of RMA-10 is given by King (1993), together with details of the solution scheme.

RMA-10 was selected for use in this study because:

- it is capable of modelling three-dimensional, density stratified flow, and already included a heat budget module and an elemental drag force parameterisation
- both the source and executable code were directly available from the primary developer of the code, and there was a substantial base of knowledge and experience in the use of RMA-10 at the Water Research Laboratory at UNSW
- use of an existing model avoided the need to create a new computer program.

The model was calibrated and validated using meteorological and water temperature data from Hopwoods Lagoon, as described in the following sections. Data collection and field monitoring of hydrodynamic behaviour were described in Section 5.5. Observed diurnal and seasonal trends in hydrodynamic behaviour are discussed in Section 6.5 and the results of model calibration and validation are presented and discussed in Section 6.6.

5.6.1 Finite Element Generation

RMA-10 requires input of a two-dimensional element grid and vertical layer information for these elements. A horizontal two-dimensional grid was prepared representing Hopwoods Lagoon from bathymetric survey data (Section 4.4.6, page 132) using the finite element generation package, RMAGEN (King, 2001). Vertical layer information was specified in the RMA-10 input data file, as absolute elevations for corner nodes beneath each surface node in the network. This allowed similar vertical resolution over a given depth range at all locations across the model domain. RMAGEN is fully documented by King (2001), and the brief overview given below is based extensively on this reference.

5.6.1.1 Creation of the Two-Dimensional Finite Element Grid

The two-dimensional grid comprised triangular and quadrilateral elements which were defined by three or four corner nodes, respectively, and an equal number of midside nodes. Midside nodes were generated automatically by RMAGEN at the precise mid-point on each element side.

The grid was designed to minimise changes in bed elevation and therefore hydrodynamic properties across any given element (King, 1993). This was achieved by following bathymetric contours as much as possible and resulted in smaller elements where the bed topography varied rapidly (for example around the shoreline) and larger elements in flat or gently undulating areas of the lagoon. Elements were also concentrated at the northern end of the lagoon where the field monitoring effort was greatest, and where the largest horizontal temperature differences were expected between the open water and macrophyte zones.

The sensitivity of the model results to the resolution of the two-dimensional grid is addressed in Section 5.6.1.4.

5.6.1.2 Creation of the Three-Dimensional Finite Elements

Three-dimensional finite elements were generated internally by RMA-10 from the two-dimensional grid. These were aligned vertically below the corresponding surface element at elevations specified in the model input. As shown in Figure 5.6, this resulted in fewer element layers in the shallow littoral zones than in the deeper regions of the lagoon. The boundary elevations were selected to limit the element depth to $\leq$0.5 m, which provided good vertical resolution in the model results. Elements were shallower near the water surface where the surface heat fluxes are most influential and where wind-induced mixing is most significant.

While the water depth should strictly be zero at the shoreline, RMA-10 introduces the convenient approximation of a small depth along the shoreline to avoid numerical difficulties associated with a zero water depth (King, 1993). This depth was arbitrarily set to Δh =0.1 m in the present study.

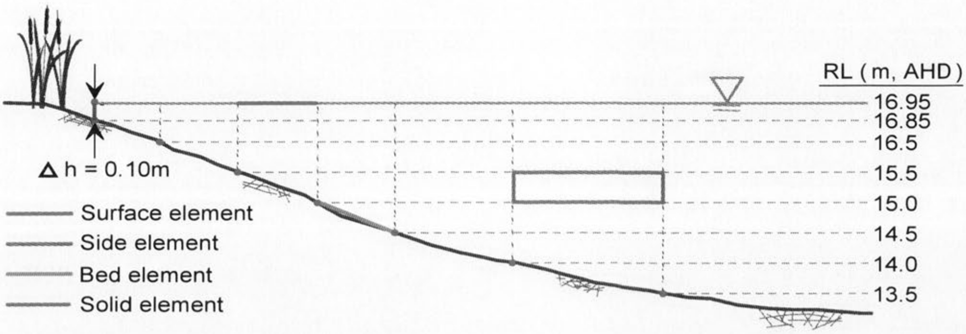

Figure 5.6: Definition of the main element types and vertical distribution of finite elements in RMA-10, with the water surface elevation at RL 16.95 m (not to scale).

5.6.1.3 Element Classification

Each two-dimensional element was assigned an element class, which allowed parameters such as surface heat flux parameters and vegetation parameters to be assigned to all elements in each element class. Three-dimensional elements were assigned the same element class as the corresponding surface element.

Three element classes were defined in the present study, representing the main wetland zones at Hopwoods Lagoon. The main features of the three zones are shown schematically in Figure 5.7:

- **Open Water Zones** (Class 1) were free of macrophytes and typically located in the deeper, central areas of Hopwoods Lagoon
- **Submerged Macrophyte Zones** (Class 2) were populated by submerged macrophytes and typically distributed around the shallow perimeter of the lagoon
- **Emergent Macrophyte Zones** (Class 3) were populated by both emergent and submerged macrophytes and typically located in distinct bands related to water depth at the northern, north-eastern and southern ends of the lagoon.

Submerged macrophytes grew in all emergent macrophyte zones at Hopwoods Lagoon.

Element classes were assigned primarily according to the observed macrophyte distribution at the time of the bathymetric survey in October 2001 (Section 4.4.6). Reference was also made to the aerial photograph from July 2000 (Figure 4.6, page 128) and other field notes and photographs from the intervening period. The distribution of the three element classes at Hopwoods Lagoon is shown in Figure 5.8.

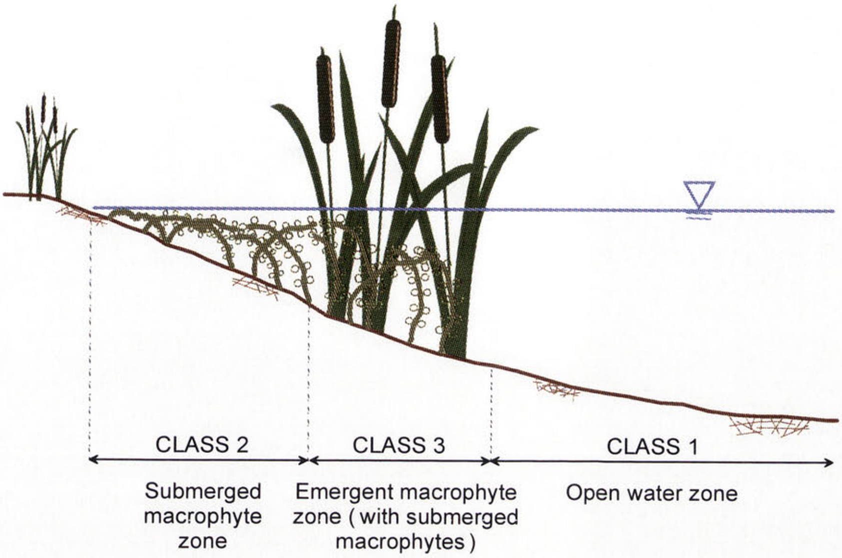

Figure 5.7: Illustration of the three main wetland zones observed at Hopwoods Lagoon, and the corresponding element classes applied in RMA-10 simulations.

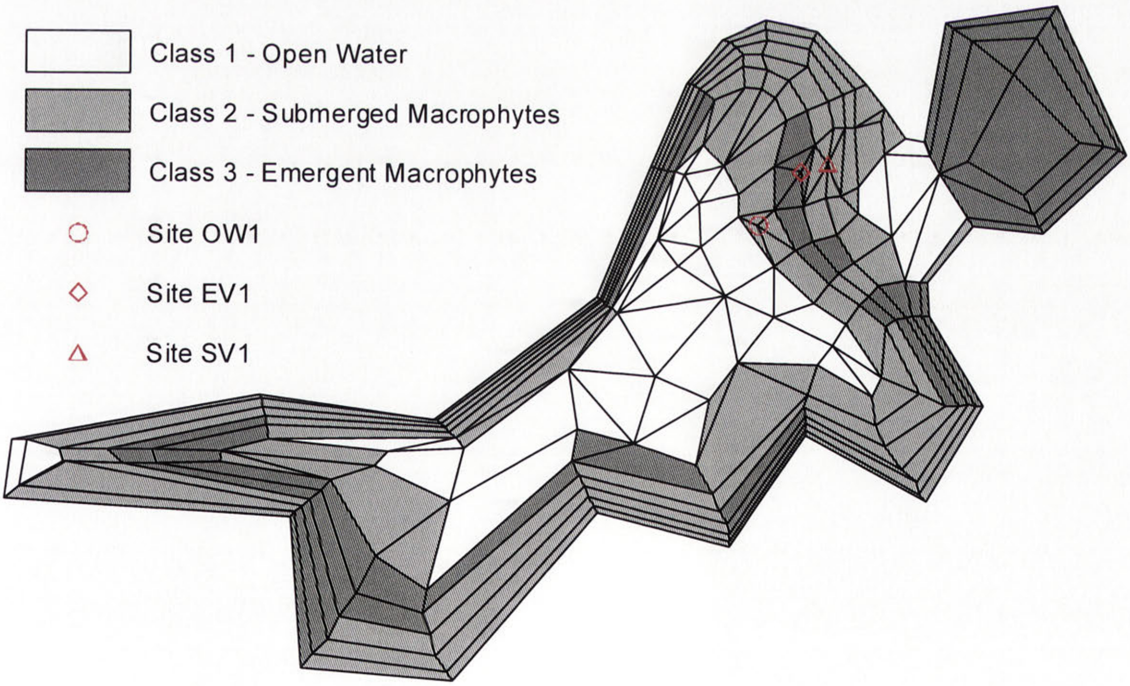

Figure 5.8: Two-dimensional finite element grid and distribution of element classes used for model simulations at Hopwoods Lagoon (water surface elevation at RL 16.95 m).

5.6.1.4 Sensitivity of the Model Output to Grid Resolution

Various grid scales were tested to ensure that the predicted temperatures and velocities were essentially independent of the two-dimensional grid resolution, and the number and spacing of element layers. Tests included an approximate doubling of the number of horizontal two-dimensional elements and a 50% increase in the number of vertical layers. The horizontal and vertical resolution were determined after considering both the sensitivity of the model output and the required computational effort. The sensitivity of the model results to changes in grid resolution was assessed using the root mean square error ($RMSE$), bias and variance statistics (Equation (5.3) and Equation (5.4) on page 169).

There were no significant differences in the water temperatures and resultant horizontal velocities predicted using a two-dimensional grid with approximately twice the number of two-dimensional elements. Temperatures predicted using the coarser horizontal grid were within 0.2°C ($RMSE$) of those predicted using the finer resolution. This is comparable with the calibration error of the monitoring thermistors (0.1°C), against which the model was calibrated. Horizontal velocities were within $1.3\,\mathrm{mm\,s^{-1}}$ ($RMSE$) over the simulation period. There was no systematic over- or under-prediction of temperatures or velocities and the variance between results from the two simulations was low. Hence, the lower grid resolution shown in Figure 5.8 was considered acceptable for modelling diurnal and seasonal variation in hydrodynamic behaviour over the wetland. Table 5.4 shows the number of elements per class corresponding to the grid shown in Figure 5.8.

Element Class	Description	No. of Elements	Approx. Area (%)
Class 1	Open Water	44	26
Class 2	Submerged Macrophytes	115	46
Class 3	Emergent Macrophytes	57	28

Table 5.4: Number of two-dimensional surface elements by class, for the geometry shown in Figure 5.8.

There were also no significant differences in the water temperatures and resultant horizontal velocities predicted using eight or twelve elements in the vertical. Temperatures predicted using the coarser vertical grid were within 0.1°C ($RMSE$) of those predicted using the finer resolution. This is comparable with the calibration error of the monitoring thermistors. Predicted horizontal velocities were within $0.8\,\mathrm{mm\,s^{-1}}$ ($RMSE$) over the simulation period. There was no systematic over- or under-prediction of temperatures or velocities and the variance between results from the two simulations was low. Given the substantial saving in computational time (around 50%), all simulations were run with the lower vertical resolution, using eight element layers.

5.6.2 Initial Conditions

Initial conditions for model simulations were created using a dynamic spin-up from a "cold start", employing a restart file capability in RMA-10. A similar restart capability was created in the new bed heat flux module to generate an initial vertical sediment temperature distribution. Each "cold start" simulation commenced with an isothermal water temperature distribution and near-zero velocities ($1.0 \times 10^{-4}\,\mathrm{m\,s^{-1}}$) everywhere throughout the modelling domain. The model was run for a warm-up period of at least 24 hours using actual meteorological data to create a near-isothermal temperature distribution and non-zero velocities. As discussed in Section 6.5.2, water temperature monitoring at Hopwoods Lagoon indicated that this was a reasonable approximation during the early hours of the morning for most times of the year.

The suitability of the initial conditions were assessed by comparing simulated temperature profiles with field data from the primary monitoring locations (Sites OW1, EV1 and SV1). Goodness of fit at the end of the warm-up period was quantified using the root mean square error ($RMSE$) which quantifies the average difference between the simulated and measured water temperatures over the depth of the water column:

$$RMSE = \sqrt{\frac{1}{n}\sum_{i=1}^{n}\left\{T_{sim}(i) - T_{meas}(i)\right\}^{2}} \tag{5.3}$$

where $T_{sim}(i)$ = simulated water temperature at point i in space or time (°C)

$T_{meas}(i)$ = measured water temperature at point i (°C)

n = number of points considered.

The bias (B) and variance (S) were used to assess the significance of systematic and random errors between the two simulations, respectively, where:

$$B = \frac{1}{n}\sum_{i=1}^{n} T_{sim}(i) - \frac{1}{n}\sum_{i=1}^{n} T_{meas}(i) \qquad \text{and} \qquad S = RMSE^{2} - B^{2} \tag{5.4}$$

The goodness of fit statistics for the four simulation periods are summarised in Table 5.5. Where the depths of temperature simulation did not correspond exactly with measured temperature depths, linear interpolation was applied between the nearest simulated temperatures to estimate the model temperature at that depth. The average errors in the initial water temperatures at the three primary monitoring sites were lowest at around 0.1 to 0.15°C in October 2001 (Spring) and December 2000 (Summer), and highest at up to 0.26°C in May 2001 (Autumn). The bias calculations indicated that initial water temperatures were often slightly underestimated at the beginning of the simulation period (B <0). Possible explanations included insufficient surface heating, insufficient vertical mixing and underestimation of the heat flux between the water column and the sediments. The results of the model calibration and validation are discussed further in Section 6.6.1.

Date	Time	Site	n^1	$RMSE$ (°C)	B (°C)	S (°C^2)
30 Dec 2000	05:00	OW1	6	0.166	-0.138	0.008
		EV1	7	0.145	-0.131	0.004
		SV1	8 [2]	0.153	-0.046	0.022
15 May 2001	05:00	OW1	6	0.176	-0.022	0.030
		EV1	7	0.262	0.210	0.025
20 Aug 2000	05:00	OW1	6	0.145	-0.142	0.001
		EV1	7	0.222	-0.156	0.025
21 Oct 2001	06:00	OW1	6	0.111	-0.025	0.012
		EV1	7	0.141	-0.088	0.012

Notes to Table:

1. n is the number of thermistors at each site.
2. Thermistors T21 to T28 were deployed at Site SV1 on 30 December 2000, in addition to T15 and T16.

Table 5.5: Suitability of initial conditions for the four calibration and validation periods.

Velocity data were not available at Hopwoods Lagoon, and comments therefore cannot be made regarding the simulated velocity initial conditions.

Sediment temperature data were also not available at Hopwoods Lagoon. Instead, the initial sediment temperatures generated by the preliminary simulation were assessed by considering temporal variation over the warm-up period, at Sites OW1 and EV1. Temperatures at the sediment-water interface were required to reflect the diurnal variation in near-bed water temperatures, while the temperature at the base of the sediment layer (the thermal depth of influence, h_s) was required to remain essentially constant with time.

Sediment temperatures at the thermal depth of influence were set equal to the initial water temperatures at the beginning of the warm-up period.

5.6.3 Data Requirements

Input data and parameter values required by RMA-10 are summarised in Table 5.6, and can be grouped as follows into:

- meteorological data
- surface heat flux parameters
- bed heat flux parameters
- macrophyte parameters
- mixing parameters.

Type of Data / Parameter	Symbol	Units	Source of Data / Parameter Value
Shortwave radiation flux	ϕ	$\mathrm{W m^{-2}}$	automatic weather station
Cloud fraction	m	–	estimated from shortwave data
Air temperature	T_a	°C	automatic weather station
Relative humidity	RH	%	automatic weather station
Atmospheric pressure	P	hPa	automatic weather station
Wind speed	u_{10}	$\mathrm{m\,s^{-1}}$	automatic weather station
Canopy air temperature	T_c	°C	thermistor T10 at Site EV1
Shortwave attenuation	η	$\mathrm{m^{-1}}$	field data, model calibration
Aerodynamic roughness length	z_0	m	literature review, model calibration
Zero-plane displacement height	d_0	m	literature review, model calibration
Depth of thermal influence	h_s	m	model calibration
Sediment thermal diffusivity	K_s	$\mathrm{m^2\,s^{-1}}$	literature review, model calibration
Sediment heat capacity	c_s	$\mathrm{J\,m^{-3}\,{}^\circ C^{-1}}$	field data
Leaf area index	LAI	$\mathrm{m^2 m^{-2}}$	field data
Coefficients for G-function	c_1, c_2, c_3	–	field data
Vegetation drag coefficients	C_{Dx}, C_{Dy}	–	estimated from literature review
Vertical viscosities	$\varepsilon'_{xz}, \varepsilon'_{yz}$	$\mathrm{Pa\,s^{-1}}$	literature review, model calibration
Vertical diffusivity	D'_z	$\mathrm{m^2\,s^{-1}}$	literature review, model calibration
Horizontal viscosities	$\varepsilon'_{xx}, \varepsilon'_{xy}, \varepsilon'_{yx}, \varepsilon'_{yy}$	$\mathrm{Pa\,s^{-1}}$	literature review, model calibration
Horizontal diffusivities	D'_x, D'_y	$\mathrm{m^2\,s^{-1}}$	literature review, model calibration
Smagorinsky coefficients	k_s, ν_s	–, $\mathrm{m^2\,s^{-1}}$	literature review, model calibration

Table 5.6: Input data and parameter values required by the modified RMA-10 model.

5.6.4 Model Calibration and Validation

The overall objective of the model calibration and validation was to prepare the model for hydrodynamic simulations at Hopwoods Lagoon. More specifically, the calibration and validation objectives were to:

- select or confirm values for the unknown parameters
- simulate diurnal water temperature profiles on selected dates at Hopwoods Lagoon, representing the four seasons
- predict water velocities over the diurnal cycle with order of magnitude and direction which were consistent with literature values and the inferences made in Chapter 6.

Subsets of the available meteorological and water temperature data were selected for model calibration using the criteria outlined in Section 5.6.4.3. These data sets were used to determine the unknown simulation parameters, which were subsequently validated using different subsets within the time series data.

5.6.4.1 Model Timestep

The model was run with a timestep of $\Delta t = 1.0$ hour. Trial simulations with $\Delta t = 10$ min produced the results illustrated in Figure 5.9 and detailed in Table 5.7.

The predicted water temperatures were slightly different for the two timesteps, primarily during the cooling phase (when $H_{NET} < 0$). The greatest differences occurred at the water surface at Site OW1, where temperatures predicted using $\Delta t = 10$ min were on average almost 0.3°C warmer than those predicted using $\Delta t = 1.0$ hour. These differences can be partly explained by the effective smoothing (averaging) of the variation in meteorological variables which resulted from using hourly data rather than 10 min data. Temperatures at depth were generally slightly cooler using the shorter timestep, again due to effective smoothing in the meteorological variables. However, the diurnal trend in the simulated water temperatures was similar for the two timestep lengths.

			Water Temperatures			Resultant Horizontal Velocities		
Site ID	Depth (m)	n	$RMSE$ (°C)	Bias B (°C)	Variance S (°C^2)	$RMSE$ (mm s^{-1})	Bias (mm s^{-1})	Variance (mm^2 s^{-2})
OW1	0.0	26	0.279	0.236	0.022	1.954	-0.968	2.882
	1.2	26	0.154	-0.067	0.019	0.196	-0.038	0.037
	2.8	26	0.045	-0.054	-0.001	0.000	0.000	0.000
	combined	78	0.186	0.038	0.033	1.134	-0.335	1.173
EV1	0.0	26	0.194	0.165	0.010	0.439	-0.071	0.187
	1.2	26	0.195	-0.120	0.024	0.734	-0.265	0.468
	2.8	26	0.117	-0.149	-0.008	0.000	0.000	0.000
	combined	78	0.173	-0.034	0.029	0.494	-0.112	0.231

Note: Calculated as [$\Delta t = 1.0$ hour] - [$\Delta t = 10$ min] in Equation (5.3).

Table 5.7: Quantification of the sensitivity of simulated water temperatures and horizontal velocities to a change in the model timestep from $\Delta t = 1.0$ hour to $\Delta t = 10$ min.

The resultant horizontal velocities predicted using the shorter timestep were generally smaller than those predicted using $\Delta t = 1.0$ hour, and fluctuated more in time. At Site OW1, these ranged from 0 to 1.3 mm s^{-1} for $\Delta t = 10$ min and 0 to 5 mm s^{-1} for $\Delta t = 1.0$ hour. While the differences between the predicted velocities for the two timesteps are significant in relative terms, they are not significant in absolute terms. These velocity ranges are also consistent with velocities inferred from the field temperature measurements and scaling analyses. To the author's knowledge, this three-dimensional finite element model was previously untested with such low velocities in a low energy environment. However, it has been applied successfully to other simulations with comparable horizontal temperature gradients. The comparison reported here is therefore considered reasonable.

The reduced fluctuation resulting from $\Delta t = 1.0$ hour was probably also due to the effective smoothing in the meteorological input. These effects were much less evident at Site EV1 than at Site OW1, presumably because of the attenuation of surface energy fluxes by the emergent canopy. The resultant horizontal velocity vectors were broadly consistent between the two simulations.

Acknowledging the slight differences between the simulations run with $\Delta t = 10$ min and $\Delta t = 1.0$ hour, all subsequent simulations were run using $\Delta t = 1.0$ hour. These produced similar results and represented a computational time saving of >80% over simulations run with $\Delta t = 10$ min.

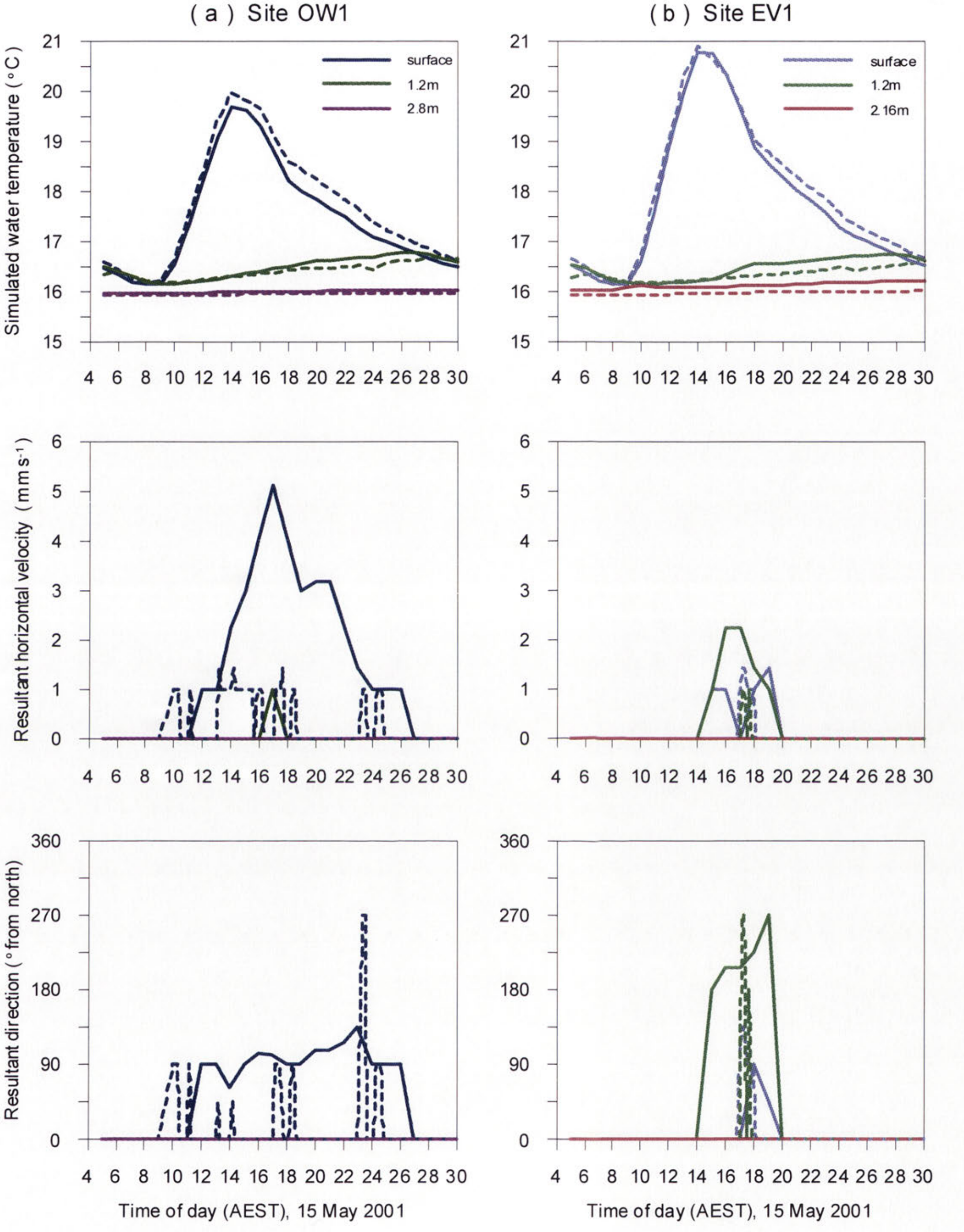

Figure 5.9: Sensitivity of the model output to the timestep: temperatures, resultant horizontal velocities $V = \sqrt{u^2 + v^2}$ and direction of resultant velocities at (a) Site OW1 and (b) Site EV1. Solid lines represent simulations using $\Delta t = 1.0$ hour and dashed lines represent simulations using $\Delta t = 10$ min.

5.6.4.2 Calibration and Validation Methodology

Predicted temperatures were compared with measured temperatures at various locations in Hopwoods Lagoon, using the $RMSE$, the bias and the variance (as defined on page 169). In this study, emphasis was placed on the heating phase of the diurnal cycle (which occurs when $H_{NET} > 0$), since the stable heating processes are considerably less complex than the physically unstable cooling and mixing processes in a density-stratified fluid. Consequently, the model was expected to perform better during heating periods. Predicted velocities were compared with velocities inferred from horizontal temperature differences measured in the field, using the scaling relationships presented in Chapter 3. No direct field velocity measurements were available.

Parameter values were progressively tuned during model calibration generally in the sequence shown in Table 5.6. That is, changes were made first to surface heat flux parameters, then bed heat flux parameters, then vertical and horizontal mixing coefficients, although the process was iterative.

5.6.4.3 Calibration and Validation Periods

Calibration and validation were undertaken on selected dates representing the four seasons, to check the consistency of the model performance over a range of conditions. Calibration periods were selected from the monitoring period using the following criteria:

(1.) availability of the full complement of meteorological and water temperature data from the primary monitoring thermistors at Sites OW1, EV1 and SV1

(2.) occurrence of approximately isothermal water temperatures at the beginning of the simulation period

(3.) absence of significant rainfall during or immediately before the simulation period

(4.) representation of weather conditions typical of the season

(5.) availability of water temperature data from the thermistors at locations additional to Sites OW1, EV1 and SV1.

Due to various data losses over the monitoring period (Appendices D and F), and because the additional thermistors were moved frequently around the lagoon, it was not always possible to satisfy all of these criteria. However, the first four criteria were generally met. The simulation periods used for model calibration and validation are listed in Table 5.8. The results of the model calibration and validation are presented and discussed in Section 6.6.1.

Season	Simulation Period	Water Temperatures used for Calibration
Summer	29 – 30 December 2000	Sites OW1, EV1, SV1 [1]
Autumn	14 – 15 May 2001	Sites OW1, EV1, SV1 [2], transect
Winter	19 – 20 August 2001	Sites OW1, EV1, SV1 [2]
Spring	20 – 21 October 2001	Sites OW1, EV1, SV1 [2], OW3

Notes to Table:

1. The additional thermistors T21 to T28 were deployed at Site SV1 on 29 and 30 December 2000, so temperatures were monitored over the full water depth.
2. Generally, only two thermistors were deployed at Site SV1, at a depth of 400 mm below the surface and at a height of 400 mm above the bed.

Table 5.8: Simulation periods used for model calibration and validation, and the monitoring locations from which field data were available.

5.6.5 Hydrodynamic Simulation Experiments

Hydrodynamic simulation experiments were undertaken using the model developed for Hopwoods Lagoon, to investigate radiation shading by varying densities of submerged and emergent macrophytes. These numerical scenarios could not be investigated directly in the field. The objectives of the simulation experiments were to examine differential heating during the heating phase due to:

- **depth differences** when the entire wetland contained no vegetation, submerged macrophytes only, and both emergent and submerged macrophytes
- **radiation shading by submerged macrophytes** of varying density
- **radiation shading by emergent macrophytes** of varying canopy density and horizontal distribution.

Simulations were run using the meteorological data sets used for model calibration. The results were used to assess the relative importance of parameters which directly affected:

(1.) the attenuation of shortwave radiation beneath the water surface, and

(2.) the net shortwave radiation flux at the water surface.

These processes are primarily responsible for heating the water column during the heating phase. In these experiments, the underwater attenuation of shortwave radiation was assumed to be due entirely to submerged macrophyte components. The shortwave radiation flux at the water surface was assumed to be dependent only on the incident flux and the foliage density of the emergent macrophyte canopy. These were the main parameters which were varied between the different simulations. Parallel simulations were also undertaken *without* the imposed surface wind stresses, to assess the relative importance of convective and advective flows when all other factors were identical.

5.6.5.1 Simulation Parameters

Submerged Macrophyte Parameters

Attenuation of net shortwave radiation beneath the water surface is a function of the density of submerged macrophytes. Density variation in the submerged macrophytes was simulated by changing the underwater attenuation coefficient, η_{SV}.

Any changes to the submerged macrophyte density would also influence the magnitude of the net vegetation drag force due to the vegetation, which would generally increase as the density increased (Section 2.3.3). However, since the vegetation resistance force was represented by a simple parameterisation in the hydrodynamic model and not directly coupled to the macrophyte density, the drag coefficient was not varied with the submerged macrophyte density during these simulations. Implications of this simplification are considered in Section 6.6.3.2 (page 321).

Parameter values used in simulations of radiation shading by submerged macrophytes are shown in Table 5.9. The lower macrophyte density was simulated by $\eta_{SV} = 4.4\,\mathrm{m}^{-1}$, which was the attenuation coefficient derived from field measurements at Hopwoods Lagoon. A moderate macrophyte density was represented by $\eta_{SV} = 6.5\,\mathrm{m}^{-1}$, which was the value determined during model calibration. The higher submerged macrophyte density was represented by $\eta_{SV} = 12.0\,\mathrm{m}^{-1}$, which corresponded to the upper limit of the range reported in the literature (Cristofor et al., 1994). In all simulations, macrophyte properties were assumed uniform throughout the submerged macrophyte zones of the wetland.

Macrophyte Density	η_{OW} (m^{-1})	η_{SV} (m^{-1})	η_{EV} (m^{-1})	LAI ($m^2 m^{-2}$)
Low	2.5	**4.4**	–	–
Moderate	2.5	**6.5**	–	–
High	2.5	**12.0**	–	–

Table 5.9: Parameter values used for model simulations of differential heating due to radiation shading by submerged macrophytes.

Emergent Macrophyte Parameters

The net shortwave radiation flux at the water surface is a function of the incident shortwave radiation flux and the density of emergent macrophytes which shade the surface. Variation in the emergent macrophyte density was simulated by changing the downward cumulative leaf area index, LAI.

In addition to modifying the attenuation of shortwave radiation, changing the density of emergent macrophytes would affect the other components of the net surface heat flux. The net shortwave radiation flux is the major component of the net surface heat flux, so an increase in the density (LAI) of an emergent macrophyte canopy could significantly reduce H_{NET} during the heating phase. The model parameterisation for the net longwave radiation flux is dependent on the canopy LAI and therefore affected by changes in the canopy density. The latent and sensible heat fluxes are affected by changes in the canopy density via complex feedback mechanisms involving T_w, T_c, RH, z_0 and u (Section 3.4).

The attenuated wind speed was not directly coupled to the canopy LAI in this model and was assumed to be uniform, regardless of the canopy density. However, variation in the LAI (canopy density) would also influence the wind stress at the water surface, the aerodynamic roughness length and the horizontal and vertical mixing coefficients within the emergent macrophyte zones, although neither was directly coupled to the canopy density in the model. The implications of these simplifications are considered in Section 6.6.3.3.

The parameter values used in the emergent macrophyte simulations are shown in Table 5.10. The foliage area was varied between $LAI = 0.5$ and $LAI = 10.0$ in the emergent macrophyte zone, which spanned the range observed in the canopy attenuation experiments (Figure 6.3, page 191). The lower value of $LAI = 0.5$ represented the sparse *Eleocharis sphacelata* canopy at Hopwoods Lagoon, the moderate value of $LAI = 2.5$ represented the *Typha domingensis* canopies at Deep Creek and Warriewood Wetlands, while $LAI = 10.0$ represented the extremely dense *Juncus kraussi* canopy at Deep Creek.

Macrophyte Density	η_{OW} (m^{-1})	η_{SV} (m^{-1})	η_{EV} (m^{-1})	LAI (m^2m^{-2})
Low	2.5	–	6.5	**0.5**
Moderate	2.5	–	6.5	**2.5**
High	2.5	–	6.5	**10.0**

Table 5.10: Parameter values used for model simulations of differential heating due to radiation shading by emergent macrophytes.

5.6.5.2 Summary of Simulation Experiments

A summary of the hydrodynamic simulation experiments is presented in Table 5.11, and the experimental methodology is summarised in the following sections. The results of the hydrodynamic simulation experiments are presented and discussed in Chapter 6.

Differential Heating due to Depth Differences

Differential heating can occur due to depth differences within an unvegetated body of water, and between zones of submerged or emergent macrophytes of different depths. This occurs in addition to differential heating between different wetland zones.

Simulations were undertaken to investigate the effects of differential heating due to depth differences alone, assuming that the entire wetland:

(1.) was unvegetated (all open water) - all Class 1 elements

(2.) contained only submerged macrophytes - all Class 2 elements

(3.) contained both emergent and submerged macrophytes - all Class 3 elements.

Each scenario used the actual bathymetry of Hopwoods Lagoon, so that differential heating effects due purely to depth differences could be isolated from other contributing factors.

Cause of Differential Heating	Open Water	Submerged Macrophytes	Emergent Macrophytes
Depth differences in:			
- open water	$\eta_{OW} = 2.5$	–	–
- submerged macrophytes	–	$\eta_{SV} = 6.5$ (M)	–
- emergent macrophytes	–	–	$\eta_{EV} = 6.5$, LAI=0.5 (L)
Radiation shading by	$\eta_{OW} = 2.5$	$\eta_{SV} = 4.4$ (L)	–
submerged macrophytes	$\eta_{OW} = 2.5$	$\eta_{SV} = 6.5$ (M)	–
	$\eta_{OW} = 2.5$	$\eta_{SV} = 12.0$ (H)	–
Radiation shading by	$\eta_{OW} = 2.5$	$\eta_{SV} = 6.5$ (M)	$\eta_{EV} = 6.5$, LAI= 0.5 (L)
emergent macrophytes	$\eta_{OW} = 2.5$	$\eta_{SV} = 6.5$ (M)	$\eta_{EV} = 6.5$, LAI= 2.5 (M)
	$\eta_{OW} = 2.5$	$\eta_{SV} = 6.5$ (M)	$\eta_{EV} = 6.5$, LAI=10.0 (H)

Notes to Table: L = low macrophyte density, M = moderate macrophyte density, H = high macrophyte density.

Table 5.11: Summary of parameter values used in hydrodynamic simulation experiments.

Simulations were run in summer and spring to examine seasonal effects, and in each season, both with and without imposed wind stresses at the water surface. Simulations run without surface wind stresses represented idealised scenarios and were designed to assess the magnitude and direction of convective flows in the absence of advective flows. Wind stresses were isolated using a switch in the model input, which did not affect calculation of the wind speed-dependent latent and sensible heat fluxes.

Radiation Shading by Submerged Macrophytes

Differential heating due to radiation shading by submerged macrophytes of various densities was investigated by varying the underwater attenuation coefficient for shortwave radiation. The effects of an emergent macrophyte canopy were removed and wetland zones were assumed to comprise either open water (Class 1 elements) or submerged macrophytes (Class 2 elements), as shown in Figure 5.10. This was the distribution of submerged macrophytes mapped during the survey of Hopwoods Lagoon in October 2001.

The effects of differential heating due to radiation shading by submerged macrophytes were assessed by comparison with simulation results for differential heating due purely to differences in depth.

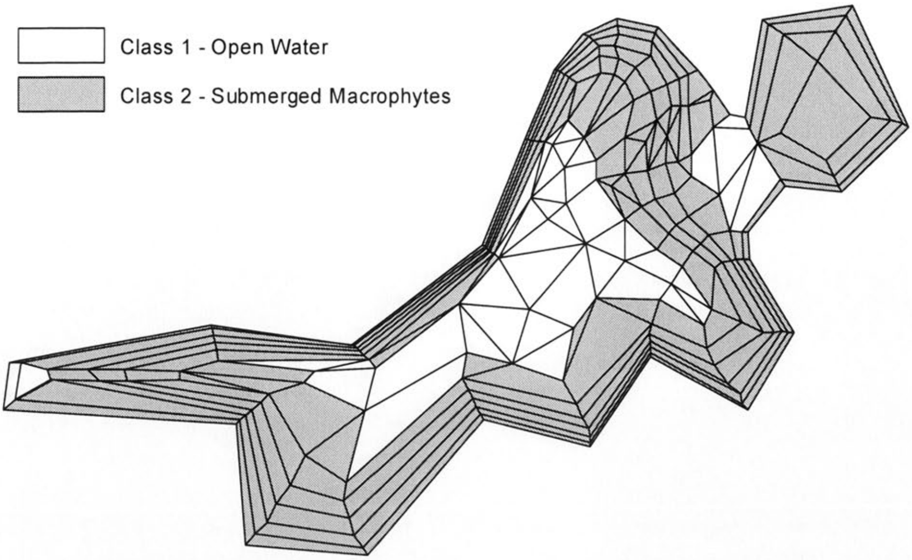

Figure 5.10: Distribution of open water and submerged macrophyte zones used for simulations of radiation shading by submerged macrophytes.

Radiation Shading by Emergent Macrophytes

The additional differential heating effects due to radiation shading by emergent macrophytes were investigated by varying the leaf area index (LAI), which quantifies the foliage area of the emergent macrophyte canopy. Because an emergent macrophyte canopy must be supported by submerged stems, submerged macrophytes were included within the emergent macrophyte zones, but the wetland was assumed to be otherwise unvegetated.

In all simulations, the macrophyte properties were assumed to be uniform in all macrophyte zones throughout the lagoon. The distribution of the emergent macrophyte and open water zones used in the radiation shading simulations is shown in Figure 5.11. This represented a greater distribution of emergent macrophytes than observed in the field, but corresponded to the distribution of submerged macrophytes mapped during the bathymetric survey, and was equal to the submerged macrophyte distribution used in the previous simulations.

The effects of differential heating due to radiation shading by emergent macrophytes were assessed by comparison with simulation results for differential heating due to depth differences and due to radiation shading by submerged macrophytes.

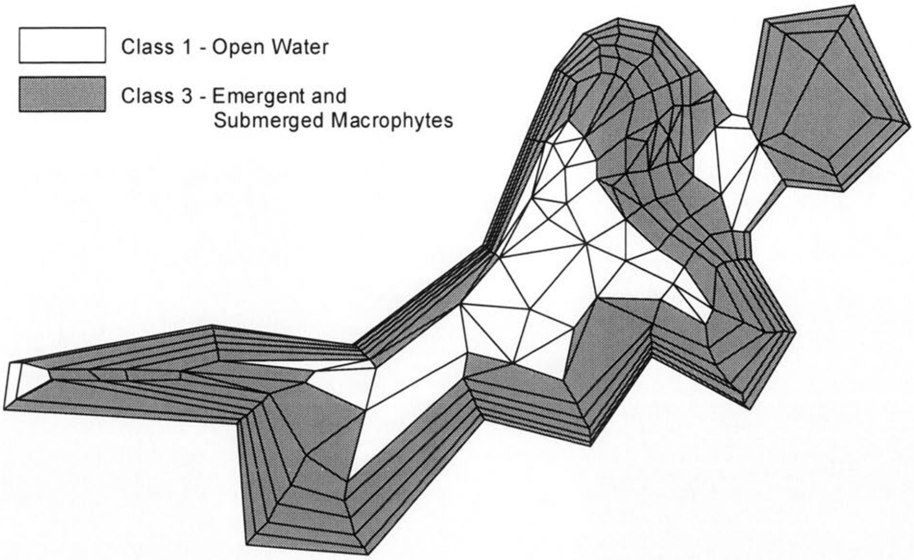

Figure 5.11: Distribution of open water and emergent (plus submerged) macrophyte zones used for simulations of radiation shading by an emergent macrophyte canopy.

Chapter 6

EXPERIMENTAL RESULTS

6.1 Introduction

This chapter presents and analyses the results the experimental programmes described in Chapter 5, including field experiments and numerical simulations.

The results of the emergent macrophyte surveys are considered in Section 6.2. These include canopy height statistics, vertical distributions of stem density and stem dimensions, foliage area density, leaf area index and foliage area inclination functions. The results characterise the foliage of the emergent macrophyte canopies at the four wetlands, and provide input into the simple models for canopy attenuation of shortwave radiation.

The results of the canopy attenuation experiments are presented and discussed in Section 6.3. The shortwave radiation profiles measured in emergent macrophyte canopies at the four wetlands are used to test simple canopy attenuation models available in the literature, and to assess their applicability in this new application. A simple canopy attenuation model is selected for incorporation into the modified hydrodynamic model, which is subsequently used for numerical simulation experiments.

The results of the underwater attenuation experiments are considered in Section 6.4. Measured underwater radiation profiles are used to estimate underwater attenuation coefficients for open water and macrophyte zones at Hopwoods Lagoon. These are used in the numerical simulation experiments.

Observed hydrodynamic behaviour at Hopwoods Lagoon is discussed in Section 6.5, including consideration of the diurnal and seasonal response of the wetland to variation in meteorological forcing. Horizontal temperature differences between open water and macrophyte zones are used to infer convective exchanges between the two, and evidence is presented supporting the existence of the inferred currents. Observations are also presented of radiation shading by submerged and emergent macrophytes.

The numerical modelling results are presented in Section 6.6. These include the results of model calibration and validation and the results of hydrodynamic simulation experiments undertaken to supplement field observations of radiation shading by submerged and emergent macrophytes.

The effects of radiation shading by macrophytes on wetland hydrodynamics are further considered in Chapter 7, which provides a summary and synthesis of the field observations and hydrodynamic simulation results, and the implications of these for wetland design and management.

6.2 Results of Emergent Macrophyte Surveys

6.2.1 Canopy Height, h_L

The maximum canopy heights measured at each wetland on each sampling occasion are shown in Table 6.1. The data show that the *Typha* canopies were taller than the *Juncus* and *Eleocharis* canopies, relative to the water surface, and that the heights of the two *Typha* canopies were similar.

Wetland and Dominant Species	Season and Date of Macrophyte Survey	Maximum Canopy Height h_L (m)
Deep Creek *Typha*	Winter, 26 Aug 1999	1.8
Typha domingensis	Spring, 26 Nov 2000	2.0
	Autumn, 17 Apr 2001	2.1
Warriewood Wetlands *Typha domingensis*	Spring, 17 Oct 1999	2.0
Deep Creek *Juncus* *Juncus kraussii*	Winter, 26 Aug 1999	1.5
Hopwoods Lagoon	Winter, 3 Sep 2000	1.2
Eleocharis sphacelata	Autumn, 1 Apr 2001	1.1

Table 6.1: Maximum canopy height above the water surface.

6.2.2 Stem Density, $n_s(z)$

Figure 6.1 shows the stem density at each site as a function of height above the water surface on each sampling occasion. The stem density included both live and dead stems of the dominant macrophyte species at each site, together with any secondary species. Stem density data for each macrophyte species are presented in Appendix B.

The stem density was similar at the Deep Creek *Typha* wetland on the three sampling occasions, and reasonably consistent between the three sites. Short, broken stems of dead *Typha* contributed significantly more to the stem density in the lower 0.5 m of the canopy than young green *Typha* stems or stems of other macrophyte species.

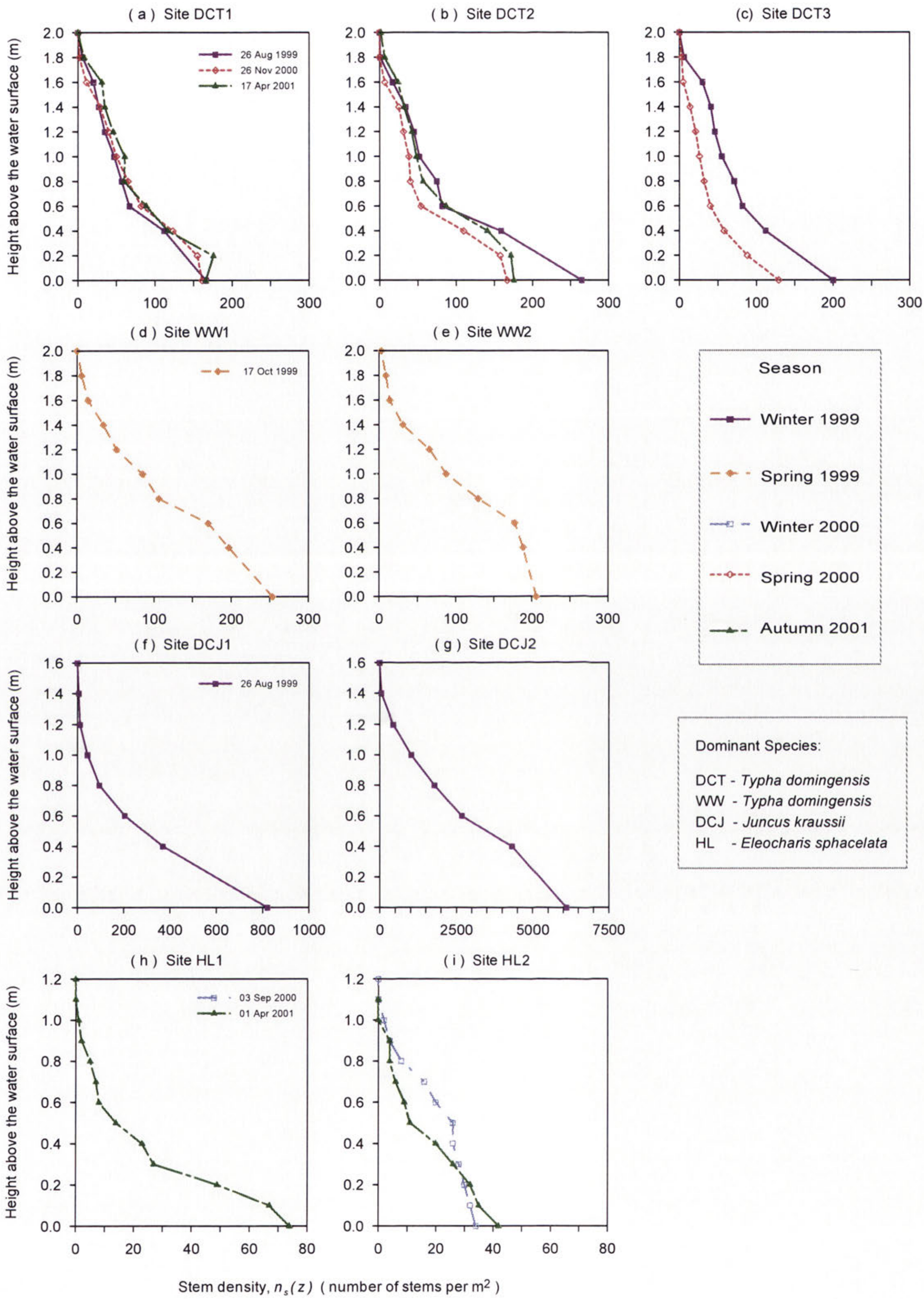

Figure 6.1: Stem density as a function of height above the water surface.

Figure 6.1(a) shows an apparently anomalous increase in stem density with elevation above the water surface at Site DCT1 on 17 April 2001. As defined in Section 5.2.2 (page 141), stems were counted if they intersected the quadrat area, irrespective of the root position (and conversely, were excluded if they exited the quadrat area in which they were rooted). The vegetation data in Table B.1 (page 385) show that there were an additional 10 stems at an elevation of 0.2 m above the water surface, compared with the number intersecting the surface. The field notes also indicate that there were many bent *Typha* stems which would have been counted twice where they intersected the planar quadrat area at a given height above the water surface.

Stem densities at Warriewood Wetlands were higher than at the Deep Creek *Typha* wetland. The *Typha* canopy at Warriewood Wetlands was surveyed approximately six weeks after the Deep Creek wetland, and it is expected that significant growth would have occurred during the intervening period in early spring.

Stem densities at the Deep Creek *Juncus* sites far exceeded those at the other wetlands, and there was significant variation between sites DCJ1 and DCJ2. This suggested that the assumption of horizontal homogeneity may have been less appropriate for the Deep Creek *Juncus* canopy than for the other wetlands. Note that the stem densities plotted on Figures 6.1(f) and (g) were calculated from the field stem densities determined from smaller quadrats.

The *Eleocharis* canopy at Hopwoods Lagoon was significantly less dense than the canopies at the three Sydney wetlands. Figures 6.1(h), (i) and (j) show that stem densities were reasonably consistent between Winter 2000 and Autumn 2001, although there was some variation between the three sites.

Collectively, the canopies of the four wetlands represented a broad range of stem densities over which the attenuation of shortwave radiation could be investigated. The results of the canopy attenuation experiments are analysed and discussed in Section 6.3.3.

6.2.3 Stem Dimensions, $d(z)$

The characteristic stem dimensions for the four wetlands are shown in Figure 6.2. Stem dimension data and statistics for the macrophyte species at each wetland are summarised in Appendix B.

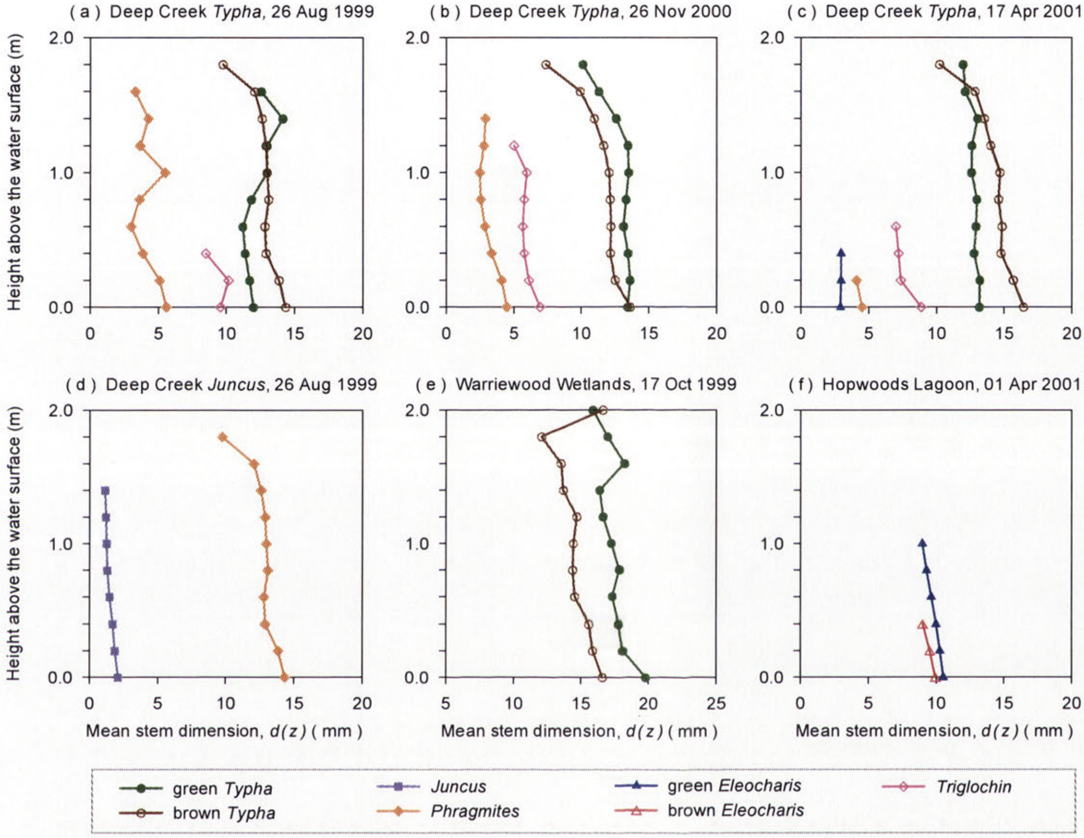

Figure 6.2: Characteristic stem dimensions as a function of height above the water surface. The stem dimension is width for the Typha and Triglochin stems, and diameter for the Juncus, Phragmites and Eleocharis stems.

The data showed a good degree of consistency for each species between the different sampling sites and dates. Note that the green *Eleocharis* species observed at the Deep Creek *Typha* site in Autumn 2001 was a smaller species than the *Eleocharis sphacelata* present at Hopwoods Lagoon throughout the monitoring period. The mean widths of the green and brown *Typha* stems were slightly higher at Warriewood Wetlands than at Deep Creek, just as the *Typha* canopy was slightly taller at Warriewood Wetlands. This was probably attributable to the six week growing period between sampling dates at the two wetlands.

For a given height above the water surface, the mean diameters of the *Phragmites australis* stems at the Deep Creek *Typha* wetland were smaller than those in the adjacent *Juncus* wetland. This was probably due to the significantly higher water depth at the *Typha* wetland, and hence the greater distance from the substrate. The mean diameter of the *Juncus kraussii* stems was smallest of the surveyed species, and always <2.5 mm.

As expected, all species exhibited a general decrease in the characteristic stem dimension with increased height above the water surface. The slight increase shown near the top of the canopy for the brown *Typha* stems was biased by a small number of wide stems at a height of 2.0 m.

6.2.4 Foliage Area Density, *a(z)*, and Leaf Area Index, *LAI(z)*

The mean *LAI(z)* for the four wetland canopies as a function of relative height above the water surface is shown in Figure 6.3.

The downward cumulative leaf area index increased monotonically with increasing depth of penetration below the top of the canopy. The mean *LAI(z)* for the *Typha domingensis* canopies was greater at Warriewood Wetlands than at the Deep Creek *Typha* wetland for $z/h_L < 0.7$. This reflects both the greater stem density and larger characteristic stem widths at the Warriewood sites.

The value of *LAI(z)* at the Deep Creek *Juncus* wetland was more than double *LAI(z)* at the other wetlands because of the very high stem density, and despite the small mean diameter of the *Juncus* stems. By contrast, the mean *LAI(z)* at Hopwoods Lagoon was very low and changed little with height above the water surface, which reflected the low stem density.

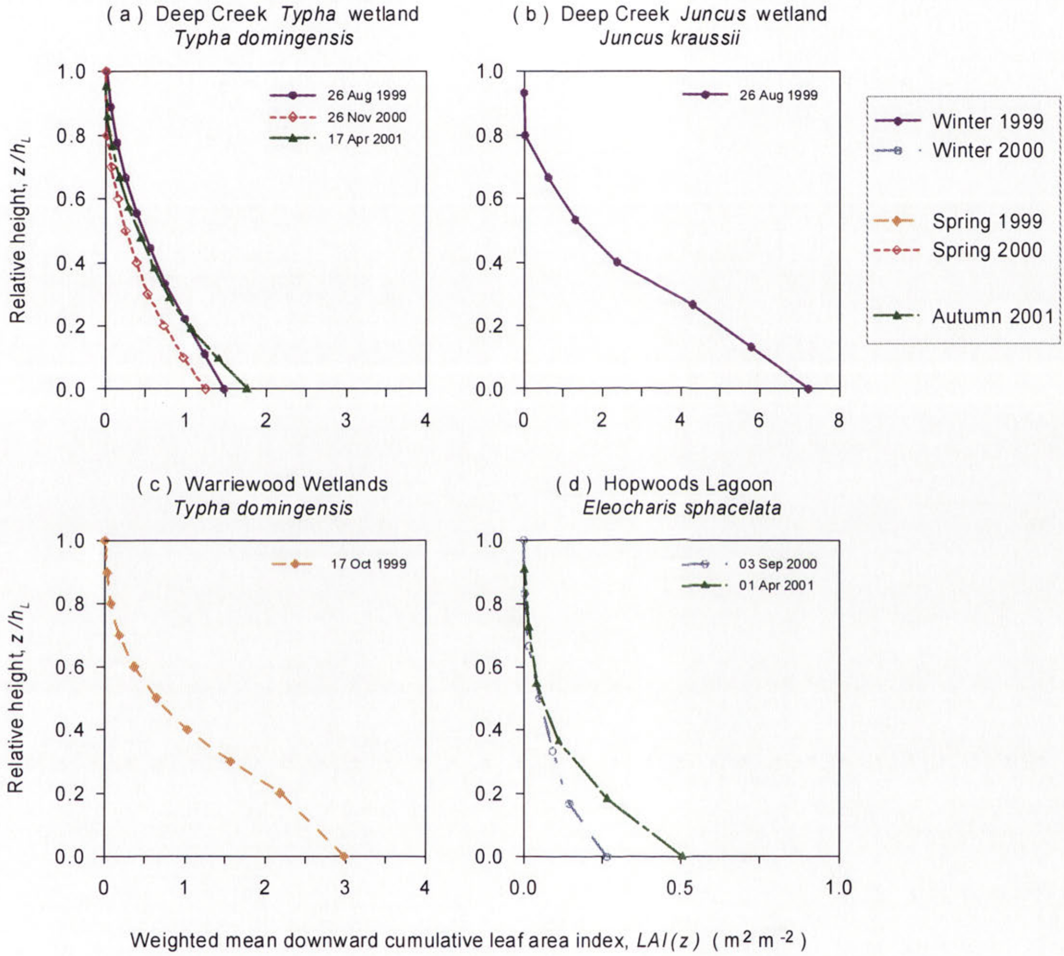

Figure 6.3: Weighted mean downward cumulative leaf area indices.

6.2.5 Foliage Area Inclination, $g_L(\theta)$

The foliage area inclination estimated for each of the four wetland canopies is reported in Table 6.2.

The majority of the emergent macrophyte stems at the four wetlands were inclined within 15° of the vertical, with the exception of the relatively short stems of *Triglochin procerum*. Many of the stems inclined at >15° were dead stems or broken stems which had fallen within the canopy.

Wetland	Macrophyte Species	Proportion of Stems (%) 0–15°	15–30°	30–45°	>45°
Deep Creek *Typha*	*Typha domingensis*	75	25	–	–
	Phragmites australis	100	–	–	–
	Triglochin procerum	50	50	–	–
	Eleocharis sp.	100	–	–	–
Warriewood Wetlands	*Typha domingensis*	75	25	–	–
Deep Creek *Juncus*	*Juncus kraussii*	75	20	5	–
	Phragmites australis	100	–	–	–
Hopwoods Lagoon	*Eleocharis sphacelata*	85	15	–	–
	Inclination Class (see p.75)	$g_{L6}(\theta_L)$	$g_{L5}(\theta_L)$	$g_{L4}(\theta_L)$	$\leq g_{L3}$

Table 6.2: Inclination distributions of foliage area in the emergent macrophyte canopies, with inclination angles taken from the vertical.

6.3 Results of Canopy Attenuation Experiments

6.3.1 Observed Relative PAR Attenuation Profiles

The results of the canopy shortwave radiation experiments at the four wetlands are presented in Figure 6.4. The radiation profiles show mean relative PAR ($\phi_{PAR(z)}$ / $\phi_{PAR(h_L)}$) as a function of relative height (z/h_L) above the water surface. The maximum canopy height for each wetland, h_L, was given in Table 6.1 (page 186). The profiles show attenuation of PAR with distance beneath the top of each canopy, and considerable variability is evident between the different macrophyte species, different sites at each wetland, different seasons and times of day. It is clear that canopy attenuation is generally not linear with depth, as proposed by Waters (1998) for a *Typha orientalis* canopy at Manly Dam, however some profiles do approximate the exponential decrease in relative PAR with depth beneath the top of the canopy suggested by Ross (1975).

Despite the 1 min averaging of 5 sec radiation data at each elevation in each vertical profile, the mean relative radiation profiles show a significant degree of scatter. Had a number of sensors been available and measurements made simultaneously at several sites through the canopy, it is expected that horizontal averaging would have provided a smoother, mean relative radiation profile for each wetland. Unfortunately, it was not possible to take a horizontal average when the profiles were measured at different times of the day using the single available sensor. Instead, many individual profiles show a counter-intuitive increase in relative radiation with increasing depth below the top of the canopy, for which there are several possible explanations.

An increase in relative PAR with depth into the canopy could suggest downwards scattering or reflection from the underside of higher canopy elements. However, as discussed previously, the absorption of PAR by green plants is very high and reflection and scattering are minimal. The apparent increase in relative PAR with depth is therefore unlikely to be due to additional downwards scattering of PAR. The canopy volume between individual canopy elements naturally contains both sunflecks (illuminated areas) and shaded areas, where the ambient PAR is clearly lower than in full sunlight. Rather than representing increases in relative PAR with depth, it is considered more likely that the observed fluctuations in PAR with depth are caused by low PAR measurements made higher in the canopy volume. For example, the sensor may have been partially obscured by an overhanging canopy element which did not shade an entire vertical slice through the canopy. Ideally, a large number of simultaneous measurements distributed through the canopy volume at each height could be averaged to minimise the overall effects of such fluctuations, and further experiments are recommended to test this.

Observations at each of the four wetlands are discussed in more detail in the following sections. The relative PAR profiles are used with the results of the emergent macrophyte surveys to assess some simple canopy attenuation models in Section 6.3.3.

6.3.1.1 PAR Attenuation by Typha domingensis at Deep Creek

Canopy attenuation experiments were conducted at three sites in the *Typha domingensis* canopy at Deep Creek between August 1999 and April 2001, although a problem with one of the telescopic poles restricted experiments to only two sites in April 2001. Figures 6.4(a) to (c) show relative PAR profiles from the Deep Creek *Typha* sites in August 1999, November 2000 and April 2001, respectively. Note that some PAR profiles were removed from the field data set, as indicated in Table 5.2, and these are not shown in Figure 6.4.

The relative radiation profiles from the Deep Creek *Typha* wetland demonstrate spatial and temporal trends according to site, time of day and season.

The relative PAR at the water surface varied throughout the day, as expected, following the movement of the sun. The maximum values at each site were typically observed around the time of solar noon, when the solar elevation was greatest above the horizon and the predominantly vertical canopy elements cast the smallest shadow area over the lower canopy layers. The maximum relative PAR at the water surface was generally $> 80\%$, and lower values were observed either side of noon, as the solar beam was intercepted by a greater proportion of the canopy elements. These minimum values ranged from around 10% at all sites in August 1999 and April 2001 and Site DCT1 in November 2000, to between 40 and 50% at Sites DCT2 and DCT3 in November 2000.

Attenuation of PAR was generally lower at the three sites in November 2000 than in August 1999 or April 2001. This was consistent with the measured *LAI* (Figure 6.3, page 191), which was lower at the beginning of the growing season in November 2000 than in August 1999 and April 2001. There was also comparatively little attenuation by the upper half of the canopy in November 2000, when the mean stem dimensions and hence the foliage area were lower than in August 1999 or April 2001.

The relative PAR profiles from the Deep Creek *Typha* wetland are compared with predictions made using simple canopy attenuation models in Section 6.3.3.

6.3.1.2 PAR Attenuation by Typha domingensis at Warriewood Wetlands

Canopy attenuation experiments were conducted at two sites within Warriewood Wetlands on 30 September 1999, and Figure 6.4(d) shows the relative PAR profiles for Sites WW1 and WW2. Access constraints restricted the number of sites available for the experiments, and only two sites were selected. These were located within 5 m of one another, and adjacent to the submerged walkway. Because of difficult access and the close proximity of the two sites which were available for experiments, it was decided not to conduct further experiments at Warriewood Wetlands.

Despite supporting the same species, the relative PAR at the water surface was generally lower at Warriewood Wetlands than at the Deep Creek *Typha* wetland. This was consistent with the higher stem density and LAI at Warriewood, particularly at Site WW1. The upper half of the canopy was comparatively sparse at Warriewood Wetlands, and only slight PAR attenuation was observed at $z / h_L > 0.6$ at Warriewood.

The mean relative PAR at the water surface ranged from approximately 5% to 40% at Site WW1 and approximately 10% to 90% at Site WW2. There was little variation with time of day at Site WW1, which suggests that the water surface was at least partially shaded at most times during the day. PAR attenuation at Site WW2 was variable throughout the day, reflecting the more open (less dense) nature of the *Typha* canopy in this location, and hence the greater temporal variability between sunflecked and shaded areas.

The relative PAR profiles from Warriewood Wetlands are compared with predictions made using simple canopy attenuation models in Section 6.3.3.

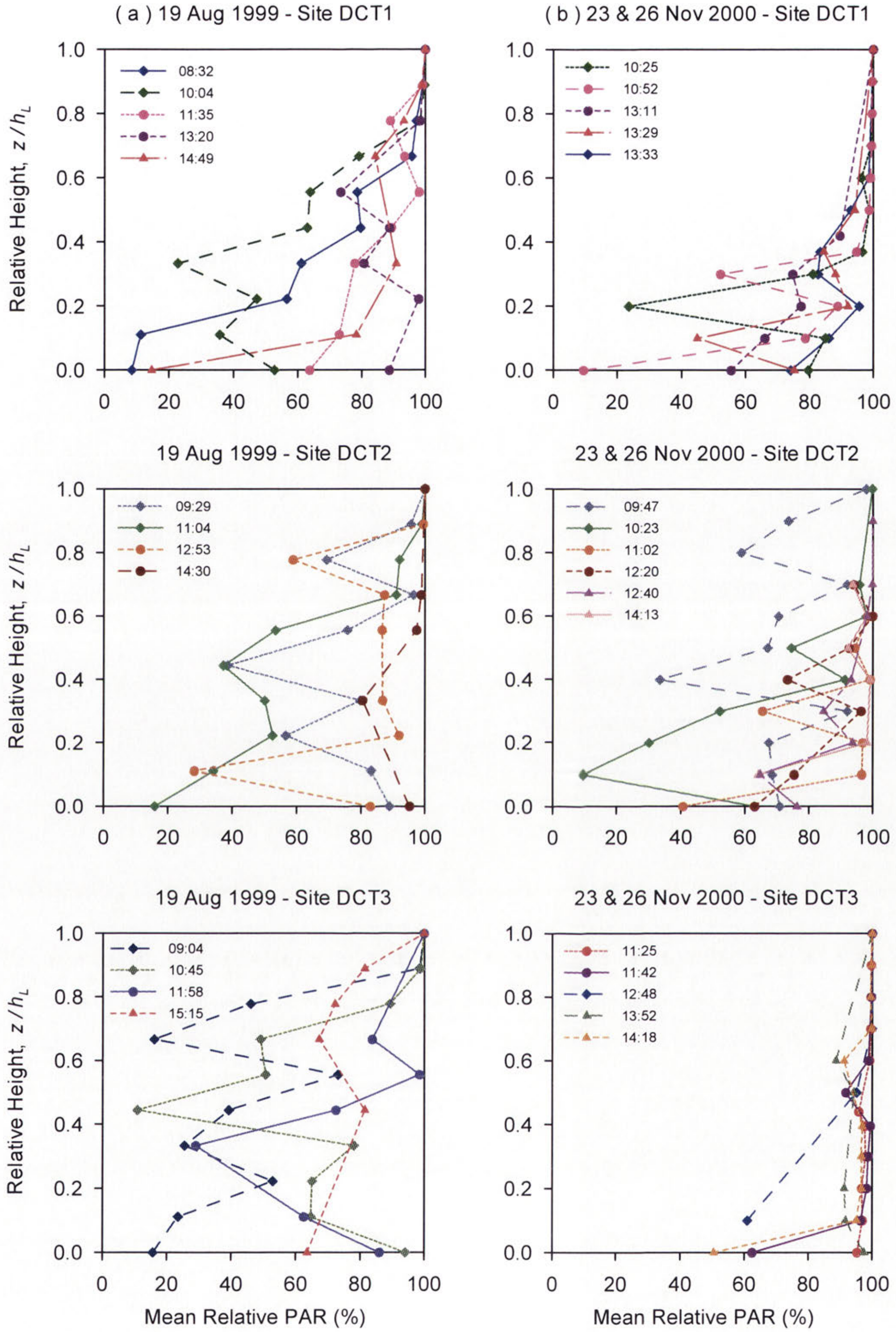

Figure 6.4: Results of canopy attenuation experiments (all times in AEST) (a) Typha domingensis canopy at Deep Creek in Winter, 19 August 1999, and (b) Typha domingensis canopy at Deep Creek in Spring, 23 and 26 November 2000.

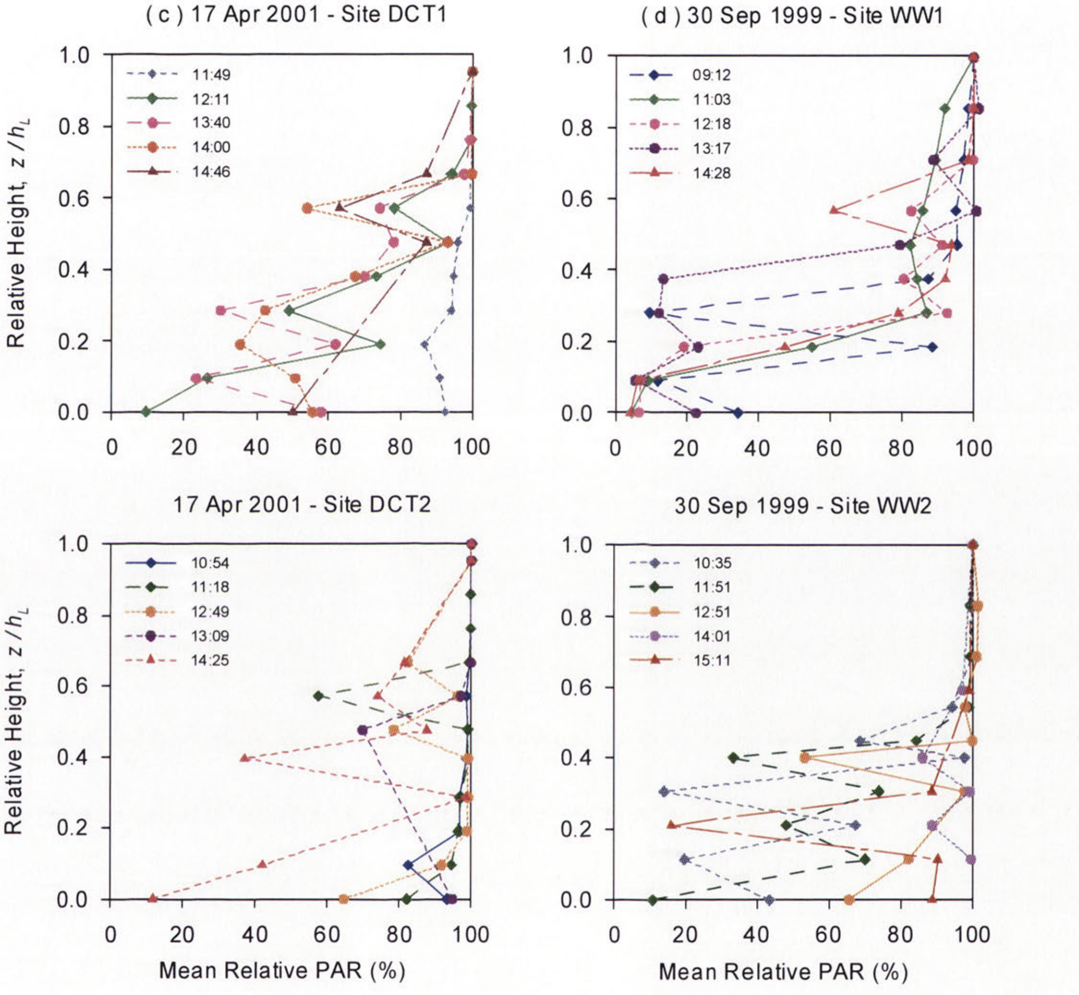

Figure 6.4 (continued): (c) *Typha domingensis* canopy at Deep Creek in Autumn, 17 April 2001, and (d) *Typha domingensis* canopy at Warriewood Wetlands in Spring, 30 September 1999. All times in AEST.

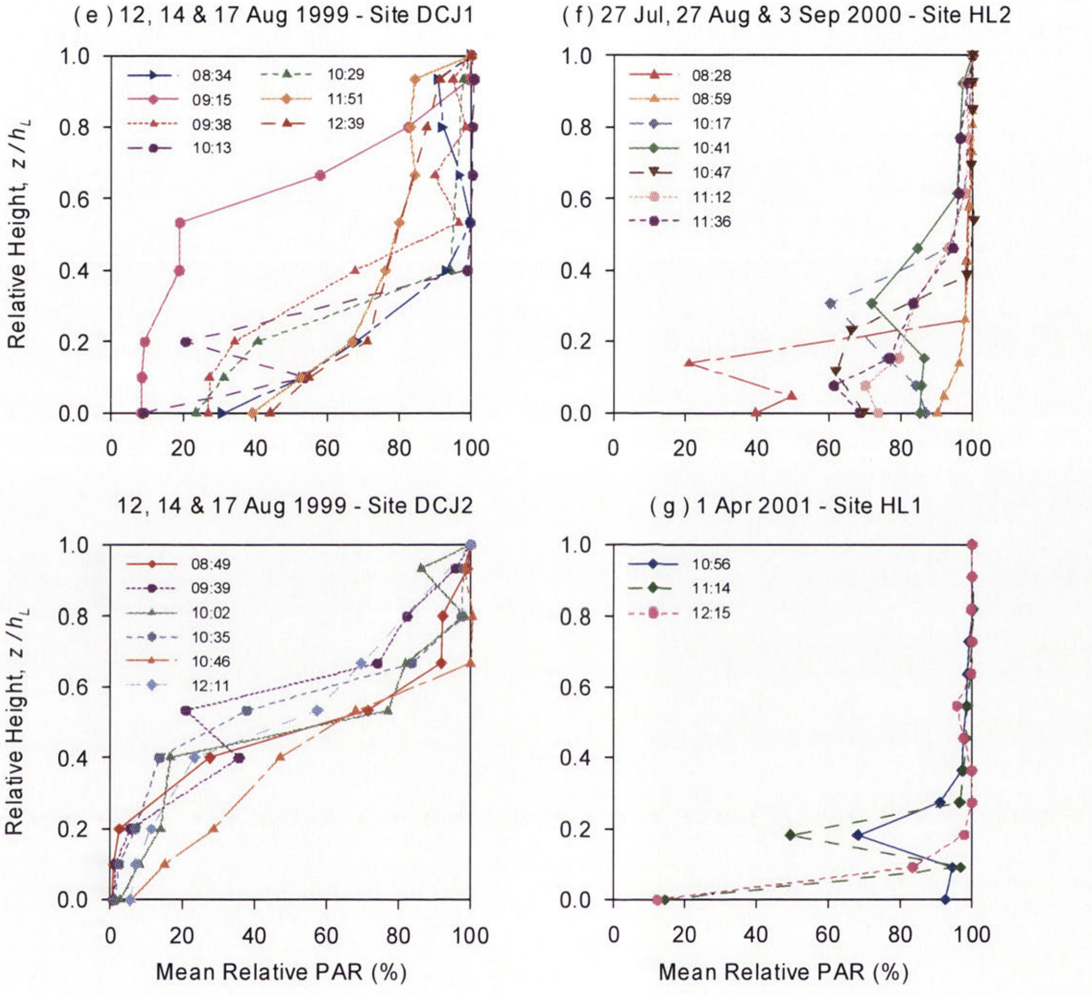

Figure 6.4 (continued): (e) Juncus kraussii canopy at Deep Creek in Winter, 12, 14 & 17 August 1999, (f) Eleocharis sphacelata canopy at Hopwoods Lagoon in Winter, 27 July, 27 August and 3 September 2000, and (g) Autumn, 1 April 2001. All times in AEST.

6.3.1.3 PAR Attenuation by Juncus kraussii at Deep Creek

Canopy attenuation experiments were conducted at two sites in the Deep Creek *Juncus* canopy on 12, 14 and 17 August 1999. As indicated in Section 5.3.1 and Table 5.2 (page 148), data could only be collected on each occasion during the morning before the sky was obscured by clouds. Some profiles were removed from the data set for the reasons indicated in Table 5.2 and have not been plotted in Figure 6.4.

Figure 6.4(e) shows the relative PAR profiles from Sites DCJ1 and DCJ2. Aside from the profile measured at Site DCJ1 from 09:15 on 12 August, the shapes and magnitudes of the relative PAR profiles were generally consistent at the two sites. There is nothing indicated in the field notes to explain the different profile shape at 09:15, as the skies were completely clear and there was no wind. However, the negligible attenuation when $z\,/\,h_L$ <0.6 suggests that the sensor was almost completely illuminated at all measurement heights within the lower canopy, in contrast to the other profiles measured at Site DCJ1.

The relative radiation at the water surface at Site DCJ2 varied little over the measurement period, and was always less than 5%, which reflected the very high foliage density (*LAI*=8.88). At Site DCJ1, the relative PAR at the water surface ranged from approximately 5% to 40%, reflecting the much lower canopy density at this site (*LAI*=1.14). There was little attenuation of PAR at $z\,/\,h_L$ >0.4 at Site DCJ1, where the stem density was low (Figure 6.1, page 187). Variation in *LAI* between the sites indicates that, while the *Juncus* canopy was generally very dense, there were some areas of lower density.

At both sites, the relative PAR at the water surface was highest near solar noon, when the shadow area cast by the dense, near-vertical canopy was smallest. Despite some scatter between the individual PAR profiles at Sites DCJ1 and DCJ2, this was considerably less than observed at the nearby *Typha* wetlands. Because of the higher stem density and more uniform canopy structure, it is suggested that the *Juncus* canopy was less influenced by local air movements so the variation between sunflecked and shaded areas was lower, and hence the profiles were more consistent with time. This concurs with Ross (1981), who stated that wind effects on the position of canopy elements are reduced with depth and less pronounced in dense stands. The relative PAR at the water surface was also much lower beneath the *Juncus* canopy than beneath the two *Typha* canopies.

Because of the extremely high density of the *Juncus* canopy and the intensive effort required to repeat macrophyte surveys at this wetland, additional canopy attenuation experiments were not conducted at the Deep Creek *Juncus* wetland. Also, because the extremely dense canopy afforded little variation in PAR attenuation with time of day, there was not expected to be significant variation with season. Instead, the results from the August 1999 experiments provided relative PAR and macrophyte data which represented the upper-bound canopy density in the present study.

The relative PAR profiles from the Deep Creek *Juncus* wetland are compared with predictions made using simple canopy attenuation models in Section 6.3.3.

6.3.1.4 PAR Attenuation by *Eleocharis sphacelata* at Hopwoods Lagoon

While the canopy experimental sites could be accessed on foot at the three Sydney wetlands, experiments had to be conducted from a boat at Hopwoods Lagoon. This limited the number of profiles which could be obtained, and unfavourable weather conditions further restricted the dates on which profile data could be collected. Problems with the data logger also resulted in some data losses. Consequently, only a limited number of canopy attenuation profiles were available from two sites at Hopwoods Lagoon. The profiles measured at Hopwoods Lagoon in Winter 2000 and Autumn 2001 represented the lower-bound canopy density in the present study.

Figure 6.4(f) shows the relative radiation profiles in the *Eleocharis* canopy in Winter 2000 and Figure 6.4(g) shows relative PAR profiles measured in Autumn 2001. The constraints mentioned above meant that profiles were not available for the same site in both seasons. However, the available attenuation profiles show that PAR was generally only slightly attenuated by the sparse *Eleocharis* canopy, compared with the macrophyte canopies at the Sydney wetlands. In Winter 2000, there was little attenuation of PAR at $z\,/\,h_L > 0.4$, while in April 2001 there was little attenuation at $z\,/\,h_L > 0.3$, due to the extremely sparse canopy density in the upper layers.

The relative PAR at the water surface varied between 40% and 90% at Site HL2 in Winter 2000, with the lower value occurring on the earliest profile of the day. At Site HL1, the sudden decreases in relative PAR at $z\,/\,h_L$=0.2 and at the water surface at all measurement times suggests that the sensor was partially obscured in each case by one or several *Eleocharis* stem(s). The differences between the two sites in the two seasons was not great, but neither was the difference in the canopy density (LAI=0.27 at Site HL2 in Winter 2000 and LAI=0.51 at Site HL1 in Autumn 2001).

The relative PAR profiles from Hopwoods Lagoon are compared with predictions made using simple canopy attenuation models in Section 6.3.3.

6.3.1.5 Summary

Consideration of mean relative PAR profiles from the sites at the two Deep Creek wetlands, Warriewood Wetlands and Hopwoods Lagoon confirm that canopy attenuation of PAR is highly site-specific, and varies not only with macrophyte species and canopy density but also with the time of day and season.

6.3.2 Net Transmission Coefficients for PAR and Global Radiation

The net transmission coefficient for photosynthetically-active radiation, τ_{PAR} quantifies the proportion of the incident PAR radiation, $\phi_{PAR(h_L)}$, which is transmitted through an emergent canopy to the water surface, $\phi_{PAR(0)}$. This is equivalent to the relative PAR at the water surface:

$$\tau_{\mathrm{PAR}} = \phi_{PAR(0)} \,/\, \phi_{PAR(h_L)} \tag{6.1}$$

Net transmission coefficients for the mean relative PAR profiles shown in Figure 6.4 are reported in Table 6.3 in Section 6.3.3.

The net transmission coefficient for global shortwave radiation, τ_S can be estimated from the net transmission coefficient for PAR (Ross, 1975) according to Equation (3.52), which is reproduced below from page 80:

$$\tau_S = 0.78\,\tau_{\mathrm{PAR}} + 0.22$$

Because the attenuation of global shortwave radiation with depth of penetration through a canopy is lower than attenuation of PAR by the same canopy, the estimated $\tau_S > \tau_{\mathrm{PAR}}$.

6.3.3 Assessment of Simple Models for Canopy Attenuation

The canopy attenuation experiments yielded radiation profile data which were used to assess simple models for PAR attenuation by the emergent macrophyte canopies. These simple models are described in the agricultural and forestry literature, but are not known to have been previously applied to attenuation by wetland macrophytes.

The objectives of the canopy attenuation modelling were to:

- test the simple exponential attenuation models based on Beers Law to determine if they could be used to describe the observed attenuation of PAR in the four macrophyte canopies
- select a simple canopy attenuation model which could be used to parameterise canopy attenuation of radiation in the wetland hydrodynamic model.

As discussed in Chapter 2, simple canopy radiation models are defined in this study as those which model net attenuation of shortwave radiation within the photosynthetically-active radiation (PAR) waveband. Reflection and scattering of PAR by the canopy foliage were not explicitly considered. It was assumed that PAR was either attenuated (absorbed) when intercepted by the canopy foliage or transmitted to greater depth in the canopy without interception. The definition of simple canopy attenuation models was further restricted to those with parameters which could be measured or estimated with relative ease, so the models could be used in applications where detailed field measurements were not available.

The PAR waveband was modelled rather than global shortwave radiation, because macrophytes are most sensitive to shortwave radiation within the PAR waveband. Transmission and reflection of PAR are also negligible compared with transmission and reflection of global shortwave radiation (Ross, 1981). The direct and diffuse components were considered together, as field measurements generally measure cumulative radiation due to both components. Net attenuation of global shortwave radiation could be estimated from the net attenuation of PAR, as shown in Section 6.3.2.

A selection of four simple models from the literature was reviewed briefly in Section 3.4.2.1. These models represent the macrophyte canopy by an array of uniform geometrical structures with characteristic dimensions, and are all variations of Beers Law. The models are distinguished by the method used to calculate the attenuation coefficient, whether:

- **empirically** from field radiation measurements and:
  - (1.) the depth of penetration into the canopy
  - (2.) the downward cumulative leaf area index, or
- **theoretically** from:
  - (3.) a shape factor which is a function of the canopy inclination and solar elevation
  - (4.) the G-function and the solar elevation.

The empirical forms of Beers Law were considered first, to determine the suitability of an exponential relationship in describing PAR attenuation by a macrophyte canopy. Empirical attenuation coefficients were calculated by curve-fitting to the relative PAR profiles shown in Figure 6.4. Geometrical shape factors and the G-function were then calculated for the theoretical models to determine if PAR attenuation could be predicted independently of the measured field data.

6.3.3.1 Empirical Forms of Beers Law

Beers Law using Depth of PAR Penetration into the Canopy

Using the depth of penetration beneath the top of a canopy, Beers Law predicts attenuation of PAR according to Equation (3.53), which is reproduced below:

$$\phi_{PAR(z)} = \phi_{PAR(h_L)} \exp\left[-\mathcal{K}_z\,(h_L - z)\right] \tag{6.2}$$

where $\mathcal{K}_z$ = attenuation coefficient as a function of depth (m^{-1})

$(h_L - z)$ = depth of penetration beneath the top of the canopy, $z = h_L$ (m).

This is shown schematically in Figure 6.5.

The attenuation coefficient $\mathcal{K}_z$ was determined by fitting Equation (6.2) to each relative PAR profile shown in Figure 6.4. The curve was forced through $\phi_{PAR(z)} / \phi_{PAR(h_L)} = 100\%$ at the top of the canopy, where $(h_L - z)$=0, and fit using least-squares regression over all data points in each measured profile. Equal weighting was given to each point. Empirical

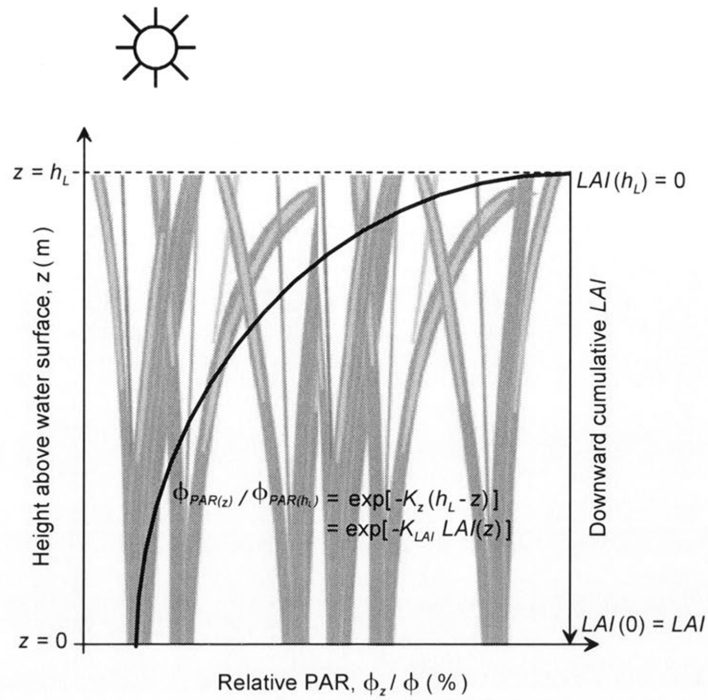

Figure 6.5: Net attenuation of PAR by an emergent macrophyte canopy, as a function of depth of penetration into the canopy ($h_L - z$) or the leaf area index (LAI).

attenuation coefficients and regression coefficients for the clear-sky relative PAR profiles are reported in Table 6.3.

Beers Law using Leaf Area Index

Attenuation of PAR due to Beers Law as a function of the leaf area index is similar to Equation (6.2), with the depth of penetration into the canopy replaced by the downward cumulative leaf area index, *LAI(z)*. This was shown schematically in Figure 6.5. Attenuation is a function of the *LAI*, as per Equation (3.54), which is reproduced below:

$$\phi_{PAR(z)} = \phi_{PAR(h_L)} \exp\left[-\mathcal{K}_{LAI}\, LAI(z)\right] \tag{6.3}$$

where $\mathcal{K}_{LAI}$ = attenuation coefficient as a function of *LAI* ($\mathrm{m^2m^{-2}}$)

LAI(z) = downward cumulative leaf area index ($\mathrm{m^2m^{-2}}$) at elevation z (m).

Similarly to $\mathcal{K}_z$, a value of $\mathcal{K}_{LAI}$ was determined for each relative PAR profile by fitting Equation (6.3) to the measured profiles, using least squares regression over all points in the profile. The empirical attenuation coefficients and regression coefficients for each profile are reported in Table 6.3.

Date	h_L (m)	Site ID	*LAI* (m^2m^{-2})	Time (AEST)	τ_{PAR} (%)	$\mathcal{K}_z$ (m^{-1})	r^2	$\mathcal{K}_{LAI}$ (m^2m^{-2})	r^2
19 Aug 1999	1.8	DCT1	1.22	08:32	9	0.86	0.59	1.53	0.75
				10:04	53	0.58	0.59	0.94	0.49
				11:35	64	0.16	0.51	0.27	0.57
				13:20	89	0.07	< 0	0.10	< 0
				14:49	15	0.34	0.24	0.64	0.34
		DCT2	1.60	09:29	89	0.26	< 0	0.29	< 0
				11:04	16	0.73	0.78	0.98	0.83
				12:53	83	0.27	0.14	0.36	0.15
				14:30	95	0.02	0.02	0.02	0.01
		DCT3	1.54	09:04	16	0.94	0.41	1.21	0.27
				10:45	94	0.43	< 0	0.49	< 0
				11:58	86	0.26	0.15	0.32	0.09
				15:15	64	0.01	< 0	0.03	< 0
23 Nov 2000	2.0	DCT1	1.58	13:33	74	0.10	0.61	0.16	0.67
		DCT2	1.22	09:47	71	0.29	< 0	0.50	< 0
				10:23	63	0.54	0.42	1.23	0.44
				11:02	41	0.17	0.30	0.43	0.47
				12:20	64	0.13	0.42	0.30	0.55
				14:13	100	0.06	0.14	0.14	0.14
		DCT3	0.85	12:48	100	0.06	0.13	0.20	0.15
26 Nov 2000	2.0	DCT1	1.58	10:25	80	0.22	0.19	0.36	0.17
				10:52	10	0.41	0.30	0.80	0.52
				13:11	56	0.19	0.64	0.33	0.89
				13:29	75	0.17	0.39	0.30	0.51
		DCT2	1.22	12:40	76	0.12	0.57	0.28	0.71
		DCT3	0.85	11:25	95	0.02	0.88	0.06	0.91
				11:42	63	0.07	0.25	0.31	0.51
				13:52	98	0.03	0.19	0.09	< 0
				14:18	51	0.11	0.25	0.44	0.51
17 Apr 2001	2.1	DCT1	1.75	11:49	93	0.05	0.67	0.07	0.69
				12:11	9	0.56	0.51	0.94	0.76
				13:40	58	0.43	0.53	0.65	0.54
				14:00	56	0.38	0.60	0.56	0.51
				14:46	50	0.11	0.10	0.17	0.13
		DCT2	1.78	10:54	93	0.04	0.40	0.06	0.54
				11:18	82	0.07	0.03	0.09	< 0
				12:49	65	0.09	0.24	0.14	0.29
				13:09	95	0.03	< 0	0.03	0.07
				14:25	12	0.44	0.37	0.77	0.54

Table 6.3: Empirical attenuation coefficients derived from PAR profiles using depth of penetration into the canopy ($\mathcal{K}_z$) and the downward cumulative leaf area index ($\mathcal{K}_{LAI}$) (a) Typha domingensis at the Deep Creek Typha wetland

Date	h_L (m)	Site ID	*LAI* (m^2m^{-2})	Time (AEST)	τ_{PAR} (%)	$\mathcal{K}_z$ (m^{-1})	r^2	$\mathcal{K}_{LAI}$ (m^2m^{-2})	r^2
30 Sep 1999	2.0	WW1	3.05	09:12	35	0.64	0.35	0.52	0.41
				11:03	5	0.79	0.46	0.69	0.69
				12:18	7	0.88	0.54	0.77	0.80
				13:17	23	1.06	0.63	0.83	0.63
				14:28	4	0.87	0.48	0.76	0.71
		WW2	2.92	10:35	44	0.55	0.38	0.46	0.44
				11:51	11	0.54	0.43	0.45	0.53
				12:51	66	0.16	0.29	0.13	0.28
				14:01	100	0.02	0.01	0.01	< 0
				15:11	89	0.23	0.12	0.20	0.16

Table 6.3 (continued): (b) Typha domingensis at Warriewood Wetlands

Date	h_L (m)	Site ID	*LAI* (m^2m^{-2})	Time (AEST)	τ_{PAR} (%)	$\mathcal{K}_z$ (m^{-1})	r^2	$\mathcal{K}_{LAI}$ (m^2m^{-2})	r^2
12 Aug 1999	1.5	DCJ1	1.14	09:15	9	1.81	0.94	2.78	0.60
				10:13	9	0.89	0.52	1.67	0.77
		DCJ2	8.88	08:49	1	2.75	0.78	0.59	0.99
				09:39	1	2.52	0.84	0.52	0.96
				10:35	1	2.39	0.88	0.49	0.97
14 Aug 1999	1.5	DCJ1	1.14	08:34	31	0.45	0.59	0.83	0.89
17 Aug 1999	1.5	DCJ1	1.14	09:38	27	0.76	0.78	1.33	0.96
				10:29	24	0.68	0.66	1.26	0.96
				11:51	39	0.46	0.80	0.77	0.81
				12:39	44	0.29	0.36	0.63	0.70
		DCJ2	8.88	10:02	3	1.81	0.82	0.37	0.94
				10:46	6	1.28	0.77	0.27	0.96
				12:11	6	1.74	0.89	0.35	0.96

(c) Juncus kraussii at the Deep Creek Juncus wetland

Date	h_L (m)	Site ID	*LAI* (m^2m^{-2})	Time (AEST)	τ_{PAR} (%)	$\mathcal{K}_z$ (m^{-1})	r^2	$\mathcal{K}_{LAI}$ (m^2m^{-2})	r^2
27 Jul 2000	1.2	HL2	0.27	10:17	87	0.22	0.38	1.12	0.10
				10:41	85	0.18	0.47	0.92	< 0
				11:12	74	0.24	0.88	1.43	0.92
				11:36	69	0.30	0.79	1.78	0.90
27 Aug 2000	1.2	HL2	0.27	08:28	40	0.67	0.51	3.43	0.46
				08:59	90	0.05	0.71	0.29	0.76
03 Sep 2000	1.2	HL2	0.27	10:47	70	0.31	0.67	1.62	0.55
01 Apr 2001	1.1	HL1	0.51	10:56	93	0.12	0.26	0.35	0.20
				11:14	15	0.56	0.27	2.21	0.56
				12:15	12	0.50	0.20	2.13	0.50

(d) Eleocharis sphacelata at Hopwoods Lagoon.

Discussion - Empirical Forms of Beers Law

From Table 6.3, it is evident that there was considerable variation in both the empirical coefficients $\mathcal{K}_z$ and $\mathcal{K}_{LAI}$ between:

- individual PAR profiles measured at different times at each site
- the different sites at each wetland
- the macrophyte species at the different wetlands
- the different seasons.

This was expected, given the variability in the observed relative PAR profiles and the comments made earlier in Section 6.3.1.

PAR Attenuation as a Function of $\mathcal{K}_z$

The empirically-derived $\mathcal{K}_z$ ranged from 0.01 to $0.94\,m^{-1}$ at the Deep Creek *Typha* wetland and from 0.02 to $1.06\,m^{-1}$ in the similar *Typha domingensis* canopy at Warriewood Wetlands. The empirical $\mathcal{K}_z$ was highest at $2.75\,m^{-1}$ at Site DCJ2 on 12 August 1999 and ranged from 0.05 to $0.67\,m^{-1}$ at Hopwoods Lagoon. The value of $\mathcal{K}_z$ was generally higher at the wetlands and sites with the higher stem densities, being the Deep Creek *Juncus* wetland and the *Typha* canopy at Warriewood Wetlands. However, $\mathcal{K}_z$ was not consistently higher in the taller canopies, which suggests that PAR attenuation is governed more by the stem density and foliage area than the canopy height.

Figure 6.6(a) shows the temporal variation in the empirical $\mathcal{K}_z$ coefficients at the four wetlands. While there are some general trends towards higher values of $\mathcal{K}_z$ in the early morning and lower values around solar noon at each site in each season, there are many exceptions. These exceptions are largely attributable to the irregular shape of many of the relative PAR profiles discussed in Section 6.3.1. Unfortunately, there are fewer PAR profiles in the afternoon, especially at the sites with higher $\mathcal{K}_z$, so it is not possible to comment on the symmetry in $\mathcal{K}_z$ around solar noon.

Seasonal effects were apparent in the values of $\mathcal{K}_z$ derived from the Deep Creek *Typha* profiles, with generally smaller values in November 2000 when the stem density and *LAI* were lower, than in the other seasons. The attenuation coefficients were generally larger in August 1999 when canopy density was higher. At Hopwoods Lagoon, the $\mathcal{K}_z$ values were

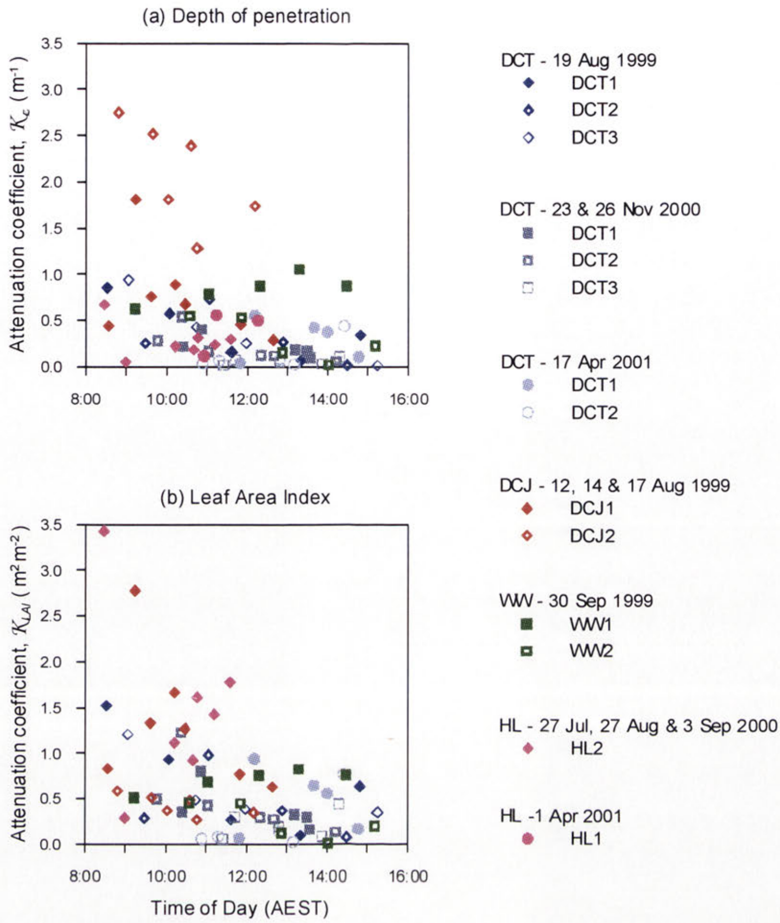

Figure 6.6: Temporal variation in attenuation coefficients derived from relative PAR profiles using Beers Law with (a) depth of penetration and (b) leaf area index.

generally smaller in Winter 2000 than following the growing season, in April 2001, despite the lower *LAI* in Winter. As at the Deep Creek *Typha* wetland, the canopy was slightly shorter in April than in Winter, which would contribute to higher $\mathcal{K}_z$ in April. Hence, it appears that some of the seasonal variation between empirical $\mathcal{K}_z$ at a given wetland can be attributed to differences in canopy height, and this would also influence comparisons between the different wetlands.

The least-squares regression coefficients for the fit of the predicted relative PAR profiles to the measured profiles at each height were highly variable between the individual profiles, and ranged from no relationship at all ($r^2 < 0$) to r^2=0.94 at the Deep Creek *Juncus* wetland. Regression coefficients were consistently higher for the Deep Creek *Juncus* sites, reflecting the generally smoother and approximately exponential attenuation profiles in the denser canopy at this wetland. The regression coefficients were widely variable for profiles measured in the *Typha domingensis* canopies at Deep Creek and Warriewood Wetlands, where the shapes of the profiles were also highly irregular. Regression coefficients were generally lowest for the profiles measured in the sparse *Eleocharis* canopy at Hopwoods Lagoon in April 2001, when there was little attenuation of PAR and where relative PAR profiles least resembled an exponential shape. This could indicate that there is a threshold canopy density below which PAR attenuation cannot be represented by an exponential relationship.

PAR Attenuation as a Function of $\mathcal{K}_{LAI}$

The values of the empirically-derived $\mathcal{K}_{LAI}$ ranged from 0.02 to 1.53 m^2m^{-2} at the Deep Creek *Typha* wetland, and from 0.01 to 0.83 m^2m^{-2} in the *Typha* canopy at Warriewood Wetlands. The $\mathcal{K}_{LAI}$ were generally more consistent between the individual profiles measured at each site in the *Typha domingensis* canopy at Warriewood Wetlands than at Deep Creek. This was similar to the variation in $\mathcal{K}_z$ between the two wetlands, and reflects the more uniform shape of the relative PAR profiles at Warriewood Wetlands, particularly at Site WW1, and the greater canopy density at Warriewood. At the Deep Creek *Juncus* wetland, $\mathcal{K}_{LAI}$ were in the range from 0.63 to 2.78 m^2m^{-2} at Site DCJ1 but only 0.27 to 0.59 m^2m^{-2} at the denser Site DCJ2. The empirically-derived $\mathcal{K}_{LAI}$ were most variable at Hopwoods Lagoon, where they ranged from 0.29 to 3.43 m^2m^{-2}, and where the canopy density was least. Note that the *LAI* are reported in Table 6.3.

Expected values of $\mathcal{K}_{LAI}$ for global shortwave radiation range from nearly zero when the solar elevation is $\beta = 90°$, to 2.4 m^2m^{-2} for a vertical canopy when $\beta < 20°$, as shown in Figure 6.7. However, as indicated by Ross (1975) and Equation (3.52) on page 201, PAR is attenuated more rapidly than global shortwave radiation, so $\mathcal{K}_{LAI}$ for PAR is expected to be slightly higher than published values for global shortwave radiation. The higher $\mathcal{K}_{LAI}$ derived from the 09:15 profile at Site DCJ1 on 12 August 1999 (Table 6.3(c)) and the 08:28 profile at Site HL2 on 27 August 2000 (Table 6.3(d)) are clearly unreasonable, while the remaining values are within the range illustrated in Figure 6.7. The 09:15 profile at Site DCJ1 was previously identified as an irregularly-shaped profile, while the 08:28 profile at

Site HL2 displayed no attenuation for $z / h_L > 0.2$ but considerably greater attenuation near the water surface than the remaining profiles measured in Winter 2000.

The empirical $\mathcal{K}_{LAI}$ values for the profiles measured at the extremely dense Site DCJ2 site are smaller than those at Site DCJ1, even though, intuitively, a larger coefficient might be expected for a denser canopy. However, according to Equation (6.3), PAR attenuation is a function of $\mathcal{K}_{LAI}$ and *LAI(z)*, so a smaller $\mathcal{K}_{LAI}$ is required if the *LAI(z)* is larger, for a given relative PAR at the water surface. The *LAI(z)* at Site DCJ2 far exceeds *LAI(z)* at all measurement heights at Site DCJ1. Because the empirical $\mathcal{K}_{LAI}$ were derived from field profiles giving all data points equal weighting, it is possible that the shape of the profiles has influenced the $\mathcal{K}_{LAI}$ towards the high side at Site DCJ1 and the low side at Site DCJ2. A similar argument applies to the generally high $\mathcal{K}_{LAI}$ derived from the profiles measured at Hopwoods Lagoon, where the canopy is sparse.

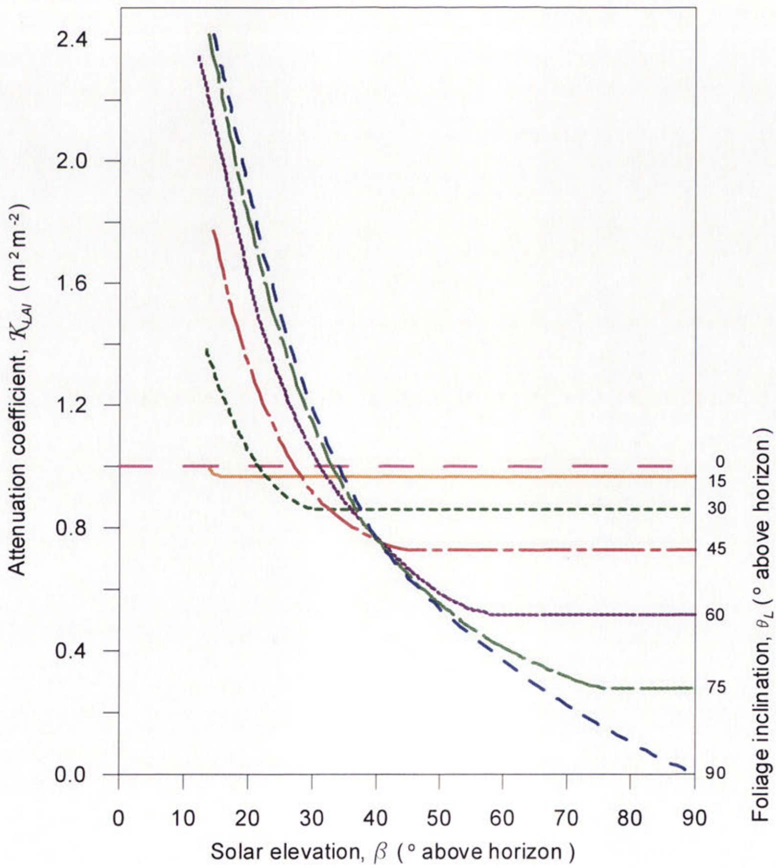

Figure 6.7: Variation in the theoretical value of $\mathcal{K}_{LAI}$ with solar elevation, β and foliage inclination, θ_L (redrawn from Anderson, 1966, p.194 in Ross, 1981).

The least-squares regression coefficients were higher for the profiles measured at Site DCJ2, indicating that these profiles more closely resemble exponential attenuation than those measured at Site DCJ1. It is also possible that the stem density and consequently the *LAI* was overestimated at Site DCJ2, which would have biased the $\mathcal{K}_{LAI}$ for Site DCJ2 towards the low side. Similarly, the stem density and *LAI* may have been underestimated at Site DCJ1. Errors of this type would have been more likely in the denser canopy at the Deep Creek *Juncus* site than at the other wetlands, although stem counting was undertaken simultaneously by two people to minimise such errors.

Figure 6.6(b) (page 208) shows temporal variation in the empirically-derived $\mathcal{K}_{LAI}$ values at the four wetlands. The expected decrease towards solar noon is present and the trend is stronger than that displayed by the empirical $\mathcal{K}_z$, shown in Figure 6.6(a). The anomalously high $\mathcal{K}_{LAI}$ values at Site DCJ1 and Site HL2 are clearly evident. Seasonal variation in the empirical $\mathcal{K}_{LAI}$ values at the Deep Creek *Typha* wetland was similar to that observed for the $\mathcal{K}_z$, with larger values in August 1999 and smaller values in November 2000. With the exception of the anomalously high $\mathcal{K}_{LAI} = 3.43$ at Site HL2 in August 2000, the empirical coefficients were generally larger in April 2001 than in Winter 2000, reflecting the observed variation in canopy density between the two seasons.

Summary - Empirical Forms of Beers Law

Figure 6.8(a) compares predicted PAR at the water surface using $\mathcal{K}_z$ with the measured PAR at the water surface, for each relative PAR profile. Figure 6.8(b) shows a similar relationship for predicted PAR at the water surface using $\mathcal{K}_{LAI}$. The regression coefficients indicate the fit of the relationship to the 1:1 slope in each case, and suggest that the net transmission coefficient (at the water surface) is better predicted as a function of *LAI*, where r^2=0.81, rather than $(h_L - z)$, where r^2=0.71. This was expected, since $(h_L - z)$ is independent of the canopy foliage area, which intercepts and absorbs radiation. The regression coefficients reported in Table 6.3 were greater for the empirically-derived $\mathcal{K}_{LAI}$ values than the $\mathcal{K}_z$ values for 80% of the individual PAR profiles. This indicates that attenuation both *within* and *beneath* the canopy (at the water surface) are better predicted using *LAI(z)* than $(h_L - z)$.

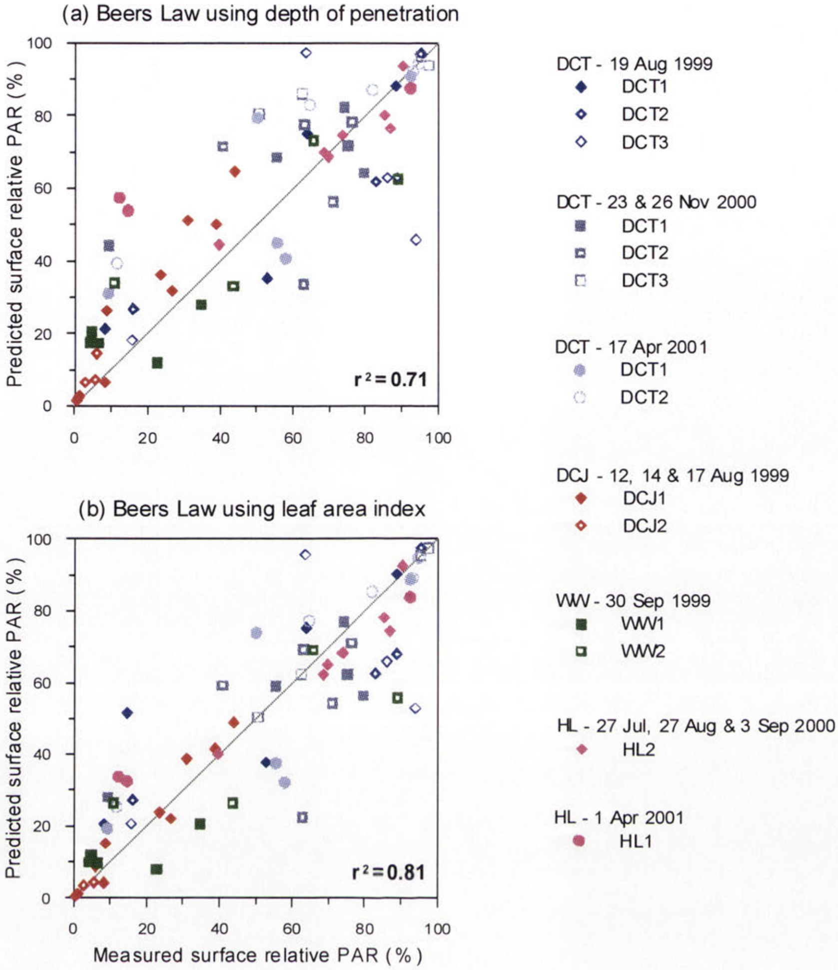

Figure 6.8: Measured and predicted relative PAR at the water surface according to Beers Law using (a) depth of penetration into the canopy and (b) leaf area index.

The results for the empirical forms of Beers Law suggest that measured relative PAR profiles within an emergent macrophyte canopy can be represented by an exponential attenuation relationship, and that a reasonable estimate can be obtained for the relative PAR at the water surface (Figure 6.8). However, the fit of Beers Law over the full height of the measured relative PAR profiles was highly variable, and for some profiles there was no apparent exponential relationship. The exponential relationship was generally stronger (higher r^2) for the dense *Juncus* canopy and weaker for the sparser canopies.

It is possible that the fit of Beers Law to the measured PAR profiles would be improved by increasing the vertical resolution in the profiles, so that a larger number of data points could be considered in each profile. The fit would almost certainly have been improved using the average of simultaneous PAR measurements made at the same height at several locations in each wetland canopy, to minimise the effects of localised differences between shaded and sunflecked areas. The results suggest that greater averaging would be required for relatively sparse canopies, such as *Eleocharis sphacelata* or *Typha domingensis*, while comparatively few profiles would produce a smooth, spatially-averaged profile in a dense *Juncus* canopy.

Empirical forms of Beers Law are unfortunately limited in their application to situations other than those represented by the field measurements, because any variation in attenuation with canopy density, time of day and season is lumped into a single attenuation coefficient and therefore not considered explicitly. A theoretical relationship is sought which can incorporate variation in canopy density and structure, and which accounts for the movement of the sun with the time of day and the season.

6.3.3.2 Theoretical Forms of Beers Law

In contrast with the empirical forms of Beers Law, where attenuation coefficients were derived from measured PAR profiles, attenuation coefficients were calculated independently of field PAR data using theoretical forms of Beers Law.

Beers Law using a Geometrical Shape Factor

The attenuation coefficient $\mathcal{K}_{LAI}$ was calculated from a purely geometrical shape factor (defined in Section 3.4.2.1, page 83), which describes the relationship between the area of shadow cast on a horizontal surface and the shadow area projected in the direction of a solar beam (Monteith and Unsworth, 1990). The shape factor is therefore a function of the canopy geometry and the solar elevation. This shape factor was used with the measured or estimated canopy LAI to predict attenuation of PAR using Equation (6.3).

As described previously and shown in photographs in Chapter 4, the structure of the macrophyte canopies at the four wetlands was close to vertical. The estimated inclination distributions for canopy foliage at the wetlands were given in Table 6.2 (page 192). When calculating the shape factor, it was assumed that each canopy could be approximated by a mean inclination angle, $\overline{\theta}_L$. This $\overline{\theta}_L$ was calculated as a weighted average of the proportions of canopy foliage inclined within six, 15° stem inclination classes, where all stems were assumed to be inclined at the midpoint of the class.

The geometrical shape factor was calculated as described in Section 3.4.2.1 and summarised below:

$$\beta \geq \overline{\theta}_L \qquad \mathcal{K}_{LAI} = \cos\overline{\theta}_L$$

$$\beta < \overline{\theta}_L \qquad \mathcal{K}_{LAI} = \frac{1}{\pi}\left[\,(\pi - 2\theta_0)\cos\overline{\theta}_L + 2\sin\overline{\theta}_L \cot\beta \sin\theta_0\,\right]$$

$$\text{where} \qquad \theta_0 = \cos^{-1}(\tan\beta\cot\overline{\theta}_L) \tag{6.4}$$

Note that the solar elevation (β) and the mean canopy inclination angle are measured from the horizon. The solar elevation was calculated for each profile as outlined in Appendix A. The two cases are required to account for situations where the solar elevation is greater or less than the mean inclination of the canopy elements. In the former, the canopy elements could be rearranged on the curved face of a conical cylinder, assuming no azimuth preference, and all would be illuminated from above Monteith and Unsworth (1990). The projected shadow area is more complex when the solar elevation is less than the mean canopy inclination, when not all elements are illuminated from above, resulting in the second expression. The full derivation is given by Monteith and Unsworth (1990).

Table 6.4 reports the $\mathcal{K}_{LAI}$ values calculated using Equation (6.4) with a geometrical shape factor for times corresponding to each measured attenuation profile. The least-squares regression coefficients compare predicted and measured relative PAR over the height of each profile.

Beers Law using the G-function

This form of Beers Law uses an attenuation coefficient calculated from the G-function. Rather than assuming a constant angle of inclination for the canopy foliage, the G-function permits a distribution of inclination angles within the canopy foliage:

$$\mathcal{K}_{LAI} = \frac{G(z,\theta,\theta_L)}{\sin\beta} = \frac{G(z,\theta,\theta_L)}{\cos\theta} \tag{6.5}$$

The G-function is traditionally calculated using the method of Ross (1975), although the simplified method of Nilson (1991) is used here, where the G-function of the subject canopy is approximated from the values for uniform, vertical and horizontal canopies, respectively (see page 75 for further details):

$$G(z, \theta, \theta_L) = c_1\left(\frac{1}{2}\right) + c_2\left(\frac{2}{\pi}\sin\theta\right) + c_3\left(\cos\theta\right) \tag{6.6}$$

Here: β = solar elevation, measured from horizon

θ = solar zenith, measured from vertical

θ_L = inclination of normal to canopy element, from vertical

$\equiv$ elevation of canopy element, from horizon.

The Nilson coefficients c_1, c_2 and c_3 were calculated as outlined on page 75, using the estimated foliage inclination distributions reported in Table 6.2 (page 192). The calculated values of Nilson's coefficients for the macrophyte canopies at the four wetlands are given in Table 6.5. The slight differences in the estimated foliage inclination distribution between the *Typha* and *Juncus* canopies were insignificant in the calculation of Nilson's coefficients, although the values of the coefficients were different for the less-vertical *Eleocharis* canopy.

The values of $\mathcal{K}_{LAI}$ calculated using the G-function are shown in Table 6.4, together with the least-squares regression coefficients comparing predicted and measured relative PAR profiles. These $\mathcal{K}_{LAI}$ are similar to those calculated using the geometrical shape factor, which assumed a mean canopy inclination angle. The attenuation coefficients calculated using the two theoretical methods were similar. It is expected that differences between the attenuation coefficients calculated using the two methods would have been greater for canopies with a larger range of canopy angles, where $\overline{\theta}_L$ would be less similar to the midpoint of the predominant 15° inclination class.

Date	$\overline{\theta}_L$ (°)	Site ID	Time (AEST)	Attenuation Coefficient, $\mathcal{K}_{LAI}$ (m^2m^{-2})					
				Empirical	r^2	Shape	r^2	G-function	r^2
19 Aug 1999	78.75	DCT1	08:32	1.53	0.75	1.50	0.75	1.45	0.74
			10:04	0.94	0.49	0.85	0.48	0.85	0.48
			11:35	0.27	0.57	0.67	< 0	0.68	< 0
			13:20	0.10	< 0	0.76	< 0	0.76	< 0
			14:49	0.64	0.34	1.16	< 0	1.16	0.01
		DCT2	09:29	0.29	< 0	1.02	< 0	1.00	< 0
			11:04	0.98	0.83	0.70	0.66	0.71	0.68
			12:53	0.36	0.15	0.70	< 0	0.72	< 0
			14:30	0.02	0.01	1.03	< 0	1.01	< 0
		DCT3	09:04	1.21	0.27	1.18	0.27	1.15	0.26
			10:45	0.49	< 0	0.74	< 0	0.75	< 0
			11:58	0.32	0.09	0.66	< 0	0.68	< 0
			15:15	0.03	< 0	1.39	< 0	1.34	< 0
23 Nov 2000	78.75	DCT1	13:33	0.16	0.67	0.35	< 0	0.41	< 0
		DCT2	09:47	0.50	< 0	0.36	< 0	0.42	< 0
			10:23	1.23	0.44	0.28	< 0	0.34	< 0
			11:02	0.43	0.47	0.22	0.31	0.29	0.41
			12:20	0.30	0.55	0.22	0.49	0.29	0.57
			14:13	0.14	0.14	0.46	< 0	0.51	< 0
		DCT3	12:48	0.20	0.15	0.26	0.14	0.32	0.05
26 Nov 2000	78.75	DCT1	10:25	0.36	0.17	0.28	0.17	0.34	0.17
			10:52	0.80	0.52	0.23	0.15	0.30	0.22
			13:11	0.33	0.89	0.30	0.88	0.36	0.88
			13:29	0.30	0.51	0.34	0.51	0.40	0.41
		DCT2	12:40	0.28	0.71	0.24	0.70	0.31	0.71
		DCT3	11:25	0.06	0.91	0.20	< 0	0.27	< 0
			11:42	0.31	0.51	0.20	0.43	0.26	0.50
			13:52	0.09	< 0	0.40	< 0	0.45	< 0
			14:18	0.44	0.51	0.48	0.52	0.52	0.50
17 Apr 2001	78.75	DCT1	11:49	0.07	0.69	0.62	< 0	0.64	< 0
			12:11	0.94	0.76	0.62	0.62	0.64	0.63
			13:40	0.65	0.54	0.77	0.48	0.78	0.48
			14:00	0.56	0.51	0.84	0.10	0.84	0.10
			14:46	0.17	0.13	1.09	< 0	1.07	< 0
		DCT2	10:54	0.06	0.54	0.66	< 0	0.68	< 0
			11:18	0.09	< 0	0.63	< 0	0.65	< 0
			12:49	0.14	0.29	0.66	< 0	0.67	< 0
			13:09	0.03	0.07	0.69	< 0	0.71	< 0
			14:25	0.77	0.54	0.96	0.48	0.95	0.48

Table 6.4: Theoretical attenuation coefficients calculated using geometrical shape factors and the G-function, for dates and times corresponding to the field PAR measurements (a) Typha domingensis at the Deep Creek Typha wetland

Date	$\overline{\theta}_L$ (°)	Site ID	Time (AEST)	Attenuation Coefficient, $\mathcal{K}_{LAI}$ (m^2m^{-2})					
				Empirical	r^2	Shape	r^2	G-function	r^2
30 Sep 1999	78.75	WW1	09:12	0.52	0.41	0.66	0.34	0.68	0.33
			11:03	0.69	0.69	0.40	0.49	0.45	0.55
			12:18	0.77	0.80	0.39	0.49	0.44	0.57
			13:17	0.83	0.63	0.48	0.35	0.52	0.41
			14:28	0.76	0.71	0.72	0.70	0.73	0.70
		WW2	10:35	0.46	0.44	0.44	0.43	0.48	0.43
			11:51	0.45	0.53	0.38	0.51	0.43	0.53
			12:51	0.13	0.28	0.44	< 0	0.48	< 0
			14:01	0.01	< 0	0.61	< 0	0.63	< 0
			15:11	0.20	0.16	0.95	< 0	0.94	< 0

Table 6.4 (continued): (b) Typha domingensis at Warriewood Wetlands

Date	$\overline{\theta}_L$ (°)	Site ID	Time (AEST)	Attenuation Coefficient, $\mathcal{K}_{LAI}$ (m^2m^{-2})					
				Empirical	r^2	Shape	r^2	G-function	r^2
12 Aug 1999	78.00	DCJ1	09:15	2.78	0.60	1.20	< 0	1.17	< 0
			10:13	1.67	0.77	0.89	0.52	0.88	0.52
		DCJ2	08:49	0.59	0.99	1.43	< 0	1.39	< 0
			09:39	0.52	0.96	1.04	< 0	1.02	< 0
			10:35	0.49	0.97	0.82	0.12	0.82	0.11
14 Aug 1999	78.00	DCJ1	08:34	0.83	0.89	1.61	< 0	1.55	< 0
17 Aug 1999	78.00	DCJ1	09:38	1.33	0.96	1.04	0.88	1.03	0.87
			10:29	1.26	0.96	0.84	0.80	0.84	0.80
			11:51	0.77	0.81	0.72	0.80	0.73	0.80
			12:39	0.63	0.70	0.74	0.67	0.75	0.67
		DCJ2	10:02	0.37	0.94	0.93	< 0	0.92	< 0
			10:46	0.27	0.96	0.79	< 0	0.80	< 0
			12:11	0.35	0.96	0.72	< 0	0.73	< 0

(c) Juncus kraussii at the Deep Creek Juncus wetland

Date	$\overline{\theta}_L$ (°)	Site ID	Time (AEST)	Attenuation Coefficient, $\mathcal{K}_{LAI}$ (m^2m^{-2})					
				Empirical	r^2	Shape	r^2	G-function	r^2
27 Jul 2000	80.25	HL2	10:17	1.12	0.10	1.03	0.10	1.03	0.09
			10:41	0.92	< 0	0.93	< 0	0.93	< 0
			11:12	1.43	0.92	0.87	0.62	0.87	0.62
			11:36	1.78	0.90	0.84	0.39	0.84	0.39
27 Aug 2000	80.25	HL2	08:28	3.43	0.46	1.95	0.31	1.91	0.30
			08:59	0.29	0.76	1.51	< 0	1.48	< 0
03 Sep 2000	80.25	HL2	10:47	1.62	0.55	1.00	0.40	1.14	0.46
01 Apr 2001	80.25	HL1	10:56	0.35	0.20	0.55	0.03	0.57	< 0
			11:14	2.21	0.56	0.53	0.13	0.54	0.14
			12:15	2.13	0.50	0.50	0.14	0.52	0.15

(d) Eleocharis sphacelata at Hopwoods Lagoon.

Wetland	Predominant Macrophyte Species	Nilson's Coefficients c_1	c_2	c_3
Deep Creek *Typha*	*Typha domingensis*	0.354	0.658	-0.012
Warriewood Wetlands	*Typha domingensis*	0.354	0.658	-0.012
Deep Creek *Juncus*	*Juncus kraussii*	0.354	0.658	-0.012
Hopwoods Lagoon	*Eleocharis sphacelata*	0.212	0.795	-0.007

Table 6.5: Calculated values of the coefficients used in Nilson's approximation to the G-function.

Discussion - Theoretical Forms of Beers Law

Similarly to the empirical attenuation coefficients, Table 6.4 shows that there was considerable variation in the values of the theoretical coefficients with wetland and species, site, season and time of day. Temporal variation in the values of the attenuation coefficient calculated from the geometrical shape factor, Equation (6.4), and the G-function, Equation (6.5) are shown in Figure 6.9. In contrast to the empirically-derived $\mathcal{K}_{LAI}$ shown in Figure 6.6, the diurnal trend for the theoretical $\mathcal{K}_{LAI}$ was very clear for both models. Attenuation coefficients increased from a minimum around solar noon to larger values in the early morning and late afternoon. This reflects diurnal variation in solar elevation and the consequent change in the shadow area cast by the macrophyte canopies. Seasonal variation was also evident, where the $\mathcal{K}_{LAI}$ were lower during Spring (denoted by squares) than during Autumn (circles) or Winter (diamonds). Although general trends were evident, the empirically-derived attenuation coefficients did not display such clear diurnal or seasonal variation, because they did not explicitly incorporate changes in solar elevation.

The values of the theoretical $\mathcal{K}_{LAI}$ ranged from 0.20 to 1.50 m^2m^{-2} using the shape factor at the Deep Creek *Typha* wetland, and 0.26 to 1.45 m^2m^{-2} using the G-function. The lower values were calculated around solar noon in November 2000, while the higher values were calculated early in the morning in August 1999, when the solar elevation was low. The range was smaller for the *Typha* canopy at Warriewood Wetlands, from 0.38 to 0.72 m^2m^{-2} according to the shape factor and 0.43 to 0.73 m^2m^{-2} using the G-function. Higher values of 0.95 and 0.94 m^2m^{-2} were calculated at Warriewood Wetlands using the two theoretical methods but discounted because there was no relationship between the predicted and measured relative PAR profiles ($r^2<0$) in these cases. The theoretical $\mathcal{K}_{LAI}$

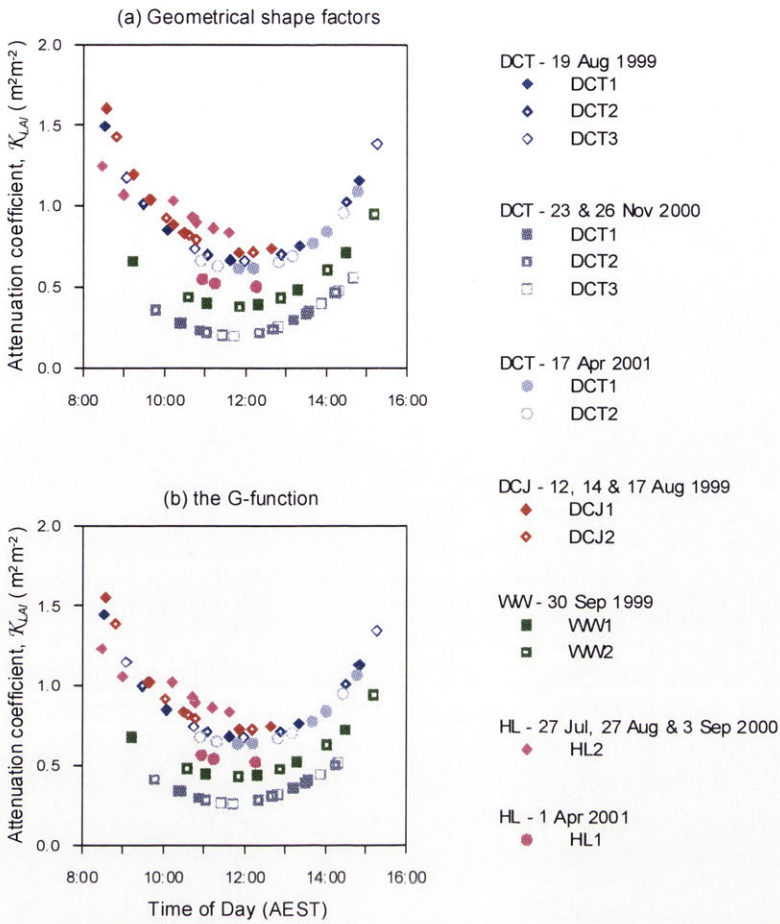

Figure 6.9: Temporal variation in attenuation coefficients calculated using (a) geometrical shape factors and (b) the G-function.

at the dense Deep Creek *Juncus* varied between 0.72 and 1.61 m^2m^{-2} using the geometrical shape factor, and 0.73 and 1.55 m^2m^{-2}using the G-function. At Hopwoods Lagoon, the ranges were 0.50 to 1.95 m^2m^{-2} and 0.52 to 1.91 m^2m^{-2}, respectively.

Strictly, the maximum values of the attenuation coefficient cannot be compared between the different sites and the different wetlands because local weather conditions dictated the number of PAR profiles obtained at each wetland and the timing of these. The profiles were therefore not evenly distributed in time between the different sites. However, comparisons over the diurnal cycle, shown in Figure 6.9, are valid.

The $\mathcal{K}_{LAI}$ values calculated using geometrical shape factors and the G-function were similar, for times and dates corresponding to the measured profiles. This was not unexpected, given the predominantly vertical canopy structure of the macrophyte species at the four wetlands. The greatest differences between the two sets of theoretical $\mathcal{K}_{LAI}$ values occurred close to solar noon when the solar elevation was close to $90\,^\circ$ and the shadow area cast by the predominantly vertical macrophyte canopies was most influenced by small changes in solar elevation and/or the inclination of canopy foliage.

Using the geometrical shape factor, the theoretical $\mathcal{K}_{LAI}$ were not highly sensitive to small changes in the mean inclination of the canopy foliage, $\overline{\theta}_L$. By way of example, in the *Typha domingensis* canopy at Warriewood Wetlands, the value of $\mathcal{K}_{LAI}$ decreased by <2.5% for $(\overline{\theta}_L + 10)\,^\circ$, and increased by <10% for $(\overline{\theta}_L - 10)\,^\circ$, with the variation slightly larger around solar noon. The net transmission coefficient at the water surface changed by less than 5% for $\overline{\theta}_L \pm 10\,^\circ$. Because the mean inclination was close to vertical, changes in $\mathcal{K}_{LAI}$ were greater when the mean foliage inclination angle was reduced. Using the simplified G-function, increases in the value of $\mathcal{K}_{LAI}$ were similar to those reported for the geometrical shape factor, when the inclination distribution of the foliage was modified from 75:25:0% to 60:30:10% in the classes 0 to 15°, 15 to 30° and 30 to 45° from the vertical, respectively. The effect at the water surface was less also than 5%.

Least-squares regression coefficients for the fit of the theoretical profiles to the measured PAR profiles were also similar whether calculated using a geometrical shape factor or the G-function, for each profile. However, there were many theoretical, exponential profiles which demonstrated no relationship to the measured relative PAR profiles ($r^2 < 0$). As discussed previously, these poor relationships are considered largely attributable to the large number of irregularly-shaped, measured relative PAR profiles.

Table 6.4 also compares the values of the theoretical $\mathcal{K}_{LAI}$ with those derived empirically from the field measurements. The ratio of the theoretical to empirical $\mathcal{K}_{LAI}$ was widely variable between 0.2 and 46.2, with a mean value of 3.13±6.25, which indicated that the theoretical values more frequently exceeded the empirical $\mathcal{K}_{LAI}$. Given that both theoretical and empirical models used the same *LAI*, the most probable reason for this is underestimation of the foliage inclination angle. As discussed above, the value of the theoretical $\mathcal{K}_{LAI}$ increased as the mean inclination angle of the foliage decreased, or the inclination distribution of the canopy departed further from vertical. Errors in estimation of the solar elevation were less likely, as several methods were used to check the calculated β. Earlier comments concerning vertical resolution and horizontal averaging in relation to improving the fit of empirical forms of Beers Law apply equally to theoretical forms.

The empirical and theoretical coefficients compared favourably only for profiles where r^2 was reasonable for the theoretical profiles, which indicated measured relative PAR profiles which closely approximated exponential attenuation. There were examples of this in the *Typha* canopies at Deep Creek and Warriewood Wetlands and at the Deep Creek *Juncus* wetland. However the fit of the theoretical attenuation profiles to the measured relative PAR profiles at Hopwoods Lagoon was poor for all profiles. This is consistent with observations made in relation to the empirical profiles, and suggested that there may be a lower canopy density (around $LAI \sim 0.5\,\mathrm{m^2m^{-2}}$) below which PAR attenuation cannot be successfully represented by an exponential relationship. It is not possible to test this proposition without additional field measurements in canopies with similar *LAI*, and further work is certainly recommended in this area.

Figure 6.10 compares the relative PAR flux predicted at the water surface using theoretical forms of Beers Law with the measured relative PAR for each of the measured profiles. The comparisons were similar for the two simple theoretical models. Not surprisingly, given the generally poor r^2 for the individual PAR profiles, no overall relationship was demonstrated between the measured and predicted relative PAR at the water surface.

6.3.3.3 Summary and Application of Simple Canopy Attenuation Models

The objectives of the canopy attenuation experiments were to:

- expand the existing data set available in the literature
- examine the applicability of some simple canopy attenuation models, and
- select a simple canopy attenuation model for incorporation into the hydrodynamic model.

The experiments have contributed relative PAR data from canopies of the emergent macrophyte species *Typha domingensis*, *Juncus kraussii* and *Eleocharis sphacelata* at four wetlands in and around Sydney. The radiation data were measured during various seasons between August 1999 and April 2001.

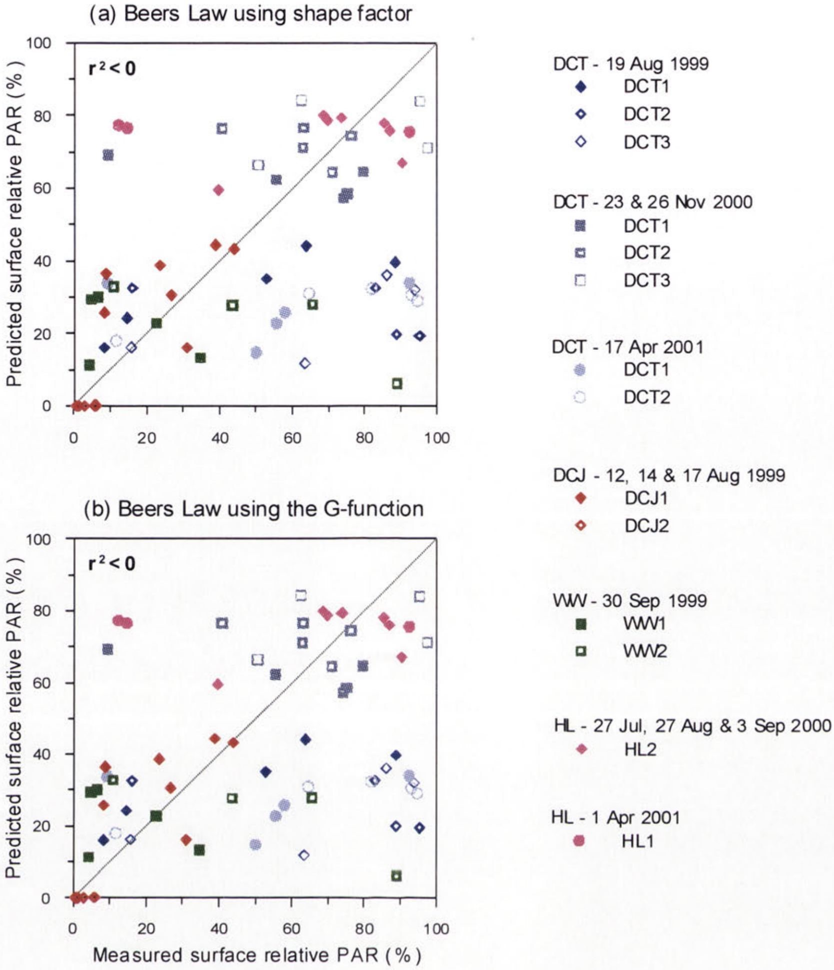

Figure 6.10: Measured and predicted relative PAR at the water surface according to Beers Law using (a) geometrical shape factors and (b) the G-function.

The simple model results for two empirical forms of Beers Law suggested that PAR attenuation could be approximated by an exponential relationship within the canopies of emergent macrophytes, although results for two theoretical forms of Beers Law were less conclusive using the full data set. The empirical forms of Beers Law lump all factors contributing to PAR attenuation into a single $\mathcal{K}_z$ or $\mathcal{K}_{LAI}$ and can only be used to model PAR attenuation in situations for which field data are available. Good agreement was obtained between theoretical and measured relative PAR profiles for measured profiles with approximately exponential form, although a large number of irregularly-shaped, measured PAR profiles could not be successfully represented by theoretical forms of Beers Law. It is expected that, with sufficient horizontal averaging to produce a smooth mean attenuation profile, the fit of the theoretical forms of Beers Law would be improved.

Despite inconclusive results for the majority of the PAR profiles using the simple theoretical forms of Beers Law, the exponential attenuation relationship has been proven valid empirically. It is therefore concluded that the theoretical forms of Beers Law can be used to predict *average* PAR attenuation by an emergent macrophyte canopy, as a function of the foliage inclination and solar elevation. Model results for both empirical and theoretical forms of Beers Law indicated that the simple models for PAR attenuation were more successful when applied to dense canopies, such as *Juncus kraussii* (LAI=8.88 at Site DCJ2) than to moderately dense *Typha domingensis* (approximately $1<LAI<3$) or sparse *Eleocharis sphacelata* ($LAI< 0.5$), given the greater horizontal uniformity in a dense canopy. Further, the attenuation model results suggested that there may be a threshold canopy density below which the exponential attenuation relationship does not apply. It was not possible to test this hypothesis with the available field data, although the results for *Eleocharis sphacelata* at Hopwoods Lagoon suggested that the threshold was higher than LAI=0.5. Clearly, there are implications for the hydrodynamic modelling of canopy attenuation at Hopwoods Lagoon (Section 6.6).

The theoretical form of Beers Law based on the G-function was adopted for the hydrodynamic modelling experiments, recognising the potential implications of using this model in a sparse emergent macrophyte canopy. This model accounts for the inclination distribution of the canopy elements and diurnal and seasonal variation in solar elevation through the G-function, and the vertical distribution of foliage area through the $LAI(z)$ term. The model requires input of the canopy LAI and the inclination distribution of the canopy foliage, which can be readily measured or estimated, while the solar elevation is calculated from standard astronomical formulae as shown in Appendix A.

6.4 Results of Underwater Attenuation Experiments

6.4.1 Observed Underwater Attenuation Profiles

The results of the underwater attenuation experiments are presented in Figure 6.11. The profiles show relative PAR as a function of depth below the water surface at Hopwoods Lagoon in open water and submerged macrophyte zones. The curves represent the mean relative PAR profile calculated for each experiment as $\overline{\phi_{PAR(z)}} / \overline{\phi_{PAR(0)}}$, using the 1 min mean of the measured 5 sec data at each depth. Errors associated with the use of $\overline{\phi_{PAR(0)}}$ were discussed in Section 5.4.1.

As for the canopy attenuation experiments, despite the averaging of 5 sec PAR data at each depth in each vertical profile, there was considerable scatter within and between the measured profiles. Horizontal averaging would have provided a smoother mean relative PAR profile had more than one sensor been available to measure PAR simultaneously at several sites. However, despite some instances where the relative PAR increased with depth below the surface, the shapes of the attenuation profiles at each of the two sites are broadly consistent and relatively smooth. As discussed in relation to the canopy attenuation profiles (page 193), these apparent increases in relative PAR with depth below the water surface are most likely due to low measurements higher in the water column, where for example, the sensor was partially obscured by suspended matter.

Observed underwater attenuation in the two wetland zones is discussed in more detail in the following sections. The relative PAR profiles are used to assess the applicability of Beers Law to underwater attenuation in Section 6.4.2. The small number of successful underwater radiation attenuation profiles meant that measurements were made only at Sites OW2 (open water) and SV2 (submerged macrophyte zone). However, measurements were made at different times of the day and on several occasions, and for the purposes of this research, taken to be representative of conditions at other open water and submerged macrophyte zones within the lagoon.

6.4.1.1 Attenuation in the Open Water Zone

Figure 6.11(a) shows the relative PAR profiles measured beneath the water surface in the open water zone at Hopwoods Lagoon on 17 January, 1 April and 22 October 2001. The

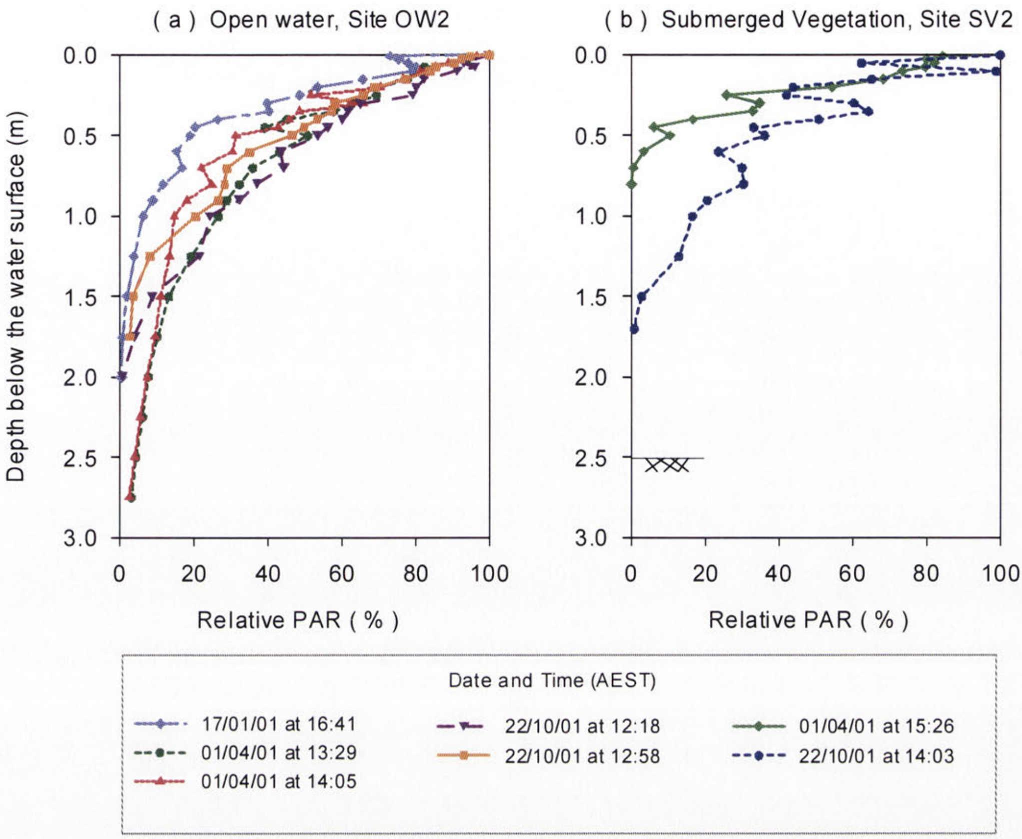

Figure 6.11: Underwater relative PAR profiles at Hopwoods Lagoon for (a) the open water zone and (b) the submerged vegetation zone, where the reference PAR, $\phi_{PAR(0)}$ was measured just below the water surface ($z < 0.005$ m).

profiles were all measured in the vicinity of Site OW2 (shown in Figure 5.5, page 161). This site was selected rather than Site OW1 because it was located further from the macrophyte zones and because the water depth was greater.

The underwater relative PAR profiles displayed temporal trends with respect to season and time of day. At Site OW2, the attenuation of PAR with depth below the surface was generally smaller for the profiles measured closest to solar noon, when the solar elevation was highest and the path length of the direct solar beam shortest. The calculated solar elevation was β=67.2° at 12:18 on 22 October 2001, compared with 42.5° at 14:05 on 1 April and 28.6° at 16:41 on 17 January 2001. The increased path length with lower solar elevation would have increased the probability of absorption or scattering of radiation by material suspended in the water column, and hence increased the attenuation of PAR with depth. The timing of the relative PAR measurements meant that solar elevation was highest in October and lowest in January 2001, for this series of measurements.

Field notes indicated that submerged vegetation was encountered at z >2.0 m on 22 October 2001, which had not been present when the earlier measurements were made. As described in Section 4.4.4 (page 130), the domain of the submerged macrophytes at Hopwoods Lagoon increased during the monitoring period, and had partly encroached on the open water zones by October 2001. This explains the otherwise unexpected decrease in relative radiation at z >2.0 m for the profiles measured on 22 October, compared with those measured in April. Because the January profile was measured relatively late in the day, the ambient PAR was almost zero at $z = 2.0$ m.

The relative PAR profiles measured in the open water zone at Hopwoods Lagoon are considered in relation to Beers Law in Section 6.4.2.

6.4.1.2 Attenuation in the Submerged Macrophyte Zone

Figure 6.11(b) shows relative PAR profiles measured beneath the water surface in the submerged macrophyte zone at Hopwoods Lagoon on 1 April and 22 October 2001. The profiles were measured in the vicinity of site SV2 (shown in Figure 5.5, page 161). This site was selected in preference to the primary thermistor monitoring site, SV1, for ease of access and because the water depth was greater. The profiles show that relative PAR was lower in the submerged macrophyte zone than in the open water zone at all depths, which indicated additional underwater attenuation by the submerged macrophyte components.

As in the open water zone, the underwater attenuation was stronger at Site SV2 for the profile measured later in the day. The solar elevation was 28.8° at 15:26 on 1 April, compared with 51.3° at 14:03 on 22 October. Seasonal variation in the movement of the sun would also have contributed to a higher solar elevation in October than in April. The increased PAR path length during the later afternoon profile would have resulted in greater attenuation with depth, as discussed above.

On 1 April, the submerged macrophytes at Site SV2 partly obstructed the lowering of the PAR sensor when z >0.7 m, and the ambient PAR was zero at z =0.8 m. No such problems were encountered on 22 October and the ambient PAR was still above zero at

z =1.7 m. This inconsistency highlighted the spatial heterogeneity within the submerged macrophyte canopy, which was potentially amplified between profile measurements made several months apart. Were a number of sensors available for use, horizontal averaging of simultaneous PAR measurements from different locations at the same depth would have created a smoother, mean attenuation profile. However, measurements made with the single sensor gave an indication of the likely order of mean underwater PAR attenuation.

6.4.2 Assessment of Beers Law for Underwater Attenuation

As well as adding to the data set available in the literature, the objectives of the underwater attenuation experiments were to examine the applicability of Beers Law to underwater attenuation of radiation and to determine underwater attenuation coefficients for use in the hydrodynamic modelling experiments. As described in Chapter 2, the underwater attenuation of shortwave radiation is commonly modelled using a form of Beers Law, which describes exponential attenuation with depth beneath the water surface. In this application, underwater attenuation of radiation is expressed mathematically by Equation (3.62), which is reproduced below from page 94:

$$\phi_{PAR(z)} = \phi_{PAR(0)} \exp\left[-\eta\, z\right] \tag{6.7}$$

where $\phi_{PAR(0)}$ = PAR flux at the water surface ($\mathrm{Wm^{-2}}$)

$\phi_{PAR(z)}$ = PAR flux at depth z ($\mathrm{Wm^{-2}}$)

η = underwater attenuation coefficient ($\mathrm{m^{-1}}$).

Underwater attenuation coefficients were determined by fitting Equation (6.7) to the relative PAR profiles shown in Figure 6.11. Each curve was forced through $\phi_{PAR(z)} \,/\, \phi_{PAR(0)}$ = 100% at the water surface, and fit to the measured relative PAR profile using least-squares regression over all data points in the profile.

The attenuation coefficients derived from each of the relative PAR profiles are reported in Table 6.6, together with the least-squares regression coefficients for the fit of Equation (6.7) to the field data. Two sets of coefficients were calculated, the first from relative PAR profiles comprised of individual 5 sec $\phi_{PAR(z)}$ measurements divided by the 1 min mean reference PAR, $\overline{\phi_{PAR(0)}}$; and the second from the 1 min mean $\overline{\phi_{PAR(z)}}$ divided by the 1 min mean reference PAR. Comparison between the two coefficients for each profile indicated the

			All $\phi_{PAR(z)}$ / $\overline{\phi_{PAR(0)}}$		$\overline{\phi_{PAR(z)}}$ / $\overline{\phi_{PAR(0)}}$	
Wetland Zone	Profile Date	Start Time	η (m^{-1})	r^2	η (m^{-1})	r^2
Open Water	17 Jan 2001	16:41	3.0	0.94	2.8	0.99
	1 Apr 2001	13:29	1.3	0.95	1.3	0.99
		14:05	1.4	0.92	1.4	0.94
	22 Oct 2001	12:18	1.8	0.87	1.8	0.88
		12:58	2.0	0.95	1.9	0.96
	Mean coefficient, $\overline{\eta}_{OW}$		1.9	N/A	1.8	N/A
Submerged Macrophytes	1 Apr 2001	15:26	3.9	0.94	6.5	0.89
	22 Oct 2001	14:03	2.4	0.86	2.2	0.84
	Mean coefficient, $\overline{\eta}_{SV}$		3.2	N/A	4.4	N/A

Table 6.6: Underwater attenuation coefficients for PAR at Hopwoods Lagoon.

variability in the individual 5 sec measurements. The mean attenuation coefficients for each wetland zone, $\overline{\eta}_{OW}$ and $\overline{\eta}_{SV}$ were calculated as the arithmetic averages of, respectively, η_{OW} and η_{SV} derived from the individual profiles.

All of the values reported in Table 6.6 are well within the published range for inland natural water bodies in Australia (Kirk, 1983). In the open water zone, the values of the attenuation coefficient η_{OW} were similar when calculated using the two sets of field measurements, which indicated relatively little variation between the individual 5 sec PAR measurements at each depth. However, the regression coefficients were consistently higher for the η_{OW} calculated from the 1 min mean $\overline{\phi_{PAR(z)}}$ and the 1 min mean reference PAR. The latter attenuation coefficients were therefore considered to give a better estimate for η_{OW}. The difference between the two η_{SV} calculated for each profile in the submerged macrophyte zone was higher than in the open water zone, although the r^2 were slightly lower for the η_{SV} calculated from $\overline{\phi_{PAR(z)}}$ than the individual $\phi_{PAR(z)}$. This indicated greater variability between 5 sec measurements at each depth in the submerged macrophyte zone, compared with the open water, but was not unexpected. Even very slight movements in the submerged *Hydrilla verticillata* canopy would have caused changes in the underwater radiation field, due to different light diffraction around the canopy elements.

The values of η_{OW} were consistent for the two profiles measured on 1 April and the two measured on 22 October, although there was variation in the values of η_{OW} between the three dates. The η_{OW} values for the October profiles were expected to have been lower than those derived from profiles measured at similar times in April, given the higher solar elevation. However, the presence of submerged vegetation at depth in October increased the attenuation coefficient because the relative PAR was reduced to zero around z=2.0 m. The value of η_{OW} was highest for the late afternoon profile measured on 17 January because the solar elevation was low. However, the mean attenuation coefficient for the open water zone was not substantially different when the 17 January profile was excluded ($\overline{\eta}_{OW}$=1.6 m^{-1} compared with 1.8 m^{-1}). The second average, neglecting the late profile on 17 January, also represented an average η_{OW} over the heating phase of the diurnal cycle. This suggested that it would be reasonable to use a constant $\overline{\eta}_{OW}$ throughout the heating phase in the hydrodynamic modelling, consistent with Kirk (1983) who reported that diurnal variation in the underwater attenuation coefficient was minimal except near sunrise and sunset.

The difference between the η_{SV} for the two profiles measured in the submerged macrophyte zone was considerable. As observed in the open water zone, the attenuation coefficient was higher for the profile measured later in the afternoon when the solar elevation was lower. The variation between the two was probably also partly due to localised differences in the submerged macrophyte density between the two measurement periods. Difficulties were also encountered lowering the PAR sensor through the dense matrix of submerged vegetation, and it is possible that any temporary path cleared by the sensor affected PAR measurements at greater depth. An alternative profiling methodology should be investigated for any further profiling experiments. The η_{SV} calculated from the 14:03 profile on 22 October is considered more representative of conditions during the heating phase, which typically continued until around 15:30 (AEST) during autumn and winter.

6.4.2.1 Summary and Application of Beers Law to Underwater Attenuation

The high regression coefficients reported in Table 6.6 indicate that the simple form of Beers Law expressed by Equation (6.7) can be used successfully to predict attenuation of PAR beneath the water surface in open water zones of a wetland. The fit of Beers Law to relative PAR profiles measured in submerged macrophyte at Hopwoods Lagoon was also reasonable, although more variable between individual profiles. This form of Beers Law is unfortunately unable to account for differences in vegetation density, although an approach based on a submerged leaf area index could be attempted, similar to that used with the simple canopy attenuation models. This is not known to have been attempted previously, and was not considered in the present investigation due to difficulties in quantifying the in-situ density and foliage area of the dense submerged vegetation. Rather, the simple form of Equation (6.7) was used to provide an estimate of a bulk η_{SV}. Further investigation is certainly warranted into underwater PAR attenuation as a function of the submerged foliage area.

From the averages reported in Table 6.6, underwater attenuation coefficients of $\overline{\eta}_{OW} = 1.8\ \mathrm{m}^{-1}$ and $\overline{\eta}_{SV} = 4.4\ \mathrm{m}^{-1}$ were selected as initial estimates during calibration of the hydrodynamic model. Given the difficulties experienced when measuring sub-surface PAR profiles in the submerged macrophyte zone, profiles were not attempted in the emergent macrophyte zone, and the value of $\overline{\eta}_{EV} \equiv \overline{\eta}_{SV} = 4.4\,\mathrm{m}^{-1}$ was used as an initial estimate when calibrating the hydrodynamic model, in both submerged and emergent macrophyte zones. However, the contribution of the relatively sparse *Eleocharis sphacelata* stems to the overall density of submerged vegetation was observed to be minimal. It was therefore assumed in the hydrodynamic modelling experiments that the underwater attenuation of shortwave radiation would be similar in the two zones.

6.5 Observed Hydrodynamics at Hopwoods Lagoon

Hydrodynamic processes are driven by the meteorological forcing to which the water body is subjected. Because Hopwoods Lagoon is usually isolated from the adjacent Macdonald River, there are no net flows through the lagoon, and water movements are generally:

- **convective** (buoyancy-driven) or
- **advective** (wind-driven).

Convective flows are the focus of the present study, and are driven by horizontal temperature and density gradients which result from differential heating or differential exposure to the surface heat fluxes.

In contrast to large lakes and reservoirs, wetlands and smaller water bodies have lower thermal inertia (Andradóttir and Nepf, 2000a) and generally respond more rapidly to changes in meteorological forcing. This means that both diurnal and seasonal timescales are important when considering wetland hydrodynamics. Heating and cooling rates within and between different wetland zones vary with time of day and season. Vertical temperature gradients within the wetland zones and horizontal temperature differences between the zones are therefore temporally and spatially variable.

The following sections provide an overview of meteorological conditions and water temperatures at Hopwoods Lagoon. The annual heat budget is considered, and diurnal, seasonal and zonal trends in the hydrodynamic response are described. Water temperatures were used to infer convective circulation patterns, since no current velocity measurements were made at Hopwoods Lagoon. These were supplemented by horizontal temperature transect data for part of the monitoring period. Temperature data do not provide direct evidence of convective currents, although the two are coupled (Ostrovsky et al., 1996), and a similar approach has been adopted by James and Barko (1991), Waters (1998) and Oldham and Sturman (2001).

6.5.1 Overview of Meteorological Conditions

This section provides an overview of diurnal and seasonal variation in the meteorological conditions at Hopwoods Lagoon between 4 February 2000 and 12 November 2001. A graphical summary of all meteorological data from this period is provided in Appendix D.

6.5.1.1 Wind Direction

Wind direction data were required to calculate vector mean wind speeds and as input data for the hydrodynamic modelling, specifically to calculate wind-induced stresses at the water surface. Wind roses showing the frequency of occurrence of winds blowing from the eight major compass points are included in Figure D.1 in Appendix D.

In October 2000, an intermittent error was discovered with the operation of the wind direction sensor. This occurred when winds swung around from the west across the sensor's deadzone at due north. The logger returned an error whenever this intermittent error occurred on any of the 20 sec measurements. An error was also returned for any 10 min mean wind direction if the error occurred on any of the intervening 20 sec measurements.

The period from April through to late October 2000 was most significantly affected by this error, and reliable wind direction results could not be presented for these months. Detailed examination of the data logger and weather monitoring instruments at the completion of the monitoring period suggested that the problem was due to a lightning strike, although there were no evident problems with the other sensors.

Prevailing winds were generally from the north and the west, largely due to funnelling by the local topography. During the warmer months from November 2000 to March 2001, winds were predominantly from the north, while westerly winds prevailed during the cooler months of the year.

6.5.1.2 Wind Speed

Wind speed data were required to calculate latent and sensible heat fluxes, and to estimate vertical and horizontal mixing coefficients in the hydrodynamic model. Time-series plots of mean wind speed are included in Figure D.2 in Appendix D, showing the 10 min vector mean and standard deviation wind speeds.

Evenings were generally relatively calm at Hopwoods Lagoon while the stronger winds usually occurred around mid-afternoon on any given day. The highest 20 sec (gust) wind speeds were recorded in November 2000 ($22.2\,\mathrm{m\,s^{-1}}$) and August 2001 ($19.4\,\mathrm{m\,s^{-1}}$), which were also the windiest months during the monitoring period. The highest 10 min mean wind speed was recorded in August 2001 ($9.8\,\mathrm{m\,s^{-1}}$). The period from May to July 2001 had consistently lower 10 min mean wind speeds than other months ($< 5\,\mathrm{m\,s^{-1}}$).

The intermittent error with the wind direction sensor during a large part of 2000 caused errors in the vector mean wind speed calculations. Mean wind speeds were incorrectly recorded as zero by the data logger for any 10 min period where the wind direction error occurred. Potentially, the entire period between 4 February and 29 October was affected. However, using the standard deviation of the 20 sec wind speed data, it was possible to determine when zero mean wind speeds had been logged incorrectly. It was assumed that the standard deviation of the wind speed should have been zero only when the mean wind speed was truly zero. All zero mean wind speeds where the standard deviation was not also zero were therefore considered erroneous and removed from the data set.

The resulting data gaps are clearly evident in the time series wind speed plots (Figure D.2 in Appendix D). Unfortunately, these periods represented a significant portion of the total record between April and October 2000, including most of the daytime measurements. The problem was rectified on 29 October 2000, after which the 20 sec wind speeds were also recorded by the data logger.

While the 10 min mean wind speeds during the periods of error could not be predicted, the standard deviation of the 20 sec wind speeds indicated the expected relative magnitudes of the mean wind speeds during the periods of error. Figure 6.12 shows that the standard deviation was approximately proportional to, but generally smaller than, the corresponding mean wind speed.

Figure 6.13 shows the maximum 10 min mean wind speed and peak 20 sec (gust) wind speed for each month during the monitoring period. Note that the period from April through to late October 2000 was most significantly affected by the intermittent problem with the wind direction sensor, and the 10 min mean wind speeds reported for these months are almost certainly underestimated. This period is represented by the dashed line in Figure 6.12. For the remaining months, the peak 20 sec wind speed was generally close to double the 10 min mean wind speed.

6.5.1.3 Air Temperature

Air temperature data were required to calculate the atmospheric longwave radiation flux and latent and sensible heat fluxes. A function of the temperature difference between the air and the water surface was also used as an indicator of atmospheric stability. Time-series mean air temperature plots are included in Figure D.3 in Appendix D.

On a typical day, the air temperature increased from a minimum near sunrise to a maximum in the early afternoon, then decreased until sunrise the following day. The diurnal air temperature range was as great as 25°C during summer and around 20°C during winter.

Figure 6.14 shows the minimum and maximum 10 min mean air temperatures during the monitoring period, together with the mean monthly temperatures. The maximum 10 min mean air temperature recorded by the weather station was 43.5°C on 23 January 2001, while the minimum was -1.6°C on 26 June 2001.

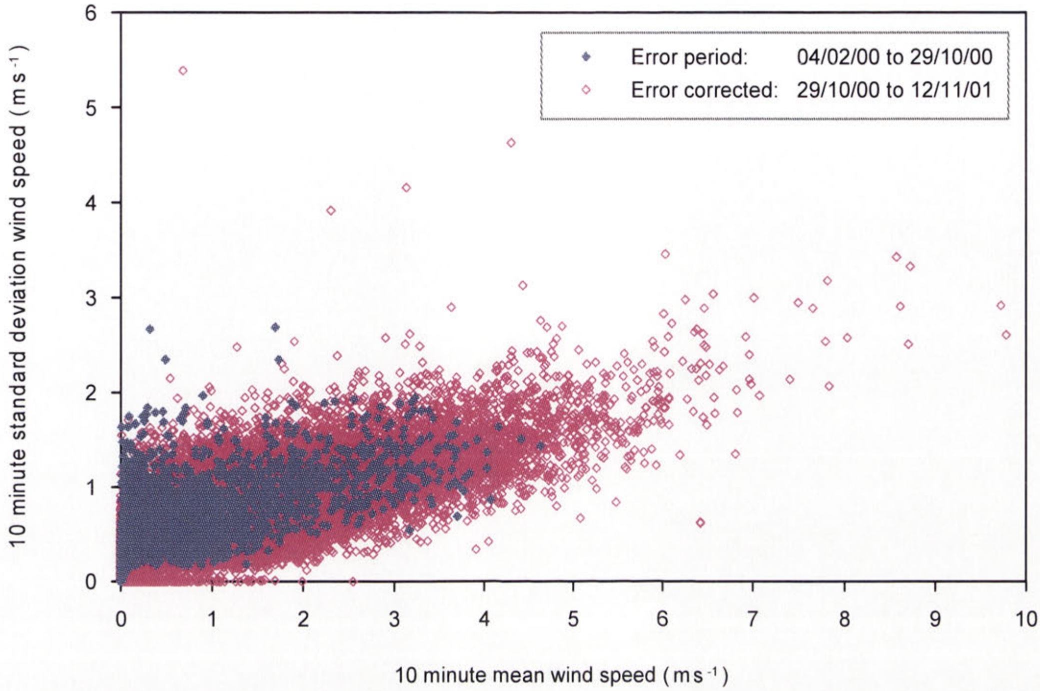

Figure 6.12: Correlation between 10 minute mean wind speed and 10 minute standard deviation of 20 sec wind speeds throughout the monitoring period.

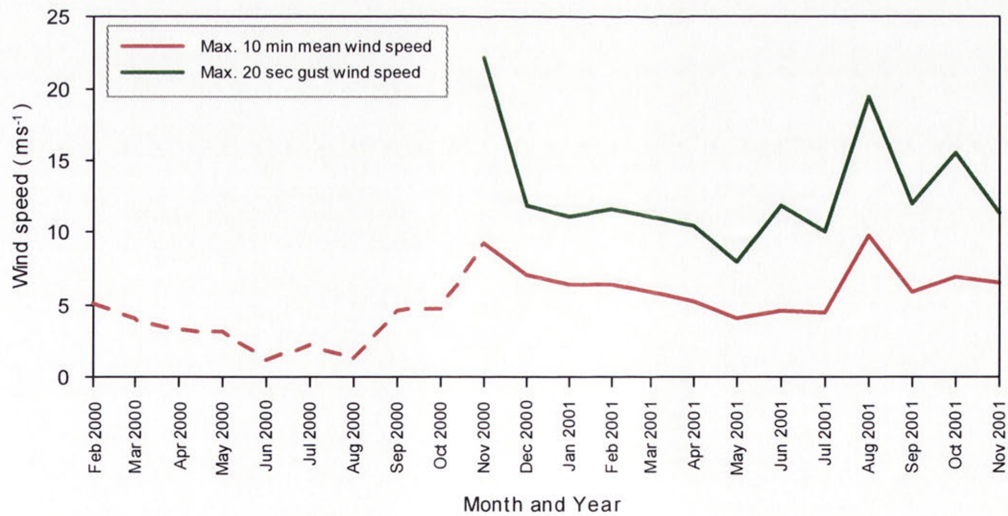

Figure 6.13: Maximum 10 minute vector mean and 20 sec (gust) wind speeds at Hopwoods Lagoon. The line is dashed for the period during which the wind direction sensor was intermittently in error.

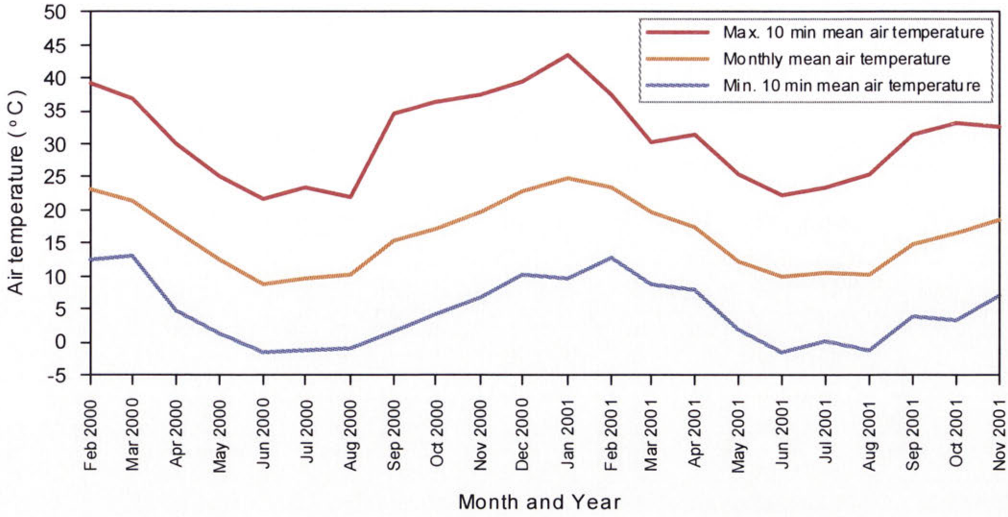

Figure 6.14: Maximum and minimum 10 minute mean air temperatures, and monthly mean air temperatures at Hopwoods Lagoon.

6.5.1.4 Relative Humidity

Relative humidity data were required to calculate latent and sensible heat fluxes, and time-series relative humidity plots are included in Figure D.4 in Appendix D.

On a typical day, the relative humidity decreased rapidly from a maximum near sunrise to a minimum in the early afternoon. The relative humidity then typically increased rapidly until sunset, and more gradually throughout the night. There were no significant seasonal trends in the relative humidity data, although the monthly minimum and mean values were higher during the cooler months of the year.

6.5.1.5 Barometric Pressure

Barometric pressure data were required to calculate latent and sensible heat fluxes, and time-series barometric pressure plots are included in Figure D.5 in Appendix D. Although there are no distinct seasonal trends in the barometric pressure data, the cyclic movement of pressure systems across the region is clear from the time-series data.

6.5.1.6 Shortwave Radiation

Shortwave radiation data were required as input for the hydrodynamic model, and time-series mean shortwave radiation plots are included in Figure D.6 in Appendix D.

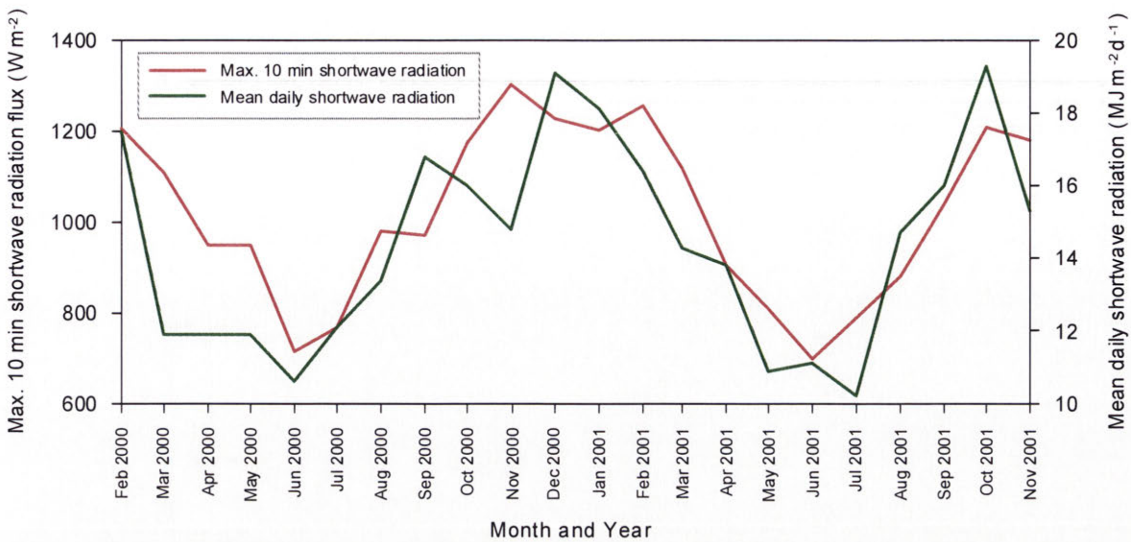

Figure 6.15: Maximum 10 minute mean shortwave radiation flux (left axis) and mean daily shortwave radiation flux (right axis) at Hopwoods Lagoon.

Figure 6.15 shows the maximum 10 min mean shortwave radiation fluxes at Hopwoods Lagoon for each month from February 2000 to November 2001. The 10 min mean shortwave radiation peaked at 1302 $\mathrm{Wm^{-2}}$ on 8 November 2000, while the maximum 10 min mean shortwave radiation flux during the winter months was only about half this value.

Figure 6.15 also shows the mean daily shortwave radiation flux for each month. The mean daily shortwave radiation flux was calculated from the total shortwave radiation energy received during the month, and was therefore strongly influenced by the degree of cloud cover. The mean daily shortwave radiation flux ranged from 10.2 $\mathrm{MJ\,m^{-2}d^{-1}}$ in July 2001 to 19.3 $\mathrm{MJ\,m^{-2}d^{-1}}$ in October 2001.

6.5.1.7 Rainfall

Rainfall had the most dramatic influence on water level variation at Hopwoods Lagoon over the monitoring period. Rainfall data were used with water level records and evaporation pan data to check the magnitude of the latent heat fluxes calculated from other meteorological variables. Time-series plots of the 10 min and 24 hr rainfall results are included in Figure D.7 in Appendix D.

Figure 6.16 shows the maximum 10 min rainfall, the maximum 24 hr rainfall (from midnight to midnight) and the total monthly rainfall recorded during each month of the

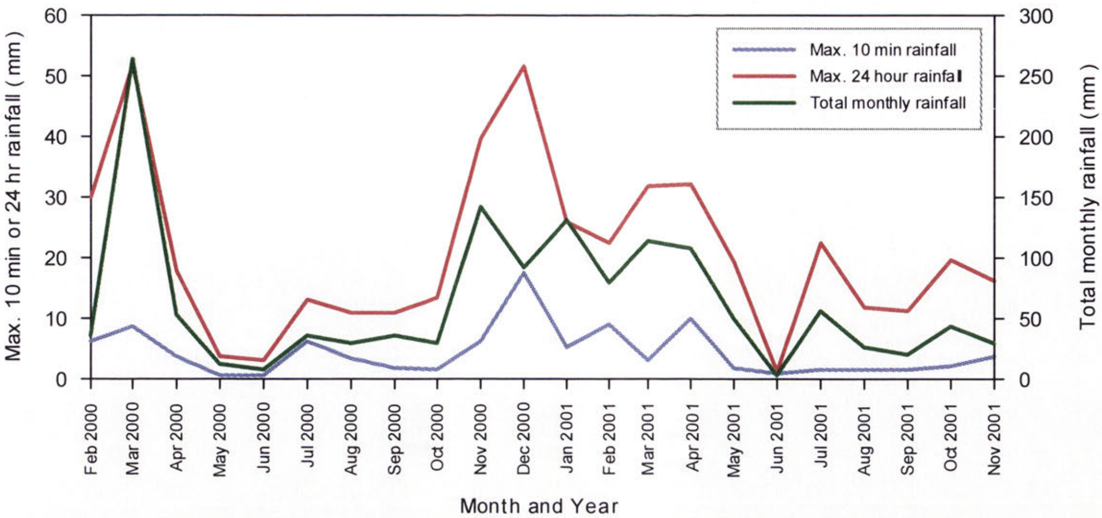

Figure 6.16: Maximum 10 minute and 24 hour rainfall (left axis) and total monthly rainfall (right axis) at Hopwoods Lagoon.

monitoring period. The rainfall total for February 2000 was for 4 to 29 February only, and the total for November 2001 was for 1 to 12 November only. The cumulative rainfall recorded by the pluviometer in 2000 was 737.4 mm, while 665.3 mm was recorded in 2001, although neither of these "annual" totals were for a complete calendar year.

March 2000 was the wettest month during the monitoring period, and the water depth in the lagoon increased by nearly 0.5 m during this period. November 2000 and January to April 2001 also received more rainfall than the remainder of the monitoring period. The highest 24 hr rainfall was 51.8 mm on 8 March 2000, and the peak 10 min rainfall was 17.6 mm between 14:10 and 14:20 (AEST) on 13 December 2000. June was the driest month, with less than 10 mm of rainfall recorded in both 2000 and 2001.

The storage rain gauge was used to verify the performance of the tipping bucket pluviometer and to predict cumulative rainfall totals when the weather station was not logging successfully. As discussed in Section D.4 in Appendix D, correlation between the cumulative rainfall measured by the tipping bucket and the storage gauge yielded a linear relationship over the period from 26 June 2000 to 12 November 2001:

$$\text{rainfall(AWS)} = 0.999 \times \text{rainfall(storage)} \qquad r^2 = 0.999 \tag{6.8}$$

The temporal distribution of rainfall was estimated when the weather station was not logging by comparison with daily rainfall totals recorded by Karen Sternbeck of Higher

Macdonald (made available by Natalie Marshall of the School of Geography at UNSW). The Sternbeck rain gauge was located approximately 500 m north-west of the weather station, on the northern side of the Macdonald River. Cumulative rainfall recorded by the weather station was 88% of that recorded at the Sternbeck's rain gauge, which indicated a highly localised rainfall distribution in the narrow Macdonald Valley. However, the cumulative rainfall curves corresponded closely in time (r^2=0.999), as discussed in Section D.4 in Appendix D.

6.5.1.8 Evaporation

The pan evaporation rate was calculated from measured net pan evaporation and rainfall data, as described in Section D.5 in Appendix D. The net evaporation record was discontinuous because the evaporation pan was operated manually and the monitoring period was irregular. However, estimated pan evaporation rates provided a useful indication of the variation in evaporation at Hopwoods Lagoon between October 2000 and October 2001.

Figure 6.17 shows the estimated pan evaporation data for Hopwoods Lagoon, together with cumulative rainfall and variation in water surface elevation. On each date, the data points for cumulative pan evaporation, cumulative rainfall and water level change are coincident in time, and apply across an equal period. Note that the intervals between successive data points were dependent on the frequency of site visits and are therefore not constant.

The mean evaporation rate at Hopwoods Lagoon was estimated from Equation (6.9), using a mean Class A Pan coefficient of $C_P = 0.7$ for south-eastern Australia (Grayson et al., 1996):

$$E_{lake} = C_P \, E_{pan} \tag{6.9}$$

Seasonal trends in the evaporation rate are evident in Figure 6.17. The mean daily pan evaporation rate was lowest between May and June and highest during the summer months. The response of the water surface elevation at Hopwoods Lagoon to rainfall and evaporation is also clearly evident from Figure 6.17. The water level increased when rainfall was sufficient to satisfy initial catchment losses, and decreased due to evaporation during dry periods.

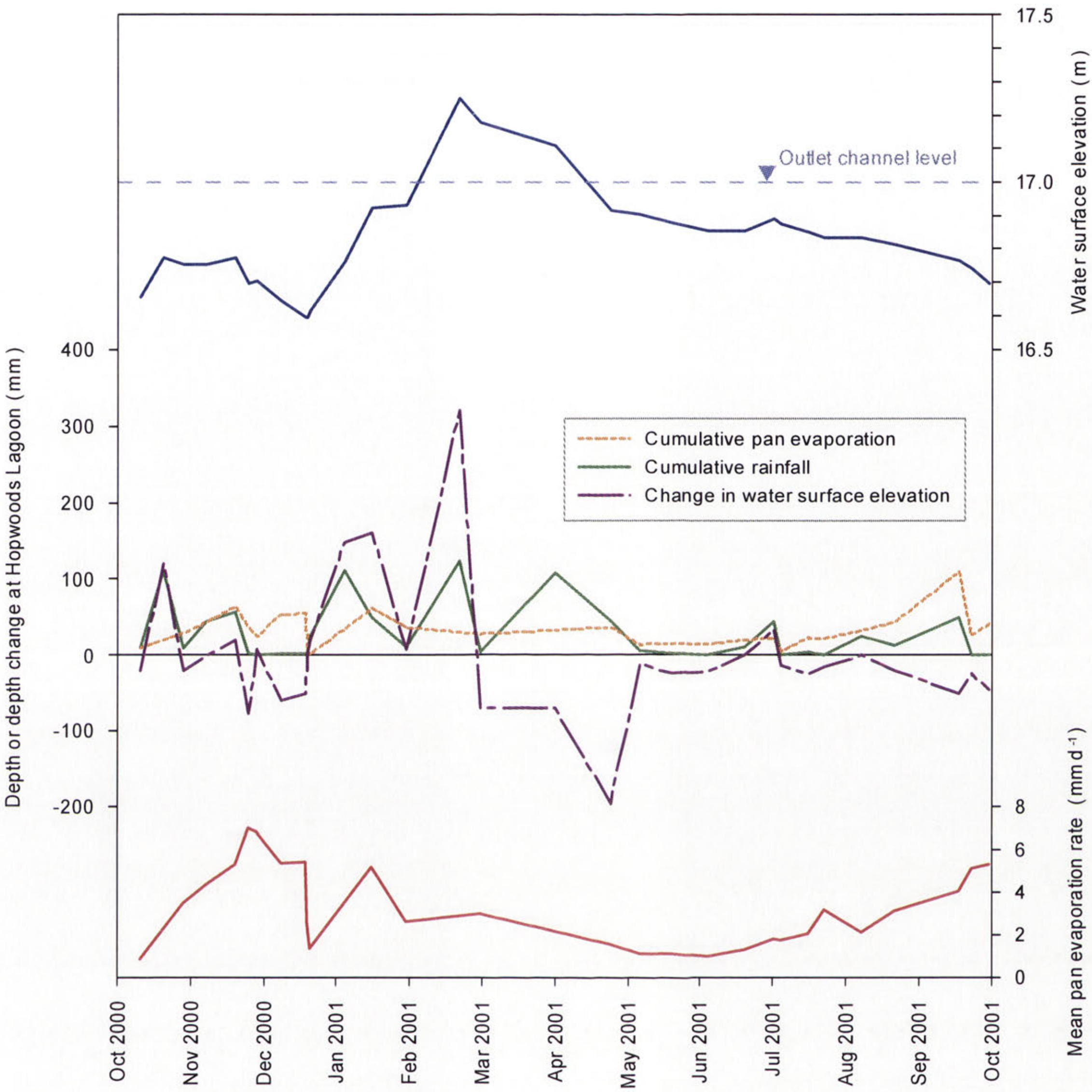

Figure 6.17: Mean pan evaporation, cumulative rainfall and water level variation at Hopwoods Lagoon.

The dramatic and apparently anomalous decrease in the water surface elevation between February and April 2001 occurred due to outflow from the lagoon to the Macdonald River, while the surface elevation exceeded that of a submerged berm within the outlet channel. Outflow ceased when the surface level receded below the channel berm. Water level variation over the entire monitoring period from February 2000 to November 2001 was presented in Section 4.4.7 (page 136).

6.5.2 Overview of Water Temperatures at Hopwoods Lagoon

This section provides an overview of the water temperature data collected at Hopwoods Lagoon between 7 May 2000 and 2 December 2001. A graphical summary of all water temperature data from this period is provided in Appendix F.

Seasonal trends at Sites OW1, EV1 and SV1 are apparent from the monthly mean temperatures shown in Figure 6.18, while the effects of depth and wetland macrophytes can be seen in Figure 6.19. The monthly mean temperatures are plotted for the period from July 2000 to November 2001 only, because some of the primary monitoring thermistors were moved in July 2000 (Table F.2 in Appendix F). The minimum and maximum temperatures measured by each thermistor are given in Table 6.7.

Monthly mean temperatures varied by 5 to 6°C between summer and winter, while the seasonal difference between absolute minimum and maximum measured temperatures was almost 30°C near the water surface. As expected, the mean monthly temperatures at Sites OW1, EV1 and SV1 generally decreased with increased depth below the water surface. The rate of change of temperature with depth was generally greater at Site EV1 than at Site OW1, despite greater depth in the open water. This indicated the importance of both macrophytes and depth in determining vertical and horizontal temperature gradients in a wetland.

Minimum temperatures recorded by the thermistors were similar over the depth at each site, which suggested that minimum temperatures occurred when the water column was mixed over the full depth and approximately isothermal. Maximum temperatures at each site generally decreased with increased depth below the water surface, consistent with the rapid underwater attenuation of shortwave radiation.

While the maximum water temperatures might appear unreasonably high, the summer months were very hot at Hopwoods Lagoon (air temperatures > 40°C) with strong insolation ($> 1200\mathrm{Wm}^{-2}$). The volume of the lagoon is relatively small (~ 104 ML below the mean water surface elevation of 16.78 m AHD), allowing substantial heating. Post-deployment verification experiments confirmed that thermistors T2 to T16 (locations shown in Figure 5.4, page 160) were within ± 0.1°C of the reference platinum resistance

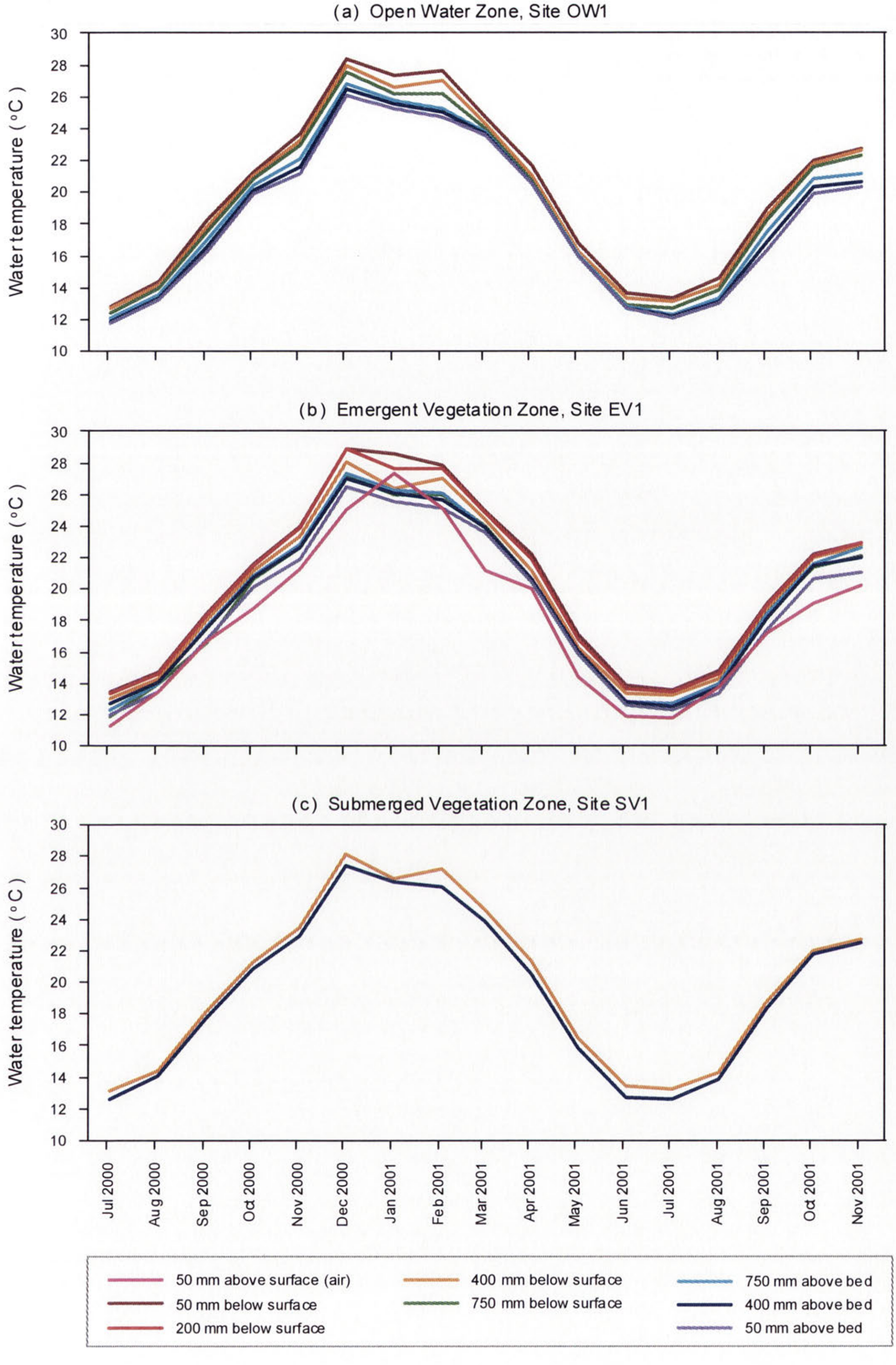

Figure 6.18: Monthly mean water temperatures at Hopwoods Lagoon between July 2000 and November 2001, for (a) Site OW1, (b) Site EV1 and (c) Site SV2.

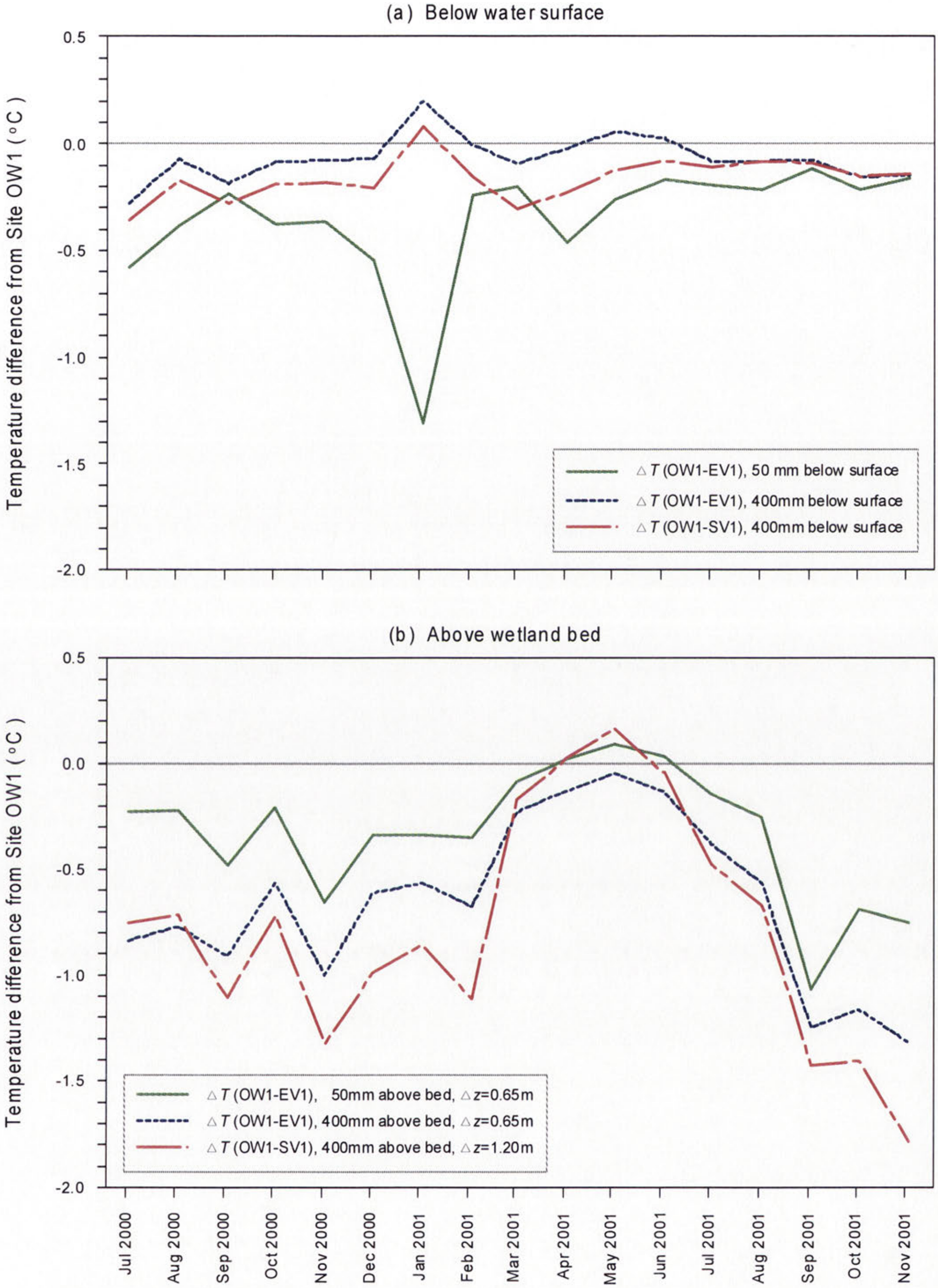

Figure 6.19: Monthly mean water temperature differentials at Hopwoods Lagoon between July 2000 and November 2001, for (a) depths of 50 mm and 400 mm below the surface and (b) heights of 50 mm and 400 mm above the wetland bed.

thermometer over the range from 11.68 to 35.47°C (Table E.9 in Appendix E). The maximum water temperatures reported in Table 6.7 are therefore considered reliable for at least $T_w \leq 35.5°C$. The maximum air temperature measured by thermistor T10 50 mm above the water surface was approximately 2 to 8°C warmer than the maximum air temperature measured by the AWS during January 2001. The thermistor was calibrated in water rather than air, which could explain some discrepancy. However, thermistor T10 was more sheltered from cooling breezes than the AWS temperature sensor, so the canopy air space was expected to be warmer than the air surrounding the AWS.

The monthly mean temperature 50 mm below the surface was always warmer at Site EV1 than at Site OW1, and the monthly temperature difference between the two sites was highest in January 2001. Monthly mean temperature differences 400 mm below the surface were smaller during summer than at 50 mm depth, but similar at both depths during winter. Site OW1 was warmer than the vegetated sites during the summer months. At similar heights above the bed, the monthly mean temperatures were generally warmest at Site SV1 and coolest at Site OW1, although mean temperatures were similar at the three sites during winter 2001.

The diurnal cycle was masked by the monthly averaging used to prepare Figures 6.18 and 6.19. Throughout the day, temperatures typically increased rapidly during a morning heating phase, from a daily minimum around sunrise to a maximum in the mid afternoon. Temperatures then typically declined throughout the afternoon and evening cooling phase. The daily water temperature cycles reflected the diurnal variation in meteorological conditions, particularly shortwave radiation and wind speed. The hydrodynamic response to diurnal changes in the meteorological forcing is discussed in more detail in Section 6.5.4.

			Minimum Temperature		Maximum Temperature	
Site	Thermistor	Depth or Height	(°C)	Month	(°C)	Month
OW1	T8	50 mm below surface	11.0	Jun 2001	35.2	Jan 2001
	T7	400 mm below surface	11.0	Jun 2001	32.8	Feb 2001
	T5	750 mm below surface	11.0	Jun 2001	31.1	Nov 2000
	T6	750 mm above bed	11.1	Jun 2001	29.1	Dec 2000
	T3	400 mm above bed	11.0	Jun 2001	28.5	Dec 2000
	T4	50 mm above bed	11.0	Jun 2001	28.1	Dec 2000
EV1	T10	50 mm above surface	-0.1	Jun 2001	47.9	Jan 2001
	T9	50 mm below surface	10.6	Jun 2001	39.5	Jan 2001
	T13	200 mm below surface	10.8	Jun 2001	35.7	Dec 2000
	T14	400 mm below surface	10.9	Jun 2001	32.9	Dec 2000
	T12	750 mm below surface	10.8	Jun 2001	30.2	Dec 2000
	T11	750 mm above bed	10.9	Jun 2001	30.5	Dec 2000
	T1 #	400 mm above bed	11.1	Jun 2001	29.7	Dec 2000
	T2	50 mm above bed	10.8	Jun 2001	28.5	Dec 2000
SV1	T16	400 mm below surface	10.8	Jun 2001	33.5	Dec 2000
	T15	400 mm above bed	10.7	Jun 2001	31.6	Dec 2000

Note to Table: Verification experiments conducted in December 2001 indicated that T1 was operating outside the calibration range of ± 0.1°C (see Appendix E).

Table 6.7: Minimum and maximum water temperatures at Sites OW1, EV1 and SV1 between July 2000 and November 2001.

6.5.3 Net Surface Heat Flux, H_{NET}

The hydrodynamic processes in a wetland are ultimately driven by the meteorological forcing, which can be parameterised by the net surface heat flux, H_{NET}. Figure 6.20 shows the components of the net surface heat flux at Hopwoods Lagoon between 29 October 2000 and 12 November 2001. The flux terms were calculated using formulae presented in Chapter 3 and H_{NET} was calculated using Equation (3.15), which is reproduced below:

$$H_{NET} = (1 - R_S)\,\phi + (1 - R_L)\,\phi_{LW\downarrow} - \phi_{LW\uparrow} + H_L + H_S$$

To ensure consistency, the daily mean net surface heat flux shown in Figure 6.20 was calculated only for those days on which meteorological and water temperature data were available for the full 24 hr.

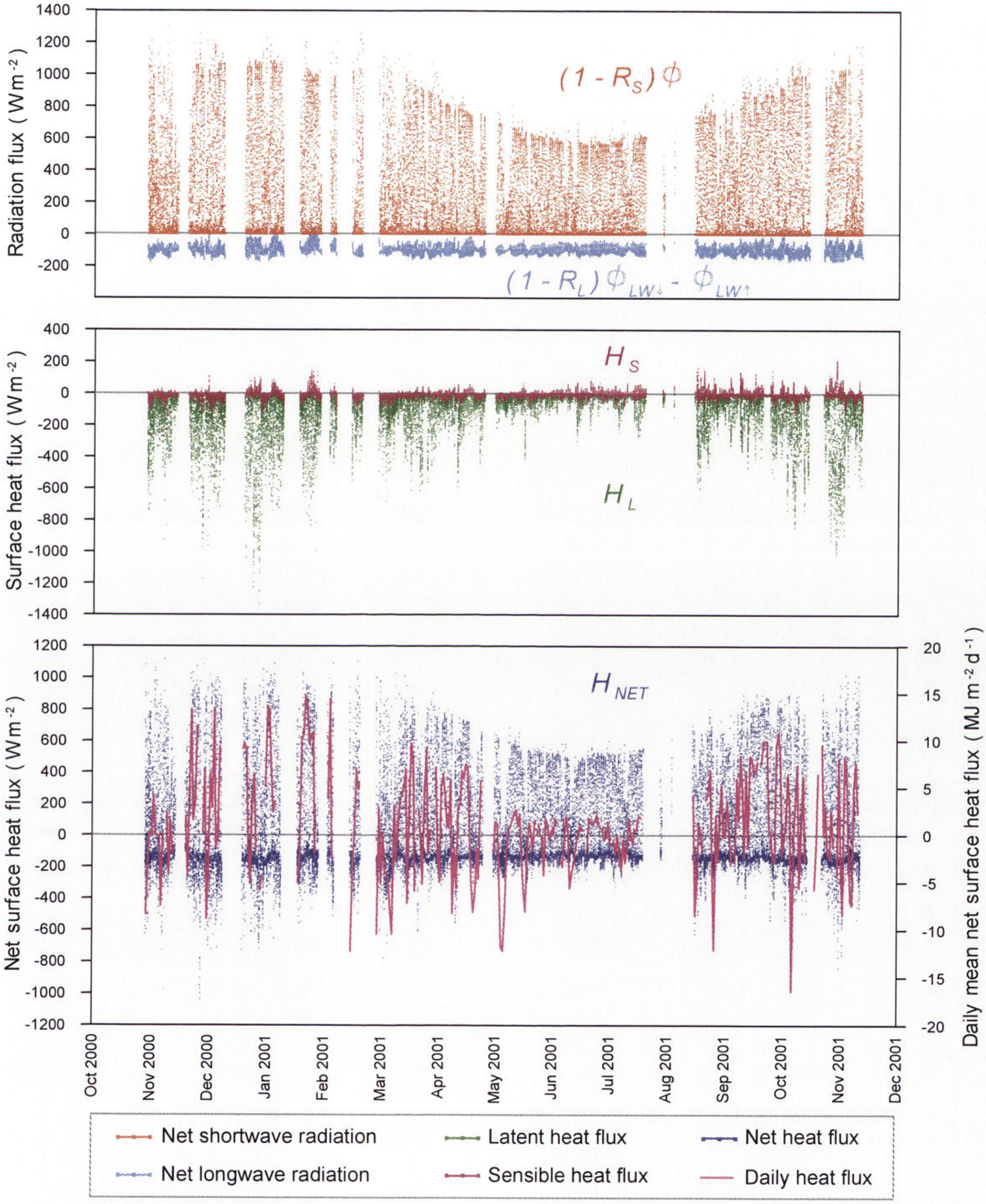

Figure 6.20: Calculated surface heat fluxes at Hopwoods Lagoon, where positive fluxes are directed into the water column.

6.5.3.1 Sensitivity of H_{NET} to Changes in Water Surface Temperature

The upward longwave ($\phi_{LW\uparrow}$), latent (H_L) and sensible heat (H_S) fluxes displayed in Figure 6.20 were calculated using the water temperature measured 50 mm below the surface at Site OW1. However, at any time the net surface heat flux varied throughout the lagoon due to differences in the water surface temperature. In the open water zones of the wetland, average surface temperature differentials with Site OW1 were:

- -0.08 ± 0.35°C at Site OW2 between 2 and 14 February 2001 ($n = 283$)
- $+0.04 \pm 0.43$°C at Site OW3 between 17 and 22 October 2001 ($n = 121$)
- -0.08 ± 0.25°C at Site OW4 between 30 October and 12 November 2001 ($n = 307$)

where n is the number of data pairs at the two sites. Figure 6.19(a) showed that monthly mean water surface temperatures at Site OW1 were generally 0.2 to 0.5°C cooler than at Site EV1, but as much as 1.3°C cooler in January 2001. Figure 6.20 therefore illustrates the relative magnitude and seasonal variation in the components of H_{NET} at a single location, Site OW1.

The sensitivity of H_{NET} and the upward longwave ($\phi_{LW\uparrow}$), latent (H_L) and sensible (H_S) heat fluxes to changes in the water surface temperature ($T_w \pm 1$°C) is summarised in Table 6.8. The calculations were made using meteorological data from 11:00 (AEST) on 29 October 2000, when the 10 min vector mean wind speed was 1.08 m s^{-1}, air temperature was 19.1°C, relative humidity was 37.5%, shortwave radiation was 590.5 Wm^{-2} and barometric pressure was 1015 hPa.

The upward longwave radiation flux ($\phi_{LW\uparrow}$) increases in magnitude with increasing T_w, and changes by < 2% for $T_w \pm 1.0$°C over the range from 10 to 30°C. The latent heat flux (H_L) also increases in magnitude with increasing T_w. Corresponding changes in H_L were as high as 20–25% at $T_w = 10.0 \pm 1.0$°C, but < 10% at $T_w = 30.0 \pm 1.0$°C. The sensible heat flux (H_S) changes sign between 10°C and 30°C (with the given meteorological conditions), and is highly sensitive to small changes in T_w around this point. However, the change in H_S is around ±10% at $T_w = 10.0 \pm 1.0$°C and $T_w = 30.0 \pm 1.0$°C. The net heat flux (H_{NET}) decreases with increasing T_w between 10 and 30°C, while the sensitivity of H_{NET} to variation in T_w increases to almost 20% at $T_w = 30.0 \pm 1.0$°C. It is clear from Table 6.8

	Upward Longwave Flux ($\phi_{LW\uparrow}$)			Latent Heat Flux (H_L)			Sensible Heat Flux (H_S)			Net Surface Heat Flux (H_{NET})		
T_w (°C)	at T_w (Wm^{-2})	T_w-1 (%)	T_w+1 (%)	at T_w (Wm^{-2})	T_w-1 (%)	T_w+1 (%)	at T_w (Wm^{-2})	T_w-1 (%)	T_w+1 (%)	at T_w (Wm^{-2})	T_w-1 (%)	T_w+1 (%)
10	-353	-1.4	1.4	-29	-20.7	24.1	45	11.1	-11.1	575	2.8	-2.8
20	-405	-1.2	1.5	-110	-9.1	10.0	-4	-100.0	125.0	392	5.4	-5.4
30	-464	-1.5	1.1	-246	-6.5	7.3	-54	-9.3	7.4	149	18.1	-19.5

Table 6.8: Sensitivity of surface heat flux components (percentage change) to variation in water surface temperature, $T_w \pm 1$°C.

that the net surface heat flux is more sensitive to the latent heat flux than to the other fluxes affected by T_w.

6.5.3.2 Annual Heat Budget

The relative magnitudes of the positive and negative surface heat fluxes shown in Figure 6.20 suggest that there should have been an overall heat gain by the wetland during this period, and the sum of the daily mean net surface fluxes over the period was 283 MJ m^{-2}. However, the water surface elevation and water temperatures were similar in October 2000 and November 2001, so the heat content of the lagoon should also have been similar. The net heat gain suggested in Figure 6.20 must therefore have been reduced through processes other than the surface heat fluxes listed above.

Other wetland energy fluxes identified in Chapter 3 which could have removed heat from the water column during the monitoring period include:

- stream inflow and outflow
- precipitation
- groundwater flux
- heat flux to the sediments.

Since there are no permanent flows into or out of Hopwoods Lagoon, they would have been unlikely to have caused any sustained cooling over the monitoring period, although dramatic cooling was observed during heavy rainfall. However, the time-series meteorological data (Appendix D) suggest that this was primarily because the net shortwave flux was low, and not directly due to the precipitation. Groundwater interaction was assessed to be negligible at Hopwoods Lagoon, and was therefore considered unlikely to have contributed to sustained cooling. Instead, heat exchange with the sediments was considered the most probable significant cooling mechanism at Hopwoods Lagoon. This was consistent with the findings of Benoit and Hemond (1996) and Fang and Stefan (1996) in shallow water bodies. The parameterisation of the bed heat flux is discussed with reference to the hydrodynamic modelling in Appendix H.

6.5.4 Seasonal and Diurnal Variation in Hydrodynamic Behaviour

The diurnal hydrodynamic cycle can be considered in terms of a heating phase and a cooling phase, where:

- the daily **heating phase** is defined as the period when the net surface heat flux is positive ($H_{NET} > 0$) and there is a net gain of heat by the water body
- the **cooling phase** occurs while the net surface heat flux is negative ($H_{NET} < 0$) and there is a net loss of heat from the water body.

The following sections provide an overview of diurnal hydrodynamic trends in the open water and macrophyte zones at Hopwoods Lagoon, and seasonal variation in these. Horizontal temperature differences observed at various depths between the primary monitoring sites (OW1 and EV1, shown in Figure 5.5 on page 161) indicate diurnal variation in buoyancy forcing between the two sites which is capable of inducing convective flows between the open water and macrophyte zones at Hopwoods Lagoon. Even in the absence of direct velocity measurements at Hopwoods Lagoon, time series vertical water temperature data and horizontal transect data are presented which support the existence of the inferred convective currents. The speed of the inferred convective flows is consistent with the estimates derived from scaling analyses in Chapter 3.

6.5.4.1 Diurnal and Zonal Hydrodynamic Trends during Summer

Typical trends in the meteorological forcing and the hydrodynamic response at Hopwoods Lagoon during the summer months (December to February) were evident between 1 and 3 January 2001. Surface fluxes during this period are shown in Figure 6.21 and water temperatures in the open water (Site OW1) and emergent macrophyte zone (Site EV1) are shown in Figure 6.22.

Meteorological Forcing and Water Temperatures during Summer

During the heating phase (approximately 07:00 to 16:00 on these days), H_{NET} was dominated by the net shortwave radiation influx and peaked at $1040\,\mathrm{Wm}^{-2}$. The latent heat efflux increased during the afternoon as wind speeds increased and was the most significant component of H_{NET} at the transition from heating to cooling phases. The sensible heat flux was the smallest component of H_{NET} throughout the period and often close to zero. The net longwave radiation flux was relatively insignificant during the heating phase but the most important component of H_{NET} overnight.

Water temperatures were warmer near the surface at Site EV1 than at Site OW1 during the day but were similar overnight, as shown in Figure 6.22. Bed temperatures were slightly cooler at Site EV1 than at the same elevation at Site OW1. The water column stratified during the day at both sites. Diurnal variation in the water surface temperatures was greater at Site EV1 than at Site OW1. Nearer the bed, the diurnal temperature variation was much smaller in magnitude and similar at both sites. These observations are consistent with those of Dale and Gillespie (1976, 1977) for temperature differences between open water and zones containing floating or submerged macrophytes. With only a sparse emergent canopy at Hopwoods Lagoon and a higher underwater attenuation coefficient than in the open water, heating due to shortwave radiation was concentrated nearer the surface in the macrophyte zones.

At Site OW1, the water cooled rapidly and mixed strongly over the upper 1 to 2 m between 16:00 and 19:00 on both 2 and 3 January. This was caused by an increase in wind speed which dramatically increased the latent heat efflux and overall surface cooling.

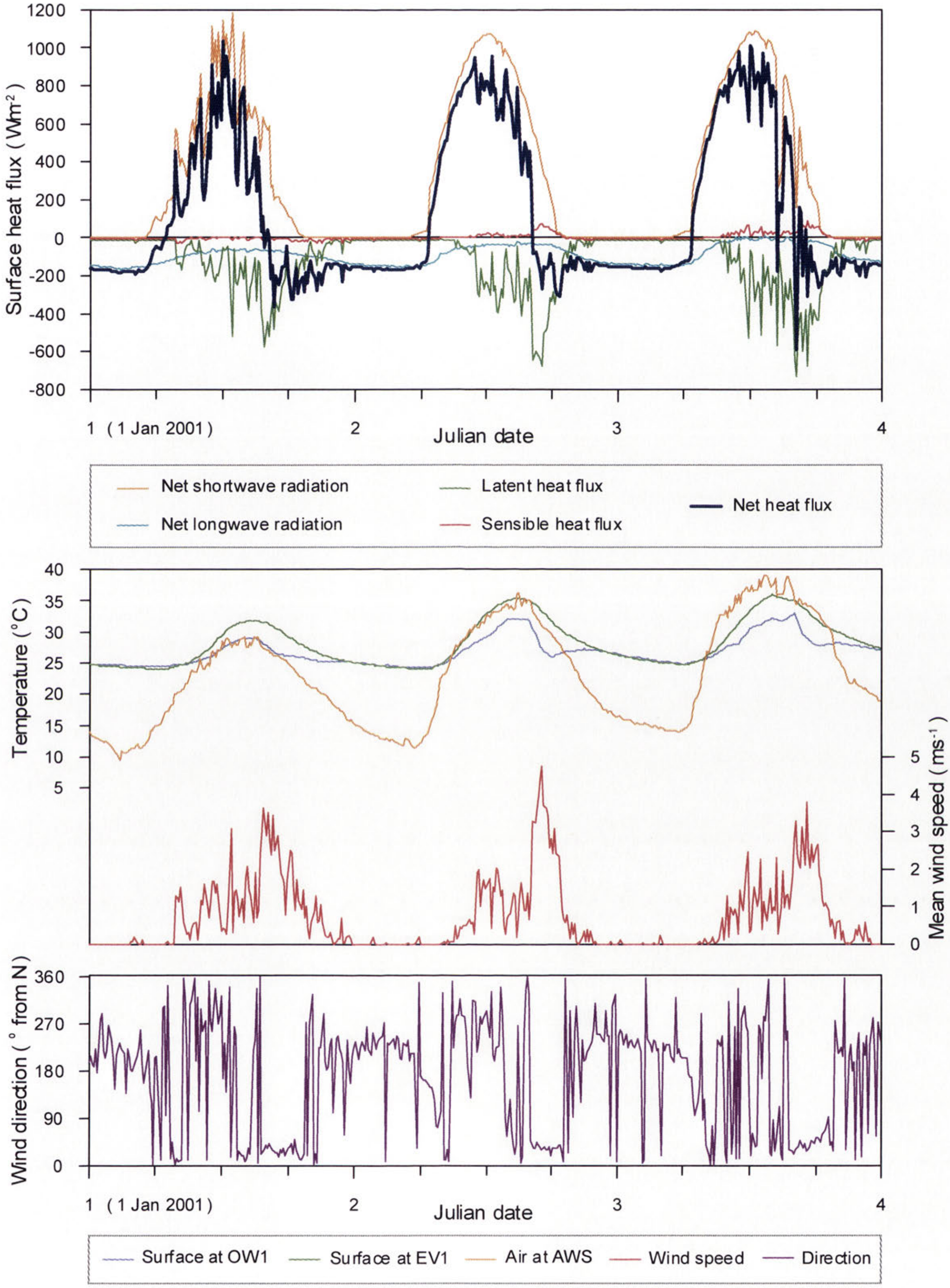

Figure 6.21: Calculated surface heat fluxes and meteorological conditions at Hopwoods Lagoon between 1 and 3 January 2001 (summer).

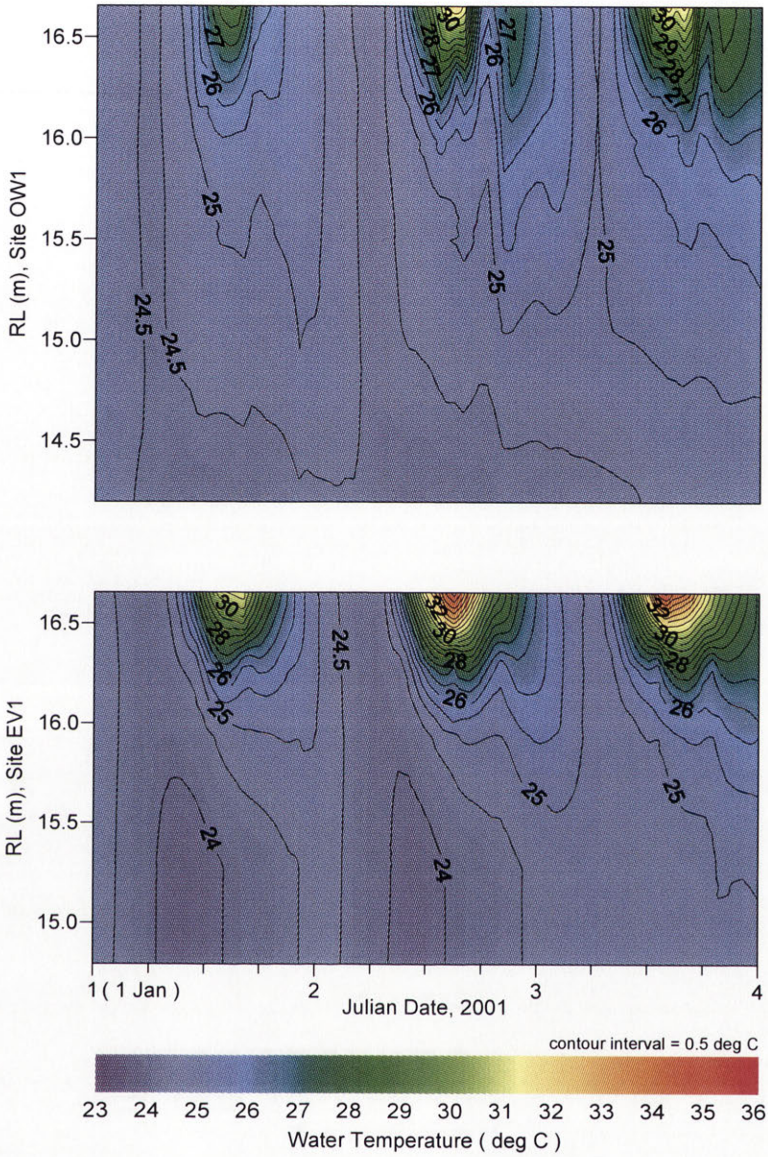

Figure 6.22: Water temperatures at Sites OW1 and EV1 between 1 and 3 January 2001 (summer). Water surface elevation at RL 16.71 m.

The near-vertical isotherms overnight at both sites indicated that the daytime stratification was completely eroded. Not only were conditions isothermal vertically at each site, but around midnight, temperatures also became isothermal *between* the two sites.

Inferred Advective Flows during Summer

During the period from 1 to 3 January 2001, winds were strongest between 16:00 and 19:00, peaking at $5\,\mathrm{m\,s^{-1}}$ on 2 January. The 10 min mean wind speeds were consistently around $3\,\mathrm{m\,s^{-1}}$ during these times and blowing from the north or north-east. Horizontal advective currents in the water surface layer would therefore have been expected to travel generally from the emergent macrophyte zone at the north-eastern end of the lagoon towards the open water in the interior (Figure 5.5 on page 161). The increase in water surface temperature at Site OW1 after sunset (18:00 AEST) on 2 and 3 January is consistent with a flow of warm water from the warmer emergent macrophyte zone.

Assuming no obstructions from the emergent macrophytes and sufficient fetch for the logarithmic wind profile to develop above the water surface, the maximum surface drift velocities in the open water are estimated, from Equation (3.79) on page 108 to be:

$$u_s \sim 0.035 \times u_{10} \sim 0.035 \times 5.0 \sim 0.175\,\mathrm{m\,s^{-1}} \tag{6.10}$$

Earlier in the day (09:00 to 16:00), wind speeds were generally $< 2\,\mathrm{m\,s^{-1}}$ and typically from the west. Making the same assumptions as above, surface advective flows with $u_s \sim 0.07\,\mathrm{m\,s^{-1}}$, would have been induced from the open water towards Site EV1, although these would have reduced speed significantly upon entering the macrophyte zones due to drag from the vegetation.

Horizontal Temperature Differences during Summer

Figure 6.23 shows horizontal temperature differences between Sites OW1 and EV1. It was not possible to calculate near-bed temperature differences directly from thermistor data, because the deeper thermistors were deployed at fixed heights above the bed, and therefore at different elevations. Instead, temperature differences at these depths were calculated using interpolated temperatures at Site OW1.

Site EV1 was considerably warmer than Site OW1 at **50 mm depth** during the day, while temperature differences were of the opposite sign at the remaining depths. The change in sign between 50 mm and 400 mm depth suggests that the surface layer was confined to a depth of < 400 mm, probably by the strong vertical temperature stratification. The only exception was between 14:00 and 19:00 on 2 January when the temperature difference reversed sign and Site OW1 was cooler than Site EV1. This coincided with the strongest wind speeds and the largest surface temperature difference between the two sites, and probably represented a deepening of the surface layer across the wetland.

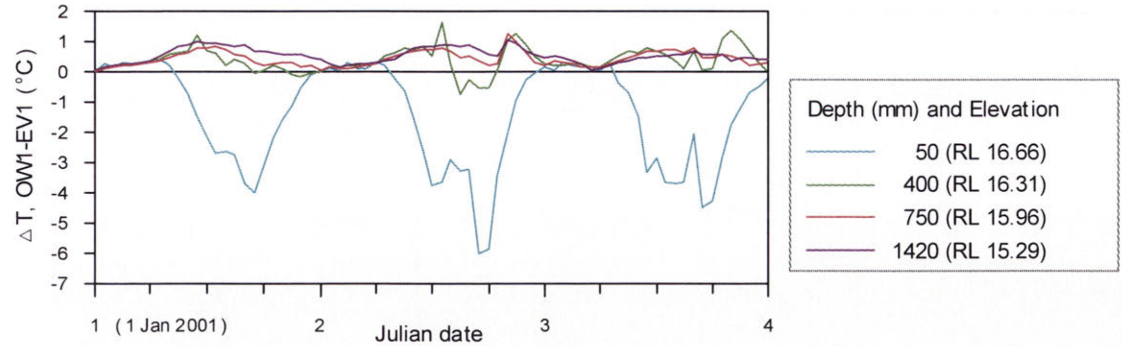

Figure 6.23: Horizontal temperature differences between Sites OW1 and EV1 from 1 to 3 January 2001 (summer). The two sites are located approximately 35 m apart.

Inferred Convective Flows during Summer

In the absence of velocity measurements, the horizontal temperature differences shown in Figure 6.23 provide an indication of the likely timing and direction of convective flows between the two sites (Ostrovsky et al., 1996; James and Barko, 1991). Between 08:00 and midnight, these temperature differences suggest a warm, surface flow of **depth** $<$ 400 **mm** from the emergent macrophyte zone towards the open water, with a return flow into the macrophyte zone over the lower depths. Between midnight and 08:00, the four horizontal temperature differences were small but approximately equal in magnitude and direction, which suggested a deeper flow from the open water towards the cooler emergent macrophyte zone. This implies that the inferred convective flow was slower but deeper during the cooling phase than during the heating phase, consistent with Monismith et al. (1990). To satisfy continuity, it is probable that there was a cool gravity current from Site EV1 towards Site OW1, as per the observations of James and Barko (1991) and Oldham and Sturman (2001), for example.

Estimates for the surface and subsurface velocities can be made based on the scaling analyses of Section 3.8. The velocity of the inferred convective surface current from the macrophyte zone towards the open water during the period from 08:00 until midnight can be estimated using Equation (3.83) (page 111). Assuming the buoyancy forcing due to the horizontal temperature gradient ($\Delta T/L = 6.0/35\,^{\circ}\mathrm{C\,m^{-1}}$) is balanced by vegetation drag, over a surface layer of depth of $H < 400\,\mathrm{mm}$ (say $H \sim 0.35\,\mathrm{m}$):

$$U \sim \left[\frac{2}{0.5} \left(\frac{0.01}{1000\,(1.1 \times 10^{-6})} \right)^{1/4} (9.81)(1.8 \times 10^{-4}) \left(\frac{6.0}{35} \right) (0.35) \right]^{4/7} \sim 0.016\,\mathrm{m\,s^{-1}} \quad (6.11)$$

The projected plant area was calculated as $A_p = n_s\, d$=50(0.01)=0.5 $\mathrm{m^2\,m^{-3}}$, based on field survey results for *Eleocharis sphacelata* at Hopwoods Lagoon.

The subsurface current, which flows in the opposite direction to the surface current, can be estimated using a similar approach. An average gradient of $\Delta T/L = 1.0/35\,{}^\circ\mathrm{C\,m^{-1}}$ in the underlying water layer with $H \sim 0.65\,\mathrm{m}$ (350 mm to 1 m depth) could give rise to a convective velocity of $\sim 0.008\,\mathrm{m\,s^{-1}}$ from the open water zone towards the emergent macrophytes.

These convective velocity estimates are much slower than the wind-induced advective flows of $u_s < 0.07\,\mathrm{m\,s^{-1}}$ from Site OW1 towards Site EV1 between 09:00 and 16:00 and $u_s < 0.175\,\mathrm{m\,s^{-1}}$ from Site EV1 towards Site OW1 between 16:00 and 19:00. The day-time advective flow from Site OW1 would probably have completely arrested the inferred convective surface flows from Site EV1 to Site OW1 during this period. However, between 16:00 and 19:00 advective flows would have been in a similar direction to, and therefore enhanced, the inferred convective flows.

The horizontal temperature differences shown in Figure 6.23 suggest horizontal convective currents between Sites OW1 and EV1, and the calculations presented above estimate their magnitude. Further support for their existence can be obtained by considering a vertical section of the water column of unit horizontal area, centred on Site OW1. Ignoring horizontal transport for the moment, the evolution of the water temperature profile over a period Δt (s) due to heating by a net shortwave radiation flux ϕ_0 ($\mathrm{Wm^{-2}}$) can be calculated using Beers Law, Equation (3.63) from page 96:

$$T_w\,(\mathrm{est}) = T_w\,(\mathrm{meas}) + \frac{\eta\,\phi_0\,\Delta t}{\rho\, c_{pw}} \exp\left(-\eta\, z\right) \tag{6.12}$$

where $T_w\,(\mathrm{est})$ = estimated water temperature at end of interval (°C)

$T_w\,(\mathrm{meas})$ = measured water temperature at beginning of interval (°C)

η = attenuation coefficient for shortwave radiation ($\mathrm{m^{-1}}$)

ρ = water density ($\mathrm{kg\,m^{-3}}$)

c_{pw} = specific heat capacity of water ($\mathrm{J\,kg^{-1}\,{}^\circ C^{-1}}$)

z = depth over which the shortwave radiation is absorbed (m).

Two pairs of water temperature profiles from Site OW1 on 1 and 2 January 2001 are shown by the solid lines in Figure 6.24. The profiles are separated by Δt=1.0 hr and predicted temperatures at the later time on each day are shown by the dashed lines. The profiles were predicted using Equation (6.12), with temperature-dependent variables ρ and c_{pw} calculated from T_w (meas) at the beginning of the period (see Appendix A). Net shortwave radiation was calculated as the average over the period (Figure 6.21), and the field value of η_{OW}=1.8 m^{-1} was adopted (Section 6.4.2.1, page 229).

From Figure 6.24(a), although the shapes of the two profiles are similar at 12:00 on 1 January, the predicted temperatures exceeded the measured temperatures by ~0.3°C at **50 mm depth**, ~1.0°C at **400 mm depth** and ~0.4°C at **750 mm depth**. The average surface heat flux due to longwave radiation, latent and sensible heat fluxes (*i.e.* $H_{NET} - \phi_0$) between 11:00 and 12:00 on 1 January was -108 Wm^{-2} (out of the wetland), which would have caused a temperature drop of ~1.3°C over the upper 0.1 m of the water column. This would have contributed to the lower T_w (meas) close to the surface. Vertical mixing would have been restricted by the strong vertical temperature stratification, so the cooling is unlikely to have caused any cooling at depth. The measured profile therefore cannot be explained completely by the shortwave radiation influx and surface heat effluxes.

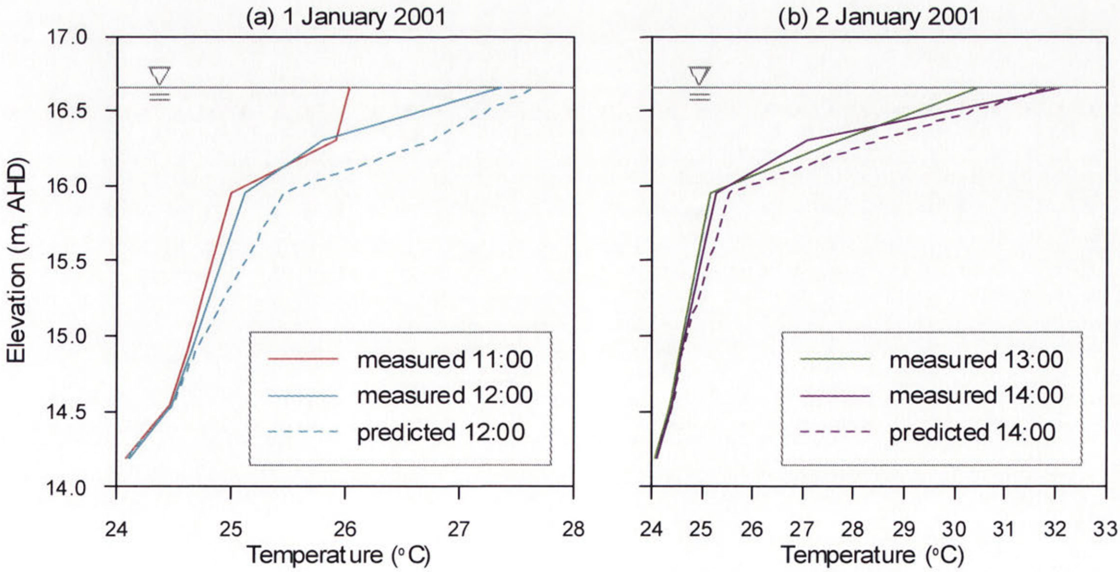

Figure 6.24: Measured and predicted water temperatures at Site OW1 on (a) 1 January 2001 at 11:00 and 12:00 and (b) 2 January 2001 at 13:00 and 14:00 (AEST).

Introducing the possibility of horizontal transport, it was shown earlier that surface advective currents would have been directed from Site OW1 to Site EV1 between 11:00 and 12:00 on 1 January. These were several times larger than, and in the opposite direction to, the inferred convective surface flows, and would have transported some heat away from Site OW1 towards Site EV1 at the surface. Near surface water temperatures would have been similar throughout the open water zones of the wetland, assuming relatively uniform η_{OW}, so advection of cooler water from the interior of the wetland is unlikely to be the cause of lower than expected heating at Site OW1.

At greater depth where surface-induced advection is minimal, the most likely explanation for the lower T_w (meas) is horizontal convection of heat to another location in the lagoon. Site OW1 was located adjacent to an emergent macrophyte zone where temperatures were substantially warmer at the surface but cooler at depth, a temperature difference conducive to horizontal convection from the warmer Site OW1 towards the cooler Site EV1. Between 350 mm and 1 m depth, an estimated convective velocity of $\sim 8\,\mathrm{mm\,s^{-1}}$ and an average horizontal temperature gradient of $\Delta T/L = 1.0/35\,°\mathrm{C\,m^{-1}}$ (page 254) could result in a temperature drop of $\sim u\,dT/dx \sim 0.8°\mathrm{C}$ over one hour at Site OW1. This is consistent with the difference between T_w (meas) and T_w (est) at these depths, and can explain the lower than predicted T_w (meas) at 12:00.

Figure 6.24(b) shows a similar trend between 13:00 and 14:00 on 2 January. Both examples are consistent with the convective flow regime inferred from the horizontal temperature differences shown in Figure 6.23, and support the existence of convective flows from the open water (Site OW1) towards the emergent macrophyte zone (Site EV1) at mid-depth.

6.5.4.2 Diurnal and Zonal Hydrodynamic Trends during Winter

Typical trends in the meteorological forcing and the hydrodynamic response at Hopwoods Lagoon during the winter months (June to August) were seen from 18 to 20 August 2001. The surface heat fluxes from this period are shown in Figure 6.25 and water temperature profiles at Sites OW1 and EV1 are shown in Figure 6.26.

Meteorological Forcing and Water Temperatures during Winter

As in summer, H_{NET} was dominated by the net shortwave radiation influx during the day and the net longwave radiation efflux overnight. However, the shortwave radiation influx was only $\sim$50% of that during summer and peaked at 670 Wm^{-2}. With the exception of 18 August which was particularly windy, wind speeds were only slightly higher than on 1 to 3 January and winds blew predominantly from the west. The latent heat flux during the day was lower in winter, chiefly because the water surface temperatures were 10 to 20°C cooler.

As in summer, water surface temperatures were warmer at Site EV1 than at Site OW1 during the day but very similar overnight. However, the surface temperature difference between the two sites was much smaller than in summer. Diurnal variation in the water surface temperatures was also considerably lower, and similar at both sites, than during summer. Near the bed, diurnal temperature variation was similar at both sites and in both seasons.

The water column was completely mixed at Site OW1 and almost isothermal at Site EV1 on 18 August, but weakly stratified in both zones on 19 and 20 August. Vertical temperature gradients during the day were much lower in August than in January, and peaked at 2.5°C m^{-1} (Site EV1) and 1.2°C m^{-1} (Site OW1), compared with 8.3°C m^{-1} and 3.4°C m^{-1} in January. The water column returned to an isothermal state overnight at both sites.

Inferred Advective Flows during Winter

Winds were strongest between 10:00 and 18:00, and blew predominantly from the west. The 10 min mean wind speeds were generally 4–5 m s^{-1}, which could have induced advective surface flows with velocities of $\sim$0.14–0.175 m s^{-1} from the open water towards Site EV1. The mean wind speed peaked at nearly 10 m s^{-1} on 18 August, which could have induced a surface flow velocity of $\sim$0.35 m s^{-1} from Site OW1 towards Site EV1.

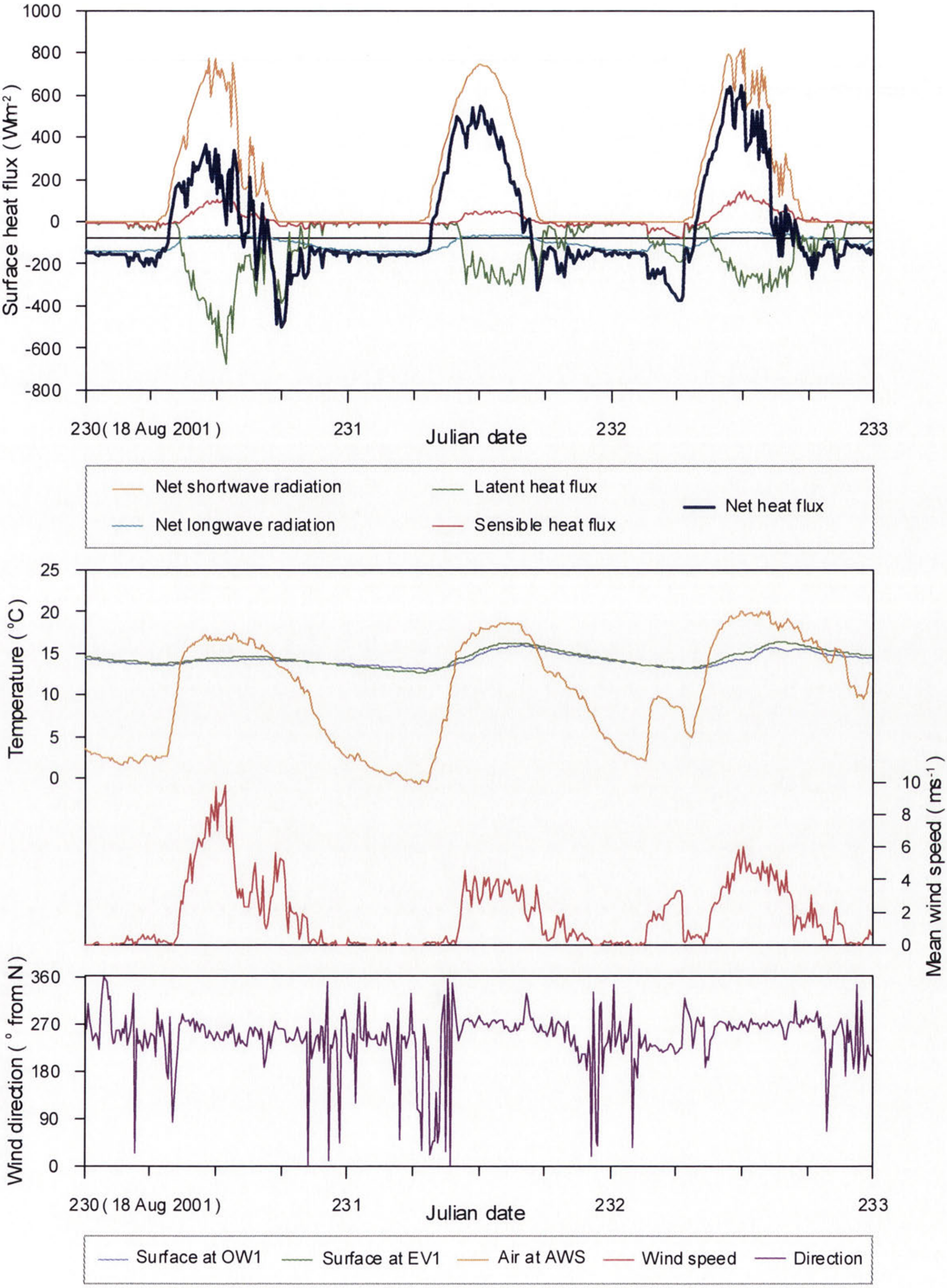

Figure 6.25: Calculated surface heat fluxes and meteorological conditions at Hopwoods Lagoon between 18 and 20 August 2001 (winter).

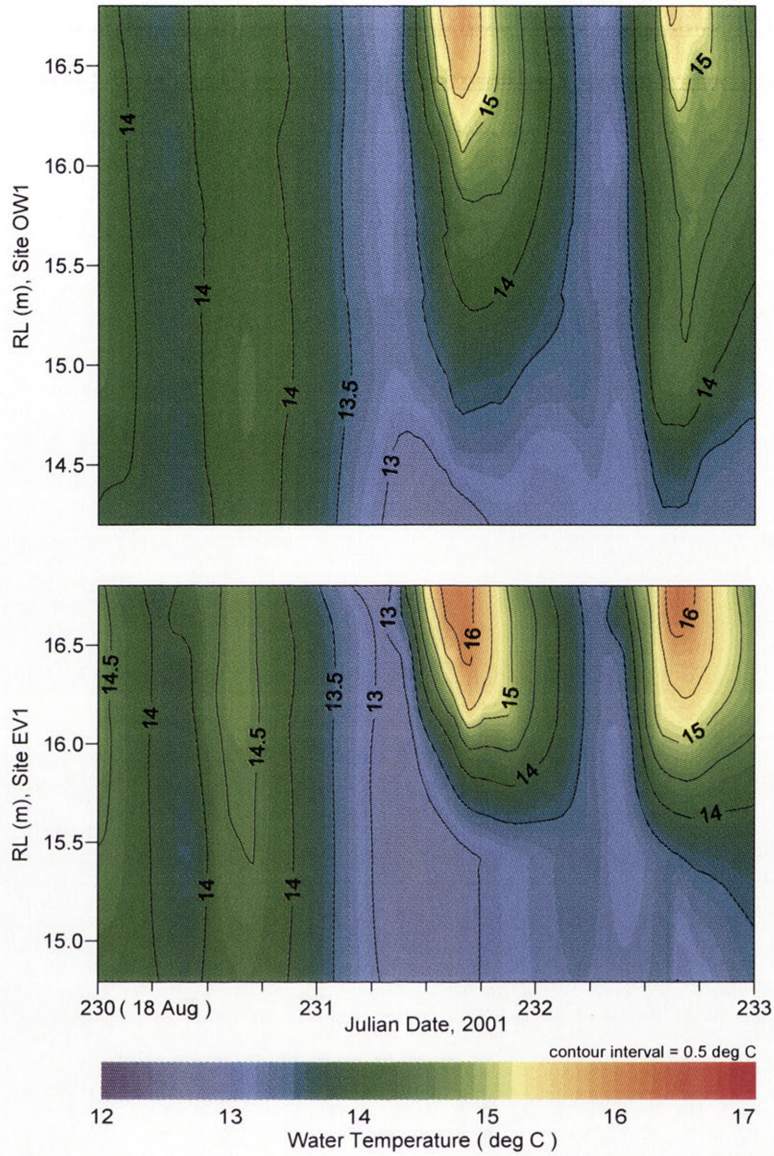

Figure 6.26: Water temperatures at Sites OW1 and EV1 between 18 and 20 August 2001 (winter). Water surface elevation at RL 16.85 m.

Horizontal Temperature Differences during Winter

Figure 6.27 shows horizontal temperature differences between Sites OW1 and EV1 from 18 to 20 August. These were distinct from the differences calculated during summer (Figure 6.23 on page 253), in both magnitude and variation throughout the diurnal cycle. The horizontal temperature differences were generally smaller at all depths in August than in January.

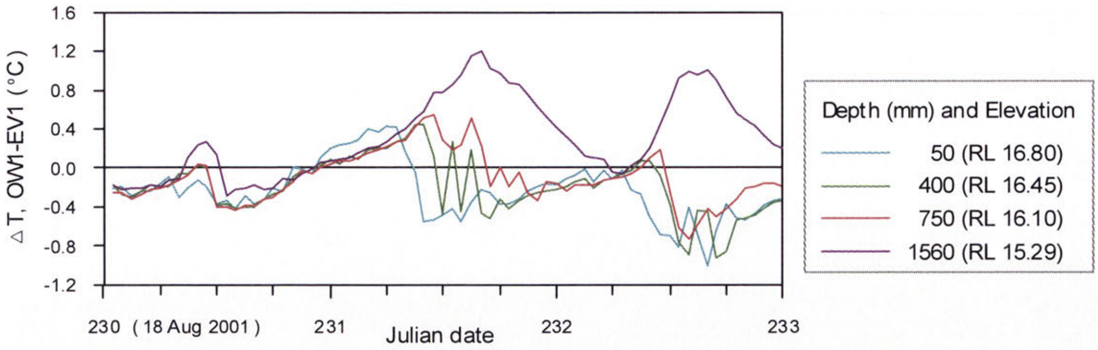

Figure 6.27: Horizontal temperature differences between Site OW1 and Site EV1 from 18 to 20 August 2001 (winter). The two sites are located approximately 35 m apart.

The trends shown in Figure 6.27 indicate that the magnitude and direction of temperature differences at **50 mm**, **400 mm** and **750 mm depth** were generally similar throughout the diurnal cycle. The similar temperature differences at all depths on 18 August suggest that the wetland was completely mixed in the vertical by the prevailing strong winds and penetrative convection resulting from the high latent heat efflux (Figure 6.25). The slightly warmer temperatures at Site EV1 were probably due partly to insulation by the emergent macrophytes and partly to the smaller depth over which available heat was mixed. The opposing sign of the near surface and deeper temperature differences on 19 and 20 August indicates that the water column was not mixed over the full depth, presumably because the winds were not as strong.

Inferred Convective Flows during Winter

The maximum horizontal temperature difference at all depths on 18 August was only 0.4 °C, which is similar to the calibration limit of the thermistors (±0.1°C), so any buoyancy forcing for flow from Site EV1 towards Site OW1 would have been minimal. Regardless, any convective flows would have been completely overcome by the strong inferred advective currents directed from Site OW1 towards Site EV1, and Figure 6.27 suggested that wind-induced vertical mixing had occurred over the full depth on 18 August.

On 19 and 20 August, the higher net surface heat influx and lower wind speeds allowed slightly larger horizontal temperature differences to develop between the two sites. At **50 mm** and **400 mm depth**, these would have established a small buoyancy forcing for flow of warm water from Site EV1 towards Site OW1 between 09:00 and 06:00. They also suggest a buoyancy forcing at **750 mm depth** in the same direction on 20 August but in the opposite direction on 19 August.

The temperature difference at **1560 mm depth** on both days suggests a convective flow of warmer water from the open water towards the emergent macrophytes. The inferred wind-induced, advective flows from Site OW1 towards Site EV1 are likely to have negated these slight inferred convective flows in the upper part of the water column. Convective flows are therefore only likely to have occurred at greater depth. As in January, bed temperatures were cooler at Site EV1 than at a similar elevation at Site OW1 (Figure 6.26), so a gravity flow would have been expected from Site EV1 towards the open water.

The greatest horizontal temperature differences occurred at depth where there is little heating due to shortwave radiation, so it is difficult to find evidence for these inferred convective flows during the heating phase (07:30 to 15:30). Instead, the overnight water temperature trends are examined.

Figure 6.28 shows measured water temperatures at Site EV1 on 19 and 20 August, together with the interpolated temperature at **1560 mm depth** at Site OW1. Figure 6.28 shows that Site EV1 was cooling strongly at **depths** $\leq$ **750 mm** after 18:00 on both days. Site OW1 was also cooling at **1560 mm depth**. By contrast, the temperature at **1560 mm** at Site EV1 continued to warm until 06:00 on 20 August, at which time the water column became isothermal. Given the cooling at higher elevations at Site EV1, this observed heating at **1560 mm depth** could not have occurred from above.

The temperature increase at **1560 mm depth** at Site EV1 (500 mm above the bed) is unlikely to have occurred by conduction from the sediments. This suggests that the observed heating occurred due to horizontal transport of warmer water from elsewhere in the lagoon. The adjacent submerged macrophyte zone is shallower than Site EV1, and therefore an improbable source of heating at **1560 mm depth** in the emergent macrophyte zone. The most likely explanation is convection of warmer water from Site OW1, as inferred from Figure 6.27.

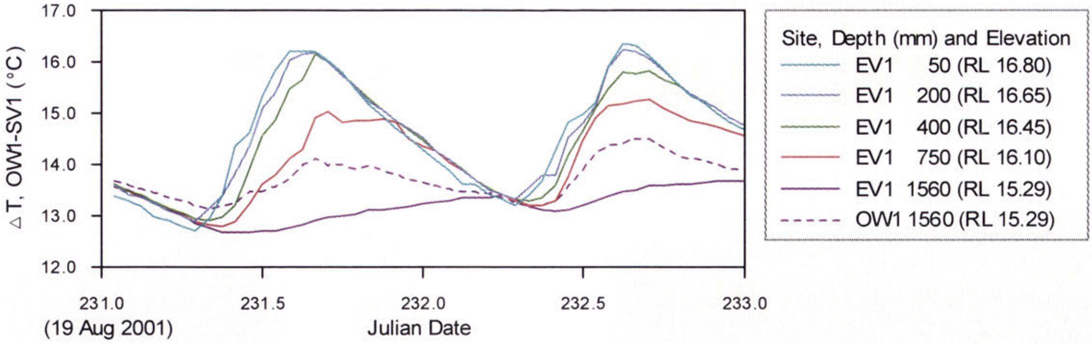

Figure 6.28: Measured water temperatures (solid lines) at Site EV1 on 19 and 20 August 2001, and the interpolated temperature at 1560 mm depth at Site OW1 (dashed line).

6.5.4.3 Diurnal and Zonal Hydrodynamic Trends during Autumn and Spring

Meteorological conditions at Hopwoods Lagoon during the transitional seasons of autumn and spring were generally intermediate between the examples in summer and winter. The horizontal temperature differences and inferred convective flow regimes varied from a diconvective (reversing) regime such as that inferred during January, to a monoconvective (single direction) regime such as that inferred during August. The primary determining factors were the magnitude and temporal variation in the net surface heat flux and the prevailing wind climate.

In summary, significant seasonal variation was demonstrated in the meteorological forcing and the hydrodynamic response at Hopwoods Lagoon. Surface heat fluxes and vertical temperature gradients were higher in the open water and the emergent macrophyte zones in summer than during winter, and horizontal temperature differences between the two zones were also higher in summer. This was not unexpected and is consistent with the detailed observations of seasonal variation reported by Waters (1998) in a partly-vegetated wetland in Sydney. However, the flow regimes inferred at Hopwoods Lagoon were not the same as those observed by Waters (1998) at Manly Dam. The distinguishing features and implications of these differences are discussed in Chapter 7.

This suggests that the hydrodynamic response of a wetland to the local meteorological forcing is highly dependent on the individual characteristics of the wetland concerned. It is expected that the type, structure and density of the wetland macrophytes strongly influence the convective flow regime in a wetland. The significance of differential heating and radiation shading by submerged and emergent macrophytes at Hopwoods Lagoon is investigated in more detail in Section 6.5.5.

6.5.4.4 Horizontal Temperature Transect Data

To further investigate the likely presence of horizontal convective flows, a horizontal transect was established between the open water and emergent macrophyte zones from April to July 2001. The transect was approximately 20 m long and comprised an array of eight thermistors (T21 to T28) at depths of 50 mm and 750 mm below the water surface. The transect was located entirely within the emergent macrophyte zone of the wetland, commencing near (but offset from) Site EV1 and extending in a south-westerly direction towards Site OW1. The bed elevation ranged from RL 14.8 m near Site EV1 to RL 14.6 m nearer Site OW1, which corresponded to a depth range of 2.2 to 2.6 m. The location and configuration of the transect is shown schematically in Figure 6.29.

Consistent with the work of Coates and Patterson (1993), it was anticipated that temporal variation in temperatures along the transect could support the presence of the convective

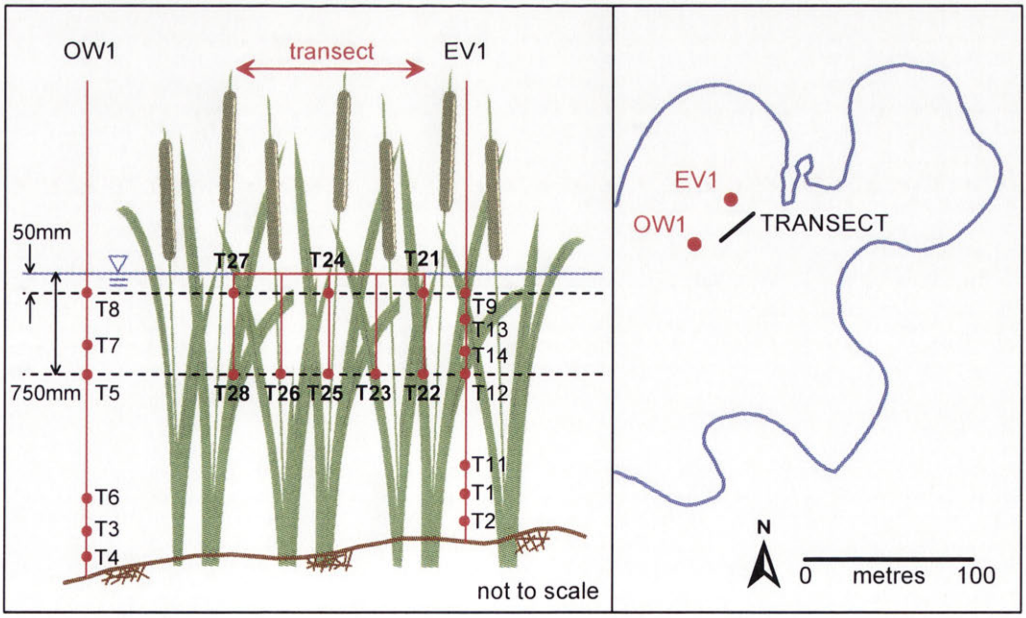

Figure 6.29: Horizontal temperature transect with Thermistors T21 to T28 established between the open water and emergent macrophyte zones from April to July 2001.

currents inferred from horizontal temperature differences between Sites OW1 and EV1. Convective velocities could also be estimated from the progress of a temperature intrusion along the transect.

Horizontal temperature differences between the two sites for the period from 13 to 15 May 2001 are shown in Figure 6.30. Meteorological fluxes for the same period are shown in Figure G.1 and water temperature profiles in Figure G.2 (Appendix G). During the early morning (from midnight until 08:00), winds of $\leq 1\,\mathrm{m\,s^{-1}}$ blew predominantly from the west, generally from Site OW1 towards Site EV1. These would have induced advective currents of $u_s < 0.035\,\mathrm{m\,s^{-1}}$ into the emergent macrophyte zone. Winds blew from the north between 08:00 and 17:00 and peaked at $2\,\mathrm{m\,s^{-1}}$, which may have induced advective flows of $u_s < 0.07\,\mathrm{m\,s^{-1}}$ from the emergent macrophyte zone towards the open water.

Figure 6.30(a) shows horizontal temperature differences between Sites OW1 and EV1 between 13 and 15 May 2001. These suggest a buoyancy-induced horizontal flow from the emergent macrophyte zone towards the open water between 08:00 and 04:00 over a

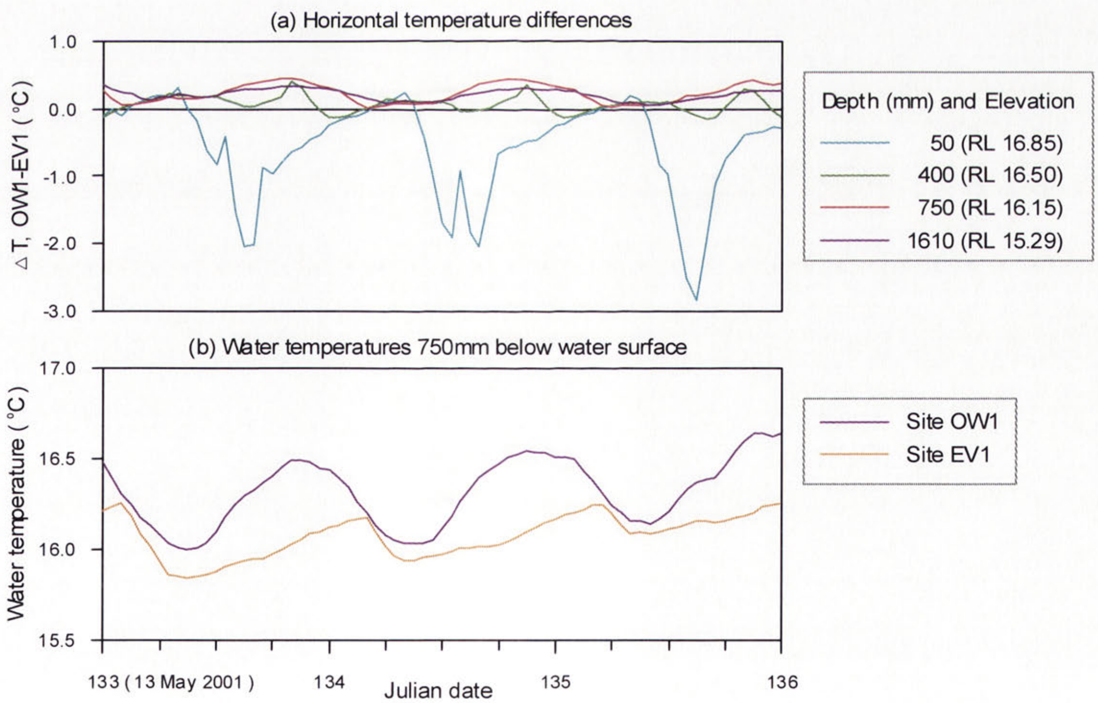

Figure 6.30: Water temperatures at Site OW1 and Site EV1 from 13 to 15 May 2001: (a) horizontal temperature differences and (b) temperatures 750 mm below the water surface.

depth of < 400 **mm**, with a deeper flow in the opposite direction over most of the diurnal cycle. The surface flow would have been enhanced by wind-induced advection (Figure G.1) between 08:00 and 17:00.

At **750 mm depth**, Figure 6.30(b) shows that Sites OW1 and EV1 commenced heating at around 08:00 on each day, and continued heating long after the commencement of the cooling phase at ~16:30. The peak temperature was attained some 7 hr later at Site EV1 than at Site OW1, which suggested a mid-depth influx of heat to Site EV1 long after the surface waters commenced cooling.

Adopting the approach of Coates and Patterson (1993), Figure 6.31 shows water temperatures along the horizontal transect between 13 and 15 May 2001, and the rate of heating at 750 mm depth. At **50 mm depth**, daily minimum and maximum transect temperatures were recorded at thermistor T27 (nearest Site OW1 but still within the emergent macrophyte zone) and lowest at thermistor T21. Considering the transect data in isolation, a convective current could be inferred during the heating phase from thermistor T27 to thermistor T21 (that is, from the open water towards the emergent macrophyte zone). This is in the opposite direction to the current suggested by the horizontal temperature difference between the nearby Sites OW1 and EV1 (Figure 6.30). However, the **50 mm deep** temperature at Site OW1 was generally lower than at Site EV1 or anywhere along the transect, so buoyant surface flow would have been directed towards the open water zone, aided by wind-driven advection. The unexpected reverse trend in the transect surface temperatures is probably due to local variation in the density of the emergent macrophyte canopy, and therefore the surface heat fluxes.

At **750 mm depth** the temperature range was significantly smaller, but the trends were suggestive of a warm current at around 750 mm depth travelling from the open water zone towards Site EV1, consistent with that inferred from Figure 6.30. The transect data suggest that a current developed during the heating phase and continued until temperature differences along the transect were equalised at around 04:00. The peak temperature and the peak rate of heating both decreased along the transect from the open water towards the emergent macrophytes, which suggested that heat was dissipated as the intrusion progressed.

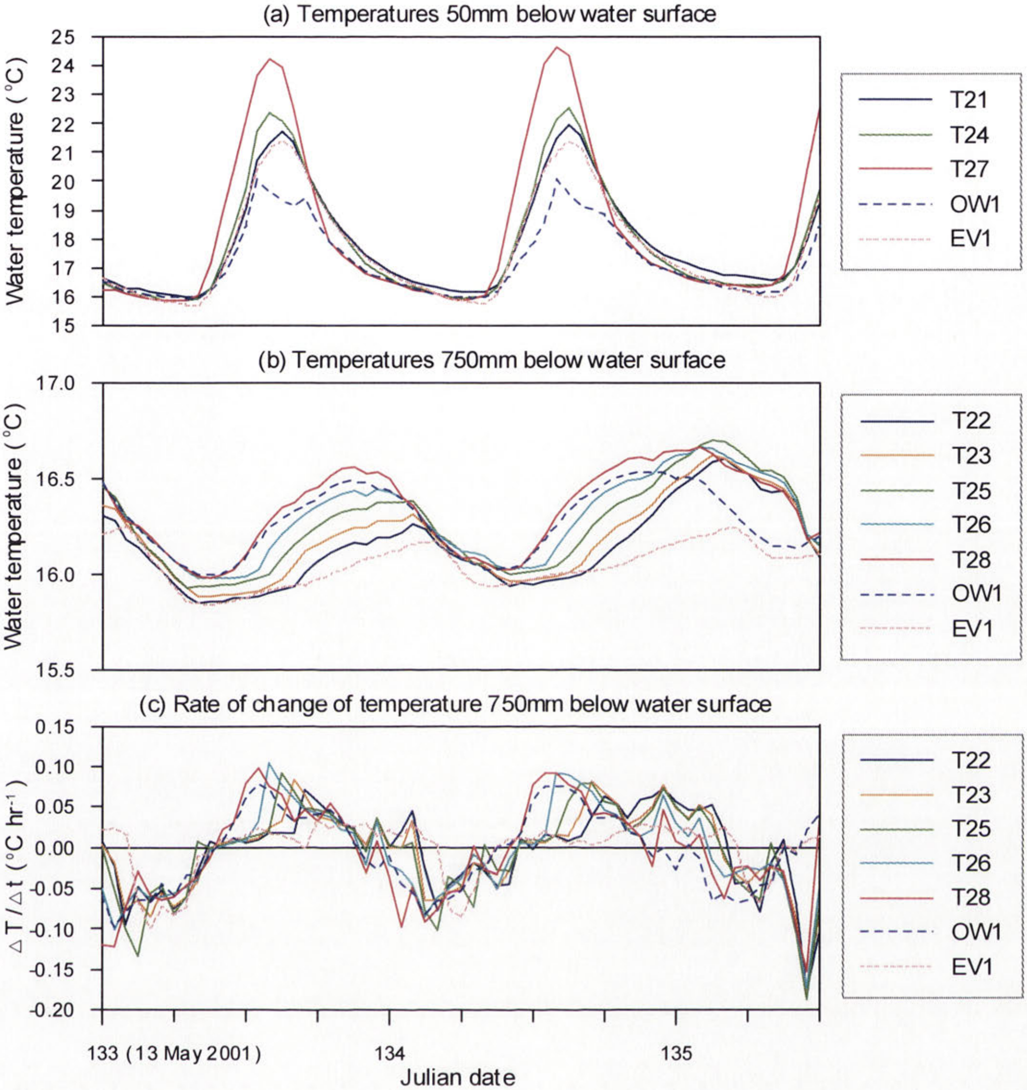

Figure 6.31: Measured water temperatures along the horizontal transect from 13 to 15 May 2001: (a) 50 mm below surface, (b) 750 mm below surface, and (c) rate of temperature change at 750 mm depth.

The progress of an inferred warm current along the transect was indicated by the timing of the peak heating rate at each thermistor. Over the 20 m transect, there was a time lag of approximately 4 hr between thermistors T28 and T22, which gives a mean convective velocity of $\sim 1.4\,\mathrm{mm\,s^{-1}}$. This estimate is comparable and broadly consistent with convective velocities reported by Waters (1998) and Oldham and Sturman (2001) in Australian wetlands and by Coates and Patterson (1993) in a differentially-illuminated cavity.

The possibility of the temperature trends along the transect being explained by a cool flow from the submerged or emergent macrophyte zones towards the open water was discounted because a cool current would be expected to move along the bed (James and Barko, 1991; Oldham and Sturman, 2001), rather than as a mid-level intrusive flow. The inferred flow and heating at **750 mm depth** continued after the commencement of the cooling phase, and therefore could not have originated from the surface. A warm convective current from the open water towards the emergent macrophytes around mid depth (750 mm) facilitates the observed heating, and is supported by the horizontal transect data.

6.5.5 Radiation Shading by Macrophytes at Hopwoods Lagoon

Radiation shading in a wetland was defined in Chapter 2 as differential heating between open water and macrophyte zones due to the presence of macrophytes. Radiation shading can be caused by:

- **emergent macrophytes**, which lower the net shortwave radiation flux at the water surface relative to open water zones, and/or
- **submerged macrophytes**, which increase the rate of absorption of shortwave radiation with depth below the water surface compared with open water zones, and therefore alter the vertical distribution of heat with depth.

Differences in depth between the macrophyte and open water zones can also contribute to differential heating and cooling, because shallow areas heat and cool more rapidly than deeper areas (Monismith et al., 1990). Macrophytes are generally restricted to the shallow, littoral zones of wetlands.

Waters (1998) examined radiation shading by emergent macrophytes in some detail, but suggested that submerged macrophytes would have no significant influence on buoyancy driven convection in a shallow wetland. Dale and Gillespie (1976, 1977) found that horizontal temperature gradients developed between open water and submerged macrophytes, but did not consider convective exchanges between the two.

The effects of depth differences and radiation shading by submerged and emergent macrophytes at Hopwoods Lagoon were assessed by comparing water temperatures at Site OW1 in the open water zone with temperatures at other locations in the lagoon. As explained in the following sections, radiation shading by the submerged macrophytes was found to be the most significant of the three effects at Hopwoods Lagoon.

6.5.5.1 Effects of Differences in Depth on Differential Heating and Cooling

The influences of depth on differential heating and cooling were examined at Hopwoods Lagoon by comparing water temperatures at Site OW1 with three additional open water sites, where the effects of macrophytes did not need to be considered. Site OW2 was located close to Site OW1 near the northern end of the lagoon, Site OW3 was located at the southern end of the lagoon and Site OW4 was located near the centre of the lagoon. Site locations were shown in Figure 5.5 (page 161).

The comparisons were also used to assess similarities in diurnal temperature trends between open water sites at the wetland, and hence if temperatures at Site OW1 were representative of the open water zones in general. The physical characteristics of the open water sites and sources of meteorological and water temperature data for the relevant investigation periods are summarised in Table 6.9.

Meteorological Forcing and Water Temperatures

Graphs showing meteorological conditions and water temperature profiles during the three investigation periods are included in Appendix G. These all occurred in the warmer months of the year, when the net surface heat flux H_{NET} was typically high during the day. Conditions were partly cloudy on most days, but heavily overcast and raining on 5 February and 9 November. Wind speeds were moderate throughout the three periods and were generally $<5\,\mathrm{m\,s^{-1}}$, often becoming stronger in the afternoon. Winds blew

Site ID	Site Location	Δh (m) OW1 - Site	Dates	Meteorological Fluxes		Water Temperatures	
OW2	15 m SW of OW1	-0.35	3 to 5 Feb 2001	Fig. G.3	p.449	Fig. G.4	p.450
OW3	205 m SW of OW1	-0.05	19 to 21 Oct 2001	Fig. G.5	p.451	Fig. G.6	p.452
OW4	115 m SW of OW1	-0.38	9 to 11 Nov 2001	Fig. G.7	p.453	Fig. G.8	p.454

Table 6.9: Physical characteristics and sources of data for the open water sites at Hopwoods Lagoon (Δh = depth difference).

predominantly from the south-west or west during the morning and the north or north-east in the afternoon. The windiest day was 19 October, when the winds blew consistently from the west with speeds $>2\,\mathrm{m\,s^{-1}}$ for most of the day.

The water temperature profiles show that the diurnal temperature cycles were similar at all open water sites over the three investigation periods, with some degree of vertical stratification developing daily. The vertical temperature gradients were weakest on 3 February and 19 October, and strongest prior to the rain storm on 5 February. Stratification decayed overnight at all sites on all days, but the water column only mixed over the full depth in the early hours of 21 October and following rainfall on 9 November.

Horizontal Temperature Differences

Horizontal temperature differences between Site OW1 and the other open water sites are shown in Figure 6.32. These were similar at all depths and generally within ± 0.5°C throughout the diurnal cycle, although there were some exceptions. During the February investigation period, the horizontal temperature differences at **50 mm** and **400 mm depth** increased to < 2.5°C in the early afternoon on the three days. This was primarily due to slight differences in the timing of the peak temperatures attained at the two sites, and the strength of vertical stratification in the upper 400 mm of the water column.

The larger temperature differences on 21 October occurred because Site OW1 experienced vertical wind-induced mixing to a depth of $\sim$2 m in the early afternoon while Site OW3 remained stratified (Figure G.6), which suggested a topographic wind sheltering effect between the two sites. A similar effect was observed near the bed between Sites OW1 and OW3 on 19 October. This was the windiest day during the period and surface heat was transported over much of the depth at Site OW1 but not at Site OW3.

Summary

These examples have demonstrated that differential heating between the four open water sites at Hopwoods Lagoon was generally small. Near surface temperatures at Sites OW2, OW3 and OW4 were generally within 0.5°C of temperatures measured simultaneously at Site OW1. Most instances with temperature differences of > 0.5°C occurred in the early afternoon, and could be explained by slight differences in the timing and magnitude of the

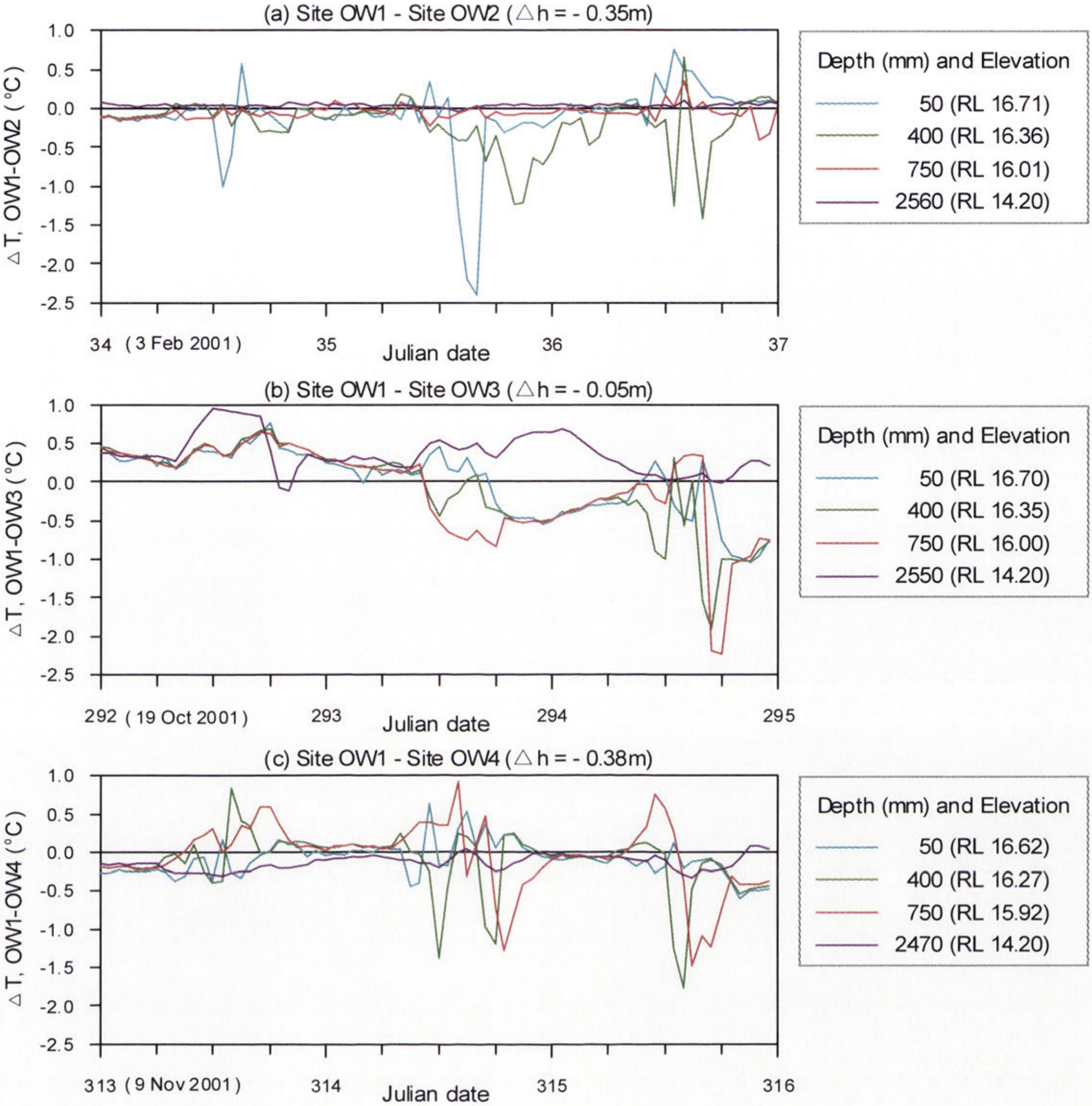

Figure 6.32: Horizontal temperature differences between Site OW1 and (a) Site OW2 from 3 to 5 February 2001, (b) Site OW3 from 19 to 21 October 2001, and (c) Site OW4 from 9 to 11 November 2001. Site details are given in Table 6.9.

peak temperatures attained at the different sites. Temperatures at Site OW1 are therefore generally representative of those in the open water zones at Hopwoods Lagoon.

The small differences in depth between the four sites ($\Delta h \leq 0.35\,\mathrm{m}$) appeared to produce little differential heating and cooling. This is consistent with the assumption of an approximately uniform underwater attenuation coefficient for shortwave radiation (η_{SV})

throughout the open water zones. As will be demonstrated in the following sections, the effects of macrophytes on differential heating and cooling are much more dramatic.

6.5.5.2 Radiation Shading by Submerged Macrophytes

As described by Dale and Gillespie (1977), radiation shading by submerged macrophytes can produce substantial horizontal temperature differences between vegetated and unvegetated areas in a water body. At Hopwoods Lagoon, radiation shading due to differential underwater absorption of shortwave radiation was examined by comparing water temperatures at submerged macrophyte sites with Site OW1.

Two submerged macrophyte sites were considered, Site SV1 located near Site EV1 at the northern end of the lagoon and Site SV2 in the deeper north-western bay. Site locations were shown in Figure 5.5 (page 161).These were free from emergent macrophytes, so any observed differential heating could be attributed to differential absorption of shortwave radiation (unequal underwater attenuation coefficients, $\eta_{SV} \neq \eta_{OW}$) and/or depth differences. Physical characteristics of the submerged macrophyte sites and sources of meteorological and water temperature data for the comparison periods are summarised in Table 6.10.

The predominant submerged macrophyte species at Hopwoods Lagoon was *Hydrilla verticillata*, which occurred in dense, continuous mats growing to within 0.2–0.3 m of the water surface. The domain of the *Hydrilla verticillata* increased throughout the monitoring period, and it had encroached on Site OW1 by October 2001. However, the impact of the *Hydrilla* at Site OW1 was assessed to be minimal in December 2000 and March 2001, when the following comparisons were made.

Site ID	Site Location	Δh (m) OW1 - Site	Dates	Meteorological Fluxes		Water Temperatures	
SV2	60 m N of OW1	0.3	14 to 16 Mar 2001	Fig. G.9	p.455	Fig. G.10	p.456
SV1	50 m NE of OW1	1.2	28 to 30 Dec 2000	Fig. G.11	p.457	Fig. G.12	p.458

Table 6.10: Physical characteristics and sources of data for comparisons between Site OW1 and the submerged macrophyte sites at Hopwoods Lagoon (Δh = depth difference).

Meteorological Forcing and Water Temperatures

Graphs showing the meteorological conditions, surface heat fluxes and water temperature profiles between 14 and 16 March 2001 and 28 and 30 December 2000 are included in Appendix G. All days were partly cloudy or overcast, and a small amount of rain was recorded on 28 and 30 December. Prevailing winds blew from the north or north-west during the morning and the north or north-east during the afternoon, and were generally stronger during the afternoon. Wind speeds peaked at $4\,\mathrm{m\,s^{-1}}$ during the March period and nearly $5\,\mathrm{m\,s^{-1}}$ during the December period. The most consistently windy day was 14 March, when wind speeds exceeded $2\,\mathrm{m\,s^{-1}}$ for most of the day. Conditions were calm overnight during the March period while wind speeds of $< 1.5\,\mathrm{m\,s^{-1}}$ were recorded overnight during the December period.

The water temperature profiles indicate that diurnal temperature cycles were similar throughout the two investigation periods. Site OW1 and the two submerged macrophyte sites became stratified to some extent on all days. Vertical temperature gradients were considerably stronger at the submerged macrophyte sites than at Site OW1, and stronger at Site SV1 than at Site SV2. The vertical stratification decayed overnight, with mixing evident over the entire water depth during December, and most of the depth during the March period.

Horizontal Temperature Differences and Inferred Convective Flows

Horizontal temperature differences between Site OW1 and the submerged macrophyte sites are shown in Figure 6.33. These were highly consistent between the two, and quite distinct from horizontal temperature differences between the various open water sites (Figure 6.32).

At **50 mm depth**, the submerged macrophyte sites were both warmer than Site OW1 during the day but slightly cooler overnight. For the moment neglecting advective effects, these temperature differences create a buoyancy forcing for convective surface flow from the submerged macrophyte zones towards the open water during the day, and in the opposite direction overnight.

The temperature difference at **400 mm depth** was generally in the opposite direction to that at 50 mm depth. This suggested that the surface convective flow was restricted to

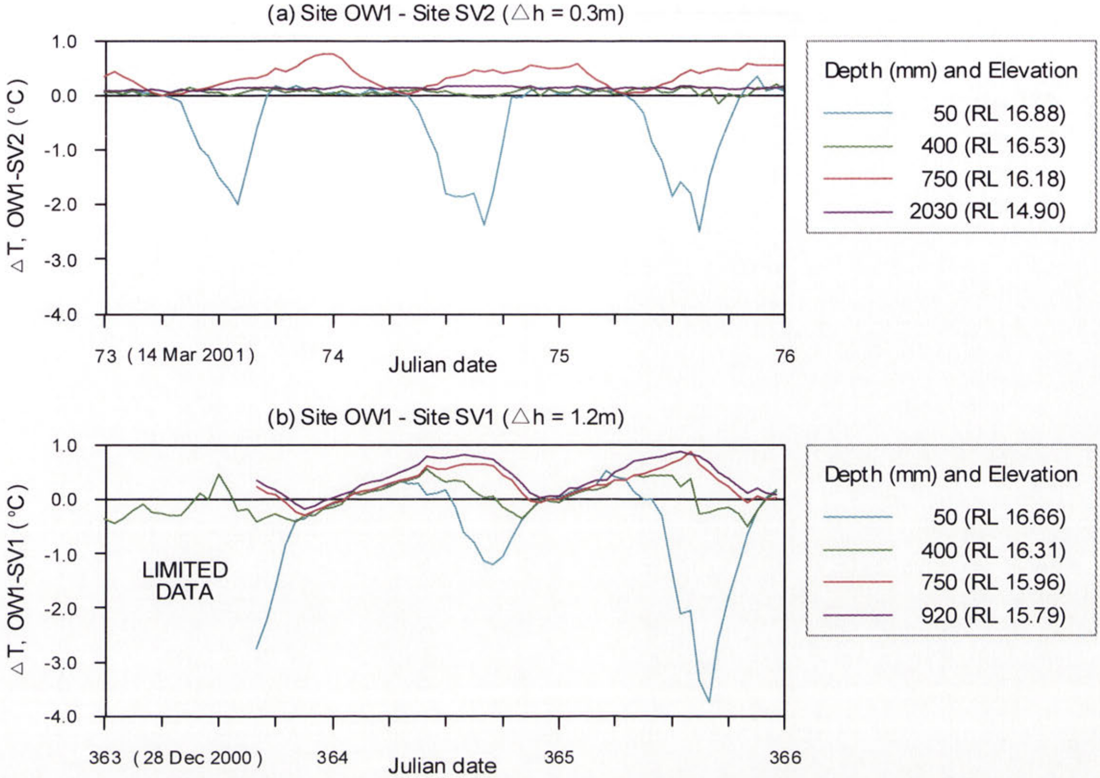

Figure 6.33: Horizontal temperature differences due to radiation shading by submerged macrophytes between Site OW1 and (a) Site SV2 from 13 to 15 March 2001, and (b) Site SV1 from 28 to 30 December 2000. Site details are given in Table 6.10.

a depth of less than 400 mm at Site SV2, while at Site SV1 it implied a deeper surface flow during the afternoon and evening ($>$ 400 mm) than during the morning heating phase ($<$ 400 mm depth).

The horizontal temperature differences at around **750 mm depth** suggested a warm intrusive flow from the open water towards the submerged macrophyte zones. This developed throughout the day and continued overnight until the early hours of the following morning when the temperatures again equalised between the two zones.

400 mm above the bed at the submerged macrophytes sites, Sites SV1 and SV2 were generally cooler than Site OW1. This suggested that the inferred intrusive flow from the open water at 750 mm depth extended towards the bed. Although there was insufficient data to examine horizontal temperature differences immediately above the bed in the submerged macrophyte zones, there may also have been a cold gravity current along the bed from the cooler submerged macrophyte zones towards the open water (James and Barko, 1991; Oldham and Sturman, 2001).

Summary of Radiation Shading by Submerged Macrophytes

The horizontal temperature differences presented in Figure 6.33 have demonstrated differential heating due to radiation shading between Site OW1 and submerged macrophyte sites at Hopwoods Lagoon. The observed trends at Site OW1 and the submerged macrophyte sites were highly consistent between the March (SV2) and December (SV1) data sets. In the absence of an emergent canopy at these sites, the observed differential heating is due to differential absorption of shortwave radiation within the water column and/or differences in depth.

Water temperature differences between the submerged macrophyte sites and Site OW1 were not consistent with differential heating due to the depth differences alone. The depth difference between Sites SV2 and OW1 (Δh=0.3 m) was similar to that between Sites OW1 and OW2 and Sites OW1 and OW4 (Δh=0.35–0.38 m), which both displayed only very small horizontal temperature differences. The water depth at Site OW1 was almost double the depth at Site SV1 (Δh = 1.2 m), but near-bed temperatures were cooler at Site SV1 throughout the diurnal cycle. This is inconsistent with differential heating due to depth differences alone, and suggests variation in the vertical distribution of heat between the open water and submerged macrophyte zones of the wetland. It was therefore concluded that the differential heating between Sites OW1 and SV1 was due primarily to radiation shading by submerged macrophytes and less significantly due to the depth difference between the two sites.

It was demonstrated in Section 6.5.5.1 that temperatures at Site OW1 are representative of the open water zones at Hopwoods Lagoon. It was also shown above that diurnal temperature trends were highly consistent between submerged macrophyte sites. The inferences made above can therefore be generalised across the open water and submerged macrophyte zones at Hopwoods Lagoon. If conditions were sufficiently calm and advective effects were minimal, horizontal temperature differences due to radiation shading by submerged macrophytes would be expected to drive the diurnal convective circulation regime illustrated schematically in Figure 6.34. Evidence for the existence of inferred convective flows such as these was presented earlier in Section 6.5.4 (Figure 6.24, p.255 and Figure 6.28, p.262). The implications of radiation shading by submerged macrophytes and the inferred convective flow regime are discussed in Chapter 7.

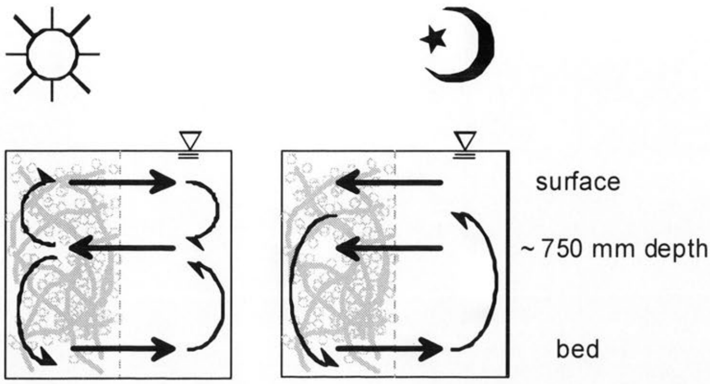

Figure 6.34: Inferred diurnal convective circulation regimes due to radiation shading by submerged macrophytes.

6.5.5.3 Effects of Submerged Macrophytes in Emergent Macrophyte Zones

At Hopwoods Lagoon, the emergent *Eleocharis sphacelata* did not occur without the submerged *Hydrilla verticillata*, so any differential heating between the emergent macrophyte and open water zones was also partly due to differential underwater absorption of radiation by submerged macrophytes. Section 6.5.5.1 considered the effect of depth differences and Section 6.5.5.2 addressed the effects of submerged macrophytes on differential heating. This section considers the additional influences of the emergent macrophytes on differential heating between shallow macrophyte and deeper open water zones.

Temperature differences between open water and submerged macrophyte sites which were examined in Section 6.5.5.2 are compared with horizontal temperature differences between the Sites OW1 and EV1 when subjected to the same meteorological forcing. Table 6.11 provides a summary of the physical characteristics and sources of meteorological and water temperature data used in these comparisons.

Site ID	Site Location	Δh (m) OW1 - Site	Dates	Meteorological Fluxes		Water Temperatures	
SV2	60 m N of OW1	0.30	14 to 16 Mar 2001	Fig. G.9	p.455	Fig. G.13	p.459
EV1	35 m NE of OW1	0.65					
SV1	50 m NE of OW1	1.20	28 to 30 Dec 2000	Fig. G.11	p.457	Fig. G.14	p.460
EV1	35 m NE of OW1	0.65					

Table 6.11: Physical characteristics and sources of data for comparisons between Site OW1 and the submerged and emergent macrophyte sites at Hopwoods Lagoon (Δh = depth difference).

Horizontal Temperature Differences and Inferred Convective Flows

Figure 6.35 shows horizontal temperature differences between Site OW1 and the macrophyte sites in March 2001 and December 2000. These showed many similarities between the emergent and submerged macrophyte sites, despite the depth differences. Meteorological fluxes and water temperature profiles for these periods are shown in Figures G.9 to G.14 in Appendix G.

At **50 mm depth**, both the submerged and emergent macrophyte sites were warmer than the open water between the start of the heating phase and the late evening. Overnight, both the emergent macrophyte zones were cooler than the open water. In the absence of wind-induced advective surface currents, these temperature differences established a buoyancy forcing for horizontal convective flow from the macrophyte zones towards the open water zone during the day, and in the opposite direction overnight.

At **400 mm depth**, the horizontal temperature differences were much smaller than at 50 mm depth. They were generally in the same direction as surface differences during the afternoon and the early evening but in the opposite direction overnight and during the morning. This suggested that the inferred convective surface flow out of the macrophyte zones towards the open water was confined to a relatively shallow layer (< 400 mm) during the day, while the reverse flow overnight was deeper than 400 mm.

At **750 mm depth**, the horizontal temperature differences were smaller than at the surface but larger than at 400 mm depth, and generally in the opposite direction to the surface

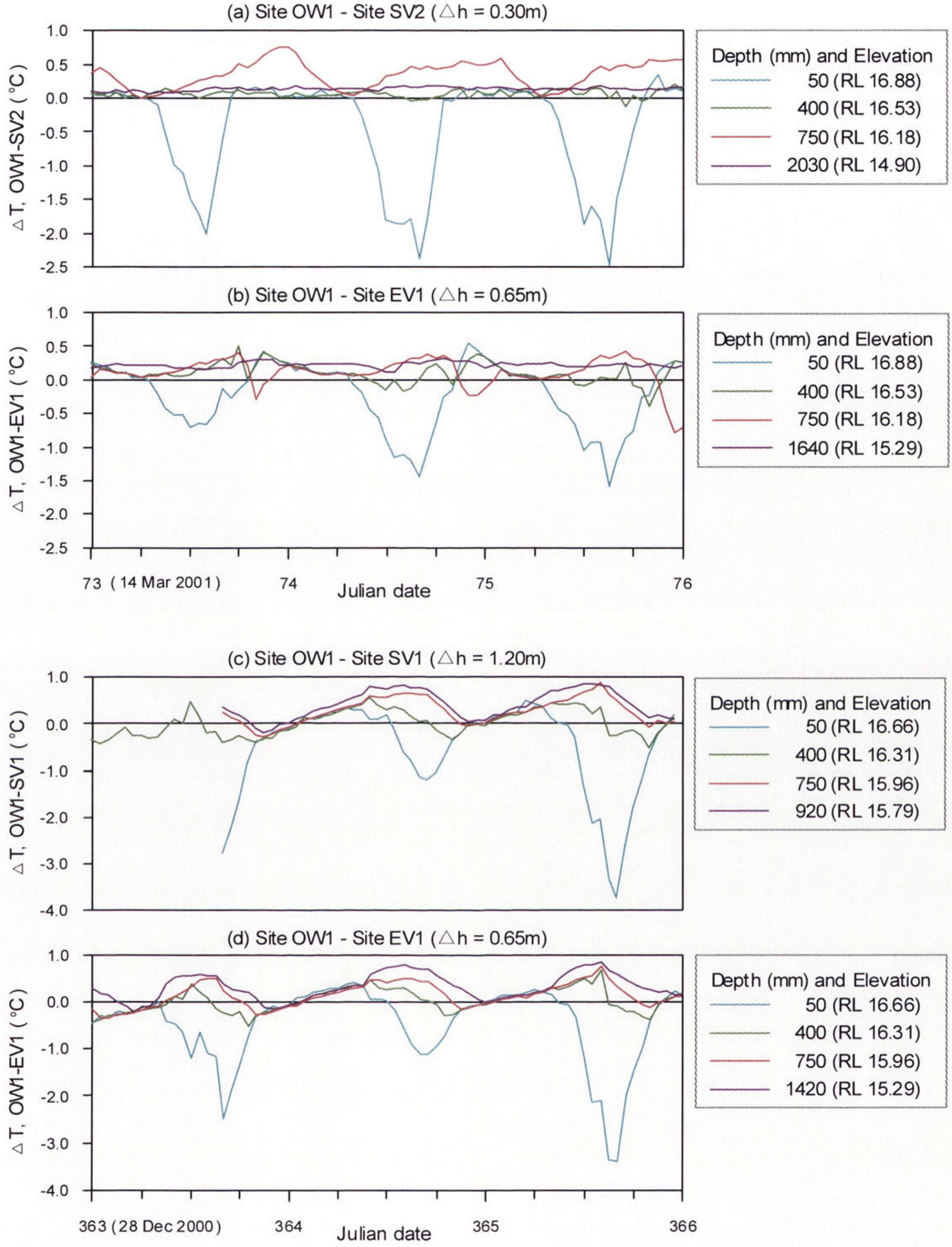

Figure 6.35: Horizontal temperature differences due to radiation shading by submerged and emergent macrophytes between Site OW1 and (a) Site SV2 from 14 to 16 March 2001, (b) Site EV1 from 14 to 16 March 2001, (c) Site SV1 from 28 to 30 December 2000, and (d) Site EV1 from 28 to 30 December 2000.

temperature difference. This could have driven a warm intrusive flow from the open water towards the macrophyte zones throughout much of the diurnal cycle.

Around **400 to 500 mm above the bed** in the macrophyte zones, the macrophyte sites were marginally cooler than Site OW1 throughout the diurnal cycle. These implied that the inferred intrusive flow from the open water towards the macrophyte zones at 750 mm depth extended close to the bed during the December period, although the temperature differences were weaker during the March period.

Summary of Effects of Submerged Macrophytes in Emergent Macrophyte Zones

Comparisons between the emergent and submerged macrophyte sites during these two investigation periods suggest that:

- radiation shading by the sparse emergent *Eleocharis sphacelata* canopy at Hopwoods Lagoon is minimal in addition to radiation shading by the submerged *Hydrilla verticillata*
- the shallow surface layer above the top of the submerged *Hydrilla* mat heats and cools more rapidly than the partly shaded surface layer in the emergent macrophyte zones, creating stronger horizontal temperature differences between the open water and submerged macrophyte sites
- radiation shading by either submerged macrophytes or a combination of submerged and emergent macrophytes leads to significant differential heating and cooling, which establishes a buoyancy forcing for convective flows between open water and macrophyte zones.

6.5.5.4 Radiation Shading by Emergent Macrophytes

In an attempt to isolate the effects of radiation shading due to emergent macrophytes, comparisons were made between a number of sites in the emergent macrophyte zones at Hopwoods Lagoon. Details of these sites and sources of meteorological and water temperature data for the comparison periods are listed in Table 6.12. Site locations were shown in Figure 5.5 (page 161). Site EV2 was located close to Site EV1 in the main emergent macrophyte zone at the northern end of the lagoon. Site EV3 was located near the centre of the semi-enclosed embayment at the northern end of the lagoon, and largely isolated from the main body of the lagoon by a shallow sill across its entrance. Site EV4 was located at the southern end of the lagoon.

Site ID	Site Location	Δh (m) OW1 - Site	Dates	Meteorological Fluxes		Water Temperatures	
EV2	50 m NE of OW1	0.95	18 to 20 Feb 2001	Fig. G.15	p.461	Fig. G.16	p.462
EV1	35 m NE of OW1	0.65					
EV3	115 m NE of OW1	0.95	25 to 27 Mar 2001	Fig. G.17	p.463	Fig. G.18	p.464
EV1	35 m NE of OW1	0.65					
EV4	270 m SW of OW1	1.00	23 to 25 Oct 2001	Fig. G.19	p.465	Fig. G.20	p.466
EV1	35 m NE of OW1	0.65					

Table 6.12: Physical characteristics and sources of data for comparisons between Site OW1 and the emergent macrophyte sites at Hopwoods Lagoon (Δh = depth difference).

Meteorological Forcing and Water Temperatures

Meteorological conditions, surface fluxes and water temperature profiles for the three investigation periods are shown in Figures G.15 to G.20 in Appendix G. With the exception of clear skies on 27 March 2001, all days were partly cloudy, and it was overcast with some rain on 25 March and 24 October. Wind speeds were generally $< 4\,\mathrm{m\,s^{-1}}$ throughout the investigation periods, but increased to $\sim 5.5\,\mathrm{m\,s^{-1}}$ on the afternoon of 25 October, while 25 March was comparatively calm ($u_{10} < 2\,\mathrm{m\,s^{-1}}$ all day). Winds blew predominantly from the north or north-east during the day from 18 to 20 February and 23 to 25 October and the west or south-west between 25 and 27 March. The only appreciable overnight winds were from the west early on 18 February and from the south on 25 March.

The water temperature profiles in Appendix G show that vertical temperature stratification developed at both the open water and emergent macrophyte sites on all days, with the exception of 25 February 2001 when it was raining. The vertical temperature gradients were stronger at the emergent macrophyte sites than at Site OW1. These decayed overnight to approximately isothermal conditions during the February and March investigation periods, but all sites remained weakly stratified overnight during the period in October.

Horizontal Temperature Differences and Inferred Convective Flows

Horizontal temperature differences between Sites OW1 and EV1 and the other emergent macrophyte sites are shown in Figure 6.36. As for comparisons involving submerged macrophyte sites, the horizontal temperature differences shown in Figure 6.36 were generally consistent between the four emergent macrophyte sites, and distinct from those observed between the different open water sites (Figure 6.32).

At **50 mm depth**, the emergent macrophyte zones were warmer than the open water from the beginning of the heating phase until several hours after the beginning of the cooling phase and cooler overnight than the open water. In each investigation period, the temperature differences were similar between the two emergent macrophyte sites, with the exception of Sites EV1 and EV4 during the windier October period. These sites were located at opposite ends of the lagoon and separated by a much larger distance than the remaining emergent macrophyte sites (Figure 5.5). Neglecting wind-induced advective effects, these horizontal temperature differences provide the buoyancy forcing for a convective surface flow from the emergent macrophyte zones towards the open water during the day with a weaker reverse flow overnight.

At **400 mm depth**, the horizontal temperature differences followed similar trends to those observed at 50 mm depth, with small differences in timing. These similarities imply that the inferred surface currents were at least 400 mm deep.

At **750 mm depth**, the emergent macrophyte zones were generally cooler than the open water during the day, with the exception of Site EV4 which was warmer than Site OW1 on 23 October. The emergent macrophyte sites generally remained cooler than the open water overnight and temperature differences were similar in magnitude to those at shallower depths. These observations suggested a warm intrusive flow from the open water towards the emergent macrophyte zones throughout much of the diurnal cycle.

Around **500 mm above the bed** at the emergent macrophyte sites, the horizontal temperature differences were similar in magnitude and generally in phase with those at 750 mm depth, which suggested that the inferred intrusive flow at 750 mm depth extended close to the bed. It is also probable that a dense gravity current developed at the bed during the

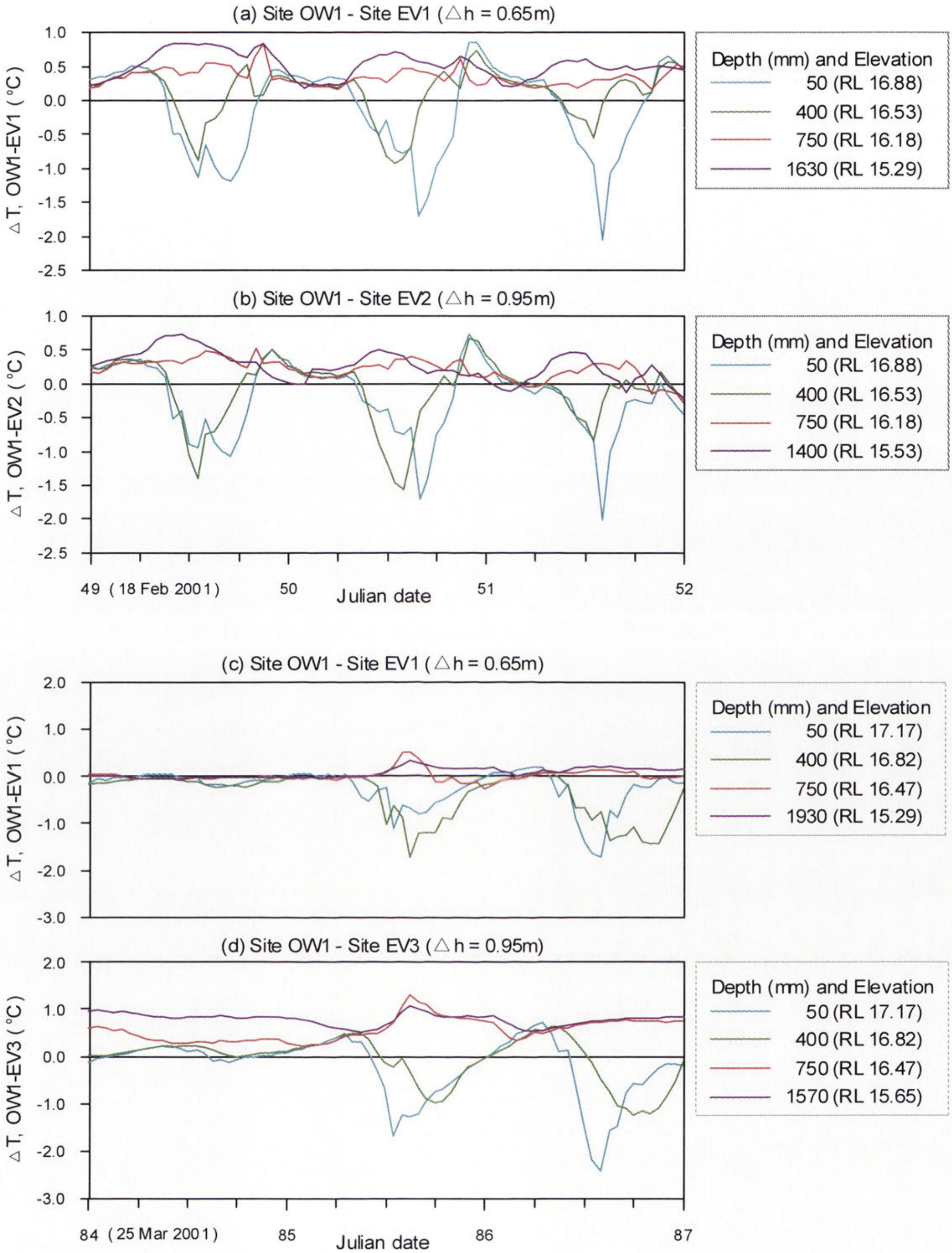

Figure 6.36: Horizontal temperature differences due to radiation shading by emergent macrophytes between Site OW1 and (a) Site EV1 from 18 to 20 February 2001, (b) Site EV2 from 18 to 20 February 2001, (c) Site EV1 from 25 to 27 March 2001, and (d) Site EV3 from 25 to 27 March 2001

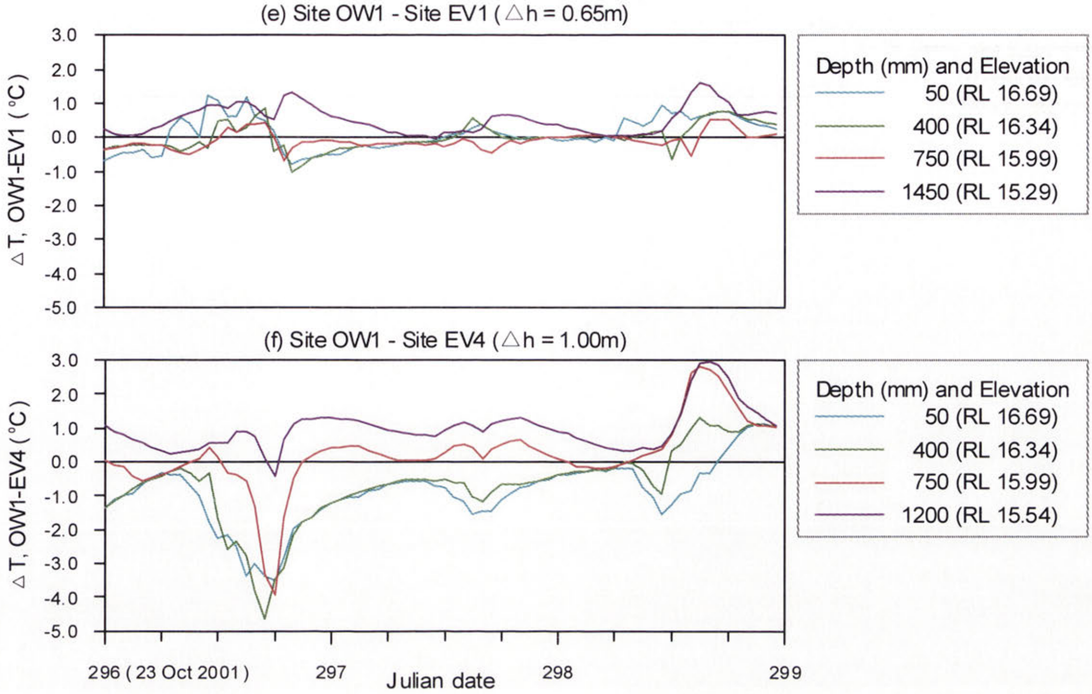

Figure 6.36 (continued): Horizontal temperature differences due to radiation shading by emergent macrophytes between Site OW1 and (e) Site EV1, and (f) Site EV4 from 24 to 26 October 2001.

day from the cooler emergent macrophyte zone towards the deeper, warmer open water (James and Barko, 1991; Oldham and Sturman, 2001), although there is insufficient data to demonstrate this.

The inferred convective flow regime was essentially the same as for the examples of radiation shading by submerged macrophytes, which suggests that additional radiation shading by emergent *Eleocharis sphacelata* is insignificant at Hopwoods Lagoon.

Summary of Radiation Shading by Emergent Macrophytes

It was earlier demonstrated (Section 6.5.4) that water temperatures at Site OW1 are representative of those in the open water zones at Hopwoods Lagoon. Figure 6.5.5.4 shows generally consistent trends between emergent macrophyte sites distributed throughout the lagoon. The temperature differences between Site OW1 and the emergent macrophyte sites can therefore be considered representative of those between open water and emergent macrophyte zones at Hopwoods Lagoon.

In the absence of strong wind-driven currents, temperature differences between the open water and emergent macrophyte sites establish a buoyancy forcing for convective exchanges between the two zones, as shown schematically in Figure 6.37. These are essentially the same as the convective flows inferred to result from radiation shading by submerged macrophytes alone (Figure 6.34). The only significant distinction is a differential cooling effect: a slight lag was observed in the change of sign of the horizontal temperature difference at 50 mm depth due to insulation from the emergent canopy. The implications of radiation shading by emergent and submerged macrophytes and the inferred convective flow regimes are discussed in Chapter 7.

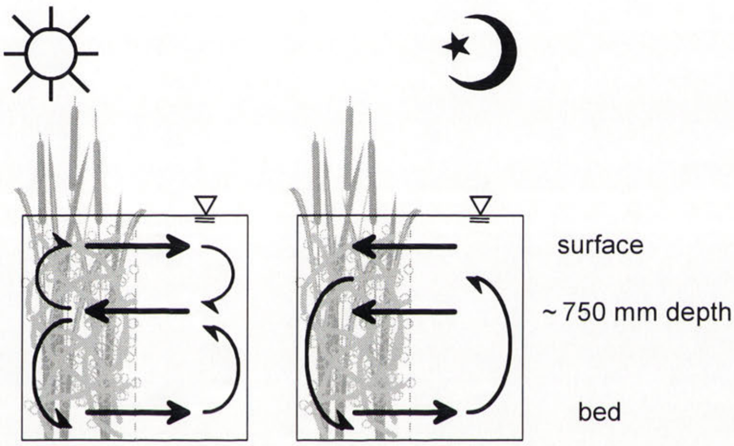

Figure 6.37: Inferred diurnal convective circulation regimes due to radiation shading by submerged and emergent macrophytes in the emergent macrophyte zones.

6.5.5.5 Summary of Radiation Shading at Hopwoods Lagoon

These examples of radiation shading between submerged and emergent macrophyte zones and open water have demonstrated significant differential heating at Hopwoods Lagoon. This appears to have resulted primarily from radiation shading by submerged *Hydrilla verticillata*, with only a minimal contribution from the sparse emergent *Eleocharis sphacelata* canopy. The relative importance of differences in depth and radiation shading by submerged and emergent macrophytes are discussed in Chapter 7.

6.6 Numerical Modelling Results

6.6.1 Results of Model Calibration and Validation

The values of the model parameters for the four calibration periods shown in Table 5.8 (page 177) are summarised in Table 6.13. These are consistent with values quoted in the literature, and were determined as discussed in the following sections. Simulated water temperatures and velocities during the four calibration periods are subsequently presented in Figure 6.38 and goodness of fit statistics are summarised in Table 6.14 (page 287).

Model Parameter	Units	Open Water	Emergent Macrophytes	Submerged Macrophytes	Further Details
η	m^{-1}	2.5	6.5	6.5	Section 6.6.1.2
z_0	m	see Table 6.15	see Table 6.15	see Table 6.15	
d_0	m	0.0	0.67	0.0	
h_s	m	1.9	1.9	1.9	Section 6.6.1.3
K_s	$m^2\,s^{-1}$	7.5×10^{-7}	7.5×10^{-7}	7.5×10^{-7}	
c_s	$J\,m^{-3}\,^{o}C^{-1}$	3.39	3.39	3.39	
LAI	m^2m^{-2}	–	0.5	–	Section 6.6.1.4
c_1	–	–	0.212	–	
c_2	–	–	0.795	–	
c_3	–	–	-0.007	–	
$C_{Dx} = C_{Dy}$	–	–	3.2	3.2	
$\varepsilon'_{xz} = \varepsilon'_{yz}$	$Pa\,s^{-1}$	1.0	1.0	1.0	Section 6.6.1.5
D'_z	$m^2\,s^{-1}$	see Figure 6.44	see Figure 6.44	see Figure 6.44	
$\varepsilon'_{xx} = \varepsilon'_{xy} = \varepsilon'_{yx} = \varepsilon'_{yy}$	$Pa\,s^{-1}$	1.0	1.0	1.0	
$D'_x = D'_y$	$m^2\,s^{-1}$	1.4×10^{-7}	1.4×10^{-7}	1.4×10^{-7}	
k_s	–	1.0	1.0	1.0	
ν_s	$m^2\,s^{-1}$	1.0×10^{-3}	1.0×10^{-3}	1.0×10^{-3}	

Table 6.13: Parameter values determined during the four calibration periods for simulations at Hopwoods Lagoon.

Only the aerodynamic roughness length and the vertical diffusivity were varied between the four seasons, as discussed in the following sections. It was found during model calibration and validation that the simulated temperatures and velocities were more sensitive to these parameters than to the underwater attenuation coefficients, the vegetation parameters or the horizontal mixing parameters.

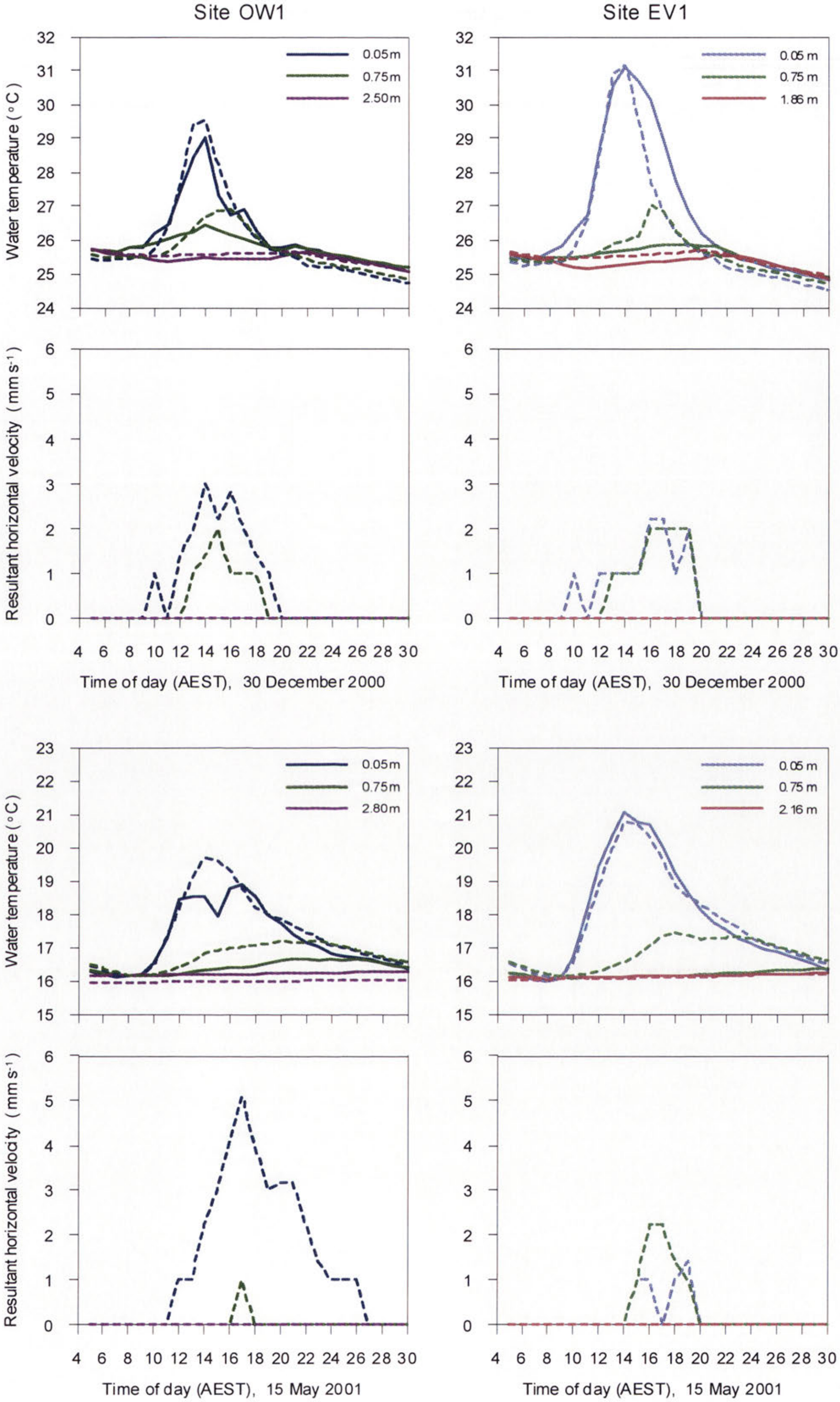

Figure 6.38: Simulated (– – –) and measured (——) water temperatures and horizontal velocities for the model calibration periods: 30 December 2000 and 15 May 2001

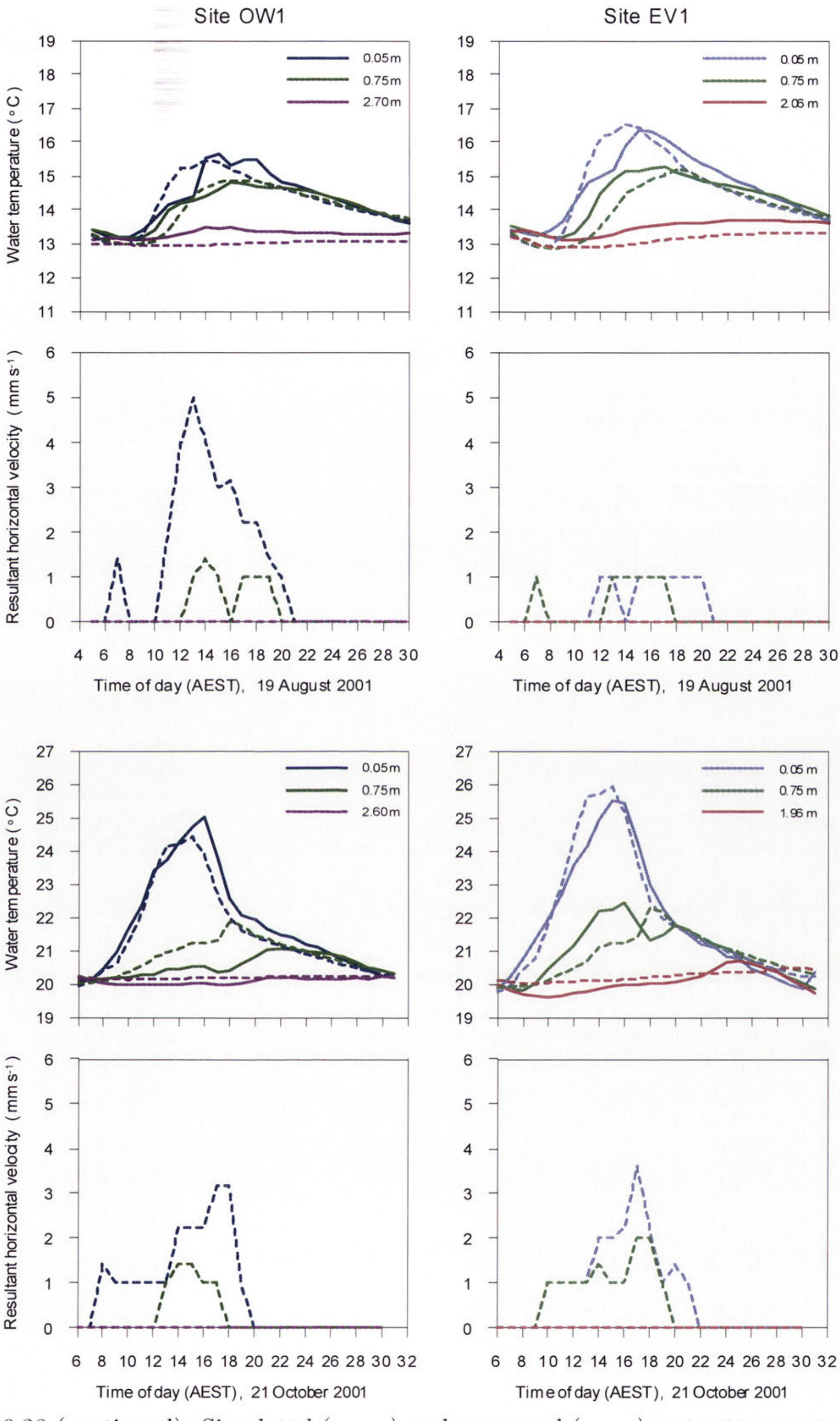

Figure 6.38 (continued): Simulated (- - -) and measured (——) water temperatures and horizontal velocities for model calibration periods: 19 August 2001 and 21 October 2001.

Calibration Period	Site ID	Depth (m)	n	$RMSE$ (°C)	Bias (°C)	Var (°C^2)
30 December 2000 05:00 to 06:00 31 Dec	OW1	0.05	26	0.434	-0.148	0.166
		0.75	26	0.328	-0.108	0.096
		2.50	26	0.098	0.057	0.006
		overall	156	**0.329**	**-0.099**	**0.099**
	EV1	0.05	26	0.801	-0.517	0.374
		0.75	26	0.369	0.017	0.136
		1.86	26	0.178	0.130	0.015
		overall	156	**0.565**	**-0.123**	**0.304**
15 May 2001 05:00 to 06:00 16 May	OW1	0.05	26	0.455	0.219	0.159
		0.75	26	0.396	0.334	0.045
		2.80	26	0.228	-0.228	0.000
		overall	156	**0.397**	**0.086**	**0.150**
	EV1	0.05	26	0.260	0.005	0.068
		0.75	26	0.734	0.608	0.168
		2.16	26	0.041	-0.033	0.001
		overall	156	**0.630**	**0.403**	**0.234**
19 August 2001 05:00 to 06:00 20 Aug	OW1	0.05	26	0.352	-0.046	0.122
		0.75	26	0.197	-0.068	0.034
		2.70	26	0.296	-0.278	0.011
		overall	156	**0.371**	**-0.198**	**0.098**
	EV1	0.05	26	0.458	-0.098	0.200
		0.75	26	0.391	-0.284	0.073
		2.06	26	0.361	-0.352	0.007
		overall	156	**0.379**	**-0.177**	**0.112**
21 October 2001 06:00 to 07:00 21 Oct	OW1	0.05	26	0.418	-0.283	0.095
		0.75	26	0.516	0.278	0.189
		2.60	26	0.123	0.106	0.004
		overall	156	**0.298**	**-0.138**	**0.070**
	EV1	0.05	26	0.472	0.099	0.213
		0.75	26	0.540	-0.130	0.275
		1.96	26	0.304	0.160	0.067
		overall	156	**0.442**	**0.131**	**0.178**

Table 6.14: Root mean square error, bias and variance for the model calibration results shown in Figure 6.38. The "overall" statistics for each period were calculated using measured and simulated temperatures from all monitoring depths at Sites OW1 and EV1.

6.6.1.1 Simulated Water Temperatures

The simulated water temperatures during the four model calibration periods are compared with the measured water temperatures at Site OW1 and EV1 in Figure 6.38, and goodness of fit statistics were summarised in Table 6.14.

Diurnal Temperature Simulation

The model reproduced the observed diurnal water temperature variation at Sites OW1 and EV1 during the four calibration periods, from approximately isothermal conditions at the commencement of the heating phase to approximately isothermal conditions at the end of the cooling phase.

The **timing of the peak water surface temperature** coincided with the measured peak surface temperature at both sites on 30 December 2000, and at Site EV1 on 15 May and 21 October 2001. The predicted peak preceeded the observed peak temperature by about =1.0 hr at both sites on 19 August and at Site OW1 on 21 October 2001. During the August calibration runs (top of page 286), the model had difficulty simulating the observed stepped heating profile during the later stages of the morning, and reached the peak temperature earlier than observed. Mean wind speeds experienced during August were significantly higher than those in the other calibration periods, which suggested the problem involved parameterisation of the wind-induced mixing processes or the wind-influenced surface heat fluxes, H_L and H_S at higher wind speeds. The early predicted peak at Site OW1 on 21 October resulted from slight under-prediction of heating during the morning. The cause of the observed double hump in the surface temperature data at Site OW1 on 15 May 2001 is not known. This feature made it difficult to determine the true time of the peak surface temperature.

With the exception of Site OW1 on 15 May 2001, the **magnitude of the peak surface temperatures** predicted by the model were within $\pm 0.5°C$ of the corresponding peak measured surface temperature at both sites. The model generally slightly over-predicted the maximum surface temperature. Over the entire calibration period on each of the four selected dates shown in Figure 6.38, the average error ($RMSE$) between the predicted and measured water surface temperatures was $< 0.5°C$, with the exception of Site EV1 on 30 December 2001 (see Table 6.14). Here, although the model successfully simulated surface temperatures during the heating phase, it over-estimated surface cooling during the cooling phase. Near-bed temperatures were well simulated on 30 December and 15 May, with $RMSE < 0.25$°C at both sites. The average error over the remaining calibration periods was within ±0.4°C. These results suggested that errors in water temperature simulation were associated more with parameterisation of the surface heat fluxes than the bed heat flux.

The model success in predicting mid-depth temperatures was more variable. Temperatures around mid-depth (at z=0.75 m in Figure 6.38) were generally over-predicted by the model during the heating phase. The $RMSE$ over the four calibration periods was generally > 0.3°C, and as high as 0.7°C at Site EV1 on 15 May 2001, when near-isothermal conditions were measured over most of the water column but the model predicted some degree of vertical stratification. These results suggested simulation errors associated with the model parameterisation of the vertical transport of heat in the wetland.

Wetland Heat Content

Figure 6.39 compares the heat content of a 1 m^2 column of water surrounding Site OW1 and Site EV1 when calculated using the measured water temperatures and those predicted by the model, for the four calibration periods. The heat content over the depth of the water column (H) was calculated by adding the heat content of a number (n) of horizontal layers, as follows:

$$H = \sum_{i=1}^{n} H_i = \sum_{i=1}^{n} T_i \, \rho_w(T_i) \, c_{pw}(T_i) \, V_i \tag{6.13}$$

where

H_i	=	heat content of layer i with a base area of 1 m^2 (J)
T_i	=	average temperature of layer i, calculated from the temperatures at the top and bottom of the layer (°C)
$\rho_w(T_i)$	=	average density of layer i, calculated using Equation A.13 (kg m^{-3})
$c_{pw}(T_i)$	=	average specific heat capacity of layer i, calculated using Equation A.15 in Appendix A (J kg^{-1} °C^{-1})
V_i	=	volume of layer i (m^3).

The plots show that there was generally very good agreement between the heat content calculated using the measured and simulated water temperatures at Sites OW1 and EV1, despite the variable success of the model in predicting water temperatures around mid-depth. The model hourly heat content was within 2% of the field hourly heat content over the full calibration period on 30 December 2000 and 21 October 2001, and within 3.6% on 15 May and 19 August 2001. The close agreement between the heat content calculated using the measured and the predicted water temperatures throughout the entire calibration period in each season suggested that there was no systematic tendency for the model to accumulate or lose heat.

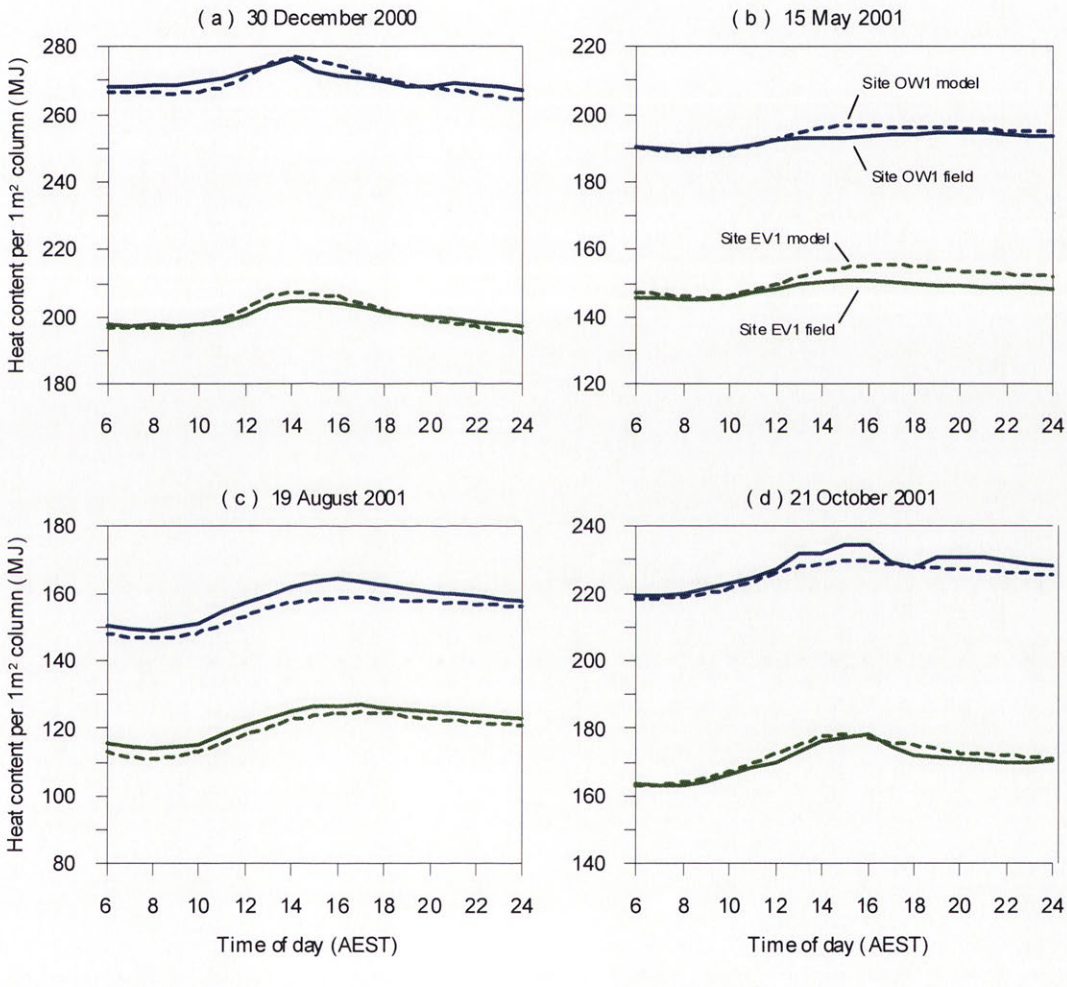

Figure 6.39: Measured (field, ——) and simulated (model, - - -) heat content per 1 m^2 *column of water at Sites OW1 and EV1 over the four calibration periods.*

6.6.1.2 Surface Heat Flux Parameters

The net surface heat flux formed the upper thermodynamic boundary condition in the model and represented the major source of energy to the wetland. The calibration effort focused first on the heating phase of the diurnal cycle, and then on the cooling phase. Heating in the model is due primarily to absorption of shortwave radiation, while evaporation is the dominant surface heat loss mechanism during the cooling phase.

Underwater Attenuation of Shortwave Radiation, η

The attenuation coefficient for shortwave radiation determines the vertical distribution of shortwave radiative heating over the water depth. Higher values for η concentrate heating near the water surface with minimal heating at the bed, causing a strong vertical temperature gradient. Lower values of η allow greater radiative heating at depth, with the lower limit of $\eta = 0$ corresponding to uniform vertical heating of the water column. Underwater attenuation coefficients calculated from field measurements (Section 6.4.2, page 227) were used as initial estimates during the model calibration.

Figure 6.40 shows measured and simulated temperatures and simulated resultant horizontal velocities for the field η and the final model η values for 15 May 2001. The irregular measured surface temperature profile at Site OW1 is difficult to explain from the meteorological data. Although there was some broken cloud around midday, it did not significantly affect the air temperatures at the AWS or the water surface temperatures at Site EV1, and was not sufficient to reduce the surface water temperature so dramatically at Site OW1. Instead, it can only be supposed that there was some transitory interference with the surface thermistor or float by waterfowl or fish in the lagoon. However, while the surface temperatures appear suspicious around midday at Site OW1, they are reasonable and consistent with surrounding days in May during the remainder of the diurnal cycle.

The mean field values of $\eta_{OW} = 1.8\,\mathrm{m}^{-1}$ in the open water and $\eta_{SV} = 4.4\,\mathrm{m}^{-1}$ in the emergent and submerged macrophyte zones were found to be too low to replicate the observed heating phase. Temperatures predicted using the field values for η_{OW} and η_{SV} were up to 1.3°C too low near the surface and up to 1.3°C too high at mid-depth in both zones, although within 0.2°C near the bed. At Site OW1, the calculated $RMSE$=0.486°C,

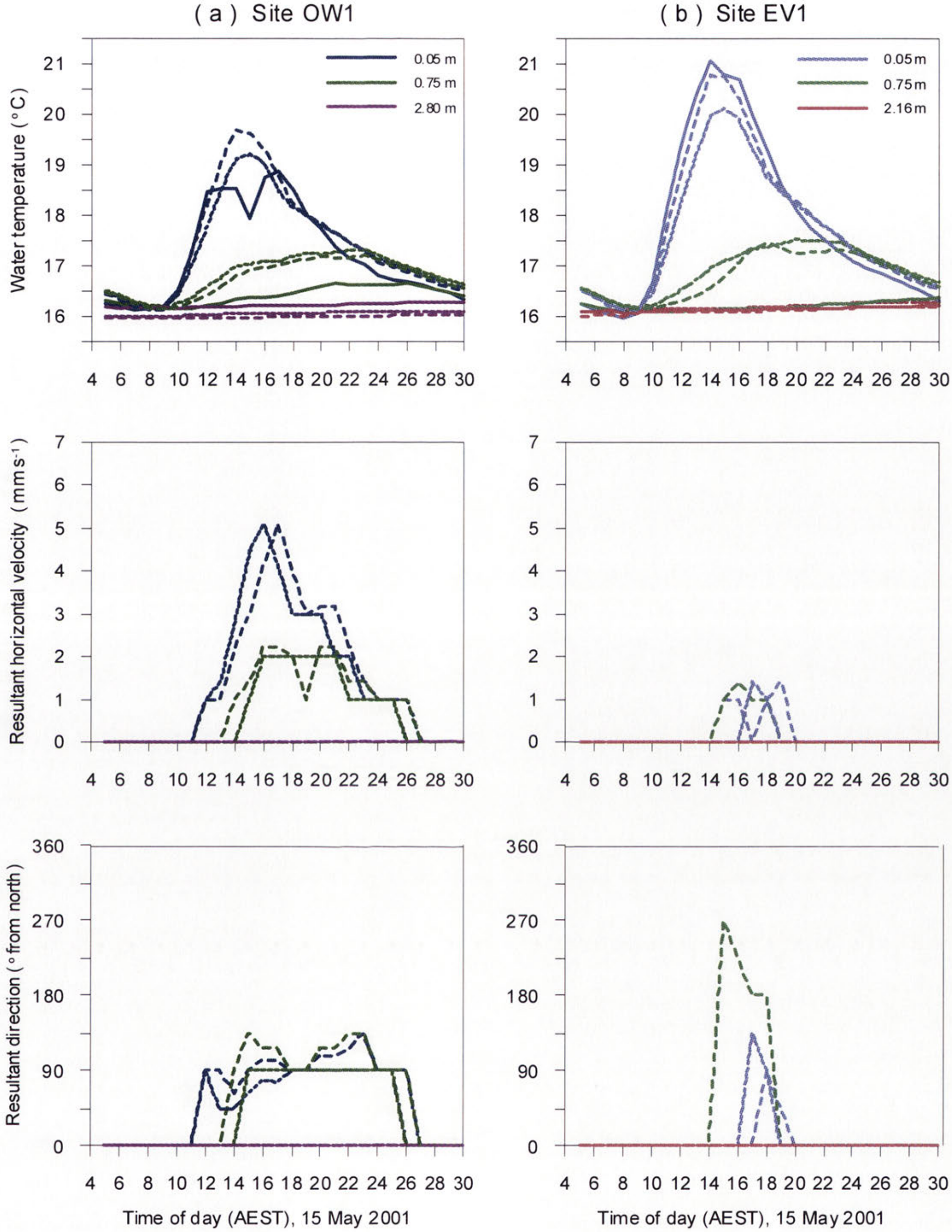

Figure 6.40: Effect of underwater attenuation coefficients at (a) Site OW1 and (b) Site EV1: water temperatures and resultant horizontal velocities on 15 May 2001, using field values (.......) of $\eta_{OW} = 1.8\,\mathrm{m}^{-1}$ and $\eta_{SV} = 4.4\,\mathrm{m}^{-1}$, and model values (– – –) of $\eta_{OW} = 2.5\,\mathrm{m}^{-1}$ and $\eta_{SV} = 6.5\,\mathrm{m}^{-1}$. Solid lines (——) represent measured temperatures.

B=0.425°C and S=0.055°C^2 at mid-depth were all larger (indicating a poorer fit to the field data) than those calculated using the model values of $\eta_{OW} = 2.5\,\mathrm{m}^{-1}$ and $\eta_{SV} = \eta_{EV} = 6.5\,\mathrm{m}^{-1}$ (reported in Table 6.14). The statistics were similar near the bed for the field and model η values. At Site EV1, the $RMSE$, B and S were higher at all three depths shown in Figure 6.40 for the field η than for the model η, again indicating a poorer fit to the measured temperatures ($RMSE = 0.523, 0.842, 0.059$°C for z=0.05, 0.75, 2.16 m, respectively). Resultant horizontal velocities were similar in magnitude and direction for the field and model η values. Similar temperature and velocity comparisons were observed for the other calibration periods.

Constant values were adopted for η_{OW} and η_{SV} with time and day and season, despite slight theoretical and observed changes with solar elevation. This was consistent with Kirk (1983), as discussed in Section 6.4.2. The density of emergent *Eleocharis sphacelata* at Hopwoods Lagoon was so low ($LAI \leq 0.51$) that it was considered to make a negligible contribution to the underwater attenuation of shortwave radiation. Submerged *Hydrilla verticillata* occurred in all locations supporting *Eleocharis*, and it was therefore assumed that $\eta_{EV} = \eta_{SV}$.

There are several possible reasons for the discrepancy between the field and model values of the attenuation coefficients. The simple form of Beers Law implemented in RMA-10, Equation (6.7), may not adequately describe attenuation of PAR near the surface in shallow highly coloured waters, such as Hopwoods Lagoon. This suggests that the empirical models of Henderson-Sellers (1984) and Zaneveld and Spinrad (1980) could warrant further investigation, although there was insufficient data from the present study to pursue this. The apparent field underestimation in η_{OW} and η_{SV} could also indicate overestimation of the downwards vertical heat transport in the model, which was commented upon earlier in relation to the calibration results. However, some increase over the field η is consistent with an expectation that η for global shortwave radiation should exceed η for PAR. The mean field values were approximately 70% of those adopted in the model, although the ratio of η_{model} to η_{field} was similar in both the open water and macrophyte zones.

Aerodynamic Roughness Length, z_0

The aerodynamic roughness length influences the fluxes of momentum, water vapour and heat across the water surface, and hence directly affects the latent and sensible heat fluxes. The value of z_0 is lowest over a smooth water surface and increases with surface irregularities caused by stronger winds.

Initial values estimated following the literature review were $z_0 = 0.23$ mm in the open water (Brutsaert, 1982) and submerged macrophyte zones, and $z_0 = 150$ mm in the emergent macrophyte zone (Garratt, 1992). Figure 6.41 shows measured and simulated temperatures and simulated horizontal velocities for the literature value of $z_{0OW} = 0.23$ mm and the final model value of $z_{0OW} = 6$ mm for 15 May 2001, with $z_{0EV} = 10$ mm in both simulations.

The initial (literature-based) estimate for z_0 in the open water zone led to insufficient cooling during the cooling phase:

- water surface temperatures were <0.5°C too warm at both Sites OW1 and EV1 during the evening and early morning
- mid-depth water temperatures were <0.8°C too warm at Site OW1 and <1.4°C too warm at Site EV1
- bed temperatures were within 0.2°C of the measured temperatures at both sites.

At both sites, the calculated goodness of fit statistics to the field data improved at the surface and mid-depth using the model values shown in Table 6.15, over the initial, literature-based estimate for z_{0OW}. By way of comparison with the statistics reported in Table 6.14 (page 287), for the literature values on 15 May 2001 $RMSE$=0.547°C and 0.515°C at z=0.05m and z=0.75m (Site OW1) and $RMSE$=0.308°C and 0.826°C at z=0.05m and z=0.75m (Site EV1).

Figure 6.41 shows that the magnitude and direction of resultant horizontal velocities was similar for literature-based and model z_0 values. Similar trends were observed for temperatures and velocities in the other model calibration periods.

The aerodynamic roughness length associated with the submerged macrophyte zones was set equal to z_0 in the open water zones, since the submerged *Hydrilla* did not penetrate

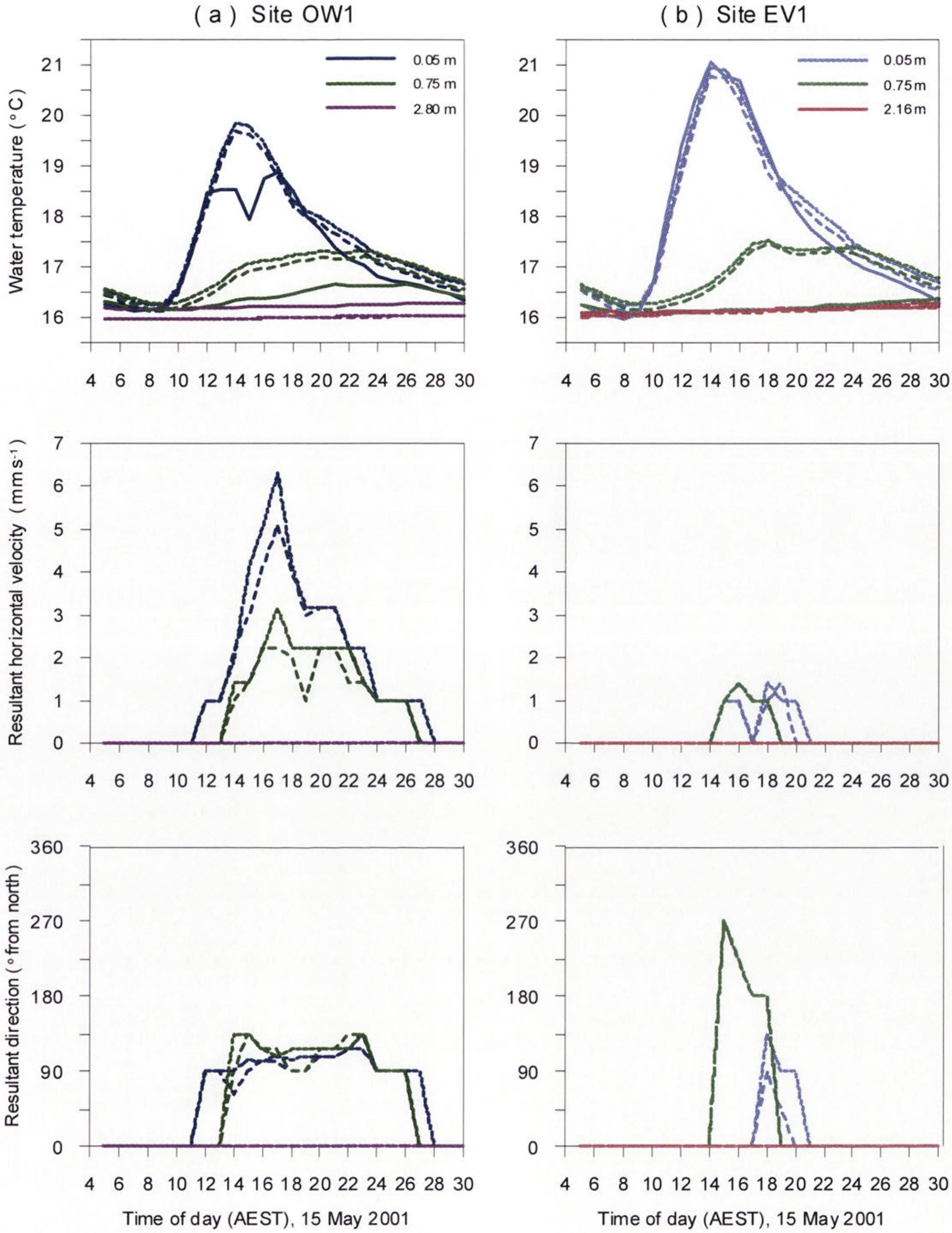

Figure 6.41: Effect of aerodynamic roughness length at (a) Site OW1 and (b) Site EV1: water temperatures and resultant horizontal velocities on 15 May 2001, using literature values (.......) of $z_{0\,OW} = 0.23$ mm and $z_{0\,EV} = 10$ mm, and model values (– – –) of $z_{0\,OW} = 6$ mm and $z_{0\,EV} = 10$ mm. Solid lines (——) represent measured temperatures.

Calibration Date	Season	Open Water	Emergent Macrophytes	Submerged Macrophytes
30 Dec 2000	Summer	3	10	3
15 May 2001	Autumn	2	10	2
19 Aug 2001	Winter	6	10	6
21 Oct 2001	Spring	3	10	3

Table 6.15: Seasonal variation in the aerodynamic roughness length, z_0 (mm) determined during the model calibration and validation.

the water surface and was not observed to dramatically affect the water surface roughness characteristics. Lower values were adopted for z_0 in the open water and submerged vegetation zones during the calmer months of summer and autumn than during the windier months of spring and winter, because the water surface was generally smoother.

However, even the lower values of z_0 determined during the model calibration were much larger than those reported in the literature over shallow water bodies. Equation (3.60) on page 93 shows that the latent heat flux is proportional to $1 / [\ln(z_M / z_0)] [\ln(z_V / z_{0V})]$, with all other variables unchanged, whereby H_L increases by 250% if z_0 is increased from 0.23 mm to 6 mm. The model requirement for such a high z_0 to simulate surface water temperatures in the open water zone during the cooling phase could indicate a potential problem with the latent heat flux parameterisation or the vertical transport of heat, or both. This was discussed in Section 6.6.1.1. The latent heat flux in the model assumes the validity of the logarithmic wind profile over the water surface, corrected for atmospheric stability. Any substantial deviation from this form would alter the physical significance of the aerodynamic roughness parameter.

Alternative, literature-based estimates for z_0 in the emergent macrophyte zone, $z_0 \sim 0.15\,h_L = 0.15$ m (Garratt, 1992) were excessive, as the water surface cooled too strongly during the cooling phase. A value of $z_0 = 10$ mm was found to be more appropriate during all four calibration periods, and is consistent with values reported in the literature for sparse grass canopies (Table 3.7 on page 90). This lower value is consistent with the very low density of the *Eleocharis* canopy at Hopwoods Lagoon ($LAI \leq 0.51$), compared with the agricultural crops and grasses on which the initial estimate was based (generally

$2 \leq LAI \leq 3$). The values cited in the literature also apply over a land surface while z_0 values over water are typically much lower. Further reductions in values of z_0 would be expected for a canopy emerging from the water surface, which is less horizontally-restrained than a canopy emerging from a solid substrate.

Zero-Plane Displacement Height, d_0

The zero-plane displacement height accounts for the apparent displacement of the logarithmic wind profile above a rough surface. The displaced logarithmic wind profile, Equation (3.59), is not highly sensitive to the value of d_0 when the wind measurement height is much greater than the canopy height, $z_M \geq 10\,h_L$ (Garratt, 1992), as is the case at Hopwoods Lagoon. The zero-plane displacement height was therfore held constant at $d_0 = 0.67\,h_L$ in the emergent macrophyte zones (Brutsaert, 1982) and $d_0 = 0$ elsewhere.

6.6.1.3 Bed Heat Flux Parameters

The bed heat flux module was used to generate temperature profiles within the sediment column, which formed the lower thermodynamic boundary condition in the model. The bed heat module incorporated direct shortwave radiative heating of the sediments and conductive heat exchange between the water column and the sediments.

Depth of Thermal Influence in the Sediments, h_s

The depth of thermal influence in the sediments is the depth below which the sediment temperature is essentially independent of the temperature of the overlying water. The sediment layers were of variable thickness in the model (Section H.7 in Appendix H), and increased with depth below the water-sediment interface. The number of sediment layers was varied during the model calibration to determine the depth of thermal influence.

Temporal variation in the temperature at the base of the sediment layer was considerable with $i_{max} = 4$ ($h_s = 0.4\,\mathrm{m}$), as shown in Figure 6.42, although the temperature variation was negligible for $i_{max} \geq 8$ ($h_s = 1.9\,\mathrm{m}$). This suggested $0.4 < h_s \leq 1.9\,\mathrm{m}$ for simulation with $\Delta\, t$=1.0 hr, and the model was subsequently run with $i_{max} = 8$.

Thermal Diffusivity of Sediments, K_s

The thermal diffusivity of the sediments controls the rate of heat transport across the interface between the water column and the sediments, and ranges from $(3.3 - 12.3) \times 10^{-6}\,\mathrm{m^2\,s^{-1}}$

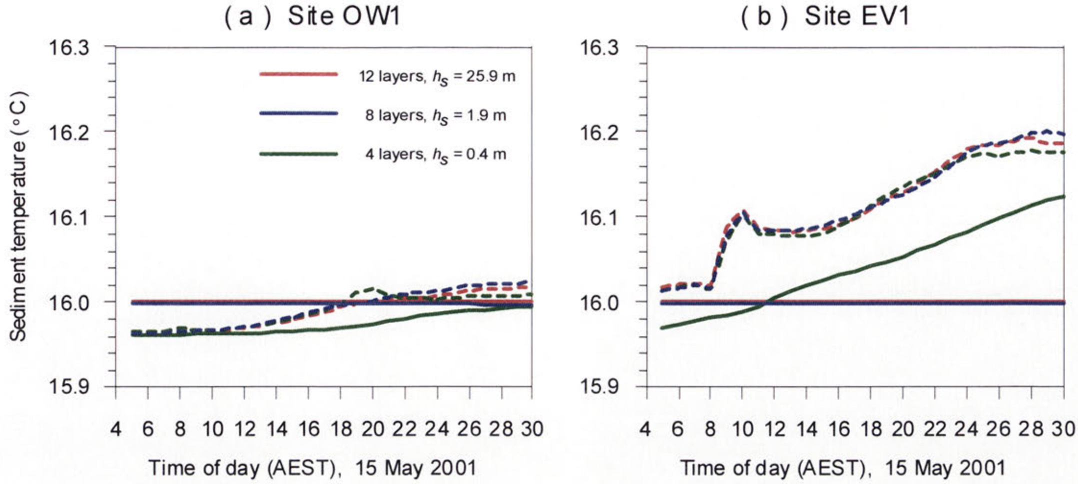

Figure 6.42: Determination of the depth of thermal influence in the sediments at (a) Site OW1 and (b) Site EV1 on 15 May 2001. Dashed lines (- - -) represent sediment temperatures 0.1 m below the water-sediment interface and solid lines (——) represent sediment temperatures at the depth of thermal influence, h_s.

for lake sediments (Benoit and Hemond, 1996; Fang and Stefan, 1998; Deas and Lowney, 2000). The model was run with K_s varying over this range, and simulated temperatures were compared with measured water temperatures at Sites OW1, EV1 and SV1. Simulated temperatures were not highly sensitive to the value of K_s within this range, and an intermediate value of $K_s = 7.5 \times 10^{-7} \mathrm{m}^2\,\mathrm{s}^{-1}$ was used in all model simulations.

Volumetric Heat Capacity of Sediments, c_s

The volumetric heat capacity is the quantity of heat involved in a temperature change by 1°C for a unit volume of sediments. It was estimated using sediment core data from Hopwoods Lagoon (Smeulders, 1999), as described in Appendix A. All simulations were run using $c_s = 3.39\,\mathrm{MJ\,m^{-3}\,°C^{-1}}$, which is within the range of $(1.4-3.8)\times10^3\,\mathrm{MJ\,m^{-3}\,°C^{-1}}$ reported in the literature (Fang and Stefan, 1998).

6.6.1.4 Macrophyte Parameters

Emergent Macrophyte Parameters: LAI and c_1, c_2, c_3

The *LAI* and the G-function were used to calculate the shortwave attenuation coefficient for the emergent macrophyte canopy, using Equations (6.5) and (6.6) on page 214. The *LAI* was determined from the results of the emergent macrophyte surveys, as reported in

Section 6.2.4), and the G-function was approximated using the simplified method of Nilson (1991). Nilson's coefficients were calculated from the canopy inclination data reported in Table 6.2 (page 192).

All model simulations at Hopwoods Lagoon were run with the field values of $LAI = 0.5$ and $c_1 = 0.212$, $c_2 = 0.795$, $c_3 = -0.007$ for Nilson's coefficients. The very sparse canopy density at Hopwoods Lagoon and small observed variation in canopy properties over the monitoring period meant seasonal variation in the model values of LAI and Nilson's coefficients was unwarranted. However, the LAI was varied during the hydrodynamic simulation experiments to investigate radiation shading by macrophytes of differing densities, as discussed in Section 6.6.3.

Vegetation Drag Coefficients, C_{Dx}, C_{Dy}

Vegetation drag coefficients were specified for both emergent and submerged macrophytes zones, since both contained submerged vegetation components. The vegetation resistance was predominantly due to submerged *Hydrilla verticillata* at Hopwoods Lagoon, and the sparse emergent *Eleocharis* was assessed to make a negligible contribution to the overall flow resistance. Identical drag coefficients were therefore used in the submerged and emergent macrophyte zones. It was assumed that the macrophytes were spatially uniform within the respective macrophyte zones, and vegetation drag was therefore made isotropic with $C_{Dx} = C_{Dy}$.

In the absence of alternative information, the projected area of the dense submerged macrophytes was assumed to be equivalent to the flow area. The *Hydrilla* at Hopwoods Lagoon was so dense that this was considered a reasonable approximation. It is also consistent with the argument of Wilson et al. (2003) that, in flexible vegetation there is a considerable momentum-absorbing area presented to the flow in addition to the traditionally applied projected frontal area. The model assumed that all Class 2 elements contained submerged macrophytes over their entire area while all Class 3 elements contained both submerged and emergent macrophytes over their entire area. Using this scheme, the edges between the open water and macrophyte zones were defined as sharp boundaries rather than comprising a transition between the two zones. This simplification may have contributed to irregularities in simulated temperatures and velocities near the boundaries of the wetland zones. Any such edge effects would have been consistent between simulations with the same horizontal distribution of macrophytes, but require consideration when comparing between results for different macrophyte distributions.

For mean flow velocities of $O(10^{-4} - 10^{-3})\,\mathrm{m\,s^{-1}}$ (Kadlec, 1990) and a mean stem diameter of 10 mm, stem Reynolds numbers are in the range $1 < Re_d < 10$. From Table 3.1 (page 46), the corresponding drag coefficients are $C_D = 10$ and $C_D = 3.2$. Drag coefficients generally decrease as vegetation density increases (Nepf, 1999), so the lower value of C_D=3.2 was selected. This is higher than the value of 1.2 determined by Nepf (1999), and $C_D \leq 0.5$ in the work of Danard and Murty (1994) for higher Re_d flows.

Because the resistance due to vegetation was not the main focus of the present study and was only represented by a simple parameterisation in the model, all simulations were run with the same drag coefficient. However, the model was also run without drag in the macrophyte zones, to give some qualitative indication of the influence of vegetation drag on wetland hydrodynamics. Temperatures and velocities predicted from otherwise identical simulations run with and without vegetation drag are compared in Figure 6.43.

Temperatures predicted by the model were identical for simulations run with and without vegetation drag. This suggested that the difference in horizontal velocities between the two simulations was insufficient to markedly affect the temperature structure at the two sites shown in Figure 6.43. As expected, by removing the vegetation resistance force, the resultant horizontal velocities were higher for $C_{Dx} = C_{Dy}$=0 than for $C_{Dx} = C_{Dy}$=3.2. At Site EV1, the no-drag peak horizontal velocities near the surface were almost three times those predicted when vegetation drag was imposed, and around double those at mid-depth. Near the surface and mid-depth at Site OW1, the no-drag peak velocities were also almost double those predicted when vegetation drag was modelled. Velocities were higher in the open water zone than in the emergent macrophyte zone due to wind speed attenuation by the emergent canopy. The directions of the resultant horizontal velocities were similar for the two simulations and generally within 45° at Site EV1, and almost identical at Site OW1.

The simulation results shown in Figure 6.43 indicated that, while the imposition of vegetation drag does not significantly influence the temperature structure or the direction

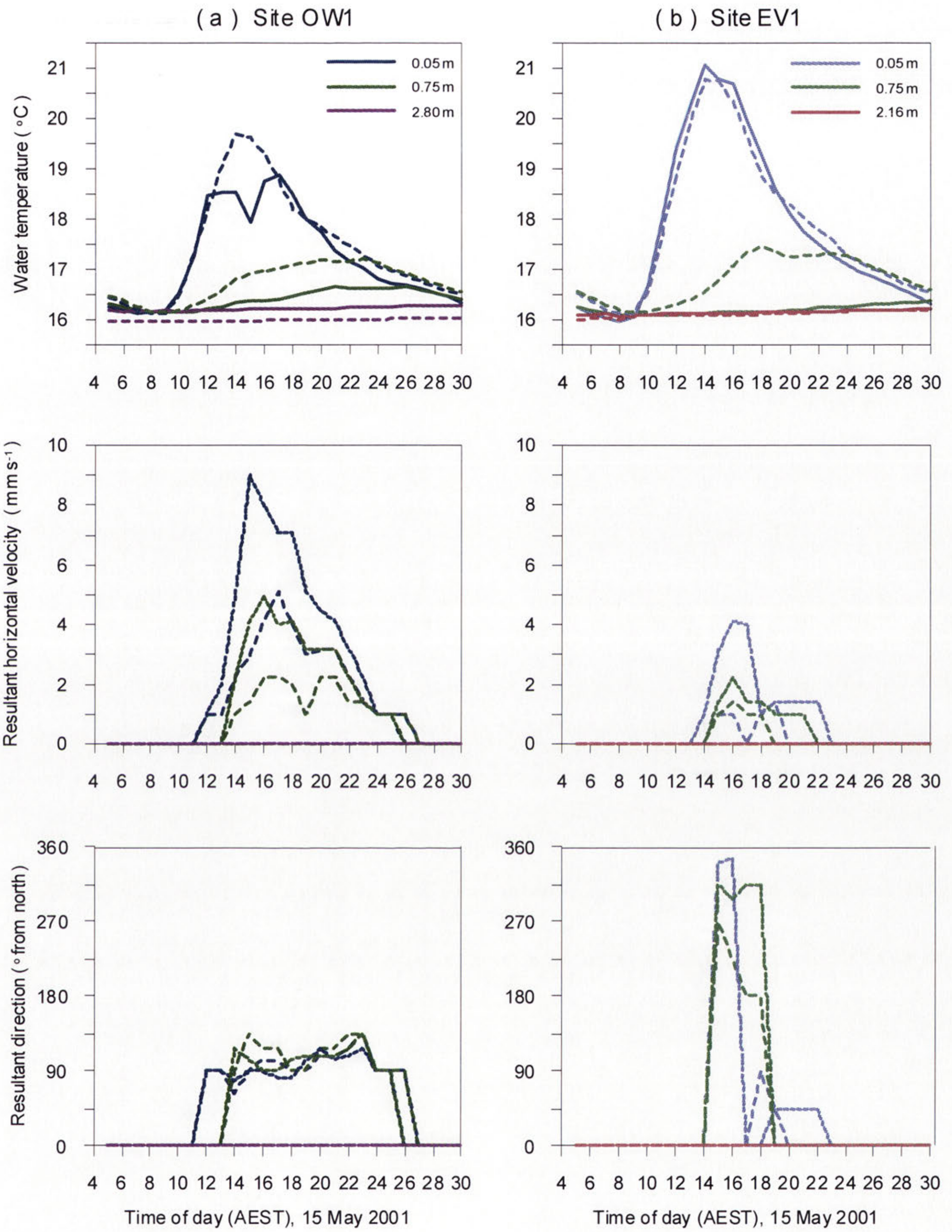

Figure 6.43: Effect of vegetation drag at (a) Site OW1 and (b) Site EV1: water temperatures and resultant horizontal velocities on 15 May 2001. Solid lines (——) represent measured temperatures, short-dashed lines (.......) represent $C_{Dx} = C_{Dy} = 0$ and long-dashed lines (– – –) represent $C_{Dx} = C_{Dy} = 3.2$. Simulated temperatures were identical for $C_D = 0$ and $C_D = 3.2$.

of the resultant horizontal velocities between the open water and macrophyte zones at Hopwoods Lagoon, it does strongly influence the magnitude of the predicted horizontal velocities. Extrapolating from this, if the vegetation resistance force remained relatively uniform throughout the macrophyte zones but the drag coefficient differed in magnitude from the cases illustrated in Figure 6.43, the temperature structure and the direction of horizontal velocities is expected to be similar in the two wetland zones, while the horizontal velocities would differ in magnitude.

6.6.1.5 Eddy Viscosities and Eddy Diffusivities

Vertical Eddy Viscosities and Diffusivities, ε'_{xz}, ε'_{yz}, D'_z

RMA-10 assumes that eddy viscosity concepts are valid in three-dimensional hydrodynamic modelling, an approach that has been adopted by others including Jin et al. (2000). The model requires specification of the minimum vertical eddy viscosities, ε'_{xz} and ε'_{yz} and the vertical eddy diffusivity, D'_z. Because there was no preferential flow direction in Hopwoods Lagoon, it was assumed that $\varepsilon'_{xz} = \varepsilon'_{yz}$ throughout the lagoon. Local values for the vertical coefficients under neutral flow conditions (E_{xz}, E_{yz} and D_h) were calculated internally using a quadratic distribution function over the depth (Equation (H.9) from page 471).

Local values of the eddy viscosities and diffusivity ($\varepsilon_{xz}, \varepsilon_{yz}$ and D_z) were calculated using the Henderson-Sellers correction, based on the local density stratification and velocity shear. The minimum eddy viscosities and diffusivity specified in the model input were based on values cited in the literature, which were varied during the model calibration process.

Few authors report the values of eddy viscosities used in three-dimensional hydrodynamic models. Additionally, because the eddy values are dependent on the processes implicitly incorporated in the model, they are often not consistent or directly comparable between different systems or hydrodynamic models. The values of the vertical eddy coefficients are also dependent on the scale of the system, and can therefore be difficult to interpret in a physical sense (Imberger and Patterson, 1990). Hence, without field velocity data against which to calibrate simulated velocities, a value of $1.0\,\mathrm{Pa\,s^{-1}}$ was adopted for ε'_{xz} and ε'_{yz}

in both the open water and vegetated zones of the wetland. This is consistent with values which are reported in the literature (for example, Johnson et al., 1993).

Vertical diffusivities for heat and other tracers in lakes and reservoirs range from the molecular scale up to $O(10^{-4})\,m^2\,s^{-1}$ (Fischer et al., 1979). Imberger and Patterson (1990) cited lake-wide $D_z \sim O(10^{-6})\,m^2\,s^{-1}$ during periods of very strong stratification and very weak winds and $O10^{-4})\,m^2\,s^{-1}$ during periods of weak thermal stratification. They also reported that direct measurements of local vertical diffusion coefficients were unknown. Johnson et al. (1993) used $D_z \geq 5.0 \times 10^{-7}\,m^2\,s^{-1}$, while Benoit and Hemond (1996) used values in the range from $(1.0\text{–}26)\times10^{-6}\,m^2\,s^{-1}$ in Lake Bickford in New England, USA ($\overline{h} = 6\,m$).

Consistent with these, the specified minimum vertical diffusivity for Hopwoods Lagoon was varied with the wind speed. A minimum value of $1.4\times10^{-7}\,m^2\,s^{-1}$ (molecular diffusion) was imposed in both open water and emergent macrophyte zones during calm periods ($u_{10} < 0.5\,m\,s^{-1}$). The value of D_z' increased non-linearly as the mean wind speeds increased. The empirical relationship shown in Figure 6.44 was developed during the calibration phase, taking into account both the wind speeds and the prevailing wind direction. Winds during summer and spring were predominantly from the north, approximately normal to the longitudinal axis of the lagoon, which presented a limited fetch. Winds during winter and autumn were generally stronger and from the west or south-west, along the major axis of the lagoon. The minimum specified D_z' values were therefore lower during summer and spring than during winter and autumn.

Consistent with Nepf et al. (1997b), lower vertical diffusivities were used in the macrophyte zones than in the open water, as shown in Figure 6.44. These diffusivities are broadly consistent with values cited in the literature for calm conditions. Due to topographic shading by the surrounding hills, even the comparatively windy periods at Hopwoods Lagoon were relatively calm compared with conditions encountered over larger, more exposed water bodies.

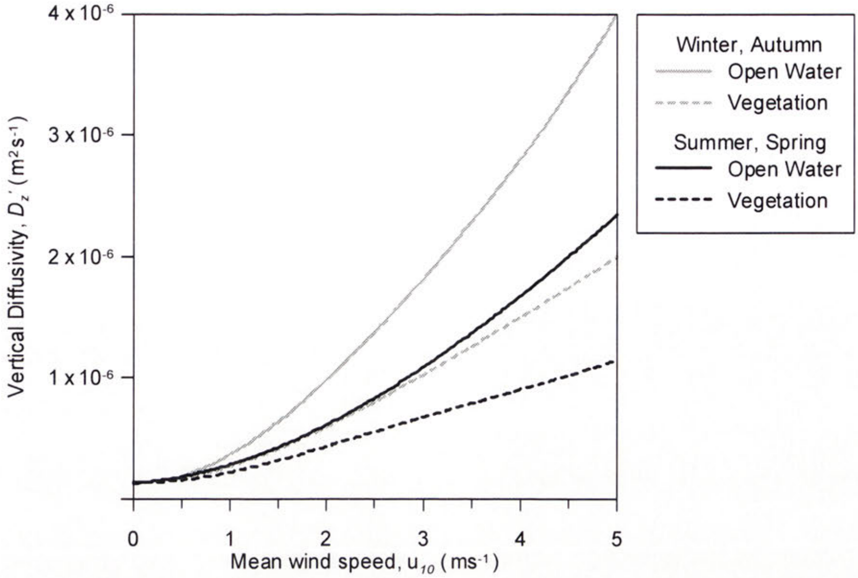

Figure 6.44: Relationship between mean wind speed, u_{10} and vertical eddy diffusivity, D_z', determined during model calibration for the open water and vegetated zones.

Horizontal Eddy Viscosities and Diffusivities, ε_{xx}', ε_{xy}', ε_{yx}', ε_{yy}', k_s, ν_s, D_x', D_y'

RMA-10 required specification of the Smagorinsky coefficient, k_s and minimum kinematic viscosity, ν_s, together with initial estimates for the horizontal eddy viscosities (ε_{xx}', ε_{xy}', ε_{yx}', ε_{yy}') and diffusivities (D_x', D_y'). The simulation results were found to be less sensitive to the value of ν_s than to k_s. The model used $k_s = 1.0$, which is within the range ($0.1 < k_s < 1.0$) suggested by Smagorinsky (1963), and $\nu_s = 1.0 \times 10^{-3}\,\mathrm{m^2\,s^{-1}}$, as for the minimum vertical eddy viscosities.

Trial simulations during model calibration indicated that the results were insensitive to the specified initial values of the horizontal eddy viscosities and diffusivities, which were used only in the first two iterations after start-up (Section H.2.3.2 in Appendix H). All model simulations were initiated using values of $\varepsilon_{xx}' = \varepsilon_{xy}' = \varepsilon_{yx}' = \varepsilon_{yy}' = 1.0\,\mathrm{Pa\,s^{-1}}$ and $D_x' = D_y' = 1.4 \times 10^{-7}\,\mathrm{m^2\,s^{-1}}$ in both the open water and macrophyte zones.

6.6.2 Model Limitations and Potential Improvements

Model calibration and validation using four independent simulation periods in different seasons provided a check on the model performance under a range of meteorologic conditions. However, additional model validation would be recommended prior to using the model in locations other than Hopwoods Lagoon.

There is scope for improvements to be made to the model, particularly if it is desired to investigate the cooling phase in more detail. For example:

- The model does not currently account for precipitation, and can only be used to simulate periods without rainfall.
- Improvements could be made to the parameterisation of the vertical mixing processes, particularly during unstable conditions, such as those experienced during the cooling phase or under extremely windy conditions.
- The parameterisation of the resistance force due to the submerged macrophyte components could be improved by further investigation and experimentation, to permit spatially-variable macrophyte density (and consequent variation in underwater light attenuation) and the vegetation resistance force.
- The wind sheltering effects of emergent macrophytes on stresses at the water surface could be further investigated and more accurately parameterised.

Regardless of these limitations, the model did reasonably simulate the observed diurnal variation in water temperatures at Sites OW1 and EV1 on the selected dates in four seasons. Velocities predicted by the model were of the order of magnitude expected from the literature.

6.6.3 Results of Hydrodynamic Simulation Experiments

6.6.3.1 Effects of Depth Differences on Differential Heating

To extend the range over which comparisons could be made in the field, a series of simulations was run to isolate the effects of differential heating due to depth differences at Hopwoods Lagoon. Three scenarios were considered which assumed, in turn, that the lagoon was:

- completely free from vegetation (open water scenario),
- completely vegetated with submerged macrophytes (submerged macrophyte scenario), and
- completely vegetated with emergent macrophytes (emergent macrophyte scenario).

The simulations were all subject to the same meteorological fluxes and uniform properties were assumed throughout the lagoon for each scenario (the relevant parameters are listed in Table 5.6 on page 172). The model was run initially without imposed surface wind stresses, which ensured that vertical and horizontal temperature profiles developed due to differences in depth alone, and that the resulting flows were convective rather than advective. The simulations were subsequently repeated with wind stresses imposed at the water surface, to examine the relative importance of convective and advective effects.

The predictions were made using meteorological data for 30 December 2000. Meteorological fluxes are shown in Figure G.11 (page 457) in Appendix G.

Inferred Convective Flows due to Depth Differences

Figure 6.45 shows the predicted horizontal temperature differences between Sites 1 and 2 for the model scenarios run without imposed wind stresses in December 2000. Note that these locations correspond to field Sites OW1 and EV1, and have been renamed in the following idealised simulations to avoid confusion. The bed elevation at Site 1 is 0.65 m lower than at Site 2. Predicted velocities at the same depths are shown superimposed on horizontal temperature contours for the ***open water scenario*** in Figure 6.46, and in Figures I.1 and I.2 in Appendix I for the two macrophyte scenarios. These results clearly show differential heating and cooling between the shallow littoral zones represented by Site 2, and the deeper open water zones of the lagoon represented by Site 1.

Figure 6.45(a) shows that appreciable horizontal temperature differences developed at the **surface** between the two sites in the early afternoon, despite being separated horizontally by only ~35 m. The shallower Site 2 was warmer than the deeper Site 1, and the peak temperature difference was largest (~1.1°C) for the ***submerged macrophyte scenario*** and smallest for the ***open water scenario*** (~0.8°C). Predicted temperature differences were smaller overnight and similar for all three scenarios. These would be expected to result in a warm surface flow from the shallower Site 2 towards the deeper Site 1 during the day with a weak flow in the opposite direction overnight.

From the scaling analyses presented in Chapter 3, and assuming a flow depth of around 0.35 m as in the field, convective velocities could be induced with estimated of u ~20 mm s^{-1}

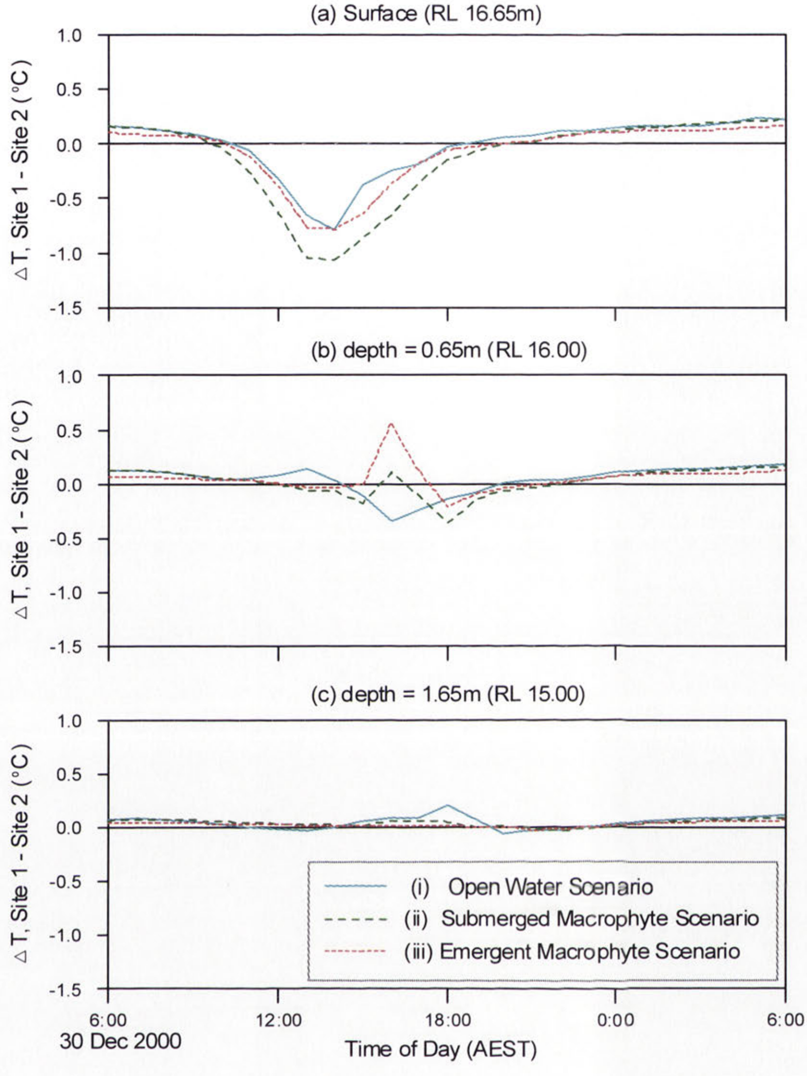

Figure 6.45: Predicted horizontal temperature differences between the deeper Site 1 and Site 2 (Δh=0.65 m) for scenarios where Hopwoods Lagoon (i) contains no vegetation, (ii) contains only submerged macrophytes and (iii) contains only emergent macrophytes. No surface wind stresses.

at 14:00 in the ***open water scenario*** (Equation 3.70, page 104) and $u \sim 6\,\mathrm{mm\,s^{-1}}$ in the ***submerged macrophyte scenario*** (Equation 3.83, page 111).

At **0.65 m depth**, Figure 6.45(b) shows distinctly different horizontal temperature differences for the three scenarios. In the ***open water*** and ***submerged macrophyte scenarios***, the shallower Site 2 was warmer than the deeper site during the afternoon, but cooler than the deeper site throughout the remainder of the diurnal cycle. This suggested a warm

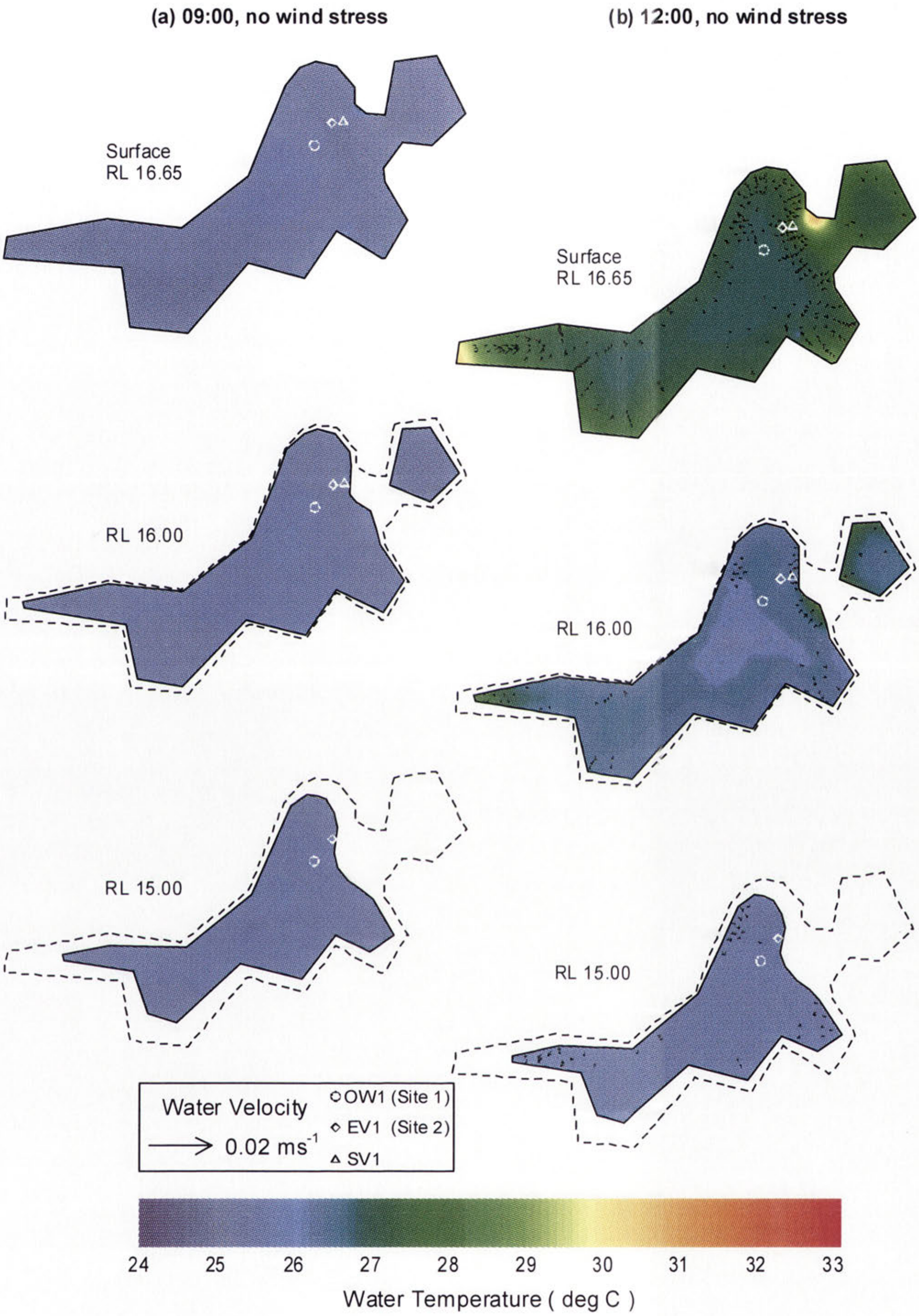

Figure 6.46: Predicted water temperatures and horizontal velocities for the open water scenario on 30 December 2000 (no wind stress)
(a) 09:00, and (b) 12:00 ($\eta_{OW} = 2.5\,\mathrm{m}^{-1}$)

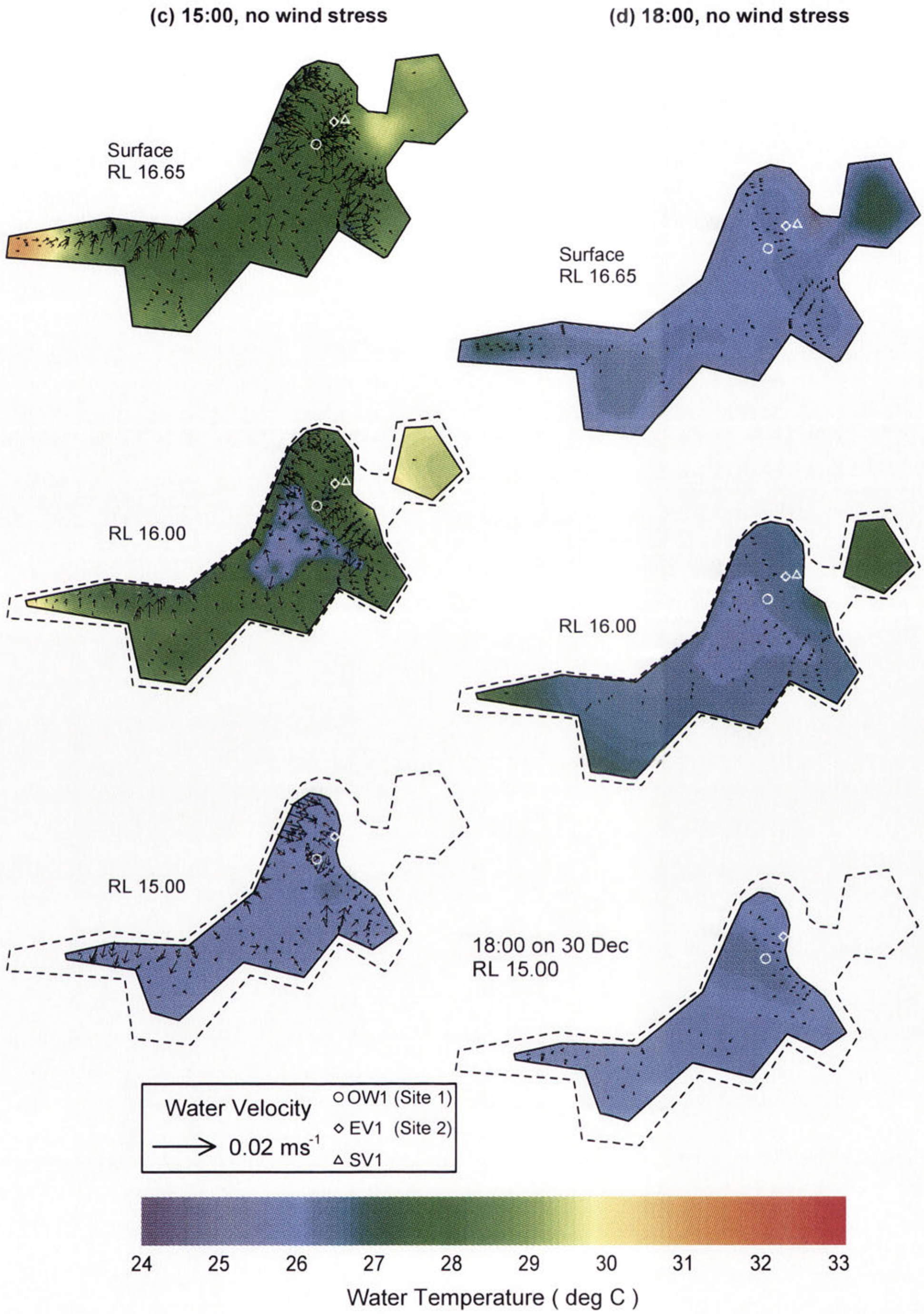

Figure 6.46 (continued): (c) 15:00, and (d) 18:00 ($\eta_{OW} = 2.5\,\mathrm{m}^{-1}$).

intrusion flow from the shallower Site 2 towards Site 1 during the afternoon, with a weak flow in the opposite direction at other times. By contrast, in the ***emergent macrophyte scenario*** the deeper Site 1 was warmer than the shallower site throughout most of the diurnal cycle. The temperature difference suggested a warm intrusion flow from the deeper zone towards the shallower Site 2 during the afternoon, while the surface flow was in the opposite direction.

At **1.65 m depth** and deeper, Figure 6.45(c) shows that the horizontal temperature differences between the two sites were generally $< 0.1°C$, which implied negligible convective exchange between the littoral and deeper zones for all three scenarios.

Differential heating between the two sites for each scenario can generally be explained by distribution of a similar surface heat load over a greater depth in the deeper zones. Heating is due primarily to shortwave radiation. With an underwater attenuation coefficient of $\eta_{OW} = 2.5\,\mathrm{m}^{-1}$, only a very small fraction of the incident shortwave radiation penetrates to the sediments where it could be absorbed and re-radiated into the water column. From Equation 3.62 (page 94), this is $< 0.2\%$ at Site 1 where h=2.5 m and $\sim 1.0\%$ at Site 2 where h=1.85 m. These fractions are even smaller for the macrophyte scenarios using larger η. However, a heat flux from the sediments becomes increasingly important as the water depth decreases (around 29% of the surface flux at h=0.5 m), and horizontal temperature differences would be larger between sites with greater $\Delta\, h$.

Differential cooling can be similarly explained. The initially warmer shallow zones cool more rapidly from the surface than the deeper areas because of decreased thermal inertia per unit horizontal area, and the earlier action of penetrative convection thermals over the full depth.

Differences between the three scenarios can be explained by variation in the surface influx of shortwave radiation, underwater attenuation coefficients and vertical mixing coefficients. Attenuation of shortwave radiation by an emergent macrophyte canopy reduced the net shortwave radiation flux and therefore the surface heat load relative to the ***open water*** and ***submerged macrophyte scenarios***. Predicted water temperatures were lower at all depths in the ***emergent macrophyte scenario*** (Figure I.2). The higher $\eta_{SV} = \eta_{EV} > \eta_{OW}$ concentrated heating nearer the water surface in both macrophyte simulations, where most of the shortwave radiation was absorbed. With the same (unattenuated) surface heat flux, predicted daytime temperatures were greater at the surface but smaller at depth in the ***submerged macrophyte scenario*** (Figure I.1) than the ***open water scenario*** (Figure 6.46). Lower vertical mixing coefficients in the macrophyte zones restricted vertical transport of heat down from the warm surface layer, so that heat was distributed less rapidly than in the ***open water scenario***.

Comparison between Inferred and Predicted Convective Flows

Predicted horizontal convective velocities for the ***open water scenario*** without imposed wind stresses are shown in Figure 6.46. Similar predictions are shown for the ***submerged*** and ***emergent macrophyte scenarios*** in Figures I.1 and I.2 (Appendix I). The predicted convective velocities were negligible overnight at all depths (not shown).

For the ***open water scenario***, predicted **surface** convective velocities were broadly consistent with convective flows inferred from the horizontal temperature differences shown in Figure 6.45 and generally directed from the shallow to deeper zones during the day. Overnight, they reversed in direction and decreased in magnitude (not shown). The predicted velocity of $\sim 5\,\mathrm{mm\,s^{-1}}$ in the afternoon was considerably lower than the $20\,\mathrm{mm\,s^{-1}}$ estimated from the temperature difference in Figure 6.45. However, the scaling relationships used to estimate the convective velocity assumed a linear flow path between the two sites, whereas the geometry of the lagoon is much more complex and the peak horizontal temperature differences were not necessarily aligned between Sites 1 and 2.

Predicted flows at **0.65 m** and **1.65 m depth** were also consistent with those inferred from the horizontal temperature differences in Figure 6.45.

For both ***submerged*** and ***emergent macrophyte scenarios***, the predicted convective flows between shallow and deeper regions of the lagoon were consistent with the flows inferred from horizontal temperature differences at the surface, and broadly consistent for inferred flows at 0.65 m and 1.65 m depth. Predicted convective velocities for the ***submerged macrophyte scenario*** (Figure I.1) and the ***emergent macrophyte scenario*** (Figure I.2) were smaller in magnitude due to the vegetation resistance. Surface velocities predicted in the ***submerged macrophyte scenario*** were $< 2\,\mathrm{mm\,s^{-1}}$, comparable with the scaling estimate ($6\,\mathrm{mm\,s^{-1}}$). Predicted velocities were slower in the ***emergent***

macrophyte scenario because the horizontal temperature differences were smaller.

Advective Effects

Figure 6.47 shows the predicted horizontal temperature differences between Site 1 and the shallower Site 2 for the ***open water scenario*** run in December 2000 with imposed wind stresses. Winds blew predominantly from the north on 30 December at speeds of $< 2.0\,\mathrm{m\,s^{-1}}$ during the morning with a peak of $5\,\mathrm{m\,s^{-1}}$ around 16:00. Wind-induced water motion is the only cause of differences between Figure 6.47 and Figure 6.45. Predicted velocities are shown superimposed over the temperatures in Figure 6.48, while predicted velocities and temperatures for the ***submerged*** and ***emergent macrophyte scenarios*** with wind stresses imposed are shown in Figures I.3 and I.4 (Appendix I).

Figure 6.47(a) shows that the magnitude and diurnal variation in predicted horizontal temperature differences were similar at the **surface** for the three scenarios, both with and without the surface wind stresses (Figure 6.45). The surface temperatures were also similar for simulations run with and without wind stresses. Horizontal temperature differences were largest for the ***submerged macrophyte scenario*** and smallest for the ***open water scenario***. The temperature differences decreased more rapidly for all three scenarios when wind stresses were imposed, due to enhanced horizontal redistribution of heat compared with the purely convective simulations (Figure 6.45).

At **0.65 m depth**, similar behaviour was predicted for the ***emergent macrophyte scenario*** both with (Figure 6.47(b)) and without surface wind stresses (Figure 6.45(b)). This suggests that wind attenuation by the emergent canopy effectively removed advective effects, and that flows predicted for the two ***emergent macrophyte scenarios*** were largely convective. The trends were distinctly different for the ***open water*** and ***submerged macrophyte scenarios***, where predicted temperature differences reversed direction between the wind and no wind simulations. The advective transport of warmer water from the shallow zones (Site 2) of the lagoon towards the interior (Site 1) throughout the morning heating phase was the most likely source of warming at Site 1. Consistent with this proposition, the peak temperature difference was higher and occurred earlier for the ***open water scenario*** than the ***submerged macrophyte scenario*** because there was no vegetation resistance.

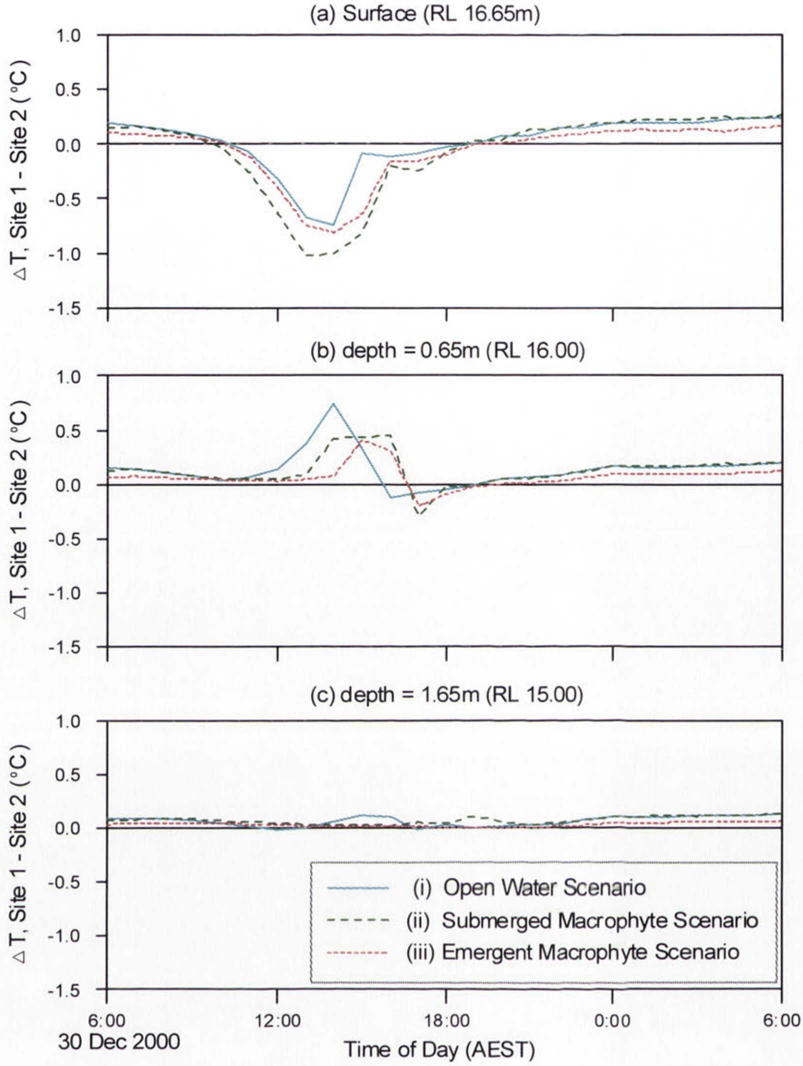

Figure 6.47: Predicted horizontal temperature differences between the deeper Site 1 and Site 2 (Δh=0.65 m) for scenarios where Hopwoods Lagoon (i) contains no vegetation, (ii) contains only submerged macrophytes and (iii) contains only emergent macrophytes. Wind stresses applied at the water surface.

Predicted horizontal temperature differences and inferred convective flows were negligible at **1.65 m** depth and deeper.

Predicted **surface** velocities for the ***open water*** and ***submerged macrophyte scenarios*** with imposed wind stresses were generally greater than those predicted without wind stresses, and the directions were different. Surface flows in littoral zones were generally consistent with predicted convective flows into the deeper interior zones, while flows in the

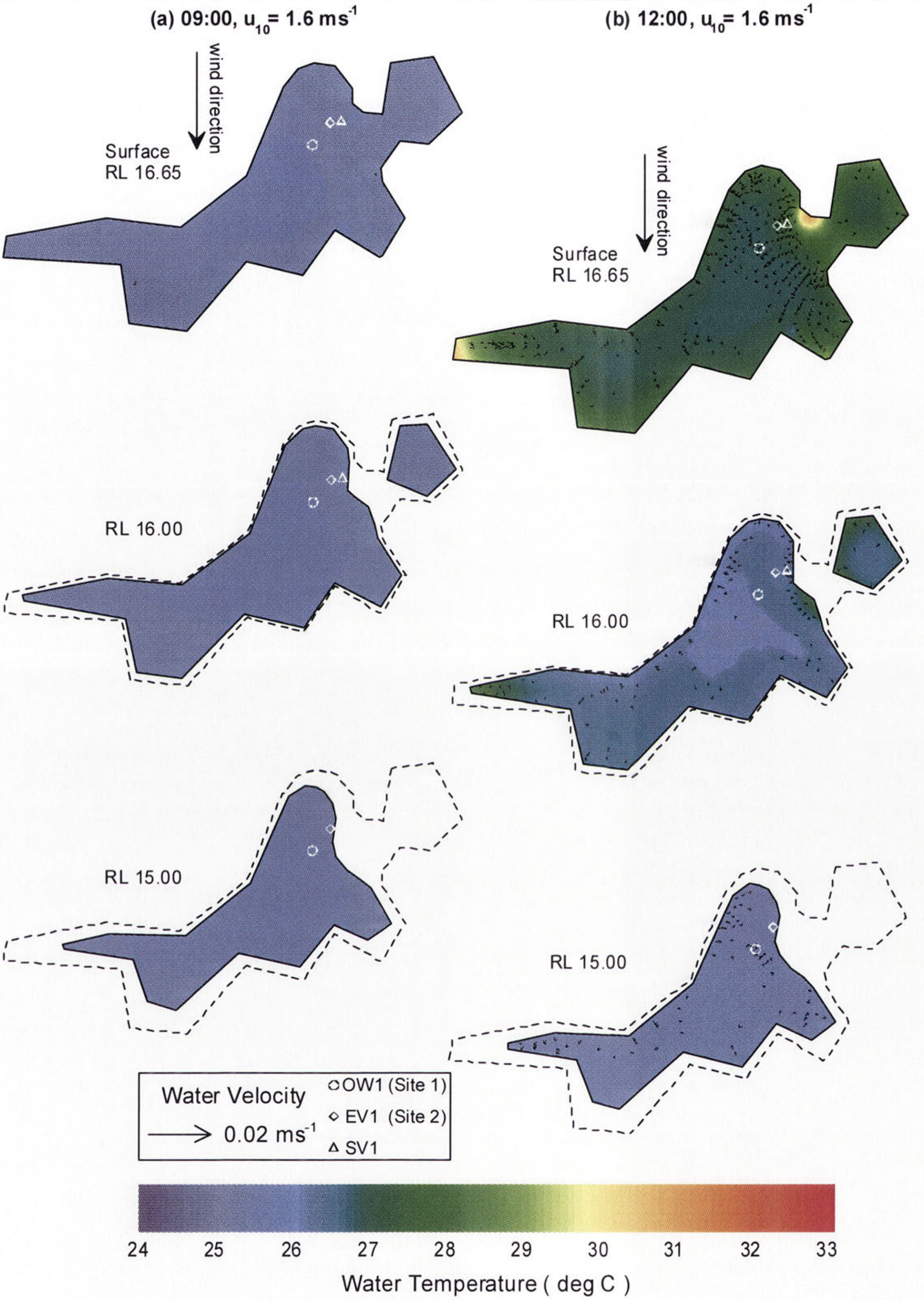

Figure 6.48: Predicted water temperatures and horizontal velocities for the open water scenario on 30 December 2000, with applied wind stress (a) 09:00, and (b) 12:00 ($\eta_{OW} = 2.5\,\mathrm{m}^{-1}$)

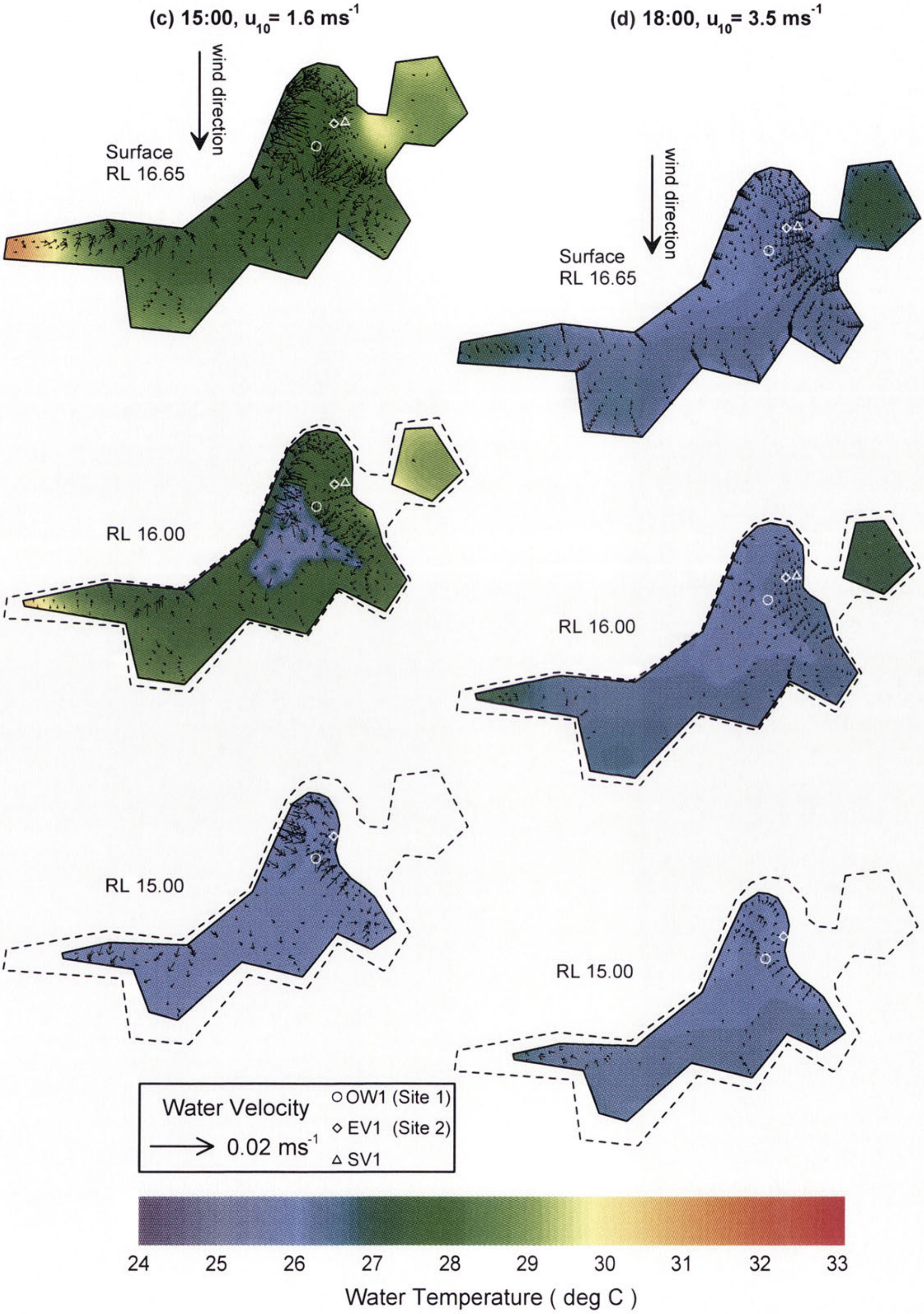

Figure 6.48 (continued): (c) 15:00, and (d) 18:00 ($\eta_{OW} = 2.5\,\mathrm{m}^{-1}$).

deeper zones were generally from the north, aligned with the prevailing winds. However, the magnitudes of the predicted advective velocities (<10 mm s^{-1}) were smaller than expected from the imposed wind speeds (u_s >100 mm s^{-1}), which suggests that there may have been a problem with the parameterisation of the surface wind stresses in the model.

Predicted flows at **0.65 m** depth were generally in a similar direction to the surface flows. In the absence of appreciable horizontal temperature differences after 18:00, predicted flows were consistent with the prevailing wind direction in the shallow zones but in an opposite, upwind direction in the deeper zones. At **1.65 m** depth, predicted flows during the day were generally in the same direction for flows predicted with and without wind stresses, although an upwind flow was evident in the wind stress simulations after 18:00, when horizontal temperature differences had equalised.

The magnitude and direction of the predicted flows for the ***emergent macrophyte scenarios*** were almost identical for the simulations run with and without surface wind stresses. This supported the inference that the emergent macrophyte canopy effectively removed advective effects.

Summary of Effects of Depth Differences on Differential Heating

The examples described above have confirmed that differential heating and cooling due purely to differences in depth can drive convective flows within a water body such as Hopwoods Lagoon. These occur on a diurnal scale whether the lagoon is unvegetated or vegetated completely with submerged or emergent macrophytes. This was expected but could not be conclusively demonstrated using field data.

Predicted horizontal surface velocities between littoral and deeper zones were similar for the ***open water*** and ***submerged macrophyte scenarios*** and lower for the ***emergent macrophyte scenario***, because the horizontal temperature gradients were lower beneath the emergent canopy. The deeper flows were slightly larger for the open water simulation than for either of the macrophyte scenarios, because the horizontal temperature differences were stronger and because there was no flow resistance due to the macrophytes. In all three scenarios, vertically and horizontally isothermal conditions were predicted overnight.

Wind-induced advective effects in open water and submerged macrophyte zones were observed to alter the magnitude and direction of horizontal flows from those due to convection alone, while advective effects were minimised beneath the emergent macrophyte canopy.

6.6.3.2 Effects of Submerged Macrophyte Density on Radiation Shading

Simulations were undertaken of radiation shading by submerged macrophytes to confirm the diurnal convective flow regimes inferred from the field data and to investigate the effects of macrophyte density on these flow regimes. The radiation shading simulations were all run with imposed wind stresses at the water surface, and the horizontal distribution of submerged macrophytes shown in Figure 5.10 (page 182). Macrophyte properties were assumed uniform through the macrophyte zones for each simulation.

Figure 6.49 shows predicted horizontal temperature differences between Site 1 in the open water zone and Site 2 in the submerged macrophyte zone for low, moderate and high densities of submerged macrophytes. Predicted temperatures and velocities for the moderate macrophyte density (represented by $\eta_{SV} = 6.5\,\mathrm{m}^{-1}$) are shown in Figure 6.50, while similar predictions for the low ($\eta_{SV} = 4.4\,\mathrm{m}^{-1}$) and high ($\eta_{SV} = 12.0\,\mathrm{m}^{-1}$) macrophyte densities are shown in Figures I.5 and I.6 in Appendix I.

Effects of Submerged Macrophyte Density on Inferred Convective Flows

Figure 6.49(a) shows that the macrophyte zone (Site 2) heated to warmer **surface** temperatures than the open water (Site 1) during the day and cooled to a lower temperature overnight. The maximum horizontal temperature difference increased as the submerged macrophyte density increased. These were larger than in both the ***open water*** and ***submerged macrophyte scenarios*** run with surface wind stresses (Figure 6.47), although the surface temperatures were slightly cooler overall than in the ***submerged macrophyte scenario*** (Figure I.3). The horizontal temperature differences suggested daytime convective surface flows from the littoral macrophyte zones into the deeper open water, with velocities of <7–8 $\mathrm{mm\,s^{-1}}$ (Equation (3.83) from page 111), using ΔT=1.0–2.0°C and H=0.35 m. Inferred flows overnight were around 2 $\mathrm{mm\,s^{-1}}$ from the deeper zones towards the submerged macrophytes.

Predicted water temperatures at **0.65 m** depth were generally cooler in the macrophyte zones than in the open water, and the horizontal temperature difference increased as den-

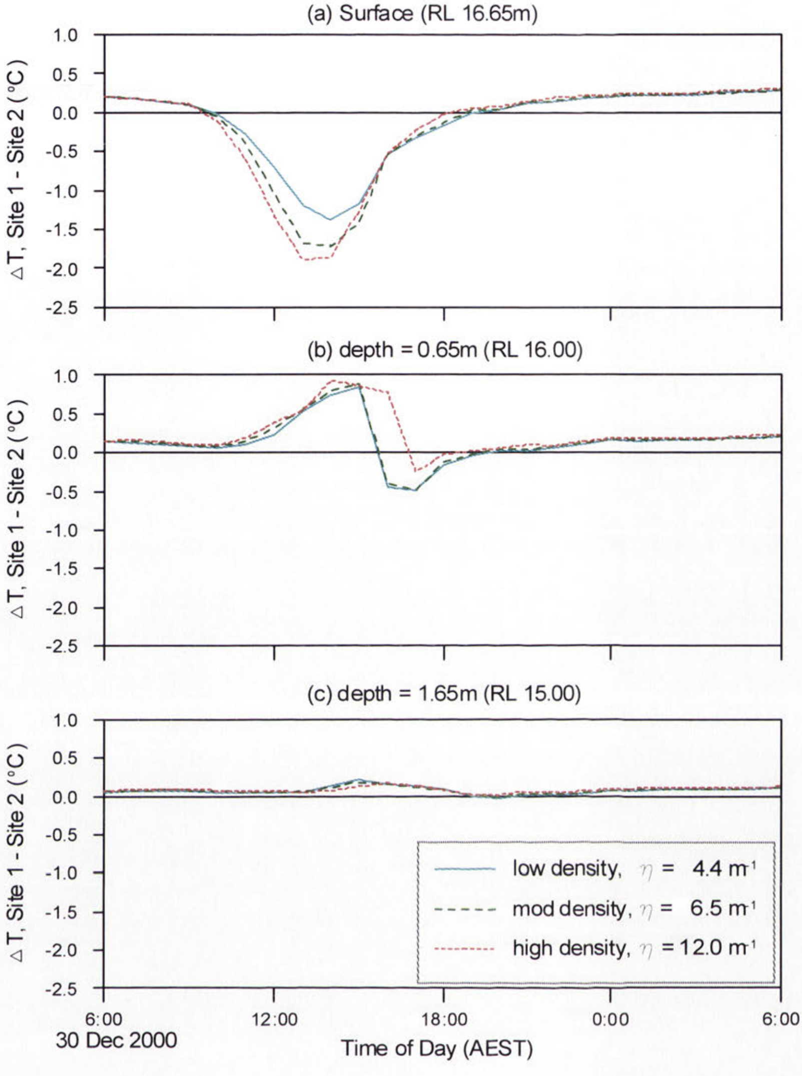

Figure 6.49: Effects of submerged macrophyte density on predicted horizontal temperature differences between the deeper Site 1 and Site 2 (Δh=0.65 m).

sity increased. The higher η_{SV} meant that a greater proportion of the available shortwave radiation was absorbed closer to the surface. Around 20% of the incident flux penetrates to 0.65 m with η_{OW}=2.5 m^{-1}, compared with 5.7% for η_{SV}=4.4 m^{-1} and <0.5% for η_{SV}=12.0 m^{-1}. Figure 6.49(b) suggested a convective flow from the open water towards the submerged macrophytes during the day, in the opposite direction to the surface flow, with a short duration flow from the macrophyte zones towards the open water in the late afternoon, and a slow overnight flow towards the macrophyte zones. Horizontal temperature differences and inferred convective flows were negligible at **1.65 m**.

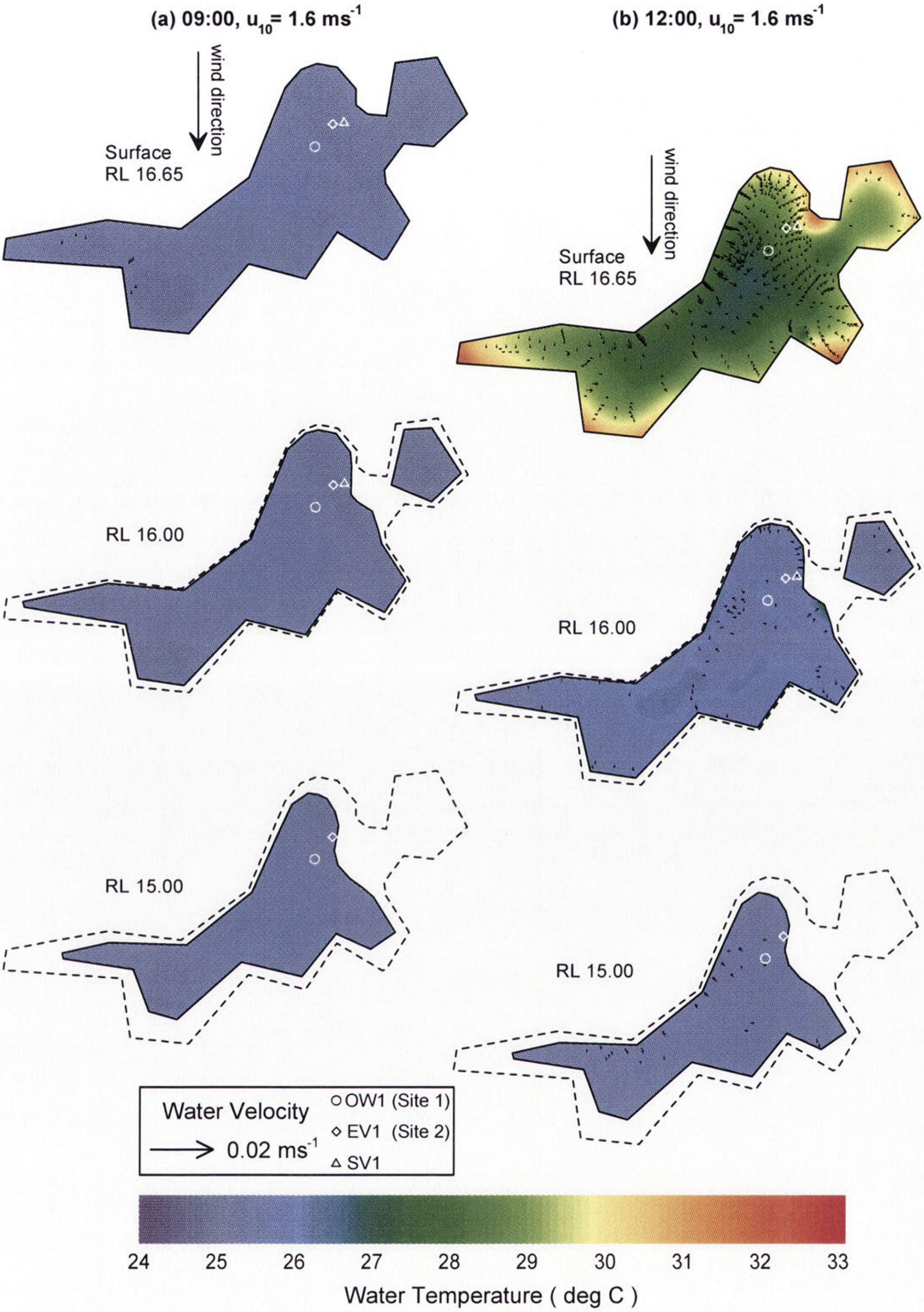

Figure 6.50: Predicted water temperatures and horizontal velocities for radiation shading by moderately dense submerged macrophytes on 30 December 2000
(a) 09:00, and (b) 12:00 ($\eta_{SV} = 6.5\,\mathrm{m}^{-1}$, $\eta_{OW} = 2.5\,\mathrm{m}^{-1}$)

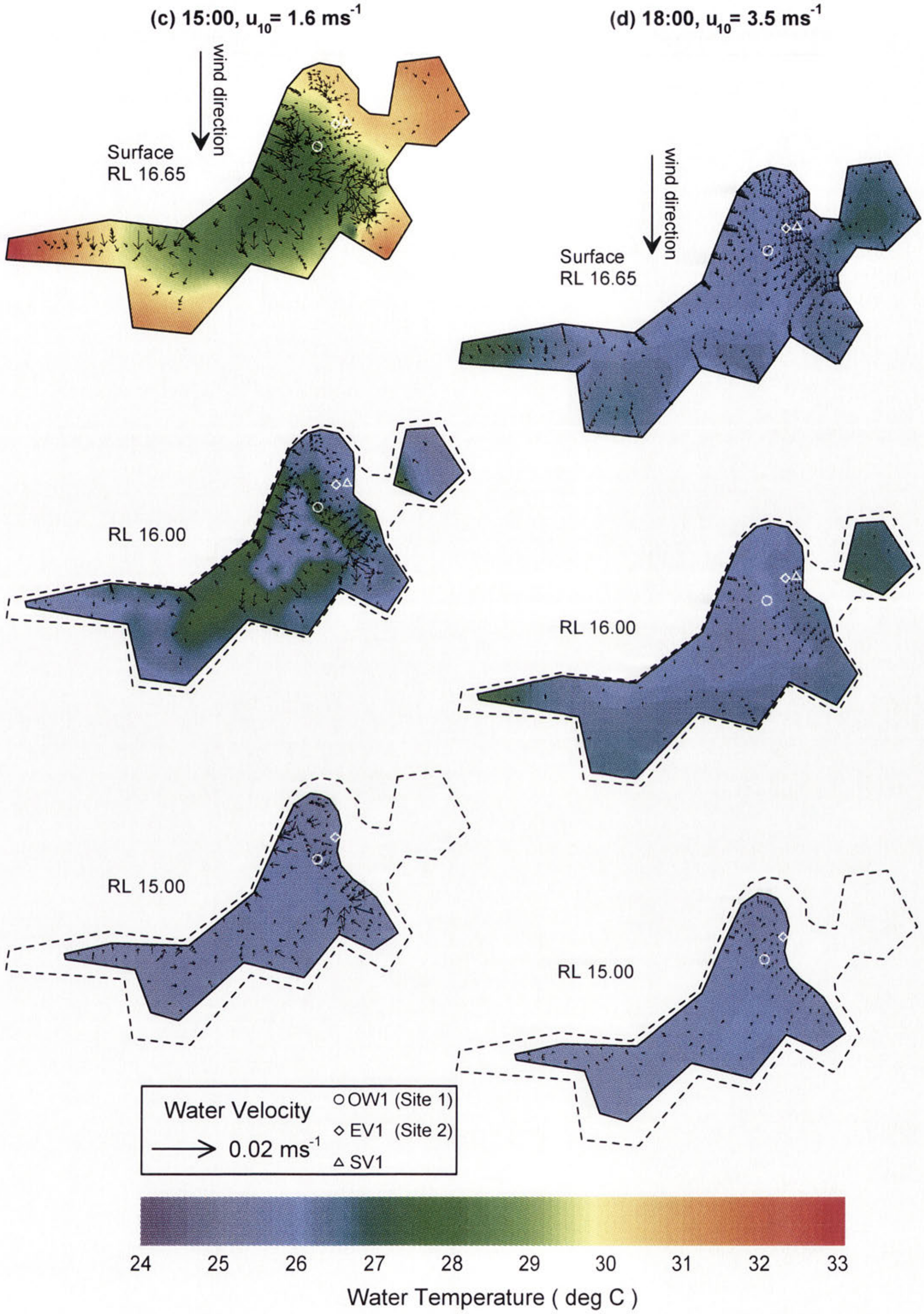

Figure 6.50 (continued): (c) 15:00, and (d) 18:00 ($\eta_{SV} = 6.5\,\mathrm{m}^{-1}$, $\eta_{OW} = 2.5\,\mathrm{m}^{-1}$).

The near surface horizontal temperature differences for the three macrophyte densities were greater than in either the ***open water*** or ***macrophyte scenarios*** (Figure 6.47). This implied that radiation shading by submerged macrophytes was a more significant cause of differential heating than differences in depth, in the model simulations at Hopwoods Lagoon.

Comparison between Inferred and Predicted Flows

The directions of the predicted velocities were broadly consistent with those inferred from the predicted horizontal temperature differences (Figure 6.49).

At the **surface**, the velocities increased in magnitude as density and η_{SV} increased. The peak predicted velocity of $\sim$4 mm s^{-1} in the macrophyte zone for the moderate macrophyte density was similar to the convective velocity estimated from the horizontal temperature difference at 15:00. The magnitude of the predicted velocities at **0.65 m** were generally consistent with inferences drawn from the horizontal temperature differences. Predicted daytime velocities at all depths increased in magnitude with increasing macrophyte density, and were larger than those predicted for the ***submerged macrophyte scenario***. Predicted velocities were negligible overnight in all simulations and at all depths.

Surface flows were dominated by advection when wind speeds increased around 18:00, and were similar to the ***submerged macrophyte scenario***.

Predicted velocities were similar for the radiation shading simulations and the ***submerged macrophyte scenario***, and comprised downwind flows through the shallow zones and weak upwind flows through the deeper, open water areas. A cool gravity current was inferred along the bed from the submerged macrophyte zones towards the open water, as observed by James and Barko (1991) and Oldham and Sturman (2001).

Implications of Model Simplifications Concerning Submerged Macrophytes

The submerged macrophyte simulations assumed a constant vegetation resistance force, independent of the density of the submerged macrophytes (simulated by η_{SV}). The major effect of this assumption would have been in the magnitude of the predicted horizontal velocities. As discussed in Section 2.3.3, the flow resistance due to submerged macrophytes generally increases with increasing macrophyte density, so velocities should be retarded more through dense submerged macrophytes than comparatively sparse vegetation. Horizontal and vertical mixing coefficients were also kept constant between the various simulations, whereas they might have been expected to decrease as the macrophyte density increased.

The modelling also assumed a uniform distribution of the vegetation resistance force over the depth of the water column, which neglected vertical variation in the subsurface macrophyte density. It also did not allow for shallow flows between the top of the submerged macrophytes and the water surface. The flow resistance would have been lower in a surface, unvegetated layer than in the underlying submerged macrophytes, although additional shear stresses would have been expected between the two layers (Danard and Murty, 1994). A more sophisticated hydrodynamic model would be required to simulate such flows, and was beyond the scope of this study.

Despite these simplifications, the model results were broadly consistent with the field observations and published findings, and can therefore be considered qualitatively valid.

Summary of Effects of Submerged Macrophyte Density on Radiation Shading

The model results suggested that radiation shading by submerged macrophytes in the littoral zones would enhance surface flows into the deeper zones of the lagoon, compared with the ***open water*** or ***submerged macrophyte scenarios*** (where properties were uniform throughout the lagoon). Deeper horizontal flows would be driven by greater horizontal temperature differences than observed in either the ***open water*** or ***submerged macrophyte scenarios***, but partly retarded by the macrophyte resistance force.

The diurnal flow regime predicted by the model is summarised schematically in Figure 6.51. This is consistent with the flow regimes inferred from temperatures measured in the field between open water and submerged macrophyte sites. The implications of radiation shading by submerged macrophytes and these inferred convective flow regimes are discussed in Chapter 7.

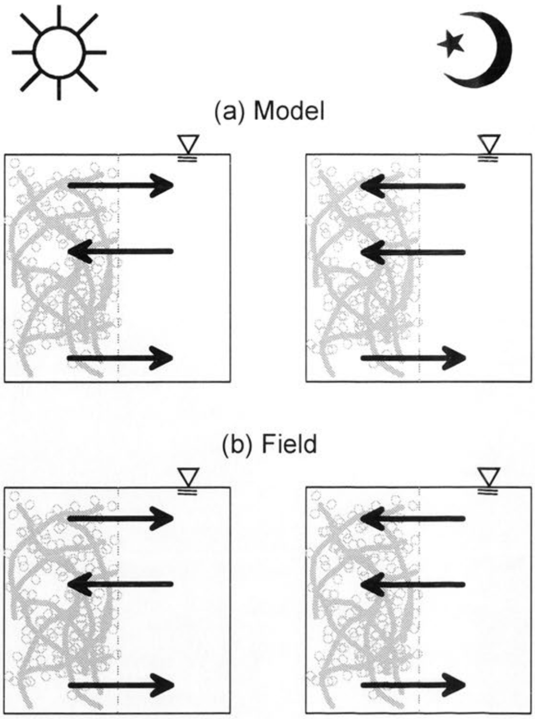

Figure 6.51: Diurnal flow regimes for radiation shading by submerged macrophytes (a) predicted by the model, and (b) inferred from the field data.

6.6.3.3 Effects of Emergent Macrophyte Density on Radiation Shading

Simulations were undertaken of radiation shading by emergent macrophytes to verify the diurnal convective flow regime inferred from the field data and to investigate the convective flow regimes predicted beneath various densities of emergent macrophytes. The emergent macrophyte canopy was modelled in addition to submerged macrophytes, so the simulation results represent the combined effects of radiation shading by emergent macrophytes and submerged macrophytes.

The radiation shading simulations were all run with wind stresses imposed at the water surface. The distribution of the macrophytes was identical for each simulation, as shown in Figure 5.11 (page 183), and macrophyte properties were assumed uniform throughout the macrophyte zones. The same submerged macrophyte density (η_{SV}=6.5 m^{-1}) was assumed for all simulations.

Figure 6.52 shows horizontal differences between predicted temperatures at Site 1 in the open water and Site 2 in the macrophyte zone for simulated low, moderate and high

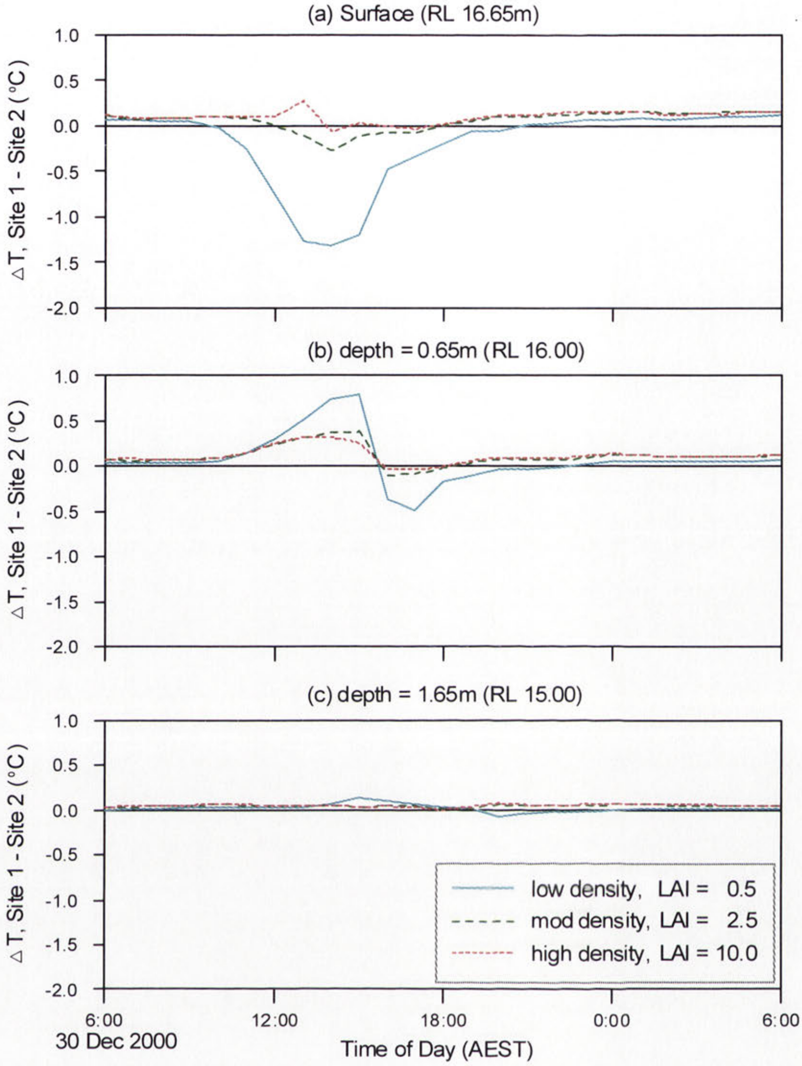

Figure 6.52: Effects of emergent macrophyte density on predicted horizontal temperature differences between the deeper Site 1 and Site 2 (Δh=0.65 m).

canopy densities. Predicted temperatures and velocities for the moderate macrophyte density (simulated by LAI=2.5) are shown in Figure 6.53, and similar predictions for the low (LAI=0.5) and high (LAI=10.0) canopy densities are shown in Figures I.7 and I.8 in Appendix I.

Effects of Emergent Macrophyte Density on Inferred Convective Flows

At the water **surface**, Figure 6.52(a) shows that temperatures at Site 2 in the emergent macrophyte zone were warmer than in the open water beneath the low and moderate

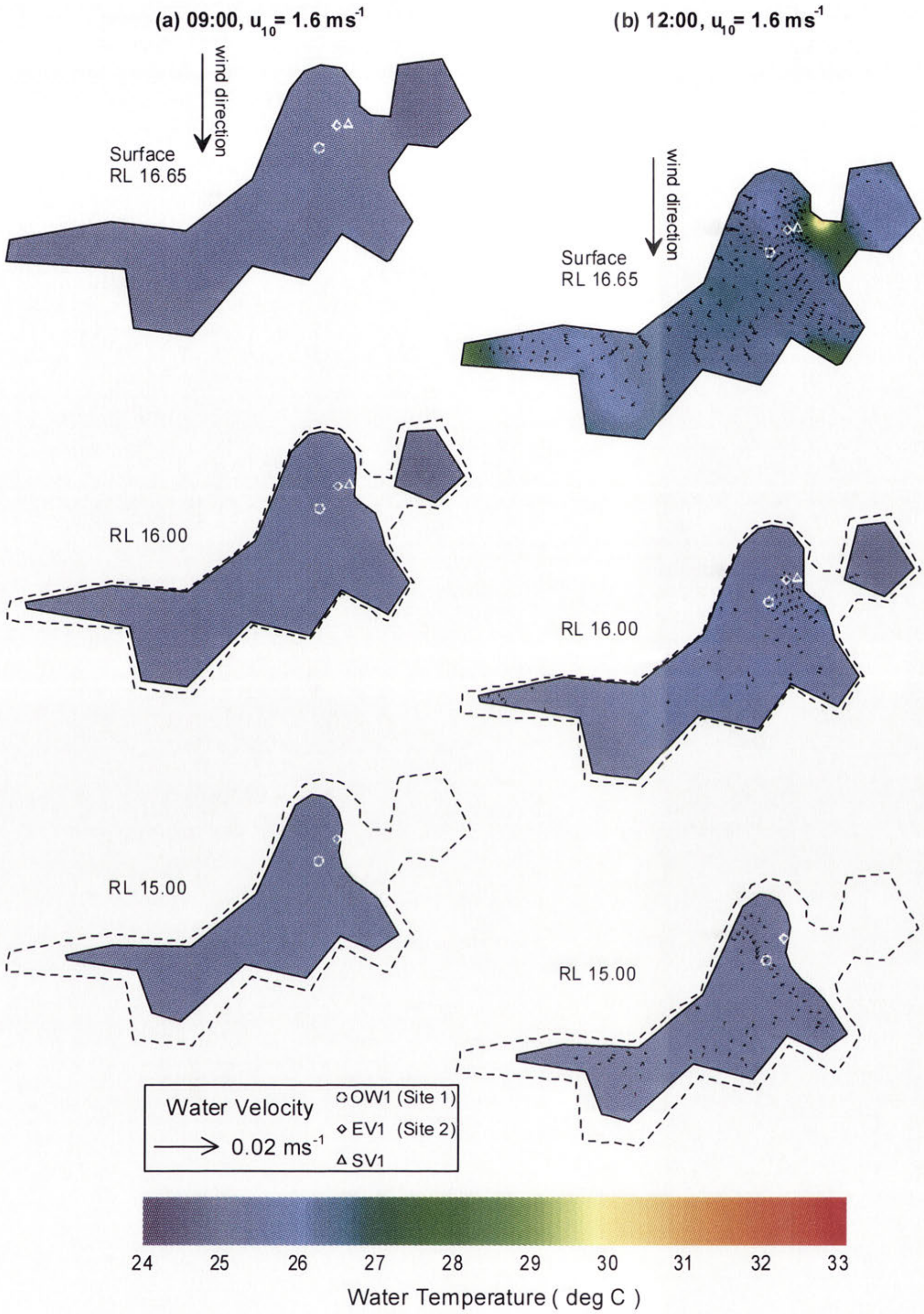

Figure 6.53: Predicted water temperatures and horizontal velocities for radiation shading by moderately dense emergent macrophytes on 30 December 2000
(a) 09:00, and (b) 12:00 ($LAI = 0.5$, $\eta_{EV} = 6.5\,\mathrm{m}^{-1}$)

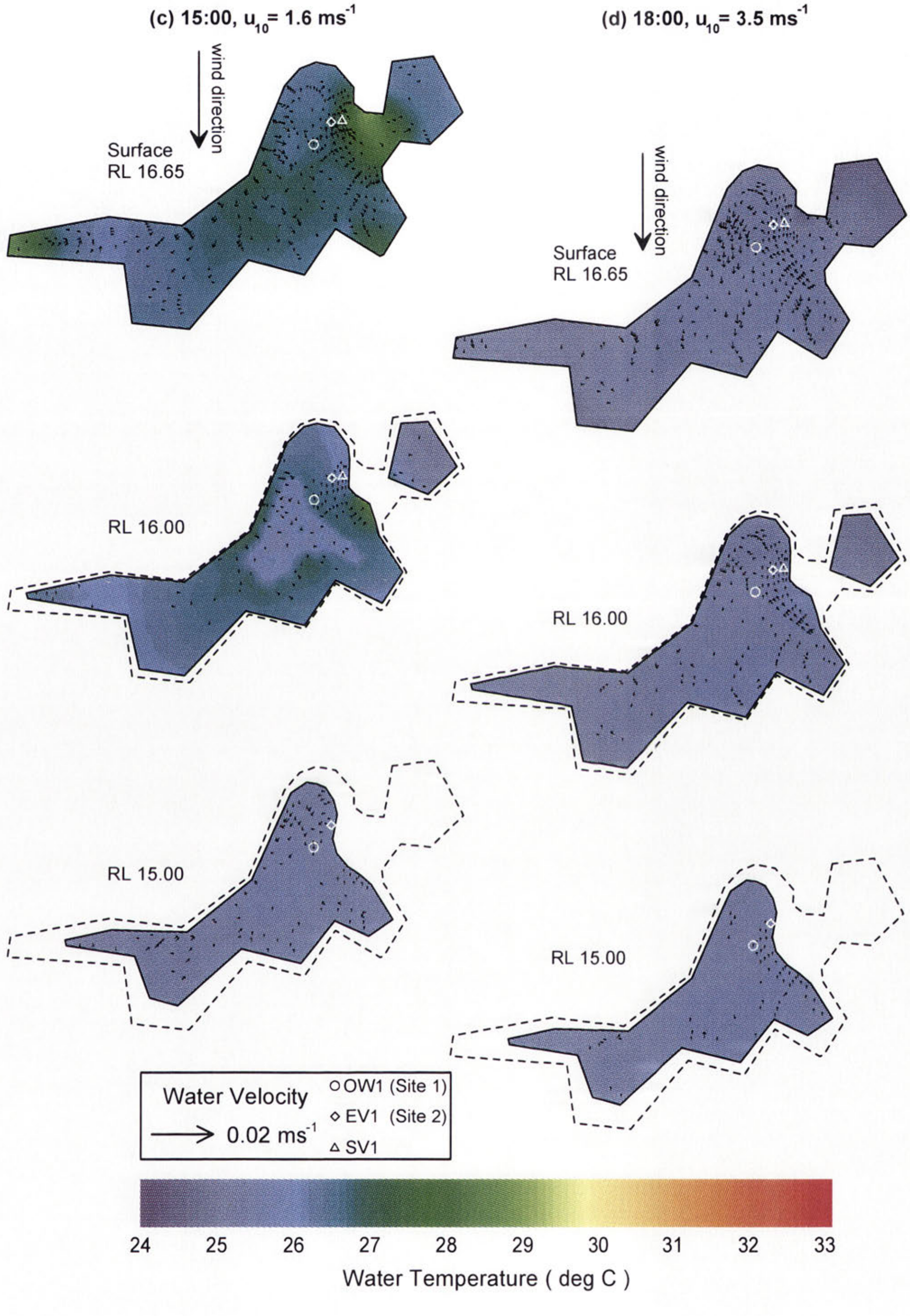

Figure 6.53 (continued): (c) 15:00, and (d) 18:00 (LAI = 0.5, $\eta_{EV} = 6.5\,\mathrm{m}^{-1}$).

canopy densities but cooler for the high canopy density. While this at first appeared counter-intuitive for the lower canopy densities, it could be explained by differential absorption of radiation beneath the water surface between the macrophyte and open water zones (η_{EV}=6.5 m^{-1}, η_{OW}=2.5 m^{-1}). The results suggest that the reduced net shortwave radiation flux beneath a moderate canopy density (LAI=2.5) almost negates differential surface heating between open water and macrophyte zones with these η_{EV} and η_{SV}. A greater canopy density would reduce surface heating compared with the open water. Approximately 78% of the incident flux is transmitted to the water surface through a canopy with LAI=0.5 but transmission is <1% through a canopy with LAI=10.0 (comparisons made using Equation (3.55) on page 84 at noon where the solar elevation is 90° and for simplicity assuming a uniform distribution of canopy foliage).

Predicted horizontal temperature differences for the low canopy density suggested a daytime **surface** convective flow from the emergent macrophyte zone (Site 2) towards the open water (Site 1) with a peak velocity of ~7 mm s^{-1} (Equation (3.83) from page 111), and a weak overnight flow in the opposite direction. A weaker surface flow from the macrophyte zone towards the open water was inferred from ΔT for the moderate canopy density. Beneath the high density canopy, a weak surface flow was inferred from the open water towards the macrophyte zone throughout most of the diurnal cycle.

At **0.65 m** depth, the horizontal temperature differences were of the same sign and in phase for the three canopy densities, although the magnitude decreased as the canopy density increased. These suggested a daytime warm convective flow from the open water towards the macrophyte zone with a weaker flow in the opposite direction beneath the low density canopy (only) in the late afternoon. At **1.65 m**, the predicted horizontal temperature differences and inferred convective flows between Site 1 (open water) and Site 2 (emergent macrophytes) were negligible throughout the diurnal cycle for the three simulated canopy densities.

Predicted temperatures were cooler for the three simulated emergent macrophyte densities than in the ***open water scenario*** and the radiation shading simulation by submerged macrophytes with η_{SV}=6.5 m^{-1}. The inferred convective behaviour for the low density emergent macrophyte simulation was very similar to that for the radiation shading by the same density of submerged macrophytes in the absence of an emergent canopy, which again suggested the minimal contribution to radiation shading by the emergent canopy with LAI=0.5.

Comparison between Inferred and Predicted Flows

The directions of the predicted velocities shown in Figures 6.53, I.7 and I.8 were quite consistent with the flows inferred from the predicted horizontal temperature differences.

At the **surface**, afternoon flows were directed generally from the emergent macrophyte zones towards the interior open water zones under the low density canopy. The peak predicted velocity at 15:00 of $\sim 8\,\mathrm{mm\,s^{-1}}$ was comparable with the convective velocity estimated from the peak horizontal temperature difference. Under the denser emergent canopies, surface flows were directed from the open water towards the macrophytes zones, consistent with flows inferred from the predicted temperature differences.

Surface flows were dominated by downwind advective flows when the wind speed increased around 18:00, and by which time the horizontal temperature differences had declined. An upwind flow was predicted through the emergent macrophyte zones at the northern end of the lagoon, where the water surface was sheltered by the emergent macrophytes and wind-induced surface stresses were lowest.

Predicted velocities at **0.65 m** depth were smaller than the surface velocities and directed generally from the open water (Site 1) towards the shallow vegetated zones (Site 2). These were consistent with the inferred flows and decreased in magnitude as the canopy density increased.

Predicted velocities at **1.65 m** depth were similar in magnitude for the three simulated canopy densities and directed generally from the shallow macrophyte zones towards the open water. When advective effects became important in the late afternoon, the flows at 0.65 m and 1.65 m depth consisted almost entirely of upwind flows through the macrophyte zones. A cool gravity current was inferred along the bed from the macrophyte zone to the deeper interior of the lagoon, as observed in field experiments by James and Barko (1991) and Oldham and Sturman (2001) between vegetated littoral zones and open water zones.

Implications of Model Simplifications Concerning Emergent Macrophytes

In the model, no distinction was made in the magnitude of the surface wind stresses beneath the various emergent canopy densities, although wind attenuation would be expected to be greater by denser emergent canopies. Wind stresses and wind-induced surface velocities would therefore also have been lower beneath a dense emergent macrophyte canopy, than under a sparse canopy. The major implication of this simplification would have been relative over-estimation of advective surface velocities beneath the denser emergent canopies.

Summary of Effects of Emergent Macrophyte Density on Radiation Shading

The model results suggested that introduction of emergent macrophytes into the littoral zones would reduce surface temperatures and surface convective velocities, compared with radiation shading by the same density of submerged macrophyte without an emergent canopy. At a sparse canopy density (simulated using $LAI = 0.5$), macrophyte zones were warmer than open water zones, and surface flows were predicted from the macrophyte zones into the open water. The reverse was true at higher canopy densities, where flows were predicted from the open water towards the cooler macrophyte zones. This suggested that differential heating due to radiation shading by submerged macrophytes and differences in depth dominated radiation shading by sparse emergent macrophytes.

The diurnal convective flow regime predicted by the model is shown schematically in Figure 6.54. This is consistent with the flow regime inferred from the predicted horizontal temperature differences. Note that convective surface flows predicted for radiation shading by dense emergent macrophytes are in the *opposite* direction to those predicted for radiation shading by dense submerged macrophytes.

The flow regime suggested by the model results for the low density emergent macrophyte canopy is also consistent with that inferred from temperature measurements beneath a sparse macrophyte canopy at Hopwoods Lagoon. Implications of radiation shading by emergent macrophytes of varying densities are discussed in Chapter 7.

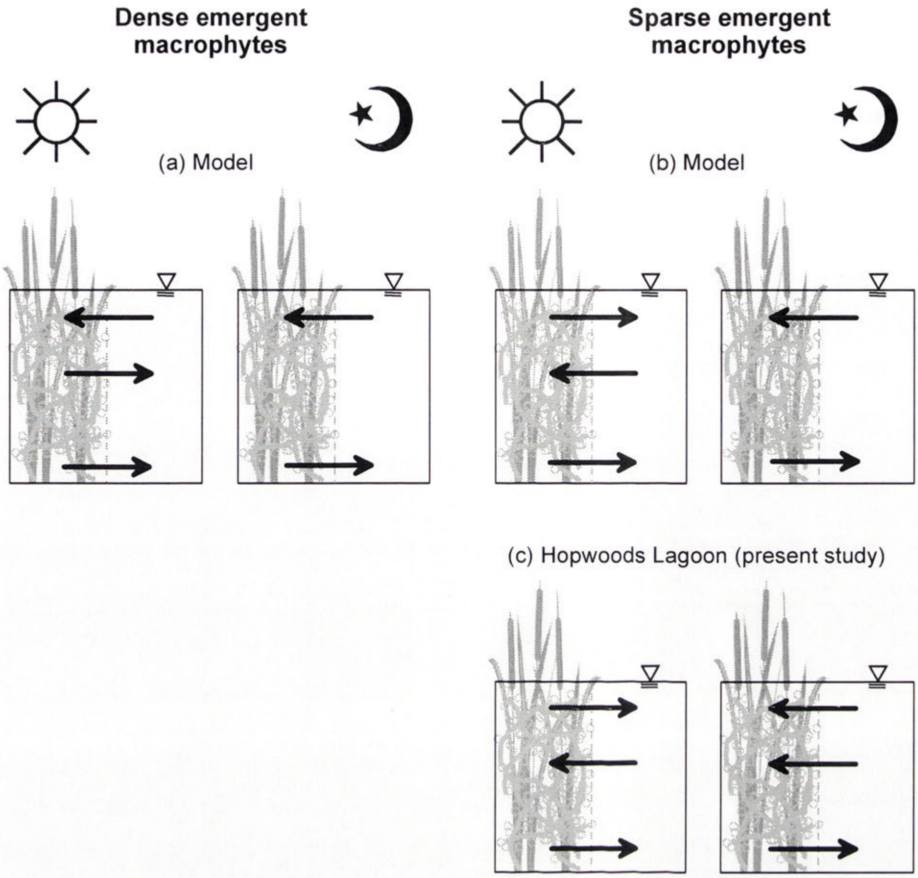

Figure 6.54: Diurnal flow regimes for radiation shading by emergent macrophytes (a) predicted by the model for a dense emergent canopy, (b) predicted by the model for a sparse emergent canopy, and (c) inferred from the field data.

6.7 Summary

This chapter has presented and discussed the results of the experimental programme described in Chapter 5.

The results of the emergent macrophyte surveys were used to characterise the physical properties of the emergent macrophytes species *Typha domingensis*, *Juncus kraussii* and *Eleocharis sphacelata* at four wetlands in and around Sydney. The leaf area indices (LAI) calculated from this macrophyte data were used as input when testing the applicability of simple canopy attenuation models available in the literature, to attenuation of shortwave radiation by macrophyte canopies. It was found that the radiation profiles measured at the four wetlands could be reasonably represented using a simple exponential attenuation relationship. A form of Beers Law using a theoretical attenuation coefficient based on the G-function (a dimensionless projection of the foliage area on a horizontal plane) was considered the most appropriate of the models tested to predict the shortwave radiation flux beneath an emergent macrophyte canopy.

Measured underwater radiation profiles were found to be reasonably well simulated by Beers Law. This attenuation relationship was used to derive mean underwater attenuation coefficients for open water and macrophyte zones at Hopwoods Lagoon, which were used in the numerical simulation experiments.

Meteorological data and water temperatures were used to assess diurnal and seasonal trends in hydrodynamics at Hopwoods Lagoon. Distinct trends were observed during the different seasons, and between the open water and vegetated zones of the wetland. Convective flow regimes were inferred from the horizontal temperature differences between wetland zones. In the absence of direct velocity measurements, the existence of the convective flows was supported by time-series water temperature data and horizontal transect data. The inferred flow regimes were compared with the observations of other researchers, and it was concluded that the diurnal and seasonal hydrodynamic response is highly site-specific and varies between different wetlands.

Radiation shading by macrophytes was found to be significant at Hopwoods Lagoon, and resulted in horizontal temperature differences of up to 6°C between sites in the open water and the vegetated zones. The field results suggested that radiation shading by the submerged macrophytes was more important than radiation shading by the sparse emergent macrophytes at Hopwoods Lagoon.

Using the calibrated and validated hydrodynamic model for Hopwoods Lagoon, differential heating due to depth differences was found to induce horizontal convective flows between littoral and deeper zones when the lagoon was unvegetated or uniformly vegetated with submerged or emergent macrophytes. Radiation shading by various densities of submerged macrophytes increased the horizontal temperature differences and therefore inferred convective flows due to depth differences between littoral and deeper zones. The effects of radiation shading by emergent macrophytes were distinctly different for sparse and dense canopy densities. Horizontal temperature differences and inferred convective flows due to radiation shading by a sparse emergent canopy were generally in the same direction as those due to depth differences, but were in the opposite direction when due to radiation shading by a denser emergent canopy. The implications of these radiation shading results are discussed in Chapter 7.

Chapter 7

EFFECTS OF RADIATION SHADING BY MACROPHYTES

7.1 Introduction

This chapter provides a synthesis of field observations and model simulations with respect to the effects of radiation shading by submerged and emergent macrophytes at Hopwoods Lagoon. These are compared and contrasted with the observations of Waters (1998), whose studies included the most significant previous investigation into radiation shading by macrophytes. The generality of his observed convective flow regimes and his proposed convective flow classification scheme are also assessed. An overview is then given of the hydrodynamic implications of radiation shading by macrophytes in wetlands. This includes the importance of depth and differences in underwater attenuation of shortwave radiation, and the significance of wind-induced (advective) process. Finally, consideration is given to implications for the design and management of constructed and natural wetlands.

7.2 Field Observations and Model Predictions of Radiation Shading

The results of the model simulations were consistent with inferences drawn from the field results. The model results demonstrated that differential heating due to depth differences and radiation shading can establish horizontal temperature differences and drive convective exchange flows between the littoral and pelagic zones in a wetland. Diurnal trends in the inferred convective currents were similar for radiation shading by submerged and emergent macrophytes at Hopwoods Lagoon. This occurred because the emergent canopy was sparse and contributed little to radiation shading, compared with the more significant differential heating observed between submerged macrophytes and open water. The main contribution of the sparse emergent macrophyte canopy appeared to be some thermal insulation during the cooling phase. However, the magnitude of the horizontal temperature differences and hence the inferred currents was larger for the submerged macrophyte zones than the zones containing both submerged and emergent macrophytes, because the emergent canopy reduced the net shortwave radiation influx at the water surface.

The predicted convective velocities were small, and generally less than $10\,\mathrm{mm\,s^{-1}}$. However, these compared well with the convective velocities estimated using the scaling relationships in Chapter 3. Such flows would be negligible in most wetlands with significant inflow, but could be highly significant in topographically-sheltered wetlands without significant net flows.

During the daytime (i.e. the heating phase), inferred and predicted buoyant surface flows were typically directed out of the macrophyte zones towards the open water, with slower overnight flows in the opposite direction. At mid-depth, convective flows were generally slower and from the open water towards the macrophyte zones throughout most of the diurnal cycle. A cool gravity current was inferred along the bed from the macrophyte zones towards the open water.

Radiation shading by submerged macrophytes in shallow littoral zones established horizontal temperature differences which were in the same direction as those created by differential heating purely due to depth differences in either (idealised) open water or submerged macrophyte simulations. However, differential heating due to radiation shading by a moderate or denser emergent macrophyte canopy ($LAI \geq 2.5$ in the simulations) created temperature differences in the opposite direction. At these moderate canopy densities, radiation shading by emergent macrophytes reduced surface temperatures in vegetated littoral zones relative to unshaded, open water zones.

The field observations and model results at Hopwoods Lagoon indicated that convective flows between shallow vegetated zones and deeper open water zones due to differences in depth were generally:

- **enhanced** by differential heating due to radiation shading by submerged macrophytes with $\eta_{SV} > \eta_{OW}$
- **opposed** by differential heating due to radiation shading by emergent macrophytes with $LAI \geq 2.5$.

The field and model results suggested that submerged macrophytes could more effectively promote convective mixing between vegetated littoral zones and open water zones than emergent macrophytes. In fact, radiation shading by a canopy of moderate or denser emergent macrophytes could oppose diurnal convective mixing driven by differential heating due to depth differences between littoral and pelagic zones.

Despite the simplifications incorporated in the radiation shading simulations, where variation in the density of macrophytes was simulated by changing only the underwater attenuation of shortwave radiation or the canopy *LAI*, the results were broadly consistent with the inferences drawn from field observations and with the published observations of others (including Waters, 1998; James and Barko, 1991; Oldham and Sturman,2001).

7.3 Observations of Radiation Shading at Manly Dam by Waters (1998)

The most significant previous study of radiation shading by macrophytes and convective exchanges between open water and emergent macrophyte zones was undertaken by Waters (1998). The results of his study led Waters to propose a convective flow classification scheme, which is summarised in Section 2.3.4 (page 36). The major findings of Waters are compared with those of the present study in the following sections, and the generality of his flow classification scheme is then assessed.

7.3.1 Physical Characteristics of the Manly Dam Wetland Sites

Field investigations were undertaken by Waters (1998) between February 1994 and June 1996 at two sites in Manly Dam, which is located in Sydney's northern suburbs. The sites were located at the northern end of the dam, approximately 1000 m from the dam wall. The majority of the experiments were conducted at Site B, which had an area of ~250 m^2 and an average water depth of ~1.0 m. This site was partially vegetated with the emergent *Typha orientalis* (Broadleaf Cumbungi), which is closely related and similar to the *Typha domingensis* studied during the present investigation at the Deep Creek *Typha* wetland and Warriewood Wetlands. The physical characteristics of the emergent macrophyte canopies at the three wetlands are compared in Table 7.1.

Wetland Site	Survey Dates	Stem Density n_s (m^{-2})	Height h_L (m)	Mean Stem Width (mm)	*LAI* (m^2 m^{-2})
Manly Dam	Jun 1996	256 – 364	1.0	12.0	see below
Deep Creek *Typha*	Aug 1999	166 – 265	1.8	13.2	1.2 – 1.5
	Nov 2000	129 – 167	2.0	13.6	0.9 – 1.6
	Apr 2001	166 – 176	2.1	14.8	1.8
Warriewood Wetlands	Oct 1999	206 – 254	2.0	18.9	2.9 – 3.0

Table 7.1: Summary of canopy characteristics at Manly Dam (Typha orientalis, from Waters, 1998) and at Deep Creek and Warriewood Wetlands (Typha domingensis, present study).

Unfortunately, it was not possible to calculate the foliage area density function or *LAI* for the *Typha orientalis* canopy, because no information was provided by Waters (1998) concerning the vertical variability in the stem density and dimensions. However, it can be seen from Table 7.1 that, while the stem density was higher at Manly Dam, this canopy was shorter and the mean stem width was smaller than that at the Deep Creek and Warriewood sites. These comparisons suggest that the *LAI* for the *Typha orientalis* canopy was probably within the range observed at the *Typha domingensis* sites (~1.0–3.0), and certainly higher than the *LAI* for *Eleocharis sphacelata* at Hopwoods Lagoon (0.2–0.5).

7.3.2 Convective Flows at the Manly Dam Wetland Sites

7.3.2.1 Convective Flows during Summer

During summer, Waters (1998) reported that differential heating and cooling between emergent macrophytes and open water zones in Manly Dam resulted in warmer temperatures in the open water during the day, but cooler temperatures overnight. Depth-averaged temperatures in the open water were rarely lower than in the emergent macrophyte zone, and horizontal temperature differences of $\leq 5°C$ persisted between the open and vegetated zones for several weeks at a time. Considering surface flows only, as the classification scheme does not consider mid-level flows, this was classified as an **ordinary monoconvective** regime (Section 2.3.4), and is shown in Figure 7.1(a). This trend is not unique to Manly Dam, however, and persistent stratification has also been reported during summer in a 1.8 m deep wetland in Massachusetts, USA (Andradóttir and Nepf, 2000b), for example.

As discussed in Section 6.5.4.1 (page 249) and shown schematically in Figure 7.1(b), the opposite was inferred at Hopwoods Lagoon. Using the scheme proposed by Waters (1998) the diurnal flow regime in summer would be classified as **diconvective**, comprising:

- reversed convection during the day, from the macrophytes towards the open water
- ordinary convection overnight, from the open water towards the macrophytes.

It was evident from the field and model results that stratification develops and decays on a diurnal timescale at Hopwoods Lagoon during summer, and is known to remain stable for many days or weeks at a time in other wetlands. From this simple comparison, it

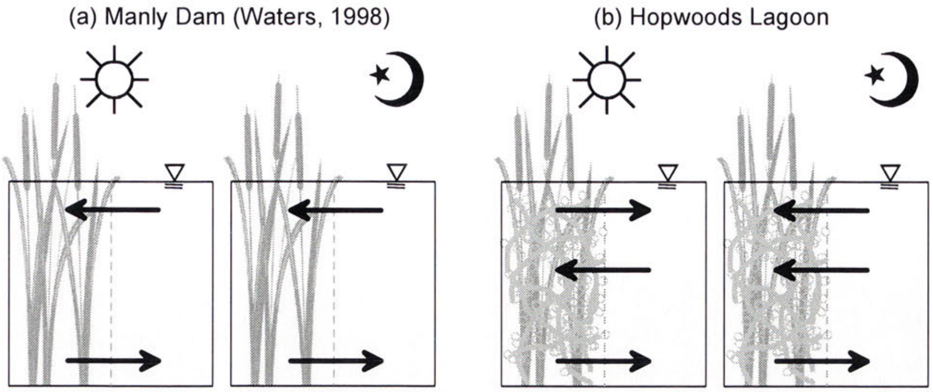

Figure 7.1: Inferred summer convective flow regimes between emergent macrophyte and open water zones at (a) Manly Dam (Waters, 1998), and (b) Hopwoods Lagoon (present study).

is also apparent that the direction of convective flows between open water and emergent macrophyte zones may vary between different wetlands.

7.3.2.2 Convective Flows during Winter

In winter, Waters (1998) observed differences in vertical temperature stratification between open water and macrophyte zones, which created horizontal temperature differences between the zones. Vertical stratification was weaker in winter than during summer but decayed rapidly overnight, and horizontal temperature differences between the zones were also lower than during summer. The wetland at Manly Dam was classified as diconvective in winter, as shown schematically in Figure 7.2(a), rather than the ordinary monoconvective regime observed in summer. By contrast, the inferred flow regime was essentially monoconvective at Hopwoods Lagoon, as shown in Figure 7.2(b).

Stratification developed and decayed on a diurnal time scale at Hopwoods Lagoon during winter as well as summer, although the strength of the vertical stratification was significantly lower in winter. The inferred convective flow regime at Hopwoods Lagoon was different in winter and summer, and in both cases, different to that observed by Waters (1998) at Manly Dam.

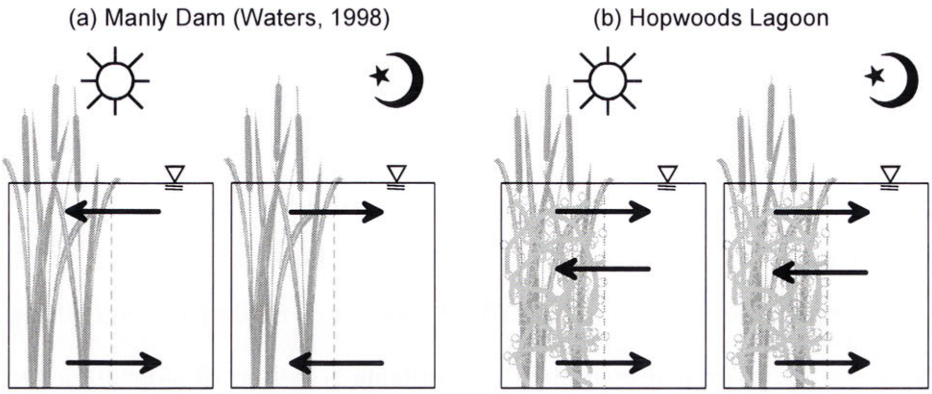

Figure 7.2: Inferred winter convective flow regimes between emergent macrophyte and open water zones at (a) Manly Dam (Waters, 1998) and (b) Hopwoods Lagoon (present study).

7.3.3 Comparisons Between Hopwoods Lagoon and Manly Dam

Although the direction and diurnal variation in horizontal temperature differences and inferred convective currents was not consistent between Hopwoods Lagoon and Manly Dam, the differences can be readily explained. The density of the emergent macrophyte canopy was higher in the experiments of Waters (estimated LAI=1.0–3.0) than at Hopwoods Lagoon (LAI=0.2–0.5). He also did not explicitly consider the effects of submerged macrophyte components, so differential heating was assumed to be primarily due to moderately dense emergent macrophytes. At Hopwoods Lagoon, radiation shading was found to be insignificant due to the sparse emergent macrophyte canopy and primarily due to differential absorption of shortwave radiation by the submerged macrophytes, which occurred in all emergent macrophyte zones. The comparisons depicted in Figure 7.3 are considered a more valid comparison than Figures 7.1 and 7.2.

It was one of the objectives of this study to examine the generality of the convective circulation regimes and classification scheme described by Waters (1998) when applied to other wetlands. Comparison with the field observations from Hopwoods Lagoon suggests that convective regimes driven by radiation shading between macrophyte and open water areas are distinctly different for shading primarily by emergent macrophytes, and shading primarily by submerged macrophytes. They are, in fact, almost opposite in direction.

In summary, the flow regimes and classification scheme described by Waters (1998):

- are broadly applicable to radiation shading by a moderately dense emergent macrophyte canopy
- were based on observations at two sites in Manly Dam and consequently do not account for other canopy densities, so are not applicable to radiation shading by a sparse emergent macrophyte canopy ($LAI<2.5$ in the model simulations)
- are not applicable to radiation shading by submerged macrophytes.

Understanding the flow regimes has important implications for the design and management of the macrophyte zones in constructed wetlands, when it is desired to promote circulation between the two zones.

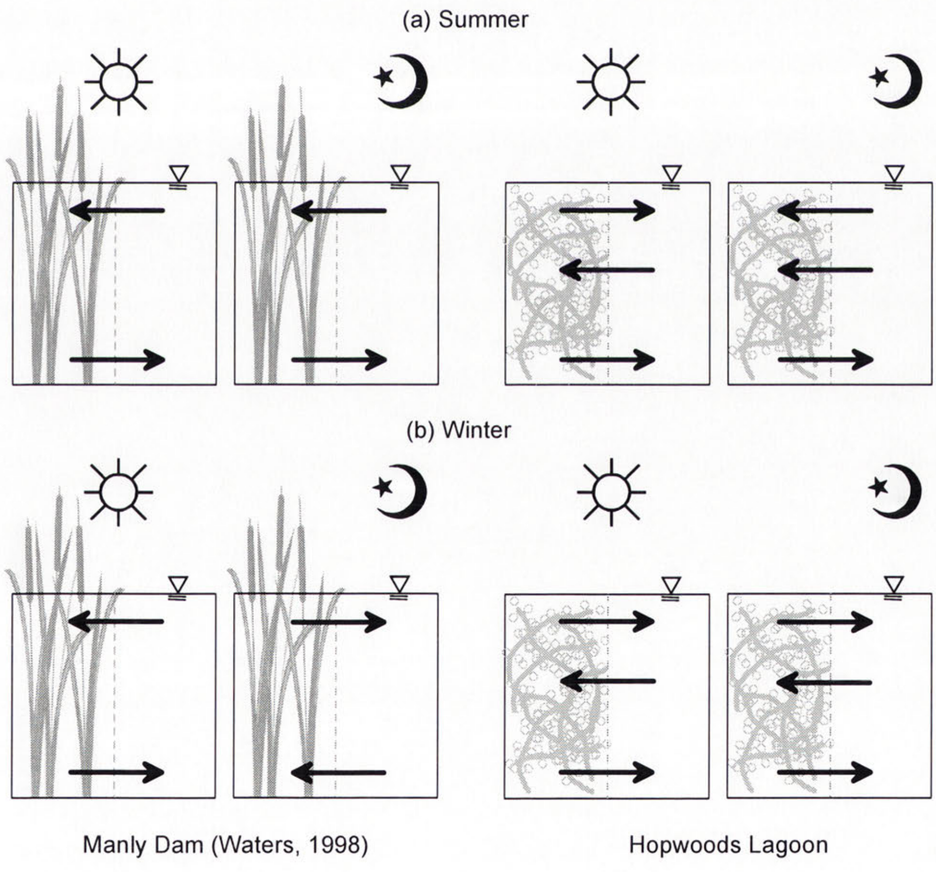

Figure 7.3: Inferred convective flow regimes due to radiation shading by moderately dense emergent macrophytes at Manly Dam (Waters, 1998) and dense submerged macrophytes at Hopwoods Lagoon (present study).

7.4 Hydrodynamic Implications of Radiation Shading by Macrophytes

Radiation shading by emergent and submerged macrophytes alters the influx and vertical distribution of shortwave radiation available for heating in a wetland. This results in vertical temperature stratification and horizontal temperature differences between different wetland zones. The strength and direction of these temperature gradients is largely dependent upon the type (emergent or submerged) and density of the macrophytes, and determines the extent of mixing within the wetland. This has important implications for vertical and horizontal transport processes within a wetland, particularly in the absence of a net flow and/or wind-induced advective mixing.

The field and model results demonstrated that vertical stratification generally develops and decays on a diurnal timescale in both open water and macrophyte zones. Vertical temperature gradients of $>10\,°\mathrm{C\,m^{-1}}$ were observed in the emergent macrophyte zones during January 2001 (summer) while vertical temperature gradients in the adjacent open water zone were $\sim 5\,°\mathrm{C\,m^{-1}}$. Winter temperature gradients were generally around half these values. Strong vertical temperature gradients are indicative of a stably stratified water column which is resistant to surface-induced vertical mixing. However, overnight cooling and penetrative convection were sufficient on most evenings to overturn the daytime stratification, and produce essentially isothermal conditions both vertically and horizontally between the wetland zones.

The rapid response of a wetland such as Hopwoods Lagoon (area $\sim$6.5 ha, maximum depth $\sim$3.2 m) to the diurnal cycles in meteorological forcing means that it is unlikely to experience the persistent stratification and hydrodynamic isolation of the hypolimnion experienced in larger lakes and reservoirs. Water quality issues such as phosphorus release (Mitsch and Gosselink, 1993), which are associated with anoxic conditions near the bed, are therefore less likely in a wetland which mixes daily both vertically and horizontally.

Observed and predicted differential heating and cooling between the open water and macrophyte zones produced horizontal temperature differences of $<6.0/35=0.2\,°\mathrm{C\,m^{-1}}$ between the two zones which drove diurnal convective flow regimes. The passive, convective mixing generally resulted in warm, shallow surface flows with $u < 0.016\,\mathrm{mm\,s^{-1}}$ out of submerged or sparse emergent macrophyte zones during the day with mid-depth intrusive flows from the open water towards the macrophytes. Overnight, surface flows were slower and deeper and generally directed from the open water towards the macrophyte zones. Surface flows were in the opposite direction in dense emergent macrophyte zones. In all cases, a cool gravity current was inferred along the bed from the macrophyte zones towards the open water (James and Barko, 1991; Oldham and Sturman, 2001), although this was not verified in the field.

Occurrence of such flows on a diurnal timescale ensures that macrophyte zones will not become stagnant, and that constituents in the water body are transported between open water and macrophyte zones. This is important for nitrogen cycling (Mitsch and Gosselink, 1993), and, for example, is known to be essential for assimilation of bioavailable nutrients (Brix, 1994). It can also influence the distribution of microorganisms, flora and fauna within a wetland (Wetzel, 1983).

It is evident from this discussion that constructed wetlands should be designed to ensure that vertical stratification is permitted to occur and decay on a daily basis. This creates horizontal temperature differences and promotes horizontal convective exchanges over the depth of the water column, between open water and emergent macrophyte zones. Similar comments apply to the management of other water bodies containing aquatic vegetation, as outlined in Section 7.5.

7.4.1 Importance of Depth and Differences in Underwater Attenuation

The model simulation results indicated that both depth differences and differences in underwater attenuation (radiation shading by submerged macrophytes) could create horizontal temperature differences and lead to convective flows between littoral and pelagic wetland zones. The results also indicated that these processes could complement one another and enhance convective flows between shallow vegetated zones and deeper open water zones in a wetland.

The relationship between depth and underwater attenuation coefficient was shown in Figure 3.10 (page 95). From this graph, it is apparent that differences in depth less significantly affect the available shortwave radiation flux in clear waters or unvegetated zones with a low attenuation coefficient (η). In more turbid waters or macrophyte zones with higher η, even small changes in depth between two sites can lead to appreciable differences in heating.

The relationship between depth differences and differences in underwater attenuation should therefore be considered in design and management of wetlands, especially where it is desired to promote convective exchanges between different wetland zones.

7.4.2 Importance of Convection and Advection

Although not the focus of the hydrodynamic simulation experiments, wind-induced advective currents appeared to dominate over convective flows when the horizontal temperature differences were small and wind speeds increased during the late afternoon. Scaling analyses (Figure 3.12, page 109) suggested that only a moderate wind speed of u_{10} ~1–4 m s^{-1} would be required to arrest a 0.5 m deep surface flow driven by a horizontal temperature gradient of ~0.01°C m^{-1}. These low wind speed thresholds would be exceeded often in the field, so advective flows could be expected much of the time in wetlands which were not topographically or otherwise sheltered from prevailing winds.

The results from simulations run *with* and *without* surface wind stresses suggested that wind sheltering by the emergent macrophyte canopy provided a preferential upwind flow path at the water surface, against the prevailing wind direction. Convective flows driven by horizontal temperature differences were either enhanced or opposed by the advective currents, depending on the directions of the temperature gradients and the winds.

The radiation shading simulations could be extended in the future to a more focused consideration of the relative importance of advective and convective flows. The hydrodynamic model developed for Hopwoods Lagoon would require refinement of the vegetation drag, wind stress and mixing parameterisation schemes. Ideally, the flow resistance, wind stress coefficients and mixing coefficients would be parameterised as functions of the density of the submerged and/or emergent macrophytes. Simple approximations were used in the hydrodynamic model for Hopwoods Lagoon, but further investigation is warranted into wind sheltering and the relative importance of advective and convective processes using a more sophisticated model.

7.5 Implications For Wetland Design and Management

Macrophytes are an intrinsic and essential component of natural or constructed wetland systems. The type, density and spatial distribution of macrophytes influences the differential heating and mixing between wetlands zones, as has been observed in the field and demonstrated through the hydrodynamic simulation experiments. In the design of a wetland, these parameters can be managed to enhance horizontal convective mixing and hence improve water quality in wetlands, particularly where there is little or no through flow. Wetland design and management is highly site-specific because they are open systems which are strongly influenced by the surrounding environment (Brady and Riding, 1996). However, the following principles can be applied to the design and management of any partly-vegetated freshwater water body with no significant through flow.

The macrophyte zones in a wetland are the sites of highest microbial activity, where physical and biochemical processes which remove nutrients and other pollutants are most concentrated (Brix, 1994). Wetland design should therefore aim to emulate and optimise the natural treatment processes occurring in these zones, especially the assimilation of bioavailable nutrients, filtration and sedimentation. This requires promotion of natural (passive) convective mixing between open water and macrophyte zones. The necessary differential heating and cooling between the wetland zones can be achieved using depth differences, radiation shading above the water surface by emergent macrophytes or differential underwater absorption of radiation by submerged macrophytes, or a combination of the three.

The study results suggested that **radiation shading by submerged macrophytes** would most effectively promote differential heating and convective exchanges between shallow macrophyte zones and deeper open water areas. The main design factors to consider would be the density of the submerged macrophytes, and hence the vertical distribution of heat within the water column, and the distribution of open water and macrophyte zones. Although not directly investigated in the present study, flow resistance due to submerged macrophytes typically increases with increasing macrophyte density (Tsihrintzis and Madiedo, 2000). Too high a density would greatly retard horizontal flows with open water zones, regardless of the temperature gradients and buoyancy forcing.

To maximise contact with macrophytes, the vegetation should ideally be established in bands situated normal to any dominant flow direction (for example, due to prevailing wind-induced surface currents or event flows). Alternatively, vegetation should be located in continuous zones around the perimeter of the wetland to prevent short-circuiting and preferential flow paths which do not include the macrophyte zones (Kadlec, 1995).

Radiation shading by emergent macrophytes can also be used to promote differential heating and convective exchanges between shallow macrophyte zones and deeper open water areas, providing the water surface is permitted to warm more during the day than the adjacent open water areas. This is jointly dependent on the difference in underwater attenuation of radiation between the open water and emergent macrophyte zones and sufficiently low attenuation of shortwave radiation by the emergent canopy. At higher canopy densities ($LAI \geq 2.5$ in the model simulations), the net shortwave radiation flux at the water surface will be too low to create a positive horizontal temperature difference at the surface between the macrophyte zone and the open water. Convective flows would then be expected to occur in the opposite direction (as observed by Waters, 1998) and against those promoted by the depth difference, thus reducing the effectiveness of either mechanism. Comments made above concerning the spatial distribution of macrophyte and open water zones apply equally to wetlands containing emergent macrophytes.

Selection of macrophyte species may also be influenced by other objectives, such as aesthetics or habitat creation (DLWC, 1998). However, to achieve and retain the water quality advantages offered by convective mixing between open water and macrophyte zones, it is important that the hydrodynamic implications are considered. Maintenance of the macrophytes at a relatively uniform density over time is also important, to avoid transition from the design convective flow regime to an unfavourable regime. This could, for example, occur due to a significant increase in the density of an emergent macrophyte canopy.

In addition to the passive convective mixing processes between macrophyte and open water zones, it can be advantageous to promote some wind-induced mixing. As shown through scaling analyses (Section 3.8) and observed in the field, horizontal advective flows are more effective in transporting water between different macrophyte zones at the surface and mixing the water column in the vertical. However, excessive wind-induced mixing in shallow systems can cause resuspension of sedimentary materials from the bed (Blom et al., 1994). This is clearly undesirable from a water quality perspective, because it potentially releases nutrients and other pollutants from long-term storage in the sedimentary matrix.

Chapter 8

CONCLUSIONS AND RECOMMENDATIONS

8.1 Conclusions

This thesis reports on research into the effects of radiation shading by macrophytes on wetland hydrodynamics. The specific objectives of the research were to:

(1.) test the applicability of existing simple models for attenuation of shortwave radiation by a vegetation canopy in a new application to emergent macrophytes in a wetland

(2.) assess the hydrodynamic response of a natural wetland to diurnal and seasonal changes in meteorological forcing, and the consistency of these responses with observations made by other researchers in different wetlands

(3.) investigate the effects of radiation shading by emergent and submerged macrophytes on convective hydrodynamics in wetlands, and the effectiveness of these in promoting horizontal flows between vegetated littoral zones and deeper open water areas.

The study included field experiments and numerical modelling using a version of the existing three-dimensional, finite-element hydrodynamic model RMA-10 (King, 1993), which was modified by the present author. While addressing the research objectives, this study also contributed several unique data sets which may be useful to future researchers. These data sets:

- quantify the structural properties of three emergent macrophyte species endemic to the greater Sydney region (*Typha domingensis*, *Juncus kraussii* and *Eleocharis sphacelata*), and
- record the annual variation in meteorological conditions and water temperatures at Hopwoods Lagoon in the Macdonald Valley, 75 km north of Sydney.

The major findings from the study are outlined below.

Four simple canopy attenuation models were tested using radiation profiles measured in the canopies of the three emergent macrophyte species. The models included:

- empirical forms of Beers Law which describe exponential attenuation of radiation using attenuation coefficients derived from field measurements, and
- theoretical forms of Beers Law which predict attenuation as a function of theoretical attenuation coefficients.

The empirical model results demonstrated that measured PAR profiles within emergent macrophyte canopies can be represented by an exponential attenuation relationship. The models could predict the radiation flux at the water surface beneath a wetland canopy. Empirical attenuation coefficients based on the downward cumulative leaf area index (LAI) were found to better represent canopy attenuation, than coefficients based on the penetration depth beneath the top of the canopy.

Without an extensive database of measured radiation profiles, empirical attenuation coefficients are unable to account for the variation in canopy properties, the time of day and season. They are therefore only strictly applicable to the conditions under which they are derived. Theoretical models using attenuation coefficients calculated independently of field data were found to be generally less successful at predicting the radiation flux at the water surface. However, they should be used in the absence of empirical information across the range of modelling conditions.

It was concluded that a form of Beers Law based on the G-function (a dimensionless projection of the foliage area on a horizontal plane) was the most appropriate of the simple theoretical models. In this model, attenuation of radiation is a function of the canopy LAI, foliage area inclination and solar elevation. Calculated theoretical attenuation coefficients ranged from $\mathcal{K}_{LAI}$=0.26 – 1.45$\mathrm{m^2m^{-2}}$ in the *Typha domingensis* canopies at Deep Creek and Warriewood Wetlands, and 0.73 – 1.55 $\mathrm{m^2m^{-2}}$ in the *Juncus kraussi* canopy at Deep Creek, with the lower values applying close to solar noon and the higher values early in the morning. These were within the expected range (Ross, 1981). The results were less conclusive for the sparse *Eleocharis sphacelata* canopy at Hopwoods Lagoon, which suggested that there may be a threshold canopy density (around LAI=0.5) below which the exponential relationship does not apply.

The underwater attenuation of shortwave radiation in the PAR waveband was found to be reasonably well represented by a form of Beers Law in both the open water and macrophyte zones at Hopwoods Lagoon. Mean attenuation coefficients derived empirically from field measurements were $\overline{\eta}_{OW} = 1.8\,\mathrm{m^{-1}}$ in the open water zone and $\overline{\eta}_{SV} = 4.4\,\mathrm{m^{-1}}$ in the submerged macrophyte zone. These were well within the published range for PAR attenuation in natural inland water bodies in Australia (Kirk, 1983).

The hydrodynamic response at Hopwoods Lagoon to the meteorological forcing displayed distinct trends over diurnal and seasonal timescales. On most days throughout the annual cycle, the wetland was found to stratify vertically during the heating phase (while the net surface heat flux $H_{NET} > 0$) and to destratify to an approximately isothermal state overnight. Horizontal water temperature differences were observed between open water and macrophyte zones throughout much of the diurnal cycle, but generally moving in opposite directions throughout the day and overnight. The strength of the vertical and horizontal temperature gradients varied throughout the year, depending on the magnitude of H_{NET}. These were generally strongest in summer (>10°C m^{-1} in the vertical and < 0.17°C m^{-1} in the horizontal) and weakest in winter (approximately half the summer values).

At Hopwoods Lagoon during summer, the inferred convective flows typically comprised daytime shallow surface flows (h <0.4 m) with u <0.016 mm s^{-1} out of the macrophyte zones towards the open water, but with mid-depth intrusive flows in the opposite direction. Overnight surface flows were typically directed from the open water towards the macrophyte zones, and were slower and deeper than the daytime flows. During winter, the currents were slower but persisted throughout most of the diurnal cycle. They comprised a shallow flow from the macrophyte zones towards the open water and a mid-depth return flow. A cool gravity current was inferred along the bed from the macrophyte zones towards the open water, throughout the diurnal cycle.

Diurnal and seasonal variation in the convective flows at Hopwoods Lagoon displayed some similarities with the observations of other researchers in different wetlands. However, the flow regimes were almost opposite to those reported from similar experiments conducted by Waters (1998) in Manly Dam, Sydney. The differences were due to the effects of radiation shading by macrophytes with different physical characteristics (growth form, density and spatial distribution). The sensitivity of the flow regime in a wetland to the vegetation structure indicates the highly site-specific hydrodynamic response of a wetland to the local meteorological forcing.

Using field observations and the results of hydrodynamic simulation experiments, a major conclusion of the present research is that the effects of radiation shading by emergent and submerged macrophytes on convective flows are distinctly different. Noting that macrophytes are generally restricted to the shallow, littoral zones of wetlands, the following conclusions were drawn.

- **Radiation shading by submerged macrophytes** created horizontal temperature differences between open water and macrophyte zones in the same direction as those due to depth differences between the zones. These temperature differences were complementary and radiation shading by submerged macrophytes therefore enhanced convective flows between shallow macrophyte zones and deeper open water areas.
- **Radiation shading by emergent macrophytes** produced different effects, depending on the density of the canopy.
  - Beneath a **sparse to moderately dense canopy** ($LAI < 2.5$ in the model simulations), horizontal temperature differences were in the same direction as those due to depth differences, but smaller than those due to radiation shading by submerged macrophytes. The effect of temperature differences between macrophyte and open water zones were also complementary and slightly enhanced the convective flows.
  - Beneath a **denser canopy**, horizontal temperature differences were in the opposite direction to those due to depth differences. These opposing tendencies arrested or reversed the convective flows due to depth differences between the macrophyte and open water zones.

While these conclusions may appear intuitive, the different effects of radiation shading by submerged and emergent macrophytes on convective hydrodynamics are not known to have been previously investigated or reported. These findings explain the distinctly different convective flow regimes observed during the present study at Hopwoods Lagoon (sparse emergent macrophytes occurring with moderately dense submerged macrophytes) and the study by Waters (1998) at Manly Dam (moderately dense emergent macrophytes).

The field and modelling results demonstrated that convective flows between macrophyte and open water zones can be significant when there is little or no flow through a wetland. Although not the focus of this study, wind-induced (advective) processes were found to generally dominate over the convective flows. Scaling analyses suggested that only moderate wind speeds of u_{10} ~1–4 m s^{-1} would be required to arrest a 0.5 m deep surface flow driven by a horizontal gradient of ~0.01°C m^{-1}. Advective flows could therefore be expected to dominate much of the time in wetlands which were not topographically or otherwise sheltered from prevailing winds.

The findings of this study have important implications for design of constructed wetlands and management of all water bodies containing macrophytes, particularly where it is desired to promote passive convective mixing between open water and macrophyte zones. Differential heating and cooling between these zones can be achieved using depth differences or radiation shading by emergent and/or submerged macrophytes. The field and model results suggest that submerged macrophytes would more effectively promote convective mixing between shallow macrophyte zones and open water, than emergent macrophytes. Dense emergent macrophytes could mitigate or even prevent diurnal convective mixing between the zones, depending on depth differences between the two.

Aesthetic and other design objectives may dictate the type of macrophytes required in a particular application, but to achieve the water quality benefits enhanced by convective mixing between the wetland zones, it is essential that the hydrodynamic implications of any proposed plantings be fully considered.

8.2 Recommendations for Future Research

The results of this investigation have contributed to the knowledge of the effects of radiation shading by macrophytes on convective hydrodynamics in wetlands. However, analysis of the results of field experiments and hydrodynamic simulations has highlighted a number of areas which would benefit from further investigation. These are summarised below.

- The canopy radiation profile experiments were conducted using a single PAR sensor to measure the radiation flux *sequentially* at various levels in the canopy foliage. It is recommended that additional experiments be conducted using a number of sensors to measure the radiation flux *simultaneously* above the canopy, at the water surface, and at various levels within the canopy foliage. This would allow greater certainty in the calculation of relative PAR profiles than could be achieved in the present study. It is also recommended that additional measurements be made simultaneously using a number of sensors mounted at the same elevation but distributed horizontally throughout an emergent canopy. This would allow spatial averaging between relative PAR profiles, and should provide mean profiles which are more representative of mean canopy conditions.

- Testing of empirical forms of Beers Law against the field relative PAR profiles suggested there may be a threshold canopy density below which attenuation of shortwave radiation is not well represented by an exponential relationship. This could not be further tested during the present study, but should be confirmed using additional field studies.

- The field measurements demonstrated differential heating due to radiation shading by macrophytes at Hopwoods Lagoon, where the density of emergent macrophytes was low and the density of submerged macrophytes was moderate to high. However, the emergent macrophyte zones were all colonised by submerged macrophytes so the effects of the two types could only be interpreted by difference. A more direct quantitative comparison of the relative effects of radiation shading by emergent and submerged macrophytes would be facilitated by additional studies in wetlands with substantial but separate stands of emergent and submerged macrophytes. Using simultaneous measurements of meteorological conditions, water temperatures and water velocities, it should be possible to isolate the effects of radiation shading due to emergent macrophytes and submerged macrophytes.

- The hydrodynamic modelling results supplemented field observations and allowed qualitative comparison of the relative effects of radiation shading by submerged and emergent macrophytes on convective hydrodynamics. It is recommended that refinements be made to the modified numerical model prior to undertaking a more rigorous, quantitative investigation into the effects of radiation shading by submerged and emergent macrophytes. These include:
  - validation of the model using data collected in a different wetland
  - development and testing of a more sophisticated parameterisation for the vegetation resistance force, which is directly related to the density of the macro-

phytes and can vary both horizontally and with elevation in the water column

  - development and testing of an alternative parameterisation for wind sheltering by emergent macrophytes, which estimates wind attenuation as a function of the physical properties of the canopy
  - review of the parameterisation of vertical mixing processes in the model, particularly during the unstable, cooling phase
  - validation of the bed heat flux module introduced into the three-dimensional hydrodynamic model RMA-10, using simultaneous water and sediment temperature data.

- Given the importance of advective effects in wetlands which are not topographically or otherwise sheltered from prevailing winds, it is also recommended that a quantitative investigation be undertaken into the relative effects of radiation shading and wind sheltering on wetland hydrodynamics.

Chapter 9

REFERENCES

Abtew, W., (1996), 'Evapotranspiration measurements and modeling for three wetland systems in South Florida', *Water Resources Bulletin*, **32**(3), 465–473.

Adrian, R. J., Ferreira, R. T. D. S., and Boberg, T., (1986), 'Turbulent thermal convection in wide horizontal fluid layers', *Experiments in Fluids*, **4**, 121–141.

Anderson, M. C., (1966), 'Stand structure and light penetration. II. A theoretical analysis.', *Journal of Applied Ecology*, **3**(1), 41–54.

Anderson, M. G., and Idso, S. B., (1987), 'Surface Geometry and Stomatal Conductance Effects on Evaporation from Aquatic Macrophytes', *Water Resources Research*, **23**(6), 1037–1042.

Andradóttir, H. O., and Nepf, H. M., (2000a), 'Thermal mediation by littoral wetlands and impact on lake intrusion depth', *Water Resources Research*, **36**(3), 725–735.

Andradóttir, H. O., and Nepf, H. M., (2000b), 'Thermal mediation in a natural littoral wetland: Measurements and modelling', *Water Resources Research*, **36**(10), 2937–2946.

Asrar, G., and Myneni, R. B., (1991), 'Applications of Radiative Transfer Models for Remote Sensing of Vegetation Conditions and States', in Myneni, & Ross (Myneni and Ross, 1991), pp. 537–558.

Ayra, S. P., (1988), *Introduction to Micrometeorology.* Academic Press, Inc, San Diego.

Benoit, G., and Hemond, H., (1996), 'Vertical eddy diffusion calculated by the flux gradient method: Significance of sediment-water heat exchange', *Limnology and Oceanography*, **41**(1), 157–168.

Blom, G., van Duin, E. H. S., and Lijklema, L., (1994), 'Sediment resuspension and light conditions in some shallow Dutch lakes', *Water Science and Technology*, **30**(10), 243–252.

Brady, A., and Riding, T., (1996), *The Importance of Wetlands in Water Resource Management - A Literature Review.* Wetlands Section, Technical Services Division, Department of Land & Water Conservation, NSW Government.

Brix, H., (1994), 'Functions of macrophytes in constructed wetlands', *Water Science and Technology*, **29**(4), 71–78.

Brown, L. C., and Barnwell, T. O., (1987), *The Enhanced Stream Water Quality Models QUAL2E and QUAL2E-UNCAS: Documentation and User Manual.* Environmental Research Laboratory, Office of Research and Development, U.S. Environmental Protection Agency.

Brutsaert, W., (1982), *Evaporation into the atmosphere.* D. Reidel Publishing Company, London.

Bukata, R. P., Jerome, J. H., Kondratyev, K. Y., and Pozdnyakov, D. V., (1995), *Optical Properties and Remote Sensing of Inland and Coastal Waters.* CRC Press, Boca Raton.

Burman, R., and Pochop, L. O., (1994), *Evaporation, evapotranspiration and climatic data.* Elsevier Science Publishing Company, Amsterdam.

Central Mapping Authority of New South Wales, (1976), *Auburn 9031–1–S. Scale 1:25 000.* (1st edition).

Central Mapping Authority of New South Wales, (2000), *Mona Vale 9130–1–S. Scale 1:25 000* (3rd edition).

Chapra, S. C., (1997), *Surface water-quality modeling.* McGraw-Hill Book Company, New York.

Chen, C.-L., (1976), 'Flow resistance in broad shallow grassed channels', *Journal of the Hydraulics Division*, **102**(HY3), 307–322.

Cheung, T. K., and Street, R. L., (1988), 'The turbulent layer in the water at an air-water interface', *Journal of Fluid Mechanics*, **194**, 133–151.

Chow, V. T., Maidment, D. R., and Mays, L. W., (1988), *Applied Hydrology.* McGraw-Hill Book Company, New York.

Cionco, R. M., (1972), 'A wind-profile index for canopy flow', *Boundary-Layer Meteorology*, **3**, 255–263.

Coates, M., and Ferris, J., (1994), 'The radiatively driven natural convection beneath a floating plant layer', *Limnology and Oceanography*, **39**(5), 1186–1194.

Coates, M. J., and Patterson, J. C., (1993), 'Unsteady natural convection in a cavity with non-uniform absorption of radiation', *Journal of Fluid Mechanics*, **256**, 133–161.

Collier, R. D., (1982), 'Calibration with Confidence: The Assurance of Temperature Accuracy', in Schooley, J. F. (Ed.), *Temperature: Its Measurement and Control in Science and Industry*, pp. 1311–1315. American Institute of Physics, New York.

Cowardin, L. M., Carter, V., Folet, F. C., and La Roe, E. T., (1979), *Classification of Wetlands and Deepwater Habitats of the United States.* US Department of the Interior, US Fish and Wildlife Service.

Craig, P. D., and Banner, M. L., (1994), 'Modelling Wave-Enhanced Turbulence in the Ocean Surface Layer', *Journal of Physical Oceanography*, **24**(12), 2546–2559.

Cristofor, S., Vadineanu, A., Ignat, G., and Ciubuc, C., (1994), 'Factors affecting light penetration in shallow lakes', *Hydrobiologia*, **275–276**, 493–498.

Dale, H. M., and Gillespie, T., (1976), 'The influence of floating vascular plants on the diurnal fluctuations of temperature near the water surface in early spring', *Hydrobiologia*, **49**(3), 245–256.

Dale, H. M., and Gillespie, T., (1977), 'The influence of submersed aquatic plants on temperature gradients in shallow water bodies', *Canadian Journal of Botany*, **55**, 2216–2225.

Danard, A. M. B., and Murty, T. S., (1994), 'Storm Surge Mitigation through Vegetation Canopies', *Natural Hazards*, **9**, 155–166.

Deas, M. L., and Lowney, C. L., (2000), *Water Temperature Modeling Review, Central Valley.* Bay Delta Modeling Forum.

Del Pozo, A., and Dennett, M. D., (1999), 'Analysis of the distribution of light, leaf nitrogen, and photosynthesis within the canopy of Vicia faba L. at two contrasting plant densities', *Australian Journal of Agricultural Research*, **50**, 183–189.

Dennis, W. M., and Isom, B. G. (Eds.)., (1984), *Ecological Assessment of Macrophyton:*

Collection, Use and Meaning of Data. ASTM Special Technical Publication 843, Philadelphia.

DLWC, (1998), *The Constructed Wetlands Manual.* New South Wales Department of Land and Water Conservation, Sydney.

Donelan, M., (1990), *Air-Sea Interaction.* John Wiley & Sons, Inc. reprinted from *The Sea: Ocean Engineering Science.* Volume 9 - Two Volume Set.

Dyer, A. J., and Hicks, B. B., (1970), 'Flux-gradient relationships in the constant flux layer', *Quarterly Journal of the Royal Meteorological Society*, **96**, 715–721.

Fang, X., and Stefan, H. G., (1996), 'Dynamics of heat exchange between sediment and water in a lake', *Water Resources Research*, **32**(6), 1719–1727.

Fang, X., and Stefan, H. G., (1998), 'Temperature variability in lake sediments', *Water Resources Research*, **34**(4), 717–729.

Farrow, D. E., and Patterson, J. C., (1993), 'On the response of a reservoir sidearm to diurnal heating and cooling', *Journal of Fluid Mechanics*, **246**, 143–161.

Fathi-Maghadam, M., and Kouwen, N., (1997), 'Nonrigid, nonsubmerged, vegetative roughness on floodplains', *Journal of Hydraulic Engineering*, **123**(1), 51–57.

Feng, K., and Molz, F. J., (1997), 'A 2-D, Diffusion-based wetland flow model', *Journal of Hydrology*, **196**, 230–250.

Finnigan, J., (2000), 'Turbulence in Plant Canopies', *Annual Review of Fluid Mechanics*, **32**, 519–571.

Fischer, H. B., List, E. J., Koh, R. C. Y., Imberger, J., and Brooks, N. H., (1979), *Mixing in Inland and Coastal Waters.* Academic Press, Inc, San Diego.

Gangopadhyaya, M., Harbeck, G. E., Nordenson, T. J., Omar, M. H., and Uryvaev, V. A., (1966), *Measurement and estimation of evaporation and evapotranspiration.* World Meteorological Organization. Technical Note No. 83.

Garratt, J. R., (1992), *The atmospheric boundary layer.* Cambridge University Press, Cambridge.

Garratt, J. R., and Hicks, B. B., (1973), 'Momentum, heat and water vapour transfer to and from natural and artificial surfaces', *Quarterly Journal of the Royal Meteorological Society*, **99**, 680–687.

Gates, D. M., (1980), *Biophysical Ecology.* Springer-Verlag, New York.

Gertz, S. M., (1984), 'Biostatistical Aspects of Macrophyton Sampling', in Dennis, & Isom (Dennis and Isom, 1984), pp. 28–35.

Goldsmith, F. B., Harrison, C. M., and Morton, A. J., (1986), 'Description and analysis of vegetation', in Moore, & Chapman (Moore and Chapman, 1986), pp. 437–524.

Goudriaan, J., (1977), *Crop Micrometeorology: a simulation study.* Centre for Agricultural Publishing and Documentation, Wageningen, The Netherlands.

Grayson, R. B., Argent, R. M., Nathan, R. J., McMahon, T. A., and Mein, R. G., (1996), *Hydrological Recipes. Estimation Techniques in Australian Hydrology.* Cooperative Research Centre for Catchment Hydrology, Clayton, Victoria.

Guyot, G., (1998), *Physics of the Environment and Climate.* John Wiley & Sons, Inc, Chichester.

Hammer, D. A. (Ed.)., (1989), *Constructed Wetlands for Wastewater Treatment: Municipal, Industrial and Agricultural.* Lewis Publishers, Inc, Chelsea.

Hammer, D. E., and Kadlec, R. H., (1986), 'A Model for Wetland Surface Water Dynamics', *Water Resources Research*, **22**(13), 1951–1958.

Henderson-Sellers, B., (1982), 'A simple formula for vertical eddy diffusion coefficients under conditions of nonneutral stability', *Journal of Geophysical Research*, **87**(C8), 5860–5864.

Henderson-Sellers, B., (1984), *Engineering Limnology.* Pitman Advanced Publishing Program, Boston.

Henry, H. M., (1977), 'Catastrophic Channel Changes in the Macdonald Valley, New South Wales, 1949-1955', *Journal and Proceedings, Royal Society of New South Wales*, **110**, 1–16.

Hicks, B. B., (1972), 'Some evaluations of drag and bulk transfer coefficients over water bodies of different sizes', *Boundary-Layer Meteorology*, **3**, 201–213.

Hicks, B. B., Drinkrow, R. L., and Grauze, G., (1974), 'Drag and bulk transfer coefficients associated with a shallow water surface', *Boundary-Layer Meteorology*, **6**, 287–297.

Hornbeck, R. W., (1975), *Numerical Methods.* Prentice-Hall, Inc., Englewood Cliffs.

Horsch, G. M., and Stefan, H. G., (1988), 'Convective circulation in littoral water due to surface cooling', *Limnology and Oceanography*, **33**(5), 1068–1083.

Hosokawa, Y., and Furukawa, K., (1992), 'Surface Flow and Particle Settling in Reed Field', in *Wetlands Down Under: Wetland Systems in Water Pollution Control. Proceedings. 30 November - 3 December 1992* Sydney. University of New South Wales.

Hounam, C. E., (1973), *Comparison between pan and lake evaporation.* World Meteorological Organization. Technical Note No. 126.

Hsu, M.-H., Kuo, A. Y., Kuo, J.-T., and Liu, W.-C., (1999), 'Procedure to calibrate and verify numerical models of estuarine hydrodynamics', *Journal of Hydraulic Engineering*, **125**(2), 166–182.

Hunt, R. J., Krabbenhoft, D. P., and Anderson, M. P., (1996), 'Groundwater inflow measurements in wetland systems', *Water Resources Research*, **32**(3), 495–507.

Hutchinson, G. E., (1957), *A Treatise on Limnology.* John Wiley & Sons, Inc, New York.

Hutter, K., (1984), 'Linear Gravity Waves, Kelvin Waves and Poincare Waves, Theoretical Modelling and Observations', in Hutter, K. (Ed.), *Hydrodynamics of Lakes. CISM Courses and Lectures No. 286. International Centre for Mechanical Sciences* Vienna. Springer-Verlag.

Idso, S. B., and Anderson, M. G., (1988), 'A Comparison of Two Recent Studies of Transpirational Water Loss from Emergent Aquatic Macrophytes', *Aquatic Botany*, **31**, 191–195.

Idso, S. B., and Jackson, R. D., (1969), 'Thermal Radiation from the Atmosphere', *Journal of Geophysical Research*, **74**(23), 5397–5403.

Imberger, J., (1985), 'The diurnal mixed layer', *Limnology and Oceanography*, **30**(4), 737–770.

Imberger, J., and Parker, G., (1985), 'Mixed layer dynamics in a lake exposed to a spatially variable wind field', *Limnology and Oceanography*, **30**(3), 473–488.

Imberger, J., and Patterson, J. C., (1990), 'Physical Limnology', *Advances in Applied Mechanics*, **27**, 303–475.

Jackson, P. S., (1981), 'On the displacement height in the logarithmic velocity profile', *Journal of Fluid Mechanics*, **111**, 15–25.

James, W. F., and Barko, J. W., (1991), 'Estimation of phosphorous exchange between littoral and pelagic zones during nighttime convective circulation', *Limnology and Oceanography*, **36**(1), 179–186.

Jensen, M. E., Burman, R. D., and Allen, R. G. (Eds.)., (1989), *Evapotranspiration and Irrigation Water Requirements.* American Society of Civil Engineers, New York.

Jin, K. R., Hamrick, J. H., and Tisdale, T., (2000), 'Application of three-dimensional hydrodynamic model for Lake Okeechobee', *Journal of Hydraulic Engineering*, **126**(10), 758–771.

Johnson, B. H., Kim, K. W., Heath, R. E., Hsieh, B. B., and Butler, H. L., (1993), 'Validation of Three-Dimensional Hydrodynamic Model of Chesapeake Bay', *Journal of Hydraulic Engineering*, **119**(1), 2–20.

Kadlec, R. H., (1990), 'Overland Flow in Wetlands: Vegetation Resistance', *Journal of Hydraulic Engineering*, **116**(5), 691–706.

Kadlec, R. H., (1995), 'Overview: Surface Flow Constructed Wetlands', *Water Science and Technology*, **32**(3), 1–12.

King, I. P., (1993), *Sydney Deepwater Outfalls Environmental Monitoring Program Post-Commissioning Phase Interim Report. A Finite Element Model for Three-Dimensional Density Stratified Flow.* AWACS Interim Report 93/01/04, March 1993.

King, I. P., (1998), *Documentation: RMA-11 - a Three Dimensional Finite Element Model for Water Quality in Estuaries and Streams. Version 2.6, July 1998.*

King, I. P., (2001), *RMAGEN. A Program for Generation of Finite Element Networks. User Instructions. Version 6.2, October 2001.*

Kirk, J. T. O., (1983), *Light and photosynthesis in aquatic ecosystems.* Cambridge University Press, Cambridge.

Koch, M. S., and Rawlik, P. S., (1993), 'Transpiration and stomatal conductance of two wetland macrophytes *(Cladium jamaicense and Typha domingensis)* in the subtropical Everglades', *American Journal of Botany*, **80**(10), 1146–1154.

Landsberg, J. J., and James, G. B., (1971), 'Wind Profiles in Plant Canopies: Studies on an Analytical Model', *Journal of Applied Ecology*, **8**, 729–741.

Lantinga, E. A., Nassiri, M., and Kropff, M. J., (1999), 'Modelling and measuring vertical light absorption within grass-clover mixtures', *Agricultural and Forest Meteorology*, **96**, 71–83.

LaPerriere, J. D., and Edmundson, J. A., (2000), 'Limnology of two lake systems of Katmai National Park and Preserve, Alaska: Part II. Light penetration and Secchi depth', *Hydrobiologia*, **418**, 209–216.

Larsen, D. R., and Kershaw, J. A., (1996), 'Influence of canopy structure assumptions on predictions from Beer's law. A comparison of deterministic and stochastic simulations', *Agricultural and Forest Meteorology*, **81**, 61–77.

Lawrence, I., and Breen, P., (1998), *Design guidelines: Stormwater pollution control ponds and wetlands.* Cooperative Research Centre for Freshwater Ecology.

LI-COR, Inc, (1990), *LI-COR Underwater Radiation Sensors, Type SA, Instruction Manual.*

Linacre, E., (1975), 'Swamps', in Monteith, J. L. (Ed.), *Vegetation and the Atmosphere, Vol.2. Case Studies*, pp. 329–347. Academic Press, London.

Linacre, E. T., Hicks, B. B., Sainty, G. R., and Grauze, G., (1970), 'The evaporation from a swamp', *Agricultural Meteorology*, **7**, 375–386.

Linforth, S., Yu, S., and Constandopolous, J., (1995), 'On the Hydrodynamics of Constructed Wetlands', in *Proceedings of National Conference on Wetlands for Water Quality Control. Townsville, Australia. 25-29 September, 1995.*

List, R. J., (1968), *Smithsonian Meteorological Tables.* Smithsonian Institution Press, Washington.

Liu, W. T., Katsaros, K. B., and Businger, J. A., (1979), 'Bulk Parameterization of Air-Sea Exchanges of Heat and Water Vapour Including the Molecular Constraints at the Interface', *Journal of the Atmospheric Sciences*, **36**(9), 1722–1735.

Luketina, D., and Kay, K., (2000), 'The Development of Temperature Stratification and Convective Circulations in Partially Vegetated Freshwater Wetlands', in *Proceedings: International Water Association conference. Paris, July 2000.*

Marshall, N., (2001), 'Geomorphology and Physical Limnology of Floodplain Lakes - Two Case Studies of Stratification in the Macdonald River Valley, NSW', in *Proceedings Third Australian Stream Management Conference. Brisbane, 27-29 August, 2001.*

Maxworthy, T., and Monismith, S. G., (1988), 'Differential mixing in a stratified fluid', *Journal of Fluid Mechanics*, **189**, 571–598.

Miller, D. H., (1981), *Energy at the Surface of the Earth. An Introduction to the Energetics of Ecosystems.* Academic Press, New York.

Mitsch, W. J., and Gosselink, J. G., (1993), *Wetlands* (2nd edition). Van Nostrand Reinhold, New York.

Monismith, S. G., Imberger, J., and Morison, M. L., (1990), 'Convective motions in the sidearm of a small reservoir', *Limnology and Oceanography*, **35**(8), 1676–1702.

Monteith, J. L. (Ed.)., (1975), *Vegetation and the Atmosphere, Vol.1. Principles.* Academic Press, London.

Monteith, J. L., and Unsworth, M., (1990), *Principles of Environmental Physics* (2nd edition). Arnold, London.

Moore, P. D., and Chapman, S. B. (Eds.)., (1986), *Methods in Plant Ecology* (2nd edition). Blackwell Scientific Publications, Oxford.

Myneni, R. B., Marshak, A., Knyazikhin, Y., and Asrar, G., (1991), 'Discrete Ordinates Method for Photon Transport in Leaf Canopies', in Myneni, & Ross (Myneni and Ross, 1991), pp. 45–109.

Myneni, R. B., and Ross, J. (Eds.)., (1991), *Photon-Vegetation Interactions - Applications in Optical Remote Sensing and Plant Ecology.* Springer-Verlag, Berlin.

Naot, D., Nezu, I., and Nakagawa, H., (1996), 'Hydrodynamic Behaviour of Partly Vegetated Open Channels', *Journal of Hydraulic Engineering*, **122**(11), 625–633.

Nepf, H. M., (1999), 'Drag, turbulence and diffusion in flow through emergent vegetation', *Water Resources Research*, **35**(2), 479–489.

Nepf, H. M., Mugnier, C. G., and Zavistoski, R. A., (1997a), 'The Effects of Vegetation on Longitudinal Dispersion', *Estuarine, Coastal and Shelf Science*, **44**, 675–684.

Nepf, H. M., Sullivan, J. A., and Zavistoski, R. A., (1997b), 'A model for diffusion within emergent vegetation', *Limnology and Oceanography*, **42**(8), 1735–1745.

Niedoroda, A. W., Sheppard, D. M., and Devereaux, A. B., (1991), 'The effect of beach vegetation on aeolian sand transport', in *Proceedings. Coastal Sediments '91. Volume 1. Seattle, Washington. June 25-27, 1991.*

Nilson, T., (1991), 'Approximate Analytical Methods for Calculating the Reflection Functions of Leaf Canopies in Remote Sensing Applications', in Myneni, & Ross (Myneni and Ross, 1991), pp. 161–190.

Norman, J. M., (1975), 'Radiative Transfer in Vegetation', in de Vries, D. A., and Afgan, N. H. (Eds.), *Heat and Mass Transfer in the Biosphere*, Vol. 1, pp. 187–205. Hemisphere Publishing Company, Washington.

Oldham, C. E., and Sturman, J. J., (2001), 'The effect of emergent vegetation on convective flushing in shallow wetlands: Scaling and experiments', *Limnology and Oceanography*, **46**(6), 1486–1493.

Ostrovsky, I., Yacobi, Y. Z., Walline, P., and Kalikhman, I., (1996), 'Seiche-induced mixing: its impact on lake productivity', *Limnology and Oceanography*, **41**(2), 323–332.

Panofsky, H. A., and Dutton, J. A., (1984), *Atmospheric Turbulence. Models and Methods for Engineering Applications.* John Wiley & Sons, Inc, New York.

Patterson, J., (1984), 'Unsteady natural convection in a cavity with internal heating and cooling', *Journal of Fluid Mechanics*, **140**, 135–151.

Penman, H. L., (1948), 'Natural evaporation from open water, bare soil and grass', in *Proceedings of the Royal Society of London. Series A. Mathematical and Physical Sciences*, Vol. 193, pp. 120–145.

Petryk, S., and Bosmajian, G., (1975), 'Analysis of Flow Through Vegetation', *Journal of the Hydraulics Division, ASCE*, **101**(7), 871–884.

Phillips, O. M., (1966), 'On turbulent convection currents and the circulation of the Red Sea', *Deep Sea Research*, **13**, 1149–1160.

Raupach, M. R., (1992), 'Drag and drag partition on rough surfaces', *Boundary-Layer Meteorology*, **60**, 375–395.

Raupach, M. R., and Thom, A. S., (1981), 'Turbulence in and above plant canopies', *Annual Review of Fluid Mechanics*, **13**, 97–129.

Roig, L. C., (1994), 'Hydrodynamic Modeling of Flows in Tidal Wetlands', University of California, Davis. Ph.D. Dissertation.

Rosenberg, N. J., (1974), *Microclimate: The Biological Environment.* John Wiley & Sons, Inc, New York.

Ross, J., (1975), 'Radiative Transfer in Plant Communities', in Monteith (Monteith, 1975), pp. 13–55.

Ross, J., (1981), *The radiation regime and architecture of plant stands.* Dr W. Junk Publishers, The Hague.

Rubin, H., and Atkinson, J., (2001), *Environmental Fluid Mechanics.* Marcel Dekker, Inc., New York.

Ryan, K., Fisher, M., and Schaeper, L., (1996), 'The natural vegetation of the St Albans 1: 100 000 map sheet', *Cunninghamia*, **4**(3), 433–481.

Sainty, G. R., and Jacobs, S. W. L., (1981), *Waterplants of New South Wales.* Water Resources Commission, New South Wales.

Sainty, G. R., and Jacobs, S. W. L., (1994), *Waterplants in Australia* (3rd edition). Sainty and Associates, Sydney.

Salen¸con, M.-J., and Th´ebault, J.-M., (1996), 'Simulation model of a mesotrophic reservoir (Lac de Pareloup, France): MELODIA, an ecosystem reservoir management model', *Ecological Modelling*, **84**, 163–187.

Sanchez-Carrillo, S., Alvarez-Cobelas, M., and Benitez, M., (2001), 'A simple method for estimating water loss by transpiration in wetlands', *Hydrological Sciences Journal*, **46**(4), 537–552.

Schlichting, H., (1962), *Boundary layer theory* (4th edition). McGraw-Hill, New York.

Shaw, R. H., and Pereira, A. R., (1982), 'Aerodynamic Roughness of a Plant Canopy: A Numerical Experiment', *Agricultural Meteorology*, **26**, 51–65.

Smagorinsky, J., (1963), 'General circulation experiments with the primitive equations. I. The basic experiment', *Monthly Weather Review*, **91**(3), 99–152.

Smeulders, D. M., (1999), 'A Late Holocene Environmental Reconstruction Using Lake Sediments from Hopwoods Lagoon, NSW', University of New South Wales, Sydney. Bachelor of Science (Honours in Geography) Thesis.

Smith, M., (1991), *Report on the expert consultation on procedures for revision of FAO guidelines for prediction of crop water requirements. Held in FAO, Rome, Italy. 28-31 May 1990.* Land and Water Development Division, Food and Agriculture Organisation of the United Nations.

Smith, S. D., (1989), 'Water vapour flux at the sea surface', *Boundary-Layer Meteorology*, **47**, 277–293.

Somes, N., Bishop, W., and Wong, T., (1999), 'Numerical simulation of wetland hydrodynamics', *Environment International*, **25**(6–7), 773–779.

SonTek, (1998), *SonTek ADV, Acoustic Doppler Velocimeter. Technical Documentation.* San Diego.

Souch, C., Wolfe, C. P., and Grimmond, C. S. B., (1996), 'Wetland evaporation and energy partitioning: Indiana Dunes National Lakeshore', *Journal of Hydrology*, **184**, 189–208.

Spigel, R. H., Imberger, J., and Rayner, K. N., (1986), 'Modeling the diurnal mixed layer', *Limnology and Oceanography*, **31**(3), 533–556.

Stefan, H. G., Cardoni, J. J., Schiebe, F. R., and Cooper, C. M., (1983), 'Model of Light Penetration in a Turbid Lake', *Water Resources Research*, **19**(1), 109–120.

Stevens, C., and Imberger, J., (1996), 'The initial response of a stratified lake to a surface shear stress', *Journal of Fluid Mechanics*, **312**, 39–66.

Stevens, C., Lawrence, G., Hamblin, P., and Carmack, E., (1996), 'Wind forcing of internal waves in a long narrow stratified lake', *Dynamics of Atmospheres and Oceans*, **24**, 41–50.

Sturman, J. J., and Ivey, G. N., (1998), 'Unsteady convective exchange flows in cavities', *Journal of Fluid Mechanics*, **368**, 127–153.

Sturman, J. J., Ivey, G. N., and Taylor, J. R., (1996), 'Convection in a long box driven by heating and cooling on the horizontal boundaries', *Journal of Fluid Mechanics*, **310**, 61–87.

Sturman, J. J., Oldham, C. E., and Ivey, G. N., (1999), 'Steady convective exchange flows down slopes', *Aquatic Sciences*, **61**, 260–278.

Styles, J. M., (1997), *A Wind Tunnel Study of the Velocity Field Above a Model Plant Canopy* . CSIRO. BSc(Hons) Thesis, The Australian National University, Canberra ACT Australia. CSIRO Technical Report No.36-97 (November 1997).

Swinbank, W. C., (1963), 'Long-wave radiation from clear skies', *Royal Meteorological Society Quarterly Journal*, **89**, 339–348.

Tennekes, H., and Lumley, J. L., (1972), *A first course in turbulence.* The MIT Press, Cambridge, Massachusetts.

Thermometrics Inc., (1986), *Thermistor Sensor Handbook.*

Thom, A. S., (1975), 'Momentum, Mass and Heat Exchange of Plant Communities', in Monteith (Monteith, 1975), pp. 57–109.

Torssell, B. W. R., and McPherson, H. G., (1977), 'An improved model for simulating the penetration, propagation and absorption of radiation within plant canopies', *Australian Journal of Ecology*, **2**, 245–256.

Townsend, A. A., (1976), *The Structure of Turbulent Shear Flow* (2nd edition). Cambridge University Press, Cambridge.

Tsihrintzis, V. A., and Madiedo, E. E., (2000), 'Hydraulic Resistance Determination in Marsh Wetlands', *Water Resources Management*, **14**, 285–309.

Turner, J. S., (1973), *Buoyancy Effects in Fluids.* Cambridge University Press, Cambridge.

Wallace, S. L., (2003), 'The Effect of Seagrass Canopies on Shallow-Water Dynamics', University of New South Wales. Ph.D. Dissertation.

Waters, M., and Luketina, D. A., (1998), 'The development of temperature stratification in freshwater wetlands', in *Proceedings Australian Fluid Mechanics Conference. Melbourne Australia, 13-18 December 1998.*

Waters, M. T., (1998), 'Effects of Vegetation on the Hydrodynamics of Freshwater Wetlands', University of New South Wales. Ph.D. Dissertation.

Waters, M. T., Luketina, D. A., and Ball, J. E., (1994), *Wetland Hydraulics Scaling Analyses. Part 1: External Influences on Mixing Processes.* The University of New South Wales Water Research Laboratory. Research Report No. 185. September 1994.

Webb, E. K., (1970), 'Profile relationships: the log-linear range, and extension to strong stability', *Quarterly Journal of the Royal Meteorological Society*, **96**, 67–90.

Wells, M. G., and Sherman, B., (2001), 'Stratification produced by surface cooling in lakes with significant shallow regions', *Limnology and Oceanography*, **46**(7), 1747–1759.

Wetzel, R. G., (1983), *Limnology* (2nd edition). Saunders College Publishing, Fort Worth.

Wetzel, R. G., and Likens, G. E., (1991), *Limnological Analyses* (2nd edition). Springer-Verlag, New York.

Wilson, C. A. M. E., Stoesser, T., Bates, P. D., and Batemann Pinzen, A., (2003), 'Open channel flow through different forms of submerged flexible vegetation', *Journal of Hydraulic Engineering*, **129**(11), 847–853.

Wong, T. H. F., Breen, P. F., Somes, N. L. G., and Lloyd, S. D., (1998), *Managing Urban Stormwater Using Constructed Wetlands. Industry Report.* Cooperative Research Centre for Catchment Hydrology.

Wong, T. H. F., and Somes, N. L. G., (1995), 'A stochastic approach to designing wetlands for stormwater pollution control', *Water Science and Technology*, **32**(1), 145–151.

Wu, F.-C., Shen, H. W., and Chou, Y.-J., (1999), 'Variation of roughness coefficients for unsubmerged and submerged vegetation', *Journal of Hydraulic Engineering*, **125**(9), 934–942.

Wu, J., (1980), 'Wind-Stress Coefficients over Sea Surface near Neutral Conditions - A Revisit', *Journal of Physical Oceanography*, **10**, 727–740.

Zaneveld, J. R. V., and Spinrad, R. W., (1980), 'An Arc Tangent Model of Irradiance in the Sea', *Journal of Geophysical Research*, **85**(C9), 4919–4922.

Zhang, J. Q., Fang, X. P., Zhang, H. X., Yang, W., and Zhu, C. C., (1997), 'A heat balance model for partially vegetated surfaces', *Infrared Physics & Technology*, **38**, 287–294.

Appendix A

CALCULATION OF ADDITIONAL PARAMETERS

A.1 Solar Elevation Calculations

Standard formulae are available to calculate the solar elevation for a given site at a given time, as shown in the following sections. These are sourced from Burman and Pochop (1994) and (Guyot, 1998).

Equation of Time, EOT

The equation of time compensates for the earth's elliptical orbit around the sun and its axial tilt when calculating solar time from local time. The equation of time (min) is calculated from:

$$EOT = 0.258\cos\Gamma - 7.416\sin\Gamma - 3.648\cos(2\Gamma) - 9.228\sin(2\Gamma) \quad (A.1)$$

where

$$\Gamma = \frac{2\pi}{365}(D_Y - 1) \quad (A.2)$$

and D_Y is the Julian date.

Correction to Local Time, t_{corr}

The equation of time is applied as a correction (min) to the local time, as follows:

$$t_{corr} = 4(L_e - L_s) + EOT \quad (A.3)$$

where L_e = local site longitude (°)

L_s = longitude of the local standard meridian (°).

The longitude of the local standard meridian is calculated from the time difference between local time and Greenwich Meridian Time, Δt_{GMT} (hr):

$$L_s = 15(\Delta t_{GMT}) \quad (A.4)$$

Solar Time, t_{solar}

Solar time is the time according to the position of the sun in the sky, which varies with longitude. Solar time can be calculated from local time, as follows:

$$t_{solar} = t + (t_{corr}/60) \quad (A.5)$$

where t is the local civil or clock time (hr).

Hour Angle, ω_h

The hour angle expresses the difference between local solar time and solar noon, using angular units. The hour angle is negative before solar noon and positive after solar noon, and calculated as follows:

$$\begin{aligned} \omega_h &= 15\,(12 - t_{solar}) && t_{solar} < 12 \\ &= 0 && t_{solar} = 12 \\ &= -15\,(t_{solar} - 12) && t_{solar} > 12 \end{aligned} \tag{A.6}$$

Solar Declination, δ

The solar declination is the angular distance of the sun to the north or south of the earth's equator, which is calculated as follows:

$$\delta = 23.45 \cos\left(\frac{2\pi}{365}\,(172 - D_Y)\right) \tag{A.7}$$

Solar Elevation, β

The solar elevation is a function of the site location (latitude and longitude) and the solar time. It is calculated as follows:

$$\sin\beta = \cos\theta = \sin\varphi \sin\delta + \cos\varphi \cos\delta \cos\omega_h \tag{A.8}$$

where β = solar elevation above the horizon ($^\circ$)

θ = solar zenith from the vertical ($^\circ$)

φ = site latitude ($^\circ$)

δ = solar declination, negative for southern hemisphere ($^\circ$)

ω_h = hour angle ($^\circ$).

Local Time at Solar Noon

By definition, the hour angle is zero at solar noon. The local clock time at solar noon can therefore be calculated using Equations (A.1) to (A.5) with $\omega_h = 0$ and $t_{solar} = 12$.

Times of Sunrise and Sunset, $t_{sunrise}$ & t_{sunset}

The elevation of the sun above the horizon is zero at sunrise and sunset ($\beta = 0$), when from Equation (A.8):

$$\cos\omega_h = -\tan\varphi \tan\delta \tag{A.9}$$

The apparent motion of the sun is symmetrical around solar noon, so the time between sunrise and solar noon is equal to the time between solar noon and sunset. The local time of sunrise (hr) is calculated from the local time at solar noon and the hour angle when the solar elevation is zero, as follows:

$$t_{sunrise} = t_{noon} - \frac{12}{\pi}\cos^{-1}(-\tan\varphi\,\tan\delta) \quad \text{(A.10)}$$

The local time at sunset (hr) is calculated similarly:

$$t_{sunset} = t_{noon} + \frac{12}{\pi}\cos^{-1}(-\tan\varphi\,\tan\delta) \quad \text{(A.11)}$$

where t_{noon} = local time at solar noon (hr)

$t_{sunrise}$ = local time at sunrise (hr)

t_{sunset} = local time at sunset (hr)

φ = site latitude (°)

δ = solar declination, negative for southern hemisphere (°).

The day length (hr) is simply the difference between the times of sunrise and sunset:

$$DL = t_{sunset} - t_{sunrise} \quad \text{(A.12)}$$

A.2 Latent Heat Flux Calculations

Table A.1 lists the most common methods available for calculating the latent heat flux, together with comments relating to the applicability of each. Notes to the table are presented below.

Notes to Table A.1:

1. World Meteorological Organisation (Gangopadhyaya et al., 1966).
2. E_{lake} = estimated open water evaporation rate (mm/d)
   E_{pan} = evaporation rate from a Class A evaporation pan (mm/d)
   C_P = Class A pan coefficient.
3. E_{energy} = evaporation rate calculated using an energy balance method (mm/d)
   ρ = water density (kg m^{-3})
   L_w = latent heat of vaporisation of water (MJ kg^{-1})
   R_{NET} = net radiation (Wm^{-2})
   G = heat storage flux term (Wm^{-2}), which is equivalent to the H_{NET} term in Equation (3.15)
   K_1 = conversion factor for units ($K_1 = 1/86.4$).
4. E_{aero} = evaporation rate calculated using an aerodynamic method (m s^{-1})
   $f(u)$ = wind-dependent vapour transport coefficient (m s^{-1}per hPa)
   e_{sat} = saturation vapour pressure (hPa)
   e_a = ambient vapour pressure (hPa)
   K_2 = conversion factor for units ($K_2 = 1 \times 10^6$).
5. Δ = rate of change of the saturation vapour pressure with temperature (hPa °C^{-1})
   γ = psychrometric coefficient (hPa °C^{-1}).
6. ρ_m = density of moist air (kg m^{-3})
   q' = fluctuation in specific humidity
   w' = horizontal fluctuation in the wind speed (m s^{-1})
   C_L = dimensionless transfer coefficient for latent heat (also known as the Dalton number)
   u_z = wind speed (m s^{-1}) at height z (m)
   q_z = specific humidity at height z (m)
   u_s = mean water surface velocity (m s^{-1})
   q_s = saturation specific humidity at the water surface temperature.

Water Balance Methods
Balance water inputs against moisture losses
Very difficult to obtain sufficient data
Inaccurate for periods of less than several years
Inappropriate for the present investigation
References: WMO [(1)], Linacre (1975)
Evaporation Pan Methods
A form of water balance using an evaporation pan
$E_{lake} = C_P \, E_{pan}$ [(2)], where $C_P \sim 0.65$ to 0.75 for south-eastern Australia
Considerable variation between locations and seasons
Limitations are similar to those for water budget methods
Inaccurate for $\Delta t \leq 1$ week; not applicable for $\Delta t \leq 1$ hr
Used only for verification in the present investigation
References: Hounam (1973), Chow et al. (1988), Grayson et al. (1996)
Energy Balance Methods
Estimate evaporation from the supply of energy required to provide L_w
Assume that transport of water vapour from the surface is not a limiting factor
$R_{NET} - G = \rho L_w K_1 E_{energy} + H_S = H_L + H_S$ [(3)]
References: Chow et al. (1988), Burman and Pochop (1994)
Aerodynamic Methods
Estimate evaporation from the available sink for water vapour
$E_{aero} = f(u) \, (e_{sat} - e_a)$ [(4)] and $H_L = -\rho \, L_w K_2 \, E_{aero}$
Assume the supply of energy to provide L_w is not limiting
Suitable for $\Delta t \leq 1$ hr
Must account for the effects of atmospheric stability
References: Penman (1948), WMO [(1)], Brutsaert (1982), Chow et al. (1988)
Combination Methods
Combine energy balance and aerodynamic methods
$E_r = \frac{\Delta}{\Delta+\gamma} E_{energy} + \frac{\gamma}{\Delta+\gamma} E_{aero}$ [(5)]
Require heat storage term for short time intervals
Must account for effects of atmospheric stability
References: Brutsaert (1982), Chow et al. (1988), Smith (1991)
Eddy Measurement Methods
Best method for instantaneous or short term fluxes
Require simultaneous measurement of momentum and water vapour fluxes
Can approximate by a bulk transfer equation in neutral stability
$H_L = \rho_m L_w \overline{q' w'} \sim -C_L \, (q_z - q_s) \, (u_z - u_s)$ [(6)]
References: Fischer et al. (1979), Donelan (1990), Imberger and Patterson (1990)

Table A.1: Summary of methods commonly adopted to estimate evaporation rate and latent heat flux from water bodies, and sources of more detailed information.

A.2.1 Calculation of Intermediate Parameters

Standard formulae are available to calculate the intermediate quantities required to estimate evaporation and latent heat fluxes from open water. These are given in the following sections.

Water Density, ρ

The water density is a function of the water temperature, and can be calculated using a form of the UNESCO equation of state, as follows (List, 1968):

$$\rho = 999.84 + 6.79 \times 10^{-2}\, T_w - 9.06 \times 10^{-3}\, T_w^2 + 1.0 \times 10^{-4}\, T_w^3 \tag{A.13}$$

where ρ = water density ($\mathrm{kg\,m^{-3}}$)

T_w = water temperature (°C).

Latent Heat of Vaporisation of Water, L_w

The latent heat of vaporisation is defined as the quantity of energy required to evaporate a unit mass of a substance. It is a function of the temperature of the substance, and can be calculated as follows (Smith, 1991):

$$L_w = 2.501 - (2.361 \times 10^{-3})\, T_w \tag{A.14}$$

where L_w = latent heat of vaporisation of water ($\mathrm{MJ\,kg^{-1}}$)

T_w = water surface temperature (°C).

Specific Heat Capacity of Water, c_{pw}

The specific heat capacity is defined as the quantity of energy required to raise the temperature of a unit mass of a substance by 1°C. It is a function of the temperature of the substance and can be calculated as follows (Henderson-Sellers, 1984):

$$c_{pw} = 4180 + \exp\left[46.40 - 0.156\,(T_w + 273)\right] \tag{A.15}$$

where c_{pw} = specific heat capacity of water ($\mathrm{J\,kg^{-1}\,{}^\circ C^{-1}}$)

T_w = water surface temperature (°C).

Vapour Pressure Deficit, $(e_{sat} - e_a)$

For short periods of around an hour or less, the vapour pressure deficit is simply the difference between the saturation vapour pressure at the water surface temperature and the vapour pressure at the ambient air temperature (Burman and Pochop, 1994).

The saturation vapour pressure is calculated using the Tetens formula (Smith, 1991):

$$e_{sat} = 6.11 \exp\left(\frac{17.27\, T_w}{T_w + 237.3}\right) \tag{A.16}$$

and the vapour pressure at the ambient air temperature is also calculated using the Tetens formula:

$$e_a = (RH/100)\ 6.11 \exp\left(\frac{17.27\, T_a}{T_a + 237.3}\right) \tag{A.17}$$

where e_{sat} = saturation vapour pressure (hPa) at the water surface temperature, T_w (°C)

e_a = vapour pressure (hPa) at the air temperature, T_a (°C)

RH = relative humidity (%).

Density of Moist Air, ρ_m

The density of moist air is a function of the atmospheric pressure and the virtual temperature of the air, and can be calculated as follows (List, 1968):

$$\rho_m = 0.34838 \frac{P}{T_V} \tag{A.18}$$

where ρ_m = density of moist air ($\mathrm{kg\,m^{-3}}$)

P = atmospheric pressure (hPa)

T_V = virtual temperature of the air (K).

Virtual Temperature, T_V

The virtual temperature is defined as the temperature which a parcel of dry air would attain at the same density as moist air with given specific humidity, temperature and pressure (Brutsaert, 1982):

$$T_V = \frac{T_a}{1 - 0.378\,(e_a/P)} \approx 1.01\, T_a \tag{A.19}$$

where T_a = absolute air temperature (K)

e_a = ambient vapour pressure (hPa)

P = atmospheric pressure (hPa).

Psychrometric Coefficient, γ

The psychrometric coefficient is calculated according to the method of Brunt, as given by Smith (1991):

$$\gamma = \frac{c_p\, P}{\epsilon\, L_w} \times 10^{-3} = 0.00163 \frac{P}{L_w} \tag{A.20}$$

where γ = psychrometric coefficient (hPa °C^{-1})

c_p = specific heat capacity of moist air (1.013 J kg^{-1} °C^{-1})

P = atmospheric pressure (hPa)

ϵ = ratio of the molecular weight of water vapour to the molecular weight of dry air (0.622)

L_w = latent heat of vaporisation of water (MJ kg^{-1}).

A.2.2 Comparison between Forced and Free Convection Fluxes

As discussed in Section 3.3.3.3, comparisons were made between the latent heat fluxes calculated for forced convection, using Equation (3.38), and free convection, using Equation (3.43). Calculations were made over a range of air and water temperatures (10°C< T_a <25°C and 15°C< T_w <30°C) where evaporation would be expected. As shown in Figure A.1, the results indicated that the wind speed threshold for equality between the forced and free convection latent heat fluxes was generally around 0.1 m s^{-1} and always between 0.05 m s^{-1} and 0.13 m s^{-1} for the specified temperatures, humidity and atmospheric pressure.

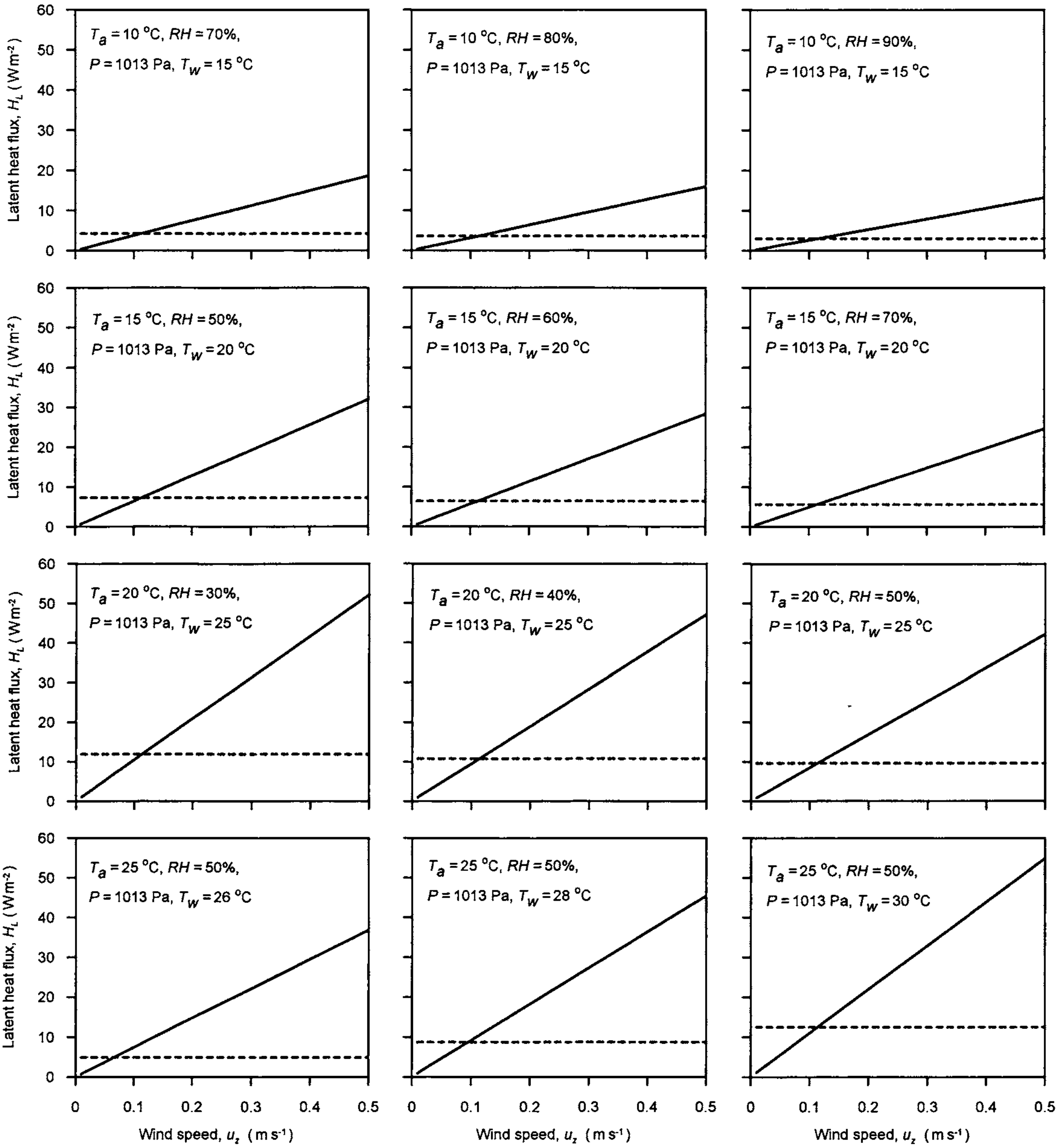

Figure A.1: Comparison between latent heat fluxes calculated for forced convection (solid line, ——) and free convection (dashed line, – – –).

A.3 Bed Heat Flux Calculations

The volumetric heat capacity of the sediments is required to calculate the bed heat flux from a known or predicted temperature distribution in the sediments. The volumetric heat capacity of a sediment matrix can be estimated from the volumetric heat capacities of the mineral component, organic component, and water, as follows (Jensen et al., 1989):

$$c_s = 1.93\,V_M + 2.51\,V_C + 4.19\,V_W \tag{A.21}$$

where V_M = volume fraction of mineral components (%)

V_C = volume fraction of organic components (%)

V_W = volume fraction of water (%)

and the coefficients represent the volumetric heat capacities of the three components.

The volume fractions of the three components of the sediments under Hopwoods Lagoon were estimated using moisture content, bulk density and organic content (loss on ignition) data obtained by Smeulders (1999) from a 1.4 m deep sediment core extracted in June 1999. The mean values of the physical parameters were determined from a total of 51 measurements over the length of the core, as summarised in Table A.2.

	Moisture Content ($\mathrm{kg\,m^{-3}}$)	Bulk Density ($\mathrm{kg\,m^{-3}}$)	Organic Content (%)
Number of Samples	51	51	51
Minimum	4.7	11.2	10.1
Maximum	8.8	16.5	25.8
Mean	**6.2**	**13.9**	**16.1**
Standard Deviation	1.02	1.46	4.25

Table A.2: Moisture content, bulk density, and organic content of sediments beneath Hopwoods Lagoon. Physical data from Smeulders (1999).

The resulting volume fractions were:

$$V_M = 28.3\,\% \qquad V_C = 9.6\,\% \qquad V_M = 62.1\,\% \tag{A.22}$$

which gave a mean volumetric heat capacity of $c_s = 3.39\,\mathrm{MJ\,m^{-3}\,{}^\circ C^{-1}}$ for the sediments under Hopwoods Lagoon.

Appendix B

VEGETATION DATA

B.1 Stem Density Data

The stem density as a function of height at each of the four wetlands was shown in Figure 6.1. The relative numbers of stems of the different macrophyte species observed at each sampling location are presented in the following tables. The quadrat area was $1.0\,\mathrm{m}^2$ for all sites except the Deep Creek *Juncus* wetland, where the quadrat area was $0.36\,\mathrm{m}^2$ for Site DCJ1 and $0.18\,\mathrm{m}^2$ for Site DCJ2.

Site DCT1 (Area = $1.0\,\mathrm{m}^2$)						
Height (m)	Total Stems	green *Typha*	brown *Typha*	*Triglochin*	*Phragmites*	*Eleocharis*
0.2	166	33	76	54	3	–
0.4	112	26	40	44	2	–
0.6	67	16	33	17	1	–
0.8	57	15	34	8	–	–
1.0	47	16	31	–	–	–
1.2	35	7	28	–	–	–
1.4	27	5	22	–	–	–
1.6	20	–	20	–	–	–
1.8	6	–	6	–	–	–
2.0	0	–	–	–	–	–

Site DCT2 (Area = $1.0\,\mathrm{m}^2$)						
Height (m)	Total Stems	green *Typha*	brown *Typha*	*Triglochin*	*Phragmites*	*Eleocharis*
0.2	265	30	115	120	0	–
0.4	159	21	57	80	–	–
0.6	82	11	43	28	–	–
0.8	75	16	43	16	–	–
1.0	52	19	33	–	–	–
1.2	45	11	34	–	–	–
1.4	34	4	30	–	–	–
1.6	17	–	17	–	–	–
1.8	1	–	1	–	–	–
2.0	0	–	–	–	–	–

Site DCT3 (Area = $1.0\,\mathrm{m}^2$)						
Height (m)	Total Stems	green *Typha*	brown *Typha*	*Triglochin*	*Phragmites*	*Eleocharis*
0.2	200	42	111	21	26	–
0.4	112	30	59	18	5	–
0.6	82	19	50	9	4	–
0.8	71	22	45	2	2	–
1.0	55	16	37	–	2	–
1.2	46	12	33	–	1	–
1.4	41	6	35	–	–	–
1.6	30	3	27	–	–	–
1.8	6	1	5	–	–	–
2.0	0	–	–	–	–	–

Table B.1: Stem density as a function of macrophyte species and height above the water surface at the Deep Creek Typha wetland.
(a) Winter, 26 August 1999.

Site DCT1 (Area = 1.0 m^2)						
Height (m)	Total Stems	green *Typha*	brown *Typha*	*Triglochin*	*Phragmites*	*Eleocharis*
0.0	161	39	57	58	7	–
0.2	155	39	49	58	9	–
0.4	123	41	45	34	3	–
0.6	82	40	29	12	1	–
0.8	65	42	23	–	–	–
1.0	50	33	17	–	–	–
1.2	40	24	16	–	–	–
1.4	29	15	14	–	–	–
1.6	11	7	4	–	–	–
1.8	2	1	1	–	–	–
2.0	0	–	–	–	–	–
Site DCT2 (Area = 1.0 m^2)						
Height (m)	Total Stems	green *Typha*	brown *Typha*	*Triglochin*	*Phragmites*	*Eleocharis*
0.0	167	24	35	108	–	–
0.2	158	22	31	105	–	–
0.4	110	22	29	59	–	–
0.6	54	18	25	11	–	–
0.8	40	18	22	–	–	–
1.0	38	17	21	–	–	–
1.2	31	12	19	–	–	–
1.4	25	7	18	–	–	–
1.6	7	3	4	–	–	–
1.8	0	–	–	–	–	–
2.0	0	–	–	–	–	–
Site DCT3 (Area = 1.0 m^2)						
Height (m)	Total Stems	green *Typha*	brown *Typha*	*Triglochin*	*Phragmites*	*Eleocharis*
0.0	129	31	30	16	52	–
0.2	88	27	11	16	34	–
0.4	58	23	11	11	13	–
0.6	40	22	9	2	7	–
0.8	32	21	6	–	5	–
1.0	26	20	4	–	2	–
1.2	21	18	3	–	–	–
1.4	14	10	4	–	–	–
1.6	5	4	1	–	–	–
1.8	3	2	1	–	–	–
2.0	0	–	–	–	–	–

Table B.1 (continued): (b) Spring, 26 November 2000.

Site DCT1 (Area = $1.0\,m^2$)						
Height (m)	Total Stems	green *Typha*	brown *Typha*	*Triglochin*	*Phragmites*	*Eleocharis*
0.0	166	21	53	37	13	42
0.2	176	21	56	39	14	46
0.4	117	21	46	30	5	15
0.6	89	21	45	18	5	–
0.8	60	18	40	–	2	–
1.0	61	17	43	–	1	–
1.2	46	11	35	–	–	–
1.4	35	3	32	–	–	–
1.6	31	2	29	–	–	–
1.8	8	1	7	–	–	–
2.0	0	–	–	–	–	–
2.2	0	–	–	–	–	–

Site DCT2 (Area = $1.0\,m^2$)						
Height (m)	Total Stems	green *Typha*	brown *Typha*	*Triglochin*	*Phragmites*	*Eleocharis*
0.0	176	30	42	104	–	–
0.2	172	33	40	99	–	–
0.4	141	29	42	70	–	–
0.6	87	19	38	30	–	–
0.8	57	19	38		–	–
1.0	48	17	31	–	–	–
1.2	42	15	27	–	–	–
1.4	32	10	22	–	–	–
1.6	24	8	16	–	–	–
1.8	7	–	7	–	–	–
2.0	2	–	2	–	–	–
2.2	0	–	–	–	–	–

Table B.1 (continued): (c) Autumn, 17 April 2001.

Site DCJ1 (Area = $0.36\,m^2$)				Site DCJ2 (Area = $0.18\,m^2$)			
Height (m)	Total Stems	*Juncus*	*Phragmites*	Height (m)	Total Stems	*Juncus*	*Phragmites*
0.2	296	224	72	0.2	1101	1066	35
0.4	133	77	56	0.4	780	748	32
0.6	74	43	31	0.6	483	452	31
0.8	34	15	19	0.8	322	304	18
1.0	16	7	9	1.0	186	173	13
1.2	4	–	4	1.2	80	72	8
1.4	2	–	2	1.4	10	8	2
1.6	0	–	–	1.6	0	–	–

Table B.2: Stem density as a function of macrophyte species and height above the water surface at the Deep Creek Juncus wetland. Winter, 26 August 1999.

Site WW1 (Area = 1.0 m^2)				Site WW2 (Area = 1.0 m^2)			
Height (m)	Total Stems	green *Typha*	brown *Typha*	Height (m)	Total Stems	green *Typha*	brown *Typha*
0.2	254	92	162	0.2	206	62	144
0.4	197	86	111	0.4	189	64	125
0.6	170	88	82	0.6	178	58	120
0.8	106	75	31	0.8	130	47	83
1.0	85	68	17	1.0	88	41	47
1.2	51	45	6	1.2	66	28	38
1.4	34	32	2	1.4	31	19	12
1.6	14	14	–	1.6	14	11	3
1.8	6	6	–	1.8	9	6	3
2.0	0	–	–	2.0	3	2	1
2.2	0	–	–	2.2	0	–	–

Table B.3: Stem density as a function of stem type and height above the water surface at Warriewood Wetlands. Spring, 17 October 1999.

(a) Winter 2000 - Site HL2 (Area = 1.0 m^2)				(b) Autumn 2001 - Site HL1 (Area = 1.0 m^2)			
Height (m)	Total Stems	green *Eleocharis*	brown *Eleocharis*	Height (m)	Total Stems	green *Eleocharis*	brown *Eleocharis*
0.0	34	17	17	0.0	74	63	11
0.1	32	16	16	0.1	67	60	7
0.2	30	15	15	0.2	49	45	4
0.3	28	14	14	0.3	27	27	0
0.4	26	13	13	0.4	23	23	0
0.5	26	13	13	0.5	14	14	0
0.6	20	10	10	0.6	8	8	0
0.7	16	8	8	0.7	7	7	0
0.8	8	4	4	0.8	5	5	0
0.9	4	2	2	0.9	2	2	0
1.0	2	1	1	1.0	1	1	0
1.1	0	0	0	1.1	0	–	–
1.2	0	–	–	1.2	0	–	–

Table B.4: Stem density as a function of stem type and height above the water surface at Hopwoods Lagoon.

(a) Winter, 03 September 2000, and (b) Autumn, 1 April 2001.

B.2 Stem Dimension Data

		Height above	Stem width (mm)				Stem thickness (mm)			
Stem Type	Count	Surface (m)	Min.	Max.	Mean	St.Dev	Min.	Max.	Mean	St.Dev
brown *Typha*	44	0.0	8.6	19.1	14.4	2.6	0.6	11.0	5.6	2.6
	51	0.2	7.8	17.6	13.9	2.2	0.7	6.4	4.0	1.0
	39	0.4	9.5	15.6	12.9	1.7	1.8	4.6	3.4	0.6
	30	0.6	9.0	15.7	12.8	1.9	2.0	4.0	2.9	0.5
	29	0.8	8.2	15.7	13.1	1.9	1.3	3.2	2.5	0.5
	27	1.0	7.5	16.0	13.0	2.1	0.6	2.6	1.9	0.5
	23	1.2	1.1	15.7	12.9	3.1	0.7	2.2	1.4	0.4
	21	1.4	2.5	15.0	12.6	2.7	0.3	1.7	0.9	0.3
	13	1.6	9.7	14.5	12.1	1.4	0.3	1.0	0.6	0.2
	2	1.8	5.7	13.8	9.8	5.7	0.2	0.6	0.4	0.3
green *Typha*	44	0.0	6.2	17.3	12.0	2.6	0.2	7.4	2.6	1.8
	40	0.2	7.2	16.7	11.7	2.6	0.3	5.3	2.0	1.1
	34	0.4	6.7	16.9	11.4	2.9	0.3	4.5	1.6	1.0
	29	0.6	4.5	16.6	11.2	2.9	0.1	3.6	1.2	0.9
	17	0.8	8.7	16.2	11.9	2.6	0.3	3.0	1.2	0.8
	10	1.0	9.1	16.4	13.0	2.6	0.3	2.1	1.0	0.6
	7	1.2	9.1	15.9	13.0	2.4	0.3	1.6	0.9	0.6
	4	1.4	11.0	15.6	14.2	2.2	0.5	0.9	0.7	0.2
	3	1.6	9.6	14.6	12.6	2.6	0.3	0.5	0.4	0.1
Triglochin	6	0.0	7.7	11.1	9.7	1.2	6.1	8.0	6.6	1.0
	6	0.2	7.2	11.5	9.4	2.0	2.1	4.8	3.5	1.2
	6	0.4	5.0	11.6	7.8	2.4	0.5	0.9	0.7	0.2

Table B.5: Stem width and thickness data for Typha domingensis *and* Triglochin procerum *at the Deep Creek* Typha *wetland.*
(a) Winter, 26 August 1999.

		Height above	Stem width (mm)				Stem thickness (mm)			
Stem Type	Count	Surface (m)	Min.	Max.	Mean	St.Dev	Min.	Max.	Mean	St.Dev
brown *Typha*	55	0.0	10.4	18.1	13.8	2.1	2.8	13.1	9.6	3.3
	55	0.2	9.7	16.2	12.5	1.4	1.7	5.3	3.8	0.7
	51	0.4	8.0	15.4	11.9	1.4	1.8	4.1	3.1	0.5
	43	0.6	8.5	16.1	12.1	1.5	1.3	3.4	2.6	0.5
	38	0.8	8.7	15.5	12.3	1.5	0.7	3.0	2.2	0.5
	36	1.0	8.1	16.1	12.1	1.7	0.5	2.5	1.6	0.5
	31	1.2	10.3	15.7	12.1	1.2	0.8	1.7	1.2	0.3
	25	1.4	1.2	15.2	11.1	2.6	0.3	1.1	0.7	0.2
	15	1.6	4.9	13.8	9.9	2.1	0.1	0.6	0.4	0.1
	3	1.8	5.4	9.0	7.4	1.8	0.2	0.2	0.2	0.0
green *Typha*	46	0.0	9.6	16.4	13.4	1.8	0.7	8.0	4.7	2.0
	46	0.2	9.5	16.4	13.6	1.8	0.4	5.9	3.5	1.4
	45	0.4	9.2	21.2	13.5	2.1	0.4	4.4	2.8	1.0
	44	0.6	1.2	16.3	13.1	2.9	0.2	3.7	2.4	0.9
	40	0.8	6.2	16.2	13.3	2.1	0.4	3.2	2.0	0.7
	37	1.0	9.2	16.4	13.5	1.8	0.3	2.4	1.5	0.5
	34	1.2	8.8	16.1	13.5	1.9	0.3	1.7	1.0	0.4
	31	1.4	3.5	16.1	12.6	2.6	0.1	1.4	0.6	0.3
	22	1.6	5.4	15.3	11.3	3.0	0.1	0.6	0.3	0.1
	7	1.8	6.1	11.7	10.1	2.1	0.1	0.3	0.2	0.1
Triglochin	43	0.0	4.5	11.2	7.0	1.6	4.0	9.8	6.1	1.4
	43	0.1	4.0	9.1	6.2	1.4	2.7	7.7	5.0	1.2
	43	0.2	3.6	10.4	5.8	1.5	1.5	6.0	3.8	1.2
	43	0.3	2.3	10.7	5.7	1.7	0.6	4.2	2.4	1.0
	39	0.4	2.2	10.5	5.8	1.9	0.4	2.7	1.2	0.8
	23	0.5	4.1	8.8	6.0	1.3	0.4	1.3	0.8	0.3
	7	0.6	3.1	6.6	5.0	1.2	0.4	0.5	0.5	0.1

Table B.5 (continued): (b) Spring, 26 November 2000.

		Height above	Stem width (mm)				Stem thickness (mm)			
Stem Type	Count	Surface (m)	Min.	Max.	Mean	St.Dev	Min.	Max.	Mean	St.Dev
brown *Typha*	46	0.0	13.1	20.1	16.4	1.5	2.1	11.7	6.4	1.9
	46	0.2	10.6	19.4	15.7	2.0	2.3	7.2	4.0	1.0
	46	0.4	10.2	17.9	14.8	1.7	2.0	4.9	3.3	0.6
	46	0.6	9.3	17.5	14.9	1.8	1.3	4.2	2.9	0.6
	46	0.8	8.6	17.5	14.6	1.8	0.7	3.8	2.4	0.7
	43	1.0	11.3	17.4	14.7	1.8	0.8	3.1	1.7	0.6
	42	1.2	8.8	17.8	14.0	2.1	0.2	3.1	1.2	0.6
	37	1.4	8.3	17.7	13.5	2.4	0.1	1.8	0.8	0.4
	26	1.6	7.1	17.1	12.9	2.8	0.1	1.2	0.5	0.3
	14	1.8	4.5	16.9	10.2	4.0	0.1	0.8	0.3	0.2
	3	2.0	11.1	15.0	12.7	2.0	0.2	0.3	0.2	0.1
green *Typha*	44	0.0	9.5	17.5	13.2	2.3	3.1	16.4	6.0	3.1
	44	0.2	9.5	17.8	13.2	2.3	2.5	14.6	4.9	2.6
	44	0.4	9.1	17.1	12.8	2.0	1.9	15.9	3.8	2.1
	44	0.6	8.7	17.3	12.9	2.0	1.4	4.8	2.9	0.8
	44	0.8	8.5	16.8	13.0	2.1	0.8	3.9	2.3	0.8
	42	1.0	6.4	16.8	12.6	2.3	0.3	3.6	1.8	0.8
	39	1.2	5.4	16.6	12.7	2.7	0.2	3.0	1.2	0.7
	32	1.4	7.7	17.1	13.1	2.1	0.2	2.3	0.9	0.6
	24	1.6	4.4	16.6	12.3	3.0	0.1	1.7	0.7	0.5
	16	1.8	9.0	15.8	11.9	2.3	0.2	1.2	0.5	0.4
	4	2.0	12.5	14.9	14.0	1.1	0.3	0.7	0.6	0.2
	3	2.2	9.2	12.4	11.3	1.8	0.2	0.3	0.3	0.1
Triglochin	46	0.0	4.6	15.5	8.9	2.5	2.6	10.6	7.1	1.8
	46	0.2	3.9	13.6	7.4	2.3	0.6	8.0	4.7	1.6
	43	0.4	2.7	14.4	7.1	2.7	0.5	5.3	2.5	1.4
	25	0.6	0.4	12.4	6.7	2.9	0.5	2.0	0.9	0.4
	1	0.8	2.6	2.6	2.6	–	0.5	0.5	0.5	–

Table B.5 (continued): (c) Autumn, 17 April 2001.

Season and Date	Stem Type	Count	Height above Surface (m)	Stem diameter (mm) Min.	Max.	Mean	St.Dev
Winter	*Phragmites*	14	0.0	3.5	9.7	5.6	2.3
26 August 1999		14	0.2	3.0	8.1	5.1	1.8
		14	0.4	1.2	6.5	3.9	1.6
		18	0.6	1.5	6.2	3.0	1.5
		6	0.8	1.1	5.9	3.6	2.0
		2	1.0	5.5	5.5	5.5	0.0
		2	1.2	3.5	3.8	3.7	0.2
		2	1.4	4.2	4.3	4.3	0.1
		2	1.6	3.2	3.4	3.3	0.1
Spring	*Phragmites*	68	0.0	2.3	9.2	4.6	1.9
26 November 2000		68	0.2	2.3	8.7	4.1	1.4
		60	0.4	0.7	6.2	3.3	1.4
		52	0.6	0.4	6.0	2.9	1.6
		34	0.8	0.2	4.6	2.6	1.4
		18	1.0	0.5	4.1	2.5	1.3
		10	1.2	1.2	3.7	2.8	0.9
		4	1.4	2.8	3.0	2.9	0.1
Autumn	*Phragmites*	90	0.0	1.7	8.7	4.5	1.5
17 April 2001		90	0.2	1.2	9.1	4.1	1.6
		68	0.4	1.4	7.7	3.8	1.6
		42	0.6	1.5	6.9	3.8	1.5
		35	0.8	1.6	7.0	3.7	1.5
		18	1.0	1.8	5.8	3.6	1.3
		8	1.2	2.2	5.2	4.0	1.2
		4	1.4	4.1	4.6	4.4	0.3
		2	1.6	4.3	4.3	4.3	0.0
		2	1.8	3.2	3.5	3.4	0.2
Autumn	*Eleocharis*	98	0.0	2.0	4.0	2.9	0.4
17 April 2001		96	0.2	2.0	4.1	3.0	0.4
		34	0.4	2.3	4.1	3.0	0.4

Table B.6: Stem diameter data for Phragmites australis and Eleocharis at the Deep Creek Typha wetland.

		Height above	Stem diameter (mm)			
Stem Type	Count	Surface (m)	Min.	Max.	Mean	St.Dev
Juncus	60	0.0	0.4	3.4	2.1	0.6
	56	0.2	0.4	2.9	1.9	0.5
	52	0.4	1.2	2.6	1.7	0.3
	49	0.6	1.0	2.3	1.5	0.3
	44	0.8	0.6	2.0	1.3	0.4
	32	1.0	0.6	2.0	1.3	0.3
	20	1.2	0.8	1.8	1.2	0.2
	8	1.4	0.7	1.6	1.1	0.3
Phragmites	38	0.0	2.5	6.2	4.1	0.9
	38	0.2	0.1	5.6	3.5	1.0
	35	0.4	2.1	4.7	3.3	0.7
	21	0.6	0.6	3.8	3.0	0.9
	16	0.8	1.0	4.0	2.9	0.9
	12	1.0	2.1	4.3	2.9	0.7
	4	1.2	3.1	3.7	3.4	0.3
	2	1.4	3.2	3.4	3.3	0.1

Table B.7: Stem diameter data for Juncus kraussii and Phragmites australis at the Deep Creek Juncus wetland. Winter, 26 August 1999.

		Height above	Stem width (mm)				Stem thickness (mm)			
Stem Type	Count	Surface (m)	Min.	Max.	Mean	St.Dev	Min.	Max.	Mean	St.Dev
brown *Typha*	19	0.0	11.6	21.0	16.6	3.0	2.0	17.1	8.1	3.8
	25	0.2	9.0	23.1	15.8	3.6	0.5	17.3	6.2	3.8
	33	0.4	8.2	24.0	15.3	3.8	1.1	14.0	5.7	3.4
	38	0.6	8.3	19.8	14.4	3.0	0.9	13.2	4.8	2.6
	37	0.8	7.3	19.1	13.8	2.8	0.2	10.3	4.7	2.5
	28	1.0	8.3	18.0	14.2	2.5	2.3	9.7	5.2	2.3
	23	1.2	7.7	17.7	14.0	2.9	2.1	9.0	4.7	2.1
	14	1.4	6.2	16.9	11.8	3.6	2.2	7.9	3.9	1.6
	7	1.6	5.5	18.1	12.0	4.7	2.1	7.0	4.4	1.9
	5	1.8	2.7	17.4	9.4	6.7	2.4	6.9	3.8	1.8
	4	2.0	4.3	17.0	11.3	6.3	2.1	6.1	3.7	1.7
	1	2.2	16.8	16.8	16.8	–	2.6	2.6	2.6	–
green *Typha*	45	0.0	2.7	28.2	19.8	4.3	0.8	10.3	5.2	2.3
	49	0.2	11.5	22.5	18.1	2.4	0.6	9.0	4.1	2.0
	49	0.4	14.5	20.4	17.8	1.5	0.2	9.2	3.4	1.9
	47	0.6	7.8	20.8	17.4	2.2	0.2	7.3	2.8	1.5
	39	0.8	14.3	20.8	17.9	1.7	0.3	5.3	2.2	1.3
	36	1.0	9.2	20.9	17.3	2.6	0.2	4.8	1.6	1.2
	30	1.2	11.2	21.3	16.7	2.9	0.2	3.1	1.1	0.9
	18	1.4	7.7	21.6	16.4	4.5	0.2	2.2	1.0	0.7
	11	1.6	12.5	21.1	18.2	2.6	0.2	1.3	0.8	0.4
	8	1.8	13.2	20.3	17.0	2.6	0.3	0.7	0.5	0.2
	3	2.0	14.6	17.6	15.9	1.5	0.2	0.3	0.3	0.1

Table B.8: Stem width and thickness data for Typha domingensis at Warriewood Wetlands.

		Height above	Stem diameter (mm)			
Stem Type	Count	Surface (m)	Min.	Max.	Mean	St.Dev
brown *Eleocharis*	30	0.0	7.9	11.5	10.0	1.0
	30	0.2	7.8	11.1	9.5	0.8
	12	0.4	8.0	10.6	9.0	0.9
green *Eleocharis*	90	0.0	9.0	11.6	10.5	0.6
	90	0.2	1.1	11.4	10.3	1.2
	84	0.4	8.5	11.4	10.0	0.6
	74	0.6	8.3	10.7	9.7	0.6
	50	0.8	7.6	10.6	9.3	0.8
	12	1.0	8.3	9.7	9.0	0.5

Table B.9: Stem diameter data for Eleocharis sphacelata at Hopwoods Lagoon. Autumn, 1 April 2001.

B.3 Calculation of Foliage Area Density Function and Leaf Area Index

The foliage area density function and the downward cumulative leaf area index were calculated for each species in each macrophyte canopy, as discrete functions defined at 0.2 m height intervals above the water surface. The foliage area densities were added for all macrophyte species at each site (quadrat) at each wetland to obtain the cumulative foliage area density function for that site. The downward cumulative leaf area index was calculated from the cumulative foliage area density for each site at each wetland. Flowering stems of *Typha, Juncus, Eleocharis, Triglochin* and *Phragmites* were few in number, and not included in the calculation of foliage area density and leaf area index.

B.3.1 Foliage Area Density Function, *a(z)*

B.3.1.1 One-Sided Incremental Stem Surface Area

For flat, rectangular stems of *Typha domingensis* and *Triglochin procerum*, the one-sided incremental stem surface area is approximately rectangular in shape:

$$\text{inc. stem surface area}(z)_i = \overline{w}(z)_i \times \Delta z \qquad (\text{m}^2 \text{per stem type}) \tag{B.1}$$

For cylindrical stems of *Juncus kraussii, Eleocharis sphacelata* and *Phragmites australis*, the one-sided incremental stem surface area is approximated by the surface area of half a circular cylinder:

$$\text{inc. stem surface area}(z)_i = \frac{1}{2}\,\pi\,\overline{d}(z)_i \times \Delta z \qquad (\text{m}^2 \text{ per stem type}) \tag{B.2}$$

$$\begin{aligned} \text{where} \quad \overline{w}(z) &= \text{mean width of stem type } i \text{ at height } z \text{ above the water surface (m)} \\ \overline{d}(z) &= \text{mean diameter of stem type } i \text{ at height } z \text{ (m)} \\ \Delta z &= \text{height increment, generally 0.2 (m).} \end{aligned}$$

The mean stem dimension for each height increment was calculated as the linear average of the characteristic stem dimensions at the lower and upper ends of the increment.

B.3.1.2 One-Sided Incremental Foliage Area

$$\text{inc. foliage area}(z)_i = n_s(z)_i \times \text{inc. stem surface area}(z)_i \quad \text{(per stem type)} \tag{B.3}$$

$$\text{inc. foliage area}(z) = \sum_{i=1}^{N} \text{inc. foliage area}(z)_i \quad \text{(per site)} \tag{B.4}$$

where $n_s(z)_i$ = density of stem type i at height z (m^{-2})

N = total number of different stem types.

B.3.1.3 Foliage Area Density Function

$$a(z) = \text{inc. foliage area}(z) \div \{\text{quadrat area} \times \Delta z\} \quad (\mathrm{m^2\,m^{-3}} \text{ per site}) \tag{B.5}$$

B.3.2 Downward Cumulative Leaf Area Index, *LAI(z)*

From Equation (3.45) on page 72:

$$LAI\,(z) = \int_z^{h_L} a(z)\,dz \quad (\mathrm{m^2\,m^{-2}} \text{ per site}) \tag{B.6}$$

B.3.2.1 Mean Downward Cumulative Leaf Area Index

The mean downward cumulative leaf area index for each wetland was calculated as the weighted mean of *LAI(z)* at all sites at that wetland. The weighting function was derived at each height z from the contributing number of stems at each site, as follows:

$$\overline{LAI(z)} = \sum_{j=1}^{M} \left(LAI(z)_j \, \frac{n_s(z)_j}{\sum_{j=1}^{N} n_s(z)_j} \right) \tag{B.7}$$

where $\overline{LAI(z)}$ = mean canopy *LAI(z)* at each wetland ($\mathrm{m^2\,m^{-2}}$)

$n_s(z)_j$ = stem density at site j at height z (m^{-2})

= $\sum_{i=1}^{N} n_s(z)_i$

M = number of sites/quadrats at each wetland.

Appendix C

SPECIFICATIONS FOR FIELD INSTRUMENTS

C.1 Photosynthetically-Active Radiation (PAR) Sensor

Photosynthetically-active radiation (PAR) was measured using a cosine-corrected, LI-COR model 192SA quantum sensor. The sensor is sensitive to the 400 to 700 nm waveband and has a response time of $10\,\mu$s (LI-COR, Inc, 1990). The sensor was factory-calibrated for use in both air and water, and used in the emergent canopy (Section 6.3) and below the water surface (Section 5.4).

The sensor output was powered by a Data Electronics model DT50 data logger and logged as a voltage signal, using a LI-COR model 2291S 1210Ω millivolt adaptor. The voltage output was converted to PAR flux units using the factory calibration factor for air or water, as outlined below.

C.1.1 Conversion to PAR Flux Units when used in Air

The factory calibration factor for air was $3.83\,\mu\mathrm{A}$ per $1000\,\mu\mathrm{E\,s^{-1}\,m^{-2}}$ (LI-COR, Inc, 1990). This is equivalent to:

$$\frac{3.83\ \mu\mathrm{A}}{1000\ \mu\,\mathrm{mol\,s^{-1}\,m^{-2}}} \times \frac{1}{10^6}\frac{\mathrm{A}}{\mu\,\mathrm{A}} \times 1210\,\Omega = \frac{0.004634\ \mathrm{V}}{1000\ \mu\,\mathrm{mol\,s^{-1}\,m^{-2}}}$$

or:

$$215.8\,\mu\,\mathrm{mol\,s^{-1}\,m^{-2}}\ \text{per mV}. \tag{C.1}$$

The quantum units were converted to PAR flux units using a factor of $0.2332\,\mathrm{Wm^{-2}}$ per $\mu\,\mathrm{E\,s^{-1}\,m^{-2}}$ as per Table C.1 ($r^2 > 0.99$ with $n = 6$, assuming a zero intercept). Note that $1\,\mu\,\mathrm{mol\,s^{-1}\,m^{-2}} \equiv 1\,\mu\,\mathrm{E\,s^{-1}\,m^{-2}}$ (Guyot, 1998). This is consistent with a conversion factor of $0.2193 \pm 0.0024\,\mathrm{Wm^{-2}}$ per $\mu\,\mathrm{E\,s^{-1}\,m^{-2}}$, cited by Monteith and Unsworth (1990).

C.1.2 Conversion to PAR Flux Units when used in Water

The factory calibration factor for water was $2.90\,\mu\,\mathrm{A}$ per $1000\ \mu\,\mathrm{E\,s^{-1}\,m^{-2}}$ for water (LI-COR, Inc, 1990). Using the conversion procedure shown above, this is equivalent to:

$$285.0\,\mu\,\mathrm{mol\,s^{-1}\,m^{-2}}\ \text{per mV}. \tag{C.2}$$

The quantum units were converted to PAR flux units as described above.

Photosynthetically Active Radiation (μ E s^{-1} m^{-2})	Photosynthetically Active Radiation (Wm^{-2})
3000	705.0
2500	587.5
2000	470.0
1500	325.5
1000	235.0
500	117.5

Table C.1: Correspondence between photosynthetically active radiation measured in natural conditions, expressed in μ E s^{-1} m^{-2} and Wm^{-2}. Data from Guyot (1998), p.55.

C.2 Relationship Between PAR and Global Shortwave Radiation

As discussed in Section 3.3.2.1, the ratio of PAR (400 to 700 nm) to global shortwave radiation (300 to 2800 nm) is approximately 47 to 50%. This ratio was examined by comparing the response of the LI-COR PAR sensor and the SolData global pyranometer over several days in March and May 2000. The measurements were made at Hopwoods Lagoon, and the two sensors were mounted at the same elevation from the mast of the automatic weather station.

Figure C.1(a) shows the temporal variation in PAR and global shortwave radiation over the measurement period. The period from 5 to 7 March was overcast and it rained heavily on 6 March. Scattered cloud was present on 8 May, but 9 May was essentially cloudless.

Figure C.1(b) shows the relationship between measured PAR and global shortwave radiation on the same days, and Table C.2 summarises the linear regression parameters for each day. The ratio of PAR to global shortwave radiation was similar for cloudless (9 May) and partly cloudy conditions (5 March and 8 May), with a range of 49.3 to 51.9%. The ratio was also similar on 6 March, when heavy rain fell and the peak 10 minute mean global shortwave radiation was less than 200 Wm^{-2}, although the ratio was considerably lower under intermittently raining skies on 7 March.

The observed ratio of 50% under clear skies was consistent with the expected value of the ratio (page **??**, and therefore adopted in the present investigation.

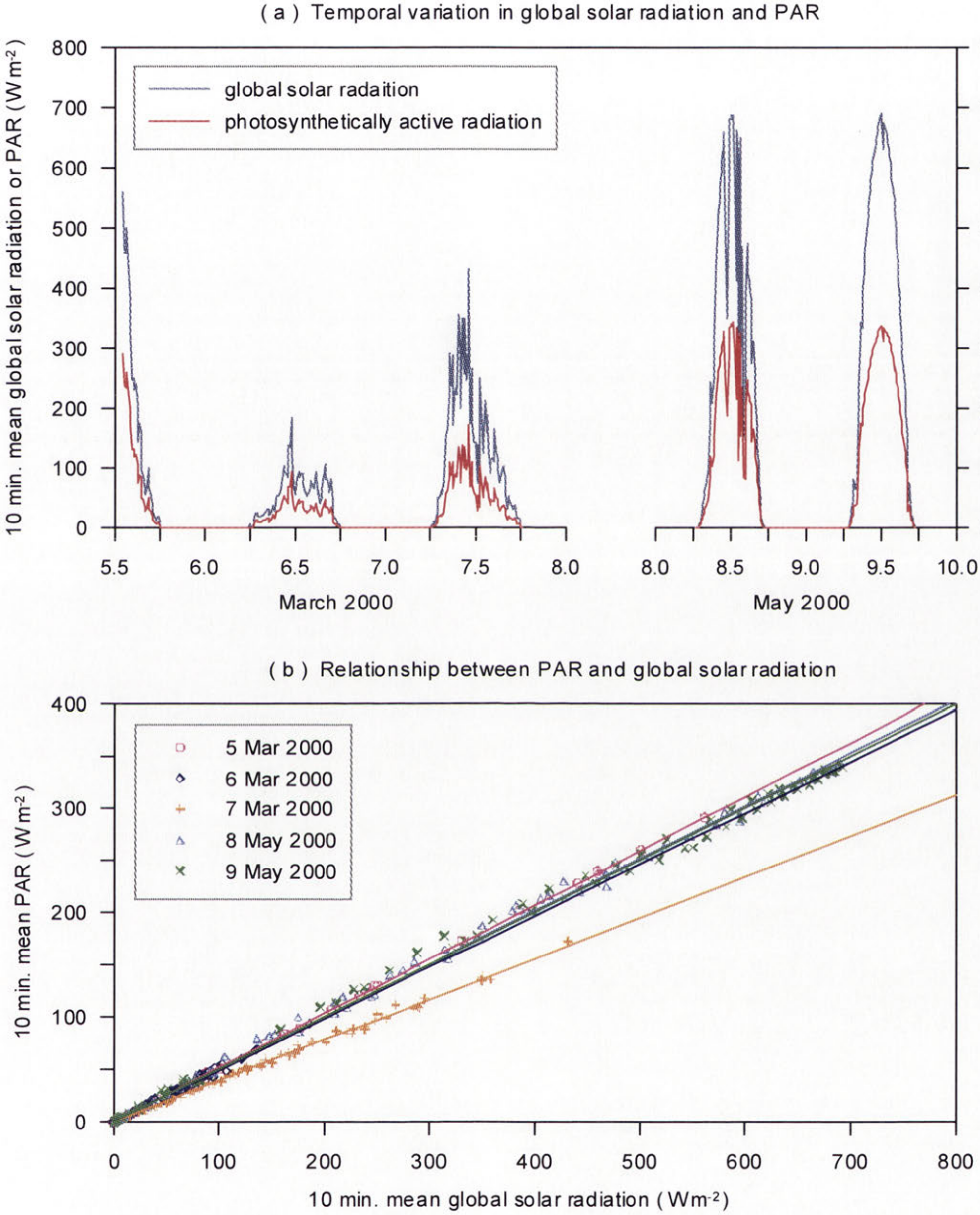

Figure C.1: Comparison between measured global shortwave radiation and PAR at Hopwoods Lagoon on 5 to 7 March and 8 to 9 May 2000.

Date of Measurement	Number of Points	Ratio of PAR to Global Shortwave Radiation	Regression Coefficient r^2
5 Mar 2000	35	0.519	0.9998
6 Mar 2000	79	0.493	0.9866
7 Mar 2000	75	0.391	0.9968
8 May 2000	67	0.505	0.9971
9 May 2000	67	0.500	0.9963

Table C.2: Regression relationships between measured PAR and measured global shortwave radiation at Hopwoods Lagoon.

C.3 Automatic Weather Station Instruments

Specifications for the monitoring instruments of the automatic weather station are given below. Note that levels are relative to AHD.

- **Wind direction** was determined using a Pacific Data Systems Model PDS-WS-10 wind vane. The wind vane was installed at one end of a 500 mm long cross arm, mounted at the top of the 10 m mast (RL 32.2 m). The 400 mm long vane was constructed of polyurethane-coated, corrosion-resistant aluminium with low friction, stainless steel bearings. The rotary potentiometer element of the wind vane had a continuous mechanical travel of 360° and a 5° deadband centred on 0°. The sensor output was logged as voltage, with a linear range of 0 to 1000 mV representing wind directions of 0 to 360° deviation from north. The wind vane was oriented during installation using a compass.

- **Wind speed** was measured using a Pacific Data Systems Model PDS-WS-10 three cup anemometer. The anemometer was also installed on the cross arm atop the 10 m mast, at an elevation of RL 32.2 m. The 60 mm diameter anemometer cups were constructed of polyurethane-coated, corrosion-resistant aluminium with stainless steel bearings. The sensor output was logged as voltage, with a linear range of 0 to 1000 mV representing wind speeds of 0 to 100 $\mathrm{km\,h^{-1}}$ (27.78 $\mathrm{m\,s^{-1}}$), above a starting threshold of 0.5 $\mathrm{m\,s^{-1}}$.

- **Air temperature** was measured using a Pacific Data Systems Model SRS/T air temperature sensor installed beneath a radiation shield at an elevation of RL 24.9 m. The 100 Ω Class A, four-wire platinum resistor was powered by the data logger and sensor output was logged as resistance. The resistance response of the sensor was linear with temperature, with an alpha coefficient of 0.00385 Ω°C^{-1} and linearity within $\pm 0.06\,\Omega$.

- **Relative humidity** was measured using a Vaisala model HMP45A capacitive thin film polymer sensor, installed within a ventilated cylindrical shelter at an elevation of RL 24.4 m. The sensor was powered by the data logger and sensor output was logged as voltage, with a linear range of 0 to 1000 mV representing relative humidity from 0 to 100 %. The sensor had a settling time of 500 ms.

- **Shortwave radiation** was measured using a SolData Model 80HDX pyranometer, comprised of a cosine-corrected, temperature-compensated photovoltaic cell mounted within a glass hemisphere. The pyranometer was installed on a cross arm mounted at an elevation of RL 25.0 m and measured global radiation (direct plus diffuse shortwave radiation) in the waveband 300 to 2800 nm. The pyranometer was powered by the data logger and logged as voltage, with a calibration factor of 7.24638 Wm^{-2} per mV.

- **Barometric pressure** was measured using a Pacific Data Systems Model PDS-TRAFAG ATM8843 barometric pressure transducer, installed within the cylindrical sensor shield at an elevation of RL 24.4 m. The sensor was powered by the data logger and the output was logged as voltage, with a linear range of 0 to 1000 mV representing 800 to 1060 hPa.

- **Rainfall** was measured using a Hydrological Services Model TB3/0.2 tipping bucket pluviometer, with a 0.2 mm tip volume and a 200 mm diameter collecting funnel. The pluviometer was installed on a concrete pad approximately 4 m from the mast of the weather station, to minimise any potential rain sheltering effects from the mast or other monitoring instruments while remaining within the fenced enclosure. The rim of the funnel was surveyed at RL 23.0 m.

Bucket tips were recorded by a high speed digital counter on the data logger, then multiplied by the bucket volume and logged as millimeters of rainfall. The pluviometer was factory calibrated to an accuracy of ±1.5 tips (average) of a theoretical 50 tips, and verified in the field using a Hydrological Services Model TB3 Portable Calibration Unit.

C.4 Water Temperature Monitoring Instruments

Water temperatures were monitored using Thermometrics thermistors, with the following specifications.

- **Primary Monitoring Thermistors, T1 to T16**
  - Thermometrics model A727-P60BA252M thermistors
  - encased in stainless steel
  - outer diameter of approximately 3.0 mm
- **Secondary Monitoring Thermistors, T21 to T28**
  - Thermometrics model T2204/C2-P60BA252M thermistors
  - constructed of stainless steel
  - thermistor beads enclosed in glass tips
  - outer diameter of approximately 1.5 mm

The thermistor beads were identical in all 24 instruments, with a nominal resistance of 2500Ω at 25°C (Thermometrics Inc., 1986). Each set of thermistors was calibrated in the laboratory against a platinum resistance thermometer, as described in Appendix E.

Appendix D

METEOROLOGICAL DATA

D.1 Calculation of Vector Mean Wind Speed and Direction

A 10 min vector mean wind speed and wind direction were calculated from raw wind speed and direction data collected every 20 seconds, as shown below.

$$\text{vector mean wind speed} = \frac{1}{n}\sqrt{\left(\sum(u\cos\theta_{\mathrm{w}})\right)^2 + \left(\sum(u\sin\theta_{\mathrm{w}})\right)^2}$$

$$\text{vector mean wind direction} = \tan^{-1}\left(\frac{u\cos\theta_{\mathrm{w}}}{u\sin\theta_{\mathrm{w}}}\right) \qquad \text{(D.1)}$$

where u = measured 20 sec wind speed ($\mathrm{m\,s^{-1}}$)

θ_w = measured 20 sec wind direction ($^\circ$).

D.2 Record of Meteorological Data Losses

As mentioned in Section 5.5.1.1, data was lost from the weather station on several occasions when there was a problem with the logger, the power supply or the memory capacity. The periods of data loss and reasons for these are summarised in Table D.1.

Data loss from:		Data loss to:		Reason for loss:
5 May 2000	03:20	7 May	13:40	battery recharge problem, overcast conditions
16 Oct 2000	03:20	22 Oct	13:30	logger error
15 Nov 2000	02:00	19 Nov	13:10	battery recharge problem, overcast conditions
9 Jan 2001	02:40	17 Jan	10:00	battery recharge problem, overcast conditions
6 Feb 2001	02:30	14 Feb	09:30	battery recharge problem - battery replaced
26 Apr 2001	09:30	1 May	14:40	memory full
15 Oct 2001	09:00	17 Oct	16:20	memory full

Table D.1: Periods of data loss from the automatic weather station, and the reasons for these losses.

D.3 Summary of Time-Series Meteorological Data

D.3.1 Wind Direction

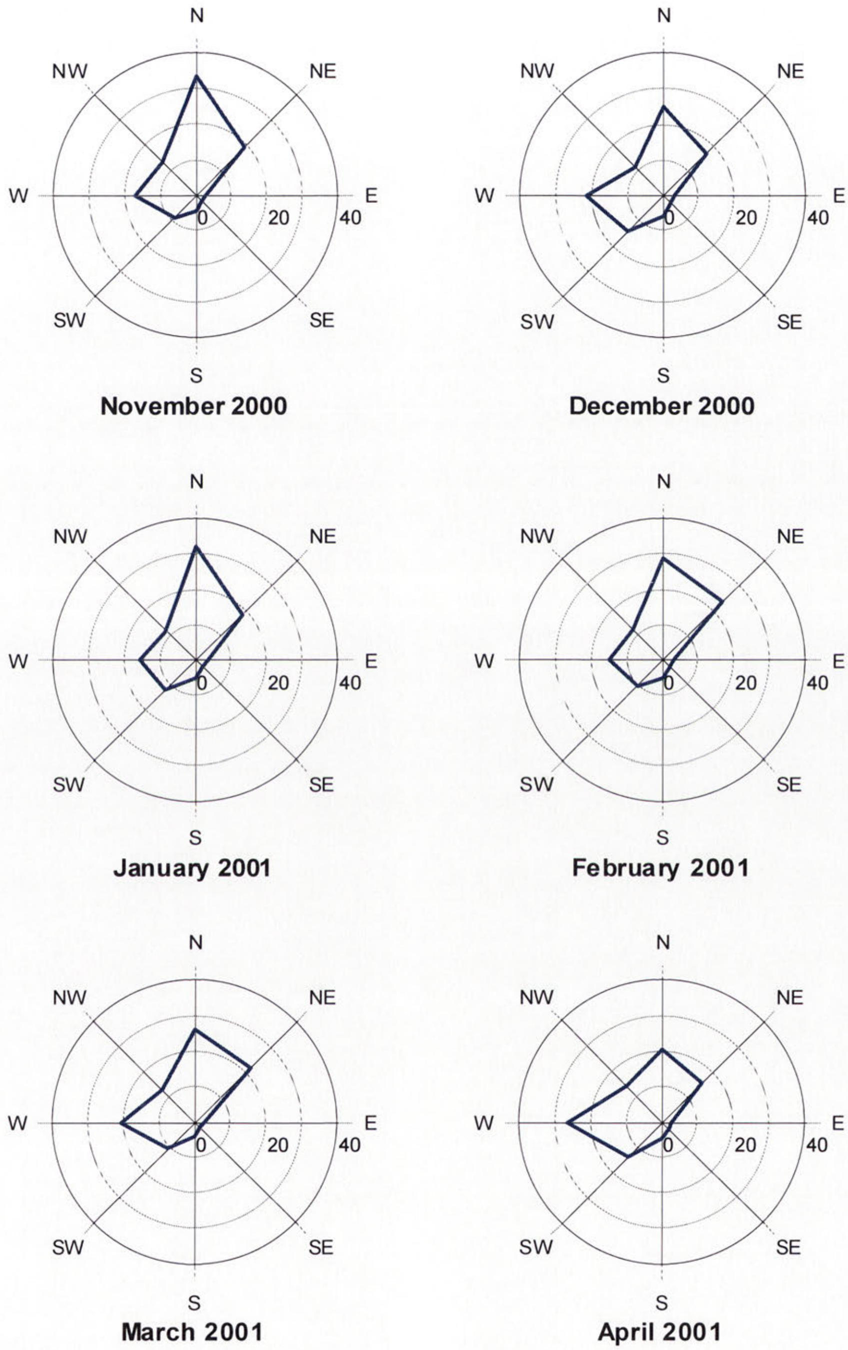

Figure D.1: Monthly wind roses at Hopwoods Lagoon, showing frequency of occurrence (%) of 10 min mean direction from which wind is blowing.

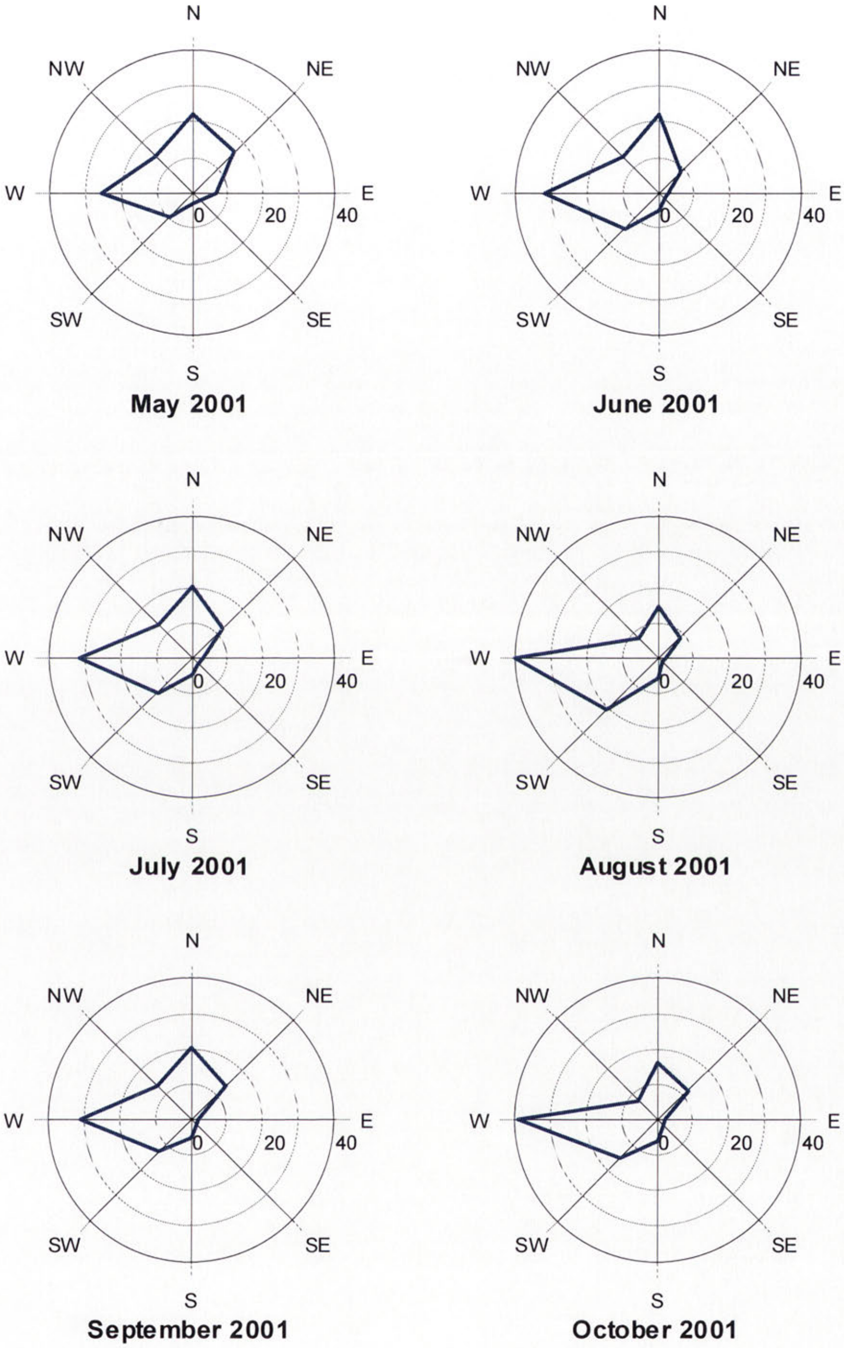

Figure D.1 (continued): Monthly wind roses at Hopwoods Lagoon, showing frequency of occurrence (%) of 10 min mean direction from which wind is blowing.

D.3.2 Wind Speed

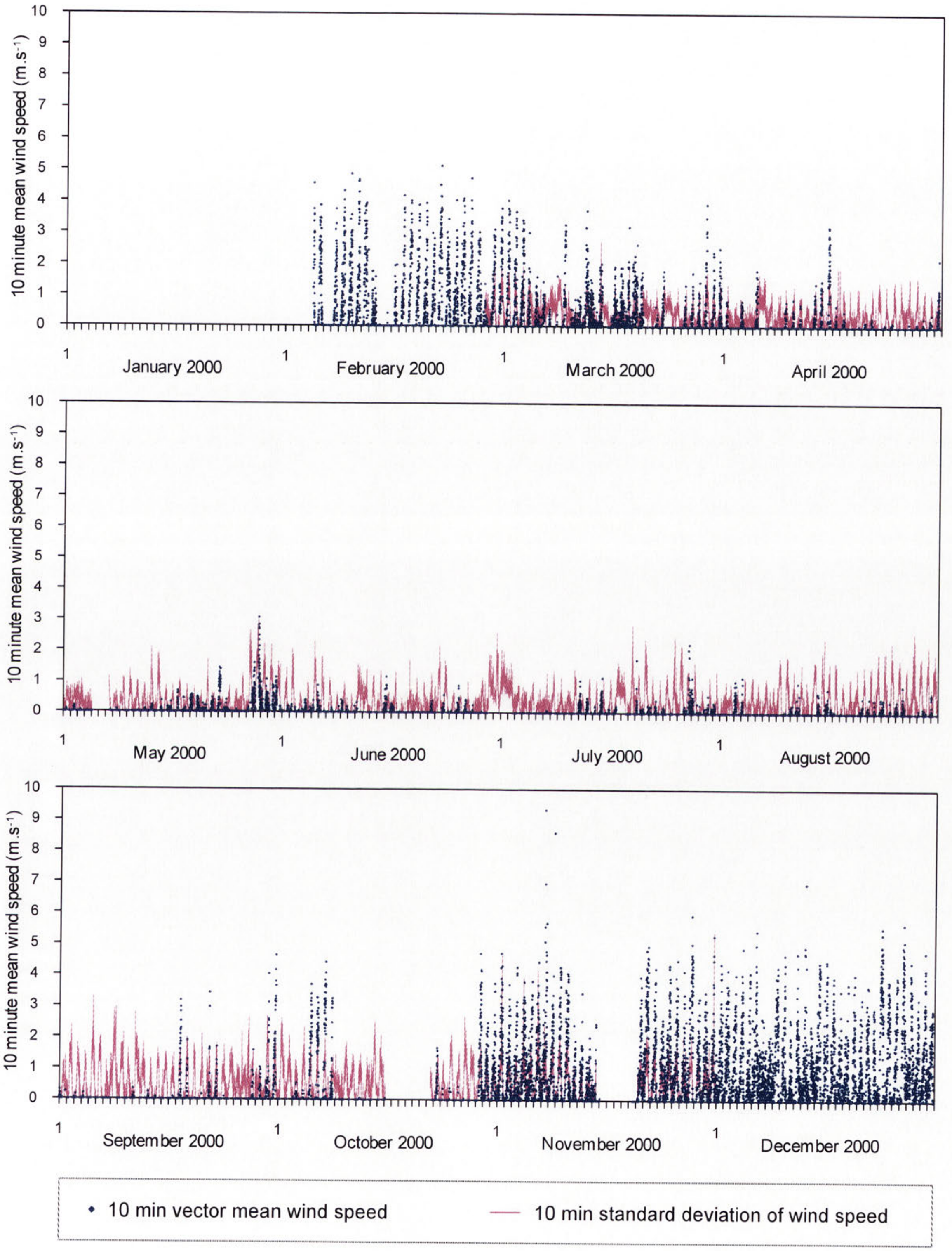

Figure D.2: Vector mean and standard deviation wind speeds at Hopwoods Lagoon.

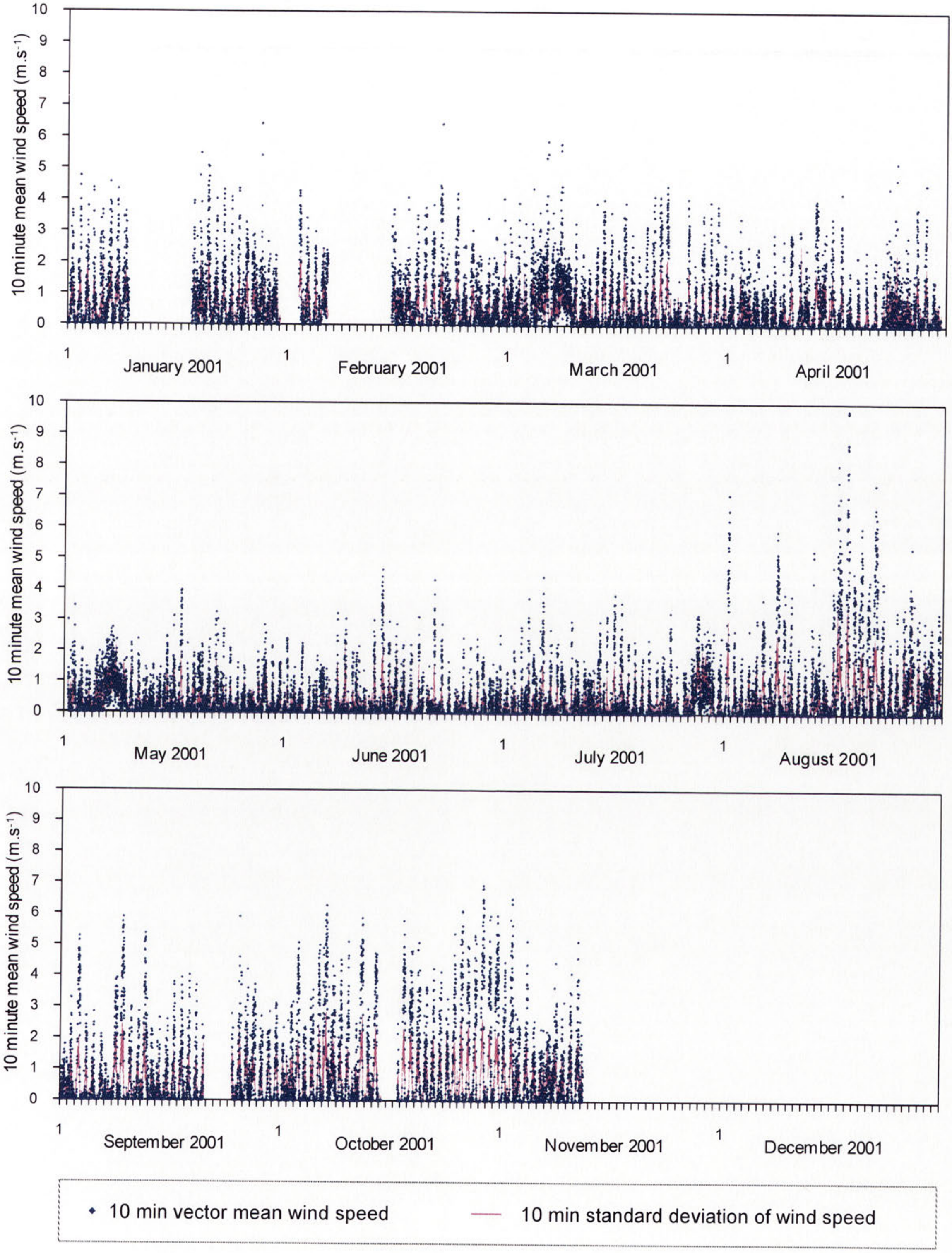

Figure D.2 (continued): Vector mean and standard deviation wind speeds.

D.3.3 Air Temperature

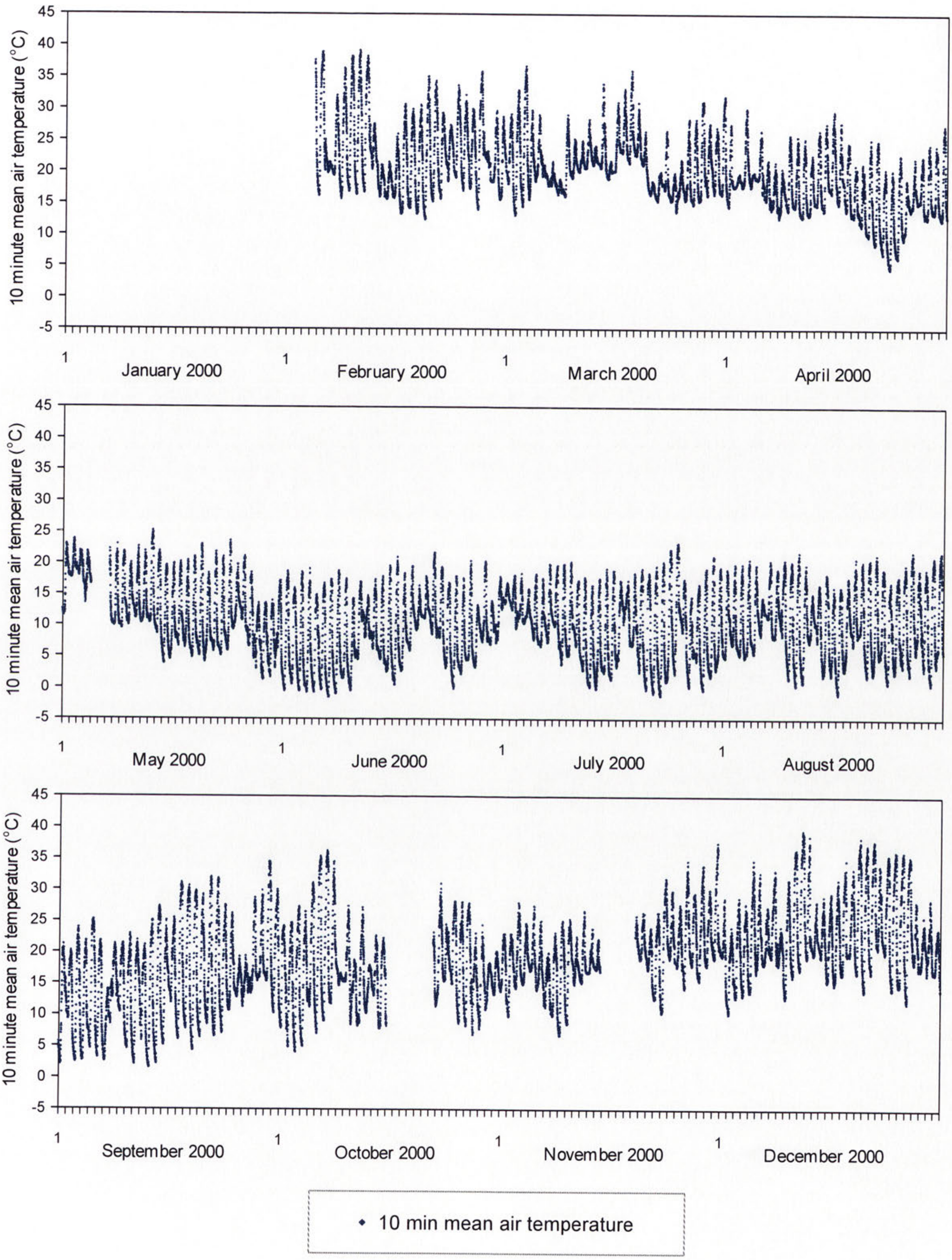

Figure D.3: Mean air temperatures at Hopwoods Lagoon.

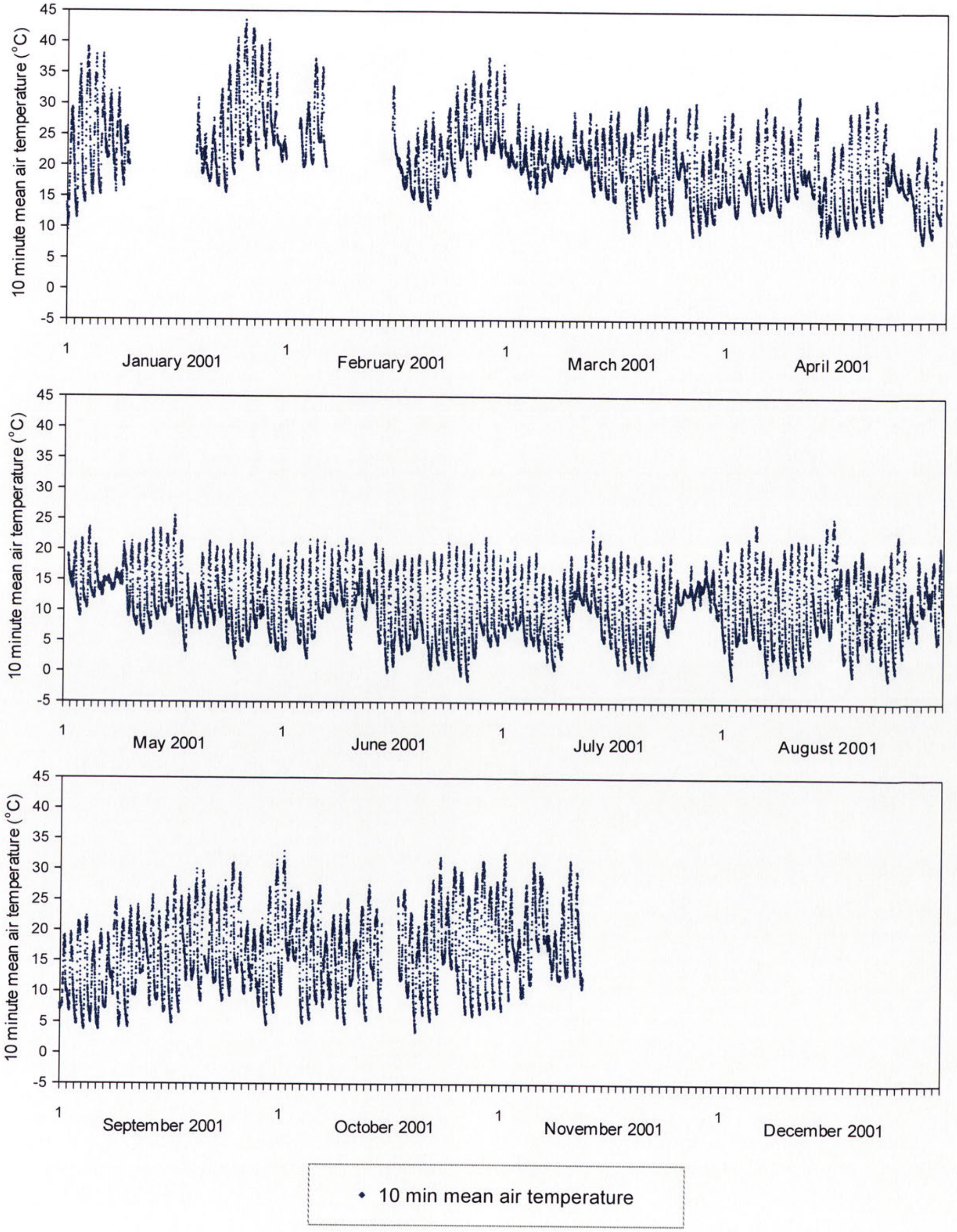

Figure D.3 (continued): Mean air temperatures at Hopwoods Lagoon.

D.3.4 Relative Humidity

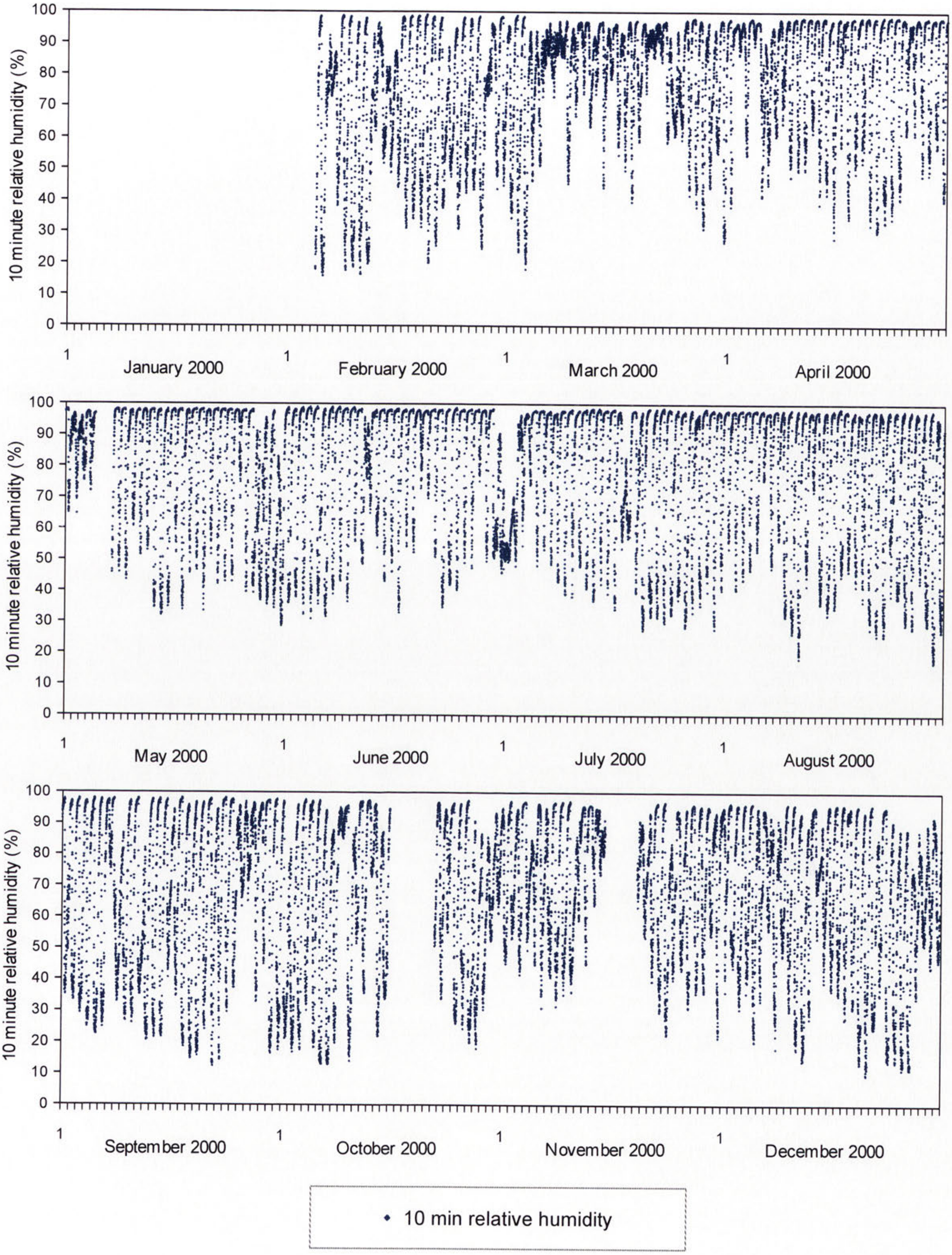

Figure D.4: Relative humidity at Hopwoods Lagoon.

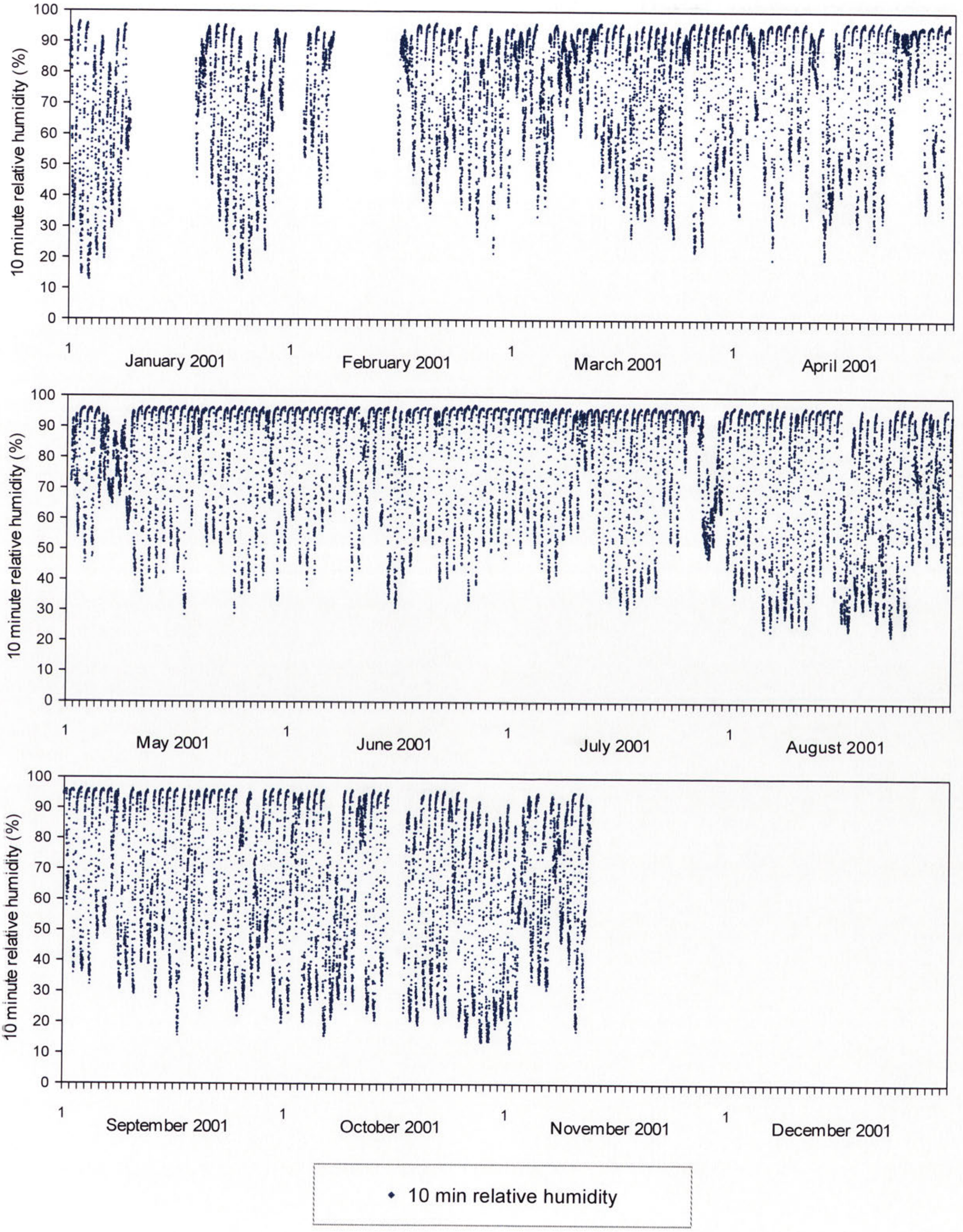

Figure D.4 (continued): Relative humidity at Hopwoods Lagoon.

D.3.5 Barometric Pressure

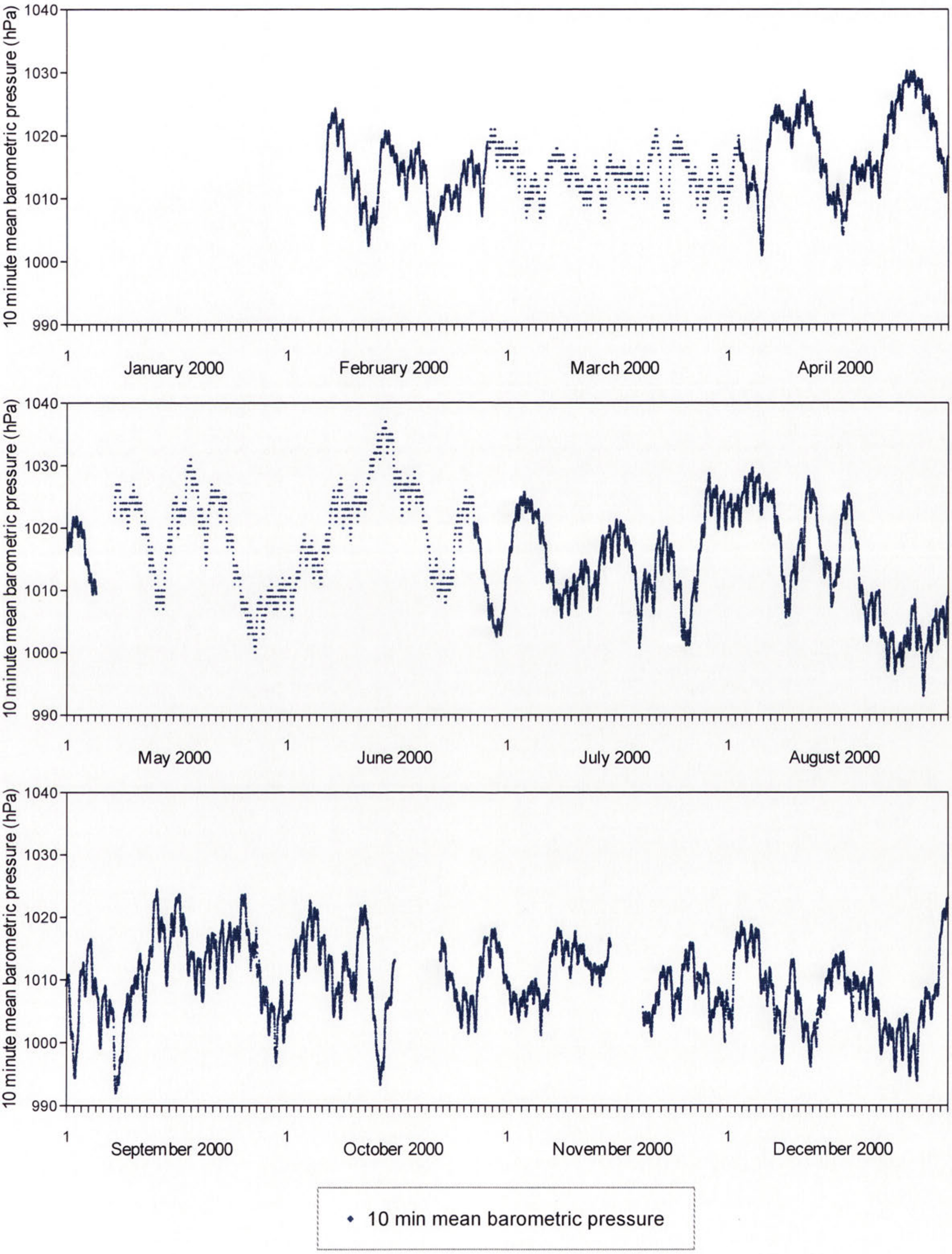

Figure D.5: Mean barometric pressure at Hopwoods Lagoon.

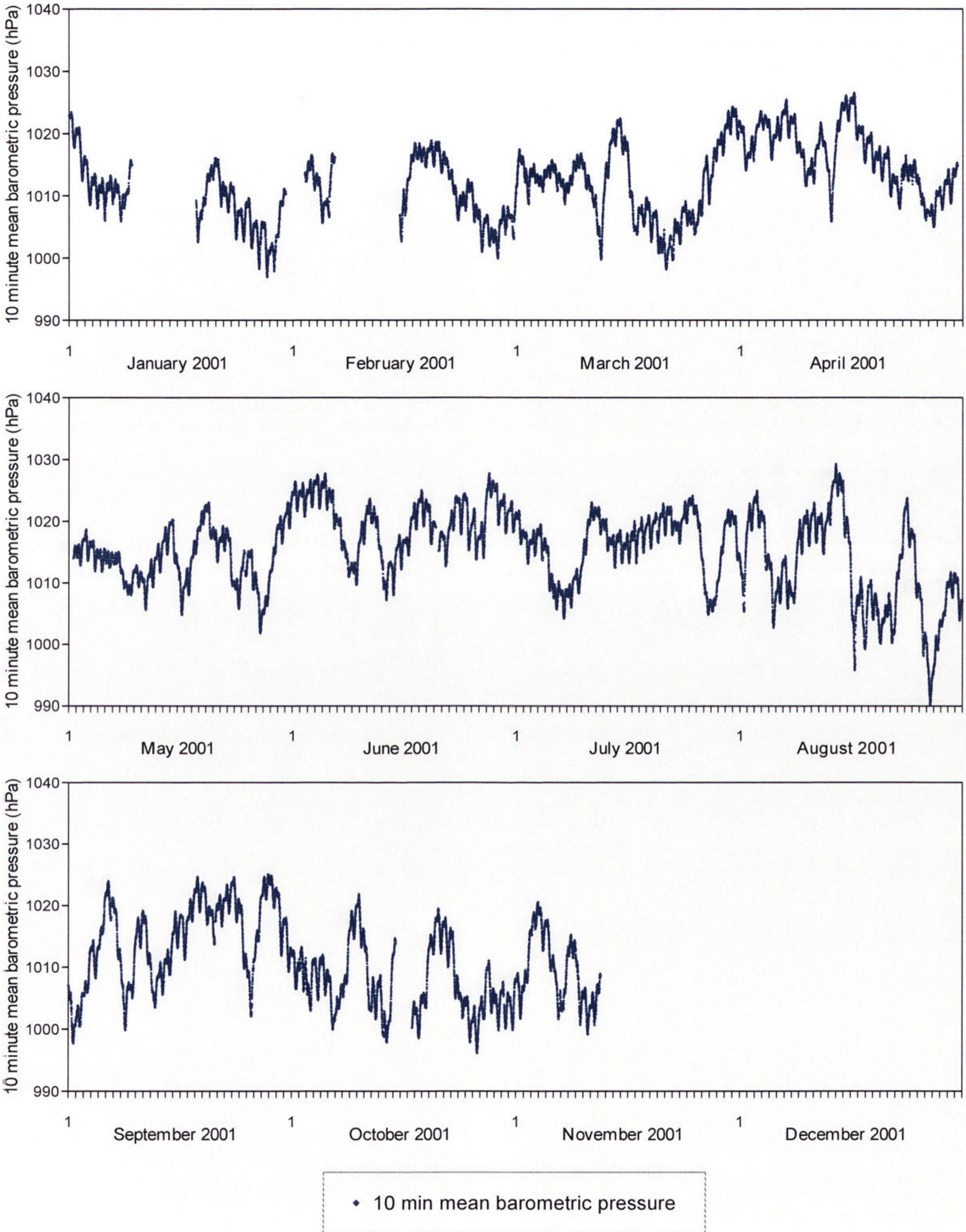

Figure D.5 (continued): Mean barometric pressure at Hopwoods Lagoon.

D.3.6 Shortwave Radiation

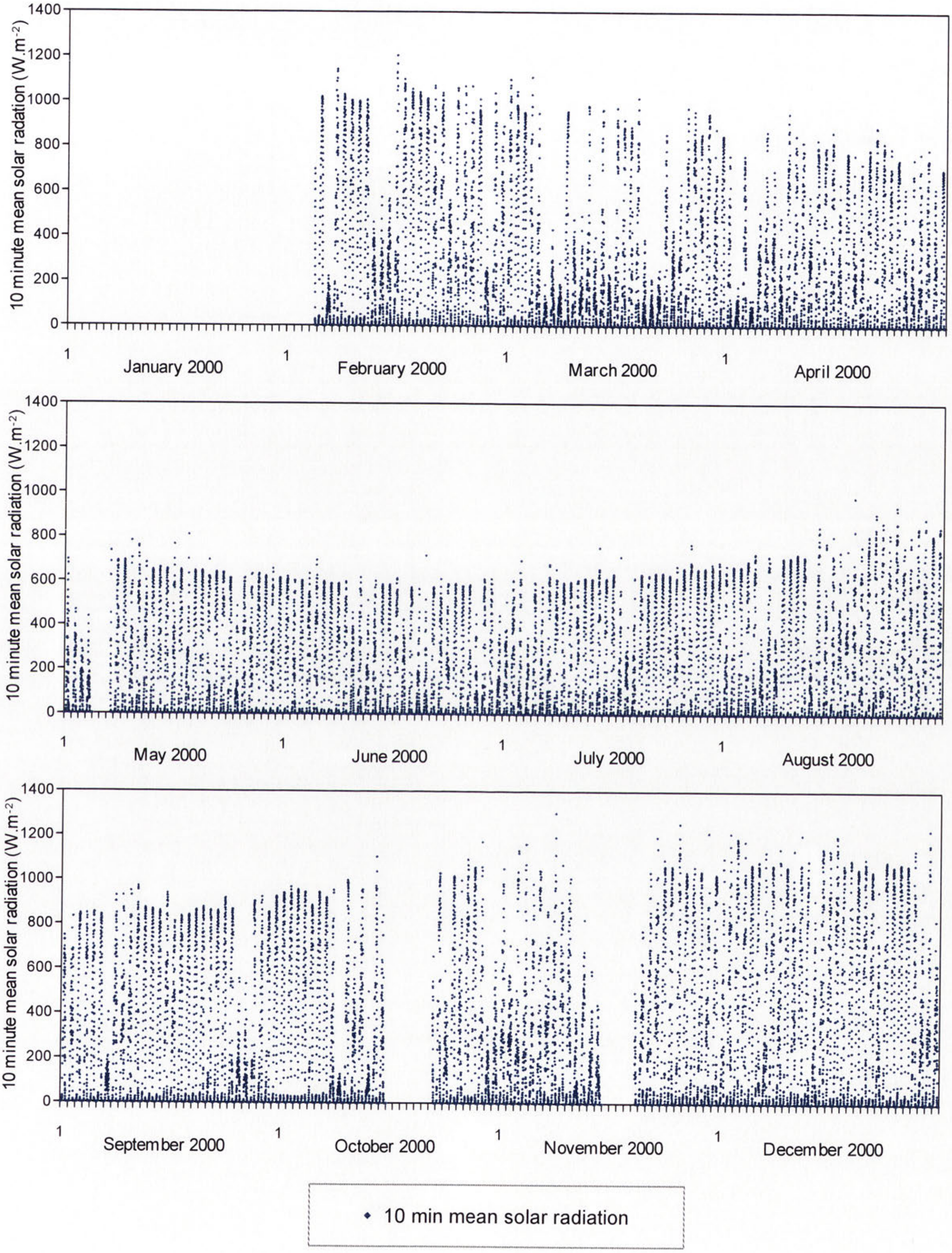

Figure D.6: Mean global shortwave radiation at Hopwoods Lagoon.

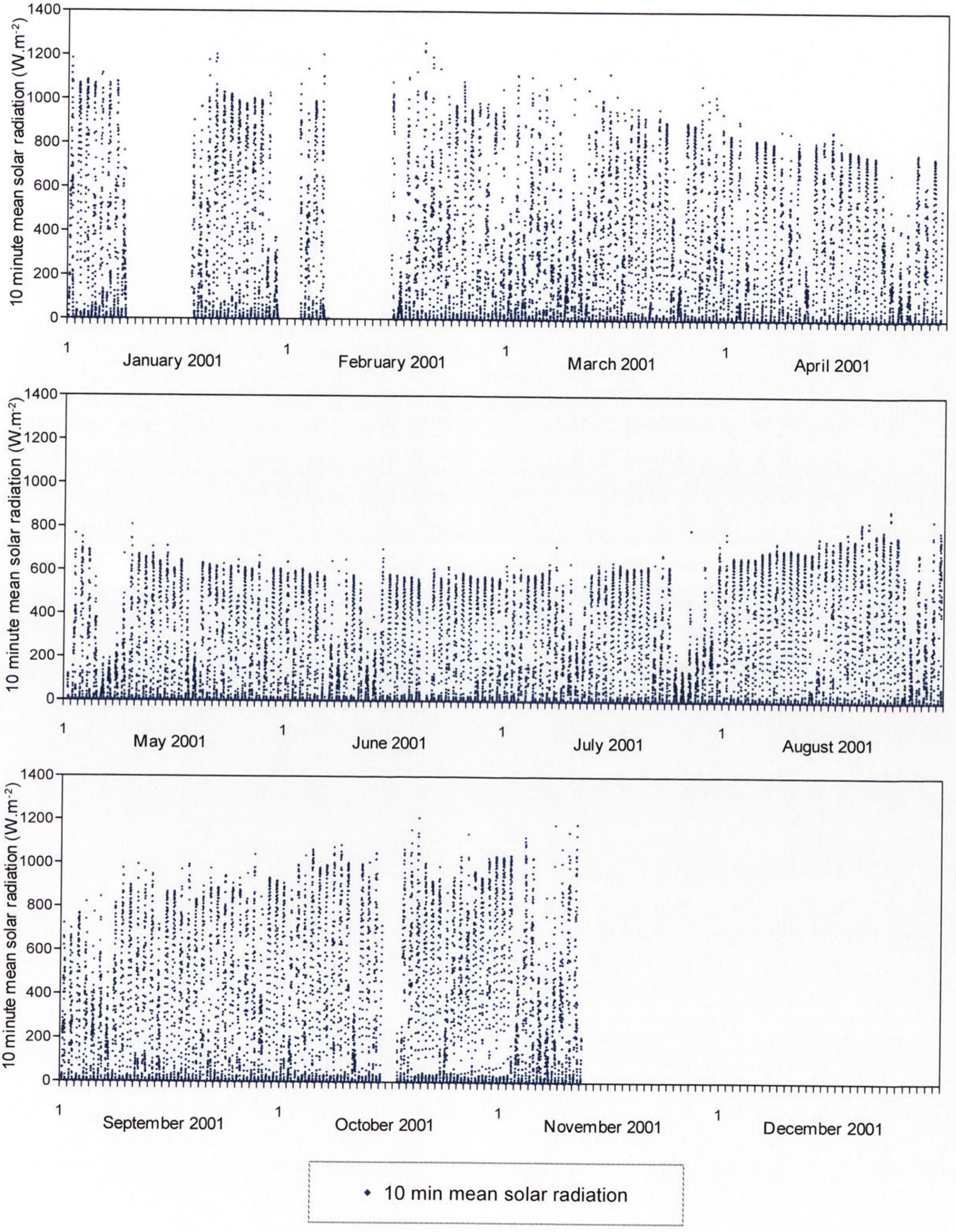

Figure D.6 (continued): Mean global shortwave radiation at Hopwoods Lagoon.

D.3.7 Rainfall

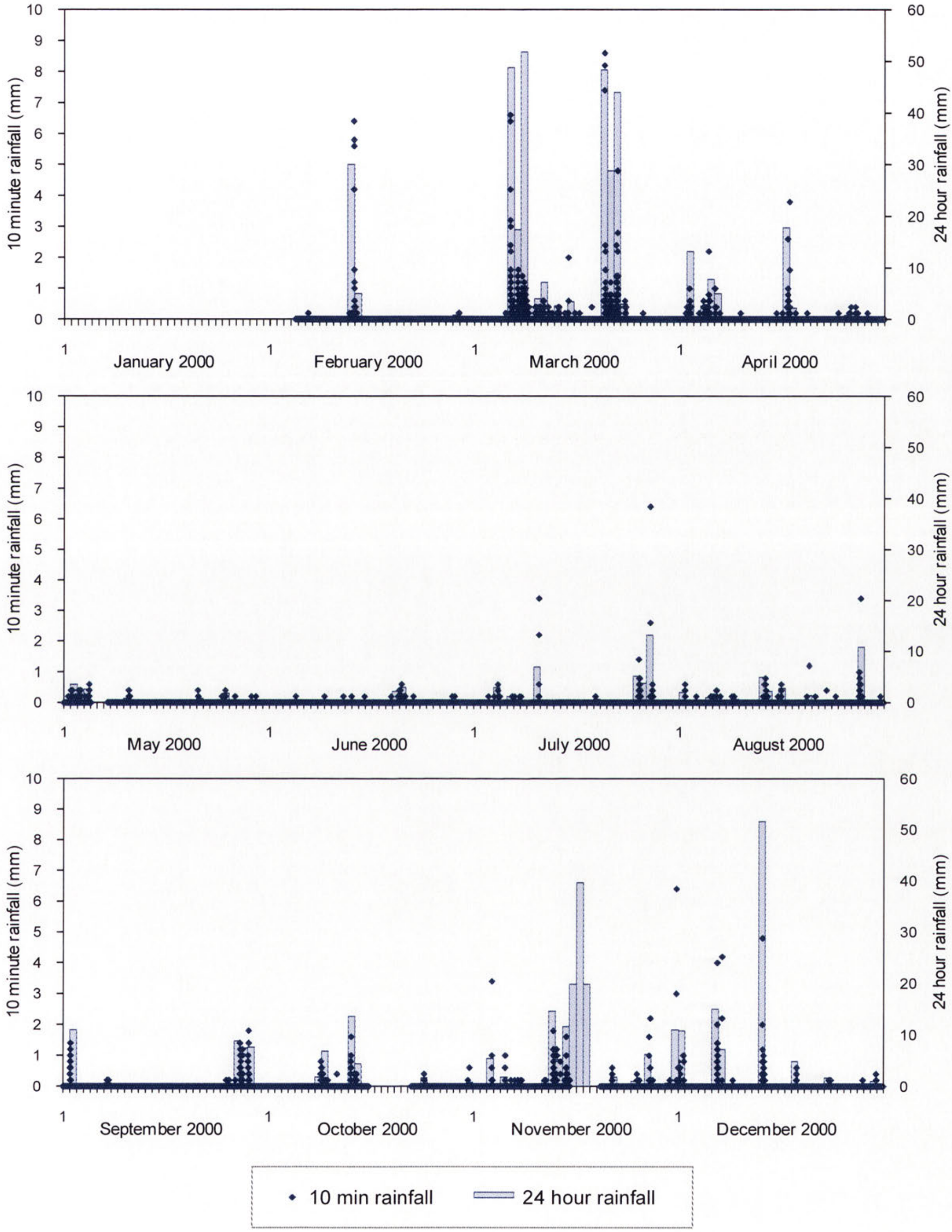

Figure D.7: Rainfall at Hopwoods Lagoon.

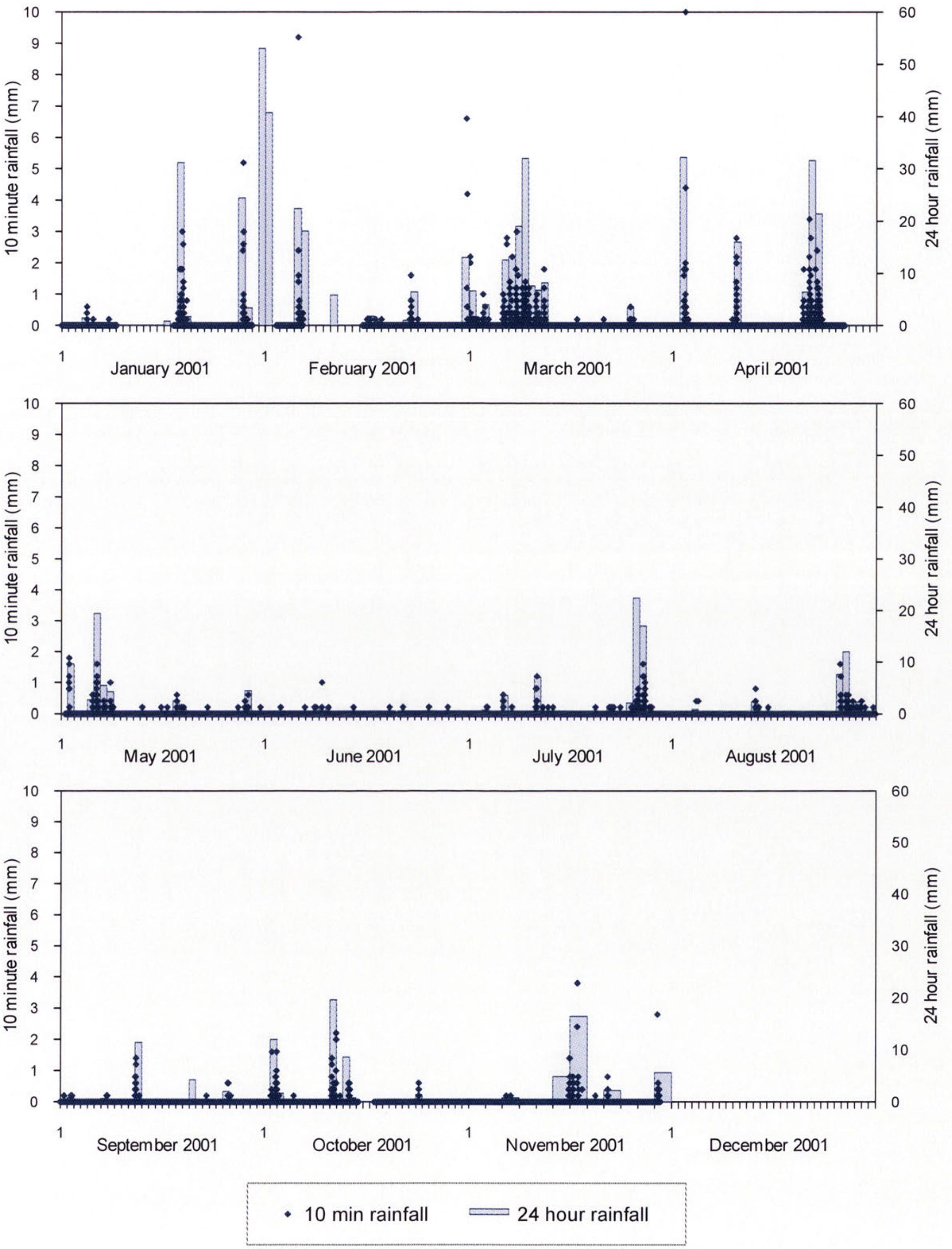

Figure D.7 (continued): Rainfall at Hopwoods Lagoon.

D.4 Cumulative Rainfall Correlation

The performance of the pluviometer attached to the automatic weather station was assessed by comparison with the adjacent storage rain gauge, and by comparison with the storage rain gauge operated by the Sternbeck family of Higher Macdonald. The results of correlation between the cumulative rainfall totals are presented below.

AWS Pluviometer and Storage Rain Gauge at Hopwoods Lagoon

Figure D.8 shows the correlation between cumulative rainfall totals recorded by the automatic weather station and the adjacent storage rain gauge. The time-series rainfall records shown in Figure D.8(a) are closely coincident in time, as expected from the adjacent instruments. The relationship shown in Figure D.8(b) is essentially linear, with a slope of 0.999 and a least-squares regression coefficient of r^2=0.999. This relationship confirmed that the total volumes of rainfall collected by the two rain gauges over the monitoring period were virtually identical. Consequently, the volumes collected by the storage rain gauge during periods where the automatic weather station was not operating could be considered representative of the volumes that would have been measured by the pluviometer during those periods.

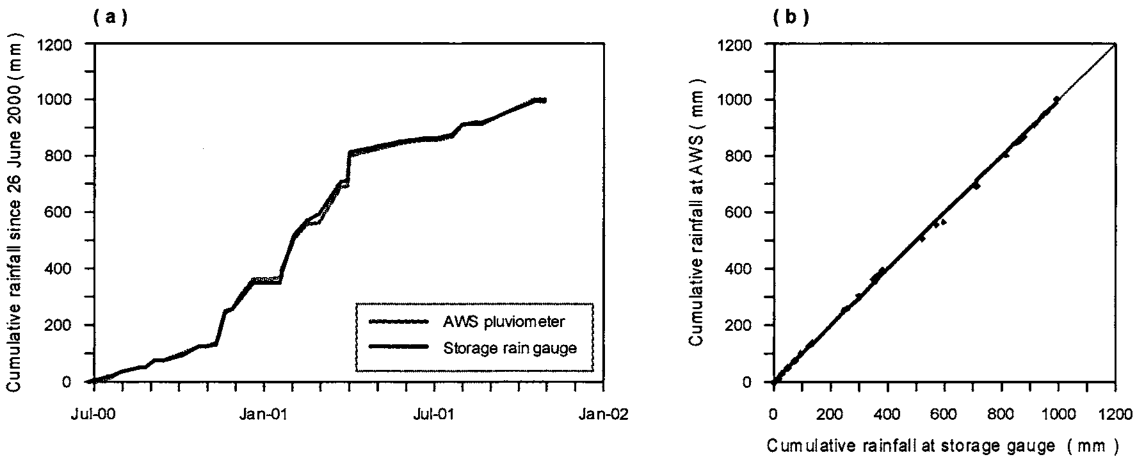

Figure D.8: Cumulative rainfall totals recorded by the AWS pluviometer and the storage rain gauge at Hopwoods Lagoon, from 26 June 2000 to 30 October 2001: (a) time-series comparison and (b) correlation of cumulative rainfall.

AWS Pluviometer and Sternbeck's Storage Rain Gauge

Figure D.9 shows the correlation between cumulative rainfall totals recorded by the automatic weather station and the storage rain gauge located at the Sternbeck's property, approximately 500 m north-west of the AWS. Figure D.9(a) shows the time-series comparison between rainfall at the two gauges, while (b) compares the cumulative rainfall totals at the two gauges.

The cumulative rainfall recorded by the pluviometer of the automatic weather station was 88% of that recorded at the Sternbeck's property, which indicated the highly localised rainfall distribution in the narrow Macdonald Valley. The correlation between cumulative rainfall totals at the pluviometer and the rain gauge at the Sternbeck's property was linear, with a least squares correlation coefficient r^2=0.999. The two cumulative rainfall curves also corresponded closely in time, which suggested that either rainfall volume could be used to predict the other. Hence, daily rainfall totals could be reported for the entire monitoring period, including estimated totals for days when the weather station was not operating successfully.

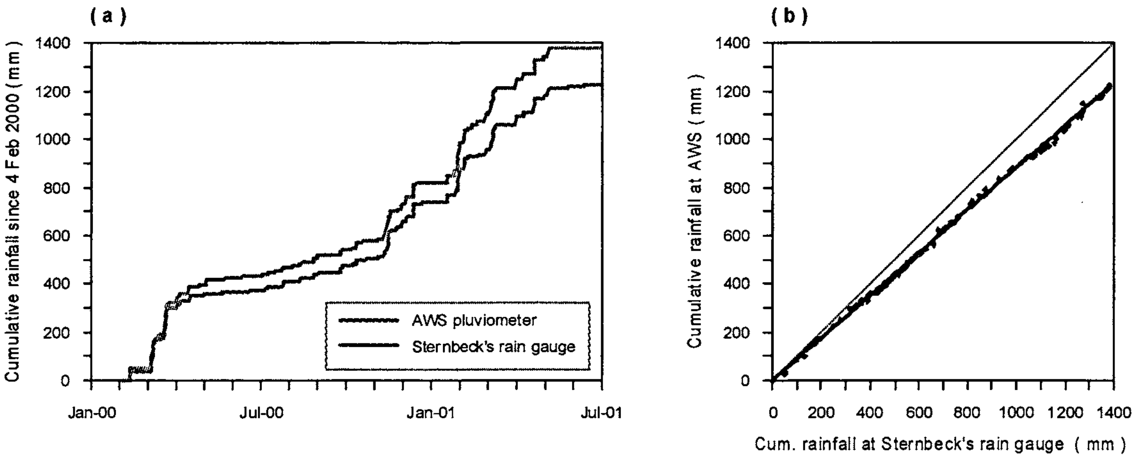

Figure D.9: Cumulative rainfall totals recorded by the AWS pluviometer and the Sternbeck's storage rain gauge, from 4 February 2000 to 30 June 2001: (a) time-series comparison and (b) correlation of cumulative rainfall.

D.5 Calculation of Mean Pan Evaporation

Net pan evaporation was measured using a calibrated cylinder and recorded to the nearest 0.2 mm. The change in storage of the evaporation pan, ΔS was measured on each visit to site. The pan evaporation, E (mm) was calculated from the change in storage of the evaporation pan and the cumulative rainfall over the same period, R (mm):

$$\Delta S = R - E \qquad \text{so} \qquad E = R - \Delta S \tag{D.2}$$

- If the water level in the evaporation pan had *decreased*:

  $\Delta S < 0 =$ net of pan evaporation over rainfall.

- If the water level in the evaporation had *increased*:

  $\Delta S > 0 =$ net of rainfall over pan evaporation.

If the evaporation pan had clearly overflowed, $\Delta S > 0$ but could not be measured, so the net or cumulative evaporation could not be estimated.

Appendix E

THERMISTOR CALIBRATION AND VERIFICATION

E.1 Introduction and Objectives

The thermistors used for water temperature monitoring at Hopwoods Lagoon required calibration prior to field deployment. Following completion of the field monitoring programme, it was necessary to verify the performance of the thermistors throughout the monitoring period. Details of the thermistor calibration and validation experiments are given in this Appendix.

These calibration procedures were derived with reference to the *Operations and Service Manual* for the Leeds and Northrup portable precision temperature bridge, and to procedures described by Waters (1998).

The resistance of a thermistor increases non-linearly with temperature, although the relationship can generally be described by a polynomial fitted to calibration data (Thermometrics Inc., 1986). The thermistors were calibrated to within ± 0.1°C using a platinum resistance thermometer (PRT). The PRT was calibrated to within ± 0.01°C, as suggested by Collier (1982).

The thermistors were calibrated or verified using the following experiments:

- the PRT was calibrated to the nominal resistance of $100.000\,\Omega$ (at 0.00 ± 0.01°C) in the laboratory prior to calibration of the monitoring thermistors
- the monitoring thermistors were calibrated against the PRT to within ± 0.1°C in the laboratory
- the performance of the monitoring thermistors was verified in the field by deploying thermistors together in pairs and examining temperature differences between each pair
- the performance of the monitoring thermistors was verified against the PRT in the laboratory, at the conclusion of the monitoring period.

Thermistors T1 to T16 were calibrated in February 2000 and then deployed at sites OW1, EV1 and SV1 between May 2000 and November 2001. Thermistors T21 to T28 were calibrated in December 2000 and then deployed until November 2001 in various locations, including sites OW1, EV1 and SV1.

E.2 Calibration Methodology and Materials

E.2.1 Calibration of Platinum Resistance Thermometer

The PRT was calibrated prior to the calibration or verification of each set of monitoring thermistors. The Leeds and Northrup model 8932 Platinum Resistance Thermometer (PRT) was connected to a Leeds and Northrup model 8078 portable precision temperature bridge and the ice point set value on the temperature bridge was adjusted, to ensure the nominal resistance of the PRT of 100.000 Ω at the ice point.

The results of the PRT calibration experiments are tabulated in Section E.3.1.

E.2.2 Calibration of Monitoring Thermistors

The thermistors were calibrated against the PRT over a range of temperatures, using a covered 26 L insulated container (esky). The container was initially filled with ice and tap water, and hot water was added periodically to create small temperature steps. The water temperature increased by approximately 1.0 °C at each temperature step from 3 °C to 39 °C. The system was allowed to stabilise at each temperature step.

The resistances of all thermistors were logged simultaneously at 5 s intervals for a period of 120 s at each temperature step. The mean resistance was calculated from the 5 s measurements at each temperature step. A least squares regression was used to construct a 6 th order polynomial to fit these mean thermistor resistances to the corresponding PRT temperatures over the calibration range. The form of the polynomial is given below:

$$T_w = C_0 + C_1 \cdot {R_T}^1 + C_2 \cdot {R_T}^2 + C_3 \cdot {R_T}^3 + C_4 \cdot {R_T}^4 + C_5 \cdot {R_T}^5 + C_6 \cdot {R_T}^6$$

where	T_w	=	water temperature (°C)
	R_T	=	mean thermistor resistance (Ω)
	$C_0 \ldots C_6$	=	polynomial coefficients.

The results of the thermistor calibration experiments for thermistors T1 to T16 and T21 to T28 are given in Section E.3.2.

E.2.3 Field Verification of Monitoring Thermistors

Field verification experiments were conducted periodically to monitor the performance of the primary monitoring thermistors T1 to T16, using thermistors T21 to T28. The additional thermistors were deployed immediately adjacent to the primary thermistors at sites OW1, EV1 and SV1, to form thermistor pairs. Temperatures were logged simultaneously and a temperature difference was calculated for each hourly measurement for each thermistor pair. The proportion of each monitoring period where the temperature difference exceeded the calibration error of $\pm 0.1°C$ was then determined.

The results of the field verification experiments are presented in Section E.3.3.

E.2.4 Laboratory Verification of Monitoring Thermistors

The monitoring thermistors were also verified in the laboratory soon after they were removed from the field. Verification of the thermistors involved comparing the temperatures recorded by the monitoring thermistors with the temperatures recorded by the PRT. The verification experiment was conducted in December 2001 and followed a procedure similar to that outlined in Sections E.2.1 and E.2.2, over a reduced number of three temperature steps. The insulated container was filled with tap water to give the first verification temperature of 19.09°C, while the second temperature of 11.68°C was achieved using chilled water. The third temperature of 35.47°C was obtained using water heated in an electric kettle.

The results of the laboratory verification experiment are given in Section E.3.4.

E.3 Calibration Results and Comments

E.3.1 Calibration of Platinum Resistance Thermometer

The results of the PRT calibration experiments conducted on 23 February 2000, 21 December 2000 and 19 December 2001 are summarised in Tables E.1, E.2, and E.3, respectively. The results show a good degree of stability once the sensor had initially stabilised.

Time	Elapsed Time (min)	PRT Resistance (Ω)	Ice Point Set Value		Temperature (°C)
			Before Adjustment	After Adjustment	
15:12	17	100.001	510	512	0.003
15:30	35	100.000	512	513	0.000
15:59	64	100.000	513	513	0.000

Table E.1: Ice point set value adjustment during calibration of the platinum resistance thermometer, 23 February 2000.

Time	Elapsed Time (min)	PRT Resistance (Ω)	Ice Point Set Value		Temperature (°C)
			Before Adjustment	After Adjustment	
09:30	15	100.001	513	512	0.000
09:51	36	100.001	512	512	0.000
10:21	66	100.000	512	512	0.000
11:00	105	100.000	512	512	0.000

Table E.2: Ice point set value adjustment during calibration of the platinum resistance thermometer, 21 December 2000.

Time	Elapsed Time (min)	PRT Resistance (Ω)	Ice Point Set Value		Temperature (°C)
			Before Adjustment	After Adjustment	
08:33	18	99.997	520	512	-0.008
08:49	34	100.000	512	512	0.000
10:21	126	100.000	513	513	0.000

Table E.3: Ice point set value adjustment during calibration of the platinum resistance thermometer, 19 December 2001.

E.3.2 Calibration of Thermistors Prior to Deployment

Thermistors T1 to T16 were calibrated on 23 February 2000 over 28 temperature steps at the temperatures shown in Figure E.1. Table E.4 shows the polynomial calibration coefficients derived for each thermistor. The variation in the coefficients between the individual thermistors is noted. This variation is primarily attributable to differences in the lengths of thermistor cables, but also to small differences which would have occurred during the manufacturing process. Resistances logged in the field by thermistors T1 to T16 were converted to temperatures using these polynomial coefficients.

Thermistors T21 to T28 were calibrated on 21 December 2000 over 28 temperature steps at the temperatures shown in Figure E.1. The derived polynomial calibration coefficients are given in Table E.5. Comparison with Table E.4 reveals that the coefficients for thermistors T21 to T28 are generally somewhat larger than the coefficients for thermistors T1 to T16. This is believed to reflect the different casing structure of the two thermistor types, the shorter length of cable connected to thermistors T21 to T28 and minor differences between the data loggers and the wiring configuration at the logger-thermistor interface.

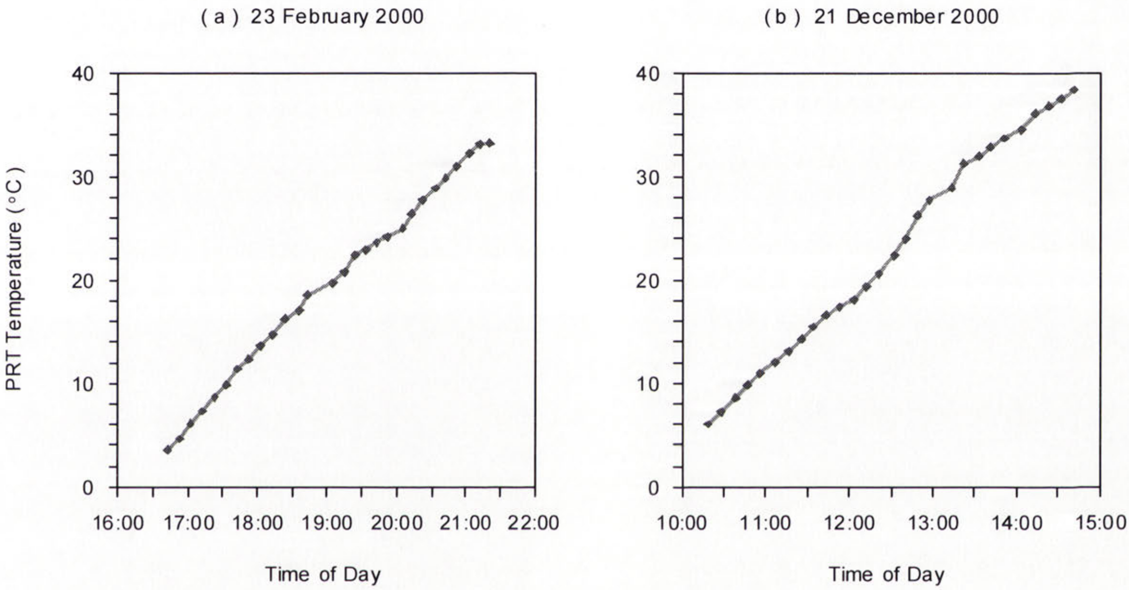

Figure E.1: Temperature ranges for calibration of the monitoring thermistors:

(a) calibration of thermistors T1 to T16 on 23 February 2000

(b) calibration of thermistors T21 to T28 on 21 December 2000.

Thermistor Number	Polynomial Coefficients						
	C0	C1	C2	C3	C4	C5	C6
T1	74.244	-3.20 E-02	3.14 E-06	2.05 E-09	-8.42 E-13	1.24 E-16	-6.63 E-21
T2	73.094	-2.62 E-02	1.24 E-06	1.79 E-09	-5.75 E-13	7.21 E-17	-3.33 E-21
T3	75.678	-2.85 E-02	3.52 E-06	6.68 E-10	-2.99 E-13	3.85 E-17	-1.74 E-21
T4	79.645	-3.96 E-02	9.90 E-06	-1.09 E-09	-5.81 E-14	2.47 E-17	-1.60 E-21
T5	78.085	-4.08 E-02	9.55 E-06	-2.99 E-10	-3.86 E-13	7.98 E-17	-4.97 E-21
T6	78.138	-3.70 E-02	7.84 E-06	-2.52 E-10	-2.46 E-13	4.65 E-17	-2.61 E-21
T7	77.853	-4.11 E-02	9.71 E-06	-3.61 E-10	-3.70 E-13	7.75 E-17	-4.84 E-21
T8	77.727	-3.76 E-02	7.66 E-06	1.10 E-10	-3.85 E-13	6.82 E-17	-3.87 E-21
T9	79.054	-3.97 E-02	1.00 E-05	-1.12 E-09	-5.97 E-14	2.55 E-17	-1.67 E-21
T10	77.423	-4.10 E-02	9.70 E-06	-2.92 E-10	-4.08 E-13	8.51 E-17	-5.35 E-21
T11	80.059	-3.93 E-02	1.02 E-05	-1.37 E-09	3.28 E-14	1.15 E-17	-8.87 E-22
T12	77.178	-3.45 E-02	6.44 E-06	1.18 E-10	-2.88 E-13	4.69 E-17	-2.45 E-21
T13	81.091	-4.14 E-02	1.12 E-05	-1.61 E-09	5.52 E-14	1.18 E-17	-1.00 E-21
T14	80.063	-3.99 E-02	1.03 E-05	-1.28 E-09	-1.10 E-14	1.87 E-17	-1.30 E-21
T15	79.838	-3.81 E-02	9.50 E-06	-1.20 E-09	1.42 E-14	1.16 E-17	-8.09 E-22
T16	78.520	-4.22 E-02	1.10 E-05	-1.10 E-09	-1.57 E-13	4.70 E-17	-3.12 E-21

Table E.4: Polynomial calibration coefficients for thermistors T1 to T16.

Thermistor Number	Polynomial Coefficients						
	C0	C1	C2	C3	C4	C5	C6
T21	91.791	-5.81 E-02	2.28 E-05	-5.87 E-09	9.08 E-13	-7.69 E-17	2.73 E-21
T22	90.681	-6.15 E-02	2.69 E-05	-7.77 E-09	1.37 E-12	-1.34 E-16	5.58 E-21
T23	89.746	-5.73 E-02	2.29 E-05	-6.02 E-09	9.54 E-13	-8.29 E-17	3.03 E-21
T24	88.446	-6.09 E-02	2.57 E-05	-7.00 E-09	1.13 E-12	-9.71 E-17	3.38 E-21
T25	90.691	-5.39 E-02	1.96 E-05	-4.63 E-09	6.52 E-13	-4.96 E-17	1.55 E-21
T26	90.017	-5.84 E-02	2.37 E-05	-6.30 E-09	1.01 E-12	-8.91 E-17	3.30 E-21
T27	88.981	-6.99 E-02	3.40 E-05	-1.08 E-08	2.05 E-12	-2.12 E-16	9.08 E-21
T28	89.021	-6.86 E-02	3.28 E-05	-1.02 E-08	1.91 E-12	-1.95 E-16	8.23 E-21

Table E.5: Polynomial calibration coefficients for thermistors T21 to T28.

E.3.3 Field Verification of Monitoring Thermistors

E.3.3.1 Site OW1: Thermistors T3 to T8.

The results of the field verification experiments on the primary thermistors at Site OW1 are shown in Table E.6.

From these results it can be concluded that thermistors T3 to T7 were performing well at all times. With the exception of the thermistor pairs incorporating T21, temperature differences were within the calibration error of $\pm 0.1°C$ more than 95% of the time during both verification experiments. On this basis, the performance of thermistors T3 to T7 and T23 to T28 was considered acceptable.

The thermistor pair of T8 and T21 deployed 50 mm below the water surface was within the calibration error of $\pm 0.1°C$ for 91% of the summer verification period, and 87% of the spring verification period. As discussed in Section E.3.4, laboratory verification experiments conducted at the conclusion of the field monitoring period found thermistor T21 to be operating outside the calibration range. It was therefore not possible to draw conclusions about the performance of thermistor T8 from the field verification experiments.

	17 January to 2 February 2001		6 to 20 September 2001	
Thermistor Location, Open Water	Thermistor Numbers	Proportion $> \pm 0.1°C$ (%)	Thermistor Numbers	Proportion $> \pm 0.1°C$ (%)
50 mm below surface	T8 & T21	9	T8 & T21	13
400 mm below surface	T7 & T23	3	no data	-
750 mm below surface	T5 & T24	1	T5 & T25	0
750 mm above bed	T6 & T26	4	T6 & T26	2
400 mm above bed	T3 & T27	0	T3 & T27	1
50 mm above bed	T4 & T28	1	T4 & T28	0

Table E.6: Proportion of hourly measurements where the temperature difference exceeded $\pm 0.1°C$ during field verification of thermistors T3 to T8 at Site OW1.

E.3.3.2 Site EV1: Thermistors T1, T2, and T9 to T14.

The results of the field verification experiments on the primary thermistors at Site EV1 are shown in Table E.7.

From these results, it can be concluded that thermistors T2 (50 mm above the bed), T12 (750 mm below the surface) and T14 (400 mm below the surface) were performing well at all times. Thermistors T9 (50 mm below the surface) and T11 (750 mm above the bed) were performing adequately, with the temperature difference within the calibration error most of the time.

The temperature difference between thermistors T10 and T21, deployed 50 mm above the water surface to measure the canopy air temperature, was outside of the calibration range nearly 80% of the time during the January 2001 experiment. However, the thermistors were calibrated in water with significantly different fluid properties to the canopy air space, so some discrepancy was expected on this basis. Furthermore, as discussed in Section E.3.4, the laboratory verification experiments found thermistor T21 to be outside the calibration error at the conclusion of the field monitoring period. The same was true of thermistor T1, deployed 400 mm above the bed.

Thermistor T13 was deployed 200 mm below surface, and the temperature difference exceeded the calibration error 16% of the time when paired with T23 in January 2001, but only 6% of the time when paired with T22 in spring 2001. Thermistor T23 was damaged and rendered inoperable during a storm in August 2001, so it was difficult to draw further conclusions on the performance of thermistor T13 from the results of field verification against thermistor T23.

E.3.3.3 Site SV1: Thermistors T15 and T16.

The results of the field verification experiment on the primary thermistors at Site SV1 are shown in Table E.8. The temperature differences between pairs T16 and T23, and T15 and T26 were always within the calibration error of $\pm 0.1°C$, indicating satisfactory performance.

E.3.4 Laboratory Verification of Monitoring Thermistors

At the conclusion of the field monitoring experiments, the thermistors were returned to the laboratory and their performance was verified against the platinum resistance thermometer (PRT). The temperatures given by the thermistors were compared against the

	7 to 16 January 2001		20 September to 17 October 2001	
Thermistor Location, Emergent Vegetation	Thermistor Numbers	Proportion > ± 0.1°C (%)	Thermistor Numbers	Proportion > ± 0.1°C (%)
50 mm above surface	T10 & T21	78	–	–
50 mm below surface	T9 & T22	5	T9 & T21	14
200 mm below surface	T13 & T23	16	T13 & T22	6
400 mm below surface	T14 & T24	0	T14 & T24	0
750 mm below surface	T12 & T25	0	T12 & T25	0
750 mm above bed	T11 & T26	1	T11 & T26	4
400 mm above bed	T1 & T27	100	T1 & T27	100
50 mm above bed	T2 & T28	0	T2 & T28	0

Table E.7: Proportion of hourly measurements where the temperature difference exceeded ± 0.1°C during field verification of thermistors T1, T2, and T9 to T14 at Site EV1.

Thermistor Location, Submerged Vegetation	Thermistor Numbers	Proportion > ± 0.1°C (%)
400 mm below surface	T16 & T23	0
400 mm above bed	T15 & T26	0

Table E.8: Proportion of hourly measurements where the temperature difference exceeded ± 0.1°C during field verification of thermistors T15 and T16 at site SV1 between 28 December 2000 and 3 January 2001.

PRT temperature at three temperatures (11.68°C, 19.09°C, and 35.47°C). These were within the range encountered during the field monitoring experiments.

The temperatures given by the thermistors at the known PRT temperatures are listed in Table E.9. The temperature residuals shown in Table E.9 are only strictly accurate to the nearest 0.1°C, as the thermistors were only calibrated to within ± 0.1°C. However, the residuals have been reported here to the nearest 0.01°C to show the variation between the individual thermistors.

The results of the verification experiments indicated a high degree of stability over the monitoring period for most thermistors. Of the sixteen primary thermistors (T1 to T16)

	PRT Temperature					
	19.09 °C		11.68 °C		35.47 °C	
Thermistor Number	Mean T (°C)	Mean T - PRT (°C)	Mean T (°C)	Mean T - PRT (°C)	Mean T (°C)	Mean T - PRT (°C)
T1	19.4	[**0.35**]	12.1	[**0.40**]	35.6	[**0.17**]
T2	19.1	0.04	11.7	0.02	35.4	-0.04
T3	19.1	0.04	11.7	0.01	35.4	-0.03
T4	19.1	0.05	11.7	0.03	35.5	0.00
T5	19.1	0.02	11.6	-0.03	35.4	-0.03
T6	19.1	0.06	11.8	0.10	35.4	-0.02
T7	19.1	0.02	11.7	0.02	35.4	-0.03
T8	19.1	0.03	11.7	0.00	35.4	-0.03
T9	19.1	0.03	11.7	0.01	35.5	0.00
T10	19.2	0.10	11.7	0.07	35.5	0.06
T11	19.1	0.04	11.7	0.03	35.5	0.01
T12	19.1	0.03	11.7	0.00	35.4	-0.03
T13	19.1	0.04	11.7	0.01	35.5	0.00
T14	19.1	0.04	11.7	0.02	35.4	-0.03
T15	19.1	0.04	11.7	0.01	35.5	0.01
T16	19.1	0.03	11.7	0.00	35.4	-0.04
T21	19.6	[**0.48**]	12.1	[**0.43**]	36.3	[**0.33**]
T22	19.2	0.08	11.7	0.01	35.9	-0.02
T23	-	-	-	-	-	-
T24	19.2	[**0.11**]	11.7	0.05	36.0	0.03
T25	19.2	0.09	11.7	0.04	35.9	0.02
T26	19.2	0.08	11.7	0.03	35.9	0.02
T27	19.1	0.06	11.7	0.02	35.9	0.01
T28	19.2	0.07	11.7	0.02	35.9	0.01

Notes to Table:

1. Mean T denotes the mean thermistor temperature, calculated from the mean resistance using the 6 th order polynomial calibration coefficients given in Tables E.4 and E.5. The mean resistance was determined from resistances logged every 5 s over a period of 120 s at each temperature.
2. Mean T - PRT denotes the error between the mean thermistor temperature and the temperature given by the platinum resistance thermometer.
3. Error values highlighted in [**bold**] and enclosed between square brackets indicate errors exceeding the thermistor calibration error of ± 0.1°C.
4. Thermistor T23 was damaged during a storm in August 2001 and not used thereafter.

Table E.9: Results of laboratory verification of thermistors T1 to T16 and T21 to T28 on 21 December 2001.

originally calibrated in February 2000, only T1 failed to give water temperatures within $\pm 0.1°C$ of the PRT temperature. Thermistor T1 had been deployed 400 mm above the bed in the emergent vegetation zone of the wetland (Site EV1). It is not possible to determine exactly why or when the drift occurred, or whether it occurred suddenly or gradually. However, it had been suspected for some time that T1 was reading slightly warmer than it should have, and field verification experiments also suggested this (see Table E.7).

The third verification temperature of 35.47°C was slightly outside the original calibration range (3.6 to 33.2°C). This may explain why many of the thermistors gave temperatures slightly lower than the PRT temperature, while they were generally slightly warmer than the PRT at the lower verification temperatures.

Of the secondary thermistors (T21 to T28) deployed in December 2000, T21 predicted somewhat warmer temperatures than the PRT at all three temperatures during the verification experiment, and T24 read slightly warmer than the PRT at 19.09°C. The temperatures predicted by thermistors T22 to T28 were otherwise within the calibration error of ± 0.1°C. The field verification experiments had previously suggested an error with thermistor T21 (Section E.3.3). Thermistor T23 was damaged during a storm in August 2001 when it broke free of its mooring, and its performance could not be verified in the laboratory.

E.4 Summary

In summary, the performance of most thermistors was demonstrated to be satisfactory over the monitoring period, with only two significant exceptions:

- temperatures measured by thermistor T1 were considered with caution, and assumed to be up to 0.4°C too high
- temperatures measured by thermistor T21 were also considered with caution, and assumed to be up to 0.5°C too high.

Appendix F

THERMISTOR DATA

F.1 Adequacy of Thermistor Sampling Regime

As discussed in Section 5.5.2.2, power requirements meant that thermistor data could not be collected more frequently than once every hour using the available equipment without making additional visits to site to change batteries. Travelling time rendered this an undesirable option. Field trials were conducted at Hopwoods Lagoon in July 2000 to examine the adequacy of the one hour sampling regime in describing time series variation in water temperatures at various depths. Measurements were made every 15 min between 10:45 on 26 July and 14:30 on 27 July at Site OW1 in the open water zone, corresponding with experiments conducted by Natalie Marshall. The results are shown in Figure F.1(a).

Water temperature data collected by Natalie Marshall at 10 min intervals between 13:00 (AEST) on 27 November 2000 and 13:00 on 29 November is shown in Figure F.1(b). These temperatures were measured near the centre of Hopwoods Lagoon using an array of three independently calibrated Yeo-Kal model 611 Intelligent Water Quality Analysers, as described by Marshall (in prep.).

Hourly temperature data were extracted from the two data sets and hourly trends are shown by the dashed lines in Figure F.1. To assess the adequacy of the hourly data in representing the 10 or 15 min water temperature data, temperatures were interpolated for the shorter intervals from the hourly data. Residuals were calculated at the 10 or 15 min intervals for each thermistor, as follows:

$$\Delta T_{\text{res}} = T_{\text{meas.}} - T_{\text{int.}} \tag{F.1}$$

where $T_{\text{meas.}}$ = measured 10 or 15 min temperature (°C)

$T_{\text{int.}}$ = 10 or 15 min temperature interpolated from hourly data (°C).

The minimum and maximum values of the residuals at each of the thermistors are shown in Table F.1. These indicate that the one hour water temperatures were representative of the 15 min measured temperatures to within ± 0.5°C over the July monitoring period, and to within ± 0.4°C over the November monitoring period. The residuals are small enough not to obscure measured diurnal temperature ranges in the open water of around 1 to 3°C in winter and 3 to 8°C in summer (Figure F.2).

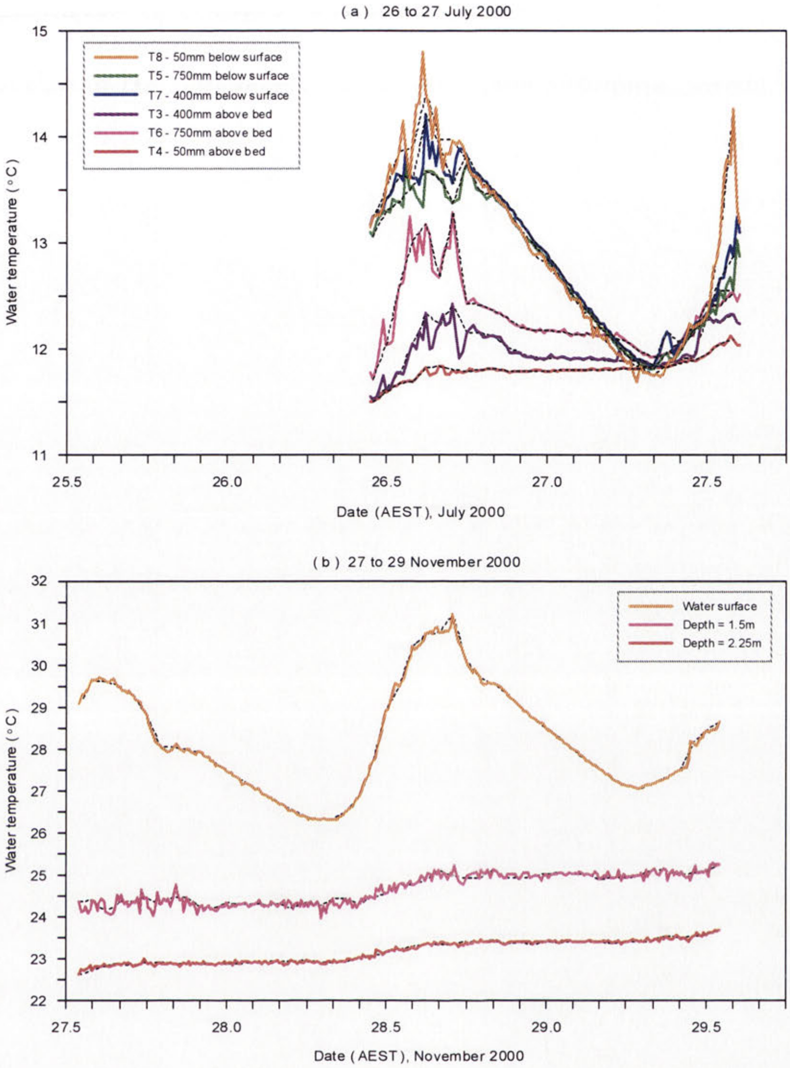

Figure F.1: Water temperature variation at Hopwoods Lagoon: (a) at Site OW1 from 26 to 27 July 2000, and (b) near the lagoon centre from 27 to 29 November 2000.

Monitoring Period	Monitoring Location	Thermistor Identification	Depth below Surface (mm)	Height above Bed (mm)	Temperature Residual	
					Min. (°C)	Max. (°C)
26 – 27 Jul 2000	Site OW1	T8	50	–	-0.29	0.51
		T7	400	–	-0.35	0.24
		T5	750	–	-0.31	0.27
		T6	–	750	-0.26	0.33
		T3	–	400	-0.37	0.14
		T4	–	50	-0.08	0.05
27 – 29 Nov 2000	centre	–	surface	–	-0.25	0.24
	of	–	1500	–	-0.36	0.31
	lagoon	–	2500	–	-0.10	0.13

Table F.1: Minimum and maximum values of the calculated temperature residuals.

F.2 Summary of Thermistor Monitoring Locations

F.2.1 Primary Thermistors, T1 to T16

Monitoring Location	Date and Time		Thermistor Identification	Depth below Surface (mm)	Thermistor Identification	Height above Bed (mm)
	from	to				
Site OW1	7 May 2000	25 Jul 2000	T8	50	-	-
			T7	400	-	-
			T5	750	-	-
			-	-	T6	750
			-	-	T3	400
			-	-	T4	50
Site EV1	7 May 2000	25 Jul 2000	T15	-50 (air)	-	-
			T16	50	-	-
			T13	200	-	-
			T14	450	-	-
			T12	700	-	-
			-	-	T11	500
			-	-	T1	250
			-	-	T2	50
Site SV1	7 May 2000	25 Jul 2000	T10	250	-	-
			-	-	T9	250
Site OW1	25 Jul 2000	2 Dec 2001	T8	50	-	-
			T7	400	-	-
			T5	750	-	-
			-	-	T6	750
			-	-	T3	400
			-	-	T4	50
Site EV1	25 Jul 2000	2 Dec 2001	T10	-50 (air)	-	-
			T9	50	-	-
			T13	200	-	-
			T14	400	-	-
			T12	750	-	-
			-	-	T11	750
			-	-	T1	400
			-	-	T2	50
Site SV1	25 Jul 2000	2 Dec 2001	T16	400	-	-
			-	-	T15	400

Table F.2: Summary of thermistor monitoring locations for the primary thermistors, T1 to T16.

F.2.2 Additional Thermistors, T21 to T28

Monitoring Location	Date and Time from	Date and Time to	Thermistor Identification	Depth below Surface (mm)	Thermistor Identification	Height above Bed (mm)
Site SV1	28 Dec 2000	3 Jan 2001	T21	50	-	-
			T22	200	-	-
			T23	400	-	-
			T24	550	-	-
			T25	700	-	-
			-	-	T26	400
			-	-	T27	200
			-	-	T28	50
Site EV1	7 Jan 2001	16 Jan 2001	T21	-50 (air)	-	-
			T22	50	-	-
			T23	200	-	-
			T24	400	-	-
			T25	750	-	-
			-	-	T26	750
			-	-	T27	400
			-	-	T28	50
Site OW1	17 Jan 2001	2 Feb 2001	T21	50	-	-
			T22	200	-	-
			T23	400	-	-
			T24	750	-	-
			-	-	T25	1050
			-	-	T26	750
			-	-	T27	400
			-	-	T28	50
Site OW2	2 Feb 2001	14 Feb 2001	T21	50	-	-
			T22	200	-	-
			T23	400	-	-
			T24	730	-	-
			-	-	T25	750
			-	-	T26	400
			-	-	T27	200
			-	-	T28	50
Site EV2	14 Feb 2001	21 Feb 2001	T21	50	-	-
			T22	200	-	-
			T23	400	-	-
			T24	730	-	-
			-	-	T25	750
			-	-	T26	400
			-	-	T27	200
			-	-	T28	50
Site SV2	28 Feb 2001	18 Mar 2001	T21	50	-	-
			T22	200	-	-
			T23	400	-	-
			T24	730	-	-
			-	-	T25	750
			-	-	T26	400
			-	-	T27	200
			-	-	T28	50
Site EV3	22 Mar 2001	31 Mar 2001	T21	50	-	-
			T22	200	-	-
			T23	400	-	-
			T24	730	-	-
			-	-	T25	750
			-	-	T26	400
			-	-	T27	200
			-	-	T28	50

Table F.3: Summary of thermistor monitoring locations for the additional thermistors, T21 to T28.

Monitoring Location	Date and Time from	Date and Time to	Thermistor Identification	Depth below Surface (mm)	Thermistor Identification	Height above Bed (mm)
Lateral Transect: Site OW1 to Site EV1	1 Apr 2001	4 Jul 2001	T21	50	-	-
			T22	750	-	-
			T23	750	-	-
			T24	50	-	-
			T25	750	-	-
			T26	750	-	-
			T27	50	-	-
			T28	750	-	-
Lateral Transect: Site OW1 to Site EV1	4 Jul 2001	15 Aug 2001	-	-	T21	300
			T22	750	-	-
			T23	750	-	-
			-	-	T24	300
			T25	750	-	-
			T26	750	-	-
			-	-	T27	300
			T28	750	-	-
Site OW1	6 Sep 2001	20 Sep 2001	T21	50	-	-
			T22	200	-	-
			T23	400	-	-
			T24	750	-	-
			-	-	T25	1250
			-	-	T26	750
			-	-	T27	400
			-	-	T28	50
Site EV1	20 Sep 2001	17 Oct 2001	T21	50	-	-
			T22	200	-	-
			T23	200	-	-
			T24	400	-	-
			T25	750	-	-
			-	-	T26	750
			-	-	T27	400
			-	-	T28	50
Site OW3	17 Oct 2001	22 Oct 2001	T21	50	-	-
			T22	200	-	-
			T23	-	-	-
			T24	400	-	-
			T25	750	-	-
			-	-	T26	50
			-	-	T27	400
			-	-	T28	750
Site EV4	22 Oct 2001	30 Oct 2001	T21	50	-	-
			T22	200	-	-
			T23	-	-	-
			T24	400	-	-
			T25	750	-	-
			-	-	T26	50
			-	-	T27	400
			-	-	T28	750
Site OW4	30 Oct 2001	12 Nov 2001	T21	50	-	-
			T22	200	-	-
			T23	-	-	-
			T24	400	-	-
			T25	750	-	-
			-	-	T26	50
			-	-	T27	1500
			-	-	T28	750

Table F.3 (continued): Summary of thermistor monitoring locations for the additional thermistors, T21 to T28.

F.3 Record of Thermistor Data Losses

Data loss from:		Data loss to:		Comments:
3 Jun 2000	22:00	9 Jun	14:00	battery problem
9 Jun 2000	14:00	26 Jun	12:00	no data for T14 (EV1 at 450mm depth) - moved to check T13 (EV1 at 200 mm depth)
20 Jun 2000	12:00	3 Jul	11:00	no data for T15 (air temperature) - moved to check T16 (EV1 at 50 mm depth)
26 Jul 2000	10:45	3 Aug	15:00	problem with T12 (EV1 at 750 mm depth)
12 Aug 2000	07:00	26 Aug	12:00	T10 (EV1 air temperature) partially submerged
28 Aug 2000	14:00	3 Sep	12:00	T10 (EV1 air temperature) partially submerged
19 Sep 2000	15:00	4 Oct	12:00	problem with T12 (EV1 at 750 mm depth)
27 Sep 2000	11:00	4 Oct	12:00	battery problem
18 Oct 2000	12:00	29 Oct	11:00	logger error
15 Nov 2000	09:00	19 Nov	15:00	battery problem
27 Nov 2000	00:00	28 Nov	16:00	battery problem
9 Dec 2000	05:00	19 Dec	10:00	suspected memory card problem
9 Mar 2001	09:00	22 Mar	13:00	T10 (EV1 air temperature) partially submerged
27 Apr 2001	14:00	1 May	16:00	battery problem
20 Jul 2001	13:00	29 Jul	14:00	battery problem
30 Jul 2001	11:00	4 Aug	13:00	suspected memory card problem
4 Aug 2001	14:00	15 Aug	13:00	failure of memory card module
3 Sep 2001	06:00	6 Sep	18:00	suspected battery problem
17 Oct 2001	11:00	22 Oct	17:00	memory full
26 Oct 2001	11:00	30 Oct	11:00	no data for T11 (EV1 at 750 mm above bed) or T12 (EV1 at 750 mm depth) - cable connection problem

Table F.4: Record of periods of data loss from the thermistors, and the reasons for these losses.

F.4 Summary of Time-Series Thermistor Data

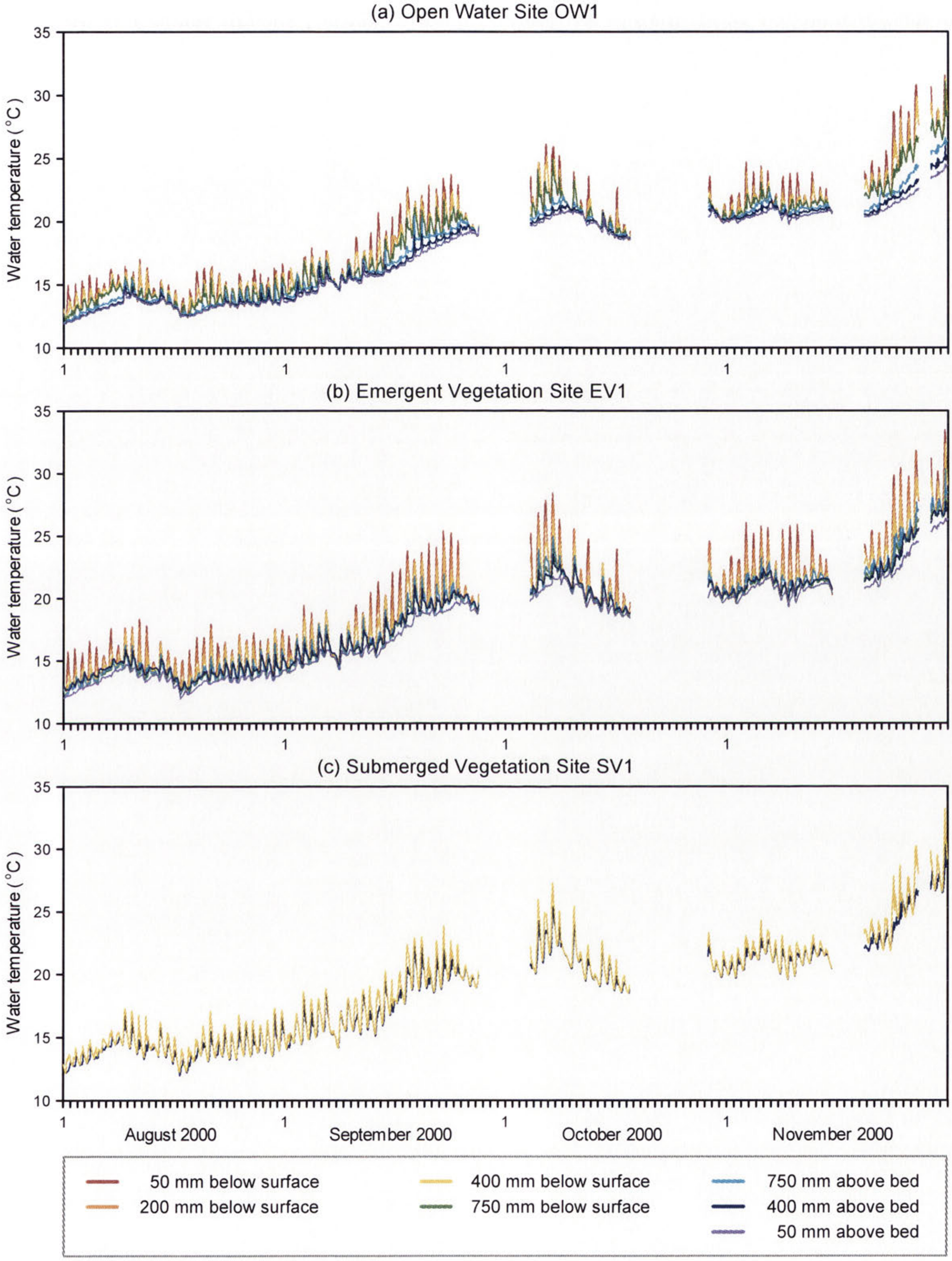

Figure F.2: Water temperatures at (a) Site OW1, (b) Site EV1 and (c) Site SV1.

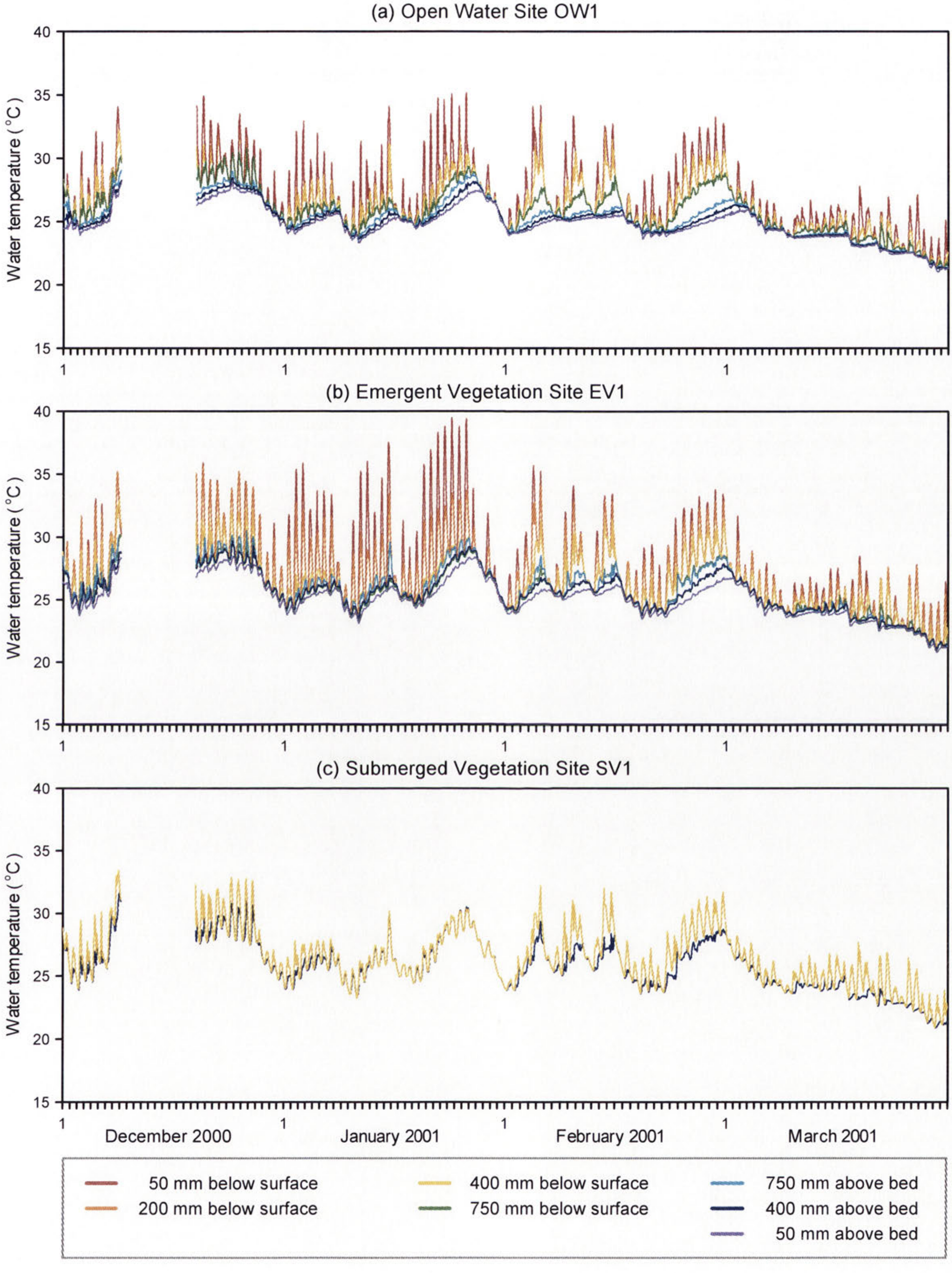

Figure F.2 (continued):

Water temperatures at (a) Site OW1, (b) Site EV1 and (c) Site SV1.

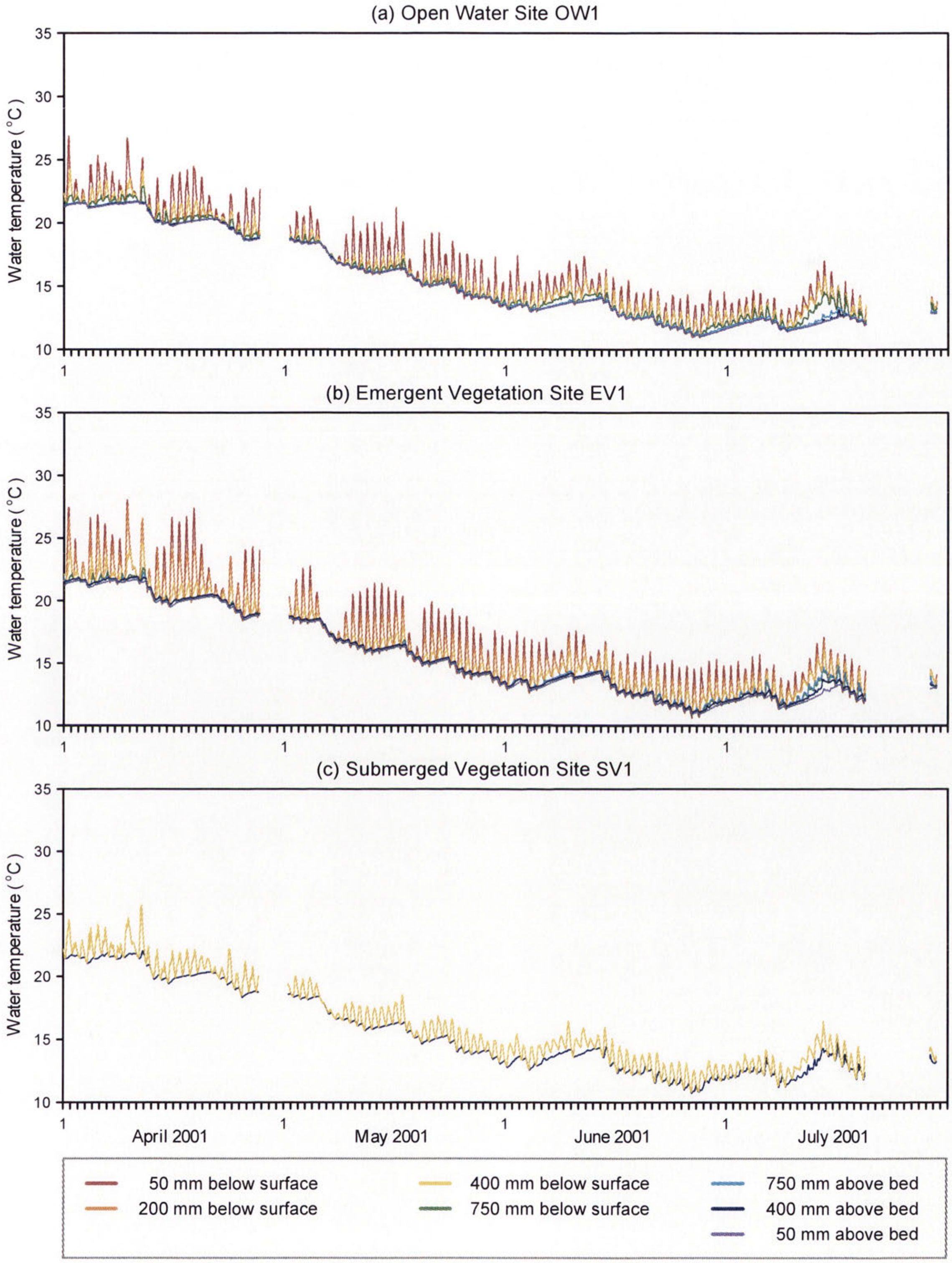

Figure F.2 (continued):

Water temperatures at (a) Site OW1, (b) Site EV1 and (c) Site SV1.

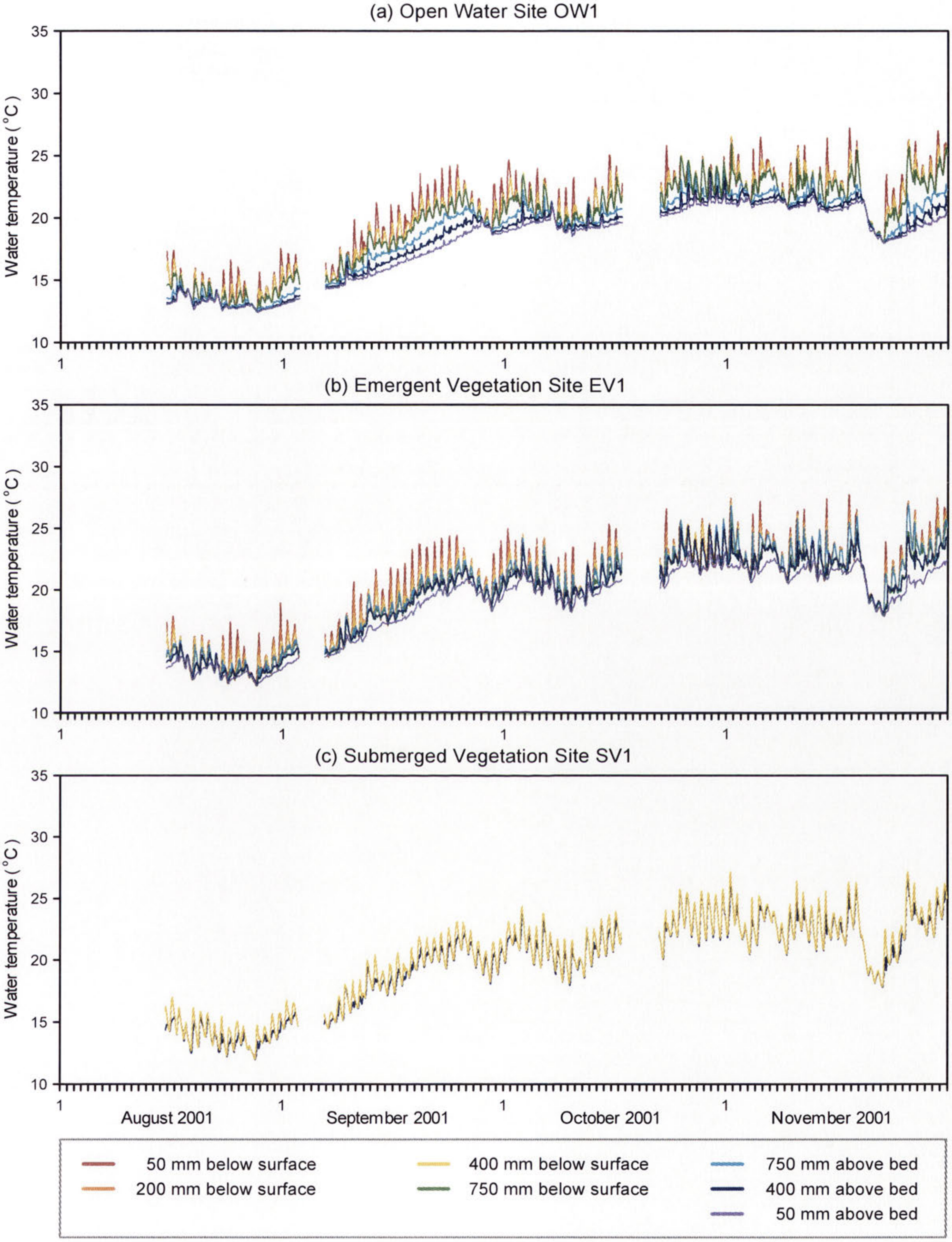

Figure F.2 (continued):

Water temperatures at (a) Site OW1, (b) Site EV1 and (c) Site SV1.

Appendix G

ADDITIONAL FIELD RESULTS

G.1 Horizontal Temperature Transect

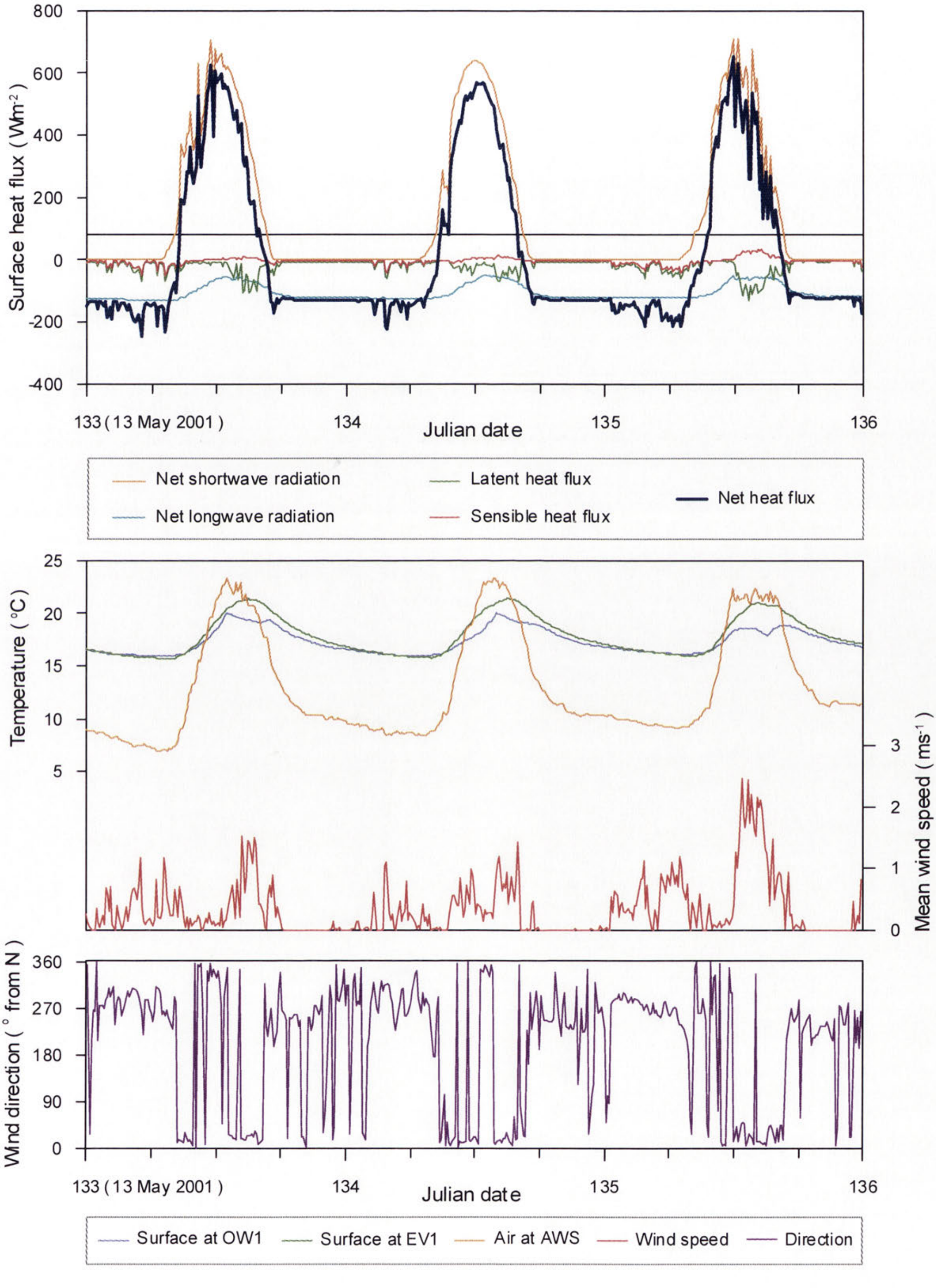

Figure G.1: Surface heat fluxes at Hopwoods Lagoon between 13 and 15 May 2001.

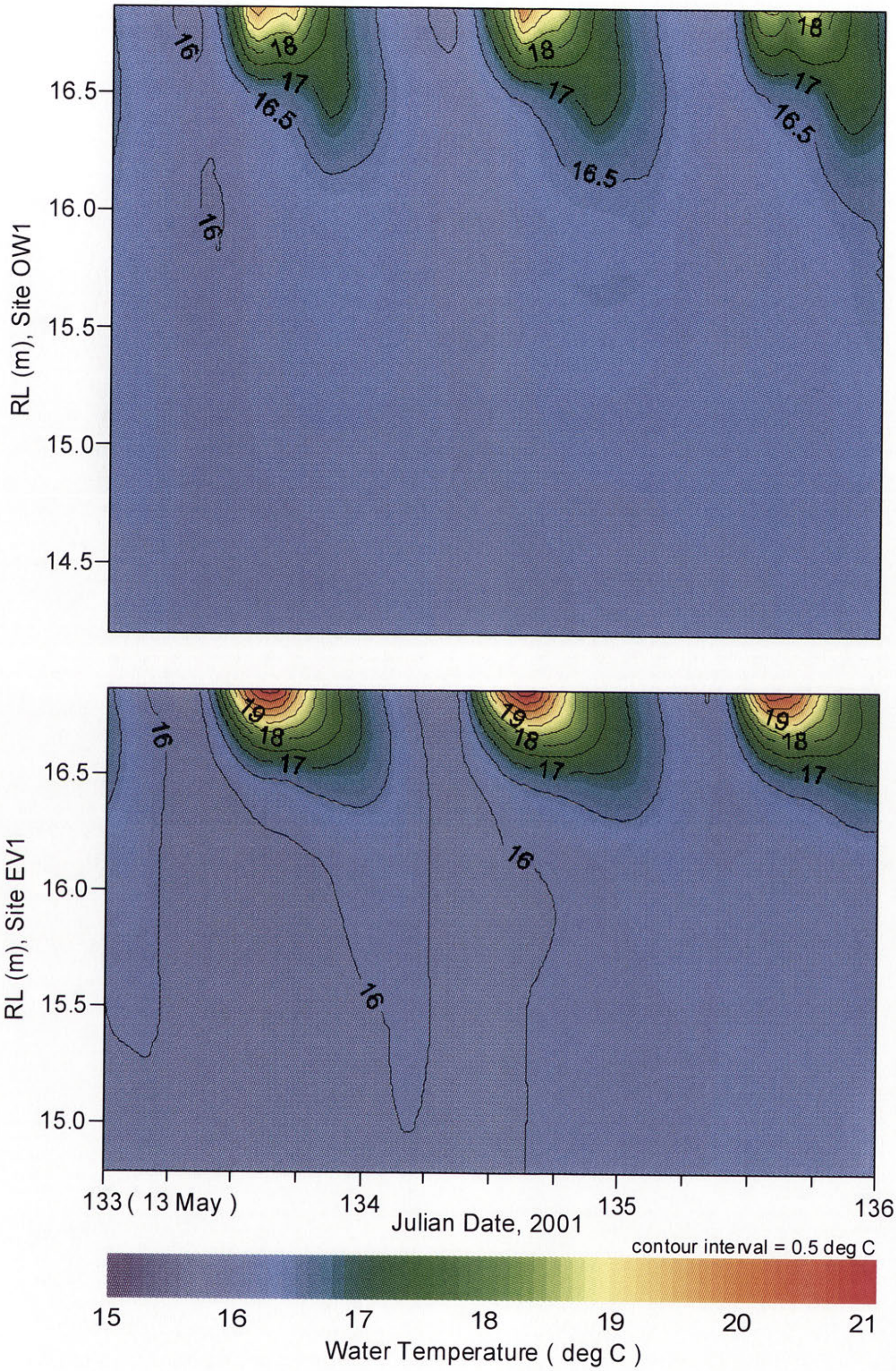

Figure G.2: Water temperatures at Sites OW1 and EV1 between 13 and 15 May 2001. Water surface elevation at RL 16.9 m.

G.2 Effects of Depth Differences

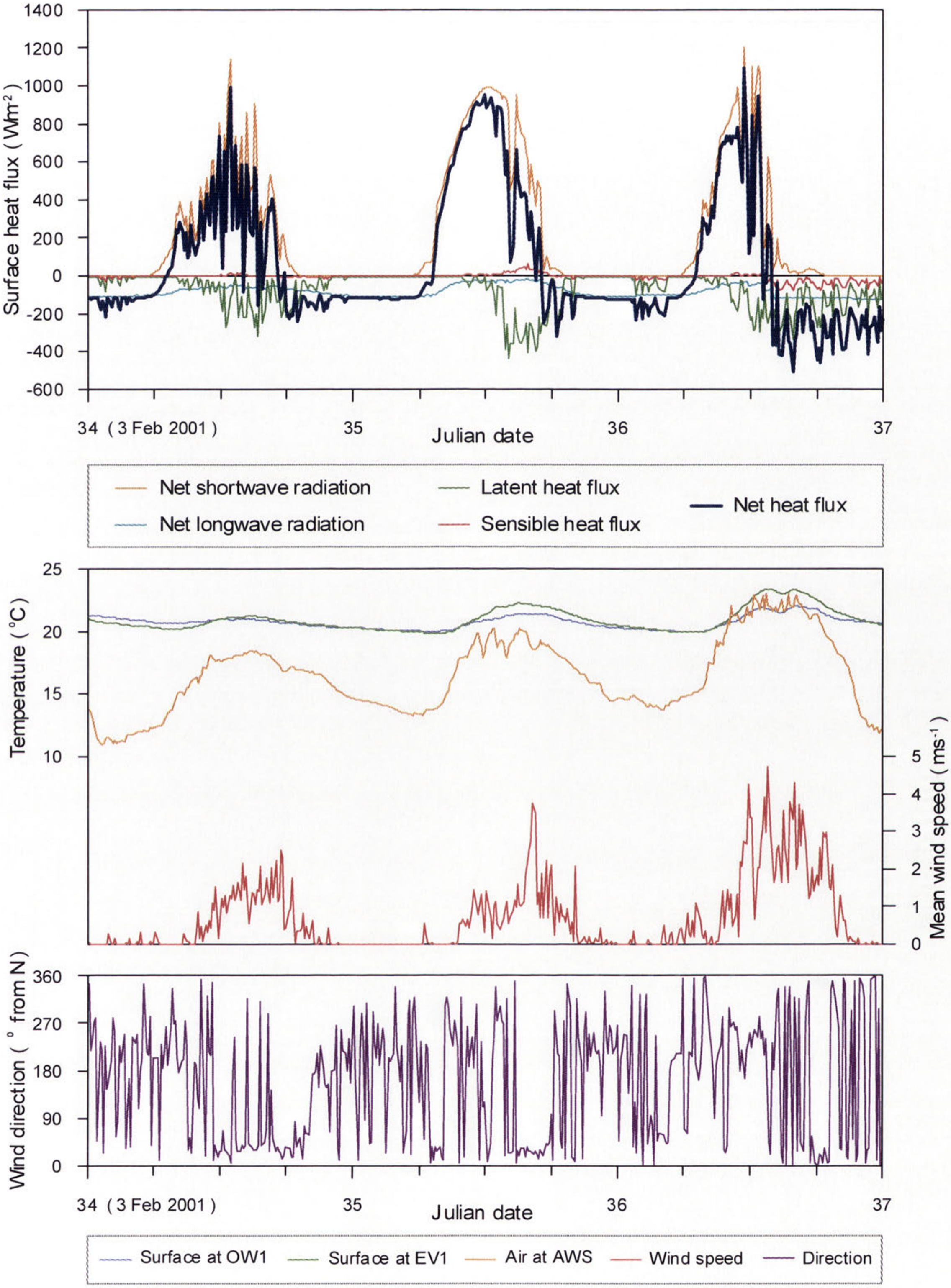

Figure G.3: Surface heat fluxes at Hopwoods Lagoon between 3 and 5 February 2001.

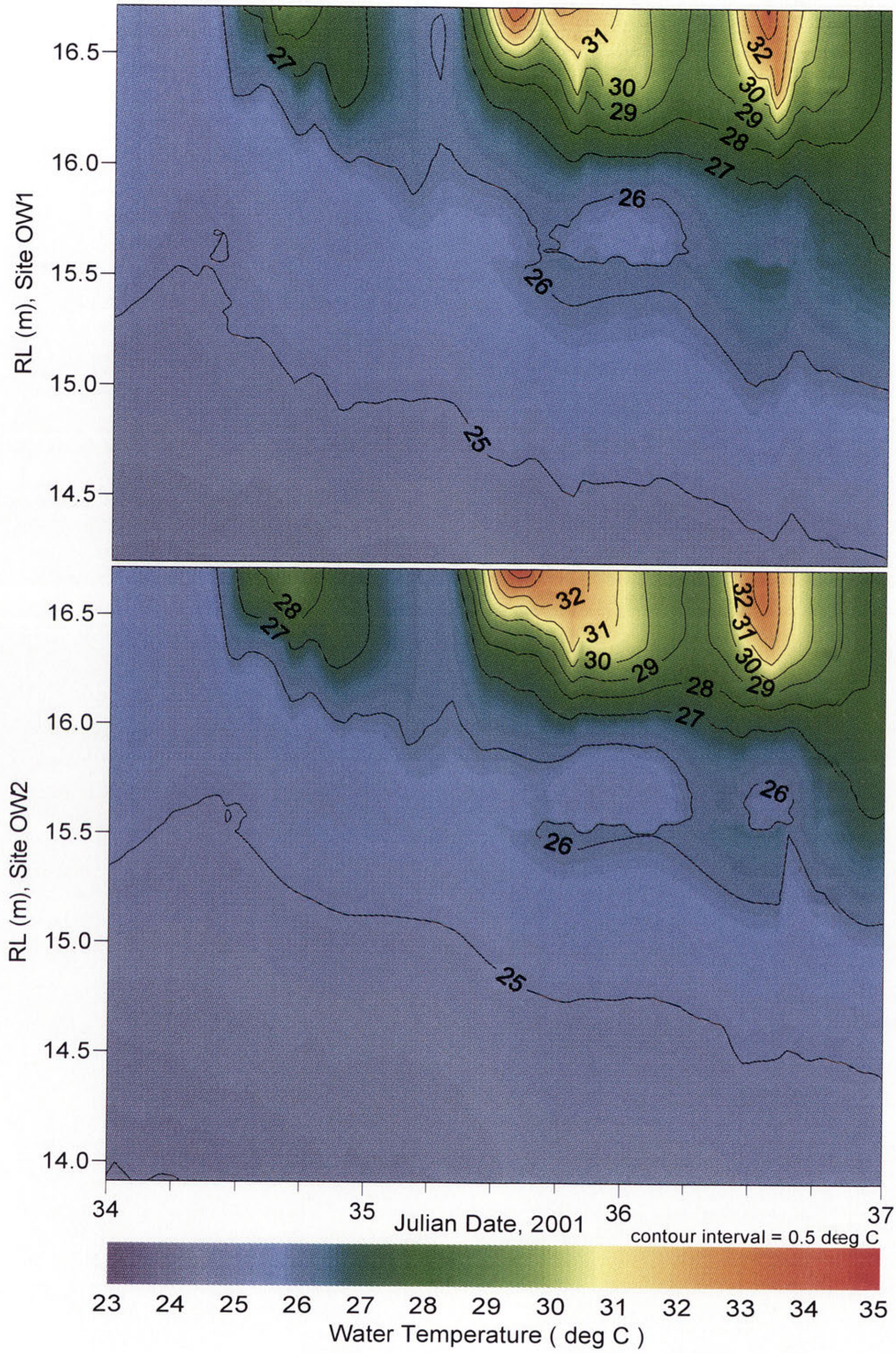

Figure G.4: Water temperatures at Sites OW1 and OW2 between 3 and 5 February 2001. Water surface elevation at RL 16.76 m.

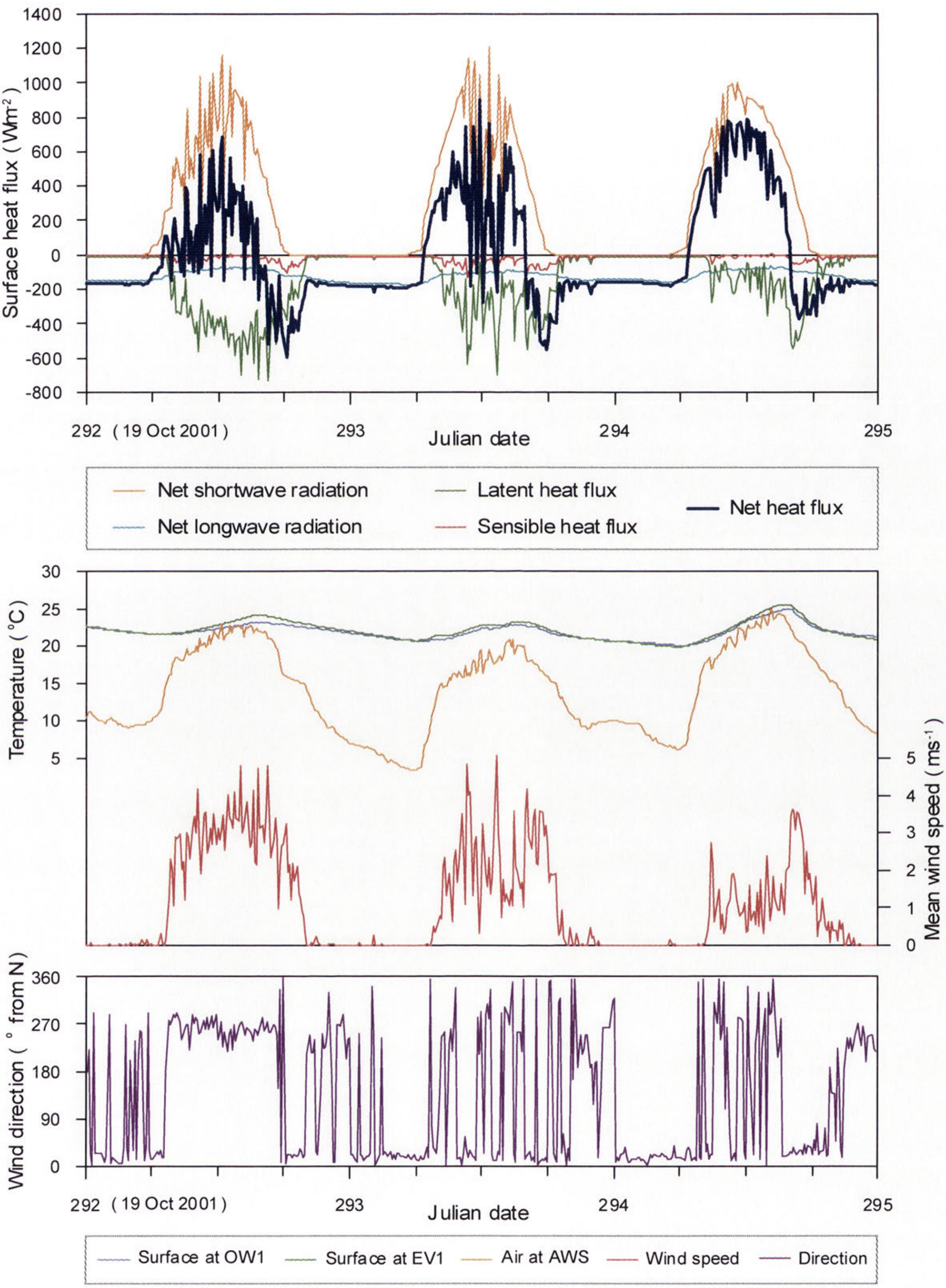

Figure G.5: Surface heat fluxes at Hopwoods Lagoon between 19 and 21 October 2001.

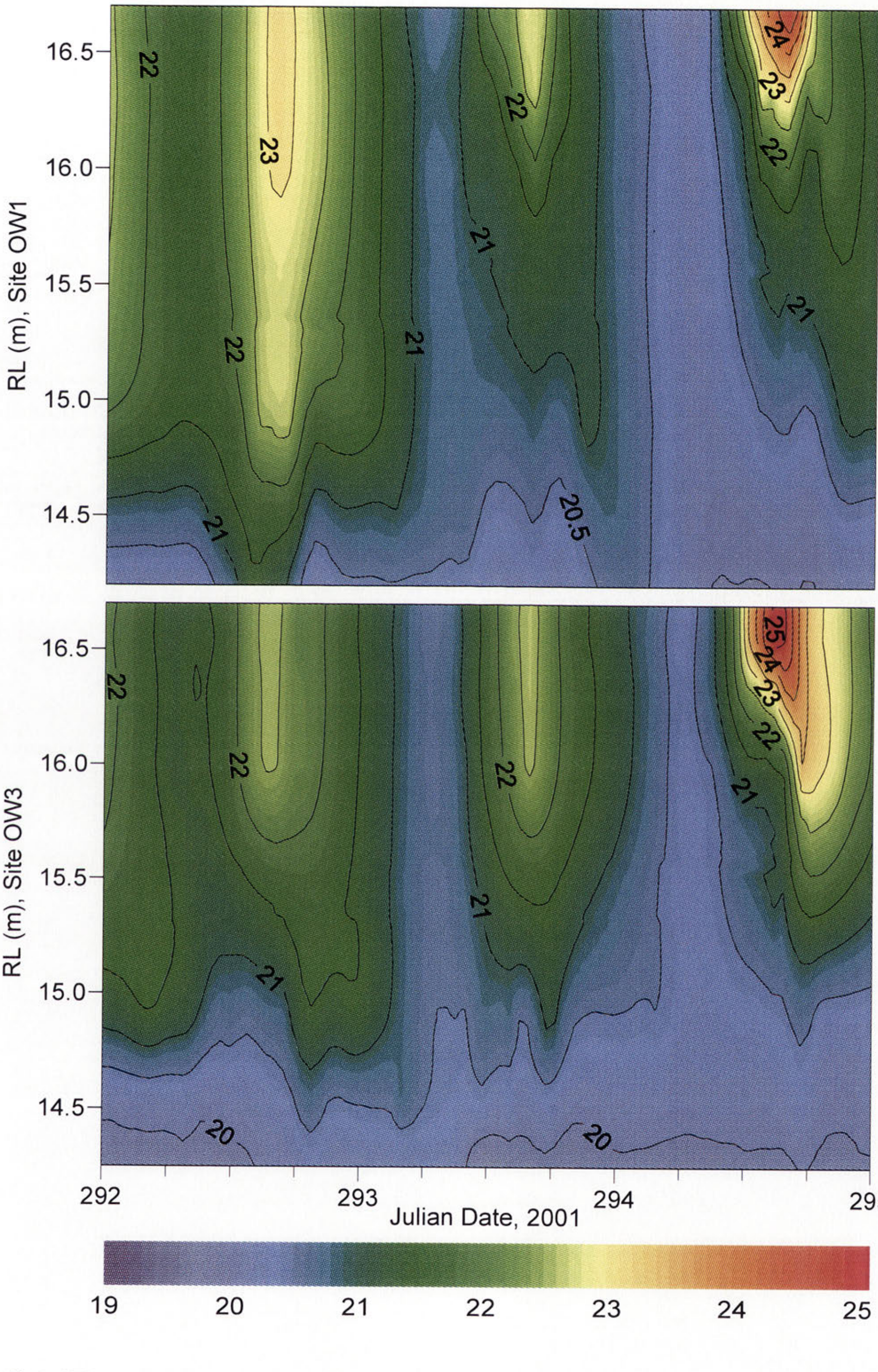

Figure G.6: Water temperatures at Sites OW1 and OW3 between 19 and 21 October 2001. Water surface elevation at RL 16.75 m.

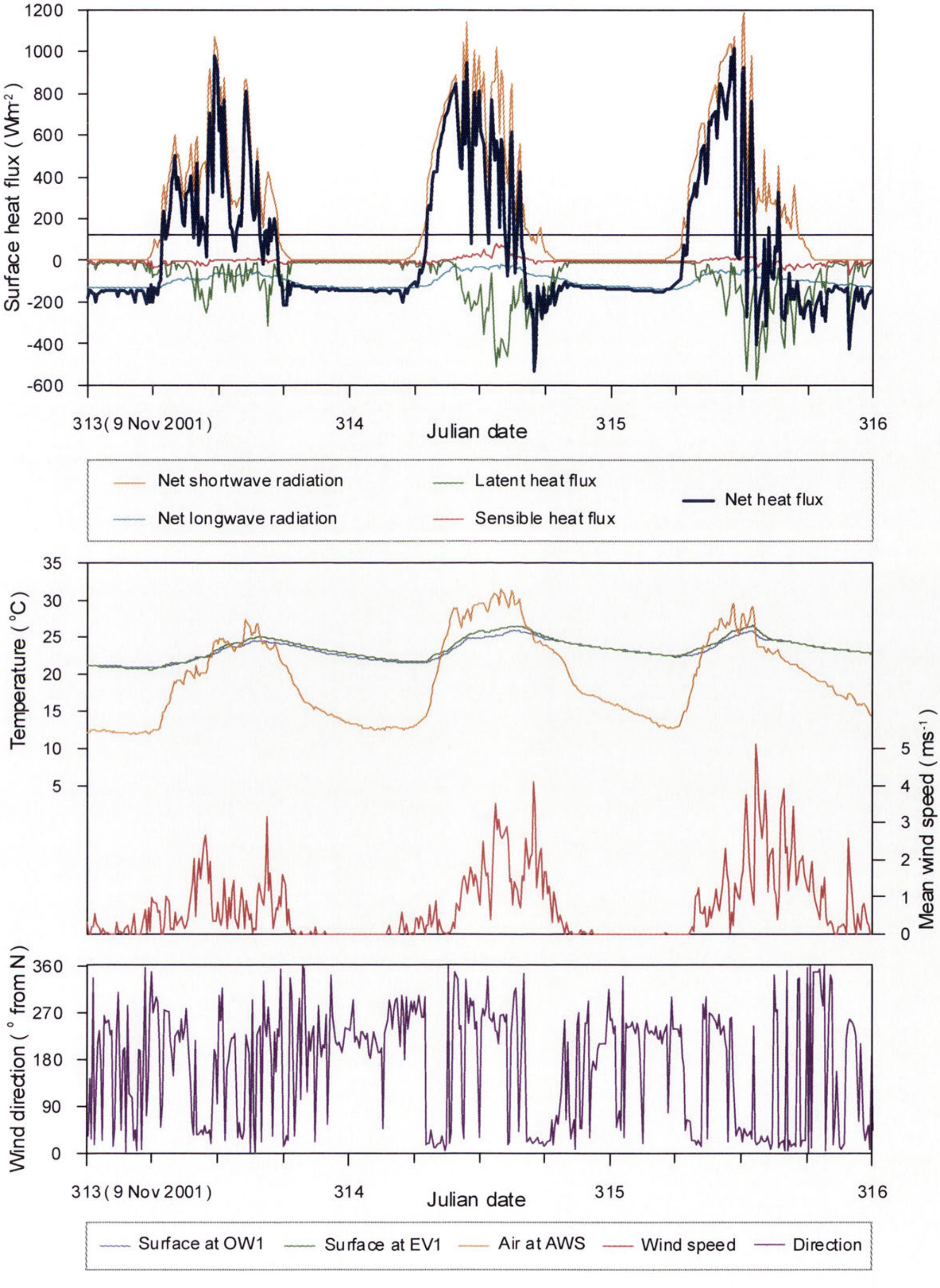

Figure G.7: Surface heat fluxes at Hopwoods Lagoon between 9 and 11 November 2001.

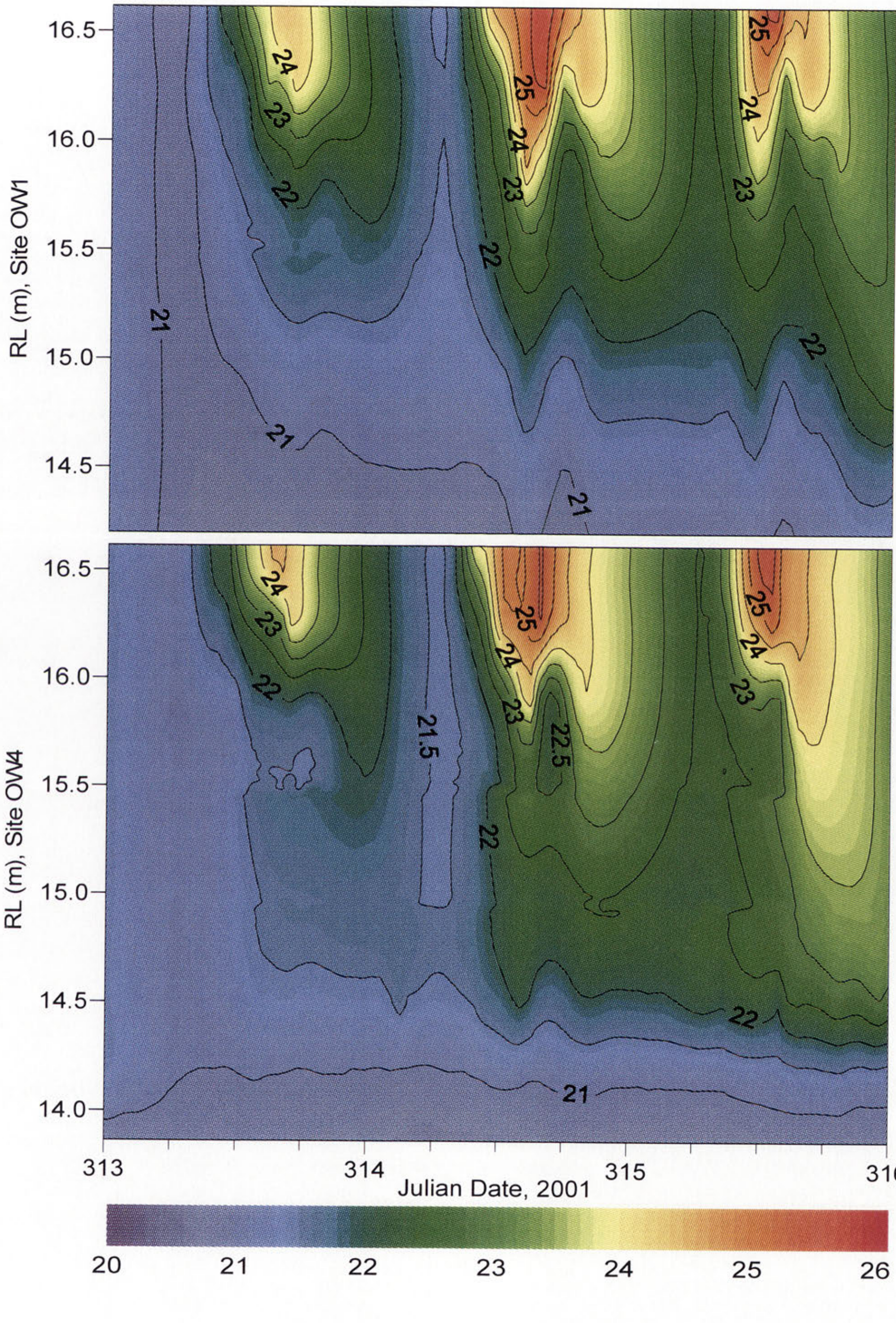

Figure G.8: Water temperatures at Sites OW1 and OW4 between 9 and 11 November 2001. Water surface elevation at RL 16.67 m.

G.3 Radiation Shading by Submerged Macrophytes

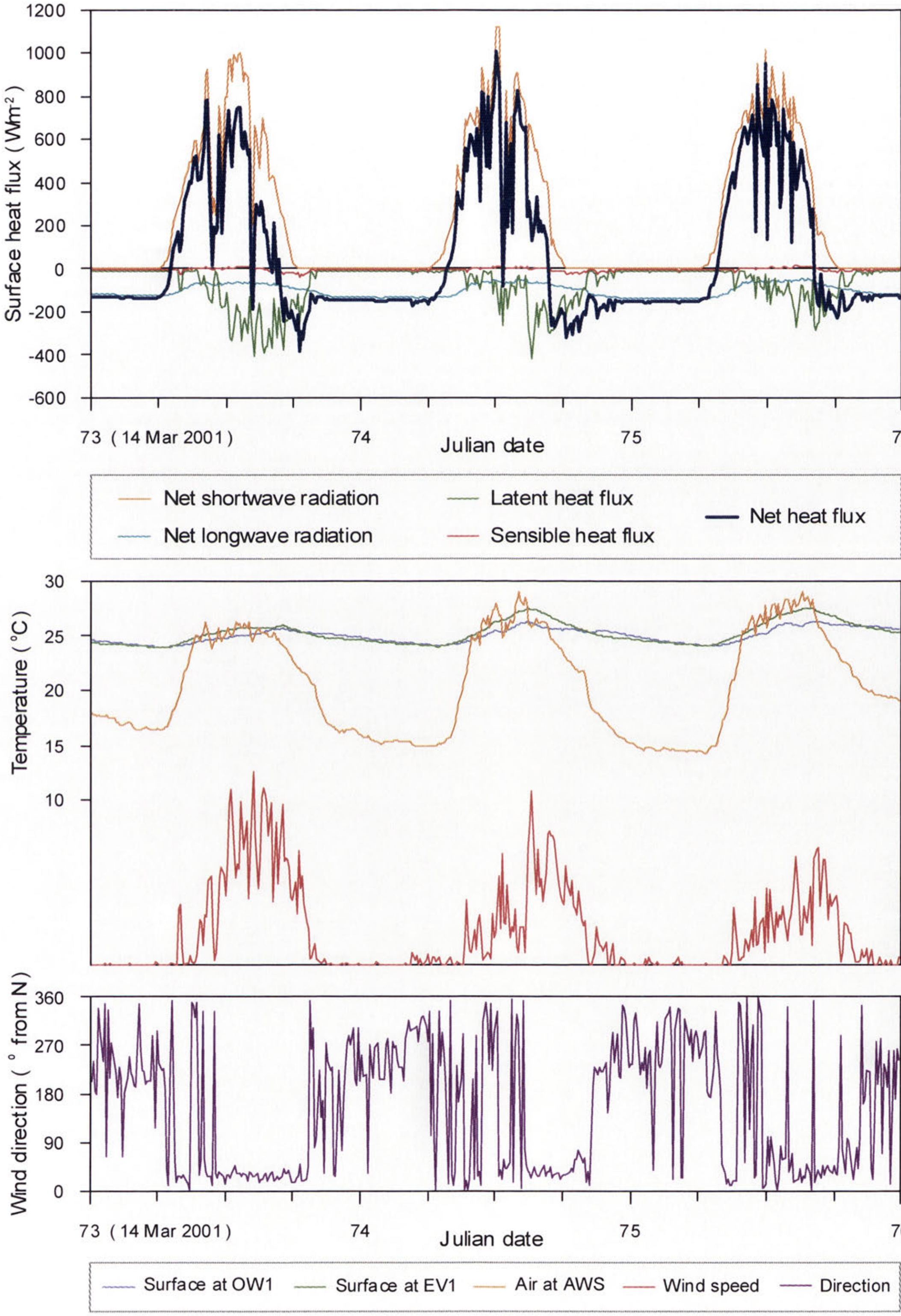

Figure G.9: Surface heat fluxes at Hopwoods Lagoon between 14 and 16 March 2001.

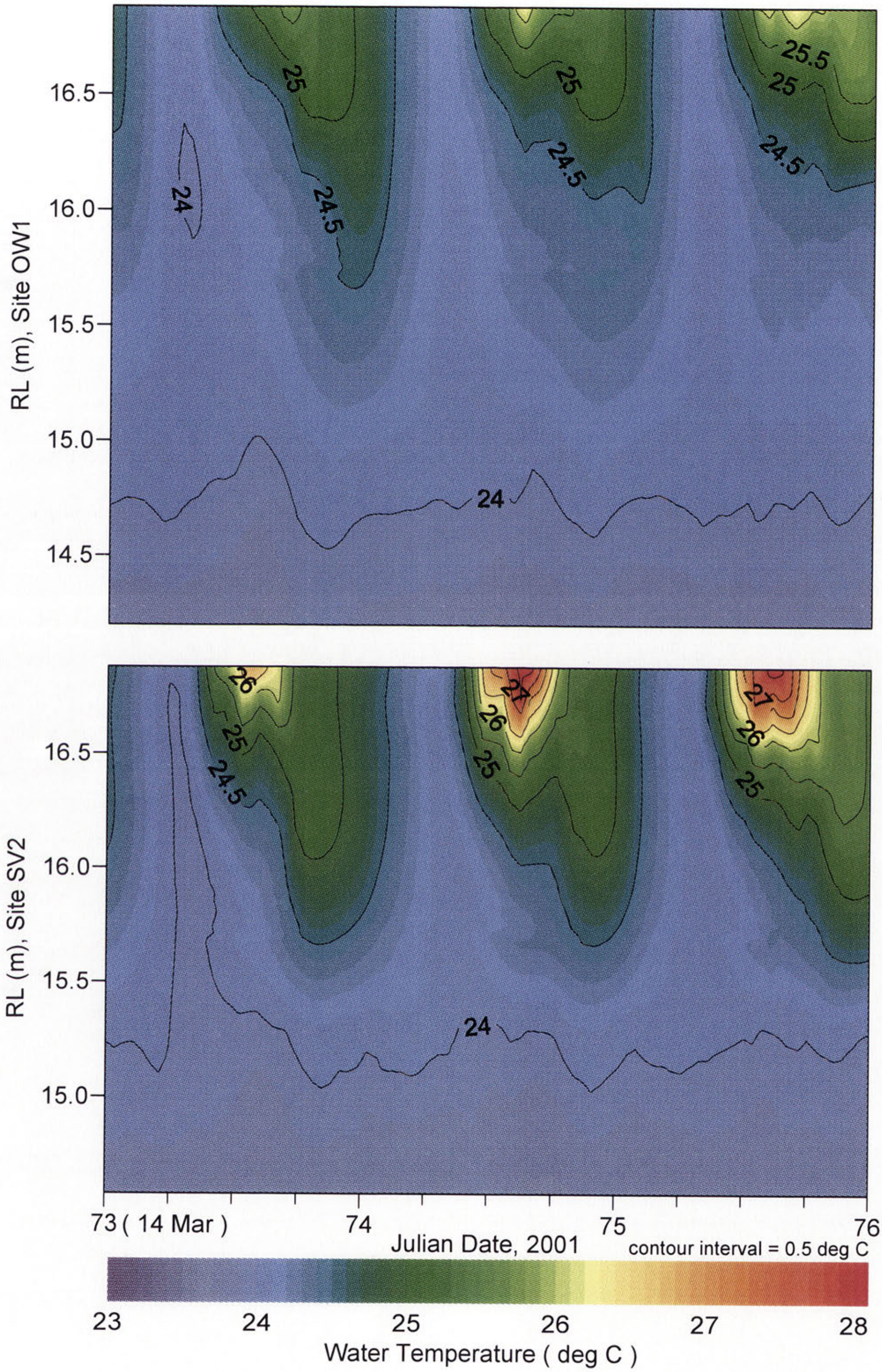

Figure G.10: Water temperatures at Sites OW1 and SV2 between 14 and 16 March 2001. Water surface elevation at RL 16.93 m.

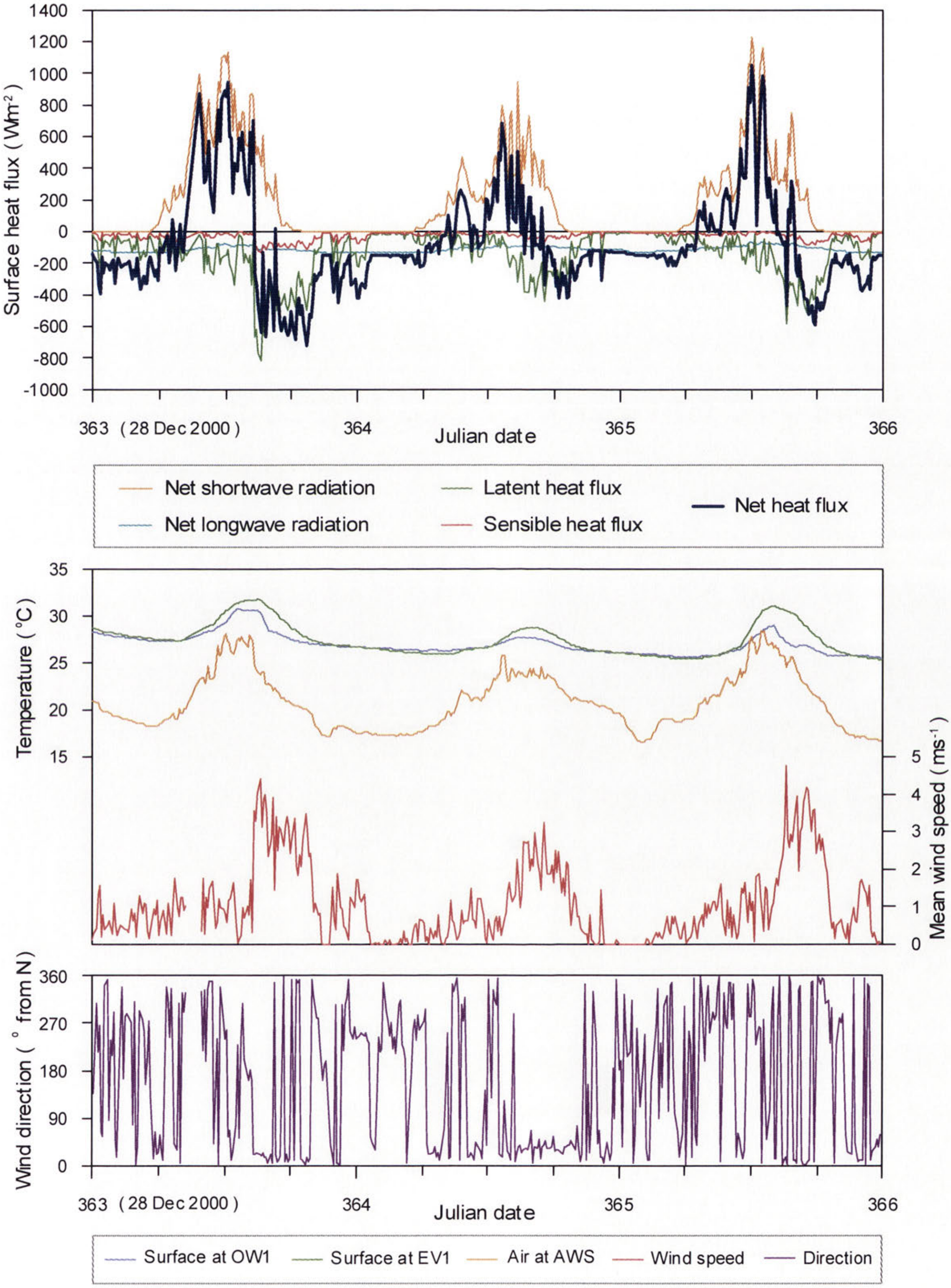

Figure G.11: Surface heat fluxes at Hopwoods Lagoon between 28 and 30 December 2000.

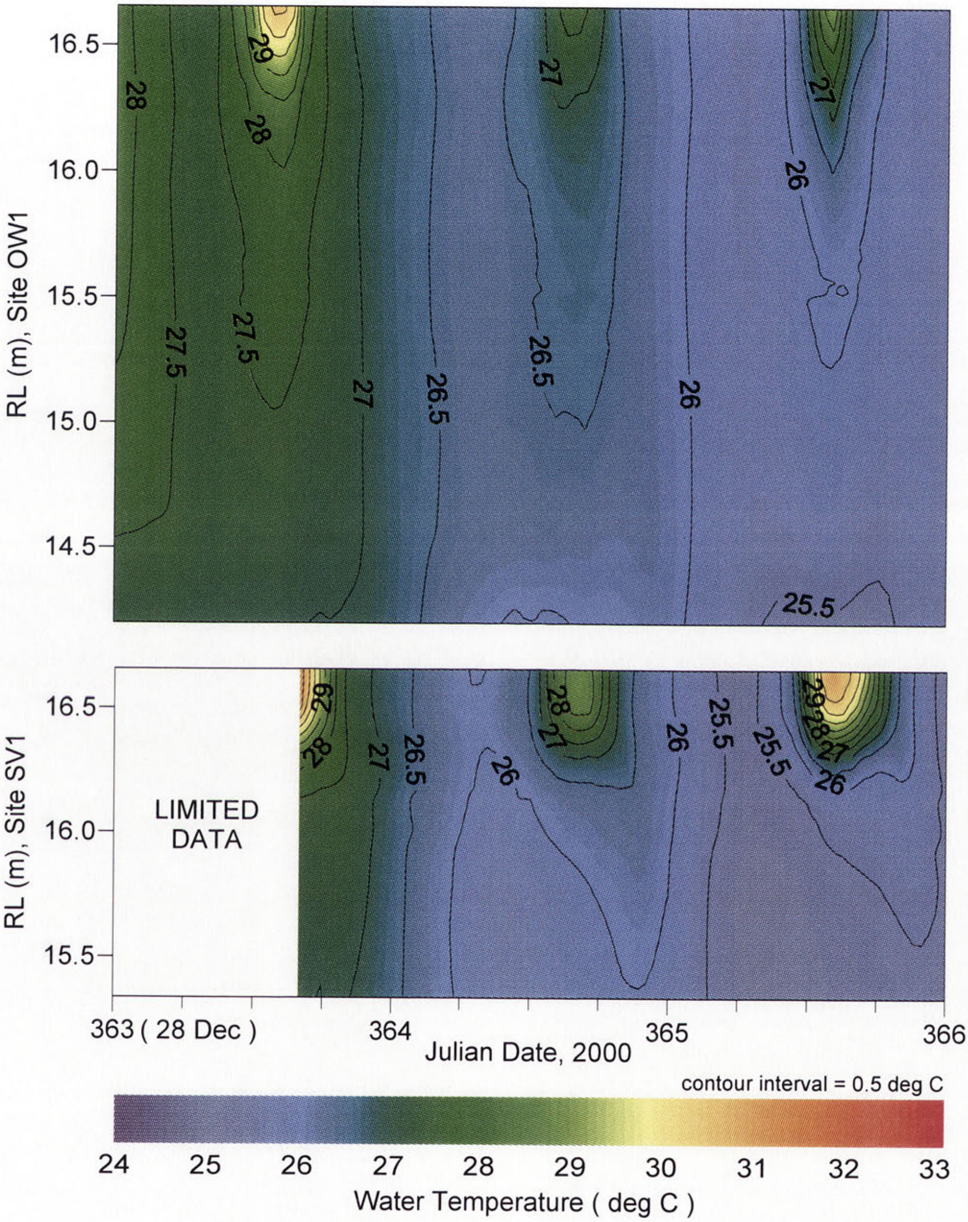

Figure G.12: Water temperatures at Sites OW1 and SV1 between 28 and 30 December 2000. Water surface elevation at RL 16.71 m.

G.4 Radiation Shading by Emergent Macrophytes

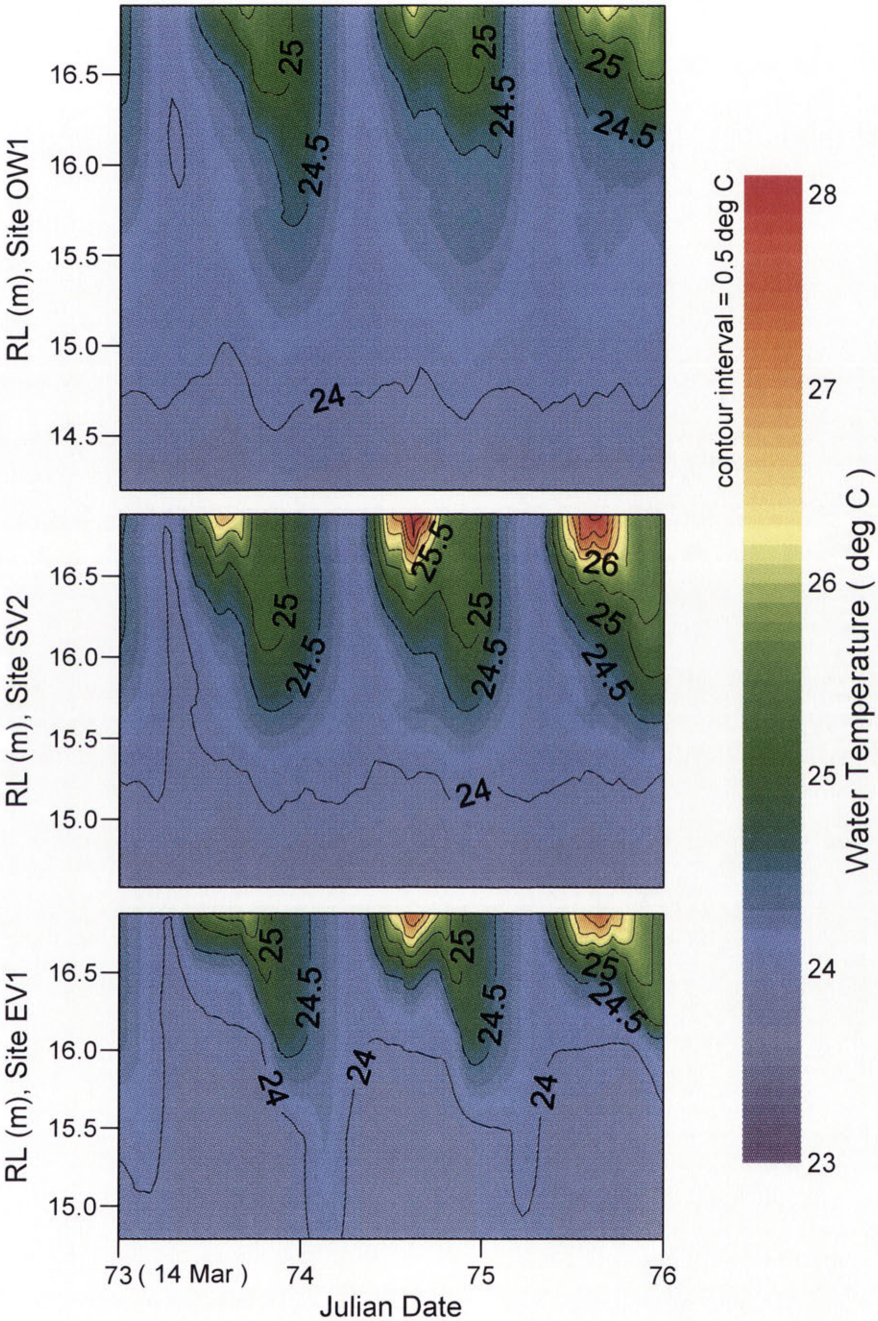

Figure G.13: Water temperatures at Sites OW1, SV2 and EV1 between 14 and 16 March 2001. Water surface elevation at RL 16.93 m.

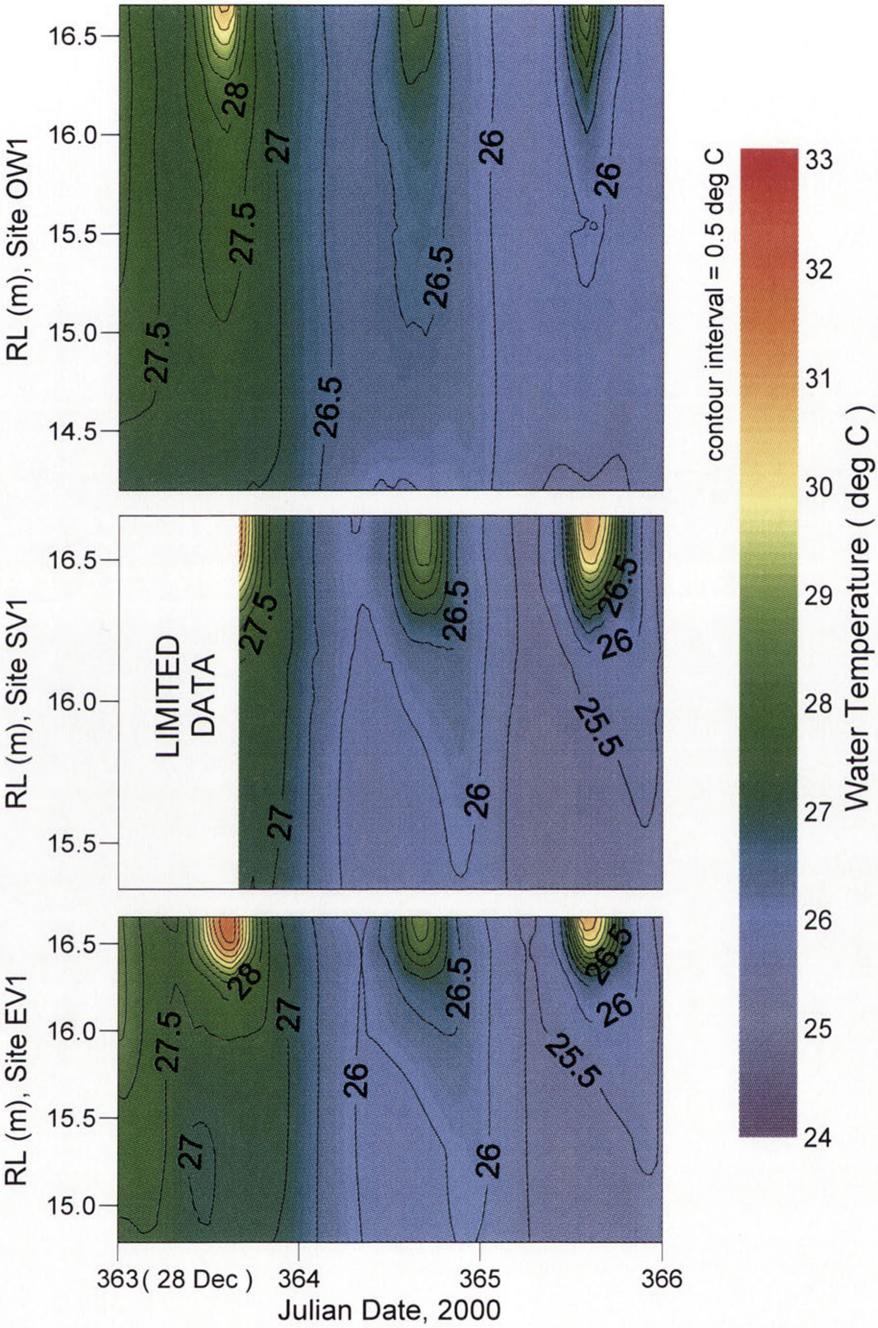

Figure G.14: Water temperatures at Sites OW1, SV1 and EV1 between 28 and 30 December 2000. Water surface elevation at RL 16.71 m.

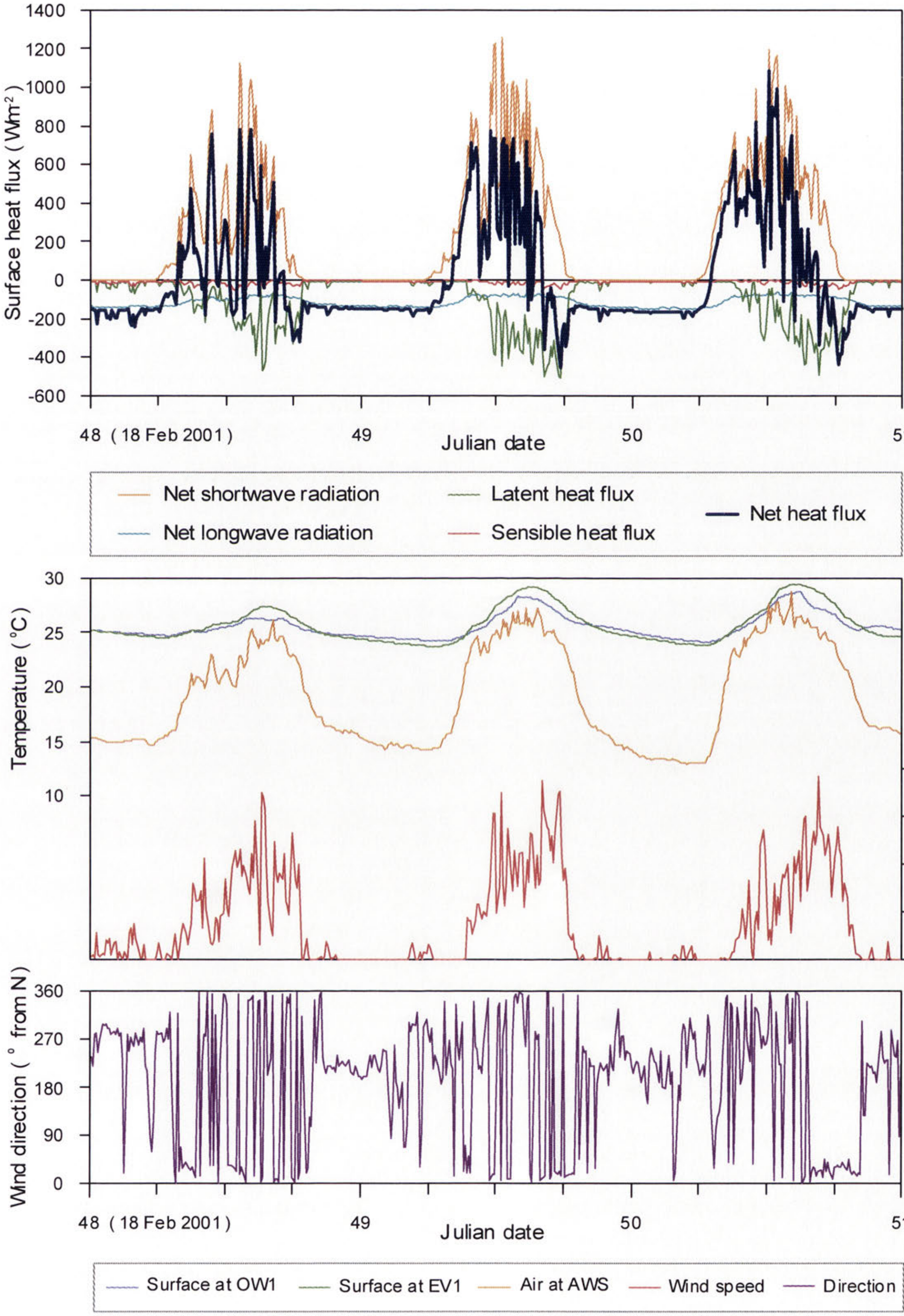

Figure G.15: Surface heat fluxes at Hopwoods Lagoon between 18 and 20 February 2001.

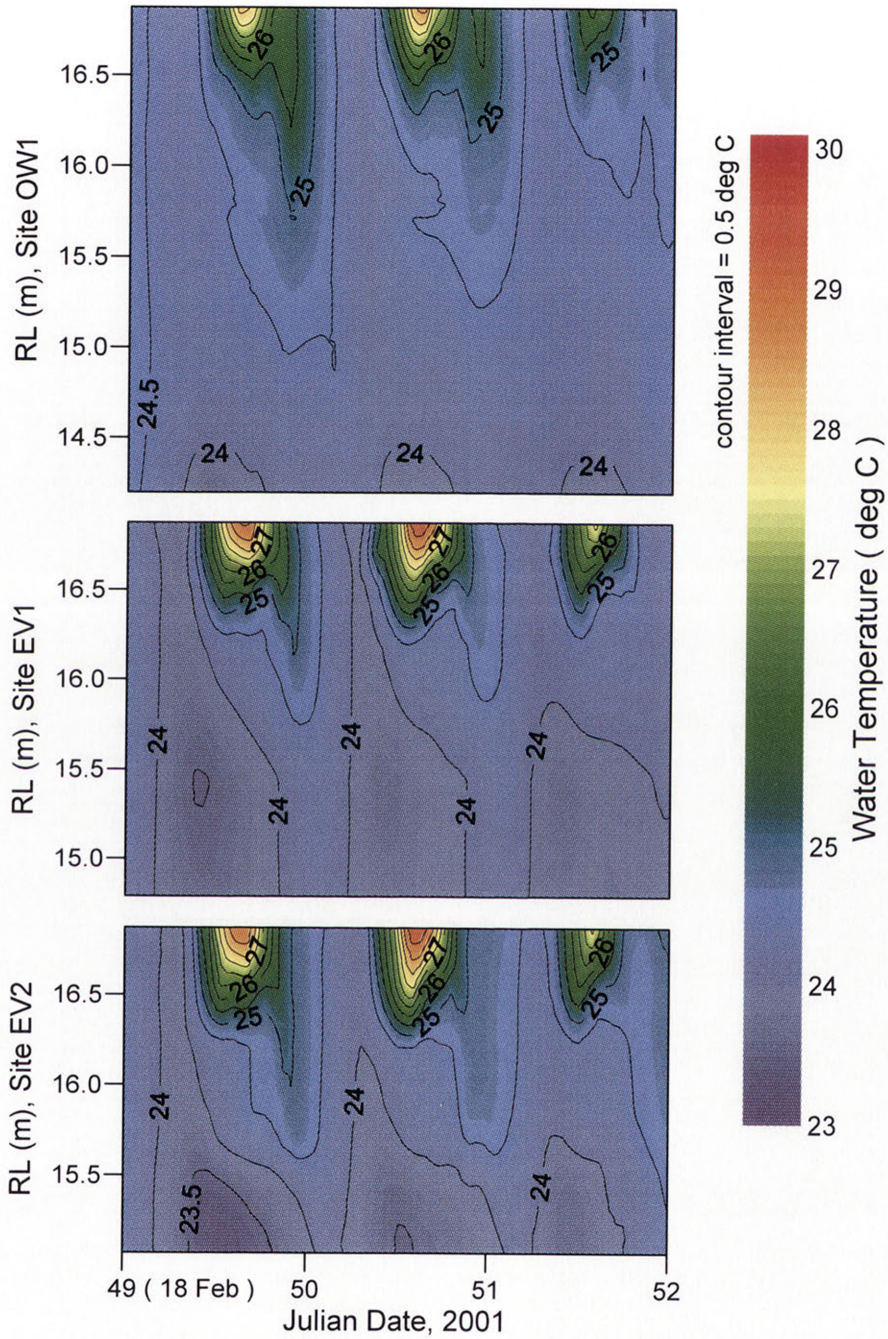

Figure G.16: Water temperatures at Sites OW1, EV1 and EV2 between 18 and 20 February 2001. Water surface elevation at RL 16.92 m.

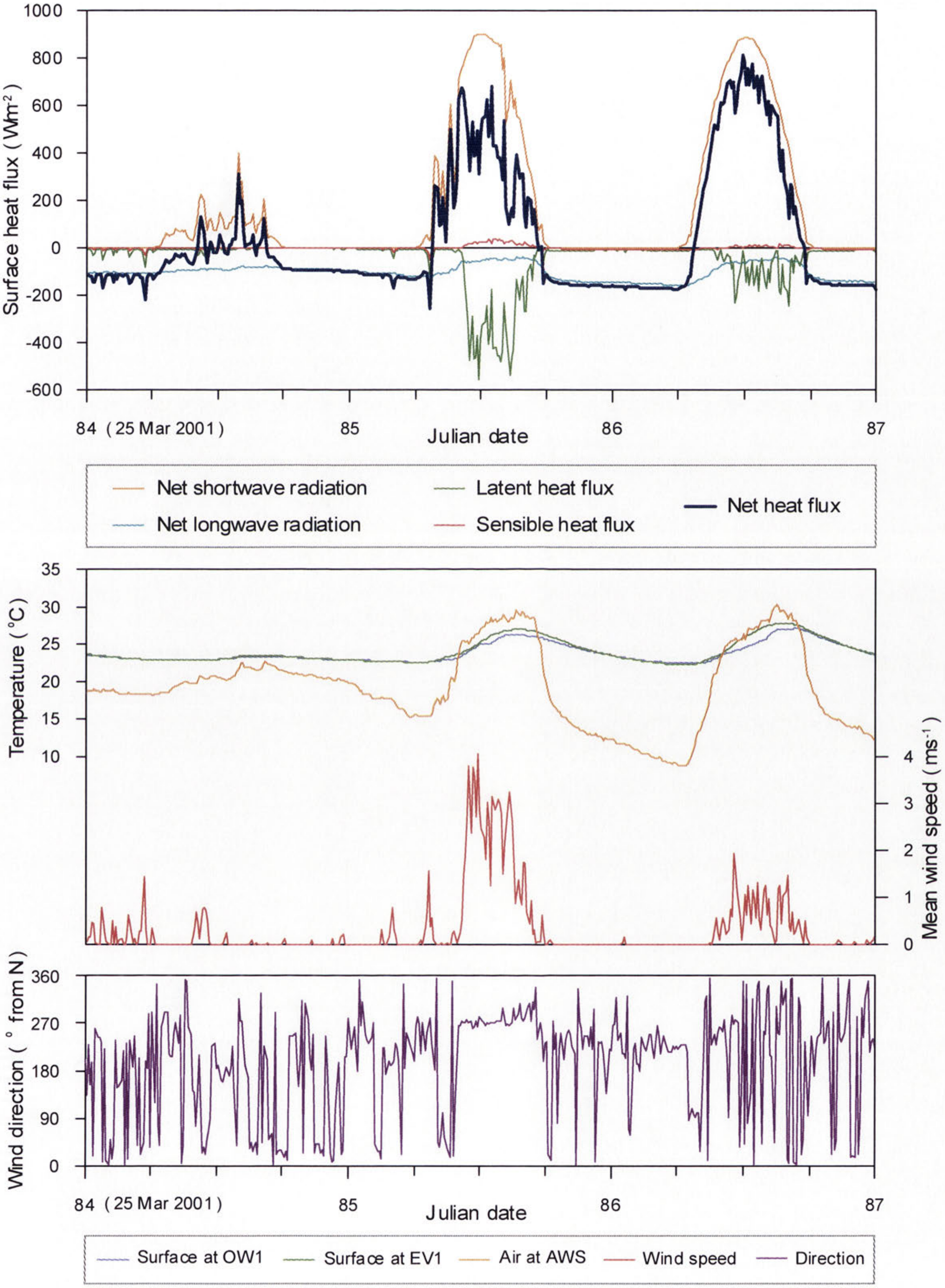

Figure G.17: Surface heat fluxes at Hopwoods Lagoon between 25 and 27 March 2001.

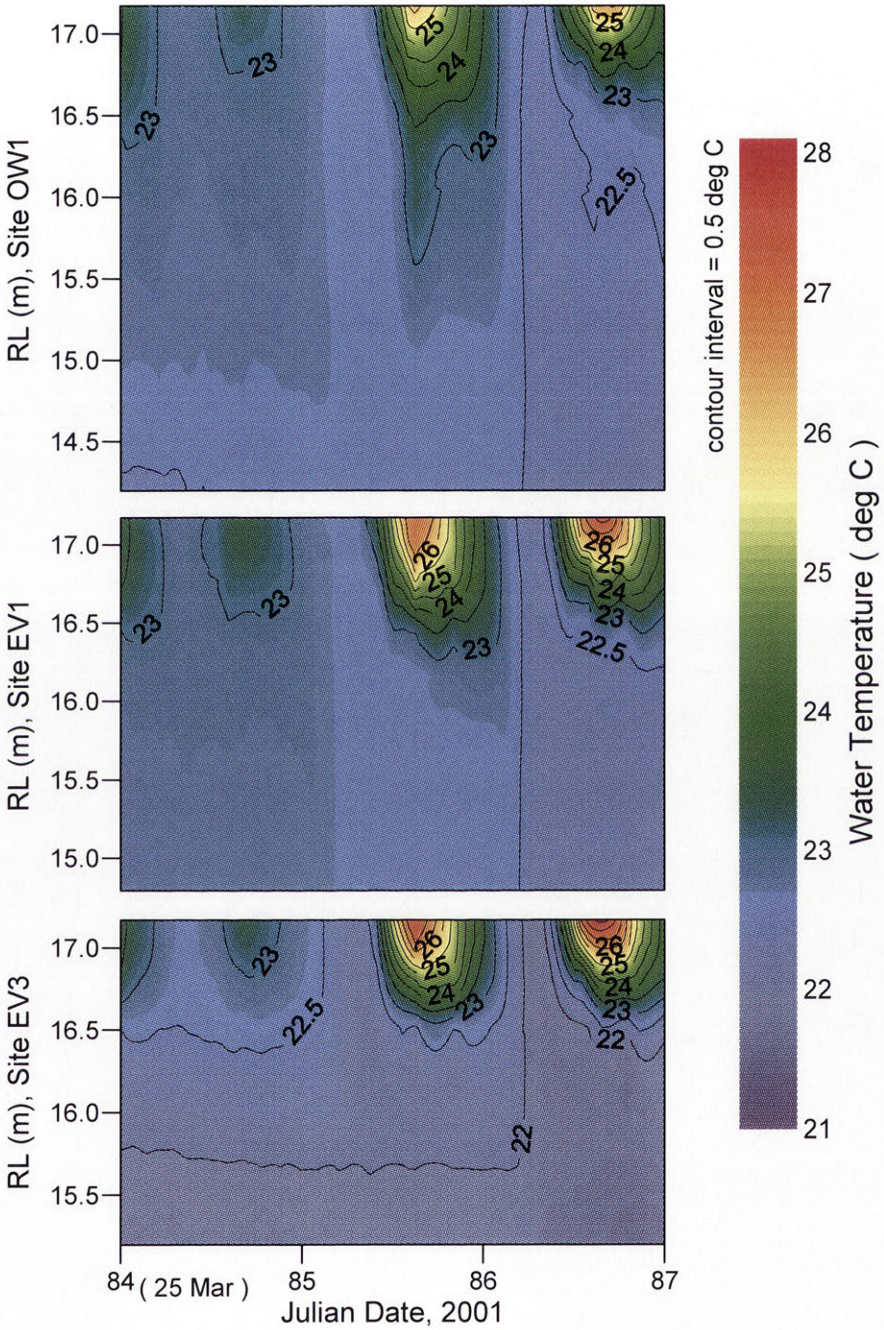

Figure G.18: Water temperatures at Sites OW1, EV1 and EV3 between 25 and 27 March 2001. Water surface elevation at RL 17.22 m.

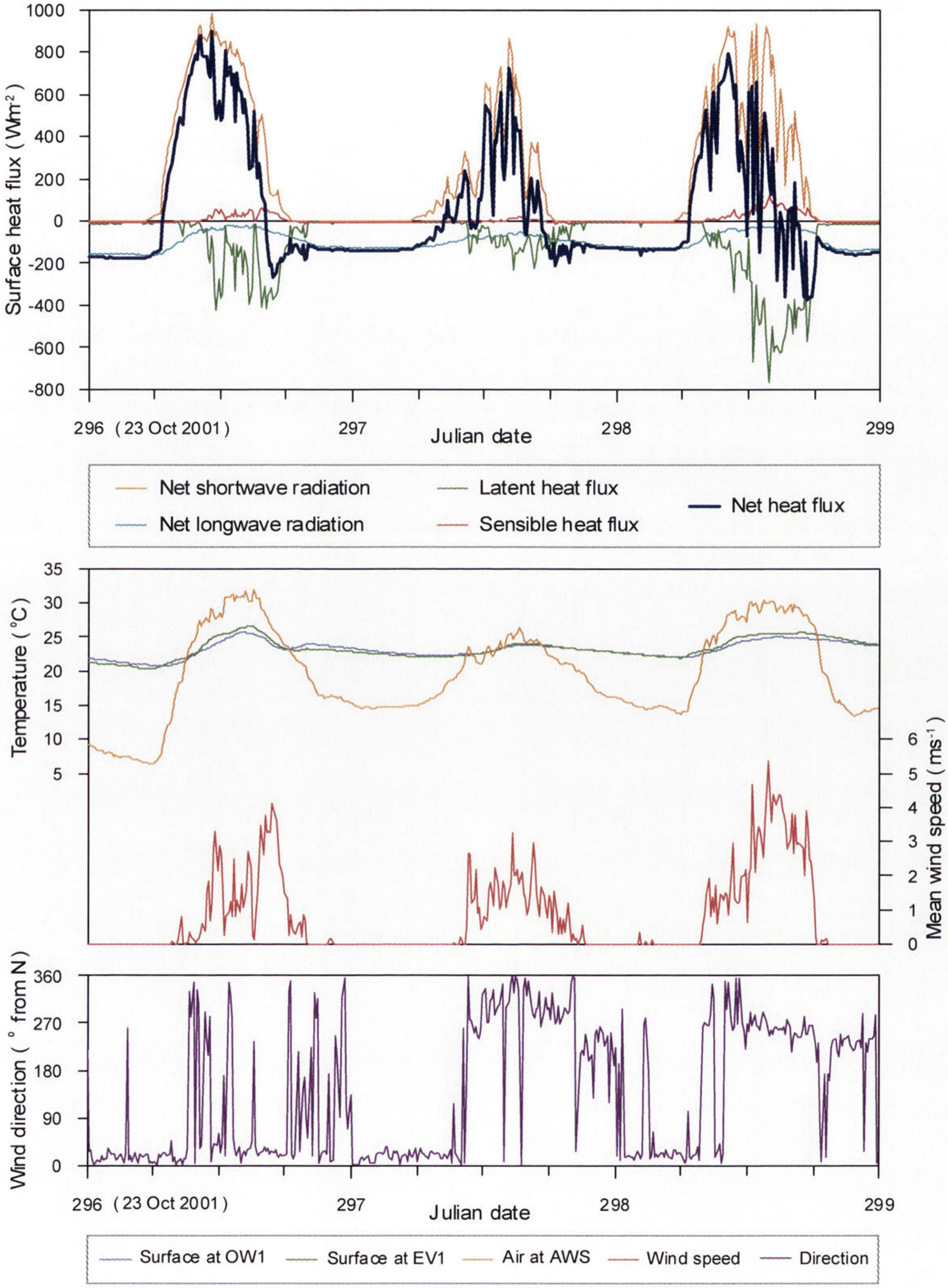

Figure G.19: Surface heat fluxes at Hopwoods Lagoon between 23 and 25 October 2001.

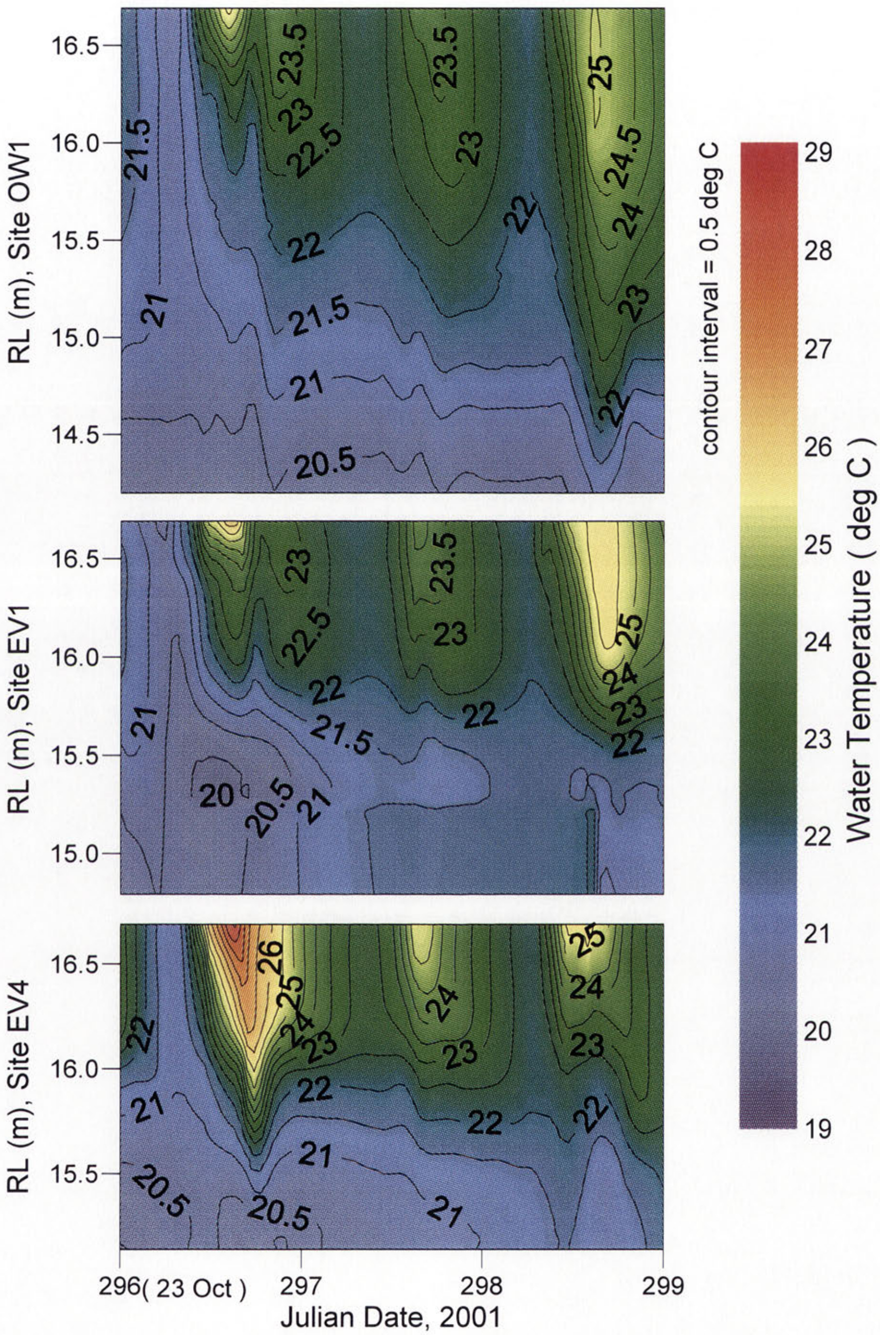

Figure G.20: Water temperatures at Sites OW1, EV1 and EV4 between 23 and 25 October 2001. Water surface elevation at RL 16.74 m.

Appendix H

DESCRIPTION OF THE HYDRODYNAMIC MODEL

H.1 Overview of Model Solution Scheme

The model adopted a decoupled approach, where the thermodynamics was imposed on the hydrodynamics, which in turn affected the thermodynamics. The feedback effects between the hydrodynamics and the thermodynamics were incorporated by repeated iteration. Trial simulations undertaken during the model calibration phase indicated that the solution converged rapidly. Most of the variation in predicted temperatures and velocities between successive timesteps was accounted for by the first iteration.

Only two temperature and two velocity iterations were implemented in all simulations using the validated model, iterating first with temperature as the dependent variable, then successively with velocity, temperature and velocity. Velocities were held constant while solving for water temperatures, and temperatures were held constant while solving for velocities. The values of the dependent variables were updated at the conclusion of each iteration step, and written to the output file.

Within each iteration, the components of the heat budget and the various force terms were computed and inserted into their respective locations in the element coefficient matrices. A Newton-Raphson iteration technique was used to solve the system of equations for changes in the values of the active dependent variables, while all inactive variables retained constant values.

H.2 Governing Equations

The governing equations for three-dimensional flow in a density-stratified fluid can be classified as either hydrodynamic or thermodynamic, as follows:

- **hydrodynamic equations**:
  - the momentum equations
  - the continuity equation
- **thermodynamic equations**:
  - the advection - diffusion equation for the transport of heat
  - an equation of state relating water density to temperature.

The following overview is sourced primarily from King (1993).

H.2.1 Hydrodynamic Equations

RMA-10 employs the Reynolds form of the Navier-Stokes equations in the three Cartesian directions (King, 1993):

$$\rho\left(\frac{\partial u}{\partial t} + u\frac{\partial u}{\partial x} + v\frac{\partial u}{\partial y} + w\frac{\partial u}{\partial z}\right) - \frac{\partial}{\partial x}\left(\varepsilon_{xx}\frac{\partial u}{\partial x}\right) - \frac{\partial}{\partial y}\left(\varepsilon_{xy}\frac{\partial u}{\partial y}\right) - \frac{\partial}{\partial z}\left(\varepsilon_{xz}\frac{\partial u}{\partial z}\right) + \frac{\partial P}{\partial x} - \Gamma_x = 0 \tag{H.1}$$

$$\rho\left(\frac{\partial v}{\partial t} + u\frac{\partial v}{\partial x} + v\frac{\partial v}{\partial y} + w\frac{\partial v}{\partial z}\right) - \frac{\partial}{\partial x}\left(\varepsilon_{yx}\frac{\partial v}{\partial x}\right) - \frac{\partial}{\partial y}\left(\varepsilon_{yy}\frac{\partial v}{\partial y}\right) - \frac{\partial}{\partial z}\left(\varepsilon_{yz}\frac{\partial v}{\partial z}\right) + \frac{\partial P}{\partial y} - \Gamma_y = 0 \tag{H.2}$$

$$\rho\left(\frac{\partial w}{\partial t} + u\frac{\partial w}{\partial x} + v\frac{\partial w}{\partial y} + w\frac{\partial w}{\partial z}\right) - \frac{\partial}{\partial x}\left(\varepsilon_{zx}\frac{\partial w}{\partial x}\right) - \frac{\partial}{\partial y}\left(\varepsilon_{zy}\frac{\partial w}{\partial y}\right) - \frac{\partial}{\partial z}\left(\varepsilon_{zz}\frac{\partial w}{\partial z}\right) + \frac{\partial P}{\partial z} + \rho g - \Gamma_z = 0 \tag{H.3}$$

where	x, y, z	=	the Cartesian coordinate system
	u, v, w	=	instantaneous velocities in the x, y, z directions ($\mathrm{m\,s^{-1}}$)
	ρ	=	water density ($\mathrm{kg\,m^{-3}}$)
	ε	=	eddy viscosities ($\mathrm{Pa\,s^{-1}}$)
	P	=	water pressure (Pa)
	$\Gamma_x, \Gamma_y, \Gamma_z$	=	external tractions operating on the system ($\mathrm{Pa\,m^{-1}}$).

Equation (H.3) can be simplified using the hydrostatic approximation if it is assumed that the water body is sufficiently shallow relative to the horizontal dimensions that the influences of vertical momentum can be neglected:

$$\frac{\partial P}{\partial z} + \rho g = 0 \tag{H.4}$$

where g is the acceleration due to gravity ($\mathrm{m\,s^{-2}}$).

Volume continuity is expressed as follows:

$$\frac{\partial u}{\partial x} + \frac{\partial v}{\partial y} + \frac{\partial w}{\partial z} = 0 \tag{H.5}$$

As described in King (1993), the pressure at any point in a non-homogeneous fluid can be determined from an integral of the water density over the depth. Using this integral, the volume continuity equation can be integrated over the depth of the water column to produce a depth-integrated volume continuity equation:

$$\int_a^{a+h} \left(\frac{\partial u}{\partial x} + \frac{\partial v}{\partial y} \right) dz + u_s \frac{\partial (a+h)}{\partial x} - u_b \frac{\partial a}{\partial x} + v_s \frac{\partial (a+h)}{\partial y} - v_b \frac{\partial a}{\partial y} + \frac{\partial h}{\partial t} = 0 \tag{H.6}$$

where	h	=	water depth (m)
	a	=	bed elevation (m)
	$a + h$	=	water surface elevation (m)
	u_b, v_b	=	x and y velocity components at the bed ($\mathrm{m\,s^{-1}}$)
	u_s, v_s	=	x and y velocity components at the water surface ($\mathrm{m\,s^{-1}}$).

The set of hydrodynamic equations thus reduces from four equations with four unknowns, to the two horizontal momentum equations and an integrated continuity equation, Equation (H.6). The principal dependent variables in the reduced equation set are u, v and h, since the vertical velocities w can be determined separately from the original volume continuity equation, Equation (H.5).

H.2.2 Thermodynamic Equations

The transport of heat is described using an advection - diffusion equation, as follows (King, 1993):

$$\frac{\partial T}{\partial t} + u\frac{\partial T}{\partial x} + v\frac{\partial T}{\partial y} + w\frac{\partial T}{\partial z} - \frac{\partial}{\partial x}\left(D_x\frac{\partial T}{\partial x}\right) - \frac{\partial}{\partial y}\left(D_y\frac{\partial T}{\partial y}\right) - \frac{\partial}{\partial z}\left(D_z\frac{\partial T}{\partial z}\right) - \theta_{SOURCE} = 0 \tag{H.7}$$

where T_w = water temperature (°C)

$D_x, D_y, D_z,$ = eddy diffusion coefficients for heat ($\mathrm{m^2\,s^{-1}}$)

θ_{SOURCE} = source or sink term for heat ($\mathrm{°C\,s^{-1}}$)

and other parameters are as defined earlier.

The equation of state relates the water density to the water temperature. The equation originally employed in RMA-10 was replaced (by the author) using a form of the UNESCO equation of state (List, 1968):

$$\rho = 999.84 + 6.79\times10^{-2}\,T_w - 9.06\times10^{-3}\,T_w^2 + 1.0\times10^{-4}\,T_w^3 \tag{H.8}$$

because it provided greater consistency between calculated and tabulated density values over the range of water temperatures recorded in the field.

H.2.3 Eddy Viscosity and Eddy Diffusivity

RMA-10 requires the eddy viscosity and eddy diffusivity to be either specified directly in the input data or calculated internally by the model. The vertical and horizontal eddy coefficients were set internally by RMA-10 using separate methods, as described below.

H.2.3.1 Vertical Eddy Viscosity and Eddy Diffusivity

In homogeneous (non-stratified) flow, RMA-10 allows the eddy viscosity and eddy diffusivity to vary with depth beneath the water surface. This depth variation is nominally based on a quadratic variation with elevation above the bed (King, 1993):

$$E_{xz} = \varepsilon'_{xz}\left[A + \frac{(z-a)}{(b-a)}\left(B + \frac{(z-a)}{(b-a)}C\right)\right] \tag{H.9}$$

where z = local elevation (m)

a = local bed elevation (m)

b = local water surface elevation (m)

ε'_{xz} = user specified minimum eddy viscosity at $z = a$ (Pa s^{-1})

E_{xz} = internally calculated local neutral eddy viscosity associated with the z direction shear of the x direction flow (Pa s^{-1})

A, B, C = quadratic coefficients specified in the model input, for each element class.

The same quadratic coefficients were applied to the values of ε'_{xz}, ε'_{xy} and $D_z{}'$ specified in the model input. These were used to generate the local, neutral values of E_{xz}, E_{xy} and D_h throughout the model domain corresponding to a non-stratified flow. The default model option specifies a constant value for the eddy viscosity and diffusivity over the depth ($A = 1.0, B = C = 0.0$). However, eddy coefficients are rarely constant with depth in natural systems (Tennekes and Lumley, 1972; Turner, 1973; Imberger and Patterson, 1990), so a quadratic variation with $A = B = C = 1.0$ was adopted to calculate the nominal, homogeneous eddy coefficients in the present study.

RMA-10 models the effects of density stratification on vertical mixing in non-homogeneous flow using a two-step process. The neutral values calculated for the vertical eddy viscosity and diffusivity terms in non-stratified flow, using Equation (H.9), are adjusted according to the stability of the density stratification.

For stable density stratified flow when

$$Ri = -\frac{g}{\rho}\frac{\partial \rho}{\partial z} \Big/ \left|\frac{\partial V}{\partial z}\right|^2 > 0.4 \qquad \text{(H.10)}$$

the local neutral values are decreased using a function of the Richardson number in a method described by Henderson-Sellers (1982):

$$\varepsilon_{xz} = \varepsilon_{yz} = \frac{E_{xz}}{(1 + 37\,Ri^2)} \qquad D_z = \frac{D_h}{(1 + 0.74\,Ri)} \qquad \text{(H.11)}$$

and $\varepsilon_{xz}, \varepsilon_{yz}$ = local values of the eddy viscosity in stratified flow (Pa s^{-1})

D_z = local value of the eddy diffusivity in stratified flow (m^2 s^{-1})

D_h = local neutral value of the eddy diffusivity (m^2 s^{-1})

V = resultant velocity (m s^{-1}).

For unstable conditions when $Ri < 0.25$ (Turner, 1973), RMA-10 increases the vertical diffusion by applying an arbitrary multiplication factor to simulate enhanced vertical mixing. Further details are given in King (1993).

H.2.3.2 Horizontal Eddy Viscosity and Eddy Diffusivity

Several options are available in RMA-10 for specification of the horizontal variation in eddy viscosity and eddy diffusivity. Of these, the Smagorinsky closure method was selected for the present study because it accounts for sub-grid scale effects as a function of the local grid scale and velocity gradients (Smagorinsky, 1963). The values of the Smagorinsky coefficient, $0.1 < k_s < 1.0$ and the minimum kinematic eddy viscosity, ν_s were specified in the model input (Section 6.6.1.5).

Initial values were specified for the horizontal eddy diffusivities, D_x' and D_y' and viscosities, ε_{xx}', ε_{xy}', ε_{yx}' and ε_{yy}'. These were used only for the first two iterations after startup (King, 1993), and were found during the model calibration to have little influence on the simulation results.

H.2.4 Vegetation Resistance Force

RMA-10 calculates the resistance force due to the macrophytes using a form of the drag equation, Equation (3.12) from page 45:

$$F_{Dx} = \tfrac{1}{2}\,\rho\, C_{Dx}\, A_p\, u\, V \qquad\qquad F_{Dy} = \tfrac{1}{2}\,\rho\, C_{Dy}\, A_p\, v\, V \tag{H.12}$$

where F_{Dx}, F_{Dy} = drag force components in the x and y directions (N)

C_{Dx}, C_{Dy} = bulk drag coefficients in the x and y directions

A_p = projected plant area over which the force acts (m^2).

This drag force parameterisation was retained despite its limitations (Section 2.3.3). At Hopwoods Lagoon, the flow resistance was predominantly due to the dense submerged macrophytes, which were assumed to project an area equivalent to the full flow area. In a dense submerged mat, this also allows for foliage hidden behind the projected frontal area of macrophytes, which also absorbs momentum, consistent with Fathi-Maghadam and Kouwen (1997). Macrophyte properties, including the vegetation resistance, were assumed to be uniform for all elements in each class.

Selection of the drag coefficient is discussed in Section 6.6.1.4.

H.3 Hydrodynamic Boundary Conditions at the Water Surface

H.3.1 Velocity Boundary Condition at the Water Surface

The flow equations were constrained by zero pressure at the water surface and no flow across the surface (King, 1993). The latter was satisfied using:

$$w_s = \frac{dh}{dt} \tag{H.13}$$

H.3.2 Wind Stresses at the Water Surface

Wind stresses were applied to the water surface as surface tractions in the horizontal momentum equations. These were calculated using:

$$\Gamma_x = \psi\, {u_{10}}^2 \cos(\theta_w) \qquad\qquad \Gamma_y = \psi\, {u_{10}}^2 \sin(\theta_w) \tag{H.14}$$

where Γ_x, Γ_y = surface tractions in the x and y directions (Pa)
ψ = a wind stress coefficient, defined below ($\mathrm{kg\,m^{-3}}$)
u_{10} = wind speed at 10 m elevation ($\mathrm{m\,s^{-1}}$)
θ_w = wind direction, measured anti-clockwise from east ($^\circ$).

In RMA-10, the wind stress coefficient varied with wind speed according to Wu (1980):

$$\psi = C_{D10}\,\rho_m \approx \tfrac{1}{2}\,{u_{10}}^{1/2}\,\rho_m \times 10^{-3} \qquad \text{when} \qquad u_{10} \leq 15 \tag{H.15}$$

where C_{D10} = dimensionless drag coefficient, referenced to u_{10}
ρ_m = density of moist air ($\mathrm{kg\,m^{-3}}$), Equation (A.18).

The model was run with wind velocities which were applied uniformly across the whole surface area of the lagoon. These velocities were used only to calculate the wind stresses at the water surface, and did not otherwise influence the hydrodynamics of the system. Mixing coefficients were updated simultaneously, although independently, as discussed in Section H.2.3.1.

H.3.2.1 Wind Stresses Beneath the Emergent Canopy

The applied wind stress coefficients were reduced in the emergent macrophyte zones to simulate wind speed attenuation, using a simple empirical approximation:

$$\psi_{veg} = 0.2\,\psi \tag{H.16}$$

where ψ_{veg} is the wind stress coefficient in the emergent macrophyte zone.

The mean wind speed attenuation factor was estimated from a series of wind speed measurements made in the emergent *Typha domingensis* canopy at Deep Creek, and the wind speed attenuation profiles are shown in Figure H.1. Although the wind data set was not analysed in detail, the reduction in wind speed below the top of the canopy is clear. The estimated attenuation factor is also consistent with velocity profile data presented by Waters (1998) for *Typha orientalis* at Manly Dam, and the wind speed reduction predicted by the mixing length model of Cionco (1972) and the constant eddy viscosity model described by Landsberg and James (1971) for a 1 m deep canopy.

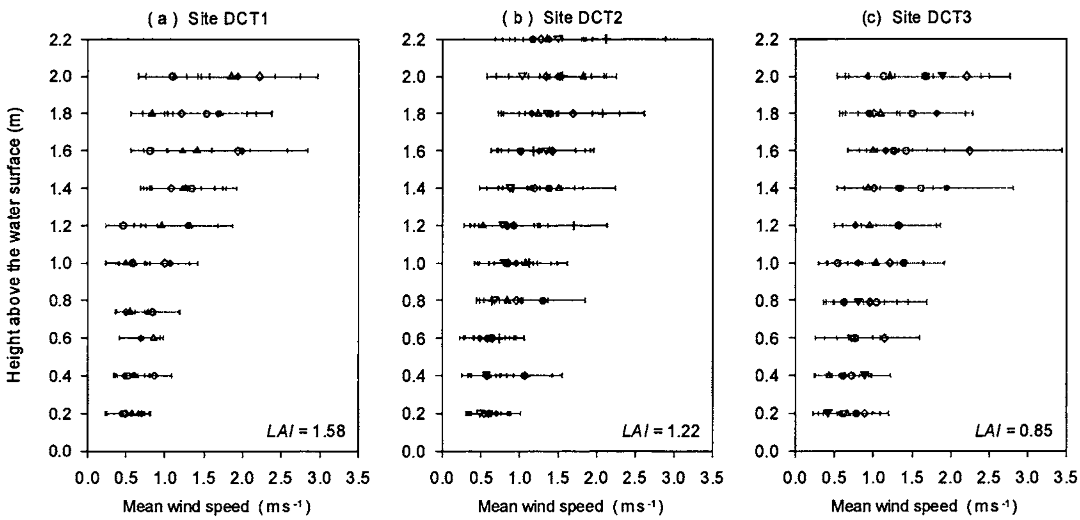

Figure H.1: Wind speed attenuation by the Typha domingensis canopy at Deep Creek, 23 and 26 November 2000, showing mean (markers) and standard deviation (error bars) of 1 sec measurements over a period of 1 min at each height. All measurements were made between 09:50 and 14:44 (AEST).

H.4 Hydrodynamic Boundary Conditions at the Bed

H.4.1 Velocity Boundary Condition at the Bed

Fluid motion at the bed was fully constrained as follows (King, 1993):

$$u_b = v_b = w_b = 0 \tag{H.17}$$

where u_b, v_b and w_b are the x, y and z components of the velocity at the bed ($\mathrm{m\,s^{-1}}$).

H.4.2 Bed Friction

RMA-10 models bed friction using the Chezy or Manning equation, neither of which is strictly applicable to a wetland where the flows are predominantly laminar or transitional rather than turbulent. However, because the velocities were constrained to zero at the bed, as per Equation (H.17), bed friction was not explicitly modelled. Neglect of bed friction is considered reasonable in this application, because the simulated system velocities were very small and because flow resistance due to the macrophytes was expected to be more important throughout the wetland, except very close to the bed Nepf et al. (1997b).

H.5 Hydrodynamic Boundary Conditions at the Shoreline

H.5.1 Horizontal Velocity Boundary Condition at the Shoreline

The flow equations at the very shallow system shorelines were constrained by the no-leakage condition, or zero normal velocity, as follows (King, 1993):

$$u \sin\left(\alpha \frac{\pi}{180}\right) - v \cos\left(\alpha \frac{\pi}{180}\right) = 0 \tag{H.18}$$

where α is the orientation of the boundary ($^\circ$).

H.5.2 Shoreline Friction

RMA-10 calculates a shear force acting over the surface area of side boundaries using the Chezy or Manning equation, similar to the approach at the bed. Shoreline friction was neglected in the present study, given the very shallow (imposed) water depth at the shoreline boundaries. The small simulated velocities would also have resulted in only negligible friction losses.

H.6 Thermodynamic Boundary Conditions at the Water Surface

The surface heat flux parameterisation adopted in the original RMA-10 was based extensively on that used in QUAL2E (described by Brown and Barnwell, 1987). At the water surface, the source rate term for heat is calculated as a function of the net heat flux across the surface (King, 1998):

$$G_T = \frac{H_{NET}}{3.6\, c_{pw}\, \rho} \tag{H.19}$$

where G_T = temperature source rate at the water surface ($\mathrm{m\,^\circ C\,s^{-1}}$)

H_{NET} = net surface heat flux ($\mathrm{kJ\,m^{-2}\,h^{-1}}$)

c_{pw} = specific heat capacity of water ($\mathrm{J\,kg^{-1}\,^\circ C^{-1}}$)

ρ = water density ($\mathrm{kg\,m^{-3}}$)

3.6 = conversion factor for units.

The net surface heat flux is defined by Equation (3.15), on page 48. The parameterisation of the components of the surface heat flux are summarised in the following sections, together with the equation and page references from earlier in the thesis. A list of symbols is presented commencing on page *xxxi*. Changes made to the original heat budget parameterisation by the author are listed in Table H.1 at the end of this Appendix.

H.6.1 Shortwave Radiation Flux

The incident shortwave radiation flux can be calculated by RMA-10 from standard astronomical formulae, as described by King (1998), or input directly via the meteorological data file. Shortwave radiation data was available from field measurements, and could therefore be used directly in the present study.

The shortwave reflection coefficient from the water surface was calculated using Equation (3.17) from page 51:

$$R_S = A\,\beta^B$$

The solar elevation was calculated for each timestep as outlined in Appendix A, using the empirical coefficients given in Table 3.2 (page 51).

H.6.1.1 Shortwave Radiation Flux beneath the Emergent Canopy

The shortwave radiation flux at the water surface beneath the emergent macrophyte canopy was modelled using Beers Law based on the G-function, Equation (6.3) from page 204:

$$\phi_{LAI} = \phi \exp\left[-\mathcal{K}_{LAI}\, LAI\right] \qquad \text{where} \qquad \mathcal{K}_{LAI} = \frac{G(z,\theta,\theta_L)}{\cos\theta} = \frac{G(z,\theta,\theta_L)}{\sin\beta}$$

The G-function was calculated using the simplified method of Nilson (1991), expressed as Equations (3.50) and (3.51) on pages 75 to 75. The LAI and inclination distribution of the canopy foliage were determined from field data, as described in Section 5.2, and specified in the model input data. The solar elevation was calculated as described in Appendix A.

Reflection of shortwave radiation from the upper surface of the canopy was assumed to be negligible (Section 3.4.2.1).

The net transmission of shortwave radiation to the water surface was calculated from the net transmission of PAR (page 80):

$$\tau_S = 0.78\,\tau_{\mathrm{PAR}} + 0.22$$

H.6.1.2 Underwater Attenuation of Shortwave Radiation

Attenuation of the shortwave radiation flux with depth below the water surface was also modelled using a form of Beers Law, Equation (6.7) from page 227:

$$\phi_z = \phi_0 \exp\left[-\eta\, z\right]$$

The original RMA-10 code was modified to permit spatial variation in the shortwave attenuation coefficient between the different element classes. Vertical attenuation coefficients were estimated from field measurements (Section 5.4), and defined in the meteorological data file. These field values were used as initial estimates during the model calibration.

H.6.2 Atmospheric (Downward) Longwave Radiation Flux

The atmospheric, downward longwave radiation flux was calculated by RMA-10 using Equation (3.19) from page 54, assuming that $R_L = 0.03$:

$$\phi_{LW\downarrow} = (1 - R_L)\,\varepsilon_{\mathrm{ac}}\,\sigma\,T_a^4\,C_f$$

H.6.2.1 Atmospheric Longwave Emissivity

The atmospheric longwave emissivity term was parameterised using the equation of Idso and Jackson (1969), Equation (3.20) from page 55, which is reportedly more accurate than the equation originally used in RMA-10 (Henderson-Sellers, 1984):

$$\varepsilon_{\mathrm{ac}} = 1.0 - 0.261 \exp\{-7.77 \times 10^{-4} (T_a - 273)^2\}$$

H.6.2.2 Cloudiness Factor

The cloudiness factor was calculated according to a form of Equation (3.21) from page 55, with the coefficients suggested by Fischer et al. (1979):

$$C_f = \left(1 + 0.17m^2\right)$$

The cloud fraction (m) was determined from inspection of the diurnal shortwave radiation data, as follows. A similar approach was described by Jin et al. (2000).

- A smooth shortwave radiation profile indicated **clear skies** ($m = 0.0$).
- A radiation profile with a peak shortwave flux less than 50% of the peak clear sky flux was interpreted as a **heavily overcast** day with complete cloud cover ($m = 1.0$).
- Irregular shortwave radiation profiles suggested the presence of discontinuous or highly variable cloud conditions throughout the day, where:
  - a peak radiation flux slightly greater than the peak clear sky flux indicated **scattered cloud** ($0.1 \leq m \leq 0.5$)
  - a peak radiation flux less than the peak clear sky flux indicated **broken cloud** ($0.6 \leq m \leq 0.9$)

This cloud cover classification is consistent with the scheme used to calculate the shortwave reflection coefficient.

H.6.2.3 Longwave Radiation Flux Beneath an Emergent Canopy

The net transmission of atmospheric longwave radiation to the water surface beneath the emergent macrophyte canopy was calculated using Equation (3.56) from page 85:

$$\phi_{LW\downarrow NET} = \{1 - \tau_d(LAI)\}\, \phi_{LW_C} + \tau_d(LAI)\, \phi_{LW\downarrow}$$

The surface transmission coefficient for atmospheric longwave radiation, $\tau_d(LAI)$ was calculated using Equation (3.57) from page 85:

$$\tau_d(LAI) = 2\int_0^{\pi/2} \exp\left[-\mathcal{K}_{LAI}\, LAI\right] \cos\theta \sin\theta \, \mathrm{d}\,\theta$$

Because the variation in solar inclination, θ was relatively small over the simulation timestep of one hour, it was assumed that the solar inclination was constant for each timestep, and Equation (3.57) then reduced to:

$$\tau_d(LAI) = \exp\left[-\mathcal{K}_{LAI}\, LAI\right]$$

This is equal to the surface transmission coefficient for shortwave radiation beneath the macrophyte canopy. Hence, the surface transmission coefficients for atmospheric longwave radiation and shortwave radiation beneath an emergent canopy were set equal in the model.

Reflection of longwave radiation by canopy foliage was assumed negligible (Section 3.4.2.2).

The longwave radiation flux from the canopy foliage was calculated using Equation (3.58) from page 85:

$$\phi_{LW_C} = \pm\, \varepsilon_{\mathrm{c}}\, \sigma\, T_c^4$$

The surface temperature of the foliage, T_c was assumed to be uniform throughout the canopy.

H.6.3 Upward Longwave Radiation Flux

The upward longwave radiation from the water surface was calculated using Equation (3.22) from page 56:

$$\phi_{LW\uparrow} = -\,\varepsilon_{\mathrm{w}}\, \sigma\, T_w^4$$

where the emissivity of the water surface was held constant at $\varepsilon_{\mathrm{w}} = 0.97$. As discussed in Section 3.4.2.2, this equation is valid irrespective of the presence of an emergent macrophyte canopy, and was hence used for both open water and vegetated zones of the wetland.

H.6.4 Latent Heat Flux

The latent heat flux at the water surface was calculated using a form of the aerodynamic equation attributed to Thornwaite and Holzman, Equation (3.60) on page 93. As discussed in Section 3.3.3.3, this approach was considered more appropriate than alternative methods, providing the effects of atmospheric stability could be incorporated:

$$H_L = -\frac{0.622\, L_w\, k^2\, \rho_m\, (\, e_{sat} - e_a\,)\, u_z}{P\, [\ln(\, z_M\, /\, z_0\,)]\, [\ln(\, z_V\, /\, z_{0V}\,)]}$$

The aerodynamic roughness lengths for momentum z_0 and water vapour z_{0V} are generally not equal (Section 3.3.3.3), and $z_{0V} = 5.7\, z_0$ was used in the open water zone (Brutsaert, 1982). The aerodynamic roughness length for momentum was used as a calibration parameter, as discussed in Section 5.6.4.

To avoid a zero latent heat flux when the winds were slight or absent, a lower threshold wind speed of $u_z \geq 0.10\,\mathrm{m\,s^{-1}}$ was imposed. As discussed in Section 3.3.3.3 (page 67), this threshold corresponds to an equivalence between free and forced convection for specified temperature, humidity and atmospheric pressure.

H.6.4.1 Latent Heat Flux beneath the Emergent Canopy

The latent heat flux beneath the emergent canopy was also calculated using a form of Equation (3.60):

$$H_L = -\frac{0.622\, L_w\, k^2\, \rho_m\, (\, e_{sat} - e_a\,)\, u_z}{P\, \{\ln\, [(z_M - d_0\,)\, /\, z_0\,)]\, [\ln(\,(z_V - d_0\,)\, /\, z_{0V}\,]\,\}}$$

Strictly, the ambient vapour pressure within the canopy, e_a is a function of the canopy air temperature and the relative humidity within the canopy. Although air temperatures were available within the canopy, relative humidity measurements were not, so the ambient vapour pressure in the canopy could not be determined. Instead, the vapour pressure in the emergent macrophyte canopy was assumed equal to the vapour pressure above the canopy, while e_{sat} was calculated as a function of the water surface temperature in each zone.

Although this is clearly a simplification, it is probably not unreasonable in a sparse canopy such as that at Hopwoods Lagoon. If RH within the canopy exceeds RH above the canopy while $T_a \approx T_c$, the canopy vapour pressure would be underestimated by incorrectly assuming them to be equal. For any given T_c the e_a term changes by between $\pm\, 1.1\%$ for $RH = 90 \pm 1\%$ and $\pm\, 10\%$ for $RH = 10 \pm 1\%$. The $(e_{sat} - e_a)$ term is therefore overestimated if RH and e_a are underestimated and *vice versa*. The error in the latent heat flux is equal to the error in the $(e_{sat} - e_a)$ term, with all other variables held constant. The canopy air temperature and relative humidity data should therefore be used when available.

In the emergent macrophyte zone, the aerodynamic roughness length for transport of water vapour was calculated from $z_{0V} = 0.11\, z_0$ (Brutsaert, 1982), as discussed in Section 3.4.3.2.

H.6.5 Sensible Heat Flux

The sensible heat flux at the surface in the open water, H_S was calculated using a form of Equation (3.44) from page 70:

$$H_S = \mathcal{B}\, H_L = \gamma \left(\frac{T_w - T_a}{e_{sat} - e_a} \right) H_L$$

The psychrometric coefficient, γ was calculated as shown in Appendix A.

H.6.5.1 Sensible Heat Flux beneath the Emergent Macrophyte Canopy

The sensible heat flux at the water surface in the emergent macrophyte zones was also calculated using Equation (3.44).

H.6.6 Effects of Atmospheric Stability

As discussed in Section 3.3.3.1, vertical transport of momentum, water vapour and heat may be either enhanced or suppressed when atmospheric conditions are non-neutral, compared with transport rates under neutral conditions. Conditions are often unstable over water bodies, particularly when winds are light, and enhanced transport under unstable atmospheric conditions was incorporated into the model.

From Equation (3.23) on page 60, the atmosphere can be classified as unstable when:

$$Ri_b = \frac{g\, z\, (\Theta_{V_z} - \Theta_{V_s})}{\Theta_{V_z}\, u_z^2} \leq 0 \tag{H.20}$$

The bulk Richardson number is proportional to the difference between the potential virtual temperatures at the measurement height, z (m) and the water surface, $(\Theta_{V_z} - \Theta_{V_s})$ (K). Enhanced transport under unstable atmospheric conditions was modelled by increasing the value of the latent heat transfer coefficient by 40% (Fischer et al., 1979) whenever $(\Theta_{V_z} - \Theta_{V_s}) \leq 0$.

The latent heat transfer coefficient is incorporated in the Thornwaite-Holzman equation as:

$$C_L = \frac{k^2}{\ln\left[(z_M - d_0)/z_0\right]\ln\left[(z_V - d_0)/z_{0V}\right]} \tag{H.21}$$

As shown in Section 6.6.1.2, even this very crude approximation dramatically improved simulation of near surface water temperatures over the diurnal cycle. The correction factor was applied to the calculation of the latent heat flux, and transferred to the calculation of the sensible heat flux via the Bowen Ratio.

Alternative schemes available in the literature, such as that suggested by Liu et al. (1979), were developed for fluxes at the ocean surface. However, ocean water depth and fetch length far exceed those in a typical wetland, and these atmospheric stability schemes are therefore not strictly applicable to the present study.

H.7 Thermodynamic Boundary Conditions at the Bed

The original RMA-10 model assumes a zero heat flux across the bed, which implies perfect heat insulation at the sediment-water interface. This may not always be valid in a shallow body of water, as discussed in Section 3.6. A bed heat flux module was introduced into RMA-10 by the author, which permitted heat conduction between the water column and the underlying sediment matrix (hereafter referred to as the "sediments"), and direct shortwave radiative heating of the sediments. Reflection of shortwave radiation from the water-sediment interface was assumed to be negligible, which is reasonable for the dark-coloured, organic materials expected at the bed of a wetland. The theory for the bed heat flux calculation was presented in Section 3.6 (page 97).

H.7.1 Sediment Temperature Distribution

The temperature distribution in the sediments was modelled using the one-dimensional, unsteady heat transport equation, Equation (3.64) from page 97:

$$\frac{\partial T_s}{\partial t} = K_s \frac{\partial^2 T_s}{\partial z^2}$$

This assumes that any horizontal heat transport is negligible compared with heat transport in the vertical (Fang and Stefan, 1996). The water temperature at the bed was used as the upper boundary condition and a zero heat flux was applied across the lower sediment boundary. The values for the depth of the lower sediment boundary (the depth of thermal influence, h_s) and the thermal diffusivity, K_s were varied and assessed for the present study during the calibration phase (see Section 5.6.4).

Equation (3.64) was solved using an explicit, finite-difference scheme (Hornbeck, 1975). The derivative with respect to temperature was approximated by a central difference expression and the derivative with respect to time was approximated by a forward difference expression, as follows:

$$\frac{T_{s\,(t,\,z+1)} - 2\,T_{s\,(t,\,z)} + T_{s\,(t,\,z-1)}}{(\Delta\, z)^2} = \frac{1}{K_s}\left(\frac{T_{s\,(t+1,\,z)} - T_{s\,(t,\,z)}}{\Delta\, t}\right) \tag{H.22}$$

where $T_{s\,(t,\,z)}$ = sediment temperature at time t and depth z (°C)

K_s = thermal diffusivity of the sediments ($\mathrm{m^2\,s^{-1}}$).

The timestep for the sediment temperature diffusion was equal to the timestep in the main RMA-10 model, subject to the stability constraint of the finite difference scheme, as follows (Hornbeck, 1975):

$$\frac{K_s\,\Delta\, t}{(\Delta\, z)^2} \leq \frac{1}{2} \tag{H.23}$$

The thickness of the sediment layers was varied as follows:

$$\begin{aligned} \Delta\, z_i &= 0.10\,\mathrm{m} && \text{when} \quad 0 < i \leq 5 \\ &= 2\,(\Delta\, z_{i-1}) && \text{when} \quad 5 < i \leq i_{max} \end{aligned} \tag{H.24}$$

where i = sediment layer number, increasing with depth

$\Delta\, z_i$ = thickness of sediment layer i (m)

i_{max} = maximum number of sediment layers.

This permitted relatively fine resolution in the sediment temperature model near the sediment-water interface with a coarser resolution at depth, to minimise the overall solution time. According to Equation (H.23), with $\Delta\, t = 1.0\,\mathrm{hr}$ and $\Delta\, z \geq 0.1\,\mathrm{m}$, the difference scheme would be stable with $K_s \leq 1.4 \times 10^{-6}\,\mathrm{m^2\,s^{-1}}$. This is consistent with values reported in the literature (see page 97).

H.7.2 Bed Heat Flux, G_{BED}

The heat flux between the sediments and the water column was calculated from the sediment temperature distribution over the depth of thermal influence using Equation (3.65) from page 98:

$$G_{BED} = -c_s \int_0^{h_s} \frac{\partial T_s}{\partial t} \, dz$$

The volumetric heat capacity of the sediments, c_s was estimated from sediment core data obtained by Smeulders (1999) at Hopwoods Lagoon. The calculation methodology and sediment core data are summarised in Section A.3 of Appendix A.

H.8 Thermodynamic Boundary Conditions at the Shoreline

RMA-10 assumes a zero flux of heat across the side boundaries, which reduces to zero diffusion because of the zero normal velocity condition. Given the very shallow, imposed water depth along the shoreline, the shoreline surface area was small relative to the bed area. The heat flux across the shoreline was therefore assumed negligible and the original insulating boundary condition was retained.

H.9 Summary of Changes to Thermodynamic Boundary Conditions

The changes made to the thermodynamic boundary conditions at the water surface in RMA-10 by the author as part of this study are summarised in Table H.1.

Flux Component	Change and Comments	References
Canopy shortwave attenuation $\mathcal{K}_{LAI}$	shortwave radiation attenuation by emergent canopy as a function of LAI and β	Section 3.4.2.1 Equation (H.20)
Canopy longwave attenuation $\{1 - \tau_d(LAI)\}$	longwave radiation attenuation by emergent canopy as a function of LAI	Section 3.4.2.2 Equation (H.20)
Shortwave attenuation η	introduce spatial variability between open water and vegetated zones	Section 3.5 Equation (H.20)
Ambient vapour pressure e_a	calculate using relative humidity, because AWS measures RH	Smith (1991) Equation (A.17)
Latent heat flux H_L	change to aerodynamic equation of Thornwaite-Holzman (open water)	Section 3.3.3.3 Equation (??)
	modify Thornwaite-Holzman equation for emergent canopy	Section 3.4.3.2 Equation (H.20)
Sensible heat flux H_S	modify for emergent macrophyte canopy	Section 3.4.3.3 Equation (H.20)
Atmospheric stability Ri_b	increase H_L and H_S in unstable atmosphere	Section 3.3.3.1 Equation (H.20)
Equation of state ρ	improve consistency between calculated and published values	List (1968) Equation (A.13)
Specific heat capacity c_{pw}	introduce temperature-dependency instead of a constant value	Henderson-Sellers (1984) Equation (A.15)
Longwave emissivity ε_{ac}	improve agreement with published values	Section 3.3.2.2 Equation (H.20)
Latent heat of vaporisation L_w	improve consistency between calculated and published values	Smith (1991) Equation (A.14)

Table H.1: Summary of changes made by the author to the surface heat flux parameterisation in RMA-10.

Appendix I

ADDITIONAL MODEL SIMULATION RESULTS

I.1 Differential Heating due to Depth Differences

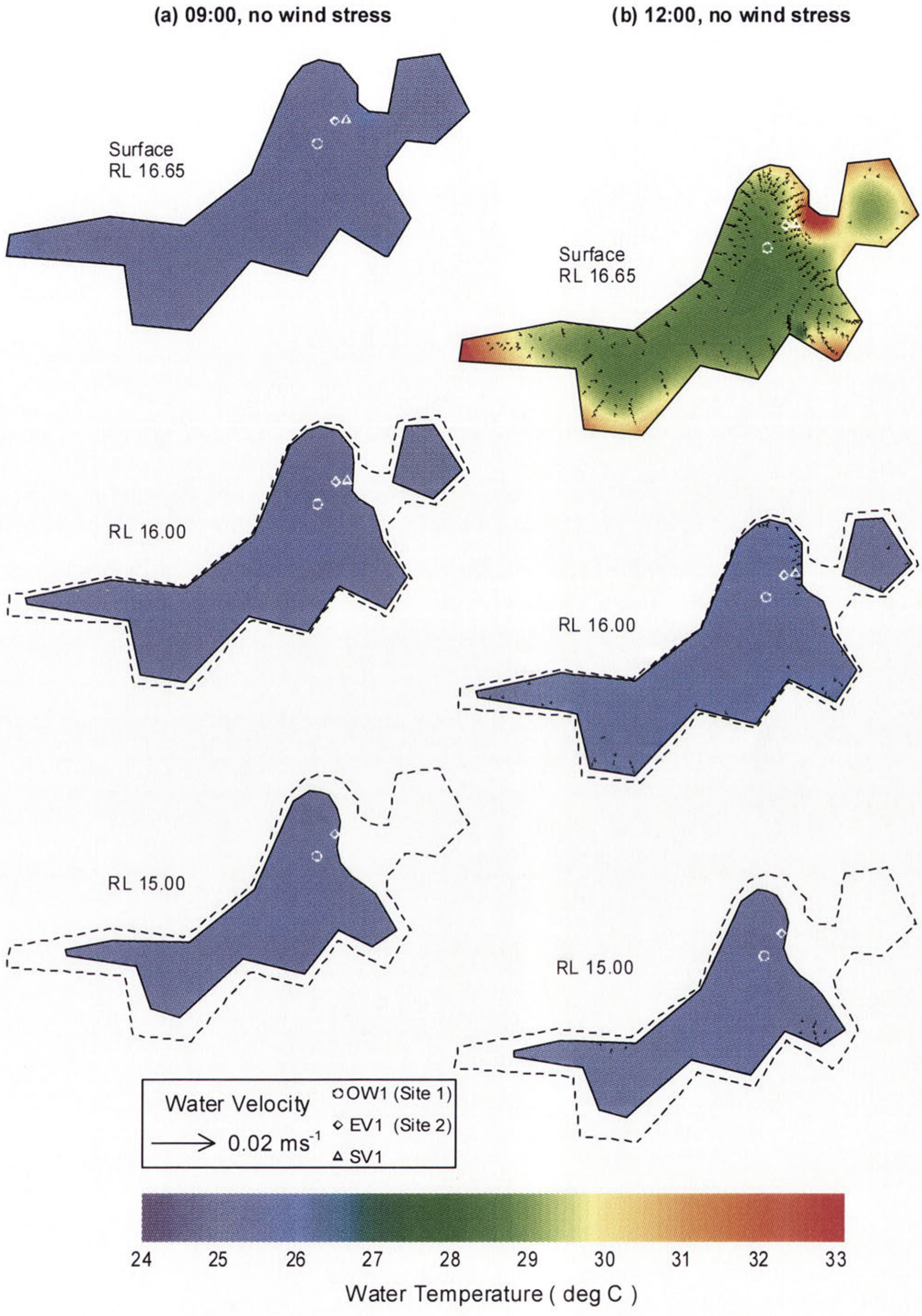

Figure I.1: Submerged macrophyte scenario: Predicted water temperatures and horizontal velocities on 30 December 2000 (no wind stress)

(a) 09:00, and (b) 12:00 ($\eta_{SV} = 6.5\,\mathrm{m}^{-1}$)

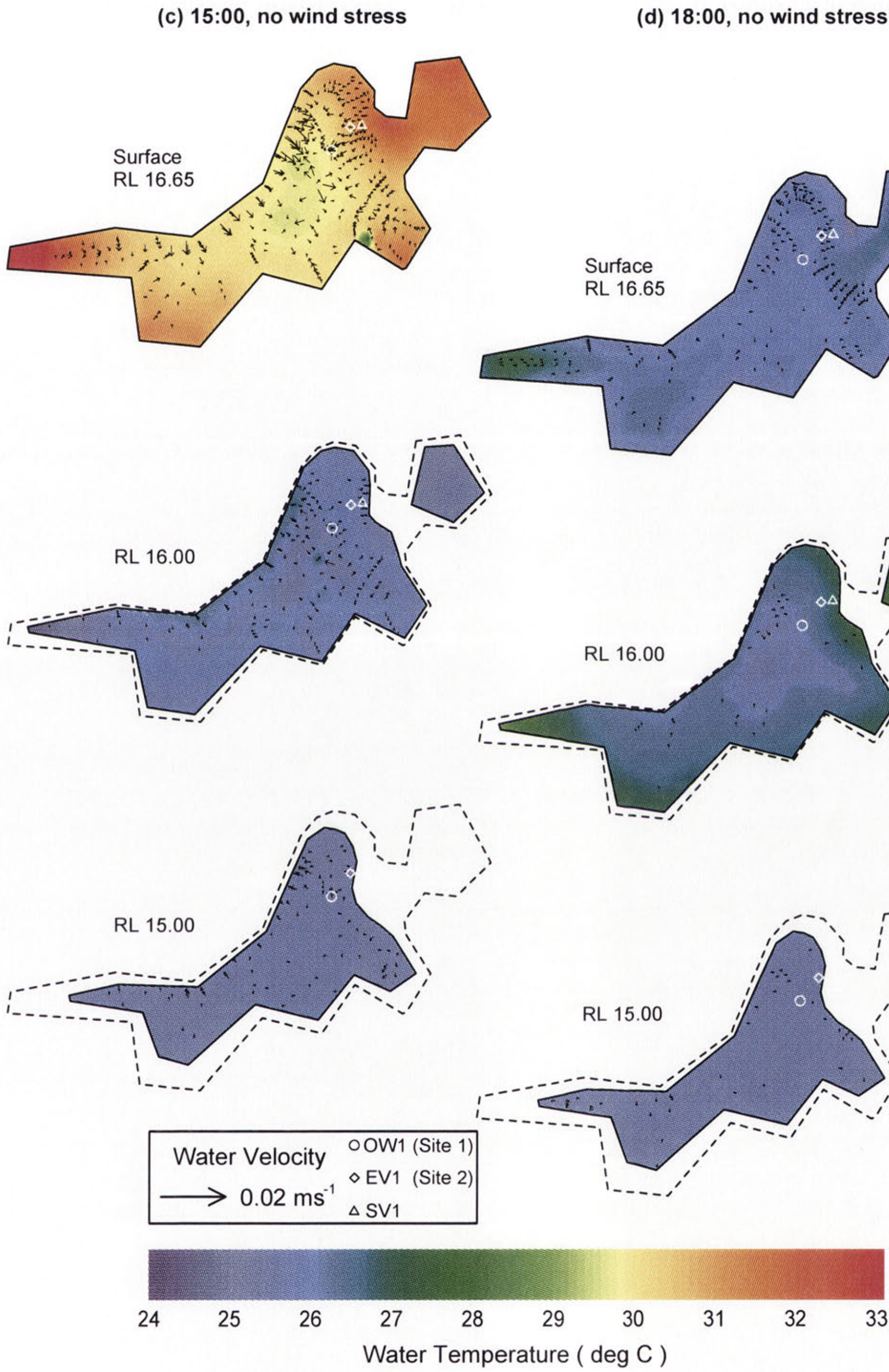

Figure I.1 (continued): (c) 15:00, and (d) 18:00 ($\eta_{SV} = 6.5\,\mathrm{m}^{-1}$).

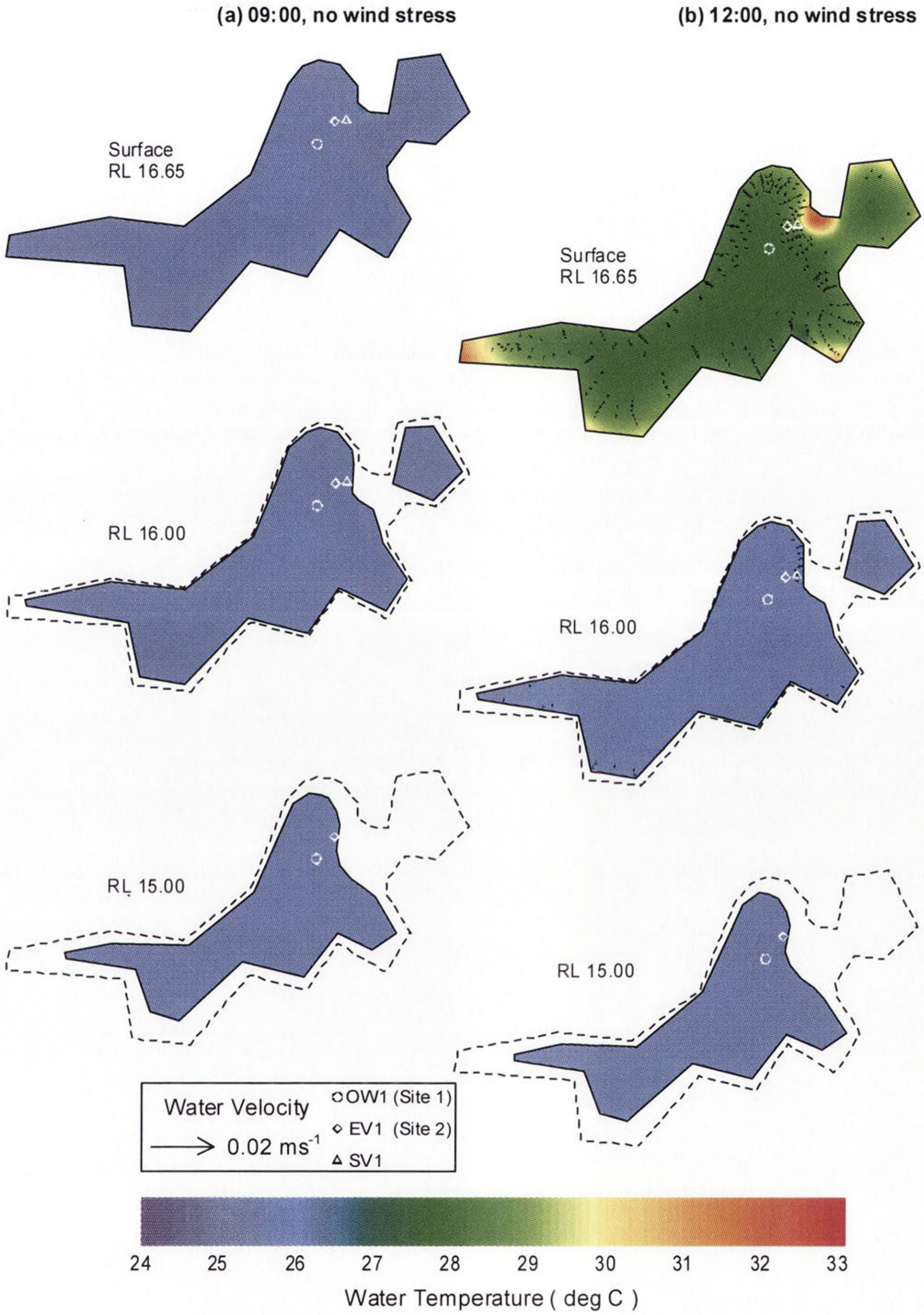

Figure I.2: Emergent macrophyte scenario: Predicted water temperatures and horizontal velocities on 30 December 2000 (no wind stress)
(a) 09:00, and (b) 12:00 ($LAI = 0.5$, $\eta_{EV} = 6.5\,\mathrm{m}^{-1}$)

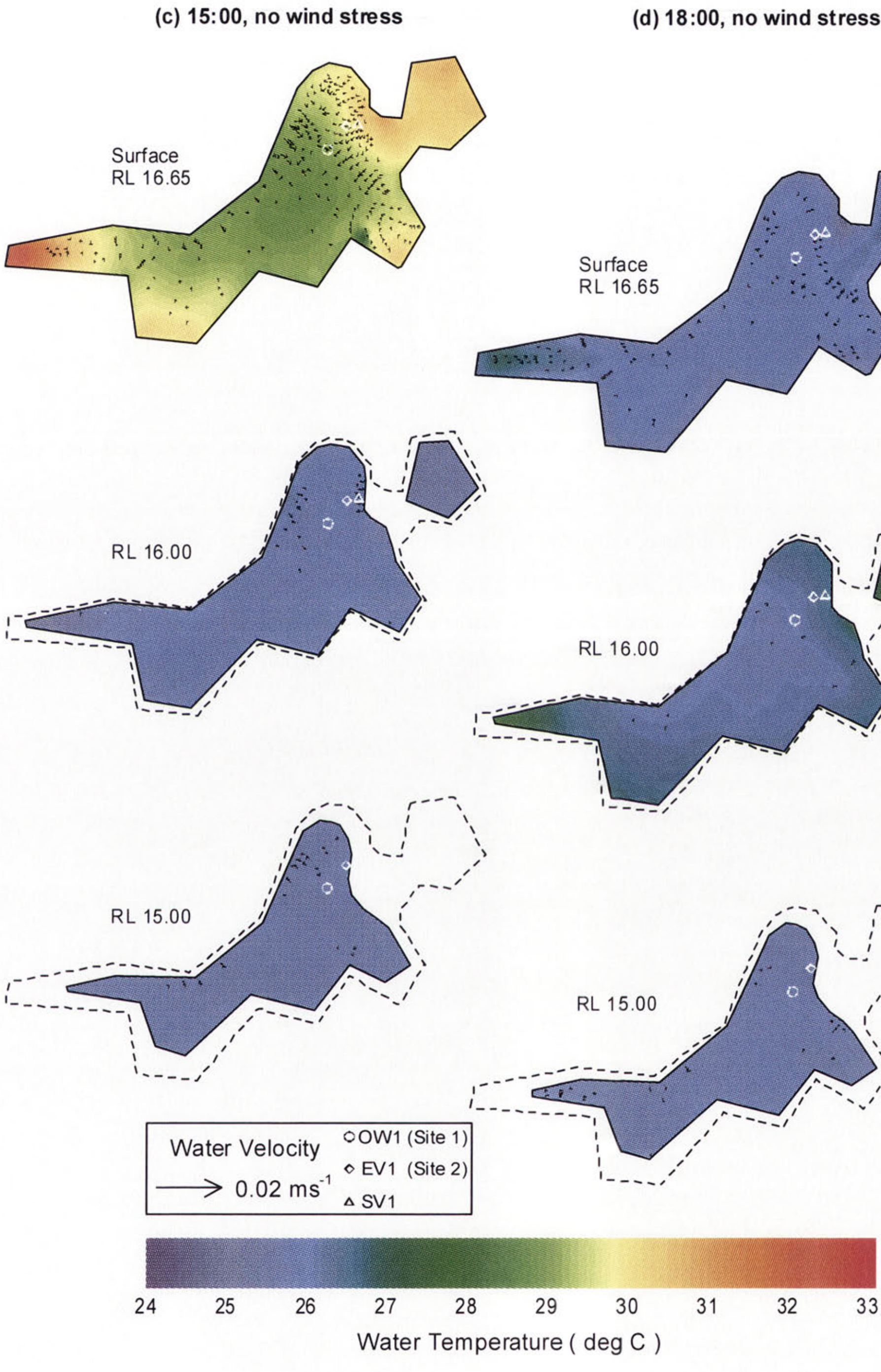

Figure I.2 (continued): (c) 15:00, and (d) 18:00 ($LAI = 0.5$, $\eta_{EV} = 6.5\,\mathrm{m}^{-1}$).

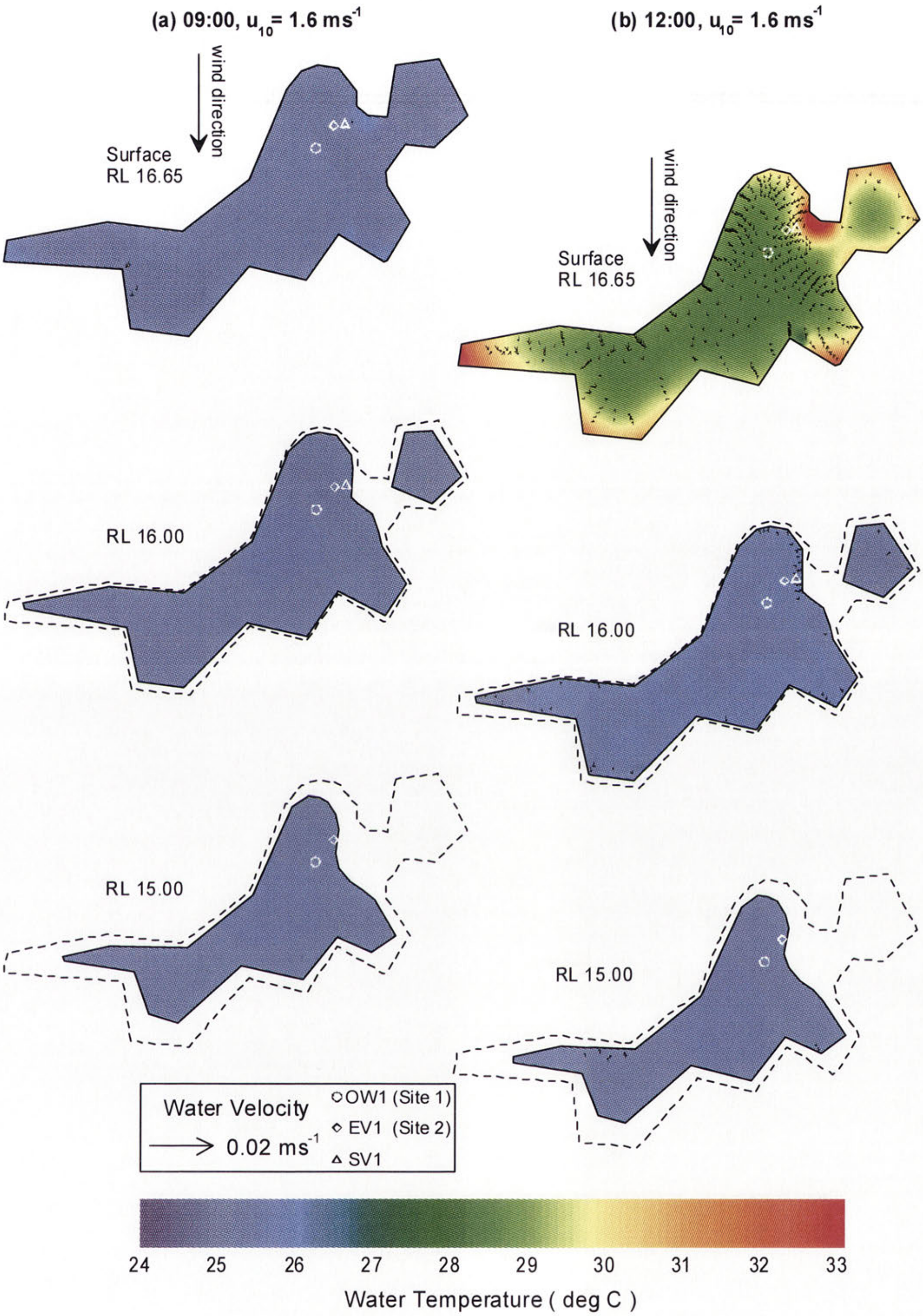

Figure I.3: Submerged macrophyte scenario: Predicted water temperatures and horizontal velocities on 30 December 2000, with applied wind stress (a) 09:00, and (b) 12:00 ($\eta_{SV} = 6.5\,\mathrm{m}^{-1}$)

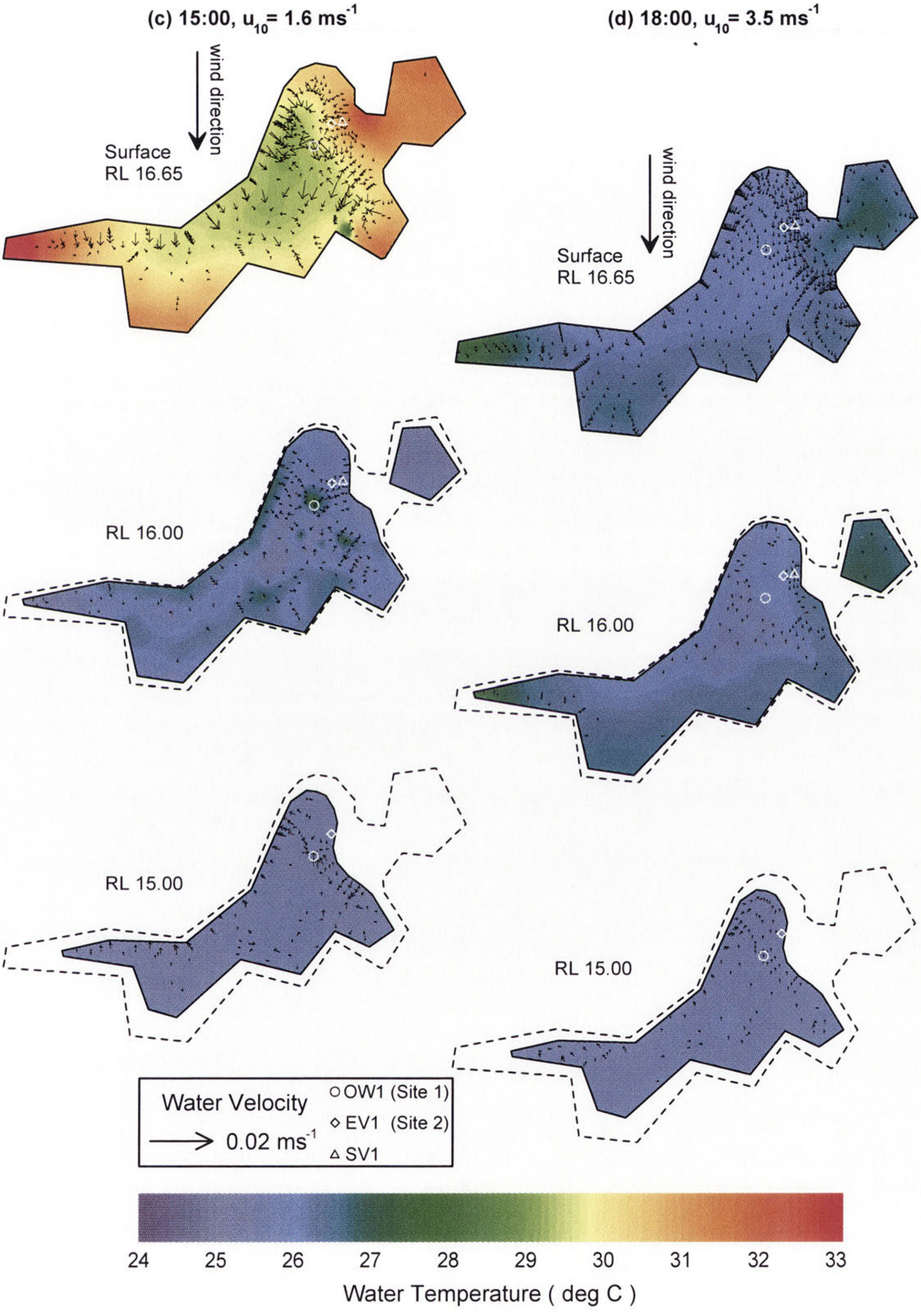

Figure I.3 (continued): (c) 15:00, and (d) 18:00 ($\eta_{SV} = 6.5\,\mathrm{m}^{-1}$).

Figure I.4: Emergent macrophyte scenario: Predicted water temperatures and horizontal velocities on 30 December 2000, with applied wind stress (a) 09:00, and (b) 12:00 ($LAI = 0.5$, $\eta_{EV} = 6.5\,\mathrm{m}^{-1}$)

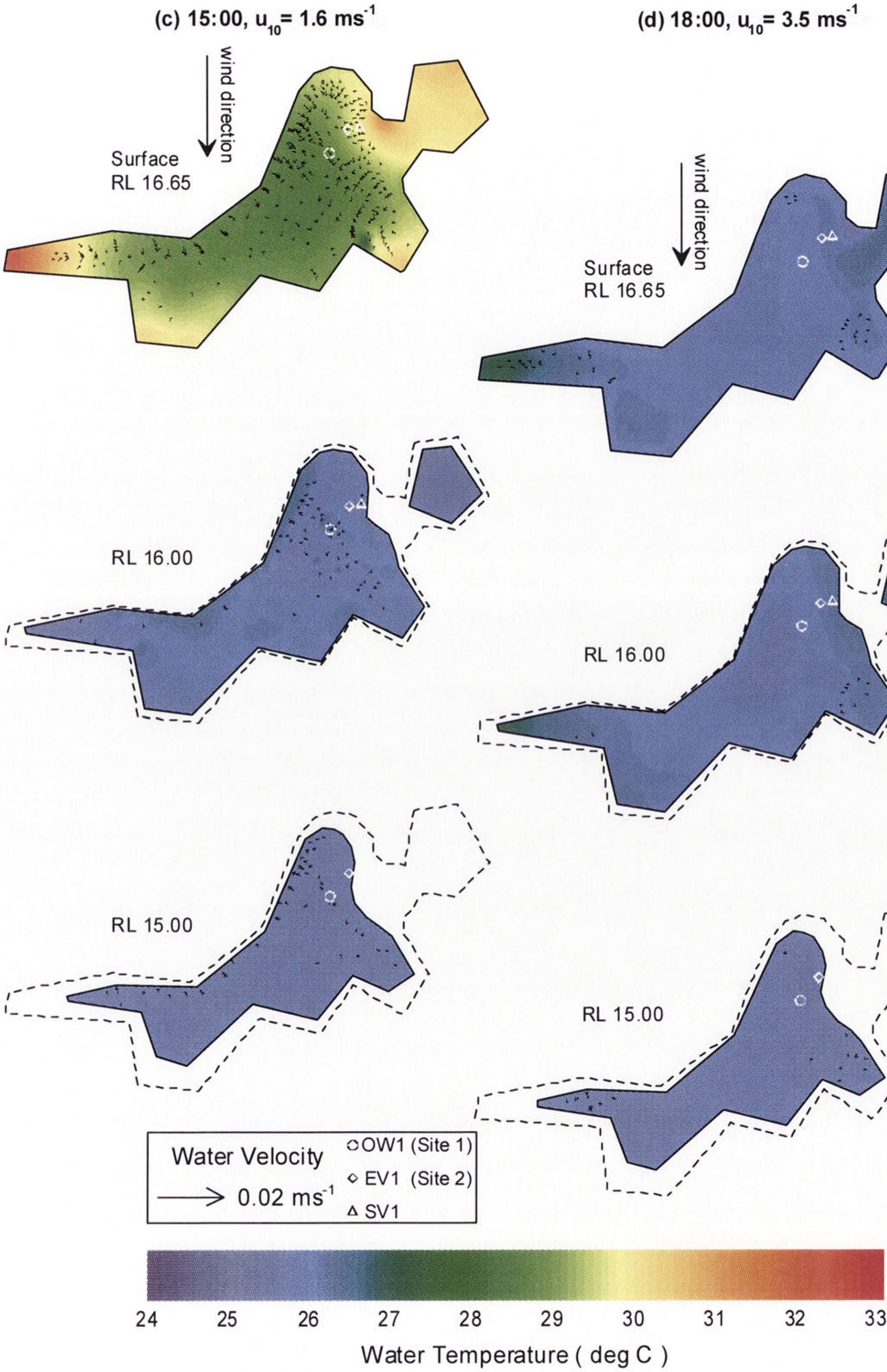

Figure I.4 (continued): (c) 15:00, and (d) 18:00 (LAI = 0.5, $\eta_{EV} = 6.5\,\mathrm{m}^{-1}$).

I.2 Radiation Shading by Submerged Macrophytes

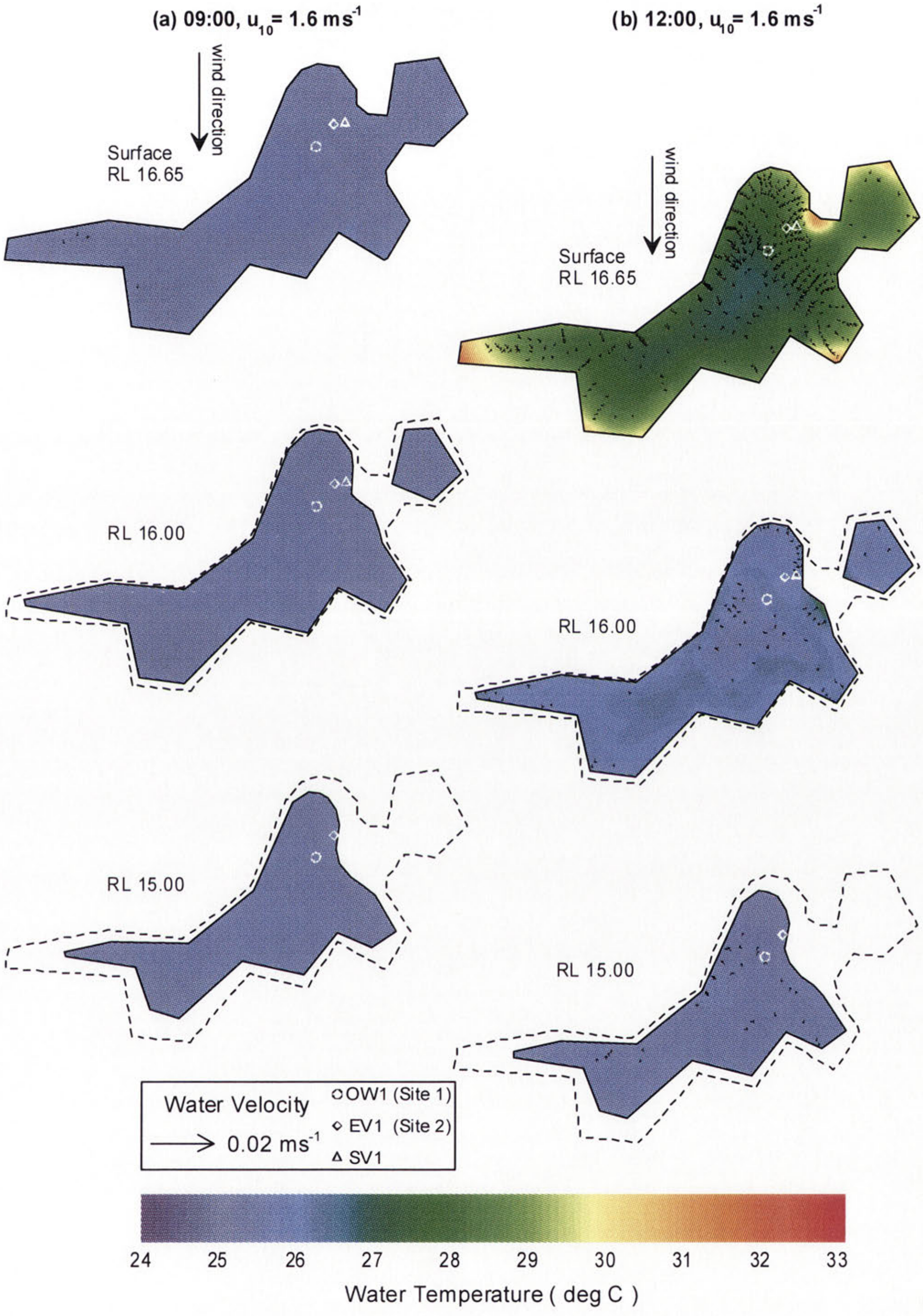

Figure I.5: Predicted water temperatures and horizontal velocities for radiation shading by low density submerged macrophytes on 30 December 2000
(a) 09:00, and (b) 12:00 ($\eta_{SV} = 4.4\,\mathrm{m}^{-1}$, $\eta_{OW} = 2.5\,\mathrm{m}^{-1}$)

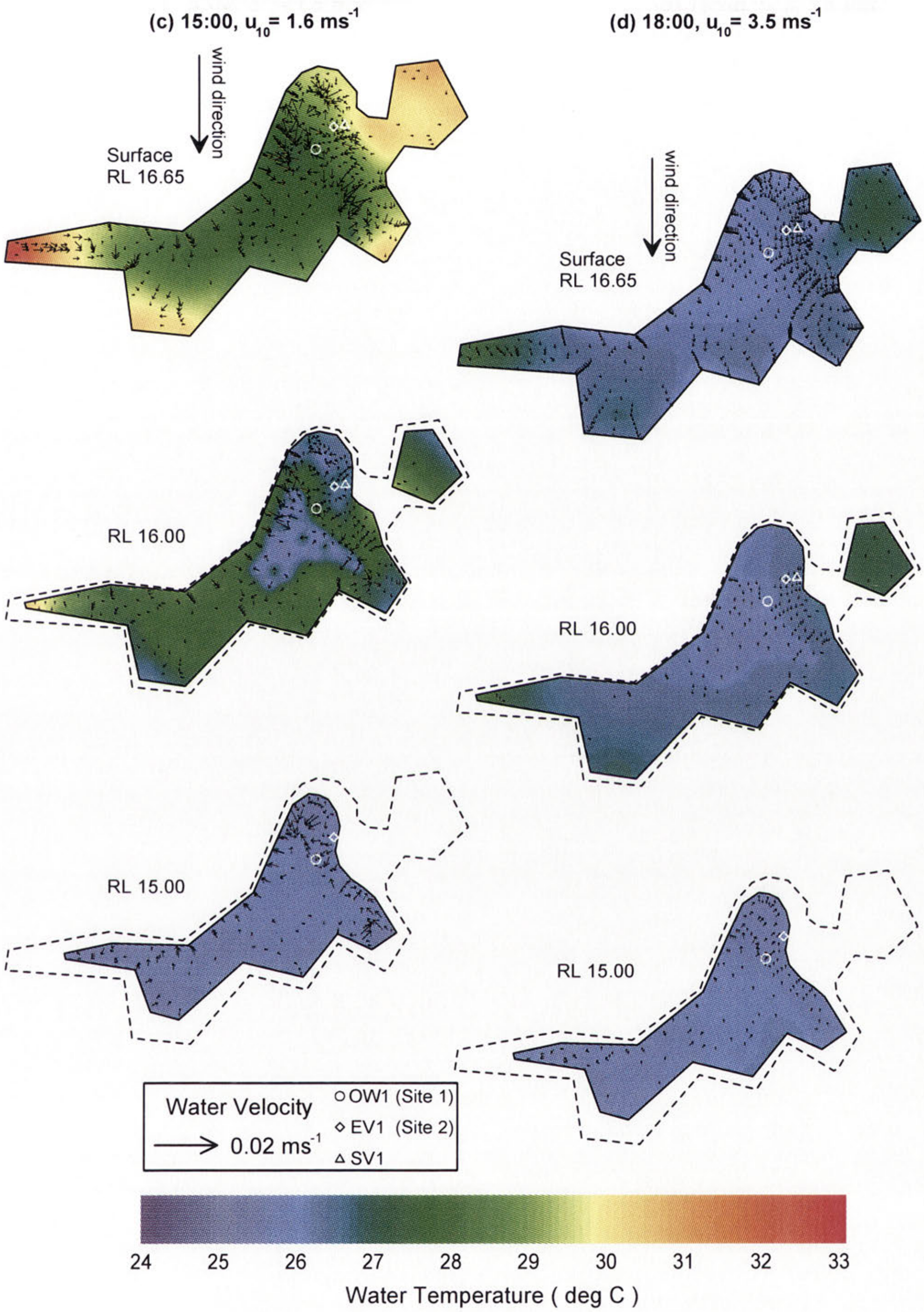

Figure I.5 (continued): (c) 15:00, and (d) 18:00 ($\eta_{SV} = 4.4\,\mathrm{m}^{-1}$, $\eta_{OW} = 2.5\,\mathrm{m}^{-1}$).

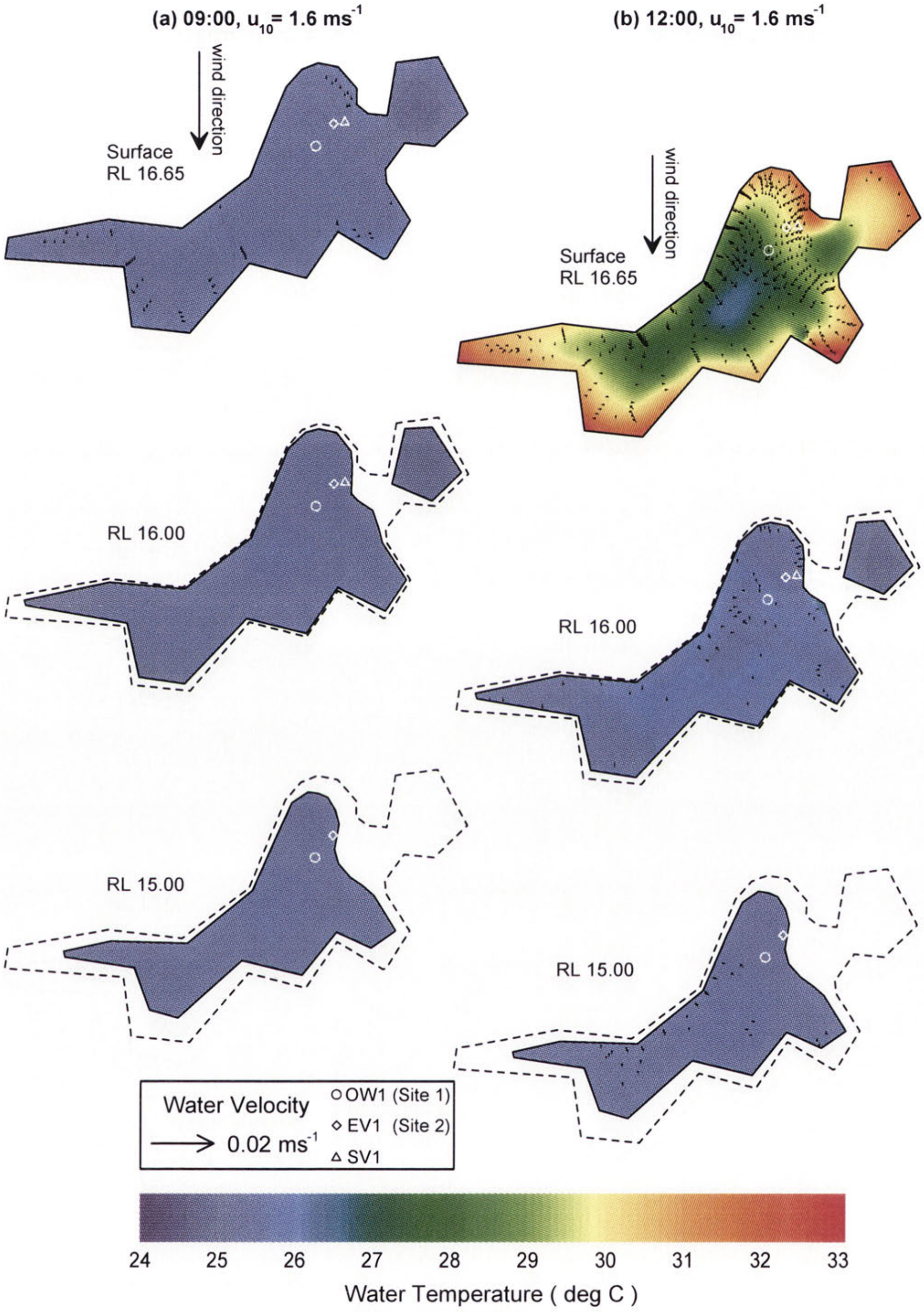

Figure I.6: Predicted water temperatures and horizontal velocities for radiation shading by low density submerged macrophytes on 30 December 2000 (a) 09:00, and (b) 12:00 ($\eta_{SV} = 12.0\,\mathrm{m}^{-1}$, $\eta_{OW} = 2.5\,\mathrm{m}^{-1}$)

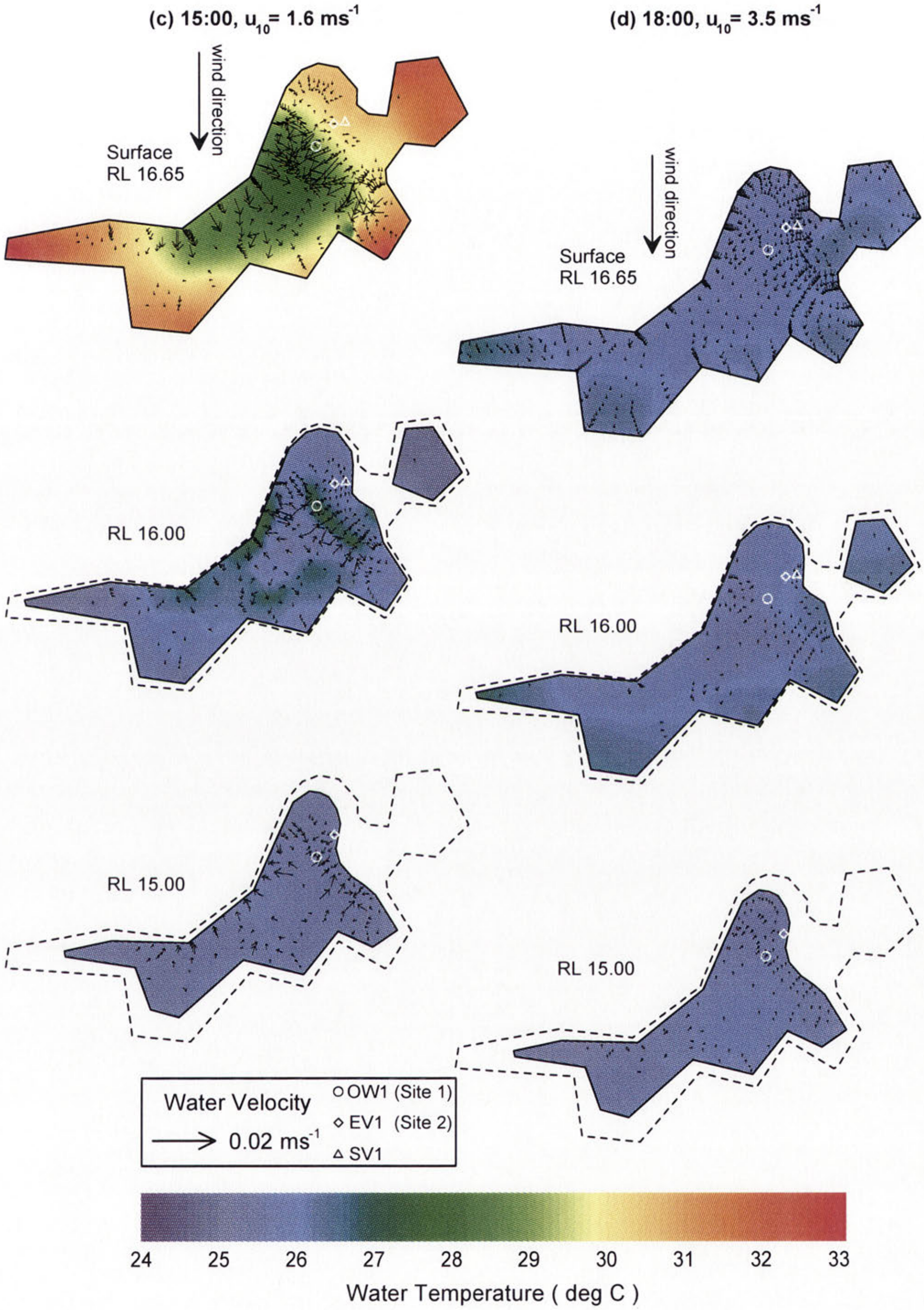

Figure I.6 (continued): (c) 15:00, and (d) 18:00 ($\eta_{SV} = 12.0\,\mathrm{m}^{-1}$, $\eta_{OW} = 2.5\,\mathrm{m}^{-1}$).

I.3 Radiation Shading by Emergent Macrophytes

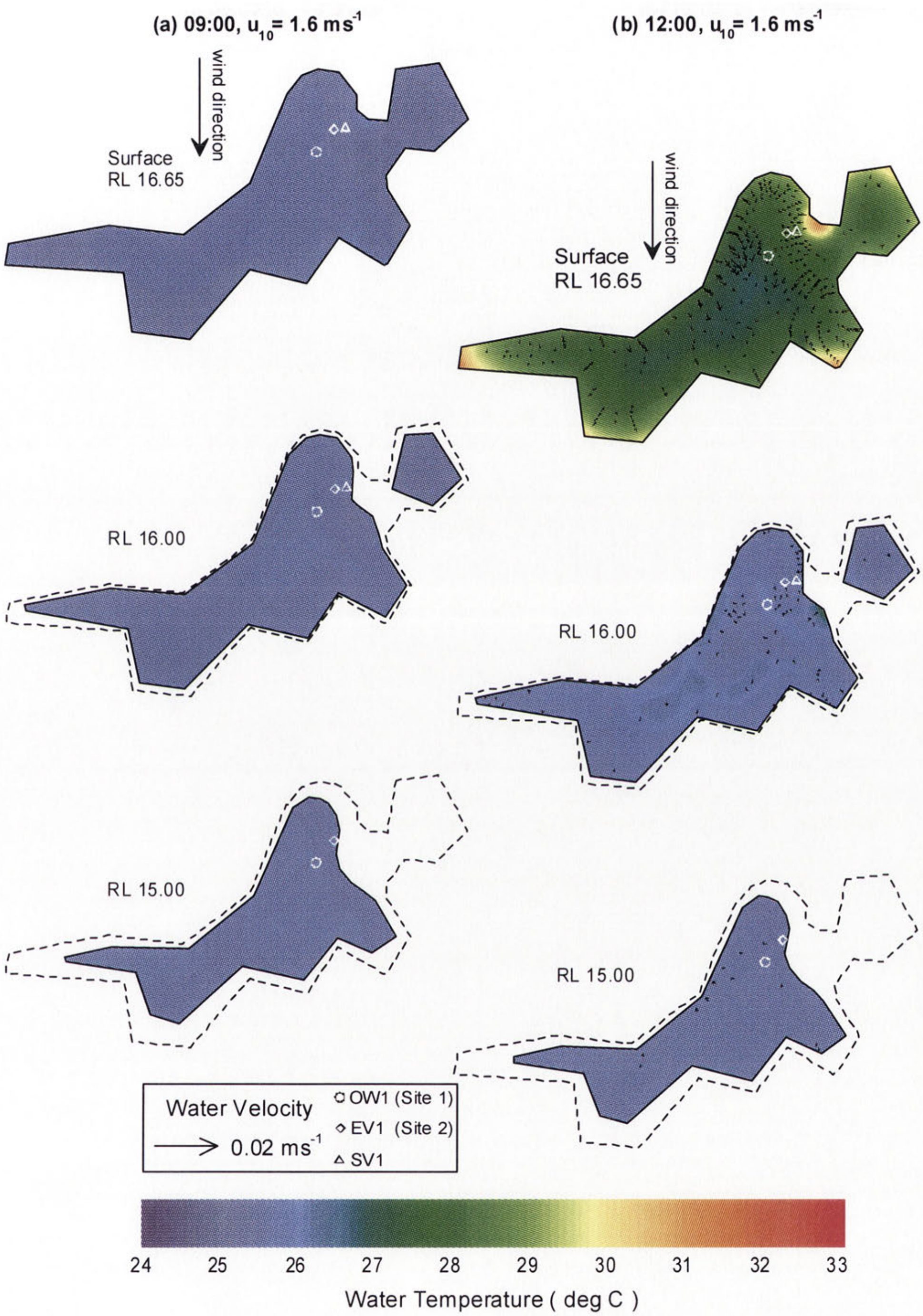

Figure I.7: Predicted water temperatures and horizontal velocities for radiation shading by low density submerged macrophytes on 30 December 2000
(a) 09:00, and (b) 12:00 ($LAI = 0.5$, $\eta_{EV} = 6.5\,\mathrm{m}^{-1}$)

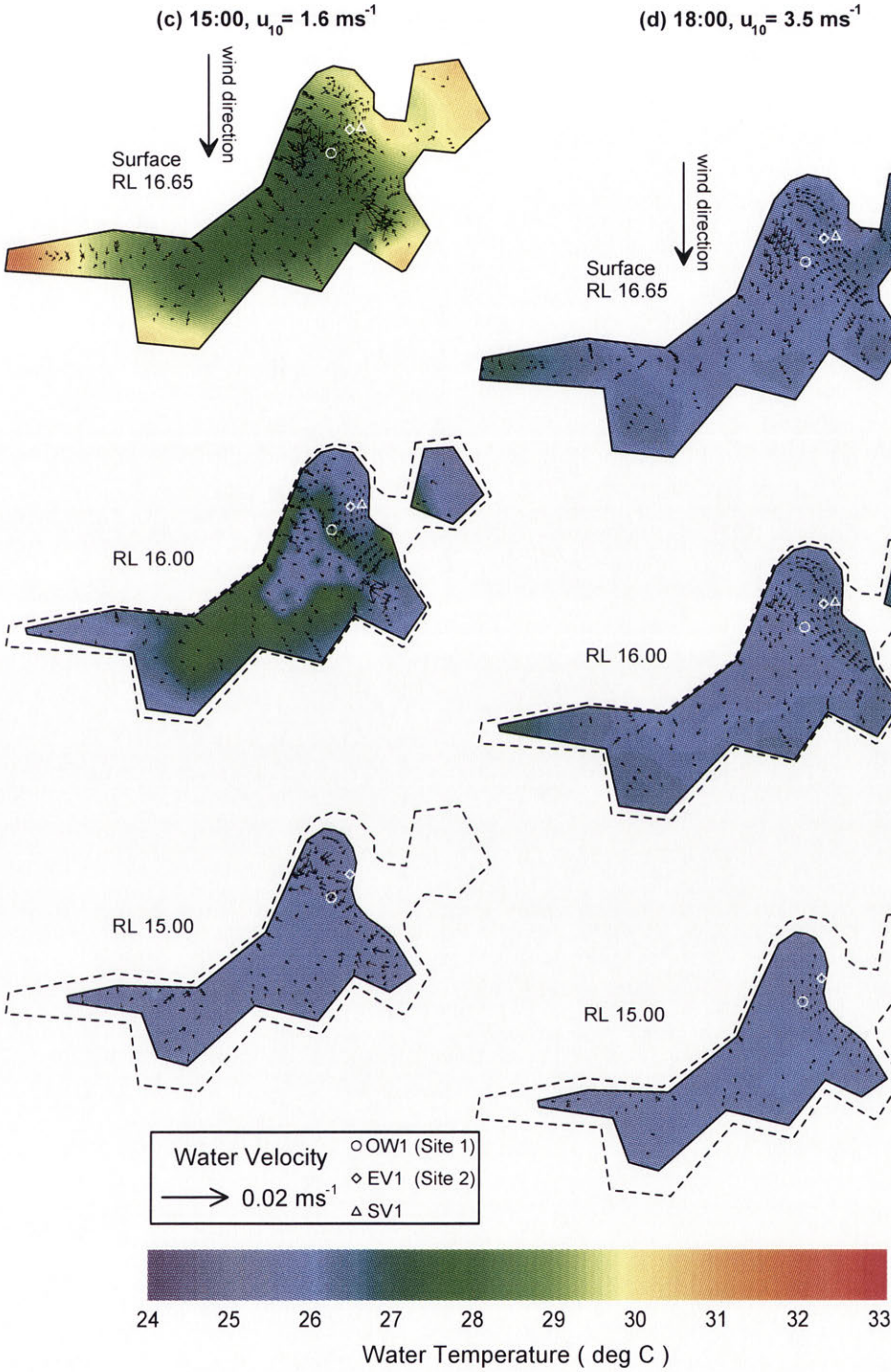

Figure I.7 (continued): (c) 15:00, and (d) 18:00 (LAI = 0.5, $\eta_{EV} = 6.5\,\mathrm{m}^{-1}$).

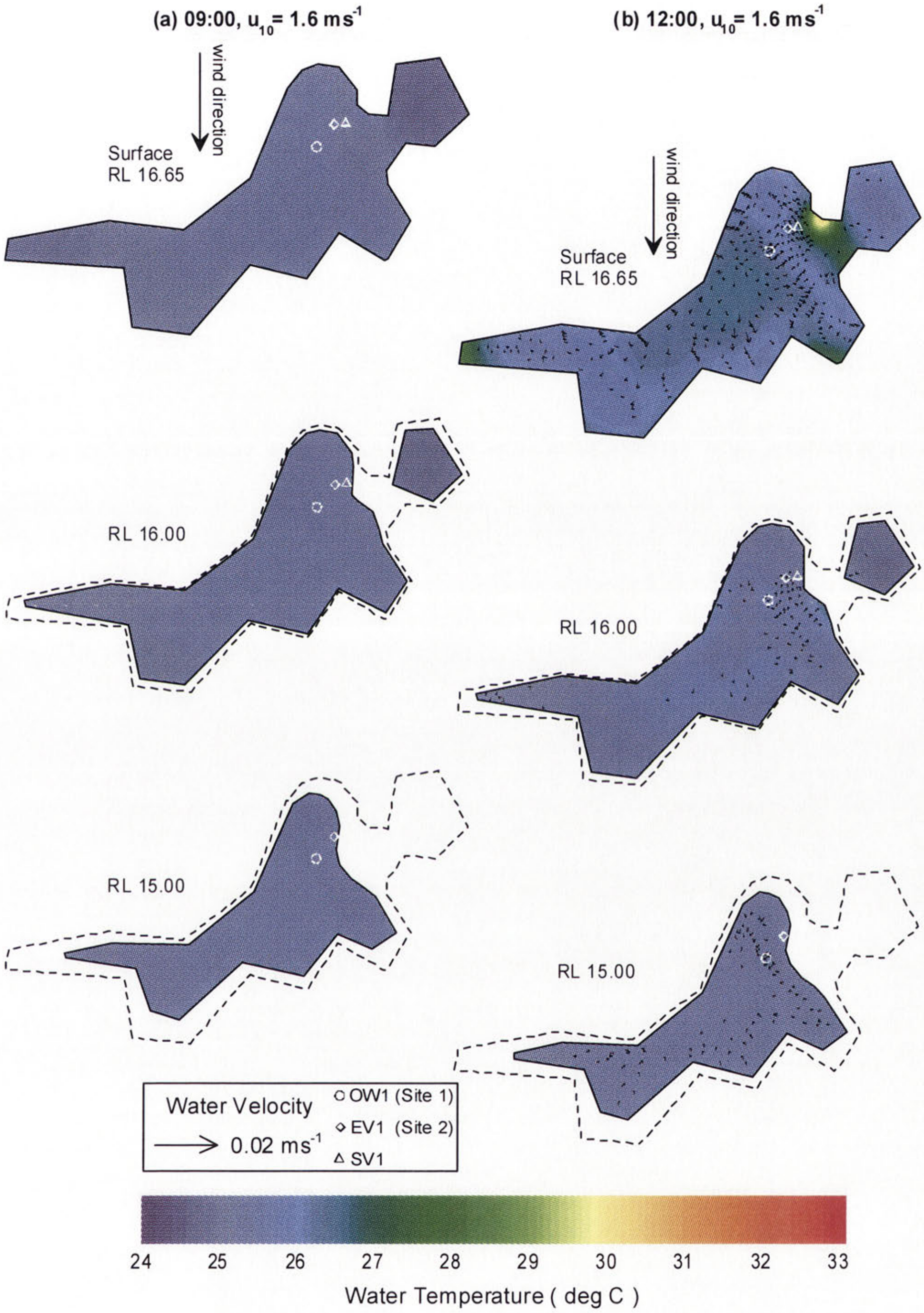

Figure I.8: Predicted water temperatures and horizontal velocities for radiation shading by low density submerged macrophytes on 30 December 2000 (a) 09:00, and (b) 12:00 (LAI = 10.0, $\eta_{EV} = 6.5\,\mathrm{m}^{-1}$)

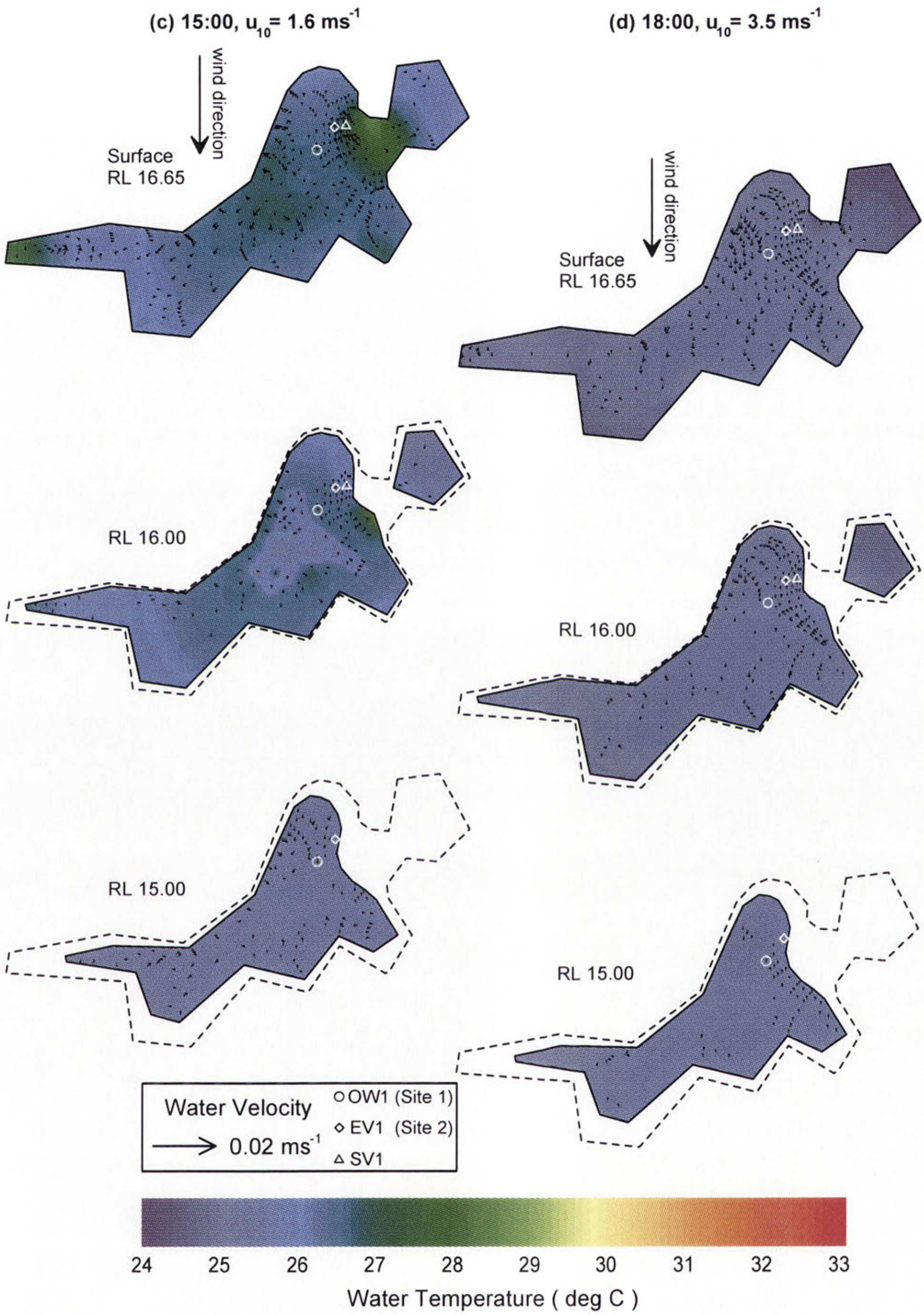

Figure I.8 (continued): (c) 15:00, and (d) 18:00 (LAI = 10.0, $\eta_{EV} = 6.5\,\mathrm{m}^{-1}$).